Practical Issues in Geriatrics
Series Editor: Stefania Maggi

Giuseppe Guglielmi
Mario Maas *Editors*

Imaging in Geriatrics

Springer

Practical Issues in Geriatrics

Series Editor
Stefania Maggi, Aging Branch
CNR-Neuroscience Institute, Padua, Italy

ALGrawany

This practically oriented series presents state of the art knowledge on the principal diseases encountered in older persons and addresses all aspects of management, including current multidisciplinary diagnostic and therapeutic approaches. It is intended as an educational tool that will enhance the everyday clinical practice of both young geriatricians and residents and also assist other specialists who deal with aged patients. Each volume is designed to provide comprehensive information on the topic that it covers, and whenever appropriate the text is complemented by additional material of high educational and practical value, including informative video-clips, standardized diagnostic flow charts and descriptive clinical cases. Practical Issues in Geriatrics will be of value to the scientific and professional community worldwide, improving understanding of the many clinical and social issues in Geriatrics and assisting in the delivery of optimal clinical care.

Giuseppe Guglielmi • Mario Maas
Editors

Imaging in Geriatrics

Springer

ALGrawany

Editors
Giuseppe Guglielmi
Clinical and Experimental Medicine
University of Foggia
Foggia, Italy

Mario Maas
Department of Radiology and Nuclear Medicine
University of Amsterdam
Amsterdam, Noord-Holland
The Netherlands

ISSN 2509-6060 ISSN 2509-6079 (electronic)
Practical Issues in Geriatrics
ISBN 978-3-031-14876-7 ISBN 978-3-031-14877-4 (eBook)
https://doi.org/10.1007/978-3-031-14877-4

This Springer imprint is published by the registered company Springer Nature Switzerland AG
The registered company address is: Gewerbestrasse 11, 6330 Cham, Switzerland

Preface

Demographic changes, due to the longer lifespan and the improvement of the quality of life, led to an aging society, where developing high-quality healthcare for older people becomes increasingly important.

Nowadays the elderly population is more informed and more demanding of better care through cutting-edge technology and treatment. Specifically, radiologists play an increasingly important role and occupy a frontline position in the evaluation of this cohort of patients, who necessitate definitive imaging.

In this perspective, the complex relationship between geriatrics and radiology must be redefined. *Imaging in Geriatrics* is the result of a teamwork of radiologists, experts in the field, with the aim to provide guidance for the appropriate use of imaging in modern geriatric care, describing how to recognize pathology from para-physiological findings in the elderly population.

The study of diagnostic imaging in geriatrics, enriched by traditional and modern imaging methods, is primarily oriented to the clinical and radiological analysis most frequently encountered in these patients and, above all, to the not easy distinction between "normal" and "pathological," especially in situations in which para-physiological changes resulting from aging processes are associated with alterations related to comorbidity and chronicity.

This volume includes a multidisciplinary approach, and it covers all major medical issues related to aging, divided by apparatus. In particular, it encloses the main pathologies in the neurological, cardiovascular, pulmonary, gastrointestinal, urogenital, hematologic, and musculoskeletal field.

This book considers all imaging techniques that have been the cornerstones of radiology, but also modern innovations. Conventional radiography is still the first approach in the diagnosis of a frequent variety of pathological conditions of elderly patients, such as fractures, often due to osteoporosis, pneumothorax, or heart failure. On the other hand, Computer Tomography (CT), with its intrinsic resolution power, allows radiologists to detect a possible ischemic or hemorrhagic cerebral focus, as well as neoplastic metastases for the staging of the primary pathology. Spinal cord injuries are best identified with Magnetic Resonance Imaging (MRI). But nowadays, and therefore modern "tailored" medicine, is changing, going towards Artificial Intelligence (AI), a technological evolution that brings with it the limits related to the training and updating of the healthcare personnel involved. For

this reason, a section about the role of AI in the management of geriatric patients could not be missed at the end of this volume.

Finally, the aim of this book is to simplify the approach and the diagnostic imaging process of geriatric diseases, bringing out the potential and limitations of each imaging technique.

We recommend the reading of this book not only to radiologists for their daily clinical practice but also to all physicians who require a basic knowledge of imaging concerning the main geriatric pathologies, because of their complex clinical presentations.

Foggia, Italy — Giuseppe Guglielmi
Amsterdam, The Netherlands — Mario Maas

Contents

Imaging Techniques in Geriatric Patients

1

Caterina Bernetti, Carlo Augusto Mallio,
Rosario Francesco Grasso, and Bruno Beomonte Zobel

1.1 Introduction: The Delicate Balance of Imaging in the Elderly

In the last decades, there has been a rising trend toward global population aging, especially in developed nations. This longevity revolution is happening faster than historical precedents and a further increase of median age is expected in subsequent years [1].

The improvement of living conditions and the advent of modern medicine carrying innovations in treatment and prevention are some of the main reasons of increased life expectancy.

This demographic change is determining a profound impact on society, in particular with regard to the healthcare system, that now has to face more age-related diseases [2, 3].

In particular, people over 65 years, defined by convention as elderly, are more prone to develop multiple chronic conditions, such as cardiovascular diseases, dementia, cancer, and also osteoporosis that could lead to fragility fractures after minor traumas [4].

In this population, there is an intrinsic difficulty in distinguishing the boundary between para-physiologic modifications determined by aging and real pathologic conditions. Furthermore, given the possibility of an incomplete medical history, the complexity of symptoms and signs determined by the coexistence of multiple comorbidities, and the reduced sensitivity of laboratory tests, the diagnosis is often difficult to achieve. In this context, radiological imaging plays an important role in the diagnostic workup of elderly patients [2, 5].

C. Bernetti · C. A. Mallio · R. F. Grasso · B. B. Zobel (✉)
Imaging Center, Diagnostic Imaging and Interventional Radiology Department, University Hospital "Campus Bio-Medico", Rome, Italy
e-mail: c.bernetti@unicampus.it; c.mallio@policlinicocampus.it; r.grasso@policlinicocampus.it; b.zobel@policlinicocampus.it

G. Guglielmi, M. Maas (eds.), *Imaging in Geriatrics*, Practical Issues in Geriatrics, https://doi.org/10.1007/978-3-031-14877-4_1

In the elderly, even more than the rest of the population, the first medical contact is often represented by the general practitioner, who necessarily needs to be equipped with adequate knowledge in order to suggest the appropriate specialist referral or radiological examination [6]. Whereas, in a hospital setting, the two main figures who will have to interface are the geriatrician and the radiologist, in association with all the other specialists who may be involved. In order to provide high-quality care, they must cooperate in the choice of the appropriate examination and in the correct management of the patient, with medical and paramedical staff trained with age-specific skills [7, 8]. Empathy is one of the main features that the health-care personnel caring for the elderly patient should own [9].

The imaging examination must be chosen wisely, must be of clinical utility, and must help modify patients management, without exposing them to unnecessary stress or risks; in fact patients' safety must be considered as the priority [10].

The goals of the exam are an improvement in the quality of life, the preservation of functionality of these frail patients, and the prevention of progression from disease to disability [3].

In the decision process to find the appropriate image technique, the clinicians must integrate several information, such as functional and mental status, and also comorbidities, for instance chronic renal impairment, cardiac disfunction, poor peripheral venous access, and dementia. Immobility and respiratory problems that impair breath holds must be taken into consideration too, because could alter image quality [3].

Handling elderly patients in the radiology department is burden by many difficulties; this population need to be treated with caution and special care as their conditions easily deteriorate. Logistical issues are one of the main challenges that need to be addressed, in fact these patients often have mobility problems, need supervision while being transferred to the radiology department and assistance while waiting to perform the exam [2].

Proper positioning is more time-consuming and the maneuvering of the patient needs more qualified trained staff [2]. Elders usually have decreased agility and strength; hence, movements could be impaired, sense of balance could be altered, and some patient could be unable to maintain required positions. In order to move them safely and position them adequately, their cooperation and compliance need to be elicited if possible. Specific movers and support devices are useful to position and immobilize them. Attention need to be paid while having more independent patients move or even walk, because they could misjudge distances [3]. The unfamiliar and cold environment of radiology rooms and equipment could frighten this fragile patients; blankets are used to offer adequate warmth, privacy, and dignity.

Healthcare providers must never leave the patient alone; moreover, they need to be aware of any sign of pain or discomfort, because in the elderly, sensation of pain could be altered, and the patients could also have trouble expressing themselves [3].

Communication abilities of geriatric patients are often impaired because of many conditions, such as reduced acuity of vision and hearing, depression, or dementia [4]. Elders can have difficulties in understanding the procedures and in complying with instructions to remain still. Speaking clearly, using gestures, beepers, and

lights could help to transmit information. In particular, for some examinations, breathing instructions are fundamental and must be carefully communicated and practiced [7]. Long diagnostic examination, that requires to be in a stationary position, is often unsuitable for this population; however, in some particular cases, sedation could be proposed and performed [9].

Sometimes it is difficult, or even impossible, to obtain written consent, because of the age-related alterations mentioned above; hence, an important point of concern that needs to be addressed and considered in the management of the senile population is family and social support. Caregivers need to be informed about the course of the exams and sometimes even involved in the preparation [11].

The purpose of this chapter is to describe the main imaging techniques used in elderly patients and the peculiar challenges and precautions that must be taken in specific conditions for the appropriate use of diagnostic and interventional exams in this complex cohort of patients.

1.2 Imaging Modalities

1.2.1 Plain Radiography in Geriatric Patients

Thanks to its availability and low costs, plain radiography often represents the initial tool for the diagnosis of many pathologic conditions, including pulmonary, cardiovascular, and musculoskeletal disorders in older adults. This technique offers as advantages low costs, celerity in execution, and with modern equipment low radiation exposure.

Correct positioning of the patient is essential to obtain quality images; however, it could require particular devices, to assure adequate posture and immobilization. Due to mental impairment or hearing loss, elderly patients often have difficulties hearing instruction and are not able to collaborate [9]. Short times reduce risk of involuntary and voluntary motion, more common in the geriatric patients, during the acquisition [12].

In order to avoid transportation from one department to another, mobile X-ray equipment with digital panels and radiolucent beds and gurneys can be used in the hospital setting.

Chest radiography (CXR) is the initial test for the diagnosis of pulmonary, pleural, and cardiovascular diseases [12]. Radiographs are usually performed in a posterior-anterior and a perpendicular lateral projection; however, due to mobility issues of elderly patients, standard projections often cannot be performed. Hence, a supine or semi-supine position radiograph has to be taken with some limitations, such as projective magnification. For lung diseases, such as pneumonia, fibrosis and lung cancer, sensitivity, and specificity of CXR are quite high. As previously said, in the elderly, there is a difficulty in recognizing pathologic versus age-related alterations, such as fibrotic changes, emphysema, airways, and rib cage calcification. Besides this problem, it is also arduous to discern overlapping pathologies in patients with multiple comorbidities; for example in the case of heart failure versus

COPD alterations or pneumonia, which is one of the leading causes of mortality from infection in older adults, versus other consolidating lung processes [2]. Hence, it is always fundamental to integrate radiological findings with clinical information and if further workup is needed, chest computed tomography (CT) should be considered. Pneumothorax, pleural thickening, and pleural effusions are also evident on chest radiographs [13].

Cardiovascular diseases are the leading cause of deaths in elderly patients. Even though chest radiographs is usually the first exam performed, it is often insufficiently sensitive to rule out pathologic conditions, in fact, often only indirect signs can be observed [2, 12].

Thoracic aortic dilation, pulmonary edema, pericardial effusion, and cardiomegaly can be evaluated. In case of any abnormality at plain radiographs or persistence of clinical concern, more sophisticated, time-consuming, and resource-intensive techniques are needed, such as ultrasound and CT [5].

Elderly population is also burdened by an high prevalence of many musculoskeletal disease, such as osteoarthritis, osteoporosis fractures, and degenerative disk disease.

Osteoarthritis is one of the most common chronic condition afflicting older adults, causing pain and disability. It can be studied with plain radiographs, usually performed in two orthogonal projections. Degenerative changes that characterize this condition are sclerotic changes of the opposing articular surfaces, joint space narrowing, and osteophyte formation [12].

Plain radiographs also allow postoperative and follow-up of joint replacement surgery with arthroplasty [14].

Radiographs are relatively insensitive in detecting early osteoporotic alteration, in fact require an important loss of bone mass to be detected objectively [12]. However, fragility fractures determined by small traumas in a osteoporosis background are common in the elderly and can be identified with plain radiographs. Vertebral bodies are the main site for insufficiency fractures in older adults, whereas femoral fracture often happens after mild traumas or falls and is associated with high morbidity and mortality [15]. In cases of a suspected fracture, dedicated oblique views may be helpful and can be added to the standard perpendicular projections [16]. Traditional radiological diagnosis may be insufficient in the initial phases in stress fractures [15]. A deepening with CT is necessary in the study of complex fractures while MRI is the gold standard for occult fractures, post-traumatic avascular necrosis, and soft tissue evaluation [5]. Plain radiographs are also used to evaluate the presence of osteolytic or osteoblastic lesions determined by myeloma, metastatic lung, breast and prostate cancers, which could also lead to malignant fractures [5].

Plain radiographs of the abdomen can be considered a valuable resource, in particular as an initial step in acute settings. Usually a supine and upright views of the abdomen are performed. If the patient is not able to stand, a left lateral decubitus view can be obtained as an alternative. This view allows to evaluate the presence of soft tissue masses, calcifications, bowel gas pattern, air-fluid levels in the intestinal loops, and free air in the abdomen [17, 18].

Radiographs are also used in hospitalized patients to verify proper positioning of medical devices, such as central venous catheter (CVC), feeding tubes, or ureteral stents.

1.2.2 Dual-Energy X-Ray Absorptiometry (DXA) in Geriatric Patients

DXA is the imaging procedure of choice to diagnose osteoporosis, which is one of the most common pathologic conditions in elders, which can lead to fragility fractures.

This is a widely accessible, well-standardize technique that quantifies, with precision, short scan times and low radiation exposure, the areal bone mineral density (aBMD, g/cm^2) using two X-ray beams of different energies (40 keV and >70 keV) [16].

Usually the regions analyzed are the lumbar spine vertebral bodies and the femoral neck; however, the forearm can be scanned as an alternative if the previous ones cannot be evaluated [16].

The risk of osteoporotic fractures is increasing in direct proportion to the average age of the world population, in fact nearly 75% of this fractures occur in geriatric patients [19].

Correct and early diagnosis of osteoporosis is fundamental, in order to start anti-osteoporotic treatment to prevent fragility fractures, which are associated with significant morbidity, mortality, and have an important economic impact on the healthcare system [16].

1.2.3 Ultrasound in Geriatric Patients

In geriatric patients, ultrasound is a useful technique, often underrated, able to provide prompt diagnosis and treatment to several chronic or acute conditions, related to splanchnic organs, musculoskeletal system, and arterial or venous vessels [20]. It is used as a technologic complement to physical examination and laboratory findings because offers numerous advantages. It is patient-friendly, safe, rapid, cost-effective, available at short notice and repeatable. Moreover, it does not require exposure to radiation or magnetic fields, hence, in comparison to CT and MRI has fewer contraindication [20].

It can also be conveniently used at the bedside at the moment of need, thus allowing a rapid evaluation of the problem, but also avoiding movements of frail patients [20].

Being a dynamic multiplanar imaging technique, it is possible to perform diagnostic and therapeutic interventional radiology procedures under real-time guidance, such as biopsies, thermal ablation, drainage positioning, thus reducing the risk of complications, such as bleeding.

However, there are some issues that need to be underlined. US images are scarcely reproducible, because it is a patient and operator dependent technique, which relies on the compliance of the patient and the skills of the radiologist. Moreover, availability of portable equipment can be limited [21].

Elderly patients are characterized by numerous age-related conditions that could affect the quality, and hence, the interpretation of the images. For instance, their tissues and vascular vectors are characterized by fibrosis and calcifications, which determine an increased sonography echogenicity and compound artifacts [10]. This cohort of patients is also characterized by reduced bowel movements with a consequent increased amount of gas in the lumen of the intestine, which could lead to difficulty in the evaluation of abdominal organs, such as the pancreas [10].

Doppler analysis represents a useful feature that allows to evaluate the blood flow. It can be used in case of suspected deep vein thrombosis (DVP) or to evaluate atherosclerotic plaques of carotid, iliac, femoral, popliteal, and tibial arteries, often present in older adults, but also to evaluate blood supply of tumors. However, motion, in particular respiratory movements, often uncontrollable in the elderly, could alter the visualization of the color maps.

Contrast ultrasound (CEUS) is performed with an intravenous contrast agent consisting of gaseous microbubbles that remain in the vascular bed and do not reach the extravascular spaces. Due to the absence of nephrotoxicity and the possibility of being repeated, CEUS could be proposed as a valid and safe alternative to CT and MRI with contrast; however, it must be performed by experienced operators in order to avoid misinterpretations [22, 23].

In addition to the most common studies (abdomen and thyroid gland), ultrasound can be used for many conditions, for instance musculoskeletal disorders, which are considered one of the major chronic conditions affecting the senile population. Vessel evaluation can be performed with color-Doppler, for instance to predict cardiovascular and neurological events measuring intima-media thickness of the carotid artery or to follow-up aneurism of the abdominal aorta [23].

1.2.4 Multidetector Spiral Computed Tomography Scan in Geriatric Patients

Computed tomography (CT) is a digital cross-sectional imaging technique that has undergone a considerable evolution over the past decades. CT scanners have isotropic data acquisition, with the possibility of multiplanar reformations and 3D reconstructions of the images, which could help depicting complex anatomical structures and understanding pathological changes [24]. The main advantages of CT are its wide availability and speed, making it ideal also in emergency settings. Modern CT scanners, due to their high spatial and temporal resolution, allow to acquire large volume in few seconds, using 1 mm or less slice thickness. Thus, reducing the risk of motion and breathing artifacts that could impair the quality of the images, often relevant in the elderly more than in the adults. Strategies to reduce breathing artifacts include a higher pitch and caudo-cranial direction of the scan [25].

This technique, however, uses higher radiation doses than plain radiographs, but in this age group the long-term risk of cancer from ionizing radiation is of diminishing concern [25].

CT allows to study in-depth findings already detected on radiography or ultrasound, but can also be used directly in case of an important clinical suspicion that requires a more targeted investigation.

Even though some studies can be performed without the use of contrast media, for instance for small lung nodules, ureteral stones, or brain after trauma, to improve the diagnostic evaluation of some pathological conditions, the use of iodinated contrast agents is mandatory. However, in the elderly, intravascular iodine contrast media should be used with caution and limited to the indications where it is strictly necessary, in order to reduce the risk of contrast medium-induced nephropathy (CIN) to which they are more exposed [26]. Geriatric patients usually have a background reduced kidney function due to age-related functional alterations and tend to be affected by multiple comorbidities, such as heart insufficiency, hypovolemia, diabetes, and hypertension that could contribute to renal impairment. Moreover, potentially nephrotoxic drugs are used in older adults [27].

When administering iodinated contrast media, the value of serum creatinine must be evaluated and according to age-appropriate guidelines for contrast agents administration, the glomerular filtration (eGFR) rate needs to be greater than 30 mg/mL [25].

Some precautions can be put into practice to reduce the risk of CIN, such as reduction of quantity of contrast media injected, modifications in kV settings, avoidance of nephrotoxic medications, pre- and post-CT hydration, and in some cases a sessions of dialysis need to be programmed [26].

Moreover, elderly patients usually have poor peripheral venous access due to fragile vessels; hence, often only small cannulas can be positioned, making them more susceptible to contrast agent extravasation. Establishing secure intravenous access and performing a saline test injection may reduce the risk of extravasation [25].

One of the main uses of CT in elderly patients is lung CT, which is able to identify, even with low-dose protocols, the presence of nodules, masses, or pneumonia [28]. Coronary CT angiography in the senile population is now considered a useful diagnostic tool for coronary assessment and risk stratification [29]. A full-body CT with contrast is often performed for tumor staging, because it offers the possibility to evaluate lymph node stations and the presence of eventual metastases, in order to adequately plan the therapeutic approach. Finally, non-contrast brain CT is one of the main tools used in the elderly, in particular in the emergency setting for stroke or after trauma [30].

1.2.5 Magnetic Resonance Imaging in Geriatric Patients

MRI is an imaging technique that exploits magnetic fields and radio waves. The main advantages are the absence of ionizing radiation, the high contrast resolution, and the direct multiplanar imaging, which make this technique suitable for a wide range of applications in medical diagnosis [24].

Due to the long acquisition times, the need to remain still, and the noisy ambient, MRI is a difficult imaging technique for elderly patients to tolerate. Moreover, in case of fragile patients that could require monitoring and, in some conditions, life support equipment, a MRI room, compared to a CT room is a more difficult environment to manage [24].

MRI is also burden by numerous contraindications, many of which are present in elderly patients, such as claustrophobia, cardiac pacemakers or old ferromagnetic surgical material. Low-field MRI equipment could be used, at the expense of the quality of the exam, for patients with claustrophobia or mental health problems, which would require the use of sedation to tolerate the positioning necessary to perform high-field MRI [2].

In case of the presence of ferromagnetic material, CT or US must be proposed in lieu of MRI.

The arrangement of the patient on the scanning table must be as comfortable as possible; in fact this population is more exposed to develop pressure ulcer if positioned for long on hard surfaces. Hence, when performing MRI in an older population, abbreviated, time-efficient MRI protocol that maintains high diagnostic accuracy could be useful in order to avoid excessive examination times that are difficult to bare and could lead to motion and breathing artifacts, but also to avoid the abovementioned complications.

Limited rapid access to MRI is another limitation that must take into consideration when choosing the right examination for elderly patients.

Even though contrast agents used in MRI are less invasive than the ones utilized for CT, it remains the risk of nephrogenic systemic fibrosis in patients with poor renal function, such as elderly. However, in some cases it is a necessary tool, for instance in the evaluation of neoplasms.

Aging is related to neurodegenerative diseases, dementia, and also stroke, which represent the main cause of disability and the second cause of death, globally, determining a high financial and social burden on the healthcare system and society [31].

One of the main use of MRI in the elderly is the study of brain ischemic events, but it is used also to indagate occult fractures and lesions of the spine [31].

1.2.6 Interventional Radiology (IR) in Geriatric Patients

In the elderly, surgical treatments are a burden because of higher risk of morbidity and mortality. Interventional radiology offers a less invasive and safer option for the diagnostic and therapeutic management of many pathologic conditions in this population. Another advantage of IR procedures is that it does not require general anesthesia, in fact a local approach with eventual deep sedation is often sufficient [5]. The main complications that might occur include infection and bleeding. The imaging methods most used as a guidance for interventional procedures are fluoroscopy, ultrasonography, and CT, the choice of which is made according to the anatomical site and type of procedure.

Many procedures can be performed, such as vascular procedures to treat arterial stenosis or pseudoneurysm; drainage positioning for ascites, abdominal fluid collections or abscess; stent or nephrostomy positioning; biliary interventions; vertebroplasty; biopsies and thermal ablations [5].

References

1. Fawcett R, McCoubrie P. Pitfalls in imaging the frail elderly. Br J Radiol. 2015;88:20140699.
2. Gossner J, Nau R. Geriatric chest imaging: when and how to image the elderly lung, age-related changes, and common pathologies. Radiol Res Pract. 2013;2013:584793. https://doi.org/10.1155/2013/584793.
3. Barba BE, Barba JR, Rankin C. Caring for older adults in the radiology department. Are you prepared? J Radiol Nurs. 2007;26:11–4.
4. Jaul E, Barron J. Age-related diseases and clinical and public health implications for the 85 years old and over population. Front Public Health. 2017;5:335.
5. O'Brien J, Baerlocher MO, Asch M, Myers A. Role of radiology in geriatric care: a primer for family physicians. Can Fam Physician. 2009;55:32–7.
6. Radiology and primary care in Europe. Insights Imaging. 2010;1:46–52.
7. Chang A, Singh N, Boyd L, Lawson C. Strategies to improve radiographic practices for patients with Alzheimer's disease: a systematic review. J Med Imaging Radiat Sci. 2016;47:362–6.
8. Sellier N, Lhoste G, Lemouchi D, Sebbane G, Seror O. [Current problems in geriatrics and radiology. Teleradiology: organization and evaluation]. J Radiol. 2003;84:1907–12.
9. Faletti C, Borrè A, Tabasso MD. Diagnostic algorithm in the elderly. In: Guglielmi G, Peh WCG, Guermazi A, editors. Geriatric imaging. Berlin: Springer; 2013. p. 21–51.
10. Chang W-H, Huang C-H, Chien D-K, Huang M-Y, Tsai W, Chang K-S, Tsai C-H. Emergency sonography for the elderly. Int J Gerontol. 2011;5:1–8.
11. Monfardini L, Vecchi V. Limitations of diagnostic radiology for frail and vulnerable elderly cancer patients. Aging Health. 2013;9:283–5.
12. Kessler R, Dean AJ. Plain radiography in the elderly. In: Fox JC, editor. Clinical emergency radiology. 2nd ed. Cambridge: Cambridge University Press; 2017. p. 178–94.
13. DeBlieux P, Mills L. Chest radiograph. In: Fox JC, editor. Clinical emergency radiology. 2nd ed. Cambridge: Cambridge University Press; 2017. p. 41–54.
14. Vanrusselt J, Vansevenant M, Vanderschueren G, Vanhoenacker F. Postoperative radiograph of the hip arthroplasty: what the radiologist should know. Insights Imaging. 2015;6:591–600.
15. Krestan C, Hojreh A. Imaging of insufficiency fractures. Eur J Radiol. 2009;71:398–405.
16. Heilmeier U, Youm J, Torabi S, Link TM. Osteoporosis imaging in the geriatric patient. Curr Radiol Rep. 2016;4:18.
17. Acute abdominal pain in the elderly. Contemp Diagn Radiol. 2017;40:8.
18. Dean AJ, Kessler R. Plain film evaluation of the abdomen. In: Fox JC, editor. Clinical emergency radiology. 2nd ed. Cambridge: Cambridge University Press; 2017. p. 55–78.
19. Melton LJ, Crowson CS, O'Fallon WM. Fracture incidence in Olmsted County, Minnesota: comparison of urban with rural rates and changes in urban rates over time. Osteoporos Int. 1999;9:29–37.
20. Can B, Kara M, Kara Ö, Ülger Z, Frontera WR, Özçakar L. The value of musculoskeletal ultrasound in geriatric care and rehabilitation. Int J Rehabil Res. 2017;40:285–96.
21. Ticinesi A, Scarlata S, Nouvenne A, Lauretani F, Incalzi RA, Ungar A, GRETA (Gruppo di Ricerca sull'Ecografia Toracica nell'Anziano) Group of the Italian Society of Gerontology and Geriatrics (SIGG). The geriatric patient: the ideal one for chest ultrasonography? A review from the chest ultrasound in the Elderly Study Group (GRETA) of the Italian Society of Gerontology and Geriatrics (SIGG). J Am Med Dir Assoc. 2020;21:447–54.e6.

22. Dietrich CF, Tana C, Caraiani C, Dong Y. Contrast enhanced ultrasound (CEUS) imaging of solid benign focal liver lesions. Expert Rev Gastroenterol Hepatol. 2018;12:479–89.
23. Recinella G, Marasco G, Tufoni M, Brizi M, Evangelisti E, Maestri L, Fusconi M, Calogero P, Magalotti D, Zoli M. Clinical role of lung ultrasound for the diagnosis and prognosis of coronavirus disease pneumonia in elderly patients: a pivotal study. GER. 2021;67:78–86.
24. Leone A, Balanika A, Cerase A. Infection and miscellaneous. In: Guglielmi G, Peh WCG, Guermazi A, editors. Geriatric imaging. Berlin: Springer; 2013. p. 141–75.
25. Sadro CT, Sandstrom CK, Verma N, Gunn ML. Geriatric trauma: a radiologist's guide to imaging trauma patients aged 65 years and older. Radiographics. 2015;35:1263–85.
26. Mehran R, Aymong ED, Nikolsky E, et al. A simple risk score for prediction of contrast-induced nephropathy after percutaneous coronary intervention: development and initial validation. J Am Coll Cardiol. 2004;44:1393–9.
27. Wilhelm-Leen E, Montez-Rath ME, Chertow G. Estimating the risk of radiocontrast-associated nephropathy. J Am Soc Nephrol. 2017;28:653–9.
28. Park JE, Kim Y, Lee SW, Shim SS, Lee JK, Lee JH. The usefulness of low-dose CT scan in elderly patients with suspected acute lower respiratory infection in the emergency room. Br J Radiol. 2016;89:20150654.
29. Nijveldt R, Pflederer T, Achenbach S. Coronary CT angiography in the elderly. Neth Heart J. 2014;22:124–5.
30. Bekelis K, Fisher ES, Labropoulos N, Zhou W, Skinner J. Variations in the intensive use of head computed tomography for elderly hemorrhagic stroke patients. Radiology. 2015;275:188–95.
31. Cole JH, Franke K. Predicting age using neuroimaging: innovative brain ageing biomarkers. Trends Neurosci. 2017;40:681–90.

Neurodegenerative Diseases in Geriatric Patients

2

Camilla Russo, Rossana Senese, and Mario Muto

Abbreviations

18FDG PET/CT	18F-fluorodeoxyglucose positron emission tomography/computed tomography
AD	Alzheimer disease
ALS	Amyotrophic lateral sclerosis
ARCA1	Autosomal recessive cerebellar ataxia type 1
Aβ	Beta amyloid plaques
BOMBS	Brain observer microbleed scale
CAA	Cerebral amyloid angiopathy
CBD	Corticobasal degeneration
CJD	Creutzfeldt–Jakob disease
CNS	Central nervous system
CSF	Cerebrospinal fluid
CT	Computed tomography
DAT	Dopamine transporter
DLB	Disease with Lewy bodies
DWI	Diffusion weighted imaging
EEG	Electroencephalogram
ERICA	Entorhinal cortical atrophy

C. Russo
Diagnostic and Interventional Neuroradiology, "A. Cardarelli" Hospital, Naples, Italy

Department of Electrical Engineering and Information Technology, Università degli Studi di Napoli "Federico II", Naples, Italy

R. Senese
Emicenter European Medical Imaging, Casavatore, Naples, Italy

M. Muto (✉)
Diagnostic and Interventional Neuroradiology, "A. Cardarelli" Hospital, Naples, Italy

G. Guglielmi, M. Maas (eds.), *Imaging in Geriatrics*, Practical Issues in Geriatrics, https://doi.org/10.1007/978-3-031-14877-4_2

FLAIR	Fluid attenuation inversion recovery
FRDA	Friedreich's ataxia
FTLD	Frontotemporal lobar degeneration
FXTAS	Fragile X-linked tremor/ataxia syndrome
GCA	Global cortical atrophy
HD	Huntington disease
MARS	Microbleed anatomical rating scale
MCI	Mild cognitive impairment
MIRAS	Mitochondrial recessive ataxia syndrome
MRI	Magnetic resonance imaging
MRPI	Magnetic resonance parkinsonism index
MSA	Multiple systemic atrophy
MTA	Medial temporal atrophy
NBIA	Neurodegeneration with brain iron accumulation
NM	Nuclear medicine
PD	Parkinson disease
PKAN	Pantothenate kinase-associated neurodegeneration
PNFA	Progressive non-fluent aphasia
PPA	Primary progressive aphasia
PrPC	Prion protein
PrPSc	Scrapie prion protein
PSP	Progressive supranuclear palsy
PWI	Perfusion weighted imaging
SD	Semantic dementia
SPECT	Single photon emission tomography
SWI	Susceptibility-weighted imaging
VRS	Visual rating scales
WMH	White matter hyperintensities

2.1 Introduction

Dementia is an umbrella term used to describe a syndrome characterized by deterioration in cognitive and behavioural functioning not consistent with normal ageing, severely interfering with daily activities; mild cognitive impairment (MCI), defined as intellectual decline greater than expected for age but still not interfering with daily life, can be an early manifestation of dementia. Dementia symptoms include memory loss, spatial and temporal disorientation, reduced concentration, sleep disturbances, up to repeated syncope and loss of consciousness, severe autonomic dysfunction, or behavioural changes including aggressiveness and depression. An early diagnosis can have a major impact on prognosis and patients' management, and the prompt identification of MCI signs is important to slow down disease progression to overt dementia.

This is even more true considering that cognitive impairment incidence among the elderly population is rapidly rising. At present dementia affects about 50 million

people worldwide, a figure that is expected to double in the next decades due to population ageing and increasing average life expectancy. Several risk factors have been called into question for dementia, including sex, ethnicity, educational level, smoking, drug and alcohol abuse; however, age and genetic factors seem to play a major role in disease onset and progression [1]. From a clinical perspective, patients suffering from a neurodegenerative disorder generally realize when their symptoms began. From here onwards the pattern of cognitive decline is variable, with a period of relative stability preceding an abrupt and inexorable deterioration. Clinical evolution speed strictly depends on the putative aetiological mechanism, ranging from few months in the most aggressive cases to several years in the slowly progressing diseases [2, 3]. In demented patients, it is supposed to be a certain discrepancy between actual disease onset and symptoms onset; indeed, due to cellular redundancy in neuronal circuits, symptoms only appear when the number of neurons spared by neurodegenerative processes is lower than required to maintain a normal neuronal activity in the affected pathway. Moreover, assuming that the rate of neuronal loss is almost constant during the whole disease course, the observed sudden clinical deterioration in late-stage dementia is probably due to a collapse in neuron number beneath a certain threshold [2]. Despite symptom severity, life expectancy in affected patients is not significantly reduced, unless in case of comorbidities or direct/indirect involvement of neurological structures responsible for vital functions (i.e. brainstem centres regulating heart rate, breathing and blood pressure).

The presence of an underlying neurodegenerative process responsible for cognitive decline defines primary dementias. However, severe cognitive impairment is not only observed in neurodegenerative disorders but also common in vascular, toxic, paraneoplastic, infectious, metabolic or traumatic insults of the central nervous system (CNS); in these cases, the definition of secondary or potentially reversible dementias may be applied, as some of these conditions may be treatable and related symptoms partially reversible [4]. Frequently, post-mortem brain examination represents the only tool for definite differential diagnosis between dementia types; nevertheless, structural magnetic resonance imaging (MRI) as well as nuclear medicine (NM) can provide important clues in excluding secondary causes and hypothesizing the presence of a specific pathogenic mechanism.

This chapter provides a comprehensive overview of the most common neurodegenerative causes of dementia in elderly, classified on the basis of the presumed underlying pathologic mechanism, focusing on clinical patterns and corresponding neuroradiological manifestations.

2.2 Neuroradiology and Its Role in Primary Neurodegeneration

Standardized CNS imaging protocols are crucial in neurodegenerative disorder assessment, in terms of both first diagnosis and longitudinal follow-up for evaluating disease progression. Anatomical imaging usually represents the first approach; MRI and, to a lesser extent, computed tomography (CT) may bring to light

structural abnormalities suggestive for a specific disorder; however, despite technological advances and increased MRI sensitivity, conventional anatomical imaging can also be unrevealing in early disease stages when clinical symptoms exceed structural alterations. In these cases, NM metabolic imaging can allow for early identification of cellular dysfunction even before anatomic alterations onset at MRI examination [5, 6]. A multimodal algorithmic approach in the evaluation of neurodegenerative disorders usually starts with structural MRI and/or CT examination, first of all to exclude possible mimics such as secondary neurodegeneration (i.e. vascular dementia, etc.) and surgical pathologies that would benefit of a different therapeutic approach. Secondly, structural MRI techniques are used to confirm clinical suspicion of primary neurodegeneration by identifying early signs when present, or to raise the suspicion of mixed dementia when brain changes suggestive for more than one dementia type coexist [7]. When anatomical imaging is silent, NM represents one last option for early dementia characterization and prognostic assessment in doubtful cases. An example of suggested algorithmic approach is shown in Fig. 2.1.

In terms of method, conventional MRI minimum protocol requires diffusion-weighted imaging (DWI) for excluding acute lesions, 3D T1-weighted and/or 3D T2-weighted imaging for volumetric measurements (with 3D fluid attenuation inversion recovery—FLAIR—preferred over T2 for white matter lesion burden assessment), and T2* gradient-recalled echo or susceptibility-weighted imaging (SWI) for deoxyhaemoglobin, ferritin, haemosiderin and dystrophic calcifications identification (with SWI up to ten times more sensitive than T2*, as well as able to differentiate between microbleeds and calcifications); gadolinium-enhanced acquisitions, MR angiography and perfusion-weighted imaging (PWI) are only used when possible mimics are highly suspected. Among the above-mentioned sequences, a prominent role is played by MRI volumetric acquisitions that harbour potential for both qualitative and quantitative atrophy assessments; in particular, quantitative assessment (carried on with several commercial and open source software) allows for a more accurate comparison to reference population and regional brain atrophy

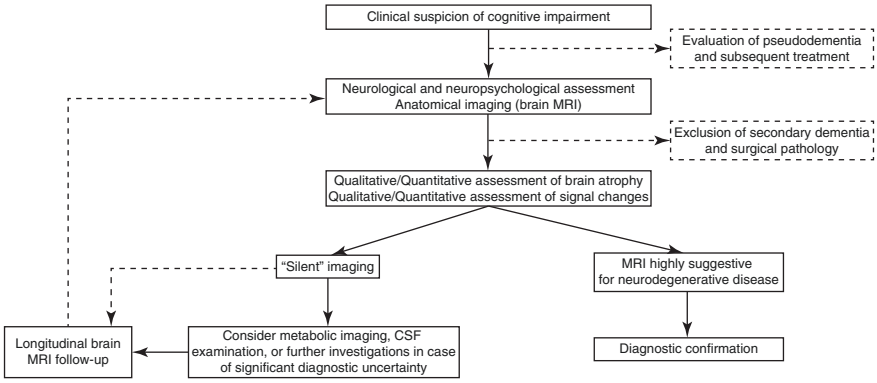

Fig. 2.1 Proposed algorithmic approach for MRI interpretation in dementia

patterns' analysis, also implementing sensitivity to minimal variations in volumes and reducing inter-rater variability (Fig. 2.2).

Among NM techniques, metabolic imaging with 18F-fluorodeoxyglucose positron emission tomography/computed tomography (18FDG PET/CT) is used to assess semi-quantitative cortical glucose uptake, whose metabolism has been found abnormal in several neurodegenerative disorders such as Alzheimer disease (AD), Parkinson disease (PD), amyotrophic lateral sclerosis (ALS) and Huntington disease (HD) [8]. In addition to 18FDG PET/CT, another commonly used second-line NM modality in case of dementia (especially if coupled to movement disorders) is represented by dopamine imaging; notably in PD and disease with Lewy bodies (DLB), dopamine transporter (DAT) single photon emission tomography (SPECT) examination can be used to assess density of dopamine receptors within the nigrostriatal extra-pyramidal pathway, and therefore confirm or exclude the suspected synucleinopathy [9–11]. Among less diffused NM techniques, the resort to amyloid precursors for PET/CT imaging (the most well-known is the Pittsburgh compound B radiotracer) is gaining an over-increasing importance in dementia diagnosis due to possibility to cross the blood–brain barrier and uniquely bind to beta amyloid plaques (Aβ); indeed abnormal accumulation of Aβ is a hallmark of amyloid angiopathy and even more importantly of AD, the latter representing the most common form of neurodegeneration in elderly. A new emerging technique similar to amyloid PET/CT is the tau PET/CT, which might become a further and more specific imaging resource for tauopathies due to the possibility to target and bind tau filaments

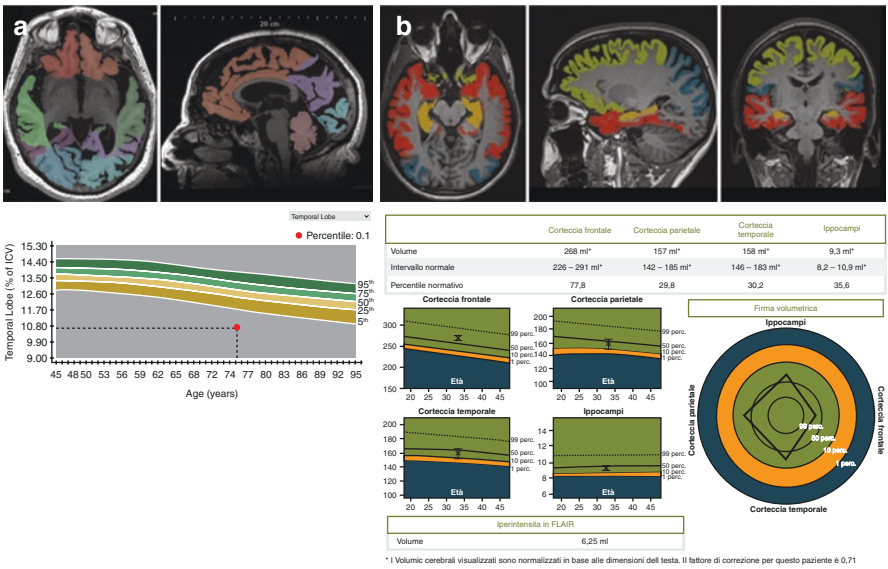

Fig. 2.2 An example of automated volume reports from two different commercial software, with reference to age/sex-matched control population and with cortical atrophy patterns: (**a**) Icobrain DM report for MRI (icometrix®) and (**b**) Quantib Neurodegenerative (Quantib® Brain)

and neurofibrillary tangles [12, 13]. However, at present NM is only indicated for those patients with significant diagnostic uncertainty after a comprehensive multi-domain evaluation, and when a timely diagnosis may affect patient's management [14].

2.3 Structured Reporting in Primary Neurodegeneration: Good Practice

As seen above dementia covers a very wide and varied spectrum of possible disorders, whose early differentiation is increasingly gaining importance especially in light of new emerging treatments and disease-modifying therapies. In this light, neuroimaging plays a pivotal role both in terms of research and diagnostic purposes. Therefore a close communication between referring clinicians and radiologists is strictly required to ensure the capitalisation of all the information provided by imaging techniques. For such purpose, the structured imaging interpretation then translated in a shared and standardized language is highly recommended [15]; in particular the introduction of semi-quantitative visual rating scales (VRS) (which have largely replaced the use of subjective terms), as well as the development of several software tools to quantify brain atrophy, is simplifying the communication among professional involved in the care of demented patients [16]. However, despite the large use for research purposes, brain atrophy quantification with dedicated tools is still far from an actual application in daily clinical routine due to its limited territorial diffusion and its cost, process, and time consumption; conversely, the use of semi-quantitative VRS is widely adopted both in non-academic and academic institutes [15, 17]. Several VRS were developed to semi-quantitatively assess the main imaging features of dementia: brain atrophy, white matter micro-vascular lesion load and cerebral microbleeds burden. Here we summarize the most relevant semi-quantitative VRS also suggesting a structured interpretation/reporting scheme to adopt in daily clinical practice.

2.3.1 Brain Atrophy

Brain atrophy is probably the most important hallmark of neurodegeneration severity. Several semi-quantitative scales have been proposed, and among them the most used include:

- Global cortical atrophy (GCA), to assess a general or localized widening of sulci due to gyral volume loss (Fig. 2.3)
- Medial temporal atrophy (MTA), to assess hippocampal and mesio-temporal atrophy (Fig. 2.4)
- Koedam score, to assess parietal lobe atrophy (Fig. 2.5)
- Entorhinal cortical atrophy (ERICA) score, to assess the entorhinal cortex for volume loss (Fig. 2.6)

	Volume of sulci	Volume of ventricles
Grade 0	Normal	No enlargement
Grade 1	Opening of sulci	Mild enlargement
Grade 2	Volume loss of gyri	Moderate enlargement
Grade 3	Knife blade atrophy	Severe enlargement

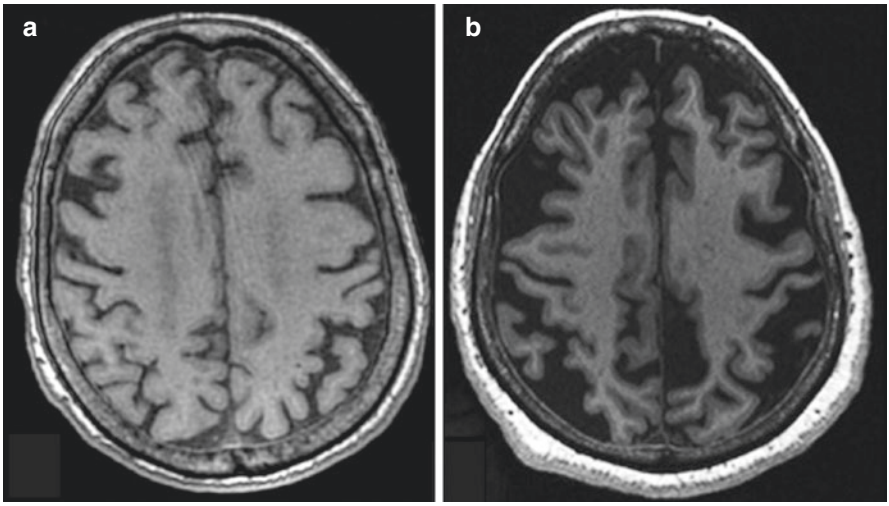

Fig. 2.3 Scheme of atrophy pattern evaluation by using the global cortical atrophy-frontal (GCA) score, to be used for each of the individual 13 brain regions assessed separately in each hemisphere; the final score is the sum of all regions. Below, an example of grade 1 (**a**) and grade 3 (**b**) atrophy

It should never be forgotten the examination of the infra-tentorial compartment (always be scrutinized to exclude PSP, MSA, and SCA), by also including qualitative or quantitative measurements (i.e., magnetic resonance parkinsonism index—MRPI, or midbrain-to-pons ratio) when applicable.

2.3.2 White Matter Lesion Burden

White matter hyperintensities (WMHs) burden on MRI can be easily assessed by using the Fazekas' score, a scale based on the visual assessment of number and the extent of periventricular and deep white matter lesions on axial T2w or T2 FLAIR images of the whole brain; to each compartment (periventricular and deep white matter) is given a score from 0 to 3 depending on size and confluence of WMH, which can then be summed to give a final grading where lower scores indicate lower lesion burden (Fig. 2.7).

	Choroid fissure	Temporal horn width	Hippocampal height
Grade 0	Normal	Normal	Normal
Grade 1	Minimal enlargement	Normal	Normal
Grade 2	Mild enlargement	Mild enlargement	Mild reduction
Grade 3	Moderate enlargement	Moderate enlargement	Moderate reduction
Grade 4	Severe enlargement	Severe enlargement	Severe reduction

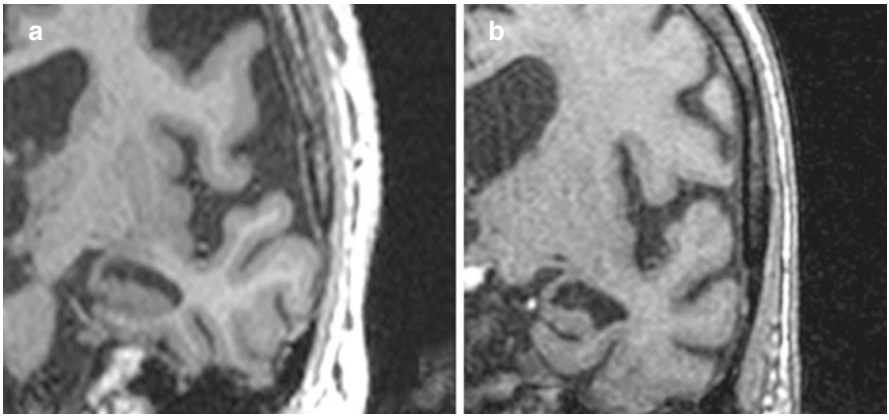

Fig. 2.4 Scheme of atrophy pattern evaluation by using the medial temporal atrophy (MTA) score, to assess hippocampal and mesio-temporal atrophy on the coronal plane. Below, an example of grade 2 (**a**) and grade 4 (**b**) atrophy

2.3.3 Cerebral Microbleeds Burden

The quantitative assessment of cerebral microbleeds highly suggestive for CAA on MRI was first included among the clinical-radiological Boston criteria [18] for the diagnosis of possible/probable CAA; the number and distribution of haemorrhages should be assessed on SWI in lobar, cortical, and/or subcortical regions, as well as on sulci surface (superficial siderosis). More recently two new scales, the Brain Observer MicroBleed Scale (BOMBS) and the Microbleed Anatomical Rating Scale (MARS), have been proposed to implement interobserver agreement about presence, number, size, and location of brain microbleeds; however, their actual application in daily practice is still limited.

2.3.4 Structured Reporting Checklist

Structured templates for MCI and dementia assessment are used to provide a checklist within which all relevant items are included and reported; for the sake of completeness, other key clinical features should always be included at the beginning of the structured report to complete the general framework.

	Parietal gyri	Parietal sulci
Grade 0	Normal	Closed sulcus
Grade 1	Mild cortical atrophy	Mild widening
Grade 2	Moderate cortical atrophy	Moderate widening
Grade 3	Knife blade atrophy	Severe widening

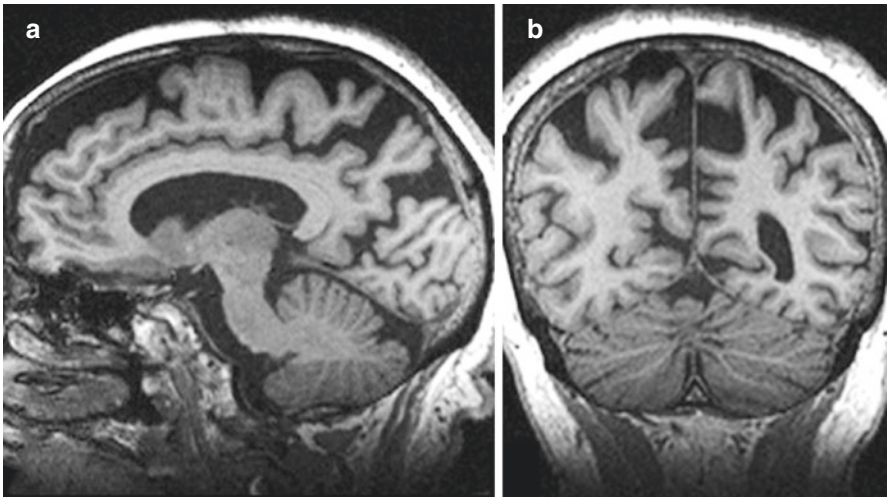

Fig. 2.5 Scheme of atrophy pattern evaluation by using the Koedam score, to assess parietal lobe atrophy especially on the sagittal and coronal plane. Below, an example of grade 3 atrophy both on the sagittal (**a**) and coronal (**b**) planes

Suggested Checklist:

- Describe the clinical presentation and state the diagnostic suspicion
- Mention the scan protocol used
- Mention previous imaging examination available for comparison
- Exclude possible mimics (mass lesions, hematomas, and any other surgical or non-surgical disorder that could explain MCI/dementia)
- Exclude the presence of hydrocephalus (communicating or non-communicating)
- Describe any diffusion abnormality
- Describe vascular pathology (quantification of WMH and microbleeds burden by using semi-quantitative scales)
- Describe atrophy pattern (symmetric or asymmetric pattern; supratentorial and/or infratentorial compartment involvement; quantification by using semi-quantitative scales)
- Summarize conclusions and final impressions (normal findings according to the age vs. vascular/neurodegenerative/mixed pathology; pattern consistent with the clinically suspected dementia disorder; suggest differential diagnosis for neurodegeneration)

	Entorhinal cortex	Enthorinal cortex
Grade 0	Normal	Closed sulcus
Grade 1	Mild cortical atrophy	Widening
Grade 2	Moderate cortical atrophy	Tentorial cleft sign
Grade 3	Severe atrophy	Wide tentorial cleft sign

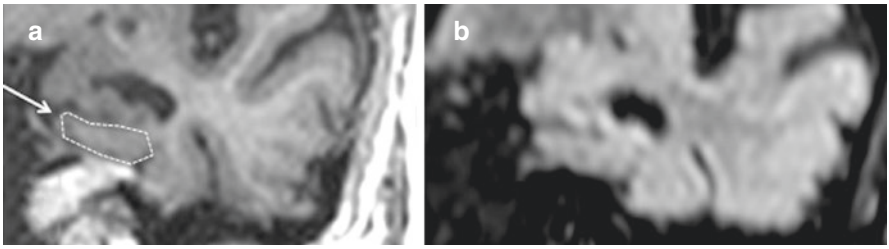

Fig. 2.6 Scheme of atrophy pattern evaluation by using the entorhinal cortical atrophy (ERICA) score, to assess the entorhinal cortex for volume loss. Below, an example of grade 2 atrophy on 3D T1w (**a**) and 3D FLAIR (**b**) images*; dotted line* indicates the entorhinal cortex, *white arrowhead* indicates the enlargement collateral sulcus (with only minimal detachment of the entorhinal cortex from the cerebellar tentorium, also known as "tentorial cleft sign")

	Fazekas score for WMHs
Grade 0	None or isolated punctate WMH lesion
Grade 1	Multiple WMH lesions
Grade 2	Initially confluent WMH lesions
Grade 3	Largely confluent WMH lesions

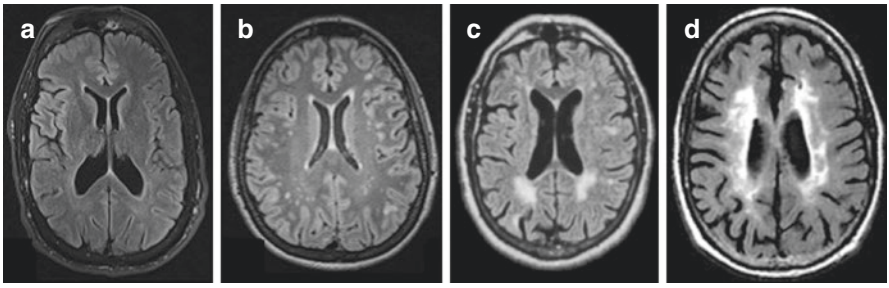

Fig. 2.7 White matter hyperintense (WMH) lesion burden evaluated by using Fazekas' score on axial FLAIR MRI. (**a**) grade 0, (**b**) grade 1, (**c**) grade 2, (**d**) grade 3

2.4 Most Common Primary Neurodegenerative Disorders in Elderly and Neuroradiological Clues for Diagnosis

The overall number of neurodegenerative disorders runs into the hundreds and some of them overlap clinically or pathologically, making the differential diagnosis quite challenging. As noted above, two main factors contribute to this phenomenon: on the one hand a same neurodegenerative disease can affect different areas of the brain, which leads to a large phenotypical variability specially in early disease stages; on the other hand some disorders share some common features, thus resembling one another in some clinical manifestations [19, 20]. In terms of classification, primary neurodegenerative disorders can be classified according to brain abnormalities location, clinical manifestations, or pathological mechanism. Following this last criterion here we give a short overview of typical findings and neuroradiological hallmarks of the most common neurodegenerative disorders in the elderly. The three most significant groups are represented by:

- Tauopathies—defined by the presence of intracellular tau-positive inclusions in the human brain, formed by neurofibrillary tangles generated by the hyperphosphorylation of a microtubular protein (called *tau)* that induce the protein to dissociate from microtubules and form insoluble aggregates
- Synucleinopathies—defined by the abnormal deposition of aggregates of *alpha-synuclein* (a protein involved in synaptic vesicle trafficking and neurotransmitter release) within neurites, axons and glial cells, interfering with normal DNA repair function
- Amyloidosis—defined by the presence within grey matter of neurotoxic amyloid plaques (or *Aβ plaques*), due to aberrant extracellular deposits of the amyloid beta protein (arising from the amyloid-beta precursor protein, a synaptic cell surface receptor regulating iron uptake and neuronal plasticity).

As final remarks, in both tauopathies and amyloidopathies, it is thought that the abnormal formation of misfolded insoluble oligomers may induce other molecules to assume the same misfolded structure, then causing protein aggregation and deposition in a sort of "cascade-effect" similar to the one observed in prion infection; however, the aetiopathogenesis of these disorders has not yet been fully elucidated. Moreover it should be noted that this arbitrary classification does not take into account the co-occurrence of some of these dementing disorders in a same patient, a phenomenon that can be at least in part attributed to a certain overlap in pathogenic mechanisms (i.e. AD and CAA) [21].

2.4.1 Tauopathies

2.4.1.1 Alzheimer Disease (AD)

AD is the most common type of dementia, with prevalence increasing from 1% between 60 and 65 years to about 30–40% over 85–90 years of age. Overall AD is

thought to be responsible for about 60–80% of all overt dementias, with an age-specific prevalence that almost doubles every 5 years in subjects aged >65 years. This exponential increase in AD prevalence in elderly suggests that AD strictly related to ageing, therefore considered the main risk factor; however, apart from ageing, other risk factors have also been described (including family history of dementia, female gender, apolipoprotein E epsilon 4 allele carrier status, smoking and mutations in the amyloid precursor protein) [22].

As per other forms of dementia, also in AD the neuropathological changes due to amyloid and tau deposition (leading to the formation of plaques) occur up to 25–30 years before clinical manifestations. From a clinical standpoint we can therefore observe a long silent (or pre-clinical) phase, followed by an overt progressive neurodegenerative disorder (starting when a certain neurotoxicity threshold has been exceeded). Clinical symptoms include memory loss and MCI in early stages, then followed by decline in praxis and visuo-spatial abilities, attention deficit and behavioural changes (with neuropsychiatric symptoms ranging from apathy, depression and anxiety up to aggressiveness, psychomotor agitation and psychosis). Apart from AD classical variant initially characterized by anterograde episodic memory loss, two other clinical (or atypical) variants may be identified: frontal variant AD (fvAD) and posterior cortical atrophy (PCA). In both cases the same neuropathological changes of AD can be observed in the brain, however with different spatial distribution and thus causing different symptoms at onset. In fvAD, the condition mainly affects frontal lobes, with dominance of behavioural changes, executive dysfunction or a combination of both over a pure memory loss. In PCA early manifestations are related to visual cortex involvement, with symptoms including difficulty in recognising faces, measuring distances and perceive the surrounding space; due to this insidious onset, PCA variant may be difficult to identify and it can take a long time before considering the proper diagnosis.

Moving to imaging in AD patients, although CT is able to detect atrophy, MRI is the golden standard to describe the pattern of cortical atrophy and exclude possible differential diagnoses. Atrophy typically occurs first in hippocampus, perirhinal and entorhinal cortex, prior to pervasive progression to diffuse cortical atrophy; this atrophy can be assessed by observing the enlargement of the parahippocampal fissures, or alternatively by using MTA and/or ERICA scores. Medial temporal lobe atrophy is found both in AD and (to a lesser extent) in other primary neurodegenerative disorders, whereas it is less commonly observed in normal ageing; however, despite a certain specificity, such volume loss does not appear early in the course of the disease, thus representing only a late AD manifestation. Posterior cortical atrophy or bilateral frontal lobe atrophy are observed in later AD stages coupled to medial temporal lobe involvement, or in atypical AD variants (PCA and fvAD) as an early finding coupled to a relative sparing of the medial temporal lobe. In addition to the above features, WMH due to chronic small vessel disease, cerebral microbleeds and microinfarcts can also be observed; in these cases, the simultaneous vascular and neurodegenerative pathologies double the risk and exacerbate the symptoms of dementia. Apart from conventional imaging, functional MRI also harbour the potential to show a reduced activation in hippocampus and related

structures within the medial temporal lobe of AD patients, either during cognitive paradigms or resting state; similarly, different advanced techniques such as diffusion tensor imaging, quantitative susceptibility mapping and magnetization transfer have also been used for analysing the damage in the same structures. However at present these applications have only been exploited for research purposes and used by limited number of research groups, therefore far from clinical widespread applications [23].

Structural MRI can be complemented by a variety of NM examinations in case AD is suspected, both for supporting the diagnosis (even before symptoms onset) and stratifying the prognosis (in case of overt dementia). SPECT and FDG-PET are used to detect regional hypoperfusion and hypometabolism, respectively, generally with a bilateral and symmetric temporo-parietal, precuneus and posterior cingulate distribution; sensorimotor cortex is generally spared, whereas frontal lobes are usually involved in later disease stages. Diagnostic specificity can also be increased by resorting to amyloid-PET and tau-PET; amyloid and tau biding tracers selectively accumulate in grey matter and medial temporal lobes respectively, with amyloid deposition occurring before tau deposition. In particular, amyloid binding tracers are used as a negative predictor of AD, as the absence of captation makes the diagnosis unlikely. Conversely tau-binding tracers are not specific for AD, as they are found positive also in other tauopathies; however, the higher is the accumulation within hippocampus, entorhinal cortex and temporoparietal cortex, the more severe is the AD cognitive decline. Therefore we can conclude that, while Aβ plaques should be considered a disease biomarker, tau-positive inclusions mainly represent a progression-related biomarker.

2.4.1.2 Corticobasal Degeneration (CBD)

CBD is a rare and probably underestimated tauopathy, with a peak incidence between the fifth and seventh decade of life and a slight male prevalence. Despite CBD is generally diagnosed as a sporadic disorder, rare familiar and isolated genetic cases have also been described; in the familiar forms, CBD has been associated with mutations in genes encoding for progranulin or microtubule-associated protein tau. Tau-positive inclusions in CBD are mainly disseminated within motor cortex (premotor, supplementary motor and somatosensory), basal ganglia and brainstem. Clinical manifestations reflect this distribution, even if the global clinical picture often overlaps with other neurodegenerative disorders with subsequent diagnostic challenges. CBD generally starts as an asymmetric, akineto-rigid syndrome with apraxia, dystonia, myoclonus and postural instability, unresponsive to levodopa; cognitive impairment and behavioural changes can also be observed in early disease stages, frequently associated to the alien limb phenomenon.

Asymmetric clusters of grey matter atrophy in specific regions invariably characterize MRI findings in CBD, mainly involving bilateral thalami, bilateral posterior fronto-median and cingulate cortex, bilateral premotor and supplementary motor area, and middle frontal and precentral gyrus; regional atrophy in frontal, parietal, temporal and occipital lobes can also be found. Left hemisphere is generally more affected; however, right-sided features of CBD can also be occasionally observed.

The most affected cerebral hemisphere is also characterized by the presence of WMH on T2/FLAIR images within subcortical and periventricular white matter [24]. Research studies concerning the use of volumetric cluster analysis and diffusion tensor imaging for CBD characterization are still ongoing, and suitable clinical applications have not yet been developed. NM only plays a marginal role in CBD at present, with SPECT and PET studies showing asymmetric metabolic changes in the same areas of atrophy on MRI; among these techniques, tau-PET probably has the larger potential for monitoring disease status, disease progression and therapeutic targeting monitoring.

2.4.1.3 Frontotemporal Lobar Degeneration (FTLD)

FTLD in an umbrella term used to describe different dementing disorders with prominent behavioural and language deterioration. Most common as a sporadic disease, at present FTLD recognizes a genetic determinant in 20% cases; most common mutations involve the progranulin and microtubule-associated protein tau genes (similar to the one described for CBD), but also *C9ORF* gene (with a certain pathogenic overlap with motor-neuron disorders involving the same genetic locus). Despite the partial understanding of its aetiology and despite its clinical heterogeneity, FTLD can be grouped in three main subtypes based on the proteinaceous inclusions observed at pathological examination: FTLD-Tau in case of misfolded tau protein; FTLD-TDP in case of transactive response DNA binding protein 43; FTLD-FUS in case of fused sarcoma protein. Most of FTLD subtypes belong to the first group; compared to other tauopathies, FTLD has the peculiarity to affect younger patients (50–60 years) at onset and to have a slower clinical progression.

From a clinical perspective, FTLD can be divided in two macro-categories according to clinical presentation: behavioural variant frontotemporal dementia (bvFTD) and language variant frontotemporal dementia (lvFTD, also known as primary progressive aphasia—PPA). bvFTD has a predominant frontal lobe involvement, while lvFTD has a predilection for the temporal lobe and is further divided into several subtypes: non-fluent variant primary progressive aphasia (nfvPPA), also named progressive non-fluent aphasia (PNFA); semantic variant primary progressive aphasia (svPPA), also named semantic dementia (SD); and the rare logopaenic variant primary progressive aphasia (lvPPA).

Imaging features described in these forms of dementia largely overlap one another [25], and only limited differences in atrophy patterns can be identified at qualitative evaluation. bvFTD is mainly characterized by changes in social behaviour and poor impulse control, while memory is generally spared and language disability generally present; in this variant at MRI examination atrophy is confined to mesio-frontal, orbito-frontal and anterior temporal cortices, with a typical anterior-to-posterior gradient and with the associated enlargement of anterior horns of the lateral ventricles. PNFA is characterized by poor speech production; in this case, atrophy is limited to bilateral insulae and inferior frontal gyri at the level of Broca's area. SD is characterized by poor language comprehension with preserved speech abilities; at MRI a severe anterior temporo-polar atrophy can be observed, usually more marked in the dominant hemisphere, associated with a variable hippocampal

atrophy. Finally, lvPPA is a disturbance in thinking of the words to use while speaking, narrow attention span, progressive hesitation and difficult comprehension of complex sentences; on MRI this variant is characterized by a selective left temporoparietal atrophy. Metabolic studies with FDG-PET confirmed the presence of hypometabolic areas corresponding to atrophic cortex, with a pattern completely superposed on the one observed at MRI examination.

2.4.1.4 Progressive Supranuclear Palsy (PSP)

PSP is a rare tauopathy of unknown aetiology, which manifests as an atypical parkinsonian syndrome. PSP shows a strong male predominance (8:1), with a mean age at onset of approximately 65 years and an overall prevalence of about 5:100,000; median survival after symptoms onset is about 6–8 years, with death frequently occurring because of complications due to brainstem damage.

Clinical PSP onset can be insidious, with axial motor abnormalities, gait instability and frequent falls as common initial manifestations; as the disease progresses, worsening parkinsonism, dysarthria, dysphagia, sleep disturbance and personality changes due to frontal cognitive decline can be observed. Unlike it might be thought, eye movement abnormalities (notably supranuclear ophthalmoplegia, which is considered the hallmark of PSP) only appear later during disease progression. Depending on the prevalence of brainstem or cortical feature, we can distinguish several clinical PSP variants: classic progressive supranuclear palsy or Richardson syndrome (PSP-RS), progressive supranuclear palsy-parkinsonism (PSP-P), progressive supranuclear palsy-pure akinesia with gait freezing (PSP-PAGF), progressive supranuclear palsy-corticobasal syndrome (PSP-CBS), progressive supranuclear palsy-behavioural variant of frontotemporal dementia (PSP-bvFTD) and progressive supranuclear palsy-progressive non-fluent aphasia (PSP-PNFA).

MRI in PSP diagnosis is poorly sensitive in early stages, with peculiar features only appearing in more advanced disease; conventional MRI is helpful in demonstrating midbrain atrophy with secondary third and fourth ventricle enlargement, fronto-temporal, pontine and cerebellar atrophy, as well as T2w signal increase within the inferior olives and the periaqueductal grey matter. In particular, midbrain atrophy results in the so-called hummingbird sign (flattening of the superior aspect of the midbrain on the sagittal plane) and morning glory sign (loss of the lateral convex margin of the tegmentum on the axial plane at mammillary body level); when midbrain atrophy is more pronounced, the so-called mickey mouse appearance of the brain stem on the axial plane (defined as a reduction in the anterior-posterior midline midbrain diameter at the level of the superior colliculi greater than 12 mm) can also be observed. These qualitative features are inconstant and dependent from the adopted acquisition planes; therefore, quantitative measurements are considered more sensitive. There are two main options to assess midbrain atrophy on MRI, the MRPI and the midbrain-to-pons area ratio, both helpful in distinguishing PSP from other movement disorders. MRPI is obtained by measuring the width of the superior cerebellar pedicle on the coronal plane, the middle cerebellar pedicle on the sagittal plane and the area of the midbrain and pons on the sagittal plane, then by multiplying the pons area to midbrain area ratio by the middle cerebellar

peduncle width to superior cerebellar peduncle width ratio; a value of more than 14 is highly suggestive for PSP. A recent version called MRPI2.0 also included ventricle enlargement in the computation, with a final figure obtained by multiplying the MRPI by the ratio of third ventricular width to frontal horn width; however, these computations can suffer from inter-rater variability and limited reproducibility. Therefore easier techniques, such as the above-mentioned midbrain-to-pons area ratio, should be preferred. The area of the midbrain and pons are calculated on the midline sagittal plan at the level of ponto-mesencephalic and ponto-medullary junctions; in PSP patients, this parameter is significantly reduced or even halved, while in PD MSA and healthy brain is approximately 0.24. An example of MRI findings in PSP is shown in Fig. 2.8. Functional imaging studies are not entirely specific for PSP; it has been described that FDG-PET can show hypometabolism in the frontal lobe and/or midbrain, while I-123 ioflupane SPECT may demonstrate loss of the normal crescent-shaped tracer uptake in the striatum.

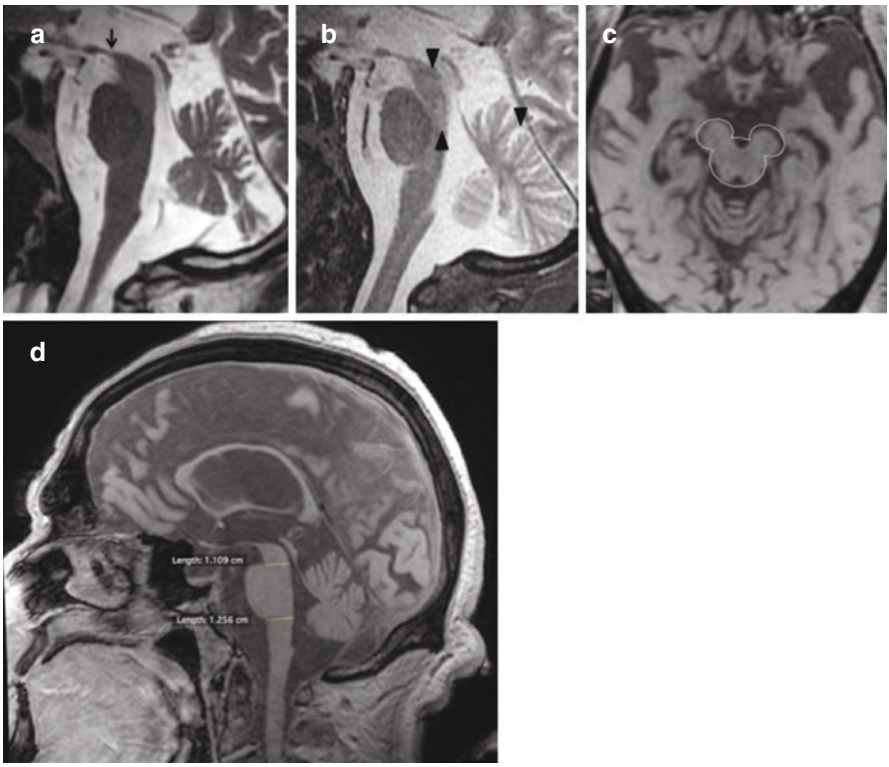

Fig. 2.8 Most prominent MRI features of PSP: atrophy of the midbrain with the hummingbird sign on sagittal images due to preserved pontine volume (**a**, *black arrow*), associated to cerebellar atrophy and periacqueductal grey matter hyperintensity (**b**, black arrowheads); mickey mouse appearance of the brain stem on the axial plane (**c**); midbrain-pons ratio <0.12 (**d**)

2.4.2 Synucleinopathies

2.4.2.1 Disease with Lewy Bodies (DLB)

DLB is the second most common synucleinopathy after PD, and the second most common neurodegenerative dementia after AD; it accounts for about 15–20% of all cases of neurodegenerative dementia, with an average age at diagnosis of 65 years. The pathologic hallmark of DLB is the abnormal accumulation of intracellular Lewy bodies (namely eosinophilic cytoplasmic inclusions whose primary structural component is represented by the alpha-synuclein protein). The underpinning genetic abnormalities are still unknown.

DLB clinical presentation is characterized by progressive memory loss, attention deficit, visual hallucinations, gait disturbances, rigidity and slowed movements, with additional manifestations that may also include sleep disorders and behavioural changes; from a clinical standpoint, to some extent DLB may resemble to AD or PD dementia, thus raising a problem related to differential diagnosis. At present genetic and laboratory findings do not contribute to solve this caveat, with the distinction made even harder to apply due to the lack of specific findings also at conventional imaging. Indeed MRI sequences show no pathognomonic sign, with the only remarkable findings represented by little hippocampal and posterior regions atrophy; on SWI the absence of the swallow tail sign (the normal imaging appearance of nigrosome-1 within the substantia nigra on axial susceptibility weighted images) is also considered a sensitive marker for both DLB and PD with high positive predictive value; however, it is generally visible only in late disease stages. In this setting, DAT scan may give a significant contribution to DLB differential diagnosis, showing deficient dopaminergic presynaptic transport in substantia nigra and striatum not consistent with AD; this deficient uptake generally results in a bilateral dot sing, instead of the normal bilateral comma-shaped appearance.

2.4.2.2 Multiple Systemic Atrophy (MSA)

MSA is a sporadic rare neurodegenerative disorder and one of the most well-recognized synucleinopathies; it has an overall prevalence of 3:100,000, with a median age at onset of approximately 66 years and a median survival time of 8 years from initial diagnosis. MSA is characterized to a variable extent by cerebellar ataxia, autonomic dysfunction, parkinsonism and corticospinal dysfunction. We can distinguish two main clinical forms of MSA, the one with predominantly parkinsonian signs (MSA-P) and the one with predominantly cerebellar signs (MSA-C), depending on the prevalent non-autonomic symptoms observed. Such symptom variability is related to the sites within the brain where neurons and glial cells are more affected by abnormal alpha-synuclein intracellular deposition, respectively, striatonigral pathway in MSA-P or olivopontocerebellar circuits in MSA-C. Parkinsonism, rigidity, postural instability and gait disturbance are typical of MSA-P, whereas ataxia, loss of movement coordination, tremor and nystagmus are typical of MSA-C. Degeneration of autonomic nuclei in the brainstem resulting in autonomic failure (more frequently urogenital and cardiovascular disorders) is an

almost constant finding in both the variants; in more advanced phases sleepiness, dysphonia, dysphagia, dystonia and excruciating pain can also occur.

MSA can be suspected based on clinical and neuroimaging findings. For MSA-P, the most reliable sign on conventional MRI is represented by putaminal atrophy, with relative central hypointensity on T2* images due to iron accumulation and peripheral hyperintensity on T2w images due to reactive astrogliosis. Conversely, in MSA-C the most evocative signs are represented by severe isolated atrophy of cerebellum and brainstem (especially olivary nuclei and middle cerebellar peduncle) coupled to a cruciform signal hyperintensity in the central pons known as hot cross bun sign (due to the selective degeneration of transverse pontocerebellar fibres and median pontine raphe nuclei with relatively spared corticospinal tracts) (Fig. 2.9). Although specific for MSA-C, hot cross bun sign only appears in case of advanced disease progression. Among NM techniques, I-123 ioflupane SPECT is usually normal in these patients. In recent times, the identification of new PET radiotracers as well as the resort to diffusivity analysis coupled to automated volume loss quantification on volumetric MRI acquisitions have been proposed as a tool for distinguish MSA from other synucleinopathies and from tauopathies; however, these studies are still embryonic and far from clinical widespread application [26].

2.4.2.3 Parkinson Disease (PD)

Also known as idiopathic parkinsonism, PD is a neurodegenerative synucleinopathy whose onset is characterized by movement disorder with the triad resting tremor, rigidity and bradykinesia; it accounts for about 80% of all parkinsonian syndromes, with a peak age at onset of 60 years. Although PD usually starts as a movement disorder, it can progress to dementia over time, with manifestations involving

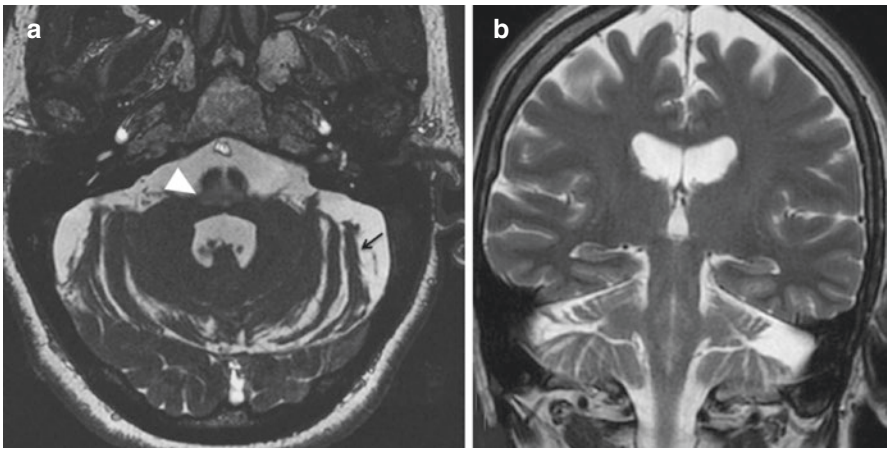

Fig. 2.9 Most prominent MRI features of MSA-C: severe isolated atrophy of cerebellum and brainstem on the axial (**a**) and coronal (**b**) planes; diffuse ex vacuo dilated cerebellar folia (**a**, *black arrow*), associated with a mild cruciform signal hyperintensity in the central pons (**a**, *white arrowhead*)

cognitive and behavioural domains. PD pathogenesis is related to the progressive degeneration of dopaminergic neurons within the substantia nigra (pars compacta), with symptoms appearing when 80% striatal dopamine is depleted. The aetiology of PD is still largely unknown, with more than 30 genetic risk loci identified till now; indeed, only a minority of all PD cases recognize a monogenic cause (rare familiar and juvenile variants), whereas the large majority of cases is sporadic and characterized by genetic complexity.

PD is responsive to dopaminergic drugs (i.e. apomorphine and levodopa) and deep brain stimulation; therefore, its early and accurate diagnosis is crucial for optimal patients management and monitoring. Initial imaging findings are subtle and inconstant, requiring an appropriate examination and an accurate interpretation to be identified. The most relevant MRI feature is the loss of the normal swallow tail appearance on axial SWI at the level of substantia nigra pars compacta (reported diagnostic accuracy of about 90%), with or without a mild hyperintensity on T1w of substantia nigra and red nuclei due to abnormal iron accumulation; non-specific diffuse cerebral volume loss can also be observed (Fig. 2.10). Also in this case DAT scan can be used to confirm the diagnostic pattern of PD, especially in patients with uncertain clinical diagnosis. Abnormal DAT scan in PD shows a marked loss of the normal comma-shaped or crescent-shaped tracer uptake in the striatum; a differentiation between PD and atypical parkinsonism is be possible by using different tracers [27].

2.4.3 Cerebral Amyloid Angiopathy (CAA)

CAA is a relatively common clinical entity in the elderly detected in approximately 10–30% of elderly brains, with a prevalence estimated to rise from about 2% at 65 years to 12% in subjects over 85 years; in addition pathological hallmarks of CAA have been found in about 80% with AD and 40% with CAA present with AD

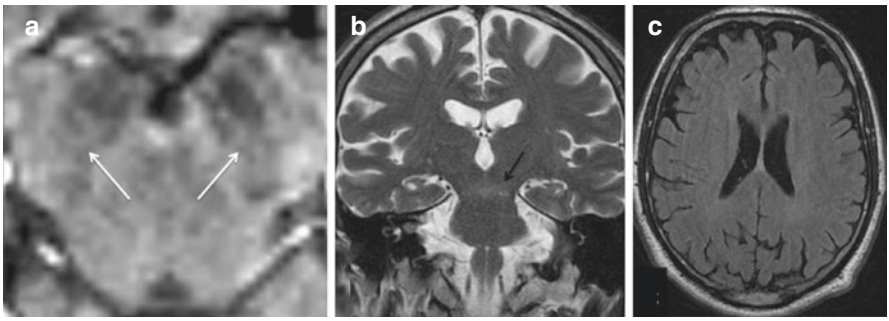

Fig. 2.10 Most relevant MRI features of PD: partial loss of the normal swallow tail appearance on axial SWI at the level of substantia nigra pars compacta (**a**, *white arrow*) coupled to mild T2w signal alteration on the coronal plane (**b**); no significant atrophy is observed in the supratentorial compartment (**c**)

symptoms during their lives. This significant overlap between CAA and AD must be framed in the common presence of amyloid deposits in brain tissue; in CAA such insoluble oligomers deposition is mainly found in blood vessel primarily at the level of smooth muscle cells, but also in pericytes and endothelial cells. It was hypothesized that amyloid produced by neurons is drained along the perivascular spaces within brain parenchyma up to the abluminal portion of the tunica media, the surrounding smooth muscle cells and in the adventitia, where it deposits under specific conditions thus causing diffuse angiopathy [28].

Generally sporadic and occasionally found as a familiar disorder, CAA is a possible cause of MCI and dementia; cognitive impairment in this setting can be both gradual (due to a vascular dementia caused by lobar cerebral microhaemorrhages and ischemic leukoencephalopathy) or rapidly progressive (in case of recurrent haemorrhages or inflammatory angiopathy).

At MRI the two primary features of CAA are represented by microbleeds and WMH (more or less confluent depending on the severity of ischemic leukoencephalopathy and generally sparing subcortical fibres), where the relation between microbleed burden and cognitive impairment severity is known to follow an exponential trend. Cerebral microbleeds are defined as perivascular deposits of haemosiderin from millimetric micro-haemorrhages, usually located at grey–white matter junction or in the cerebellum but sparing basal ganglia and pons; microbleeds can be distinguished only on T2* sequences as small foci of blooming artefact, with SWI up to 10 times more sensitive than other T2* images. Other possible findings also include lobar or cerebellar haemorrhages (that tend to spare the basal ganglia and pons), convexity subarachnoid haemorrhage and/or superficial siderosis (as a chronic manifestation of previous convexity subarachnoid haemorrhages, both symptomatic or asymptomatic), dilated perivascular spaces at the level of centrum semiovale and corona radiate, and microinfarcts or ischemic lacunae (due to acute, subacute or chronic ischemic insult).

2.4.4 Others

2.4.4.1 Creutzfeldt–Jakob Disease (CJD)

Spongiform encephalopathy encompasses a group of rare neurodegenerative disorders occurring in adult patients and in the elderly, characterized by rapid neuropsychiatric decline, cerebellar/extrapyramidal dysfunction and fatal outcome (generally within 1 year from symptoms onset). Among spongiform encephalopathies, CJD represents the most frequent disorder, with a peak onset between 60 and 75 years; in the large majority (80–90%) of cases, CJD is sporadic (sCJD) although familial, zoonotic and iatrogenic forms have also been described. The triggering event in CJD pathogenesis is the structural and conformational conversion of a naturally existing prion protein (PrPC) into a misfolded and protease-resistant form named *scrapie* prion protein (PrPSc), able to initiate a catalytic conversion of wild-type PrPC into PrPSc (where the aberrant PrPSc is the mould for the pathological conversion of more PrPC); in this pathologic process, the normal synthesis of PrPC

within brain tissues provides an over increasing substrate for this cascade effect. At histological examination, the counterparty of these events is the pathological deposition of amyloid plaques within normal brain tissue, coupled to the vacuolization of neutrophil and normal myelin. Depending on molecular markers observed in affected patients, sCJD can be further divided into subtypes based on two elements: the amino acid at codon 129 in the prion protein gene (subtype MM if methionine, VV if valine, or MV if both) and the size of the protease-resistant core of the abnormal prion protein (subtype 1 if 21 kDa, 2 if 19 kDa or 1 + 2 if both PrPSc types).

sCJD diagnosis relies on the combination of clinical features coupled to the results in one or more para-clinical tests among electroencephalogram (EEG), cerebrospinal fluid (CSF) analysis and/or MRI. EEG is generally aspecific, with the most evocative patterns of alteration only observed in late disease stages. CSF analysis is probably the most sensitive supportive examination, allowing for the detection of a specific protein called 14-3-3 (whose expression is correlated to sCJD with a sensitivity and a specificity of >90%). However MRI abnormalities still represent the most important hallmark for CJD, with alterations visible even before or in case of unremarkable findings at EEG and CSF examination [29].

Most common MRI alterations are represented by symmetric or asymmetric, diffuse or focal restriction of water diffusion associated to a less marked increase in T2-FLAIR signal within cortical and deep grey matter. The aetiology of DWI abnormalities is still poorly understood, probably related to compartmentalization within myelin vacuoles or to abnormal deposition of prion protein somehow restricting free water diffusion. The most typical patterns involve insula, cingulate cortex, superior frontal gyrus, striatum and thalamus (generally with anterior → posterior gradient); peri-rolandic cortex, pulvinar and cerebellum are usually (but not invariably) spared. Usually cortical and deep grey matters are both affected, with the exception of VV1 subtype prominent cortical involvement (almost completely sparing deep grey matter) and of MV2/VV2 exclusive basal ganglia involvement with very limited/absent cortical abnormalities (Fig. 2.11). Cerebellar atrophy can also be observed, especially in later CJD stages.

The intensity of the T2-FLAIR equivalent depends on disease severity and duration; moreover, if NM is performed, the areas of restricted water diffusion and elevated T2-FLAIR signal correspond to PET/CT areas of hypometabolism. MRI features are therefore crucial in case of sCJD clinical suspicion, supporting the diagnosis when typical imaging patterns are observed and possible mimics ruled out, thus guiding the approach to EEG/CSF interpretation.

2.4.4.2 Huntington Disease

HD is an autosomal dominant trinucleotide repeat syndrome due to the expansion of CAG (cytosine-adenine-guanine) trinucleotide in the gene encoding for a protein called *huntintin* located on chromosome 4, abnormally amplified to >35 copies (compare to the normal value <26 copies); the larger is the number of copies the more severe is the disease course, with a progressively earlier onset and a more rapid clinical deterioration. Moreover HD appears at an earlier age in descendants of affected patients, a phenomenon called genetic anticipation that is due gene

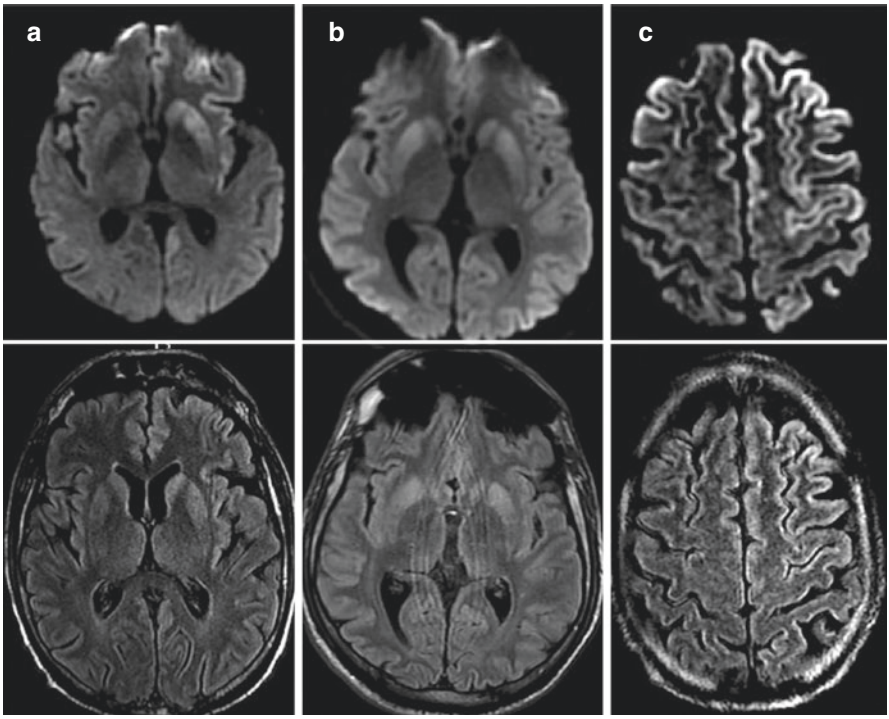

Fig. 2.11 Three possible patterns of signal alteration in sCJD (first row DWI sequences, second row FLAIR sequences): usual asymmetric basal ganglia involvement with mild DWI restriction of frontal cortex (**a**); more unusual bilateral and symmetric basal ganglia involvement (**b**); rare selective cortical involvement (**c**)

instability during cell division caused by the abnormal number of these repeats; generally the trinucleotide repeats expand until the gene stops functioning. Huntingtin protein has a prominent role in protein trafficking, vesicle transport, synaptic (i.e. dopaminergic) signalling and neural cells apoptosis; therefore, its loss or toxic gain of function is responsible for premature neurodegeneration due to disruption in many intracellular pathways.

Being HD characterized by an autosomal dominant pattern of inheritance with complete penetrance, the probability of transmitting the mutated gene is 50% and all the individuals with the pathologic allele express the clinical phenotype. Although most serious presentation is generally observed in young adults, HD can also be diagnosed in elderly in case of short CAG expansion, with the highest recorded prevalence ranging between 60 and 69 years; in these cases, atypical parkinsonism as well as cognitive or psychiatric disturbances are the first manifestations, with chorea and deficit in postural control appearing later on in more advanced stages (MCI described up to 15 years before motor symptom onset) [30].

Due to the pervasive impact on dopaminergic circuits, HD is mainly characterized by the loss of GABAergic neurons within basal ganglia, especially in caudate

and putamen nuclei; this neuronal loss is responsible for the most typical HD imaging feature at MRI, characterized by focal atrophy and secondary enlargement of frontal horns of the lateral ventricles (with increased frontal horns width to intercaudate distance ratio or intercaudate distance to inner table width ratio). Indeed it has been demonstrated that striatal atrophy is positively correlated with disease severity and negatively correlated with the number of CAG triplet repeats. Besides the striatum, extra-striatal atrophy can also be observed in thalamus, hypothalamus, globus pallidus, limbic system and cerebellum; occasional findings may also include iron deposition within basal ganglia on SWI and increased T2w signal of the putamen. In preclinical HD as well as in case of atypical clinical presentation with poor motor symptoms, FDG-PET showing striatal hypometabolism or DATscan showing decreased striatal dopamine transporter binding may support MRI findings is guiding the genetic diagnosis.

2.4.4.3 Sporadic Adult-Onset Degenerative Ataxia

Apart from MSA-C, other hereditary or non-hereditary degenerative ataxias can be responsible for sporadic adult-onset degenerative ataxias. Among the hereditary forms, the following are most frequently associated to a later onset >60 years: *Friedreich's ataxia* (FRDA), an autosomal recessive disorder due to the abnormal expansion of GAA triplet (guanine-adenine-adenine) in the *FXN* gene encoding for the protein frataxin, required for normal mitochondrial function within neural tissue; *autosomal recessive cerebellar ataxia type 1* (ARCA1) due to mutations in *SYNE1* gene, required for the synthesis of a protein responsible for the homeostasis in Purkinje cells of the cerebellum; *fragile X-linked tremor/ataxia syndrome* (FXTAS), observed in older (>58 years) pre-mutation carriers of *FMR1* gene (55–200 CGG—cytosine-guanine-guanine repeats), leading to neuronal toxicity and mitochondrial dysfunction (with women less affected than men because of the second X chromosome); *mitochondrial recessive ataxia syndrome* (MIRAS) caused by mutations of the *POLG1* gene encoding the mitochondrial DNA polymerase gamma enzyme. When neither genetic nor acquired causes of late-onset ataxia can be identified, it applies the definition of *non-hereditary sporadic adult onset ataxia (or idiopathic late-onset cerebellar ataxia)*, which further requires epidemiological and genetic studies to fully elucidate the unknown underlying pathogenic mechanism. However, both the hereditary and non-hereditary forms share the most relevant MRI features, including a constant and marked cerebellar atrophy coupled to a variable T2/FLAIR signal alteration within cerebellar lobes, cerebellar pedicles and dentate nuclei; the simultaneous involvement of cerebral white matter, thalamus and corpus callosum is inconstant, whereas brain atrophy is observed with varying degrees in most cases [31, 32].

2.4.4.4 Late-Onset Neurodegeneration with Brain Iron Accumulation (NBIA)

NBIA encompasses heterogeneous group of rare neurodegenerative disorders due to abnormal brain iron deposition, with variable neurological deficits including extrapyramidal symptoms and neuropsychiatric disturbances. At present an over

increasing number of putative genes has been identified, with variable phenotypical and MRI presentation depending on the specific causative mutation. Generally affecting children or young adults, NBIA can also be occasionally observed in elderly population; in these unusual cases, the most common manifestation is represented by a late-onset atypical parkinsonism. When clinical suspicion is raised, MRI and DATscan are required to identify typical findings as well as to rule out PD. The most common NBIA in the elderly is represented by pantothenate kinase-associated neurodegeneration (PKAN) [33], whose most remarkable MRI feature is represented by T2w hypointensity within globus pallidi and substantia nigra (corresponding on SWI/T2* to susceptibility artefacts due to abundant iron deposition) with a central hyperintense spot due to myelin vacuolisation (also known as "eye of the tiger" sign); on spectroscopy, decreased N-acetylaspartate and increased myo-inositol levels can be observed due to neuronal depletion. Other possible NBIAs, such as aceruloplasminaemia or neuroferritinopathy, are only exceptionally observed.

References

1. Chen J, Lin K, Chen Y. Risk factors for dementia. J Formos Med Assoc. 2009;108(10):754–64. https://doi.org/10.1016/S0929-6646(09)60402-2.
2. Przedborski S, Vila M, Jackson-Lewis V. Neurodegeneration: what is it and where are we? J Clin Invest. 2003;111(1):3–10.
3. Cloutier S, Chertkow H, Kergoat M, Gauthier S, Belleville S. Patterns of cognitive decline prior to dementia in persons with mild cognitive impairment. J Alzheimer's Dis. 2015;47:901–13.
4. Tripathi M, Vibha D. Reversible dementias. Indian J Psychiatry. 2009;51 Suppl 1(Suppl 1):S52–5. https://pubmed.ncbi.nlm.nih.gov/21416018.
5. Martin-macintosh EL, Broski SM, Johnson GB, Hunt CH, Cullen EL, Peller PJ. Multimodality imaging of neurodegenerative processes: part 1, the basics and common dementias. AJR. 2016;207:871–82.
6. Martin-macintosh EL, Broski SM, Johnson GB, Hunt CH, Cullen EL, Peller PJ. Multimodality imaging of neurodegenerative processes: part 2, atypical dementias. AJR. 2016;207:883–95.
7. Custodio N, Montesinos R, Lira D, Herrera-Perez E, Bardales Y, Valeriano-Lorenzo L. Mixed dementia. A review of the evidence. Dement Neuropsychol. 2017;11(4):364–70.
8. Han R, Liang J, Zhou B. Glucose metabolic dysfunction in neurodegenerative diseases—new mechanistic insights and the potential of hypoxia as a prospective therapy targeting metabolic reprogramming. Int J Mol Sci. 2021;22:5887.
9. Bega D, Cindy G, Spies W. Is there a role for DAT-SPECT imaging in a specialty movement disorders practice? Neurodegener Dis. 2015;15(2):81–6.
10. Morbelli S, Esposito G, Arbizu J, Barthel H, Boellaard R, Bohnen NI. EANM practice guideline/SNMMI procedure standard for dopaminergic imaging in Parkinsonian syndromes 1.0. Eur J Nucl Med Mol Imaging. 2020;47:1885–912.
11. Bega D, Kuo PH, Chalkidou A, Grzeda MT, Macmillan T, Brand C, et al. Clinical utility of DaTscan in patients with suspected Parkinsonian syndrome: a systematic review and meta-analysis. Park Dis. 2021;43:1–8.
12. Lemoine L, Gillberg P, Svedberg M, Stepanov V, Jia Z, Huang J, et al. Comparative binding properties of the tau PET tracers THK5117, THK5351, PBB3, and T807 in postmortem Alzheimer brains. Alzheimers Res Ther. 2017;9(96):1–13.
13. Leuzy A, Chiotis K, Lemoine L, Gillberg P, Almkvist O, Rodriguez-vieitez E, et al. Tau PET imaging in neurodegenerative tauopathies—still a challenge. Mol Psychiatry. 2019;24:1112–34.

14. Sánchez-juan P, Ghosh PM, Hagen J, Henry M, Grinberg LT, Neil JPO, et al. Practical utility of amyloid and FDG-PET in an academic dementia center. Neurology. 2014;82(21):230–8.
15. Vernooij M. Outline presentation Imaging in cognitive decline: MRI protocols. Why imaging in dementia? Conventional MR imaging: main aim. Patterns of atrophy: imaging considerations MTA: perpendicular recons needed; 2019. p. 1–12.
16. Håkansson C, Torisson G, Londos E, Hansson O, Björkman-burtscher IM, Van Westen D. Reporting frequency of radiology findings increases after introducing visual rating scales in the primary care diagnostic work up of subjective and mild cognitive impairment. Eur Radiol. 2021;31:666–73.
17. Vernooij MW, Pizzini FB, Schmidt R, Smits M, Yousry TA, Bargallo N, et al. Dementia imaging in clinical practice: a European-wide survey of 193 centres and conclusions by the ESNR working group. Neuroradiology. 2019;61:633–42.
18. Van Veluw SJ, Lauer A, Charidimou A, Bounemia N, Xiong L, Gregoire B, et al. Evolution of DWI lesions in cerebral amyloid angiopathy. Evidence for ischemia. Neurology. 2017;89:1–8.
19. Sobański M, Zacharzewska-Gondek A, Waliszewska-Prosól M, Sąsiadek MJ, Zimny A, Bladowska J. A review of neuroimaging in rare neurodegenerative diseases. Dement Geriatr Cogn Disord. 2020;49:544–56.
20. Erkkinen MG, Kim M, Geschwind MD. Clinical neurology and epidemiology of the major neurodegenerative diseases. Cold Spring Harb Perspect Biol. 2018;10(4):a033118.
21. Staffaroni AM, Elahi FM, McDermott D, Marton K, Karageorgiou E, Sacco S, et al. Neuroimaging in dementia. Semin Neurol. 2018;37(5):510–37.
22. Van Oostveen WM, de Lange ECM. Imaging techniques in Alzheimer's disease: a review of applications in early diagnosis and longitudinal monitoring. Int J Mol Sci. 2021;22:2110.
23. Oldan JD, Jewells VL, Pieper B, Wong TZ. Complete evaluation of dementia: PET and MRI correlation and diagnosis for the neuroradiologist. AJNR. 2021;42(6):998–1007.
24. Albrecht F, Mueller K, Ballarini T, Lampe L, Diehl-schmid J, Fassbender K, et al. Unraveling corticobasal syndrome and alien limb syndrome with structural brain imaging. Cortex. 2019;117:33–40.
25. Rohrer J. Structural brain imaging in frontotemporal dementia. Biochim Biophys Acta. 2012;3(1822):325–32.
26. Watanabe H, Riku Y, Hara K, Kawabata K, Nakamura T, Ito M, et al. Clinical and imaging features of multiple system atrophy: challenges for an early and clinically definitive diagnosis. J Mov Disord. 2018;11(3):107–20.
27. Gayed I, Joseph U, Fanous M, Wan D, Schiess M, Ondo W, et al. The impact of DaTscan in the diagnosis of Parkinson disease. Clin Nucl Med. 2015;40(5):390–3.
28. Biffi A, Greenberg SM. Cerebral amyloid angiopathy: a systematic review. J Clin Neurol. 2011;7:1–9.
29. Fragoso DC, Lio da Mota Gonçalves Filho A, Torres Pacheco F, Rodi Barros B, Aguiar Littig I, Hoffmann Nunes R, et al. Imaging of Creutzfeldt-Jakob disease: imaging patterns and their differential diagnosis. Radiographics. 2017;37(4):234–57.
30. McColgan P, Tabrizi SJ. Huntington's disease: a clinical review. Eur J Neurol. 2018;25(1):24–34.
31. Cocozza S, Pontillo G, De Michele G, Di Stasi M, Guerriero E, Perillo T, et al. Conventional MRI findings in hereditary degenerative ataxias: a pictorial review. Neuroradiology. 2021;63:983–99.
32. Lieto M, Roca A, Santorelli FM, Fico T, De Michele G, Bellofatto M, et al. Degenerative and acquired sporadic adult onset ataxia. Neurol Sci. 2019;40:1335–42.
33. Tofaris GK, Revesz T, Jacques TS, Papacostas S, Chataway J. Adult-onset neurodegeneration with brain iron accumulation and cortical alpha-synuclein and tau pathology. A distinct clinicopathological entity. Arch Neurol. 2007;64:280–2.

Neurovascular Emergencies in Geriatric Patients

3

Giuseppe Maria Di Lella, Luca Ausili Cefaro, and Cesare Colosimo

3.1 Introduction

"Neurovascular emergencies" represent an ample concept that comprehend not only the classical concept of "cerebrovascular disease," in which resides the ischemic and hemorrhagic arterial stroke, the effect of the cerebral venous thrombosis, and the causes of subarachnoid hemorrhage (SAH), but also the bleedings related to head trauma, such as the epidural and subdural hematomas. It is of common knowledge that cerebrovascular disease alone represents the third more common cause of death in the developed world and the first cause of disability in the adult population. In fact almost half of the patients do not regain the normal physical abilities and need long-term assistance from both their family and the healthcare systems. These concepts are much more important in the elderly, due to the higher incidence of specific risk factors, like high blood pressure, atherosclerosis, and, regarding the specific problems related to traumatic hemorrhages, the anatomical predisposition of the old people to experience various type of falls. The rate of stroke event doubles each 10 years after the age of 55 years, making clear how the vast majority of lesions occur in this group. Considering the progressive increase of elderly in the population of the developed countries, this kind of pathologies has an increasing social impact and need to be addressed in the best possible way. More disturbing is the fact that cerebrovascular disease, and in particular stroke, is increasing globally. The future does not look very bright considering that by 2050 the population aged over 65 years is expected almost to triple; in effect the percentage of the population over the age of 65 years is steadily increasing and is expected to continue in the foreseeable future, with people over the age of 80 years now among the fastest

G. M. Di Lella · L. Ausili Cefaro · C. Colosimo (✉)
Department of Radiological Sciences, Fondazione Policlinico Universitario A. Gemelli IRCCS, University of the Sacred Heart, Rome, Italy
e-mail: giuseppemaria.dilella@policlinicogemelli.it; luca.ausilicefaro@policlinicogemelli.it; cesare.colosimo@unicatt.it

G. Guglielmi, M. Maas (eds.), *Imaging in Geriatrics*, Practical Issues in Geriatrics, https://doi.org/10.1007/978-3-031-14877-4_3

growing subset of the population. Effective management of patients who have cerebrovascular disease depends on accurate diagnosis. The neuroradiological studies and treatments play a major role in the diagnosis and treatment of patients often affected also by other age-related symptoms and pathologies (i.e., dementia, diabetes, etc.). The wide diffusion, in the last two decades, of high-quality CT and MRI systems has allowed better and faster anatomic and functional evaluation, or exclusion, of ischemic and hemorrhagic lesions of arterial or venous origin, especially with the availability of fast and reliable CT and MR perfusion techniques. The "need of speed" in these often uncooperating patients is in fact of paramount importance in order to achieve a proper diagnosis. Neuroradiology plays an established role also in the therapeutic phase, due to the continuous advance of the materials and techniques available (i.e., flow diverter stent in the treatment of aneurysms). Technological advancements have led to advanced interventions such as angioplasty, stenting, and carotid endarterectomy for selected stroke patients and expanded access to acute stroke services through tele stroke programs. In the past decade, we have also enhanced our understanding of the mechanisms of brain injury, repair, plasticity, and recovery that hopefully will improve our future post stroke treatments. In the United States from 1997 to 2007, the stroke death rate fell 44.8%, and the actual number of stroke deaths declined 14.7%, making stroke the fourth instead of the third leading cause of death.

3.2 Ischemic Stroke

Stroke is the fifth leading cause of death among elderly persons in the United States [1]. While stroke can occur at any age, ischemic stroke is predominantly a disease of the elderly, as age is the most substantial nonmodifiable risk factor. Stroke risk increases with age, and in 2009, 66% of persons hospitalized for stroke were 65 years or older. The growing longevity of human populations and the associated multimorbidity explain how the number of accidental strokes is projected to double between 2010 and 2050, with most strokes occurring in adults over the age of 75 years [2]. Additionally, this age group (>75 years) experiences more hospitalization stays and higher mortality post-stroke. Over 80% of strokes result from ischemic damage to the brain due to an acute reduction in the blood supply. Around 25–35% of strokes present with large vessel occlusion, and the onset of patients in this category is often characterized by severe neurological deficits [3, 4].

Stroke is a complex disease that can be caused by multiple potential etiologies; it is really a heterogeneous disorder with more than 100 pathologies implicated in the pathogenesis. However the end result is mostly represented by the occlusion of an artery, which almost immediately leads to hypo perfusion of the tissue segment supplied by that vessel; the affected parenchyma usually consists of a severely hypo perfused (cerebral blood flow [CBF] $\leq$10 mL/100 g/min) central infarct core where the damage is irreversible. It is bordered by the critically hypo perfused (CBF 10–20 mL/100 g/min) ischemic penumbra (tissue-at-risk), where the injury may be reversed if timely reperfusion occurs. Collaterals aim at preserving as much

penumbral tissue as possible. With time (minutes to hours) the infarct core expands at the expense of the penumbra. This is also helped by the mass effect of the edematous tissue on the neighboring arteries. The penumbra is surrounded by other involved tissue, which is not at risk of infarction, the so-called benign oligemia (CBF >20 mL/100 g/min) [5] (Figs. 3.1 and 3.2).

Stroke imaging (CT and/or MR) is crucial in the handling of such patients and has to be performed in a fast and efficient manner; early diagnosis and assessment are important in the treatment of acute ischemic stroke (AIS). The main roles of imaging are: exclude an intracranial hemorrhage, define the ischemic region, distinguish between infarct core and penumbra, and finally depict the vessel status. In particular:

– Nonenhanced computed tomographic (CT) imaging represent the first imaging step and is regularly used to exclude hemorrhage (classically detected as a lesion with high CT density, 60–90 HU) and other diseases, and indicate early changes in AIS, such as obscuration of the lentiform nucleus/insular ribbon, due to the loss of the normal slight hyperdensity over the surrounding white matter structures following the onset of cytotoxic edema, hyperdensity of the feeding artery,

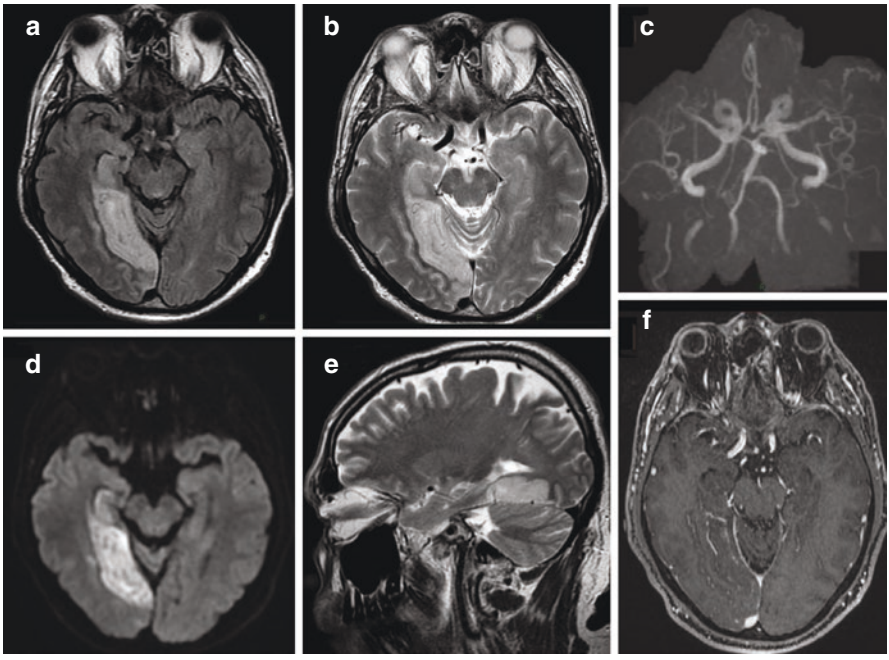

Fig. 3.1 Right occipital ischemic stroke. A 75-year-old woman with visual disturbance (hemianopsia). FLAIR (**a**), T2 (axial and coronal; **b**, **e**), and DWI (**d**) show the classic appearance and MR imaging of an acute infarct in the PCA territory, with hyperintensity in the cortex and subcortical white matter of the right deep occipital lobe. Angio-TOF sequences (**c**) and T1 C+ MR (**f**) confirm the presence of a right P2 segment occlusion

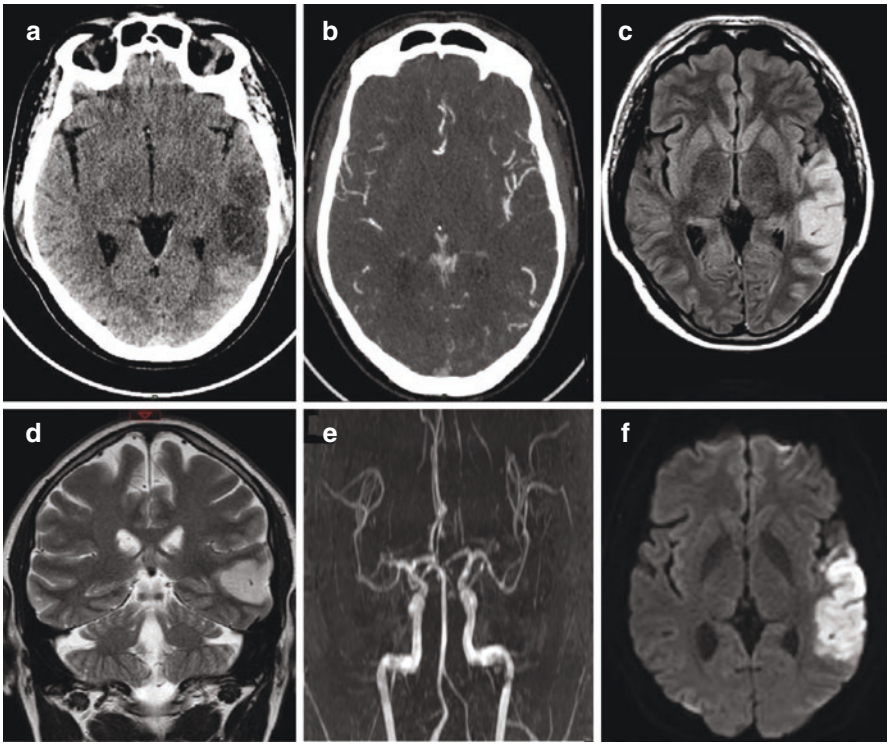

Fig. 3.2 Left temporal-parietal ischemic stroke. A 71-year-old man with aphasia and sudden right hemiparesis; classic appearance of an early subacute cerebral infarct. Axial CT scan (**a**) in the ER show a low-density area with loss of SB/SG differentiation and swollen appearance of the involved temporo-parietal cerebral convolutions; axial MIP view of the CTA (**b**) shows normal cerebral intracranial district ("circle of Willis"). MR FLAIR axial and DWI (**c**, **f**) and T2 coronal TSE (**d**) obtained 48 h after the initial onset of speech difficulties demonstrate an area of hyperintensity in the same region, associated with hyperintensity in DWI images, due to typical diffusion restriction in the acute phase (within 7 days). Angio-MRI (TOF 3D, **e**) confirms the normal parity of arterial circulation of the base of the skull

loss of the gray–white matter interface, and swelling of the cerebral tissue. The Alberta Stroke Program Early Computed (ASPECTS) is a CT score system that can be used to quantify the extent of ischemia: 10 brain regions are assessed dichotomously for the presence (or not) of early signs of ischemic stroke, resulting in a range 0–10, with 1 point subtracted for any evidence of early ischemic change in each region defined on the CT scan; baseline CT showing a large area of hypo attenuation is considered as an indicator of poor outcome (ASPECTS <7).

– Hypo perfusion abnormalities can be accurately measured using perfusion CT (PCT) and MR perfusion-weighted imaging (PWI); these are able to define the area of irreversible severe ischemia, with complete loss of oxygen and glucose supply and resultant depletion of energy stores, cellular necrosis, and cavitation ("ischemic core") and also the area surrounding the ischemic core, characterized

by moderate ischemia and cellular dysfunction but not cell death, which is potentially reversible with prompt reperfusion ("ischemic penumbra"). Perfusion CT (PCT) is one of the best imaging techniques readily available in an emergency room to evaluate acute stroke patients for the presence, quantity, and distribution of the ischemic penumbra, through a dynamic technique involving sequential CT data acquisition [6] in suspect brain areas during an intravenous bolus injection of iodinated contrast medium. The most relevant and used parameters are: cerebral blood flow (CBF), cerebral blood volume (CBV), average transit time (MTT), time-to-peak (TTP). In the ischemic penumbra, cerebral perfusion is impaired, but self-regulation is preserved; vasodilation and collateral recruitment lead to an increase in CBV. Quantification of ischemic "core" (CBF <30%) and estimation of "penumbra" or tissue at risk (T-max >6 s) can provide immediate information for treatment decision-making. Clinical trials have shown that perfusion mismatch ratios of core/penumbra greater than 1.8 may indicate the eligibility for endovascular treatment (EVT) [7, 8].

Some institutions have MRI available anytime and prefer it over CT, when the patient's condition permits, because of the additional information it provides. Diffusion-weighted magnetic resonance imaging (MRI) is the most useful method for detecting hyper acute ischemia and the "ischemic core" while PWI, in selected cases, could be used to evaluate hypo perfusion abnormalities. MRI can detect abnormal cytotoxic edema (this restricted diffusion areas are seen as bright on b1000 DWI images and with low signal on the corresponding automatically calculated apparent diffusion coefficient [ADC] maps) in the early stage and show clear discrimination between ischemic lesions and normal brain tissue. After the acute phase of decreasing ADC to the lower value, at 1–4 days, the ADC subsequently rises and "pseudo normalizes" to transient equivalence with normal brain tissue (although the tissue is infarcted), typically at 1–2 weeks, and keeps rising until the ADC values would result elevated in the chronic stage [9]. Since the signal intensity on DWI depends on ADC as well as the T2 information inherent in the $b = 0$ echo-planar image, net hyper intensity on the DWI images may be due to low ADC or T2 effects: the "T2 shine-through." The DWI-FLAIR mismatch depends on the lack of marked parenchymal hyper intensity on fluid attenuated inversion recovery (FLAIR) on early MRI study and has been used as an MRI parameter to widen the treatment window, with intravenous bolus of r-TPA, in patients with AIS with onset of symptoms beyond 4.5 h and/or in case of unknown onset time, as in the "wake-up" stroke. Neuroimaging methods, particularly MRI, based on PWI parameter and DWI lesion volumes, may allow us to identify the ischemic penumbra and predict brain tissue viability in patients with AIS, although criteria to define clinically relevant mismatch are not yet standardized [10] (Fig. 3.3).

– Obviously the evaluation of intracranial arterial vessels and collateral circulation, made possible through this kind of imaging modalities, is of paramount importance and is achieved by CT or MR angiography. The study should cover the entire arterial tree, from the aortic arch to the vertex. MRI provides the advantage of noncontrast imaging of the intracranial arteries using the flow-sensitive

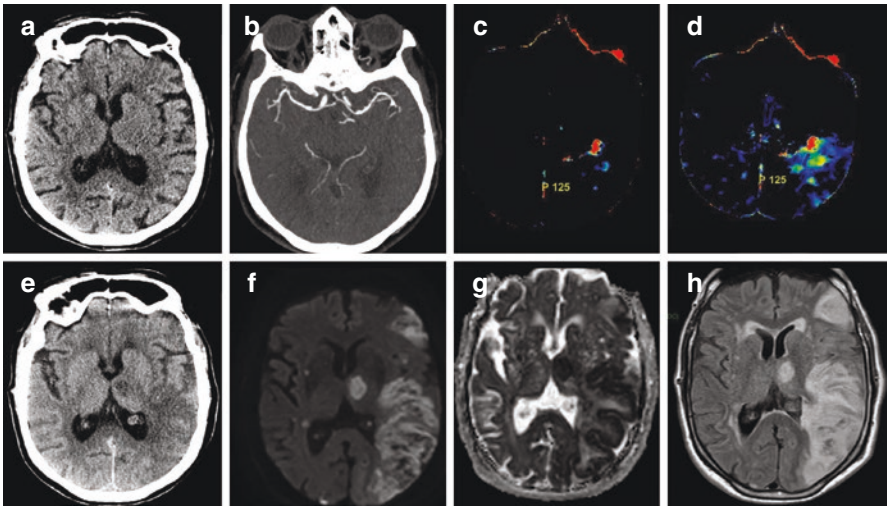

Fig. 3.3 CT, CTA, CTP, and MRI evaluation in the left MCA territory stroke. Normal appearing non-contrast CT scan in the ER of a 76-year-old female with sudden onset of aphasia (**a**). Axial MIP view of the CTA (**b**) shows a distal left MCA occlusion, while CT perfusion (**c**, **d**) shows an infarct, with core–penumbra mismatch in the left MCA territory. Non-contrast CT obtained 48 h after initial onset of speech difficulties (**e**) shows the classic appearance of an early subacute cerebral infarct. Note the wedge-shaped, low-density area involving both the gray and white matter in the left MCA distribution and in the left thalamus. Follow-up MRI with axial DWI (/ADC) image (**f**, **g**) and FLAIR (**h**) in the same patient show hyperintensity in the same region within the left MCA territory. The DWI hyperintensity is due to true diffusion restriction, typical in the acute phase (within 7 days)

time-of-flight (TOF) technique. Multiphase or dynamic CTA represents the fast scanning protocols and is timed to optimize the acquisition in the arterial phase, an independent predictor of radiological and clinical outcomes in patients with AIS [11]. CTA provides information of arterial, capillary, and venous phases of cerebral arteries. Thus the radiological report should comment upon: (a) *site of occlusion*; this is of utmost importance since large vessel occlusions produce severe neurological symptoms and eventually result in poor outcomes; and (b) *details of collateral circulation,* which are of paramount importance, since the extent of collateralization is a predictor of final infarct volume and thus the clinical outcome. The collateral circulation plays a crucial role in the pathophysiology of ischemic stroke and is closely related to the treatment response and the patient's prognosis [12]. The presence of good collateral circulation helps to sustain the penumbral area and increase the rate of successful reperfusions [13]. It was shown that the rate of neuronal loss varies greatly depending on the state of the collaterals, which can maintain a stable penumbra for several hours after the onset of occlusion (Fig. 3.4).

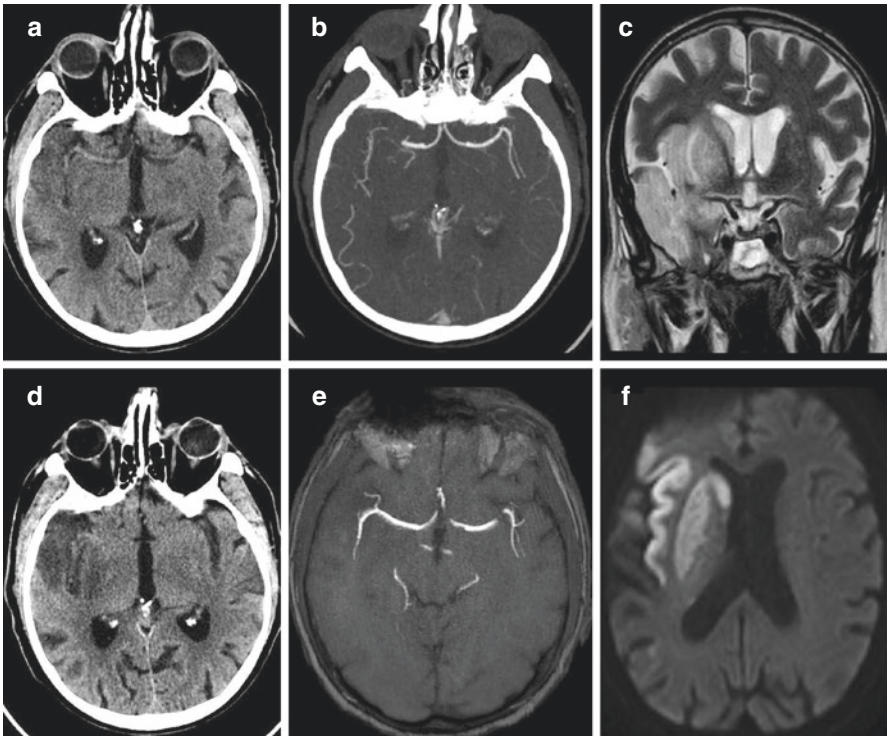

Fig. 3.4 Artery occlusion in a right temporal ischemic stroke. A 71-year-old man with confusional state and sudden onset of left hemiparesis. CT axial documents tenuous right temporo-polar hypodensity with initial loss of SB/SG differentiation (**a**). CTA demonstrates the occlusion of the M1 segment of the right middle cerebral artery (**b**); note the hyperdensity of the horizontal section of the rACM on the basal images (**a**). The CT follow-up after 6 h shows a better defined area of low-density, with loss of SB/SG differentiation and swollen appearance of the temporo-insulare cerebral convolutions involved (**d**). MR axial DWI and T2 coronal TSE confirm the lesion, represented by an area of T2 hyperintensity in the same region, associated with hyperintensity in DWI images, due to typical diffusion restriction in the acute phase (within 7 days, **c**, **f**). Angio-TOF sequences document re-habilitation of the right M1 segment of the ACM (**e**)

Treatments involve implementing strategies to obtain the reperfusion of the "at risk" brain tissue and are based on intravenous and intra-arterial administration of thrombolytic drugs and the application of various thrombectomy devices during angiographic procedure and fluoroscopic guidance (the approved devices have differing mechanisms of action: clot retrievers, aspiration device, and stent retrievers). Intravenous thrombolysis with intravenous recombinant tissue Plasminogen Activator (r-tPA; Alteplase) represents the "standard of care" drug in the case of an acute ischemic stroke. This treatment improves functional outcomes and is more effective if the administration begins in a very early phase of the stroke. Intravenous

recombinant tissue plasminogen activator (r-tPA) remains the standard of care for patients with moderate to severe neurological deficits who present within 4.5 h from symptom onset (Acute Ischemic Stroke [Study ECASS-3] and the American Heart Association/American Stroke Association [AHA/ASA]).

Treatment with intravenous thrombolysis has been tested using imaging biomarkers to select patients with unknown stroke time onset. These biomarkers comprise either penumbral imaging (i.e., perfusion-diffusion MRI or perfusion CT) or MRI-based tissue-clocking—i.e., the mismatch between a visible ischemic lesion on diffusion weighted imaging (DWI) and lack of marked parenchymal hyper intensity on fluid attenuated inversion recovery (FLAIR) on MRI (termed DWI-FLAIR mismatch). The results of recent trials (EXTEND, ECASS4-EXTEND and EPITHET) have shown, in fact, that patients with ischemic stroke 4,·5–9 h after stroke onset or with wake-up stroke with evidence of salvageable brain tissue using CT perfusion or perfusion-diffusion MRI, who were given intravenous Alteplase, have improved functional outcomes compared with those given placebo. The "benefit to risk" ratio seems to be larger in patients who meet automated perfusion mismatch criteria [14].

Outcomes for some patients with acute ischemic stroke and moderate to severe neurological deficits due to proximal artery occlusion are improved with endovascular reperfusion therapy. Efforts to hasten reperfusion therapy, regardless of the mode, should be undertaken within organized stroke systems of care [15]. It is also suggested that the EVT should not just be held back based on age, and even patients over the age of 80 years can benefit from EVT. In conclusion, studies recently demonstrated statistically that endovascular treatment (EVT) combined with intravenous thrombolysis (IVT) has good efficacy and high safety in the treatment of acute intracranial arterial occlusion, and the combination can significantly improve the patients' quality of life, therefore having a high clinical application value [16].

3.3 Nontraumatic Intracranial Hemorrhage

Hemorrhagic conditions should be separated into intracerebral hemorrhage (ICH) and subarachnoid hemorrhage (SAH). These two subtypes of hemorrhage have different causes, different clinical findings, and different treatment strategies.

3.3.1 Intracerebral Hemorrhage (ICH)

Nontraumatic intracerebral hemorrhage (ICH) results from bleeding into the brain parenchyma arising from the rupture of an arterial vessel, most often (>80%) a small arteriole affected by cerebral small vessel diseases (SVD).

Stroke is the second leading cause of death worldwide, and one of the leading causes of disability. ICH is the second most common subtype of stroke after ischemic stroke and accounts for approximately 10–20% of all strokes [17, 18]. A large meta-analysis recently concluded that most likely the incidence of intracerebral

hemorrhage has not changed between 1980 and 2006, but consistent across the various studies was the finding that the incidence of intracerebral hemorrhage increased strongly with age, with persons aged 85 years and over having an almost tenfold increase in yearly risk of intracerebral hemorrhage. Overall case fatality at 1 month for ICH is reported as 40%. ICH outcomes have been well described in the general population, but there is a paucity of data regarding complications and outcomes in the "very elderly" (age >80 years). Available data suggest that patients >85 years have an almost tenfold increase in yearly risk of ICH compared to patients aged 45–54 years. As the population ages, the incidence of ICH in the very elderly will likely increase, and the number of Americans aged >65 years is projected to more than double by 2060 [19, 20].

More than 50% of primary ICH events are directly correlated with hypertension as a risk factor, whereas ≈30% are known to be associated with cerebral amyloid angiopathy (CAA). Deep perforator arteriopathy is linked with hypertension (though not exclusively) and is a frequent cause of nonlobar or deep ICH in the basal ganglia or brainstem but also contributes to lobar hemorrhage (Fig. 3.5).

CAA is caused by amyloid beta deposition in cortical and leptomeningeal blood vessels and is a major contributory cause of lobar ICH. Other ICH risk factors are genetic factors, diabetes, alcohol intake, smoking, oral anticoagulant treatment, drug abuse, and older age. Intracerebral hemorrhage can occur as a complication of a preexisting lesion, such as vascular malformation or tumor, which is then referred to as secondary intracerebral hemorrhage (15–20%) [21–23].

The clinical presentations of ICH and ischemic stroke are similar, typically consisting of abrupt onset of a focal neurologic deficit. Decreased level of consciousness, vomiting, headache, seizures, and very high blood pressure (BP) might suggest the presence of ICH. However, none of these symptoms/signs is specific enough to distinguish hemorrhagic from ischemic stroke [24].

Intracerebral hemorrhage is therefore a life-threatening medical emergency that requires timely diagnosis; brain imaging is essential to reliably distinguish ICH from ischemic stroke, usually with a rapid noncontrast CT (NCCT) which is highly sensitive for all forms of acute intracranial hemorrhage, is a fast technique, with excellent sensitivity, also in noncooperative patients, to identify acute ICH, and given its wide availability is considered the gold standard for the diagnosis of ICH in the ER departments. Beyond the diagnosis of ICH, NCCT can provide useful elements such as ICH location, intraventricular extension, hydrocephalus, presence and degree of edema, and midline shift or brainstem compression secondary to the mass effect from the hematoma. Moreover, NCCT allows to quantify the volume of a hematoma and determine its approximate age, by evaluating the density of the lesions, measured in Hounsfield units (HU), according to the value of X-ray attenuation corrected for the attenuation coefficient of water; HU for water is equal to 0, blood is between 30 and 45, gray substance is between 37 and 45, white substance is between 20 and 30, whereas bone is between 700 and 3000. On CT, an acute ICH typically presents as a hyper dense mass within the brain parenchyma showing Hounsfield Units (HU) of 50–70. Within 1–6 weeks, the ICH becomes isodense (="subacute" ICH) typically showing a decrease of attenuation of 1.5 HU a day.

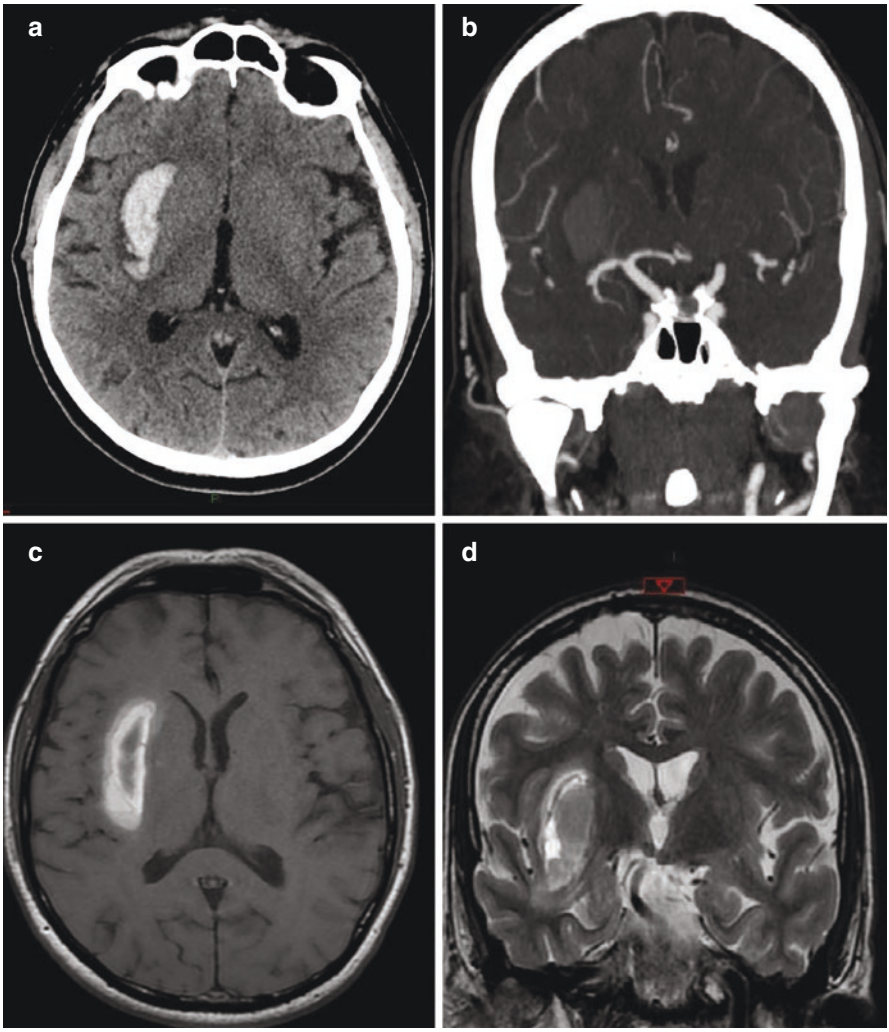

Fig. 3.5 "Typical" primary hemorrhage in the right lentiform nucleus. A 72-year-old man with hypertension and ASA therapy, the axial non-contrast CT study in ER shows the classic appearance of an acute hemorrhage in the R basal ganglia involving the putamen and external capsule (striatocapsular), with minimal surrounding edema, without significant mass effect (**a**). CTA, in the coronal plane, shows mild displacement of the lenticulostriate arteries. There is no spot sign that would indicate active bleeding. No underlying vascular lesion was found (**b**). Follow-up MRI with axial T1 TSE (**c**) and coronal T2 TSE (**d**) shows the physiological evolution in the early subacute phase of the striatocapsular hemorrhage, due to transformation in intracellular methemoglobin

"Chronic" ICHs present as a hypodense mass compared to the surrounding brain parenchyma [25, 26]. CT angiography (CTA) or MR angiography are appropriate initial investigations to detect macrovascular bleeding sources. Initial diagnostic accuracy studies (comparing acute noninvasive angiography with the gold standard,

digital subtraction angiography) suggested high specify and sensitivity. Contrast-enhanced CTA performed <96 h from symptom onset has a high accuracy for predicting underlying vascular anomalies, with sensitivities ≥95% and specificities approaching 100%. Positive and negative predictive values have also been reported to be in excess of 97% [27–29]. A comprehensive diagnostic workup of ICH etiology is needed in ICH survivors to inform patients and relatives about the risk of recurrence as well as strategies for secondary prevention. MRI is superior in detecting markers of SVD including white matter lesions, lacunas, perivascular spaces, cerebral micro bleeds, cortical superficial siderosis, and atrophy. A comprehensive workup of ICH etiology should, therefore, include an MRI in the days/weeks following the acute ICH event including T2/FLAIR, DWI, SWI/T2* and contrast-enhanced sequences, as well as MR angiography [30, 31] (Fig. 3.6).

ICH patients should ideally be treated in a comprehensive hospital environment, involving a multidisciplinary organization team comprising neurology, neurosurgery, neuroradiology, intensive care, emergency medicine, and internal medicine, possibly being admitted to a stroke unit, in order to constantly monitor the patient's

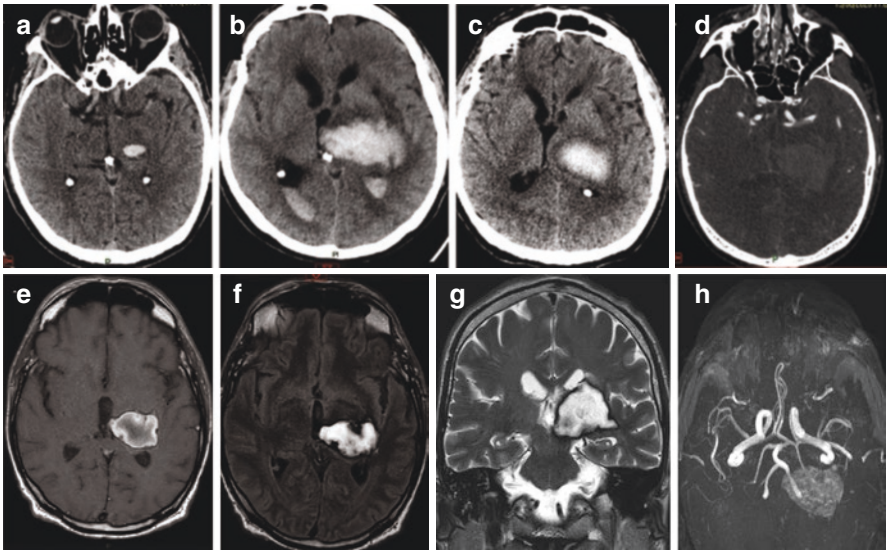

Fig. 3.6 "Typical" intra-axial hemorrhage in the left thalamus. A 72-year-old woman with sudden right loss of strength and dysarthria. Axial CT study in ER show a small hyperacute hemorrhage in the left thalamus with minimal surrounding edema ("typical" intra-axial hemorrhage, **a**). Axial CT at 24 h demonstrates huge increase of the blood collection and the mass effect, with extension of the bleeding in the ventricular system, also in the fourth ventricle (not shown) (**b**). The subsequent CT angiography did not show arterial or venous malformations, but demonstrated further enlargement of the hematoma (**d**). Follow-up MRI with angio-TOF sequences at 1 month (and CT, **c**) evidentiate size reduction of the collection, due to the disappearance of surrounding edema and physiological evolution of the blood components: hemosiderin in the periphery (black ring) and mostly deoxyhemoglobin in the core (**e**–**g**). No vascular malformation was found on the TOF angiographic sequence (**h**)

vital parameters and reduce/eliminate the factors that determine ICH (modifiable factors), with stabilization of blood pressure, suspension/reduction of anticoagulant drugs, and possibly administration of prothrombotic drugs. The role of surgical therapy remains controversial and surgical evacuation of supratentorial hematomas should be considered only as a lifesaving measure in deteriorating patients. The only condition in which there is consensus in favor of surgical intervention is in cerebellar hematomas with clinical or imaging signs of hydrocephalus and/or brainstem compression. In these cases, surgical decompression and hematoma evacuation should be performed as soon as possible in the vast majority of cases [32, 33].

3.3.2 Subarachnoid Hemorrhage (SAH)

Subarachnoid hemorrhage (SAH) is defined as blood in the cerebrospinal fluid contained in the basal cisterns and the sub-arachnoid space of the cerebral hemispheres, between the arachnoid mater and the pia mater [34].

Subarachnoid hemorrhage (SAH) is a potentially fatal disease that mainly affects middle-aged patients, with a mean age of 60 years [35, 36]. Yet, due to better general health and improved life expectancy, the number of hospital admissions of elderly SAH patients is constantly increasing; recently, the annual incidence of SAH in persons aged 70 years was estimated to exceed 25/100,000. The incidence of aneurysmal subarachnoid hemorrhage (aSAH) is known to rise with age, especially in women. Both the number of elderly patients with aSAH and the total incidence have therefore been estimated to be increasing. In addition to the characteristics of elderly aSAH, such as a high rate of poor clinical grade on admission, severe aSAH on initial computed tomography (CT) scan, and general complications, the most serious problem is a high rate of poor outcome. In particular, several studies indicate that poor outcome significantly increases in the patients over age 75 years. The death rate in patients increases with age [37, 38] (Figs. 3.7 and 3.8).

Subarachnoid bleeding usually occurs rapidly over several seconds. In some patients, it is preceded by a "warning headache," or minor bleeding, several days or weeks ahead of the major rupture. The major SAH episode presents as the sudden onset of severe, usually diffuse, headache, which patients describe as the "worst headache of their life"; vomiting, cessation of activity, and decreased level of consciousness are frequently present. Ruptured aneurysms are the cause in 85% of patients, whereas 10% fit into the pattern of so-called nonaneurysmal perimesencephalic hemorrhage, a relatively innocuous condition. The remaining 5% are caused by various rare causes (arteriovenous malformations that abut on pial surfaces can bleed. Amyloid angiopathy, severe hypertension, bleeding disorders, drugs, and occult trauma are among the less frequent causes) [34, 39, 40].

Diagnosis centers on defining the presence of an aneurysm or other bleeding lesion. CT and MRI of the brain are highly sensitive tests for detecting acute SAH. CT scanning is the first investigation if subarachnoid hemorrhage is suspected. The ability to detect subarachnoid hemorrhage is dependent on the amount of subarachnoid blood, the interval after symptom onset, the resolution of the

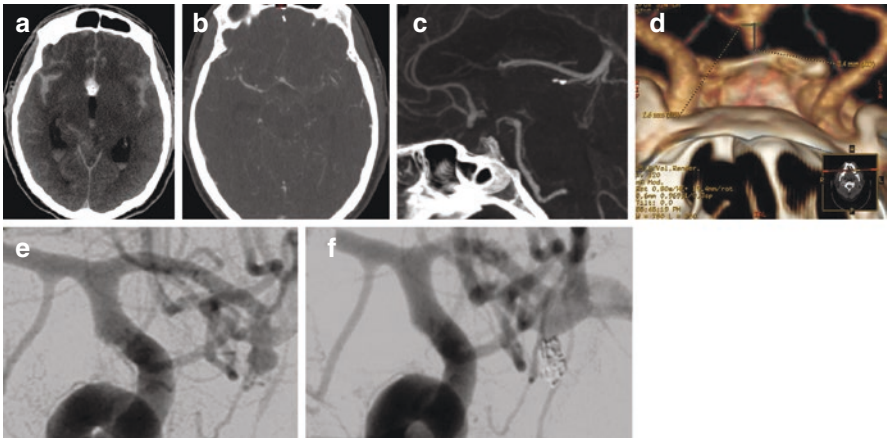

Fig. 3.7 Ruptured ACA saccular aneurysm in a 74-year-old male. (**a**) Non-contrast CT scan in ER at 11 am: widespread, bilateral, and symmetrical subarachnoid hemorrhage secondary to the rupture of an ACA saccular aneurysm. The lesion location was suspected on the non-contrast CT due to the higher blood density in the lamina terminalis cistern and confirmed with the CT angiography (**b**–**d**). (**e**, **f**) DSA, before and after embolization with GDC coils, done on the same day. Note the complete lesion occlusion and consequent exclusion from the intracranial arterial circulation. Everything went well, apparently, with progressive albeit partial diappearance of the onset symptomatology, …

scanner, and the skills of the radiologist. If performed within the first 2 days of SAH, CT scans have 95–100% sensitivity for intracranial hemorrhage. This sensitivity diminishes to 85% within 5 days, 50% after 1 week, 30% after 2 weeks, and 0% after 3 weeks [41–43].

Other than the positive diagnosis of SAH, the initial CT examination can detect the early complications of hydrocephalus, intraparenchymal hematoma with space occupying effect and ventricular hemorrhage. Hydrocephalus, which begins with dilatation of the temporal horns, and a compressive intra-parenchymal hematoma need to be diagnosed and reported, as they represent life-threatening conditions and require immediate neurosurgical treatment with the positioning of an external ventricular shunt and/or the evacuation of the hematoma before the treatment of the cause of the SAH (Fig. 3.9).

Relying on CT of the brain to make a diagnosis of SAH after 1 week is instead an uncertain and much more challenging affair. Because of the greater availability and feasibility of CT imaging in patients with suspected subarachnoid hemorrhage, few studies of MRI in the acute phase after subarachnoid hemorrhage have been reported. These suggest that in the first few hours and days, MR with proton density and, nowadays almost exclusively, FLAIR images is as sensitive as CT imaging. After the initial days, when hyperdensity on CT scans decreases, MR is better for detecting blood, with fluid attenuation inversion recovery (FLAIR) and T2* images being the most sensitive techniques [42, 43]. Vascular imaging, usually including cerebral dye contrast angiography, is needed. CT angiography (CTA) of the circle

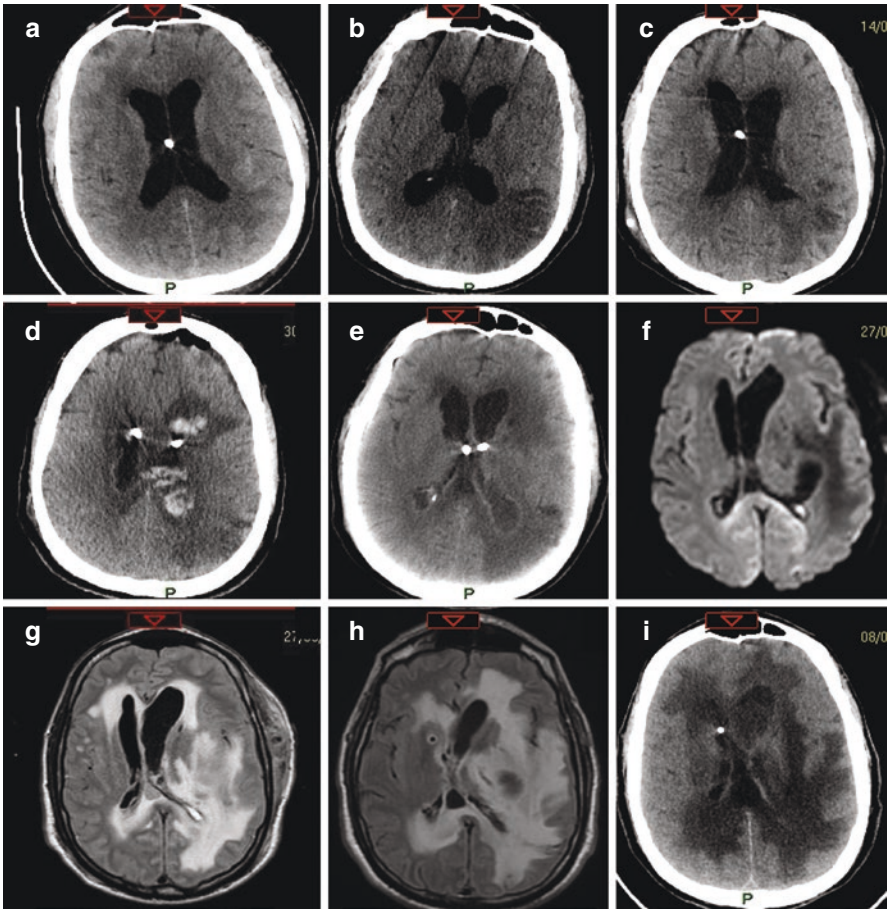

Fig. 3.8 (**a**–**i**) …but 11 days after the treatment the patient's history became the "worst case scenario" in a clinical case like this, with the onset of an almost untreatable vasospasm, followed by multiple ischemic lesions, intraparenchymal bleeding partially along the ventricular catheters, and, finally, an infectious cerebritis with massive vasogenic edema and ventricular hypertension, that led this unfortunate patient, a MD Radiologist by the way, to the exitus. This case would be a reminder that nowadays subarachnoid hemorrhage also represents, also in a "not so old" individual, a life threatening occurrence, not only at the onset, but also after a routinary successful treatment of the primary lesion

of Willis has a sensitivity of 98% to detect intracranial aneurysms, particularly because of its excellent spatial resolution, which is less than 1 mm. CTA in general is useful not only to identify one or more aneurysms as potential causes in a patient with subarachnoid hemorrhage but also to study the anatomical configuration of the aneurysm in relation to adjoining arteries, which allows optimum selection of treatment (coiling/stenting or clipping) and, therefore, the choice between the surgical or intravascular approach. CT angiography is a continuously improving technique. The sensitivity for detecting ruptured aneurysms, with conventional angiography as the gold standard, is currently about 95% [44, 45] (Fig. 3.10).

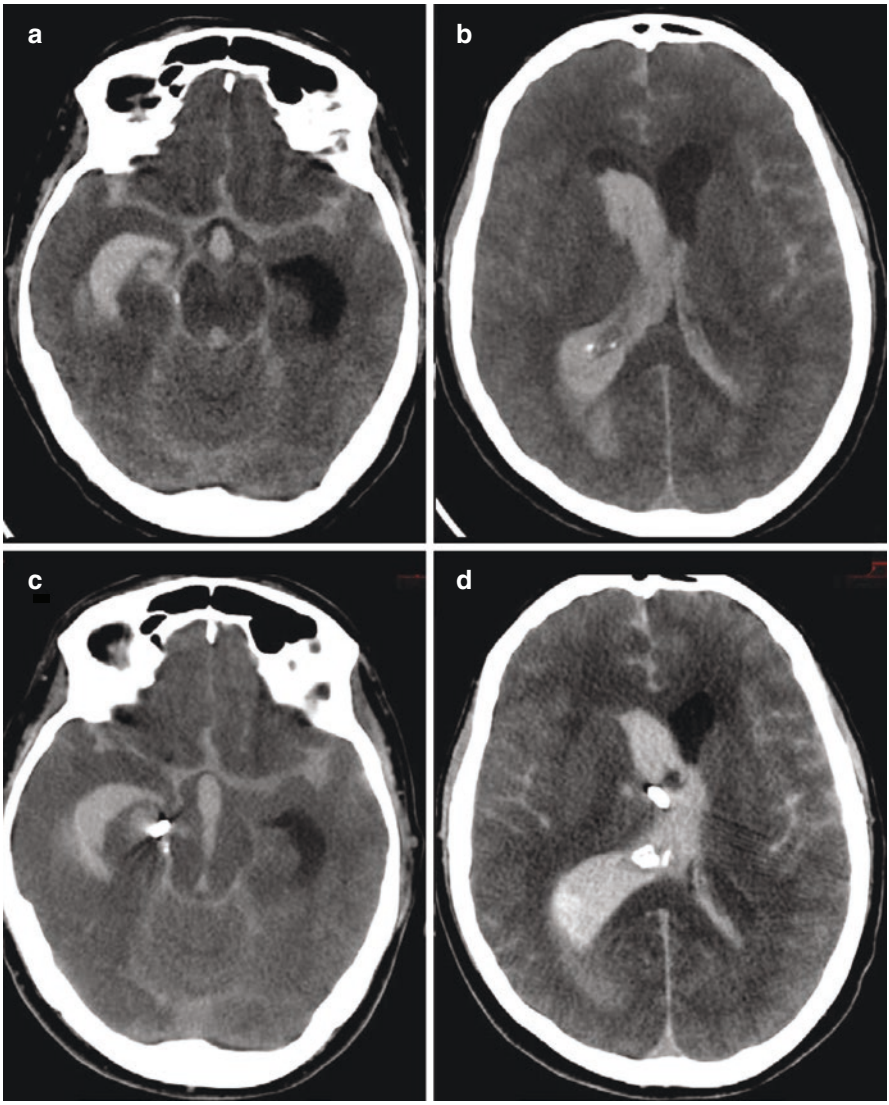

Fig. 3.9 Severe hydrocephalus in ruptured PCoA aneurysm (**a**, **b**). Non-contrast CT study in ER of a 81-year-old woman with severe headache and consciousness alteration shows diffuse subarachnoid hemorrhage (SAH) throughout the basal cisterns and massive intraventricular hemorrhage. Note the enlargement of both temporal horns of the lateral ventricles, consistent with early hydrocephalus. SAH was caused by a ruptured saccular aneurysm located in the PCoA segment of the right internal carotid artery (not shown). (**c**, **d**) Non-contrast CT after the endovascular embolization of the aneurysm and placement of an atrial-ventricular catheter for the treatment of intracranial hypertension

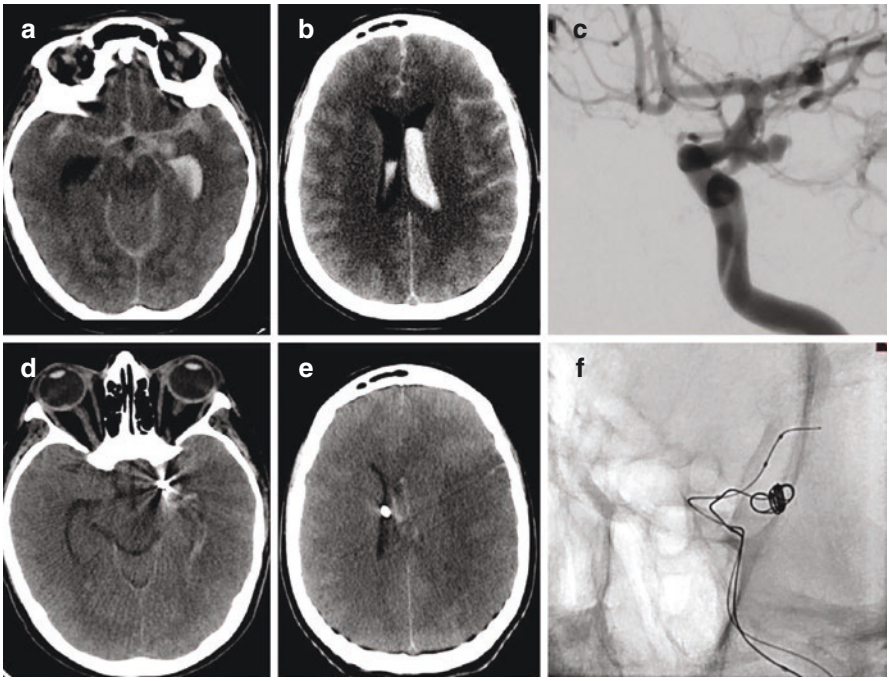

Fig. 3.10 Endovascular treatment in an SAH from a saccular L Pcom ruptured aneurysm. A 74-year-old woman with sudden, severe headache. Axial CT study in ER shows extensive subarachnoid hemorrhage (SAH) throughout the basal cisterns and intraventricular hemorrhage (left>right). Note the enlargement of both temporal horns of the lateral ventricles, consistent with early hydrocephalus (**a**, **b**). Cerebral angiography demonstrates the presence of a saccular Pcom aneurysm of the left internal carotid artery, which most likely represents the cause of the bleeding (**c**). Unsubtracted images during coiling of the aneurysm with balloon assistance for the neck coverage (**f**). Axial CT after the endovascular embolization of the aneurysm shows an ample parenchymal ischemic area (in the left frontal and parietal regions) due to SAH-related vasospasms, with mild mass effect and compression of lateral ventricles (**d**, **e**)

The appropriate treatment of this disease in elderly patients, predominantly regarding the occlusion of the ruptured intracranial aneurysms, is still controversial. About 5% of all strokes are due to SAH, and about 10% are due to ICH, depending on age, sex, educational and social status, and racial composition of the evaluated patients. Treatment of patients harboring aneurysms is aimed at eliminating the aneurysm's rebleeding potential either by direct surgical clipping or coating or by endovascular techniques that contain and thrombose the aneurysmal sac. In the latest years in particular has been developed a new "stenting" method to allow the exclusion of an aneurysmal sac from the cerebral circulation. After some unsatisfactory attempts with coated stent, in order to cover the aneurysm's origin from the parent vessel, the results of several new hemodynamic studies, allowed by the availability of new ultrafast volumetric CT scanner, with up to 320 slices contemporary acquisition, drew attention to the fact that the aneurysmal growth was largely dependent on the peculiarity of the flowing blood, both in the parent vessel and, as a consequence, in the aneurysmal sac [46, 47]. A new kind of stents with "flow diverting" features was

therefore developed, which, distorting the local hemodynamic, eliminates the excessive pressure inside the lesion, which suddenly shrinks and could finally disappear.

As a result of these continuous evolution, the percentage of aneurysm malformations that require a conventional surgical approach has been greatly diminished and is currently limited to the cases in which the endovascular treatment is not feasible, due to the patient's vascular anatomy that could not allow the catheter navigation, or the complexity of the aneurysm origin, with close relationship with adjacent vessel that needs to be savaged.

In elderly especially, the endovascular approach has the great advantage of being much less invasive and therefore more sustainable from often more fragile individuals. On the other hand, the vessels are often tortuous, with calcifications and sometime accompanying stenosis, which in some cases do not allow the catheter to reach a proper position in order to release the devices (stent and/or coils), required from the treatment [48–50].

3.4 Traumatic Intra-axial Brain Injures (TBI)

Traumatic brain injury (TBI) is among the leading causes of death and disability worldwide, with enormous negative social and economic impacts. Traumatic cerebrovascular injury (TCVI) is a common pathologic mechanism of traumatic brain injury with often possible multiple intracranial lesions (Fig. 3.11). Among the elderly, in recent years, instances of neurotrauma have been increasing [51]. As aged population grow, so the instances of traumatic brain injury (TBI) in the elderly are increasing. It has been known that the frequency curve of TBI by age groups has two peaks, in patients at 15–29 and 65–79 years of age [52]. In recent years, this curve has changed and currently shows a single peak, only in the elderly age range, resulting from both decreased frequency in the young and increased frequency in the elderly. In addition, the peak of frequency in the elderly is continuously shifting toward older ones. Such changes may be the result of the increased representation of aged individuals in the population, as well as the reduction in traffic injures, by far more common in the young people. Age has been proposed as one of the most reliable prognostic factors following TBI. Both survival and functional outcomes are significantly poorer in the elderly compared to the younger patients with TBI. It has been also reported that the duration of hospital stay is significantly longer in the elderly than younger patients with TBI [53]. The elderly patient frequently presents numerous comorbidities (diabetes mellitus, neurodegenerative diseases, arterial hypertension, chronic vascular encephalopathy) at the time of trauma, which can mask the clinical picture, postpone treatment, and influence prognosis: as an example, age-related atrophy may provide space for an intracranial hemorrhage to expand substantially before leading to clinically apparent signs or symptoms that would be detected by the GCS [54]. Morphologically, the distribution of traumatic intracranial lesion varies in the age groups. Diffuse axonal injury (DAI) is less common in the elderly than the young. In contrast, focal injury is more common in the elderly. It is well known that the subdural, contusional, and intracerebral hematomas are more common lesions in the elderly than the young, although epidural hematomas are less common in the elderly. Those

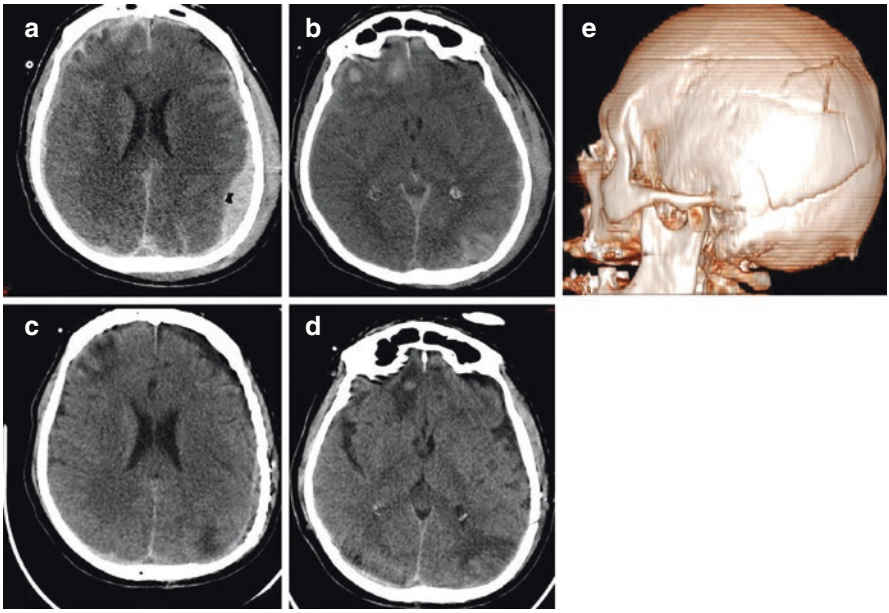

Fig. 3.11 SAH, epidural hematoma, and multiple brain contusions in polytrauma. Axial CT scans in a 69-year-old patient with severe closed head trauma show the classic biconvex configuration of an acute epidural hematoma in the left parietal region (**a**) and right frontal and left parietal hemorrhagic contusions (the right frontal lesions due to contrecoup mechanism) (**b**–**d**) with mild surrounding edema. Traumatic subarachnoid hemorrhage and tiny subdural right hematoma are also present. Bone CT reconstruction shows a nondisplaced skull fracture of the left parieto-temporal bone underlying the epidural hematoma (**e**). Note the subgaleal acute, hyperdense hematoma in the left temporal area (**a**)

characteristics of intracranial lesion have been explained by morphological changes related to aging. The elderly patients show a markedly different survival trend in comparison with other age groups. Death within 48 hours of admission is not different among all age groups. After that, only the elderly group shows a progressive decrease in survival until the rate leveled off at approximately 35%, whereas the other age groups tend to level off at approximately 60–80% survival. The "talk and deteriorate (T&D)" concept is defined as a patient who present a relatively good neurological condition in the early phase after TBI and then deteriorate to a severe neurological status within 48 hours. It is much more common in the elderly and is often induced by the delay of posttraumatic changes such as hyperemia/hyperperfusion, traumatic intracerebral hematoma, expansion of subdural hematoma, or aggravation of traumatic contusional edema. The T&D is much more common in old patients after TBI with resulting cerebral contusion. Cerebral contusional edema has been classified as early massive edema and delayed-pericontusional edema. The early massive edema is defined as a hypo intensity core on diffusion-weighted magnetic resonance image (MRI), which appears within 24 h after TBI, suggesting that intra- and extracellular components undergo disintegration and homogenization in the central area of the contusion. In contrast, delayed-pericontusional edema is defined as predominant cellular swelling in the peripheral area. There is a crescent-shaped border zone of very high

ADC value on MRI between central and peripheral area. In spite of CBF reduction, fluid amount is excessive in the area of the cerebral contusion. In addition, hyperemia/hyperperfusion subsequent to ischemia enhances the increase of post contusional edema, resulting in delayed deterioration. Delayed traumatic intracerebral hematoma and expansion of either traumatic acute subdural hematoma or intracerebral hematoma may be other important clinical entities for delayed deterioration. A peculiar entity of delayed deterioration after TBI, the delayed posttraumatic acute subdural hematoma (DASH), has been reported in elderly patients. DASH has been defined as an acute subdural hematoma that is not apparent on the initial computed tomography (CT), and suddenly arise on a follow-up CT after 9–72 h after TBI. Thus, DASH should be suspected in elderly, anticoagulated, mild TBI patients, including those who present in the ER with GCS scores of 15 and normal initial CT [55–57]. Current guidelines recommend "In case of head trauma, the head CT scan is the first line examination and is recommended for any patient without loss of consciousness or post-traumatic amnesia, if any of the following is present: neurological deficit, vomiting, severe headache, age over 65 years, suspected skull-base fracture, Glasgow score <15, coagulopathy, trauma with dangerous mechanism" [58, 59]. A fundamental role in the approach of the traumatic patient is represented by neuroimaging and in particular by CT, which through a prompt diagnosis in acute, indicates the management and helps predict patient outcomes of all ages spectrum. A fundamental role in the approach to the traumatic patient is represented by neuroimaging and in particular by CT, which through a timely diagnosis in acute indicates management and helps predict the outcomes of patients of all age groups. In particular, CT must promptly recognize pathological conditions that require urgent surgery (extensive expansive lesions) and/or intracranial hypertension. In this context and especially when fractures of the skull base are present, the integration of a dynamic CT angio study may be useful, for the evaluation of the main vascular structures in order to exclude arterial dissections, aneurysms/pseudoaneurysms, and thrombosis of the venous sinuses and of the cerebral veins. The unstable clinical conditions of the traumatic patient, the reduced availability on the territory and the duration of the examination, relegate the MR in urgency to a secondary role. The damage incurred by TBI can be differentiated into primary and secondary mechanisms. Post traumatic head lesions included both primary injuries, that are typically defined as the direct mechanical damage caused by trauma hemorrhagic parenchymal contusions, brain stem injury, traumatic axonal injury (TAI), parenchymal hematomas, subdural, subarachnoid or extra-dural hematoma, cranial vault fractures, and secondary injury mechanisms, that are varied and related to disruption of the blood brain barrier, production of reactive oxygen species and resultant oxidative stress, metabolic dysfunction, inflammation, and excitotoxicity. They may become apparent as diffuse cerebral hyperemia, cytotoxic and/or vasogenic edema, and tissue ischemia [60, 61].

3.4.1 Posttraumatic Subarachnoid Hemorrhage (t-ESA)

Posttraumatic subarachnoid hemorrhage is due to a tearing of the bridging veins or pial vessels in contact with the sub-arachnoid space; if the choroid plexuses and/or parenchymal foci contusive juxtaventricular foci are involved, the hemoventricle

can also be found. t-ESA is more focal and circumscribed than nontraumatic ESA and is frequently localized in the peri-sylvian regions and in the cerebral sulci adjacent to the and/or to epi/sub-dural blood collections [62] (Fig. 3.11).

The clinical presentation appears mostly in the form of headache, classically defined as maximal at onset and "the worst of life." The most common cause is traumatic, also representing the most common form of intracranial hemorrhage in trauma; approximately 80% of nontraumatic SAH are due to aneurysmal rupture, with the remainder from idiopathic peri-mesencephalic hemorrhage or other less common causes.

Noncontrast head CT is the primary means of diagnosis, with the advanced generation scanners approaching a 100% sensitivity, if completed within 6 h from symptom onset. The bleeding in the subarachnoid space will result in hyper density in the first hours on CT-scanner. Within the first 24 h, it is positive in 90/95% of cases; it should be noted that spontaneous hyper density gradually disappears and that after a week it is only found in 50% cases. In general, hyper density will depend on hemoglobin level, amount of blood, and delays between performing the scan and bleeding [63]. One pitfall might be that the blood and adjacent bone, which both appear white, can be difficult to distinguish from each other, especially in small bleeding and in the anemia (sensitivity decreases when the hematocrit is <30%); in addition, motion artifacts in scans of restless patients can making such scans technically suboptimal and obscure the diagnosis [64]. In these cases, the Dual Source scanners may show some edge in the demonstration of such collections.

On MRI the fluid attenuated inversion recovery (FLAIR)/gradient reversal echo (GRE)/susceptibility weighted imaging (SWI) sequences have a good sensitivity for the detection of acute SAH in the first 48 h and are complimentary to the CT scans [65]; however, they are not suitable for a rapid assessment of head injuries. SAH can be diagnosed by GRE/SWI sequences by its dark signal intensity ("blooming"), surrounded by the CSF signal intensity. More specifically, the FLAIR sequences, which are the most sensitive in the first days compared to T1, T2, T2*, show a hypersignal in the basal cisterns and the sulci of the convexity [64, 66]. The radiologist evaluation must be careful, because there are other etiologies at the origin of a hypersignal in FLAIR in the subarachnoid spaces, such as meningitis, hyperoxygenation, and metallic artefacts. After a few days from the onset T2* sequences show hemosiderin deposits, i.e., in the cisterns of the base, or in the cortical furrows. This modality does not require radiation, though several limitations exist, including limited availability in the ED, the time required for scanning, the potential for inducing claustrophobia, and the need for specialist interpretation. MRI/MRA is optimal for patients who present in a subacute or chronic timeframe [67].

3.4.2 Cerebral Contusion (PTBCs)

Posttraumatic brain contusions (PTBCs) represent one of the most frequent lesions in patients with moderate or severe traumatic brain injury (TBI). PTBCs are traditionally considered primary injuries, but they have an inherent capacity to increase

in size, generate perilesional edema, and cause mass effect [68]. These lesions are cortical and due to the impact with the bone surfaces (e.g., the petrous bone, sphenoid, cribriform plate, orbit roof) and the dura mater (more resistant and irregular). There are therefore more common localizations, such as the fronto-basal regions and the temporal and frontal poles; they typically occur at ("coup") or in front ("countercoup") with respect to the site of the blunt trauma. Bruises frequently are multifocal and bilateral, usually involving the superficial gray matter that often bleed, particularly those found in "countercoup" areas. The use in the acute phase is represented almost exclusively by NCCT; however, it can underestimate the number and size of blunt foci; there are moreover less common localizations, as is in the case of Duret hemorrhages, generally associated with other lesions (Fig. 3.12).

Therefore, MRI in a sub-acute/chronic structural phase improves prognostic modeling after TBI by identifying evidence of neurotrauma that may not be detected by head CT. They are recognized as hypo dense cortical-subcortical areas and in some cases a contextual hyper dense component of hemorrhagic significance may be highlighted.

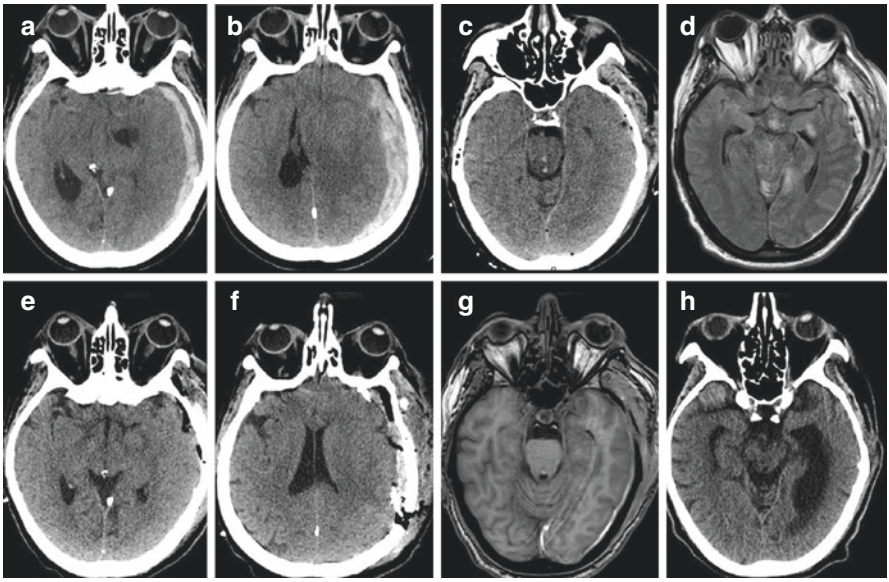

Fig. 3.12 Duret brainstem hemorrhage in posttraumatic left subdural hematoma. A 75-year-old woman with head trauma due to sudden loss of consciousness. A CT study in ER showed an acute left hemispherical subdural hematoma compressing the hemisphere and lateral ventricle, with uncal hernia and incarceration of the temporal horn of the lateral ventricle; note left-to-right midline shift (**a**, **b**). There is also the evidence of midbrain Duret hemorrhage (usually due to stretching/tearing of pontine perforators, **c**). Follow-up non-contrast CT scan after the removal of the hematoma shows re-expansion of the left ventricular hemisystem (**e**, **f**); MRI with FLAIR (**d**) and T1 TSE (**g**) sequences confirm the reduction of the subdural hemorrhage and of the associated mass effect. CT follow-up after 60 days demonstrates an "ex vacuo" dilation of the horn and trine of the left lateral ventricle (**h**)

In patients with severe cerebral contusions, early massive edema occurs within the period of 24–72 h post-trauma. This type of edema results in progressive elevation of intracranial pressure (ICP) and clinical deterioration giving rise to a clinical course termed "talk-and-deteriorate" [69]. DWI measures the freedom of molecular motion of water in tissue and is useful in identifying pathologic lesions including foci of axonal injury and infarction. DWI is best used in conjunction with its associated ADC map, which can distinguish between cytotoxic and vasogenic edema in the acute and subacute phases and is highly sensitive in the detection of secondary acute ischemic infarction associated with TBI.

Despite intensive medical therapy, the elevated ICP in patients with early massive edema is often uncontrollable and fatal.

3.4.3 Post-traumatic Intracerebral Hematomas (t-ICH)

t-ICH results from injury to intraparenchymal arteries or veins secondary to rotational strain or penetrating trauma and are usually located in the frontal-temporal white matter or basal ganglia; ICHs collect between relatively intact parenchyma, in contrast to hemorrhagic contusions where the hemorrhage is within a larger area of injured edematous brain. Prognosis of isolated ICH is generally good, but worsens when the lesion coexists with marked mass effect, traumatic axonal injury (TAI), or multiple basal ganglia hemorrhages. When CTA is also performed, the "spot sign," or active extravasation of contrast into the hematoma, predicts future expansion of the hematoma and worsens clinical outcome [61, 70] (Fig. 3.13).

3.4.4 Traumatic Axonal Injury (TAI)

Traumatic axonal injury is a condition defined as multiple, scattered, small hemorrhagic, and/or nonhemorrhagic lesions, alongside brain swelling, in a more confined white matter distribution on imaging studies, together with impaired axoplasmic transport, axonal swelling, and disconnection after traumatic brain injury [71]. TAI is thought to be caused by a variety of traumatic mechanisms involving fast acceleration and/or deceleration, including motor vehicle accidents, falls from height, and blunt assault [72]; the distribution of traumatic lesions has a predisposition for white matter tracts in the midline of the brain, including the corpus callosum, internal capsule, cerebral peduncles, brainstem, and the gray–white junction of the cerebral cortex (Figs. 3.14 and 3.15). CT is capable of identifying large TAI-related hemorrhage, but nonhemorrhagic lesions and small TAI hemorrhage are virtually impossible to identify using CT and therefore can be easily lost [73]. Conventional MRI (cMRI) has a higher sensitivity in demonstrating lesions in the brainstem and the deep white matter, making it more sensitive for identifying axonal injury

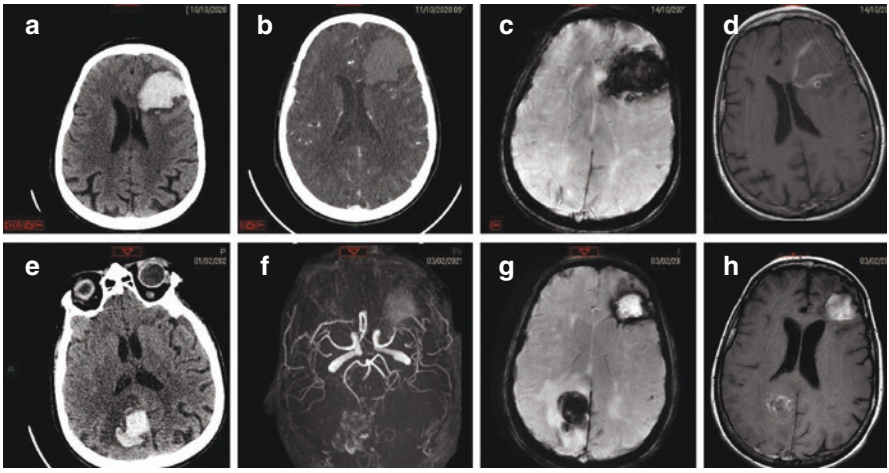

Fig. 3.13 Hemorrhagic brain contusions in head trauma. A 73-year-old patient with head trauma in ASA therapy. Non-contrast CT study in ER demonstrated an ample atypical intra-axial left frontal hemorrhage with initial surrounding edema and mass effect (**a**). The next day a CT angiographic exam showed stability of the collection, with no signs of underlying vascular malformations (**b**). The subsequent MR study confirmed the diagnosis. T1-w (**d**) evidentiates the initial peripheral methemoglobin ring surrounding the oxy-deoxyhemoglobin content of the fresh lesion, while the SWI (**c**) sequence shows a little subarachnoid spread and absence of previous hemorrhages. After another light head trauma 3 month later, axial CT showed another intra-axial hematoma in the right posterior parietal lobe with surrounding edema (**e**). The subsequent MR study with TOF sequence confirmed the diagnosis, excluding also in this case signs of vascular malformations and showing the remnants of the previous frontal hemorrhage (**f**–**h**)

compared to CT [74]. The MRI gradient echo sequence (GRE) is able to detect heme and heme breakdown products, making it a suitable method for discovering small hemorrhagic lesions. Susceptibility-weighted imaging (SWI) as a variant sequence of GRE imaging should be considered the "gold standard" for identifying TAI lesions. It has a higher sensitivity for hemorrhage than GRE, which makes it more useful for early diagnosis of TAI. Diffusion-weighted imaging (DWI) can accurately examine nonhemorrhagic lesions. High signal DWI can be used in patients with early stage TAI. Lesions found represent cellular swelling and cytotoxic edema. DWI may aid in predicting clinical outcome after TAI. DWI is more capable of determining the severity of the injury and estimating the long-term prognosis than MRI techniques [71, 75, 76].

Diffusion tensor imaging (DTI) is an improved form of DWI. It can be used to evaluate nerve alignment, white matter microstructure, and the morphology around nerve fibers. Within the first 24 h after trauma, DTI can detect white matter regions with reduced anisotropy, making it an adequate technique for detecting TAI. CT scanning is more widely used in the acute phase, due to its much shorter scanning

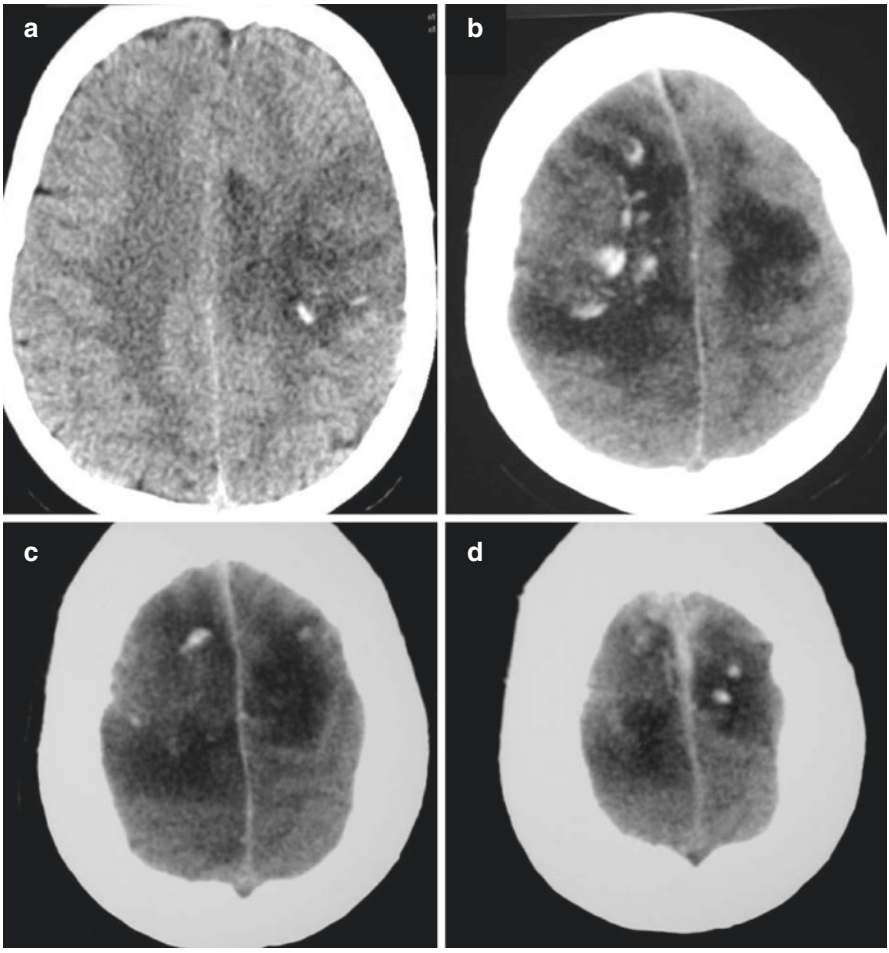

Fig. 3.14 Bilateral frontal cerebral contusions and TAI of a 65-year-old male (**a**–**d**). Non-contrast CT in ER after close head trauma due to a car accident. The images show bilateral cortical-subcortical inhomogeneous hypodense parenchymal areas, partially due to vasogenic edema, directly related with the impact. Also note the multiple small hyperdense foci, more evident in (**b**), which represent associated manifestations of traumatic axonal injures (TAI), secondary to the axonal traumatic strain, related to the tissue deformation caused by the differential kinetic energy with the skull

time. MRI scanning should be performed as soon as the condition of the patient allows it, so the full extent of trauma can be mapped and white matter volume prospectively followed-up [73, 77].

Acute treatment in the elderly with moderate to severe head injury involves an acute neurosurgical approach including intracranial pressure monitoring (ICP), craniotomy, and decompression craniotomy; tSAH may impair the absorption of CSF and may produce hydrocephalus. Posttraumatic vasospasm (PTV) is a significant

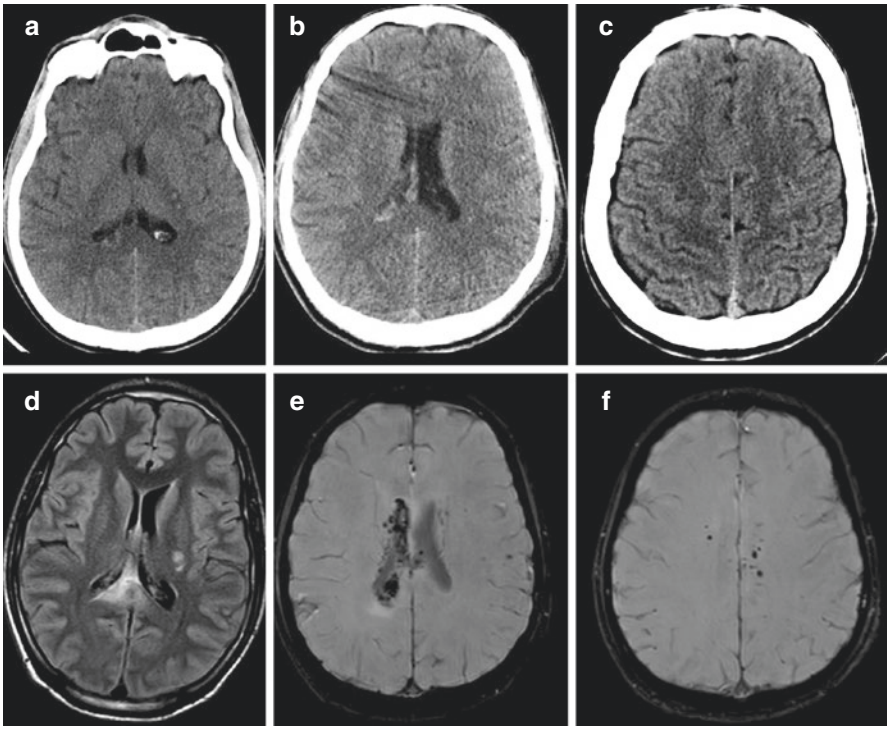

Fig. 3.15 Traumatic axonal injury (TAI). Non-contrast CT study in a 67-year-old man involved in a high-energy head trauma shows tiny hemorrhagic foci in the subcortical white matter (**c**) and in the left internal capsule (**a**). Blood is also present in the right lateral ventricle (**b**). These microbleeds are typical imaging markers of diffuse axonal injury (DAI). FLAIR images well depict the edema surrounding the tiny hemorrhagic foci in the left internal capsule (**d**), while the SWI (**e**, **f**) sequence shows other hemorrhagic foci in the subcortical white matter and in the right lateral ventricle. Note how the MRI study more accurately demonstrates the presence and the extension of diffuse axonal damage manifestations

secondary insult to the injured brain. It typically develops between 12 h and 5 days after the injury and lasts between 12 h and 30 days.

However, preexisting clinical conditions dramatically influence the prognosis in elderly patients; therefore, invasive surgical treatment in this population remains controversial.

3.5 Extra-axial Hemorrhages

3.5.1 Epidural Hematoma

Epidural hematoma (EDH) represents an extremely rare event in the elderly population: an overwhelming majority of cases arise in fact after a high energy

traumatic brain injury (TBI), with associated skull fracture that involves an artery, often represented by the middle meningeal artery (MMA). Such events are typical of the young male population. Other causes, more frequent in the elderly due to underlying comorbidity, are coagulopathy, secondary effect of thrombolysis, vascular malformation, neoplasm, epidural anesthesia, or Paget disease of skull. On the other hand, spontaneous EDHs are rare, and generally arise from a skull primary or secondary tumor. EDHs, generally unilateral and supratentorial, derive from an arterial bleeding in 90% of cases and therefore show a rapid expansion, reaching the maximum size after 36 h. EDHs have the typical shape of a biconvex lens, often also if of venous origin, are extra-axial and determine rapid compression and displacement of the underlying brain parenchyma with huge mass effect: thus a quick diagnosis followed by immediate surgical approach have paramount importance, in order to avoid a poor outcome, or the death of the patients due to the brain damage. EDH of suspected venous origin, with thickness not superior to 1 cm, could be observed with subsequent TC scan in the following 36 h. Although typical in shape, imaging features and clinical history, EDHs may pose DD with SDHs, that in some cases may have biconvex shape: in this case it is useful to remember that EDHs, differently from SDHs, do not cross the cranial sutures. Other, less frequent DDs are with extra-axial tumors, like meningiomas or soft component of skull or dural primary (lymphomas, primary sarcomas) or secondary lesions. Also some infectious/inflammatory event may pose a DD with EDH, epidural empyema from skull osteomyelitis or granulomatous tubercular osseous localizations. The NCCT exam is usually diagnostic: a second level study is not necessary and not recommended, in order to avoid a delay of the surgical treatment, which could in order cause a significant worsening of the outcome. EDHs appear as a thick biconvex homogeneously hyper dense collection located under the area of the skull trauma where, in the case of arterial origin, a fracture responsible for the torn of an arterial vessel is almost inevitably visible (Fig. 3.16). The density may also be low or inhomogeneous, due to the contemporary presence of uncoagulated blood: in this case the collection is in the hyperacute phase. The eventual presence of air (20%) is related to the fracture of a paranasal sinus or mastoid proximal to the collection. A small, iso or hypodense collection is almost always of venous origin. MRI is useful in case of nontraumatic collections. In the acute phase, the content is hypointense in T1 and variable, hypo to hyperintense on T2wi: in the subacute/chronic phase the T1 signal becomes hyperintense, while in T2 it appears hypointense in the subacute period and hyperintense in the chronic phase. The post contrast T1wi may be useful in case of venous collection in order to demonstrate displacement and patency of dural sinuses.

3.5.2 Subdural Hematoma (SDH)

Subdural hematomas (SDH) surely represent a sizeable cause of cerebrovascular emergencies in the elderly. The incidence of falls, considered to be the leading cause

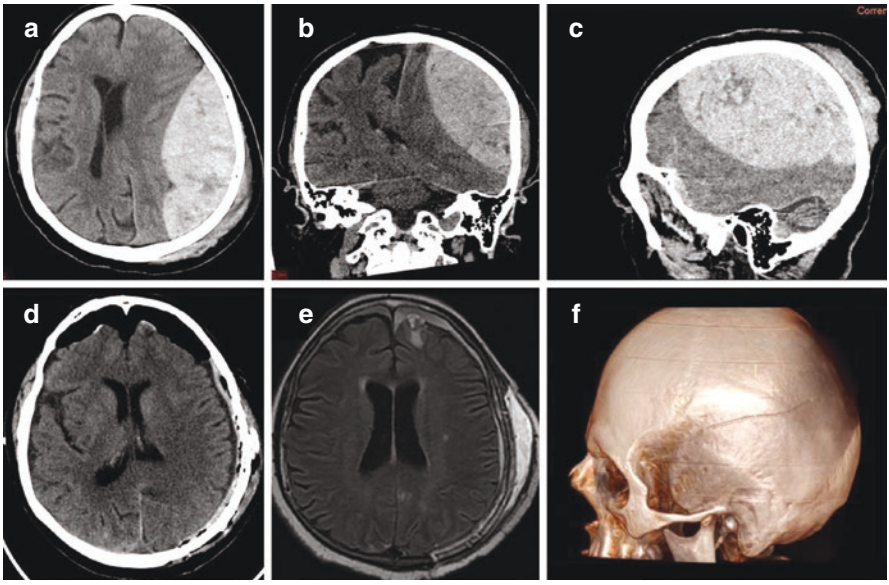

Fig. 3.16 Epidural hematoma. Non-contrast CT study in a 71-year-old woman with head trauma shows the classic biconvex appearance of an acute left epidural hematoma, associated with mass effect, compression of the left hemisphere and lateral ventricle, left-to-right subfalcine herniation and resulting ample midline shift (**a**–**c**). Note the hematoma of adjacent soft tissues (**a**). Axial CT study after surgical evacuation shows the disappearance of the epidural blood collection and consequently of the mass effect, with the presence of bilateral frontal pneumocephalus (**d**). MRI FLAIR axial image, several days after surgery, showing the presence of tiny bilateral subdural hematomas and a left subgaleal collection over the craniotomy (**e**). Bone CT 3D-reconstruction shows a non-displaced skull fracture of the temporal and parietal bone underlying the hematoma (**f**)

of SDH [78–80], has increased worldwide along with the augmented percentage of elderly in the population. Sixty percent of patients are hospitalized due to injuries sustained in a fall, according to the National Trauma Data Bank in the United States, 55,729 (61%) had sustained injuries from falling [81]. In older patients, reduced brain parenchyma has been associated with an increased risk of SDH, which may even occur following minor trauma [82]. SDH usually results from tears in bridging veins, which cross between the cerebral cortex and the dural sinus [83], or, less frequently, a rupture of the superior cortical arteries [84]. Blood accumulates in the space surrounding the brain parenchyma, between the arachnoid mater and the dura [85]. Increased intracranial pressure caused by a hematoma causes further compression and damage to the brain tissue (Fig. 3.17). Moreover as the patients grow older, there is a higher prevalence of comorbidities and increased use of medications, including anticoagulants and polypharmacy. This can heighten the risk of bleeding and developing further complications. Fortunately overtime there has been a decrease in the mortality rate: in the 1990s, the mortality rate for acute SDH was reported to be as high as 60% [79]. The mortality rate of SDH decreased to a level of 20% around the year 2000 and has fallen as low as 14% within the last decade

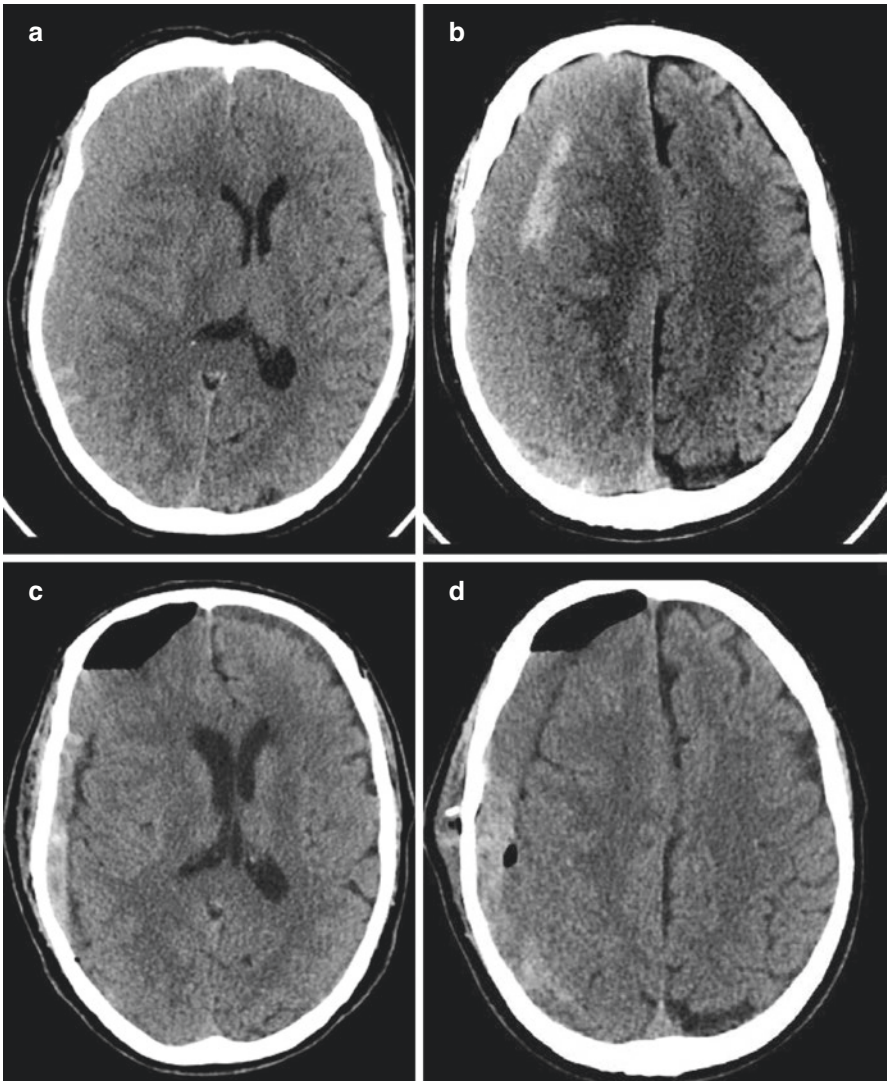

Fig. 3.17 Subdural hematoma. NCCT study in ER of a 81-year-old man with consciousness reduction and confusion showing right hemispherical subacute subdural hematoma, with signs of recent rebleeding, that compresses the right hemisphere and lateral ventricle, with right-to-left subfalcine herniation, resulting in midline shift (**a**, **b**). Immediate postsurgical NCCT shows the thickness reduction of the subdural hematoma (with presence of an air-fluid level) and the associated reduced compression on the right hemisphere and lateral ventricle (**c**, **d**)

[79]. However, acute SDH has been reported to be a poor prognostic factor for those patients with a traumatic brain injury [86], particularly in elder patients. There was in fact higher mortality for the elderly following falls compared to young adult patients, after adjusting for preexisting comorbidities and severity of injury [78].

Being an almost typical acute neurological event, the patient is generally evaluated with a noncontrast TC study (NCTC). The recent multislice CT systems generally available in the radiological departments being nowadays capable to acquire 64 or more (128, 256, 320 up to 512 sub-mm slices) simultaneously, make generally possible a good quality study even in an uncooperative patient. An SDH, regardless its phase, appears as a crescentic extra-axial collection of variable breadth and longitudinal extension along the surface of the affected hemisphere. Less frequently (15–20%), the SDH can involve both the hemispheres (Fig. 3.18), or be located in the posterior fossa. In the hyperacute phase (less than 6 h), the subdural collection appear hypodense or at least heterogeneous, due to the presence of mostly uncoagulated blood. In the acute phase, it appears homogeneously hyperdense in 60% of cases, while in 40% is mixed hyper-, hypodense with active bleeding ("swirl" sign), torn arachnoid with CSF accumulation, clot retraction. Rarely the collection is isodense, due to coagulopathy, anemia (Hgb <8–10 g/dL) ·If no new hemorrhage, density gradually decreases to become isodense to brain parenchyma in the

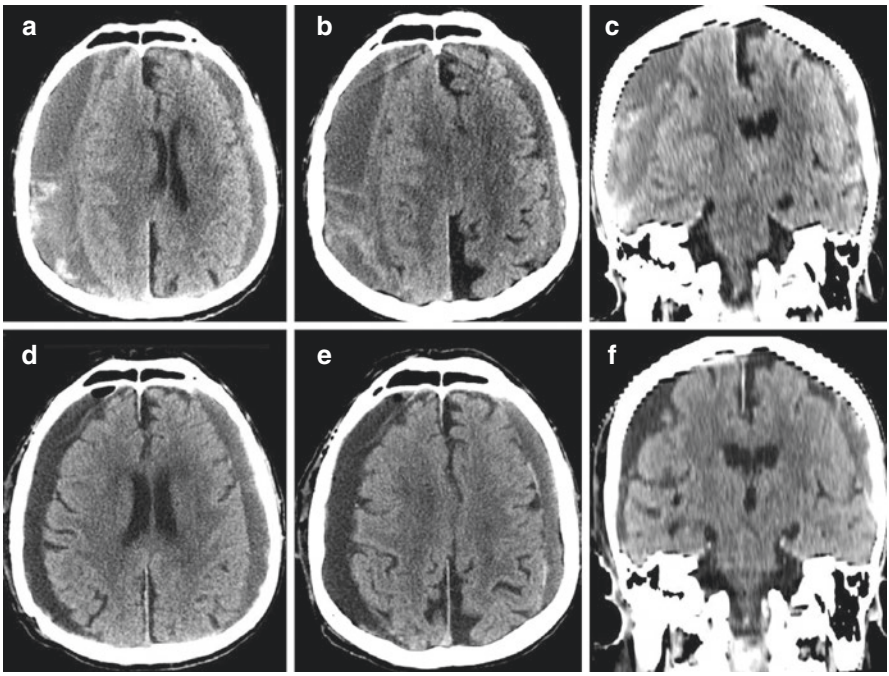

Fig. 3.18 Bilateral subdural hematomas. NCCT study in ER of a 81-year-old woman with severe headache, showing bilateral hemispherical subacute subdural hematoma (right>left): in the right, more sample collection, there are signs of recent rebleeding, represented by the irregular areas of hyperdensity (**a**). Note the bilateral compression of the cerebral hemispheres and lateral ventricles, with right-to-left subfalcine herniation, resulting in midline shift (**a**–**c**). Follow-up CT days after surgery showed the reduction of both the subdural hematomas and of the compression on the hemispheres and the lateral ventricles. (**f**) The coronal plane shows the reduction of the right-to-left subfalcine herniation (**d**–**f**)

subacute phase. Post contrast CT is generally unnecessary in this phase, while in the subacute period it could come in handy, because in certain case a thin SDH could be indistinguishable from the adjacent brain cortex.

On MRI a SDH generally often follow the fashion of intraparenchymal hemorrhage. On TlWI in the hyper acute phase (less than 12 h) appear iso to mildly hyper intense. In the acute (12 h to 2 days) is mildly hypo intense. On T2WI hyper acute is mildly hyper intense. In the acute appear hypo intense. On the FLAIR sequence, it is typically hyper intense to CSF. Signal intensity varies depending on relative Tl and T2 effects. Acute hematomas can be isointense to CSF due to T2 shortening effects of intracellular methemoglobin. FLAIR is often the most reliable sequence. On T2* GRE the collection is hypo intense unless hyper acute. Finally on DWl it shows heterogeneous signal (nonspecific), but this sequence may be useful in order to differentiate extra axial empyema (marked central hyper intensity) from hemorrhage. Among the differential diagnoses it is possible to consider other subdural collection, like hygroma, that shows clear CSF without encapsulating membranes, subdural effusion, made by xanthochromic fluid secondary to extravasation of plasma from membrane, that appears 1–3 days post-trauma; near CSF density/intensity, and empyema, that generally has peripheral enhancement and shows hyper intensity on FLAIR and restricted diffusion on DWl. The epidural hematoma is a biconvex extra-axial collection, associated with fracture. It may cross dural attachments, limited by sutures Pachymeningopathies (thickened dura) derives from chronic meningitis (may be indistinguishable), neurosarcoid, with nodular, "lumpy-bumpy" appearance, or postsurgical (e.g., shunt), caused by intracranial hypotension with "slumping" midbrain and tonsillar herniation. Tumors, like meningiomas, lymphomas, leukemia, metastases are generally dural-based, enhancing masses, which in some cases may involve the adjacent skull and extracranial soft tissue. In the peripheral brain infarction, the cortex is involved, not displaced, and is typically hyper intense on DWl.

Subacute and chronic SDH (sSDH and cSDH) are infrequently the cause of a neurovascular emergence, due to the subtle onset and slow progression of the symptoms, also if in some cases is possible to withstand a patient with sudden loss of consciousness. Nevertheless the sSDH may represent a diagnostic challenge, especially with a NCCT study; as stated above a thin crescentic collection, without signs of recent rebleeding or older, chronic component, could be difficult to diagnose from a nonexperienced radiologist. In this case the diagnosis is made easier by administration of iodinated contrast media, eventually for other morbidities, while a conventional MRI study with a FLAIR sequence never misses the collection, albeit making sometimes necessary the differential diagnosis (DD) with other pathologies.

The diagnosis is much more easy in case of chronic SDH, which appears clearly hypodense on NCCT. In these case, without signs of rebleeding or presence of membranes inside the collection, it is necessary in some cases to distinguish a cSDH

from a hygroma: the DD could be made measuring the density of the collection compared with that of the CSF in the ventricles. The density of a cSDH is generally higher.

3.6 Cerebral Venous Thrombosis

Cerebral venous thrombosis (CVT) is an overall not frequent cerebrovascular pathology (incidence of CVT is estimated nowadays to be 1.32/100,000/year in Western Europe), accounting for 1% of strokes [87], and represents a really rare disease in the adult and elderly population: the vast majority of cases being observed in the young female population after a pregnancy or during oral contraceptives therapy. Nevertheless other causes like trauma, infection, inflammation or metabolic (dehydration, cirrhosis, thyrotoxicosis), and hematological (coagulopathy) are more common in the latest decades of life. Albeit rare CVT is potentially deadly (10–20% of untreated cases), and while the symptoms are often nonspecific, it is necessary to keep this pathology in the range of the possible diagnosis, also given the possibility of accurate diagnosis offered by the venous intracranial system analysis of a CTA or an MRI PC and post-contrast 3D sequence [88]. Unfortunately a patient with VCT may describe subtle symptoms, often represented only by headache, nausea, vomiting, without neurological deficit. The NCCT may be negative or nonspecific: in the latter case, it is possible to find smooth areas of white and gray matter edema, sometimes multiple and often without a definite vascular "arterial" pattern, as in the case of superior sagittal sinus involvement, with eventual signs of concurrent hemorrhage, representing the effect of venous congestion. In the more typical cases, the NCCT may show slight hyperdensity of involved sinuses (triangle sign on SSS) while the post-contrast scan reveals the hypodensity of the blood clot [89]. The parenchymal involvement is related generally to the occluded vessel: the temporal lobe is frequently affected in transverse and sigmoid sinus or Labbe' CVT, while thalami and basal ganglia are related, often bilaterally, in case of CVT located in the deep system (Internal cerebral vein, Vein of Galen, Straight sinus). In some cases instead the thrombosis could be limited to a small vein of the deep system and the subsequent surrounding edema may mimic an expansive lesion, while in others multiple venous vessels in different cerebral areas may be involved. In 30–40% of cases CVT presents or evolves with hemorrhage, generally intraparenchimal, focal, or petechial (Fig. 3.19). Sometimes a concurrent SAH may be seen. The hemorrhage worsens the prognosis and the outcome in patients with VCT. In fact it makes much more challenging the primary treatment, which relies on the administration of anticoagulative (not antithrombotic) drugs, whose effect could worsen the size and therefore the effect of hemorrhage. This occurrence makes of paramount importance the need for an early diagnosis of VCT, before the onset of the subsequent bleeding.

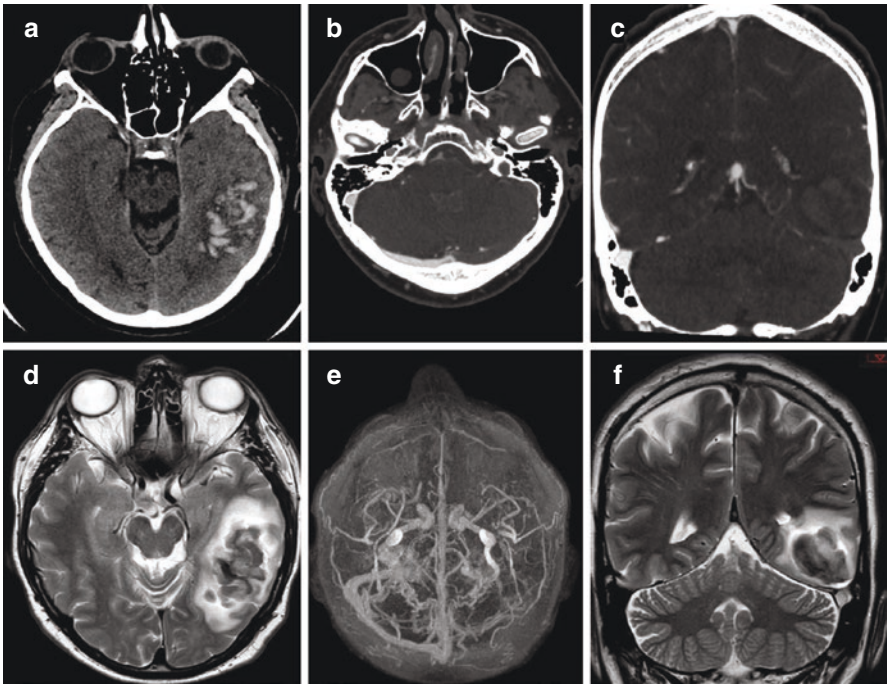

Fig. 3.19 Dural sinus thrombosis. A 74-year-old man hospitalized in a COVID+ intensive care unit for sudden and prolonged loss of consciousness. CT axial and ACT study showed an inhomogeneous hemorrhage with initial surrounding vasogenic edema in the left temporal lobe; the angio-CT demonstrated thrombosis of left transverse and sigmoid sinuses, with involvement of the homolateral Labbè vein and intracranial tract of the jugular vein (**a**–**c**). Follow-up MRI with 3D TOF angio-sequences confirmed the involvement of the venous structures, with extension to the extracranial proximal left jugular vein. Also note the enlargement of the vasogenic edema surrounding the hemorrhage (**d**–**f**)

References

1. Heron M. Deaths: leading causes for 2017. Natl Vital Stat Rep. 2019;68(6):1–77.
2. Howard G, Goff DC. Population shifts and the future of stroke: forecasts of the future burden of stroke. Ann N Y Acad Sci. 2012;1268:14–20. https://doi.org/10.1111/j.1749.
3. Saposnik G, Black S. Stroke in the very elderly: hospital care, case fatality and disposition. Cerebrovasc Dis. 2009;27(6):537–43. https://doi.org/10.1159/000214216.
4. Singer J, Gustafson D, Cummings C, Egelko A, Mlabasati J, Conigliaro A, Levine SR. Independent ischemic stroke risk factors in older Americans: a systematic review. Aging. 2019;11(10):3392–407. https://doi.org/10.18632/aging.101987.
5. El-Koussy M, Schroth G, Brekenfeld C, Arnold C. Imaging of acute ischemic stroke. Eur Neurol. 2014;72(5-6):309–16. https://doi.org/10.1159/000362719.
6. Eastwood JD, Lev MH, Provenzale JM. Correlation of early dynamic CT perfusion imaging with whole-brain MR diffusion and perfusion imaging in acute hemispheric stroke. AJNR. 2003;24:1869–75.

7. Wintermark M, Flanders AE, Velthuis B, et al. Perfusion-CT assessment of infarct core and penumbra: receiver operating characteristic curve analysis in 130 patients suspected of acute hemispheric stroke. Stroke. 2006;37(4):979–85. https://doi.org/10.1161/01.str.0000209238.61459.39.
8. Herpich F, Rincon F. Management of acute ischemic stroke. Crit Care Med. 2020;48:11. https://doi.org/10.1097/CCM.0000000000004597.
9. Schlaug G, et al. Time course of the apparent diffusion coefficient (ADC) abnormality in human stroke. Neurology. 1997;49(1):113–9. https://doi.org/10.1212/wnl.49.1.113.1997.
10. Lorenzano S, Rost NS, Muhib K, et al. Early molecular oxidative stress biomarkers of ischemic penumbra in acute stroke. Neurology. 2019;93(13):e1288–98. https://doi.org/10.1212/WNL.0000000000008158.
11. Sui B, Gao P. Imaging evaluation of acute ischemic stroke. J Int Med Res. 2020;48(1) https://doi.org/10.1177/0300060518802530.
12. Wufuer A, Wubuli A, Mijiti P, et al. Impact of collateral circulation status on favorable outcomes in thrombolysis treatment: a systematic review and meta-analysis. Exp Ther Med. 2018;15:707–18.
13. Leng X, Fang H, Leung TW, et al. Impact of collateral status on successful revascularization in endovascular treatment: a systematic review and meta-analysis. Cerebrovasc Dis. 2016;41:27–34.
14. Campbell B, Ma H, Ringleb P, et al. Extending thrombolysis to 4·5–9 h and wake-up stroke using perfusion imaging: a systematic review and meta-analysis of individual patient data. Lancet. 2019;394(10193):139–47. https://doi.org/10.1016/S0140-6736(19)31053-0.
15. Prabhakaran S, Ruff I, Bernstein RA. Acute stroke intervention: a systematic review. Clin Rev Educ. 2015;313(14):1451–62.
16. Zhu D, Wang Q, Zhao W, Li C, Xu L, Liu S. Efficacy and safety of vascular intervention combined with intravenous thrombolysis in treatment of acute intracranial arterial occlusion. Exp Ther Med. 2020;20(3):2903–8. https://doi.org/10.3892/etm.2020.9027.
17. Feigin VL, Lawes CM, Bennett DA, et al. Worldwide stroke incidence and early case fatality reported in 56 population-based studies: a systematic review. Lancet Neurol. 2009;8(4):355–69.
18. O'Donnell M, Yusuf S. Tackling the global burden of stroke: the need for large-scale international studies. Lancet Neurol. 2009;8(4):306–7.
19. van Asch CJ, Luitse MJ, Rinkel GJ, et al. Incidence, case fatality, and functional outcome of intracerebral haemorrhage over time, according to age, sex, and ethnic origin: a systematic review and meta-analysis. Lancet Neurol. 2010;9(2):167–76.
20. Bagg S, Pombo AP, Hopman W. Effect of age on functional outcomes after stroke rehabilitation. Stroke. 2002;33:179–85.
21. Hostettler IC, Seiffge DJ, Werring DJ. Intracerebral hemorrhage: an update on diagnosis and treatment. Expert Rev Neurother. 2019;19(7):1–16. https://doi.org/10.1080/14737175.2019.1623671.
22. Fisher CM. Pathological observations in hypertensive cerebral hemorrhage. J Neuropathol Exp Neurol. 1971;30(3):536–50.
23. Vinters HV. Cerebral amyloid angiopathy. A critical review. Stroke. 1987;18(2):311–24.
24. Morott A, Goldstein JN. Diagnosis and management of acute intracerebral hemorrhage. Emerg Med Clin North Am. 2016;34(4):883–99. https://doi.org/10.1016/j.emc.2016.06.010.
25. Wilson D, Charidimou A, Werring DJ. Advances in understanding spontaneous intracerebral hemorrhage: insights from neuroimaging. Expert Rev Neurother. 2014;14(6):661–78.
26. Macellari F, Paciaroni M, Agnelli G, Caso V. Neuroimaging in intracerebral hemorrhage. Stroke. 2014;45(3):903–8.
27. Yoon DY, Chang SK, Choi CS, Kim WK, Lee JH. Multidetector row CT angiography in spontaneous lobar intracerebral hemorrhage: a prospective comparison with conventional angiography. AJNR Am J Neuroradiol. 2009;30:962–7.
28. Manninen AL, Isokangas JM, Karttunen A, Siniluoto T, Nieminen MT. A comparison of radiation exposure between diagnostic CTA and DSA examinations of cerebral and cervicocerebral vessels. AJNR Am J Neuroradiol. 2012;33:2038–42.

29. Khosravani H, Mayer SA, Demchuk A, Jahromi BS, Gladstone DJ, Flaherty M, et al. Emergency noninvasive angiography for acute intracerebral hemorrhage. AJNR Am J Neuroradiol. 2013;34:1481–7.
30. Wardlaw JM, Smith EE, Biessels GJ, et al. Neuroimaging standards for research into small vessel disease and its contribution to ageing and neurodegeneration. Lancet Neurol. 2013;12(8):822–38.
31. Banerjee G, Carare R, Cordonnier C, et al. The increasing impact of cerebral amyloid angiopathy: essential new insights for clinical practice. J Neurol Neurosurg Psychiatry. 2017;88(11):982–94. Focused review on cerebral amyloid angiopathy.
32. Hilkens NA, van Asch CJJ, Werring DJ, et al. Predicting the presence of macrovascular causes in non-traumatic intracerebral haemorrhage: the DIAGRAM prediction score. J Neurol Neurosurg Psychiatry. 2018;89(7):674–9.
33. Hemphill JC, Greenberg SM, Anderson C. Guidelines for the management of spontaneous intracerebral hemorrhage: a guideline for healthcare professionals from the American Heart Association/American Stroke Association. Stroke. 2015;46(7):2032–60.
34. Caplan LR, Searls DE, Hon FKS. Cerebrovascular disease. Med Clin North Am. 2009;93(2):353–69. https://doi.org/10.1016/j.mcna.2008.09.004.
35. de Rooij NK, Linn FH, van der Plas JA, Algra A, Rinkel GJ. Incidence of subarachnoid haemorrhage: a systematic review with emphasis on region, age, gender and time trends. J Neurol Neurosurg Psychiatry. 2007;78:1365–72.
36. Fortuny LA, Adams CB, Briggs M. Surgical mortality in an aneurysm population: effects of age, blood pressure and preoperative neurological state. J Neurol Neurosurg Psychiatry. 1980;43:879–82.
37. Pobereskin LH. Incidence and outcome of subarachnoid haemorrhage: a retrospective population based study. J Neurol Neurosurg Psychiatry. 2001;70:340–3.
38. Thom T, Haase N, Rosamond W, et al. Heart disease and stroke statistics—2006 update: a report from the American Heart Association statistics committee and stroke statistics subcommittee. Circulation. 2006;113:e85–151.
39. Schöller K, Massmann M, Markl G, Kunz M, et al. Aneurysmal subarachnoid hemorrhage in elderly patients: long-term outcome and prognostic factors in an interdisciplinary treatment approach. J Neurol. 2013;260(4):1052–60. https://doi.org/10.1007/s00415-012-6758-1.
40. Ostergaard JR. Headache as a warning symptom of impending aneurismal subarachnoid haemorrhage. Cephalalgia. 1991;11(1):53–5.
41. van Gijn J, Rinkel GJ. Subarachnoid haemorrhage: diagnosis, causes and management. Brain. 2001;124:249–78.
42. Hostettler IC, Seiffge DJ, Werring DJ. Intracerebral hemorrhage: an update on diagnosis and treatment. Expert Rev Neurother. 2019;19(7):679–94.
43. Szepesi R, Szell IK, Hortobagyi T, et al. New prognostic score for the prediction of 30-day outcome in spontaneous supratentorial cerebral haemorrhage. Biomed Res Int. 2015;2015:961085.
44. Fiebach JB, Schellinger PD, Gass A, et al. Stroke magnetic resonance imaging is accurate in hyperacute intracerebral hemorrhage: a multicenter study on the validity of stroke imaging. Stroke. 2004;35:502–6.
45. Mitchell P, Wilkinson ID, Hoggard N, et al. Detection of subarachnoid haemorrhage with magnetic resonance imaging. J Neurol Neurosurg Psychiatry. 2001;70:205–11.
46. Papke K, Kuhl CK, Fruth M, Haupt C, Schlunz-Hendann M, Sauner D, et al. Intracranial aneurysms: role of multidetector CT angiography in diagnosis and endovascular therapy planning. Radiology. 2007;244(2):532–40.
47. Wintermark M, Uske A, Chalaron M, et al. Multislice computerized tomography angiography in the evaluation of intracranial aneurysms: a comparison with intraarterial digital subtraction angiography. J Neurosurg. 2003;98:828–36.
48. Tetri S, Juvela S, Saloheimo P, et al. Hypertension and diabetes as predictors of early death after spontaneous intracerebral hemorrhage. J Neurosurg. 2009;110(3):411–7.
49. Garbossa D, Panciani PP, Fornaro R, Crobeddu E, Marengo N, Fronda C, Ducati A, Bergui M, Fontanella M. Subarachnoid hemorrhage in elderly: advantages of the endovascular treatment. Geriatr Gerontol Int. 2011;12(1):46–9.

50. Nieuwkamp DJ. Subarachnoid haemorrhage in patients >=75 years: clinical course, treatment and outcome. J Neurol Neurosurg Psychiatry. 2006;77(8):933–7. https://doi.org/10.1136/jnnp.2005.0843.
51. Gardner R, Dams-O'Connor K, Morrissey MR, Manley GT. Geriatric traumatic brain injury: epidemiology, outcomes, knowledge gasp and future directions. J Neurotrauma. 2018;35(7):889–906. https://doi.org/10.1089/neu.2017.5371.
52. Kameyama M, Karibe H, Kawase M, Hayashi T, Hirano T, Tominaga T. Severe head injury and age in Japan Neurotrauma Data Bank: comparison among project 1998, 2004, and 2009. Neurotraumatology. 2013;36:10–6.
53. Timler D, Dworzyński MJ, Szarpak Ł, Gaszyńska E, Dudek K, Gałązkowski R. Head trauma in elderly patients: mechanisms of injuries and CT findings. Adv Clin Exp Med. 2015;24(6):1045–50. https://doi.org/10.17219/acem/27565.
54. Styrke J, Stalnacke BM, Sojka P, Bjornstig U. Traumatic brain injuries in a well-defined population: epidemiological aspects and severity. J. Neurotrauma. 2007;24:1425–36.
55. Eisenberg HM, Gary HE Jr, Aldrich EF, Saydjari C, Turner B, Foulkes MA, Jane JA, Marmarou A, Marshall LF, Young HF. Initial CT findings in 753 patients with severe head injury. A report from the NIH Traumatic Coma Data Bank. J Neurosurg. 1990 ; 73(5):688-698.
56. Jane JA, Francel PC. Age and outcome of head injury. In: Narayan RK, Wilberger Jr JE, Povlishock JT, editors. Neurotrauma. New York: McGraw-Hill; 1996. p. 793–804.
57. Tokutomi T, Ogawa T, Ono J, et al. Intracranial diagnosis according to the Traumatic Coma Data Bank classification of computed tomography imaging in the Japan Neurotrauma Data Bank. Neurotraumatology. 2005;28:1–5.
58. Smits M, Dippel DWJ, et al. External validation of the Canadian CT head rule and the New Orleans Criteria for CT scanning in patients with minor head injury. JAMA. 2005;294(12):1511–8.
59. Guide de bon usage des examens d'imagerie. http://www.sfrnet.org/sfr/professionnels/5-referentiels-bonnes-pratiques/guides/guide-bonusage-examens-imagerie-medicale/index.phtml.
60. Pages P-J, Boncoeur-Martel M-P, Dalmay F, Salle H, Caire F, Mounayer C, Rouchaud A. Relevance of emergency head CT scan for fall in the elderly person. J Neuroradiol. 2020;47(1):54–8. https://doi.org/10.1016/j.neurad.2019.03.004.
61. Mutch C, Talbott J, Gean A. Imaging evaluation of acute traumatic brain injury. Neurosurg Clin N Am. 2016;27(4):409–39. https://doi.org/10.1016/j.nec.2016.05.011.
62. Modi NJ, Agrawal M, Sinha VD. Post-traumatic subarachnoid hemorrhage: a review. Neurol India. 2016;64(Suppl):S8–S13. https://doi.org/10.4103/0028-3886.178030.
63. Gauvrit J-Y, Leclerc X, Ferré J-C, Taschner C-A, Carsin-Nicol B, Auffray-Calvier E, Morandi X, Carsin M. Imagerie de l'hémorragie sous-arachnoïdienne. J Neuroradiol. 2009;36(2):65–73. https://doi.org/10.1016/j.neurad.2008.06.005.
64. Edlow JA, Caplan LR. Avoiding pitfalls in the diagnosis of subarachnoid hemorrhage. N Engl J Med. 2000;342(1):29–36. https://doi.org/10.1056/nejm200001063420106.
65. Agrawal M, Modi N, Sinha VD. Neurological outcome in patients of traumatic subarachnoid haemorrhage: a study of prognostic factors and role of MRI. IJNT2014;11:10–6.
66. Boesiger BM, Shiber JR. Subarachnoid hemorrhage diagnosis by computed tomography and lumbar puncture: are fifth generation CT scanners better at identifying subarachnoid hemorrhage ? J Emerg Med. 2005;29:23–7.
67. Long B, Koyfman A, Runyon MS. Subarachnoid hemorrhage. Emerg Med Clin North Am. 2017;35(4):803–24. https://doi.org/10.1016/j.emc.2017.07.001.
68. Martinez-valverde T, Vidal-jorge M, Marrtinez-Saez E, et al. Sulfonylurea receptor 1 in humans with post-traumatic brain contusion. J Neurotrauma. 2015;32(19):1478–87. https://doi.org/10.1089/neu.2014.3706. Epub 2015 Jun 3.
69. Katayama Y, Tsubokawa T, Miyazaki S, Kawamata T, Yoshino A. Oedema fluid formation within contused brain tissue as a cause of medically uncontrollable elevation of intracranial pressure in head trauma patients. Acta Neurochir. 1990;s51:308–10.
70. Gentry LR. Imaging of closed head injury. Radiology. 1994;191(1):1–17.

71. Bruggeman GF, Haitsma IK, Dirven CMF, Volovic V. Traumatic axonal injury (TAI): definitions, pathophysiology and imaging a narrative review. Acta Neurochir. 2021;163:31–44.
72. Gennarelli TA, Thibault LE, Adams JH, Graham DI, Thompson CJ, Marcincin RP. Diffuse axonal injury and traumatic coma in the primate. Ann Neurol. 1982;12:564–74.
73. Ma J, Zhang K, Wang Z, Chen G. Progress of research on diffuse axonal injury after traumatic brain injury. Neural Plast. 2016;2016:9746313. https://doi.org/10.1155/2016/9746313.
74. Besenski N. Traumatic injuries: imaging of head injuries. Eur Radiol. 2002;12:1237–52.
75. Takayama H, Kobayashi M, Sugishita M, Mihara B. Diffusion-weighted imaging demonstrates transient cytotoxic edema involving the corpus callosum in a patient with diffuse brain injury. Clin Neurol Neurosurg. 2000;102:135–9.
76. Ezaki Y, Tsutsumi K, Morikawa M, Nagata I. Role of diffusion-weighted magnetic resonance imaging in diffuse axonal injury. Acta Radiol. 2006;47:733–40.
77. Arfanakis K, Haughton VM, Carew JD, Rogers BP, Dempsey RJ, Meyerand ME. Diffusion tensor MR imaging in diffuse axonal injury. AJNR Am J Neuroradiol. 2002;23:794–802.
78. Rau CS, Lin TS, Wu SC, Yang JC, Hsu SY, Cho TY, Hsieh CH. Geriatric hospitalizations in fall-related injuries. Scand J Trauma Resusc Emerg Med. 2014;22:63. https://doi.org/10.1186/s13049-014-0063-1.
79. Ryan CG, Thompson RE, Temkin NR, Crane PK, Ellenbogen RG, Elmore JG. Acute traumatic subdural hematoma: current mortality and functional outcomes in adult patients at a Level I trauma center. J Trauma Acute Care Surg. 2012;73:1348–54. https://doi.org/10.1097/TA.0b013e31826fcb30.
80. Leitgeb J, Mauritz W, Brazinova A, Janciak I, Majdan M, Wilbacher I, Rusnak M. Outcome after severe brain trauma due to acute subdural hematoma. J Neurosurg. 2012;117:324–33. https://doi.org/10.3171/2012.4.JNS111448.
81. Hsieh C-H, Rau C-S, Shao-Chun W, Liu H-T, Huang C-Y, Hsu S-Y, Hsieh H-Y. Risk factors contributing to higher mortality rates in elderly patients with acute traumatic subdural hematoma sustained in a fall: a cross-sectional analysis using registered trauma data. Int J Environ Res Public Health. 2018;15(11):2426.
82. Ledic D, Girotto D, Pal S, Kolbah B. Risk factors for subdural bleeding in elderly population. Coll Antropol. 2014;38:1195–8.
83. Shen J, Pan JW, Fan ZX, Zhou YQ, Chen Z, Zhan RY. Surgery for contralateral acute epidural hematoma following acute subdural hematoma evacuation: five new cases and a short literature review. Acta Neurochir. 2013;155:335–41. https://doi.org/10.1007/s00701-012-1569-9.
84. Maxeiner H, Wolff M. Pure subdural hematomas: a postmortem analysis of their form and bleeding points. Neurosurgery. 2002;50:503–8; discussion 508–9.
85. Chisholm KM, Harruff RC. Elderly deaths due to ground-level falls. Am J Forensic Med Pathol. 2010;31:350–4. https://doi.org/10.1097/PAF.0b013e3181f69c87.
86. Anandasivam NS, Russo GS, Samuel AM, Grant R, Bohl DD, Grauer JN. Injuries associated with subdural hematoma: a study of the National Trauma Data Bank. Conn Med. 2017;81:215–22.
87. Nasr DM, et al. Mortality in cerebral venous thrombosis: results from national inpatient sample database. Cerebrovasc Dis. 2013;35(1):40–4.
88. Connor SEJ, Jarosz JMJ. Magnetic resonance imaging of cerebral venous sinus thrombosis. Clin Radiol. 2002;57(6):449–61.
89. Coutinho JM, Zuurbier SM, Aramideh M, Stam J. The incidence of cerebral venous thrombosis: a cross-sectional study. Stroke. 2012;43(12):3375–7.

Head and Neck in Geriatric Patients

4

T. Popolizio, L. Cassano, A. Pennelli, R. Izzo, G. Fascia, M. Masciavè, and Giuseppe Guglielmi

Learning Objectives
After reading this chapter, readers should be able to:

- Detect the more frequent diseases in geriatric patients
- Be aware the radiologic characteristics
- Know the clinical manifestations of the main geriatric diseases of the head of the neck

4.1 Ear

4.1.1 Chronic Suppurative Otitis Media

Chronic suppurative otitis media is a very common disease that should be carefully treated, as severe complications can develop. Despite the significantly decreased incidence of chronic suppurative otitis media related complications since the

T. Popolizio · A. Pennelli · R. Izzo
Radiology Unit, Hospital "Casa Sollievo della Sofferenza", San Giovanni Rotondo, Italy

L. Cassano
Otolaryngology Unit, Hospital "Casa Sollievo Della Sofferenza", San Giovanni Rotondo, Italy
e-mail: l.cassano@operapadrepio.it

G. Fascia · M. Masciavè
Department of Clinical and Experimental Medicine, Foggia University School of Medicine, Foggia, Italy
e-mail: giacomo.fascia@unifg.it

G. Guglielmi (✉)
Clinical and Experimental Medicine, University of Foggia, Foggia, Foggia, Italy
e-mail: giuseppe.guglielmi@unifg.it, http://www.unifg.it

G. Guglielmi, M. Maas (eds.), *Imaging in Geriatrics*, Practical Issues in Geriatrics, https://doi.org/10.1007/978-3-031-14877-4_4

introduction of antibiotics, this clinical problem has not been eliminated. Chronic suppurative otitis media remains a serious concern, particularly in developing countries and socioeconomically poor regions [1–4].

Complications of CSOM can be classed as extracranial (EC) or intracranial (IC). Extracranial complications include mastoid abscess, petrositis, labyrinthitis, facial nerve paralysis (FNP), and Bezold's abscess. Intracranial complications comprise intracranial abscess (including extradural, epidural, subdural, perisigmoid sinus, and brain abscesses), lateral sinus thrombophlebitis (LST), meningitis, and otitic hydrocephalus. The pathophysiology of complications of CSOM remains somewhat of a mystery. The pathways of EC and IC complications include thrombophlebitis of the venules of the adjoining cranial bones, bone erosion by pressure or enzymatic actions, preformed pathways, and hematogenous spread [5–8].

4.1.1.1 Extracranial Complication

Coalescent Mastoiditis

The treatment for acute mastoiditis can fail and sometimes there is an enzymatic destruction of the mastoid septa and the development of an intramastoid empyema. TC can visualize these erosive changes very early [9, 10].

Subperiosteal Abscess

It typically occurs via direct extension of the inflammatory debris through a defect in the external context of the mastoid sinus. This passage can occur in any direction: post-auricular, common as the bone is particularly thin (Macewan's triangle) or infero-medial, medial to the attachment of sternocleidomastoid (resulting in a Bezold's abscess) [11].

Bezold's abscess is comparable to the subperiosteal abscess but takes place through a bony defect at the mastoid tip, medial to the insertion of the posterior belly of digastric.

CT can demonstrate coalescent mastoiditis with erosion of the medial mastoid tip [12].

This defect could let infection expand into the neck.

CT also shows thickening of the omolateral sternocleidomastoid muscles with surrounding inflammatory changes, heterogeneous post contrast enhancement with rim enhancing cystic lesion [13, 14].

Petrositis

It is an infection with involvement of bone at petrous apex of the temporal bone.

CT is the modality of choice to evaluate bony changes in the temporal bone, revealing debris within the petrous apex, air cells, and erosive lysis of bony septa [15–18].

Disruption of the anterior or posterior bony cortex may occur resulting in fulminant intracranial complication (meningitis, empyema, dural sinus thrombosis, cranial neuropathy).

At the onset diagnosis of petrus, apex inflammatory disease is best made with high-resolution CT. Later MR imaging becomes important to assess intracranial complications [19, 20].

Labyrinthitis

The acute stage results when bacteria and other pathogenic noxae filled the perilymphatic spaces, inducing acute inflammatory response.

The CT is normal at this stage, and the endolymphatic space is spared.

The majority of patients will not have enhancement or any imaging findings. Sometimes there is enhancement of the normally not enhanced fluid-filled spaces of the labyrinth on T1-weighted images [21, 22].

The enhancement may persist long after symptoms, there is an accumulation of gadolinium within inflamed labyrinthine membrane because of the breakdown of the labyrinthine vasculature [10].

The combination of pathological labyrinthine enhancement and thickening/enhancement of the seventh nerve should induce suspicion of EAC [23, 24].

If acute labyrinthitis does not resolve, the progression to chronic disease results first in fibrous change and then in ossification.

The fibrous stage is characterized by fibroblastic proliferation within the perilymphatic spaces (begins after 2 weeks after the onset of infection). CT is normal while T2-weighed MR images show replacement of the normal high signal of the fluid-filled spaces of the labyrinth, detected at the cochlear apex [25, 26].

The ossify stage consists of pathological ossification of the membranous labyrinth [27, 28].

The CT appearance is characterized by high-density bone deposition within the membranous labyrinth, from hazy increase in density within fluid spaces of the membranous labyrinth (mild disease) or focal areas of bony invasion on fluid spaces (moderate disease) or with total obliteration by bony replacing fluid spaces (severe disease) [29, 30].

MRI will show loss of normal signal fluid in membranous labyrinth in T2-weighted images as hypointense foci in labyrinth.

Facial Nerve Involvement

It may occur facilitated by the development of dehiscence that allows the passage of inflammatory products. CT and MRI are helpful for identifying bony facial canal and soft tissue abnormalities, respectively. When using CT to evaluate the facial nerve, pathology often can only be deducted by visualization of erosion or destruction of the adjacent bony facial nerve canal [31]. MRI, instead, visualizes soft tissues well and so is more appropriate for evaluating soft tissue facial nerve abnormalities. In high-resolution T2-weighted images or CISS images, the normal facial nerve appears as a hypointense linear structure extending from the brainstem to the IAC, anterior to the vestibulocochlear nerve, surrounded by T2 hyperintense cerebrospinal fluid. The labyrinthine, tympanic, and mastoid segments of the facial nerve are not typically well visualized in non-contrast images. Mastoiditis and acute otitis media occur simultaneously determining engorgement of the normal aeration

of the mastoid cells and reducing the vascular perfusion of the mucosa and decreases the tissue penetration of antibiotics [32]. The inflammatory process on the facial nerve canal, through canal dehiscence or invasion of infectious microorganisms, results in inflammation and edema of the nerve inside its canal. The venous return decreases and the pressure increases on the nerve, which leads to nerve dysfunction. As the limits of the facial nerve canal are narrow, the accumulation of purulent secretion inside the canal leads to mechanical compression and ischemic neuritis. Persistent inflammation of the middle ear can also cause dehiscence of the facial nerve canal, which leads to consequent facial paralysis [33].

Gradenigo's Syndrome

It consists of the triad: suppurative otitis media, abducent nerve palsy, retroorbital pain due to the extension of inflammation into Meckel cave. In patients with suppurative otis media infection may spread to the petrous apex of the temporal bone and may be via pneumatized air cell tracts, through vascular channels or as a result of direct extension through fascial planes. Abducent nerve is close to the petrous apex separated from it only by dura mater, lies medial and adjacent to the trigeminal ganglion, passing through Dorello canal. Extradural inflammation secondary to apical petrositis may affect the above structures and generate the symptoms of Gradenigo's syndrome [34–40].

4.1.1.2 Intracranial Complications

Intracranial complications secondary to chronic otitis media (COM) include extradural abscess, subdural abscess, meningitis (with or without encephalitis), otogenic brain abscess, and lateral or sigmoid sinus thrombosis. Age (first decade or elderly), immunosuppression, and presence of cholesteatoma are among the common influencing factors for the development of intracranial complications [41].

Otogenic Brain Abscess

Otogenic brain abscesses are one of the most significant life-threatening complications of otologic infections. Given their low prevalence, otogenic brain abscesses require a high index of suspicion for diagnosis [42, 43].

CT shows a soft tissue mass in the middle ear and mastoid with erosion of the middle ear ossicles, expansion of the aditus of antrum, and erosion of the tegmen [44].

A well-demarcated oval mass with hypo-intense content and faint hyperintense rim, with considerable mass effect on the brainstem. On FLAIR it has mixed content, thin hypointense rim, surrounding edema and mass-effect, hyperintense signal in petrous bone. Following administration of contrast, there is rim enhancement of the lesion and continuity with adjacent dural enhancement. The content demonstrates intense diffusion restriction in DWI [45].

Sinus Thrombophlebitis

Sinus thrombophlebitis is caused by spread of infection to the inner wall of the venous sinus, leading to the formation of a thrombus through the action of fibrin and platelets, a process called endophlebitis [46].

CT scan is useful in demonstrating the classic "delta sign" of perisinus dural enhancement and filling defect of the lateral sinus and also can avoid by excluding other intracranial complications.

MRI is more sensitive than CT in detecting the thrombus. It shows blood flow, sinus obstruction, and subsequent reversal of flow.

MRI can show increased signal intensity of the thrombus and detect LST not identified on a routine CT. On T1-weighted MRI after contrast, thrombus appears as soft tissue signal associated with vascular bright appearance of the dural wall: the "delta" sign. MR venography, additionally, can demonstrate the loss of signal and the absence of flow in the sinus. MRI is the investigation of choice and should be performed in conjunction with CT, thereby fully evaluating associated otologic and cerebral pathology. Magnetic resonance imaging is also useful for excluding an adjacent subdural empyema, cerebritis, or cerebral abscess. Complete occlusion of the sinus may occur, and presence of organisms may promote the formation of an intrasinus abscess, whereby a septic emboli will have systemic manifestations in the form of septicemia. Distal and proximal extensions may occur (Fig. 4.1) [47, 48].

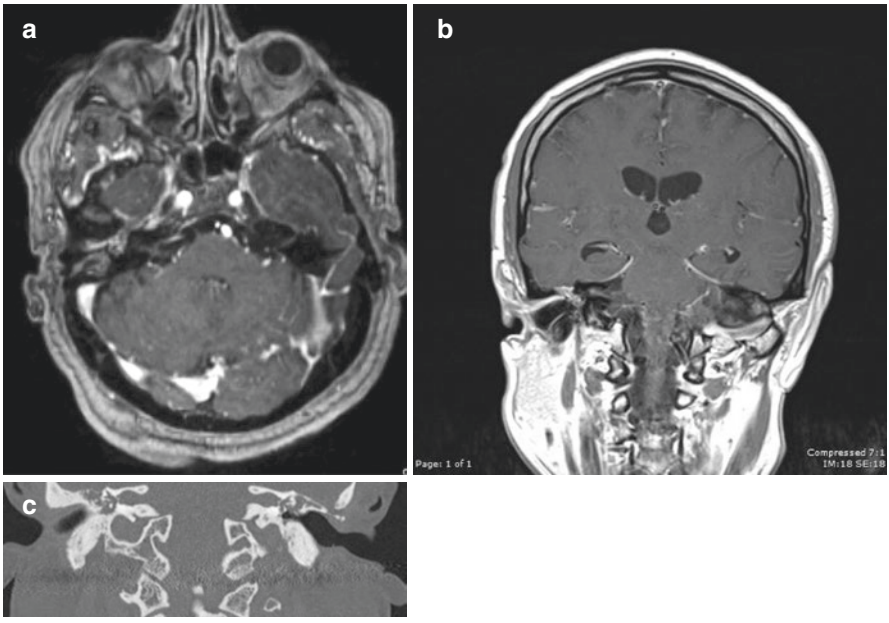

Fig. 4.1 Necrotizing external otitis. Meningo-encephalitis complication. Post-contrast T1-w coronal (**a**) and axial (**b**): high contrast enhancement of right middle ear and mastoid with focal thickening of the meningeal sheets in the middle crania fossa close to the petrous bone. In the late sequences (**b**) a small area of vivid contrast enhancement with blurred borders can be appreciated in the adjoining brain parenchyma. Findings are suggestive for meningo-encephalitis. NCCT coronal MPR reconstruction (**c**): the right residual middle ear is filled with homogeneously hypodense tissue. No erosions of the epitympanic recess are evident. The stapes shows some bone changes. The tegmen tympani is eroded. The superior semicircular canal is not well depicted. On the left, a small amount of homogeneous hypodense tissue is attached to the cochlear promontory

4.1.2 Malignant Otitis Externa

Malignant (necrotizing) otitis externa (MOE) is an aggressive form of skin inflammation of the external ear with a tendency to spread the infection to the temporal cortical bone, leading to potential skull base osteomyelitis. The condition was first reported by Toulmouche in 1838 [5] and is mentioned as the first case report of this disease. The most common causative pathogen is *Pseudomonas aeruginosa*, especially in immunocompromised patients with diabetes, HIV, leukemia, granulocytopenia, anemia, on immunosuppressive therapy. In addition, some species of fungi have been described as a causative agent, such as *Aspergillus* and *Candida* species. Several cases of methicillin-resistant *Staphylococcus aureus* (MRSA) have been described, and there is an ongoing increase in the MOE causative agents, such as *Klebsiella* and *Proteus* mirabilis [26, 49].

The mechanism of tissue damage involves coagulation tissue necrosis because of microangiopathy of small blood vessels. The most common clinical findings are severe otalgia, otorrhea, impaired hearing, and granulation polyps. The facial nerve is the most commonly involved cranial nerve, but glossopharyngeal, vagus, accessory, or hypoglossal nerves could also be affected [50, 51].

Diagnosis was based on anamnesis, clinical examination, audiological assessment, microbiological analysis of ear swab, and CT (computed tomography) scan of the temporal bone, skull base, and endocranium. Notably, the diagnostic criteria have changed over time [52, 53].

The primary treatment of MOE is long-term antimicrobial therapy. Other treatment strategies include close follow-up of blood glucose levels and inflammation markers and repeated local debridement of necrotic tissue. Lately, increased use of the hyperbaric oxygen chamber has been noted as one of the therapeutic modalities.

CT and MRI are complementary in the evaluation of NEO [54, 55].

CT can better study cortical bone erosion in the region of external auditory canal, especially at initial diagnosis, as small cortical erosions are better seen. On contrast-enhanced CT, there can be thickening and enhancing soft tissue and, in cases of abscess, it can be observed cartilaginous bone ring enhancing collection with a center of necrotic low attenuation [56].

MRI demonstrates soft tissue extension, cranial nerve involvement, parenchymal and meningeal disease.

Subtemporal soft tissue abnormalities had low signal intensity on T1- and T2-weighted images. Soft tissue changes improve but did not disappear completely with treatment.

Either modality can be used to follow up soft tissue evolution. Nuclear imaging studies are useful for continued surveillance of disease activity (Fig. 4.2).

4.1.3 Hearing Loss and Cognitive Decline

Alterations in sensory functions, vision, balance, and hearing are some of the most common disturbances seen in the aging population and lead to dramatic social and

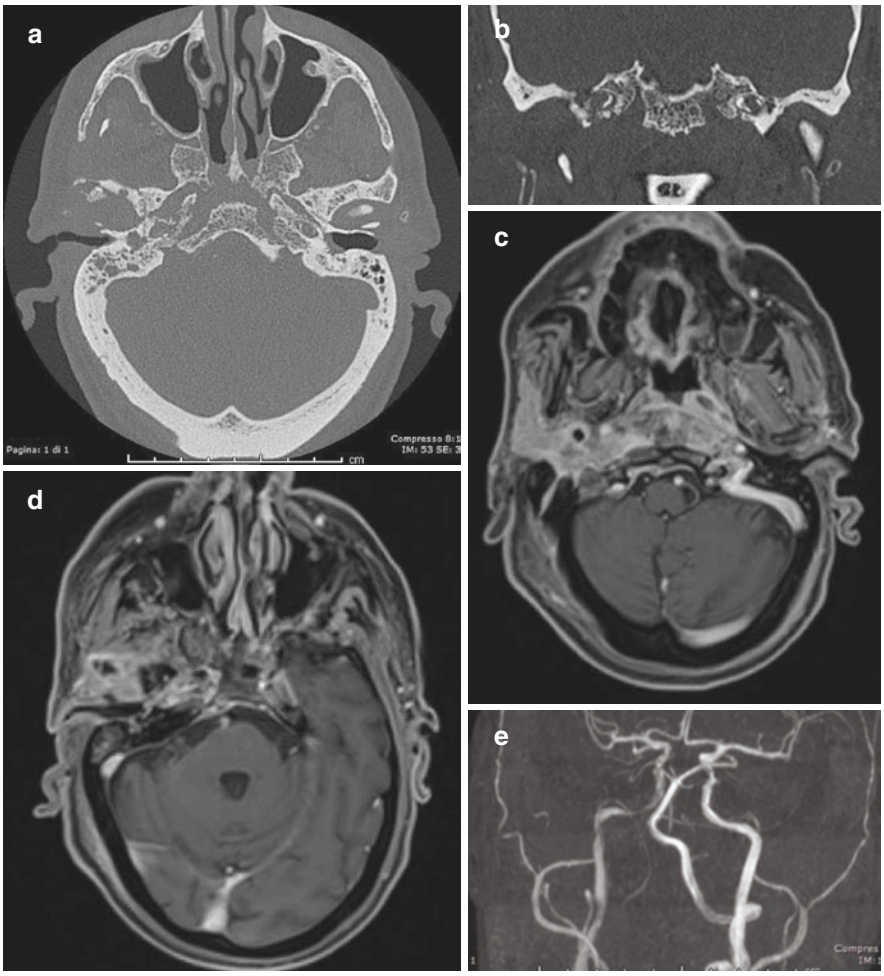

Fig. 4.2 Necrotizing external otitis. Carotid stenosis complication. Axial (**a**) CT and coronal (**b**) CT images show on the right side erosion of the glenoid joint, the jaw condyle, the apex of the petrous part of the temporal bone, the carotid canal, and clivus. Hypodense tissue fills the middle ear and mastoid cavities. There are no signs of bone or ossicular chain erosion. Post-contrast T1-w MRI (**c** and **d**) shows avid enhancement of temporo-mandibular joint that extends to the petrous part of the temporal bone, clivus pterygoid space, skull base, and cavernous sinus. Encasement of the intrapetrous segments of the internal carotid artery can also be appreciated, which appear stenotic as depicted in the 3D MRI TOF (**e**). Also, the lesion expands through the masticatory space, engaging the lateral pterygoid muscles, and the prevertebral space involving the posterior wall of rhinopharynx, which is swelled. It focally overpasses the midline affecting the left lateral pterygoid muscle. Autologous 99mTc-HMPAO-labeled leukocyte scintigraphy (**f**) shows accumulation in the right mastoid bone, skull base, rhinopharynx, and clivus

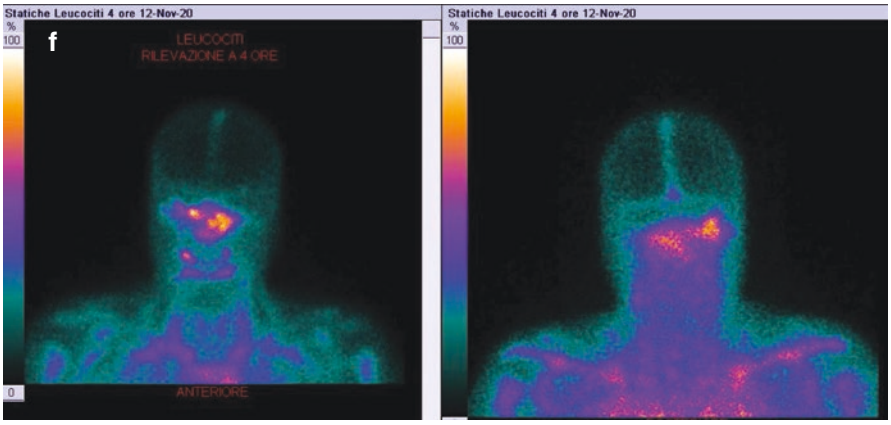

Fig. 4.2 (continued)

functional disability. Among the senses affected by increasing age, hearing loss is the most common. Presbycusis, or age-related hearing loss (ARHL), is a term that refers to hearing loss as a result of physiologic and pathologic changes associated with increasing age. As the aging population continues to grow, greater focus is placed on understanding and attempting to reverse this sensory loss for the benefit of geriatric patients. Today, there is an established although still evolving concept of the workings of the outer ear, middle ear, and inner ear.

Presbycusis may present insidiously and be confounded by various medical, psychological, and pharmacologic factors. Only after thorough history, examination, and audiological testing can a diagnosis of presbycusis be made after excluding concurrent medical and pharmacologic effects. In general, the first signs of ARHL can be seen in late middle age with high-frequency hearing losses in the realm of conversation frequencies, ultimately progressing subtly to lower frequency tones. The range of human auditory frequencies spans 20–20,000 Hz, with speech frequencies ranging from 400 to 5000 Hz, with the greatest loss in hearing seen in frequencies greater than or equal to 2000 Hz. The loss of this linguistic information results in many of the complaints in presbycusis. The loss of meaning is seen in deterioration of speech intelligibility, the loss of clear separation between words results in speech sounding mumbled, and the loss of syllables causes difficulty discerning similarly sounding words. Patients with presbycusis rely on conversational, emotional, and postural context clues to compensate for their hearing impairment, requiring a greater amount of higher order cognitive functioning to understand daily conversations.

4.1.3.1 Osseointegrated Auditory Implants

Osseointegrated auditory implants like the bone-anchored hearing aid (BAHA) systems are approved in the United States for patients with single-sided deafness (SSD) or those with a conductive/mixed hearing loss (CMHL) who cannot use traditional amplification. The use of BAHA systems began in patients with dental implants.

These individuals noted the perception of sound through an osseointegrated dental implant. BAHA systems use an external processor to amplify sound waves as vibrations that are delivered to the inner ear. Older patients fitted with a BAHA experience substantially improved hearing and word and speech recognition and obtain greater sound localization, and substantial numbers report improvement in quality of life.

4.1.3.2 Cochlear Implantation

Although most older patients are appropriate candidates for amplification, up to 10% of older patients with hearing loss suffer from hearing loss severe enough that amplification cannot provide significant benefit. Cochlear implants, devices placed into the inner ear to restore the perception of sound, are an effective intervention for older patients who do not benefit from amplification. Unfortunately, the rate of cochlear implant use in older adults who meet candidacy criteria is less than 5%. Outcomes of cochlear implantation are closely related to the duration of deafness, and counseling patients and their families on reasonable expectations is essential. Cognitive evaluations can help guide assessment and counseling. Cochlear implantation is a surgery commonly performed under general anesthesia, lasting less than 2 h. Despite the short nature of the surgery, careful attention must be paid to medical comorbidities [57–59].

Older cochlear implant users show greater confidence and participation in social settings than they did preoperatively. Moreover, older cochlear implant users and their families also reported high levels of satisfaction and hearing benefits from their devices.

Radiologists play an essential role in the pre- and postoperative evaluation and selection of CI candidates. Preoperative imaging is important to diagnose any type of inner ear malformations and to identify other abnormalities in the temporal bone that may be encountered. It allows the best insight into all relevant anatomical details and potential situations which preclude surgery or require modifying standard surgical approaches. Postoperative imaging is important to confirm and document the intended electrode position and to demonstrate any scalar dislocation, cochlear dislocation, electrode fold, or malposition, which can be a possible source of CI malfunction [60–62].

Preoperative imaging in CI candidates is based on high-resolution computed tomography (HRCT) and magnetic resonance imaging.

The strength of HRCT is the detailed visualization of the bony structures of the middle and inner ear, helping to determine the probability of success of the procedure, influencing the choice of implants, and allowing the surgeon to choose the best side of implantation. CT is ideal for ossific disease in chronic labyrinthitis because such condition, if very extensive, can preclude the implantation [63, 64].

An absent cochlear nerve, congenital or acquired, is the only complete contraindication to successful cochlear implantation [65].

Bilateral acoustic and disruptive fractures of the cochlea are relative contraindication to implantation.

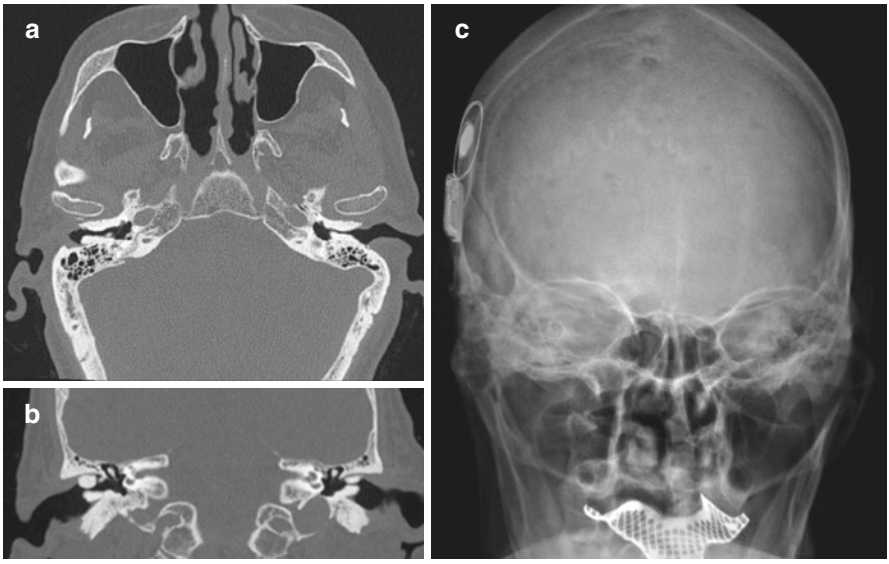

Fig. 4.3 External auditory canal exostoses—hearing loss. NCCT Ax (**a**) and Cor (**b**): broad-based and focal circumferential bony overgrowth of the osseous external auditory canal causing stenosis of the left auditory canal. Stenosis external acoustic. X-ray (**c**) of implant shows how well it is the curve of the skull

MRI can visualize the fluid content of the membranous labyrinth. Visualization of the vestibulocochlear nerve in the fluid-filled internal auditory canal and cerebellopontine angle is only possible by the MRI [66, 67].

Postoperative imaging is required when a malfunction of the device is suspected [63]. However, the authors perform—and recommend to do so—a postoperative examination in every patient to confirm the correct position of the implant electrode. Information regarding basal electrode location helps improving programming accuracy, associated frequency allocation, and audibility with appropriate deactivation of extracochlear electrodes [68, 69].

Postoperative CT has turned out to be useful in visualizing position of the electrode array by using HRCT or cone-beam computed tomography (CBCT). Successful cochlear implantation requires that the electrode be confined to the scala tympani. In general, CBCT is associated with lower dose and less metal artifacts when compared to HRCT (Fig. 4.3) [70].

4.2 Nose

4.2.1 Rhinosinusitis

Based on the Medical Expenditure Panel Survey for 2007, which concerned 225.1 million Americans, Bhattacharyya estimated the prevalence of chronic rhinosinusitis (CRS) (with nasal polyps or without nasal polyps) at 0.2% or 490/10,000

population. When analyzing the information obtained on 57,128 people aged 15–75 years who lived in 19 centers in 12 European countries, the Global Allergy and Asthma Network of Excellence study concluded that the overall prevalence of CRS, based on European position paper on rhinosinusitis and nasal polyps (EP3OS) criteria, was 10.9% (range, 6.9–27.1%) [71, 72].

The size of the geriatric population is on the increase in developed countries: the U.S. Census Bureau estimated that 20% of the U.S. population will be at least 65 years old by 2030. Recently, the prevalence of CRS among people 60 years was calculated at 4.7%, and rhinosinusitis was judged to be the sixth most common chronic condition in the elderly [73, 74].

There are several factors that predispose the elderly to chronic paranasal sinus inflammatory disease. Age-related changes in the nasal and paranasal mucosa include:

- An increase in the volume and a decrease in the elasticity of the nasal mucosa [75, 76]
- A reduced or absent nasal cycle, partly due to a declining ciliary efficacy
- Atrophy of the supporting fibro fatty tissues of the nose, with a potential loss of support for the nasal structures (narrowing of the nasal valve), which gives rise to more nasal obstruction
- A higher incidence of rhinorrhea with more mucus due to increased glandular activity and more viscous secretions and excess mucus crusting [77]

Aging in patients with CRS is also characterized by an increasing likelihood of comorbid conditions and the use of several types of medication, such as bisphosphonates, non-steroidal anti-inflammatory drugs, antihypertensive agents, antidepressants, and vitamins.

There are several forms of chronic sinonasal inflammation including chronic bacterial sinusitis, allergic sinusitis, fungal, and vasomotor sinusitis.

The two primary diagnostic imaging technique for evaluating the paranasal sinus are CT and MRI [78].

The main role of CT is to aid the diagnosis and management of recurrent and chronic disease, to define anatomy and to help the preoperative planning of FESS. CT can differentiate pathologic variation and better shows, because of its 3D high resolution, anatomic structures inaccessible by physical examination or endoscopy [79].

CT is more readily available than MRI.

The use of a bone algorithm provides resolution of osteomeatal complex and other anatomic factors. The characteristic findings include: air-fluid level, mucosal thickening, and opacification of the normal aerated lume [80, 81].

CT is superior to MRI for the delimitation of the fine bone structures of the infundibular complex, orbital lamina, orbital floor, and cribriform lamina [82].

MRI might be used to assess therapeutic success in patients with inflammatory disease with the advantage of avoiding radiation exposure. It can be used in screening for foci of septic disease before implantation of organs and prostheses, in the diagnosis of complication of sinus infection or FESS (Fig. 4.4).

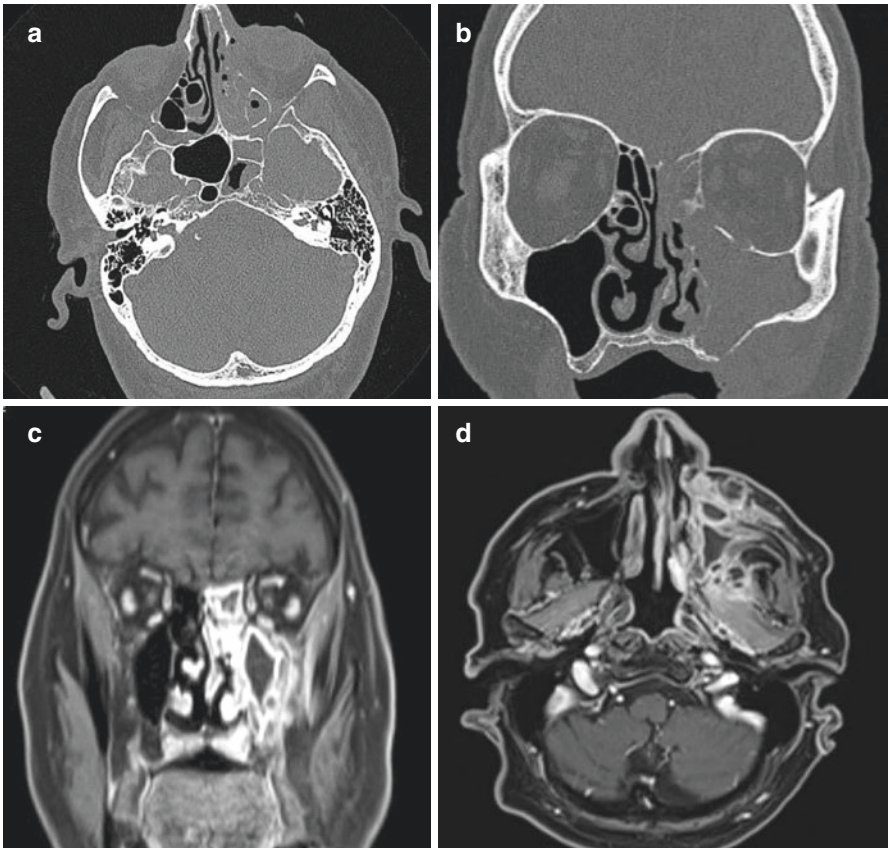

Fig. 4.4 Acute rhinosinusitis. NCCT bone algorithm, axial (**a**) and coronal MPR (**b**). The maxillary sinus is filled with hypodense tissue that also involves the upper and middle ethmoid cells and the sphenoid sinus. Focal interruptions of lamina papyracea, cribriform plate, orbital floor, and the maxillary bone are evident. Reticulation of the medial intraorbitary fat tissue is present suggesting involvement. On post-contrast T1-w MRI, axial (**c**) and coronal (**d**) images, the pathologic tissue has low signal on T1-w and intermediate on T2-w (not shown), fuzzy margins and determines structural bone changes and focal interruptions. Internal fluid components are present, which show proton diffusion restriction on DWI (not shown), compatible with abscess. Also, there is involvement of pterygopalatine fossa, infratemporal fossa, lateral pterygoid muscle, the choana, and the let nasal cavities

4.2.2 Inverted Papilloma

Sinonasal inverted papilloma (IP) is one of the most common benign epithelial tumors of the nose and paranasal sinuses. It accounts for 0.5–4% of all nasal tumors, with a male/female ratio of 2–4:1.1 It originates from the Schneiderian membrane that lines both nasal and paranasal areas. The invagination of such epithelial

membrane within the submucosal stroma is the typical histological aspect of this tumor. The age at onset varies, but it is mostly encountered between the fifth and sixth decades of life. Although the precise etiology is not clear, several external factors and a relationship with some subtypes of the human papilloma virus are reported in almost 40% of patients. It has been suggested that sinonasal IP can progress to squamous cell carcinoma; some recent articles stated that alteration of cell cycle–related proteins may contribute to the malignant transformation from IP to squamous cell carcinoma. As initially reported, the origins of tumor were observed in the lateral nasal wall (82%), maxillary sinus (53.9%), ethmoid sinus (31.6%), frontal sinus (6.5%), and sphenoid sinus (3.9%) [83–85].

The proposed treatment for IP has always been a radical surgical removal based on the recurrence rates and the possibility of malignant transformation/association with malignant lesions. As stated in the literature, we confirmed that the tumor presented a pedicle and a single site of attachment. The research of the pedicle's attachment is facilitated by radiological examination because, according to several recent articles, the site of tumor attachment can be frequently predicted by both computed tomography (CT) and magnetic resonance imaging (MRI) scans. Moreover, in most cases, the tumor's pedicle and the site of attachment can be accurately unveiled during surgery, and the tumor's extension can be precisely studied [86, 87].

Even though combined CT and MRI are useful for preoperative assessment of sinonasal IP, differentiation of IP from other malignant sinonasal tumors is often difficult because the overlap of imaging features. CT demonstrates soft tissue density mass with enhancement. The location of the mass leads toward the correct diagnosis. As the mass enlarges, it results in bony remodeling and resorption [85, 88, 89].

In 40% of cases, intralesional calcifications can be observed, representing residual bone fragments. The presence of focal hyperostosis has been correlated to the point of origin of the lesions [90].

MRI often demonstrates a distinctive gross mucosal morphology of IP, called convoluted cerebriform pattern (CCP), a "striated" imaging, seen on both T2 and contrast-enhanced T1-weighted images, with characteristic alternating hypointense and hyperintense bands.

In T1-weighted images, it appears isointense to muscle, in T2 generally hyperintense to muscle with alternating lines. In roughly 50% of cases IP enhance, the lesions are heterogeneous with alternating hypointense and hyperintense bands [91, 92].

The presence of central necrosis requires consideration of an associated malignancy [93–96].

IP can show an aggressive pattern of bone destruction because it may cross the cribriform plate into the cranial anterior fossa.

They can erode the skull base comparable to aggressive cancer and because of this signal intensity characteristics place on those of malignancies [97, 98].

Recurrences may be distinguished from postoperative thickening by dynamic enhanced MRI because they have earlier and greater enhancement than granulation tissue (Fig. 4.5) [99].

4.2.3 Dacryocystitis

Dacryostenosis is an acquired or congenital condition that can cause epiphora but can progress to dacryocystitis in children and in adults. This activity reviews the pathogenesis, evaluation, and management of dacryostenosis infection and

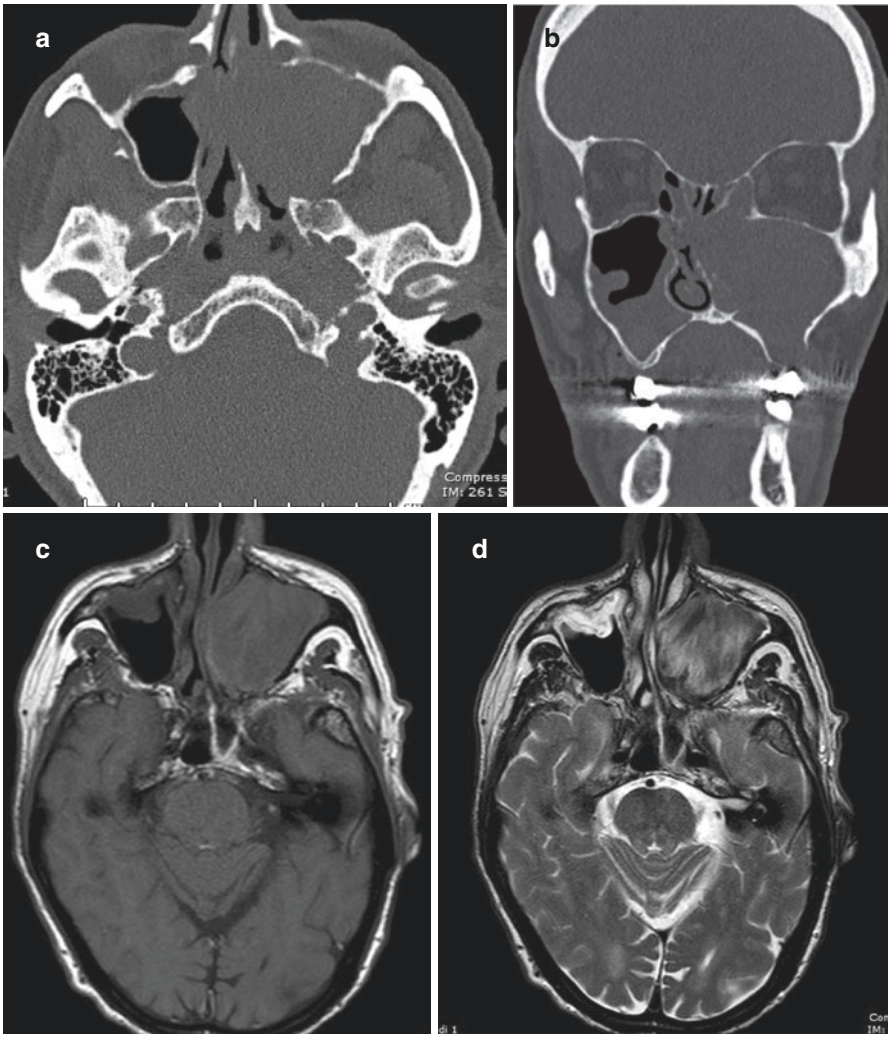

Fig. 4.5 Inverted papilloma. NCCT axial (**a**) and coronal MPR reconstruction (**b**): expansive dense mass in the left maxillary sinus erodes the lamina papyracea and invades the nasal fossa. There are signs of bone remodeling (thinning and bowing) and resorption. The cribriform plate is intact. On MRI, the lesion has low signal on T1-w (**c**), axial (**d**), and coronal (**e**) T2-w images showing a "striated pattern" sign. On post-contrast T1-w MRI image (**f**), the lesion shows peripheral enhancement. DWI coronal image (**g**) shows restricted diffusion

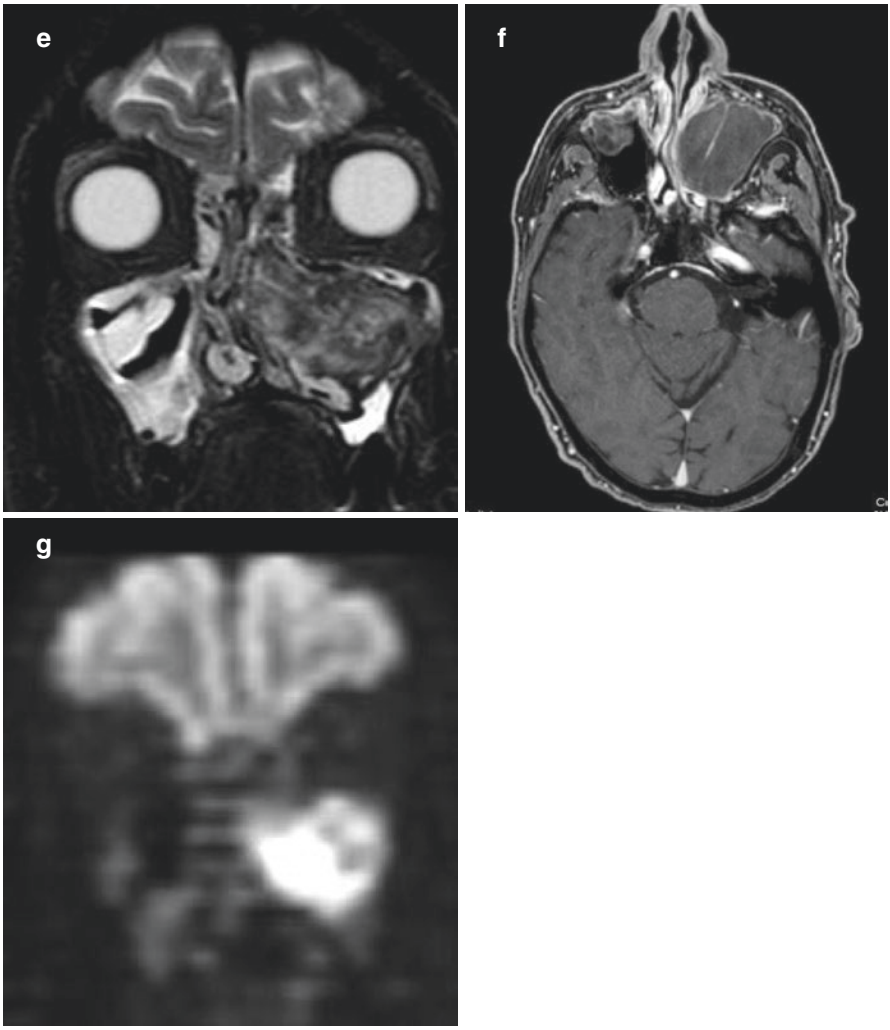

Fig. 4.5 (continued)

highlights the role of the interprofessional team in the care of patients with this condition [100, 101].

The etiology of acquired dacryostenosis is multifactorial and is not fully understood. Some cases may be related to trauma, neoplasm, systemic disease, radiotherapy, or chemotherapy. However, in most cases, the cause is "involutional" and classified as "idiopathic." Some authors have reported that the cause is secondary to anatomic changes in the diameter of the bony lacrimal canal, which occurs with aging. Women, in particular, have a smaller diameter of the lacrimal duct that tends to narrow with time. A congenital narrowness within the lacrimal drainage system is generally regarded as a disposition for lacrimal stenosis [102].

Some authors suggest that the cause may be from ascending inflammation from the region of the nose and sinus cavities. A descending infection from the conjunctiva has also been suggested as a cause of acquired dacryostenosis. Clinical studies indicate that nasal disease is sporadic in patients undergoing DCR [103].

Familial predisposition and osteoporotic changes have also been suggested as being predisposing factors.

The obstruction is more frequently situated at the level of the nasolacrimal duct or puncta and less frequently at the level of the canaliculi. The incidence is higher among older people and in women [104].

Diagnosis is usually made clinically; however, imaging may help to exclude complications. It is important distinguishing between acute and chronic dacryocystitis [100].

Acute dacryocystitis is commonly associated with preseptal cellulitis. Complications include orbital cellulitis (limited to preseptal tissues), corneal involvement, lacrimal sac mucocele and, rarely orbital abscess. The most common organisms implicated are *Staphylococcus aureus* in acquired cases and *S. pneumonia* in congenital cases although cultures and smears expressed punctual secretions as desirable [105].

Chronic dacryocystitis is a result of chronic obstruction due to systemic disease, repeated infection, dacryoliths, and chronic inflammatory debris of the nasolacrimal system. Some common systemic diseases include Wegener's granulomatosis, sarcoidosis, and systemic lupus erythematosus.

Acquired states are typically due to repeated trauma, surgeries, medications, and neoplasms. Among traumatic causes of nasolacrimal obstruction, nasoethmoid fractures seem to be most common.

Imaging features pointing to acute dacryocystitis include thick rim enhancement and extensive adjacent soft tissue preseptal cellulitis.

MRI is the imaging modality of choice in the evaluation of orbital cellulitis because of its superior soft tissue and contrast resolution. It is essential to evaluate the extent of the orbital infection, underlying paranasal sinus involvement, as well as detect complications of orbital cellulitis, especially intracranial spread. Orbital cellulitis causes diffuse, edematous infiltration of the orbital connective tissue that is best demonstrated by the high signal intensity in T2-weighted fat-saturated sequences. Other findings are swelling and ill-defined margins of the extraocular muscles and exophthalmos. Orbital cellulitis may be complicated by an abscess, which may form in the extraconal or intraconal orbit separate from the bone.

Periorbital cellulitis is a preseptal process, which is limited to the soft tissues anterior to the orbital septum. It usually occurs due to the contiguous spread of infection from adjacent structures such as the teeth and face. Computed tomography and MRI demonstrate diffuse soft tissue thickening anterior to the orbital septum. Infection in orbit, whether as a result of periorbital cellulitis extending across the orbital septum or due to sinusitis, constitutes an emergency.

MRI is better than CT, in fact it provides excellent contrast resolution in the orbit with the demonstration of pathologies in the intraconal and extraconal compartments. The ability to depict cross-sectional anatomy and pathology with better tissue characterization and even without administering intravenous gadolinium-based

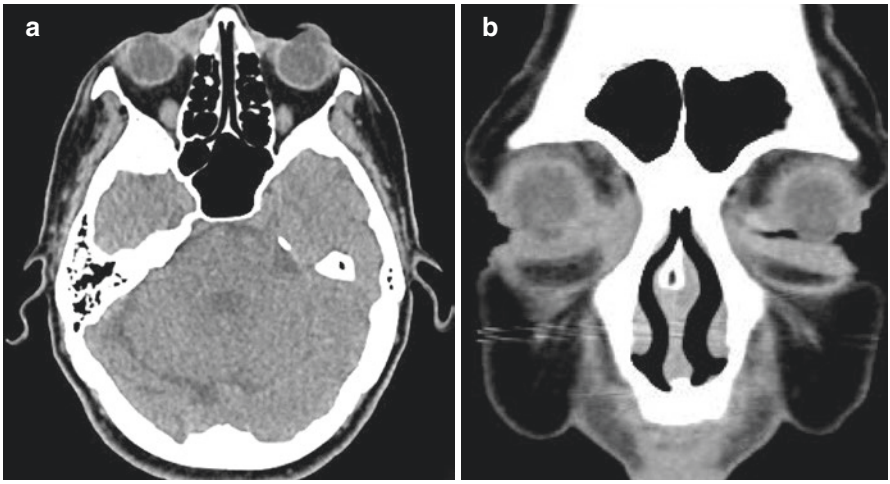

Fig. 4.6 Dacryocystitis. NCCT Ax (**a**), e Cor MPR reconstruction (**b**). Well-circumscribed round lesions with fluid core around the inner canthus, with adjacent soft tissue thickening and fat stranding, scalp melanoma is noticed

contrast agent is a distinct advantage of MRI over CT scanning, especially intracranial spread.

Although T1-weighted contrast-enhanced imaging with fat suppression is widely held as the gold standard in the detection and characterization of orbital pathology, T2-weighted fat-suppressed sequences have similar sensitivity for detecting orbital lesions and readily identify postseptal disease. Contrast enhancement, however, is essential for distinguishing abscess from edema and phlegmon.

Abscesses show a well-described phenomenon of diffusion restriction, likely related to the viscosity and dense cellular packing purulent material, strongly hyperintense on trace DW images and with reduced apparent diffusion coefficient (ADC) images within the central, non-enhancing portion of the abscess cavity (Fig. 4.6).

4.3 Skin Tumors

Cutaneous squamous cell carcinoma (cSCC) accounts for approximately 20% of all non-melanoma skin cancers, which is the most common malignancy worldwide.

Although less than 5% of head and neck cSCC (HNcSCC) metastasize, lymph node metastases in the parotid and/or neck are potentially lethal and require morbid multimodal regional therapy with surgery and adjuvant radiotherapy (RT). Although the fundamental treatment approach has remained largely unchanged, there have been several advances that may impact survival.

There have been very few studies examining trends in survival of HNcSCC, particularly metastatic HNcSCC. Gnanasekaran et al. recently examined the trends in prognosis of patients with metastatic HNcSCC over the last 30 years within a single Australian institution. The authors reported improved cancer-specific survival over

time despite treating increasing numbers of elderly patients and more aggressive cancers.

The radiologist's roles include evaluating the full local extent of the primary, detecting perineural tumor, and assessing regional nodal and distant spread of disease.

CT scanning or MRI can be helpful in defining the extent of disease. CT scanning is useful for determining the presence of bone or soft tissue invasion and for evaluating cervical lymph nodes at risk for metastasis.

cSCCs predominantly exhibited a flattened configuration, superficial ulcer formation, protrusion into the subcutaneous tissue, ill-demarcated deep tumor margin, and peritumoral fat stranding.

Conventional MRI sequences are also superior to CT for a variety of findings that influence the therapeutic choice such as laryngeal cartilage invasion, invasion of the skull base, perineural spread, detection of retropharyngeal lymph nodes in nasopharyngeal carcinoma, extranodal spread in metastatic neck nodes and vascular and lymphatic invasion.

On T2-weighted MRI the show ill-demarcated, flattened, cutaneous lesion, with superficial ulcer formation and protrusion and infiltration into subcutaneous fat tissue. Fat-suppressed T2-weighted image is useful for the evaluation of peritumoral fat stranding. MRI criteria based on the analysis of signal intensity and enhancement patterns after injection of gadolinium have had a major impact on the assessment of deep tumor spread. In most HNSCCs, the actual invasion of bony and cartilaginous structures is often preceded by tumor-induced inflammation. In laryngeal and hypopharyngeal HNSCCs, careful analysis of signal intensities on T1 and T2 sequences has improved differentiation between tumor and inflammation: moderate enhancement on T1 and moderately high signal on T2 indicate tumor involvement, whereas high signal on T2 and vivid enhancement correspond histologically to peritumoral inflammation (Fig. 4.7).

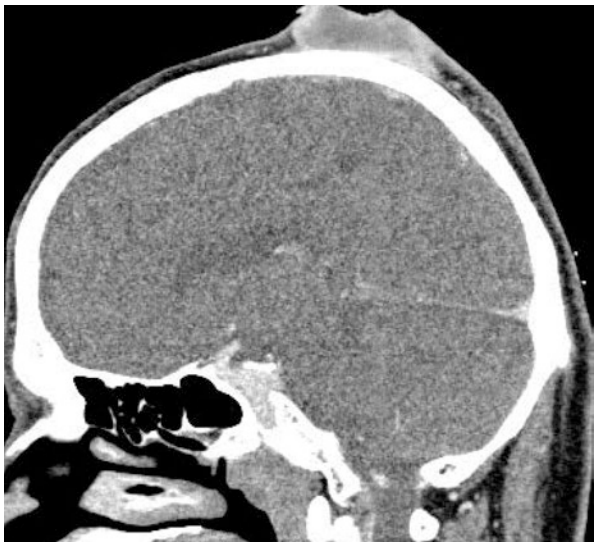

Fig. 4.7 Contrast enhancement CT (CECT) scan: subcutaneous expansive lesion with avid contrast enhancement and central necrosis that infiltrates fat and the aponeurosis

4.4 Tumors of the Oral Cavity

The population in developed countries is aging rapidly, which is associated with a significant increase in the total cancer burden over the last decades and, specifically, also with an increase in the incidence of the head and neck squamous cell carcinoma (HNSCC) after 50 years of age. Although the age of most of the HNSCC patients ranges between 50 and70 years, the occurrence of this tumor type in older patients is not rare.

The medical literature provides no clear definition of an elderly person. According to the National Institute on Aging and the National Institutes of Health, elderly persons can be classified into three categories: young old, aged 65–75 years; old, aged 76–85 years; and oldest old, older than 85 years.

Because aging is a highly individualized process and the elderly population is very heterogeneous, chronological age alone is an inappropriate parameter for treatment selection. More important is functional age, which should be defined individually for each patient based on the functional status, comorbidities, and presence of geriatric syndromes. Several authors concluded that traditional oncology measures of functional status alone (e.g., Karnofsky performances status score) do not appear to reflect the comorbidity burden and its prognostic potential in elderly patients. A long-lasting history of tobacco and alcohol abuse that is characteristic for a substantial proportion of HNSCC patients, an advanced age per se, and the history of other factors or events increase the probability for severe comorbidity. According to literature, the prevalence of comorbidity in the general population of HNSCC patients is approximately 60%, whereas the rate of moderate and severe comorbid burden is in the range of 20%. As may be expected, these figures rise with age, impacting the prognosis of the patients significantly and independently from other factors. In older patients with cancer, a full onco-geriatric evaluation is warranted prior to any treatment decision-making to avoid overlooking any relevant information about the ability of an older patient to cope with the proposed treatment. This assessment is probably the most critical step, as its results have a profound effects on all downstream decisions (i.e., the aim of treatment—palliation vs. curative, the extent of diagnostics and mode(s) of therapy employed) and, thus, also on the prognosis.

Unlike other evaluation instruments, which are mostly focused on some specific issues, the CGA uses standardized instruments to employ a multidimensional and interdisciplinary approach. The CGA encompasses a spectrum of important clinical domains, namely an evaluation of different aspects of patient functioning, comorbidity, polypharmacy, nutritional status, cognitive function, socio-economic issues, and geriatric syndromes, thus allowing for the identification of patient groups with different frailty levels and selection of the appropriate therapeutic strategy.

There are features distinctive for HNSCC patients of older age groups. First of all, in the elderly, there is a significantly higher proportion of female patients compared to the younger population. The reason for this is most probably longer life expectancy among females. In addition, a history of alcohol abuse and smoking is less frequently reported in the advanced age groups than in the general population of HNSCC patients [106].

The most prevalent primary tumor sites in the head and neck region in elderly patients seem to be—depending on the series—the oral cavity or the larynx, each comprising up to one half of all primaries, with the tendency to overcome their incidence among younger-aged patients. A trend of fewer hypopharyngeal cancer cases in the elderly patient group was also observed. Considering the tumor stage at presentation, it appears that the occurrence of an advanced disease (T3, T4) at the primary site is comparable to or even reduced when matched with that observed in younger age groups, but the regional lymphatics are primarily less frequently infiltrated by cancer cells in older patients. Apparently, an increase in the disease severity that would be expected from the usual delay in diagnosis in older people, probably reflecting age-related inequalities in access to health care due to a variety of social and behavioral factors is successfully compensated by a less aggressive biology of the disease in the elderly [107–109].

4.5 Salivary Gland Tumors

Incidence of benign and malignant salivary gland tumors in major portion of the world ranges from 1 to 2 cases per 100,000 people per year There is no specific predilection of occurrence of these tumors in any particular gender, although Warthin's tumor is more common in males and acinic cell tumor in females. Site-wise incidence varies for both benign and malignant tumors. Seventy-five to eighty percent of benign tumors occur in the parotid glands, 5–10% in submandibular glands, and only 1–2% in sublingual glands. Malignant tumors are more common in sublingual glands (80%) and least in parotid glands (17–20%). Benign tumors affect a mean age group of 40 years, and malignant tumors affect an age group of 55 years [110–114].

4.5.1 Pleomorphic Adenoma

Most frequently found in the superficial lobe of the parotid gland, it presents as a firm, slow-growing asymptomatic mass which is smooth, rounded, lobular, and mobile with a rubbery consistency causing ear lobule to be raised [115, 116].

On light microscopy, morphologically complex and diverse cellular elements are seen. Both epithelial and myoepithelial elements are present myxoid to extreme cellular [117].

Surgical excision is the treatment of choice. Historically, enucleation was practiced which resulted in inadequate surgery and recurrences. Superficial parotidectomy is the most widely accepted technique in the treatment of pleomorphic adenomas in the superficial lobe of the parotid gland, and total gland excision with facial nerve preservation is carried out [118, 119].

4.5.2 Warthin's Tumor

Warthin's tumor, also known as papillary cystadenoma lymphomatosum and adenolymphoma, is the second most common benign tumor of the salivary glands, around 5% of neoplasms [120].

The majority of the tumors arise in the parotid gland, more often bilaterally, in the elderly and occurs in the fifth and sixth decades of life. A predilection for male sex is seen, more in Caucasians. Both the tumors do not occur simultaneously but are metachronous in their manifestation.

Surgical removal is the established treatment for Warthin's tumor. Treatment philosophies given are:

- Tumor enucleation with resection of minimal amount of surrounding normal tissue
- Superficial parotidectomy, which is more aggressive than enucleation
- Local excision of parotid gland [121, 122]

4.5.3 Mucoepidermoid Carcinoma

Mucoepidermoid carcinoma is the most common malignant salivary gland neoplasm. They are classified as grade I (low grade) which are well differentiated, grade II (intermediate grade) which are moderately differentiated, and grade III (high grade) which are poorly differentiated tumors [107, 123–126].

Mucoepidermoid carcinomas occur more commonly in the minor salivary glands with a female predilection.

It occurs as a painless, circumscribed, mobile solitary enlargement of the body or tail of the parotid or the submandibular region with over a year duration generally.

Complete, adequate, and radical surgical excision is the treatment of choice for all grades of mucoepidermoid carcinomas.

4.5.4 Adenoid Cystic Carcinoma

Adenoid cystic carcinoma (ACC) is a highly aggressive, destructive, and clinically unpredictable tumor of the head and neck region.

Adenoid cystic carcinoma occurs in adults between 50 and 70 years of age with equal prevalence in males and females.

Clinically adenoid cystic carcinoma manifests in the major and intraoral accessory salivary glands as a slow growing swelling or mass.

Histopathologically, ACC are classified into cribriform pattern, tubular pattern, and solid pattern. A major microscopic feature in most adenoid cystic carcinomas is the propensity for the tumor to involve peripheral nerves, reported to occur in 20–80% of the patients.

Complete excision like all other tumors is the treatment of choice. Elective regional lymph node dissection is not indicated, because distant metastasis is more common than cervical (regional) node involvement [127–131].

4.5.5 Squamous Cell Carcinoma

The diagnosis of primary squamous cell carcinoma is limited to the major glands.

It occurs between 7 and 95 years of age, the mean age being 60.5 years with a male predilection of 2:1. Parotid gland is the most commonly involved followed by submandibular and sublingual glands [132].

Surgical management is the mainstay of treatment. Parotidectomy with or without facial nerve preservation depending on the case is needed for parotid tumors. Submandibular sialoadenectomy is needed for submandibular gland tumors. A neck dissection is done in clinically positive necks at the slightest suspicion [116].

4.5.6 Pleomorphic Adenoma

Pleomorphic adenoma is the most common salivary gland tumor and is characterized by cytomorphological and architectural diversity. On CT and MR images, PAs are shown as well-circumscribed rounded masses, most commonly located within the parotid gland, sometimes joined by characteristic lobulated contour enhancement. On T2-weighted images, typical PAs show marked hyperintensity, which reflects the abundant myxochondroid stroma, with a hypointense rim indicating the fibrous capsule. The intensity signal within the tumors varies due to the cellular density, proportion of epithelial and stromal components, and type of stromal components. In addition, a variety of secondary histological changes, including fibrosis, lipometaplasia, ossification, cystic degeneration, and infarction, occur rarely in PAs. T1-weighted images after contrast administration usually demonstrate homogeneous enhancement [133, 134].

4.5.7 Whartin's Tumor

It is the second most common benign tumor arising in the parotid gland after benign mixed tumor. On CT, Warthin's tumors usually appear as small (2–4 cm, rare >10 cm), ovoid, smoothly marginated masses. They are homogenous soft tissue density lesions without calcifications. Cyst formation with homogenous material is common (30%). The cyst wall is usually thin and fairly smooth. The presence of a mural nodule helps to distinguish Warthin's tumors with large cystic components, septa or multiple adjacent cystic lesions from first branchial cleft cysts or lymphoepithelial cysts [135–137].

On MRI solid and cystic components show low T1-weighted signal, but cystic areas may show high signal secondary to proteinaceous debris and/or hemorrhage. In T1-weighted images after contrast administration solid components show minimal contrast enhancement. In T2-weighted images, solid components appear intermediate to high signal, with high signal in cystic foci, intermediate signal in Proton Density-weighted images, while in STIR images the lesions become more conspicuous, especially the cystic components. Warthin's tumors show significant restriction of diffusion. The differential diagnosis of Warthin's tumor includes benign mixed tumor, benign adenopathy, lymphoma, benign lymphoepithelial lesions—HIV, adenoid cystic or mucoepidermoid carcinoma, as well as squamous cell carcinoma and melanoma nodal metastasis [138–140].

4.5.8 Mucoepidermoid Carcinoma

MEC has been classified histologically as low, intermediate, or high grade according to intracystic components, mitotic figures, neural invasion, necrosis, and cellular anaplasia.

MRI findings are variable reflecting their histological nature, which seems to have certain tendencies depending on the tumor grade.

Tumors show inhomogeneous low to intermediate signal intensity on T2-weighted images, reflecting high cellularity, with an ill-defined margin, reflecting peritumoral inflammatory changes rather than invasive tumor growth. In the intermediate-grade MECs, tumors showed intermediate signal intensity on T2-weighted images. Among the low-grade MECs, most tumors had a hyperintense area on T2-weighted images because of the existence of abundant mucin-secreting cells. High-grade tumors, on the other hand, have lower signal on T2 and poorly defined margins and infrequent cystic areas. On T1 images following administration of contrast, there is heterogeneous enhancement of solid components [141–144].

Lymph node metastasis was seen often in high-grade MECs.

On CT images, low-grade tumors appear as well-circumscribed lesions, usually with cystic components. The solid components enhance and calcification is sometimes seen. They have appearances similar to benign mixed tumors. High-grade tumors have poorly defined margins, infiltrate locally, and appear solid.

4.5.9 Adenoid Cystic Carcinoma

Adenoid cystic carcinoma has a propensity for perineural spread. A high-grade variant is evidenced by a copious of pleomorphic cells, loss of the classic biphasic epithelial-myoepithelial growth pattern, and comedonecrosis. CT and MRI are

considered reliable and convenient methods for diagnostic and prognostic prediction, they can both be helpful for demonstrating the extent of invasion in oral cavity-associated adenoid cystic carcinoma, which can reach the inferior alveolar nerve for perineural spread by direct invasion through the mandible. It is usually best depicted on MRI. Low-grade tumors tend to be well-defined, in contradistinction to high-grade tumors, which appear infiltrative. However, on T1-weighted images both the subtypes are usually hypo to isointense, on T2 slightly hyperintense, with higher grades being markedly hypointense and homogeneously enhancing after contrast administration. In particular, involvement of cranial nerves and tumoral infiltration around the nerves and osseous structures is optimally assessed via non-contrast T1-weighted and contrast-enhanced, fat-suppressed T1-weighted MR sequences. Perineural spread typically appears as enlargement and abnormal enhancement of the affected nerve and widening or obliteration of the nerve canal. Considering adenoid cystic carcinoma of the oral cavity can attain, overrun, and infiltrate the inferior alveolar nerve by first eroding through the mandibular cortex, and infiltrating through the bone marrow, CT can be complementary to MRI.

4.5.10 Squamous Cell Carcinoma

MRI features showed large tumor size, irregular shape, ill-defined margin, extraparotid infiltration, low-intermediate signal intensity in the solid portions on T2-weighted images and the presence of central necrosis. On contrast-enhanced T1-weighted image with the fat-suppression technique, the mass has a central unenhanced area and can infiltrate the subcutaneous fat, mandibular ramus, and parapharyngeal space.

The ill-defined margins and extraparotid infiltration, which reflect the invasive growth of the tumor cells. The appearances of SCC originating in the parotid gland on MRI can be similar to other more common parotid malignancies (e.g., adenoid cystic carcinoma and muco-epidermoid carcinoma) (Figs. 4.8 and 4.9) [125, 145].

Fig. 4.8 Parotid gland adenocarcinoma. CECT (**a**) shows an expansive lesion with avid enhancement located in the superficial lobe and in the deep portion of the gland. Peripheral stranding and central fluid areas are evident. MRI confirms the presence of an infiltrating lesion with fuzzy borders that shows isointense signal on T1 (**b**) and low signal on T2-w (**c**) and high contrast enhancement on post-contrast T1-w (**d**). Irregular stranding can be appreciated in the adipose tissue around and posteriorly to the deep portion on the gland (sagittal post-contrast T1-w (**e** and **f**)). Bulky and coalescent nodal metastases are also present

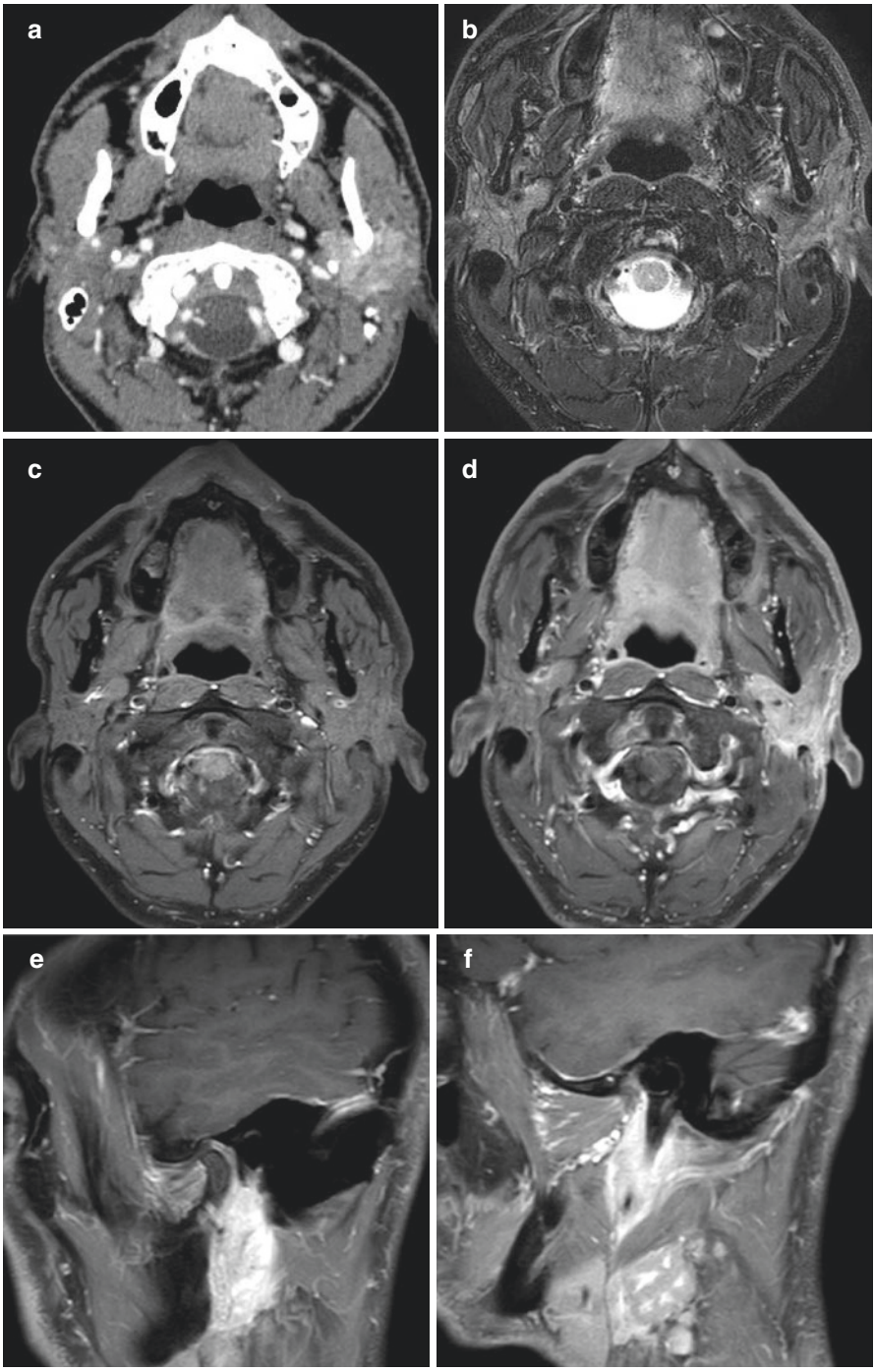
a
b
c
d
e
f

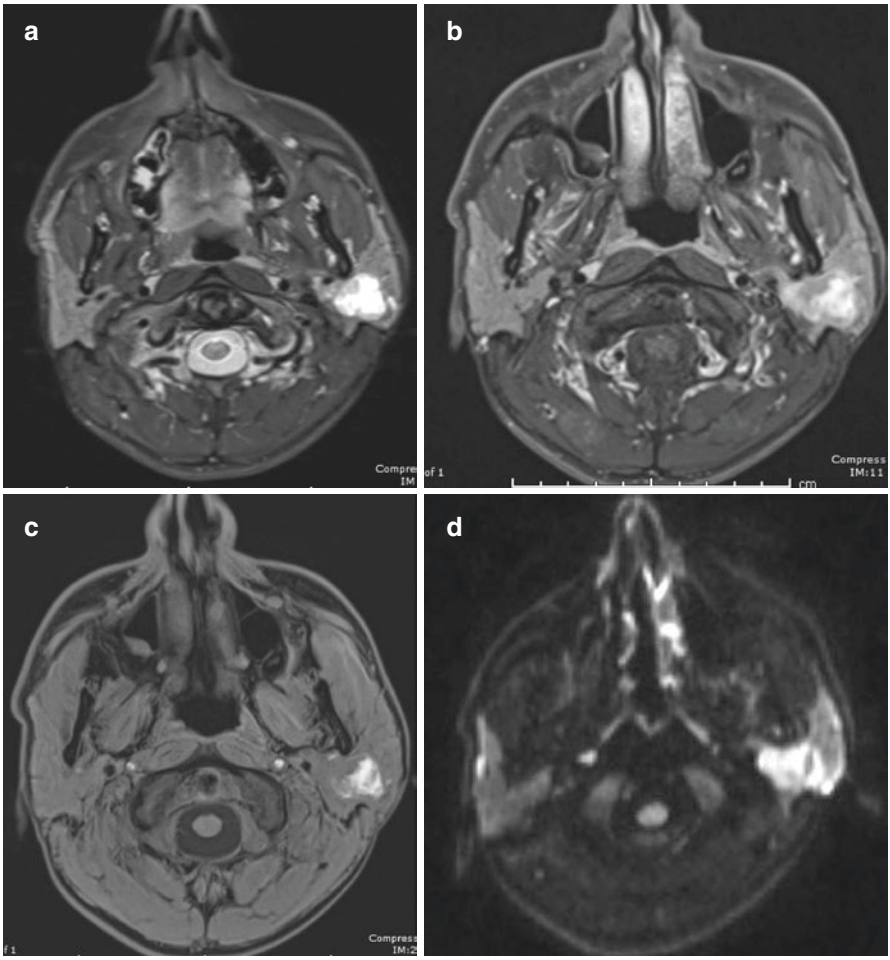

Fig. 4.9 Parotid gland cystadenoma. The MRI shows expansive lesion located in the deep part of the parotid gland that deforms its contour and comes close to the external carotid and the internal jugular vein, without imaging findings of infiltration. The lesion has high signal intensity on T2-w (**a**) with an isointense small central component with corresponding high signal intensity on fat saturated T1-w without contrast (**b**), suggesting proteinaceous components. On post-contrast T1-w (**c**), contrast enhancement is avid in the deeper part of the lesion, while it is more nuanced and inhomogeneous in the superficial portions. A fluid component with peripheral enhancement is also noticed. On DWI (**d**) the lesion shows restriction in the diffusion of proton density. There are also two lymph nodes in the superficial layers of the gland

4.6 Osteonecrosis

The bisphosphonates play a major role in the treatment and prevention of these skeletal related events, together with radiation therapy, surgery, analgesics, and standard anticancer therapy. The primary goal of these therapeutic strategies is to

improve the quality of life, as the disease is usually incurable at this stage. The occurrence of osteonecrosis of the jaw (ONJ) associated with the use of bisphosphonates is a potentially new side effect that can have a severe impact on the daily functioning of the affected individuals, causing great concern among patients, dentists, and the medical community [146–148].

Osteonecrosis of the jaw has historically been linked with exposure to white phosphorous ("phossy jaw") and in more recent times with radiotherapy and chemotherapy.

Changes in the socioeconomic fabric of society, resulting in safer working environments and the banning of white phosphorus, have caused phossy jaw to be nothing more than a historical curiosity. Osteoradionecrosis, on the other hand, is a well-defined entity that can be adequately managed with combined hyperbaric oxygen therapy and surgery, although it can develop many years after initial treatment [6]. Chemotherapy as a cause of ONJ has been infrequently reported in the literature and is poorly understood, but the presence of infection and dentures seems to be important in the development of this disorder.

Diagnostic criteria put forward by an expert panel have been published and confirm ONJ as a clinical diagnosis. The disorder is defined as the persistence of exposed bone in the oral cavity after adequate treatment for 6 weeks, in the absence of local metastatic disease and without previous radiation therapy to the affected area. This definition is, however, deceptively simple, as the differentiation between osteonecrosis complicated by infection and osteomyelitis with secondary osteonecrosis can be difficult, if not impossible. Although these criteria will help uniform reporting, there is some ambiguity regarding the role of other diagnostic procedures, such as pathology, imaging, and microbiology. Moreover, it is unclear what an "adequate treatment" should entail [119, 149].

Clinical examination reveals an exposed alveolar ridge with sequestra of necrotic bone, often with a foul smelling discharge. The surrounding gingival and mucosal tissues are usually inflamed and painful to touch. The lesions can become multiple, as one study identified 2.3 areas of ONJ per patient. The mandible is affected in the majority of cases (60–80%), with the lingual posterior area being particularly susceptible, which may relate to the thinness of the mucosa in this region and can be easily traumatized during normal mastication. Fistulization to the maxillary sinus and the skin can occur and pathological fractures of the mandible have also been reported [150].

The aspect of ONJ at radiography, CT, and MR imaging is variable and is nonspecific at both anatomic imaging and functional imaging. Imaging takes part in determining the extent of the disease, diagnosing early stages of osteonecrosis, identifying a potential association between metastasis to the jaw and ONJ lesions, excluding other diseases of the jaws, diagnosing complications such as fractures, and evaluating the jaw before performance of orofacial procedures [151].

The appearance of ONJ at radiography and CT is variable and includes ill-defined areas of lucency or low attenuation, permeative appearance, cortical destruction, bony sequestrum, periosteal reaction, or sclerotic changes [152].

The bone changes may be mixed, predominantly lytic or prevalently sclerotic. The lytic areas may represent foci of bacterial infection. Persistent alveolar sockets have been described as a typical radiographic feature of ONJ [153].

On MRI ONJ shows in T1-weighted images decreased marrow signal intensity, in T2-weighted images has increased marrow signal intensity, and in contrast-enhanced fat-saturated T1-weighted images shows enhancement of marrow and soft tissue and associated increased signal intensity and soft tissue prominence (Fig. 4.10) [148].

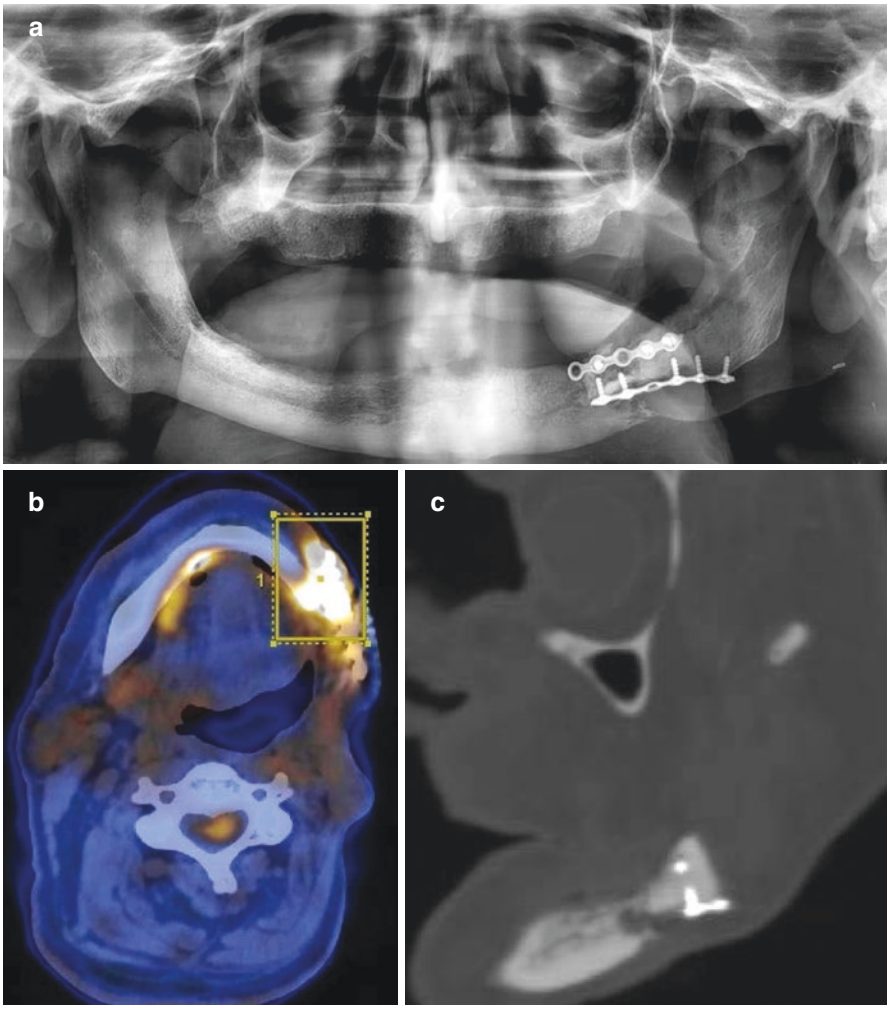

Fig. 4.10 Osteonecrosis. Patient with history of retromolar trigone carcinoma that underwent surgery and radiation therapy. Orthopantomography (**a**) documents fixation device in the left mandibular bone and the presence of osteolysis discontinuity of bone fragments. Tumefaction of adjoining small parts is also evident. NCCT with bone algorithm (**b**) better demonstrates bone rarefaction and microfractures. On PET 18F-FDG (**c**) there is high metabolic activity (SUV max 7.09) suggesting inflammation

References

1. Lin Y-H, Lin M-Y. Bezold abscess. Ear Nose Throat J. 2015;94(6):E45–6.
2. Abada RL, Mansouri I, Maamri M, Kadiri F. Complications of chronic otitis media. Ann Otolaryngol Chir Cervicofac. 2009;126(1):1–5. https://doi.org/10.1016/j.aorl.2008.10.006.
3. Pont E, Mazón M. Indications and radiological findings of acute otitis media and its complications. Acta Otorrinolaringol Esp. 2017;68(1):29–37.
4. Govea-Camacho LH, Pérez-Ramírez R, Cornejo-Suárez A, Fierro-Rizo R, Jiménez-Sala CJ, Rosales-Orozco CS. Diagnosis and treatment of the complications of otitis media in adults. Case series and literature review. Cir Cir. 2016;84(5):398–404.
5. Chengazi HV, Desai A, Bhatt AA. Emergency radiologic approach to mastoid air cell fluid. Emerg Radiol. 2021;28(3):633–40.
6. Kovoor JM, Kademian J, Moritani T, Neal MH, Birkeland AC, Spector ME. Head and neck. p. 715–75.
7. Mansour S, Magnan J, Nicolas K, Haidar H. Complications of chronic otitis media. p. 383–414.
8. Nelson D, Jeanmonod R. Bezold abscess: a rare complication of mastoiditis. Am J Emerg Med. 2013;31(11):1626.e3–4.
9. Bhutta MF, Monono ME, Johnson WD. Management of infective complications of otitis media in resource-constrained settings. Curr Opin Otolaryngol Head Neck Surg. 2020;28(3):174–81.
10. Lemmerling M. Acute otomastoiditis and its complications. p. 53–9.
11. Lyoubi H, Berrada O, Lekhbal A, Abada RA, Mahtar M. Bezold's abscess: an extremely rare complication of suppurative mastoiditis: case report and literature review. Int J Surg Case Rep. 2020;77:534–7.
12. Minks DP, Porte M, Jenkins N. Acute mastoiditis—the role of radiology. Clin Radiol. 2013;68(4):397–405.
13. Lesser FD, Derbyshire SG, Lewis-Jones H. Can computed tomography and magnetic resonance imaging differentiate between malignant pathology and osteomyelitis in the central skull base? J Laryngol Otol. 2015;129(9):852–9. https://doi.org/10.1017/S0022215115001991.
14. Meltzer PEKG. Pyocutaneous osteomyelitis of the temporal bone, mandible, and zygoma. Laryngoscope. 1959;169:1300–16.
15. McKellop JA, Bou-Assaly W, Mukherji SK. Emergency head & neck imaging: infections and inflammatory processes. Neuroimaging Clin N Am. 2010;20(4):651–61.
16. El-Kashlan HK, Harker LA, Shelton C, Aygun N, Niparko JK. Complications of temporal bone infections. In: Flint PW, Haughey BH, Lund VJ, Niparko JK, Richardson MA, Robbins KT, editors. Cummings otolaryngology head and neck surgery. 5th ed. Philadelphia, PA: Mosby; 2010. p. 1979–98.
17. Chole RA, Donald PJ. Petrous apicitis: clinical considerations. Ann Otol Rhinol Laryngol. 1983;92(6 Pt 1):544–51.
18. Finkelstein Y, Marcus N, Mosseri R, Bar-Sever Z, Garty BZ. Streptococcus acidominimus infection in a child causing Gradenigo syndrome. Int J Pediatr Otorhinolaryngol. 2003;67(7):815–7.
19. Chole RA, Sudhoff HH. Chronic otitis media, mastoiditis, and petrositis. In: Flint PW, Haughey BH, Lund VJ, Niparko JK, Richardson MA, Robbins KT, editors. Cummings otolaryngology head and neck surgery. 5th ed. Philadelphia, PA: Mosby; 2010. p. 1963–78.
20. Watkyn-Thomas FW. The treatment of petrositis: (section of otology). Proc R Soc Med. 1936;29(3):267–74.
21. Wanna GB, Dharamsi LM, Moss JR, Bennett ML, Thompson RC, Haynes DS. Contemporary management of intracranial complications of otitis media. Otol Neurotol. 2010;31(1):111–7.
22. Penido Nde O, Borin A, Iha LC, Suguri VM, Onishi E, Fukuda Y, Cruz OL. Intracranial complications of otitis media: 15 years of experience in 33 patients. Otolaryngol Head Neck Surg. 2005;132(1):37–42.

23. Booth TN, Roland P, Kutz JW, Lee K, Isaacson B. High-resolution 3-D T2-weighted imaging in the diagnosis of labyrinthitis ossificans: emphasis on subtle cochlear involvement. Pediatr Radiol. 2013;43(12):1584–90.
24. Mattiola LR, Makowiecky M, Guimarães de Salles CE, Cardoso MP, Cahali S. Labyrinthitis ossificans. Report of one case and literature review. Int Arch Otorhinolaryngol. 2008. Accessed 20 May 2019.
25. Paparella MM, Sugiura S. The pathology of suppurative labyrinthitis. Ann Otol Rhinol Laryngol. 1967;76:554–86.
26. Torok N. Tympanogenic labyrinthitis. Otolaryngol Clin N Am. 1972;5:45–57.
27. Cody Larson MD, Scott A, Jorgensen MD, Alexander J, Towbin MD, Richard Towbin MD. Labyrinthine ossificans. Appl Radiol. Accessed 30 May 2019.
28. Page N, Kearns D. Radiology quiz case 2. Labyrinthitis ossificans secondary to suppurative labyrinthitis. Arch Otolaryngol Head Neck Surg. 2011;137:303–5.
29. Swartz JD, Mandell DM, Faerber EN, Popky GL, Ardito JM, Steinberg SB, et al. Labyrinthine ossification: etiologies and CT findings. Radiology. 1985;157(2):395–8.
30. deSouza C, Paparella MM, Schachern P, Yoon TH. Pathology of labyrinthine ossification. J Laryngol Otol. 1991;105:621–4.
31. Laurens MB, Becker RM, Johnson JK, Wolf JS, Kotloff KL. MRSA with progression from otitis media and sphenoid sinusitis to clival osteomyelitis, pachymeningitis and abducens nerve palsy in an immunocompetent 10-year-old patient. Int J Pediatr Otorhinolaryngol. 2008;72(7):945–51.
32. Sternberg I, Ronen S, Arnon N. Recurrent, isolated, post-febrile abducens nerve palsy. J Pediatr Ophthalmol Strabismus. 1980;17(5):323–4.
33. Lee NH, Ban JH, Park CY, Kim CC. A case of petrositis with abducens palsy. Korean J Otolaryngol-Head Neck Surg. 2006;49(8):869–72.
34. Kong SK, Lee IW, Goh EK, Park SE. Acute otitis media induced petrous apicitis presenting as Gradenigo syndrome: successfully treated by ventilation tube insertion. Am J Otolaryngol. 2011;32(5):445–7.
35. Lutter SA, Kerschner JE, Chusid MJ. Gradenigo syndrome: a rare but serious complication of otitis media. Pediatr Emerg Care. 2005;21(6):384–6; Marianowski R, Rocton S, Ait-Amer JL, Morisseau-Durand MP, Manach Y. Conservative management of Gradenigo syndrome in a child. Int J Pediatr Otorhinolaryngol. 2001;57(1):79–83.
36. Burston BJ, Pretorius PM, Ramsden JD. Gradenigo's syndrome: successful conservative treatment in adult and paediatric patients. J Laryngol Otol. 2005;119(4):325–9; Shin HS, Yoo HK, Suh YR. A case of unusual petrositis. Korean J Otolaryngol-Head Neck Surg. 1964;7(2):59–62.
37. Gillanders DA. Gradenigo's syndrome revisited. J Otolaryngol. 1983;12(3):169–74.
38. Peters GB III, Bakri SJ, Krohel GB. Cause and prognosis of nontraumatic sixth nerve palsies in young adults. Ophthalmology. 2002;109(10):1925–8.
39. Lee KC, Chio C, Park KY, Park MS. A case of Gradenigo's syndrome combining epidural abscess and Bezold's abscess. Korean J Otolaryngol-Head Neck Surg. 1989;32(3):567–71.
40. Minotti AM, Kountakis SE. Management of abducens palsy in patients with petrositis. Ann Otol Rhinol Laryngol. 1999;108(9):897–902.
41. Colpaert C, Van Rompaey V, Vanderveken O, Venstermans C, Boudewyns A, Menovsky T, de Veuster I, Van de Heyning P, Hamans E. Intracranial complications of acute otitis media and Gradenigo's syndrome. B-ENT. 2013;9(2):151–6. PMID: 23909122.
42. Derić D, Arsović N, Dordević V. [Pathogenesis and methods of treatment of otogenic brain abscess]. Med Pregl. 1998;51(1–2):51–5.
43. Mattos JL, Colman KL, Casselbrant ML, Chi DH. Intratemporal and intracranial complications of acute otitis media in a pediatric population. Int J Pediatr Otorhinolaryngol. 2014;78(12):2161–4.
44. Swartz JD, Hagiwara M. Inflammatory diseases of the temporal bone. p. 1183–229.
45. Goldstein NA, Casselbrant ML, Bluestone CD, Kurs-Lasky M. Intratemporal complications of acute otitis media in infants and children. Otolaryngol Head Neck Surg. 1998;119(5):444–54.
46. Graß SK, Welkoborsky HJ, Bersch C. Lateral sinus thrombosis—a rare complication of an acute mastoiditis or infected cholesteatoma. Laryngorhinootologie. 2016;95(1):37–42.

47. Park SN, Yeo SW, Rhyoo JY, Lee HY. A case of cavernous sinus thrombophlebitis and abducence nerve palsy secondary to petrositis. Korean J Otolaryngol-Head Neck Surg. 2002;45(1):82–5.
48. Hendershot EL, Wood JW, Bennhoff D. The middle cranial fossa approach to the petrous apex. Laryngoscope. 1976;86(5):658–63.
49. Chandler JR. Malignant external otitis. Laryngoscope. 1968;1968(78):1257–94.
50. Mahdyoun P, Pulcini C, Gahide I, Raffaelli C, Savoldelli C, Castillo L, et al. Necrotizing otitis externa: a systematic review. Otol Neurotol. 2013;34(4):620–9.
51. Sylvester MJ, Sanghvi S, Patel VM, Eloy JA, Ying YM. Malignant otitis externa hospitalizations: analysis of patient characteristics. Laryngoscope. 2016;127(10):2328–36.
52. Kwon BJ, Han MH, Oh SH, Song JJ, Chang KH. MRI findings and spreading patterns of necrotizing external otitis: is a poor outcome predictable? Clin Radiol. 2006;61(6):495–504. Spreading patterns with MRI imagings with clear examples of intracerebral complications.
53. Glikson E, Sagiv D, Wolf M, Shapira Y. Necrotizing otitis externa: diagnosis, treatment, and outcome in a case series. Diagn Microbiol Infect Dis. 2017;87(1):74–8.
54. Stevens SM, Lambert PR, Baker AB, Meyer TA. Malignant otitis externa: a novel stratification protocol for predicting treatment outcomes. Otol Neurotol. 2015;36(9):1492–8.
55. Soudry E, Hamzany Y, Preis M, Joshua B, Hadar T, Nageris BI. Malignant external otitis: analysis of severe cases. Otolaryngol Head Neck Surg. 2011;144(5):758–62.
56. Chawdhary G, Pankhania M, Douglas S, Bottrill I. Current management of necrotising otitis externa in the UK: survey of 221 UK otolaryngologists. Acta Otolaryngol. 2017;137(8):818–22.
57. Marsot-Dupuch K, Meyer B. Cochlear implant assessment: imaging issues. Eur J Radiol. 2001;40:119–32.
58. Berrettini S, Baggiani A, Bruschini L, et al. Systematic review of the literature on the clinical effectiveness of the cochlear implant procedure in adult patients. Acta Otorhinolaryngol Ital. 2011;31:299–310.
59. Carlson ML, Sladen DP, Gurgel RK, Tombers NM, Lohse CM, Driscoll CL. Survey of the American Neurotology Society on cochlear implantation: part 1, candidacy assessment and expanding indications. Otol Neurotol. 2018;39:e12–9.
60. Vesseur A, Free R, Snels C, et al. Hearing restoration in cochlear nerve deficiency: the choice between cochlear implant or auditory brainstem implant, a meta-analysis. Otol Neurotol. 2018;39:428–37.
61. Peng KA, Kuan EC, Hagan S, Wilkinson EP, Miller ME. Cochlear nerve aplasia and hypoplasia: predictors of cochlear implant success. Otolaryngol Head Neck Surg. 2017;157:392–400.
62. Birman CS, Brew JA, Gibson WPR, Elliott EJ. CHARGE syndrome and cochlear implantation: difficulties and outcomes in the paediatric population. Int J Pediatr Otorhinolaryngol. 2015;79:487–92.
63. Frau GN, Luxford WM, Lo WW, Berliner KI, Telischi FF. High-resolution computed tomography in evaluation of cochlear patency in implant candidates: a comparison with surgical findings. J Laryngol Otol. 1994;108:743–8.
64. Aldhafeeri AM, Alsanosi AA. Management of surgical difficulties during cochlear implant with inner ear anomalies. Int J Pediatr Otorhinolaryngol. 2017;92:45–9.
65. Deep N, Dowling E, Jethanamest D, Carlson M. Cochlear implantation: an overview. J Neurol Surg Part B Skull Base. 2018;80:169–77.
66. Sennaroglu L. Cochlear implantation in inner ear malformations—a review article. Cochlear Implants Int. 2010;11:4–41.
67. Sennaroğlu L, Bajin MD. Classification and current management of inner ear malformations. Balkan Med J. 2017;34:397–411.
68. Birman CS, Elliott EJ, Gibson WPR. Pediatric cochlear implants: additional disabilities prevalence, risk factors, and effect on language outcomes. Otol Neurotol. 2012;33:1347–52.
69. Hellingman CA, Dunnebier EA. Cochlear implantation in patients with acute or chronic middle ear infectious disease: a review of the literature. Eur Arch Otorhinolaryngol. 2009;266:171–6.
70. Amin N, Sethukumar P, Pai I, Rajput K, Nash R. Systematic review of cochlear implantation in CHARGE syndrome. Cochlear Implants Int. 2019;20:266–80.

71. Fasunla AJ, Nwaorgu OGB. Adult chronic rhinosinusitis: spectrum of clinical features in a tertiary health institution and literature review. East Cent Afr J Surg. 2011;16(1):12–8.
72. Lanza DC, Kennedy DW. Adult rhinosinusitis defined. Otolaryngol Head Neck Surg. 1997;117(3 pt 2):S1–7.
73. Benninger MS, Ferguson BJ, Hadley JA. Adult chronic rhinosinusitis: definitions, diagnosis, epidemiology, and pathophysiology. Otolaryngol Head Neck Surg. 2003;129(3 Suppl):S1–32.
74. Bhattacharyya N. A comparison of symptom scores and radiographic staging systems in chronic rhinosinusitis. Am J Rhinol. 2005;19(2):175–9.
75. Fokkens W, Lund V, Bachert C, Clement P, Hellings P, Holmstrom M, Jones N, Kalogjera L, Kennedy D, Kowalski M, Malmberg H, Mullol J, Passali D, Stammberger H, Stierna P. EAACI position paper on rhinosinusitis and nasal polyps executive Summary. Allergy. 2005;60(5):583–601.
76. Lund VJ, Kennedy DW. Staging for rhinosinusitis. Otolaryngol Head Neck Surg. 1997;117(suppl):S35–40.
77. Hopkins C, Browne JP, Slack R, Lund V, Brown P. The Lund-Mackay grading system for chronic rhinosinusitis: how is it used and what does it predict. Otolaryngol Head Neck Surg. 2007;137(4):555–61.
78. Bhattacharyya N. The role of CT and MRI in the diagnosis of chronic rhinosinusitis. Curr Allergy Asthma Rep. 2010;10(3):171–4.
79. Arango P, Kountakis SE. Significance of computed tomography pathology in chronic rhinosinusitis. Laryngoscope. 2001;111(10):1779–82.
80. Kenny TJ, Duncavage J, Bracikowski J, Yildirim A, Murray JJ, Tanner SB. Prospective analysis of sinus symptoms and correlation with paranasal computed tomography scan. Otolaryngol Head Neck Surg. 2001;125(1):40–3.
81. Bhattacharyya N, Fried MP. The accuracy of computed tomography in the diagnosis of chronic rhinosinusitis. Laryngoscope. 2003;113(1):125–9.
82. Karkos PD, Khoo LC, Leong SC, Lewis-Jones H, Swift AC. Computed tomography and/or magnetic resonance imaging for pre-operative planning for inverted nasal papilloma: review of evidence. J Laryngol Otol. 2009;123(7):705–9.
83. Loevner L, Sonners A. Imaging of neoplasms of the paranasal sinuses. Neuroimaging Clin N Am. 2004;4:625–46.
84. Wassef SH, Batra PS, Barnett S. Review article: Skull base inverted papilloma: a comprehensive review. ISRN. 2012:1–34.
85. Jeon TY, Kim HJ, Chung SK, Dhong HJ, Kim HY, Yim HJ, Kim ST, Jeon P. Sinonasal inverted papilloma: value of convoluted cerebriform pattern on MR imaging. AJ Neuroradiol. 2007;29:1556–60.
86. Wright EJ, Chernichenko N, Ocal E, Moliterno J, Bulsara KR, Judson BL. Benign inverted papilloma with intracranial extension: prognostic factors and outcomes. Skull Base Rep. 2011;1:145–50.
87. Chawla A, Shenoy J, Chokkappan K, Chung R. Imaging features of sinonasal inverted papilloma: a pictorial review. Curr Probl Diagn Radiol. 2015;10:1–7.
88. Maroldi R, Farina D, Palvarini L. Magnetic resonance imaging findings of inverted papilloma: differential diagnosis with malignant sinonasal tumors. Am J Rhinol. 2004;18:305–10.
89. Anari S, Carrie S. Sinonasal inverted papilloma: narrative review. J Laryngol Otol. 2010;124:705–15.
90. Head CH, Sercaz JA, Luu Q, Collis J, Blackwell K. Radiographic assessment of inverted papilloma. Acta Otolaryngol. 2007;127:515–20.
91. Alba JR, Armengot M, Díaz A, Pérez A, Rausell N, Basterra J. Inverted papilloma of the sphenoid sinus. Acta Otorhinolaryngol Belg. 2002;56(4):399–4.
92. Lisan Q, Laccourreye O, Bonfils P. Sinonasal inverted papilloma: from diagnosis to treatment. Eur Ann Otorhinolaryngol Head Neck Dis. 2016;133(5):337–41.
93. Ozturk K, Gawande R, Gencturk M, Boegel K, Caicedo-Granados E, Cayci Z. Imaging features of sinonasal tumors on positron emission tomography and magnetic resonance imaging including diffusion weighted imaging: a pictorial review. Clin Imaging. 2018;51:217–28.

94. Salomone R, Matsuyama C, Filho G, De Alvarenga ML, Neto EM, Chaves AG. Bilateral inverted papilloma. Case report and review of literature. Rev Bras Otorrinolaringol. 2008;74(2):293–6.
95. Strek P, Zagolski O, Skladzien J, Oles K, Konior M, Hydzik-Sobocinska K. Endoscopic surgical treatment of patients with isolated sphenoid sinus disease. Otolaryngol Pol. 2007;61(3):254–9.
96. Lee JT, Bhuta S, Lufkin R, Castro DJ. Isolated inverting papilloma of the sphenoid sinus. Laryngoscope. 2003;113(1):41–4.
97. Lee DK, Chung SK, Dhong H-J, Kim HY, Kim H-J, Bok KH. Focal hyperostosis on CT of sinonasal inverted papilloma as a predictor of tumor origin. AJNR Am J Neuroradiol. 2007;28:618–21.
98. Bhalla RK, Wright ED. Predicting the site of attachment of sinonasal inverted papilloma. Rhinology. 2009;47:345–8.
99. Liang N, Huang Z, Liu H, Xian J, Huang Q, Zhou B. Bone involvement: histopathological evidence for endoscopic management of sinonasal inverted papilloma. Laryngoscope. 2017;127:2703–8.
100. Wilkins RB, Pressly JP. Diagnosis and incidence of lacrimal calculi. Ophthalmic Surg. 1980;11:787–9.
101. Weber AL, Rodriguez-DeVelasquez A, Lucarelli MJ, Cheng HM. Normal anatomy and lesions of the lacrimal sac and duct: evaluated by dacryocystography, computed tomography, and MR Imaging. Neuroimaging Clin N Am. 1996;6:199–216.
102. Kassel EE, Schatz CJ. Anatomy, imaging, and pathology of the lacrimal apparatus. In: Som PM, Curtin HD, editors. Head and neck imaging. 5th ed. St. Louis, MO: Elsevier-Mosby; 2011. p. 757–853.
103. Hurwitz JJ, Edward Kassel EE, Jaffer N. Computed tomography and combined CT-dacryocystography (CT-DCG). In: Hurwitz JJ, editor. The lacrimal system. New York: Lippincott-Raven; 1996. p. 83–5.
104. Choi SC, Lee S, Choi HS, Jang JW, Kim SJ, Lee JH. Preoperative computed tomography findings for patients with nasolacrimal duct obstruction or stenosis. Korean J Ophthalmol. 2016;30:243–50.
105. Tawfik KO, Ishman SL, Altaye M, Meinzen-Derr J, Choo DI. Pediatric acute otitis media in the era of pneumococcal vaccination. Otolaryngol Head Neck Surg. 2017;156(5):938–45.
106. Taxy JB. Squamous carcinoma in a major salivary gland: a review of the diagnostic considerations. Arch Pathol Lab Med. 2001;125:740–5.
107. Christe A, Waldherr C, Hallett R, et al. MR imaging of parotid tumors: typical lesion characteristics in MR imaging improve discrimination between benign and malignant disease. AJNR Am J Neuroradiol. 2011;32:1202–7.
108. Batsakis JG, McClatchey KD, Johns M, et al. Primary squamous cell carcinoma of the parotid gland. Arch Otolaryngol. 1976;102:355–7.
109. Ying YL, Johnson JT, Myers EN. Squamous cell carcinoma of the parotid gland. Head Neck. 2006;28:626–32.
110. Heaton CM, Chazen JL, van Zante A, Glastonbury CM, Kezirian EJ, Eisele DW. Pleomorphic adenoma of the major salivary glands: diagnostic utility of FNAB and MRI. Laryngoscope. 2013;123(12):3056–60.
111. Yarington CT Jr, Yonkers AJ, Carter WS. Salivary gland tumors. Nebr State Med J. 1971;56(4):146–51.
112. Spiro RH. Salivary neoplasms: overview of a 35-year experience with 2,807 patients. Head Neck Surg. 1986;8:177–84.
113. Abdel Razek AAK, Mukherji SK. State-of-the-art imaging of salivary gland tumors. Neuroimaging Clin N Am. 2018;28:303–17.
114. Thoeny HC. Imaging of salivary gland tumors. Cancer Imaging. 2007;7:52–62.
115. Phillips PP, Olsen KD. Recurrent pleomorphic adenoma of the parotid gland: report of 126 cases and a review of the literature. Ann Otol Rhinol Laryngol. 1995;104:100–4.

116. Tsushima Y, Matsumoto M, Endo K, et al. Characteristic bright signal of parotid pleomorphic adenomas on T2-weighted MR images with pathological correlation. Clin Radiol. 1994;49:485–89; Ikeda K, Katoh T, Ha-Kawa SK, et al. The usefulness of MR in establishing the diagnosis of parotid pleomorphic adenoma. AJNR Am J Neuroradiol. 1996;17:555–59.
117. Motoori K, Yamamoto S, Ueda T, et al. Inter- and intratumoral variability in magnetic resonance imaging of pleomorphic adenoma: an attempt to interpret the variable magnetic resonance findings. J Comput Assist Tomogr. 2004;28:233–46.
118. Mandelblatt SM, Braun IF, Davis PC, et al. Parotid masses: MR imaging. Radiology. 1987;163:411–4.
119. Epstein JB, Wong FL, Stevenson-Moore P. Osteoradionecrosis: clinical experience and a proposal for classification. J Oral Maxillofac Surg. 1987;45(2):104–10.
120. Minami M, Tanioa H, Oyama K, et al. Warthin's tumor of the parotid gland: MR-pathologic correlation. AJNR Am J Neuroradiol. 1993;14:209–14.
121. Liu XW, Xie CM, Li H, Zhang R, Geng ZJ, Mo YX, et al. Nasopharyngeal adenoid cystic carcinoma: magnetic resonance imaging features in ten cases. Chin J Cancer. 2012;31:19–28.
122. Shimamoto H, Chindasombatjaroen J, Kakimoto N, Kishino M, Murakami S, Furukawa S. Perineural spread of adenoid cystic carcinoma in the oral and maxillofacial regions: evaluation with contrast-enhanced CT and MRI. Dentomaxillofac Radiol. 2012;41:143–51.
123. Joe VQ, Westesson PL. Tumors of the parotid gland: MR imaging characteristics of various histologic types. AJR Am J Roentgenol. 1994;163:433–8.
124. Tian Z, Li L, Wang L, Hu Y, Li J. Salivary gland neoplasms in oral and maxillofacial regions: a 23-year retrospective study of 6982 cases in an eastern Chinese population. Int J Oral Maxillofac Surg. 2010;39:235–42.
125. Goode RK, Auclair PL, Ellis GL. Mucoepidermoid carcinoma of the major salivary glands: clinical and histopathologic analysis of 234 cases with evaluation of grading criteria. Cancer. 1998;82:1217–24.
126. Jansisyanont P, Blanchaert RH Jr, Ord RA. Intraoral minor salivary gland neoplasm: a single institution experience of 80 cases. Int J Oral Maxillofac Surg. 2002;31:257–61.
127. Khalek Abdel Razek AA. Diffusion-weighted magnetic resonance imaging of head and neck. J Comput Assist Tomogr. 2010;34:808–15.
128. Meyers M, Granger B, Herman P, Janot F, Garrel R, Fakhry N, et al. Head and neck adenoid cystic carcinoma: a prospective multicenter REFCOR study of 95 cases. Eur Ann Otorhinolaryngol Head Neck Dis. 2016;133:13–7.
129. Coca-Pelaz A, Rodrigo JP, Bradley PJ, Vander Poorten V, Triantafyllou A, Hunt JL, et al. Adenoid cystic carcinoma of the head and neck—an update. Oral Oncol. 2015;51:652–61.
130. van Weert S, Lissenberg-Witte BI, Bloemena E, Leemans CR. Mucoepidermoid carcinoma of the head and neck: CRTC1/3 MAML 2 translocation and its prognosticators. Eur Arch Otorhinolaryngol. 2021;279(5):2573–81. https://doi.org/10.1007/s00405-021-07039-2.
131. Takashima S, Wang J, Takayama F, et al. Parotid masses: prediction of malignancy using magnetization transfer and MR imaging findings. AJR Am J Roentgenol. 2001;176:1577–84.
132. Casselman JW, Mancuso AA. Major salivary gland masses: comparison of MR imaging and CT. Radiology. 1987;165:183–9.
133. Celebi I, Mahmutoglu AS, Ucgul A, Ulusay SM, Basak T, Basak M. Quantitative diffusion-weighted magnetic resonance imaging in the evaluation of parotid gland masses: a study with histopathological correlation. Clin Imaging. 2013;37:232–8.
134. Yoshino N, Yamada I, Ohbayashi N, et al. Salivary glands and lesions: evaluation of apparent diffusion coefficients with split-echo diffusion-weighted MR imaging–initial results. Radiology. 2001;221:837–42.
135. Thompson L. World Health Organization classification of tumours: pathology and genetics of head and neck tumours. Ear Nose Throat J. 2006;85:74.
136. Habermann CR, Gossrau P, Graessner J, et al. Diffusion-weighted echo-planar MRI: a valuable tool for differentiating primary parotid gland tumors? Rofo. 2005;177:940–5.

137. Lechner Goyault J, Riehm S, Neuville A, Gentine A, Veillon F. Interest of diffusion-weighted and gadolinium-enhanced dynamic MR sequences for the diagnosis of parotid gland tumors. J Neuroradiol. 2011;38:77–89.
138. Okahara M, Kiyosue H, Hori Y, et al. Parotid tumors: MR imaging with pathological correlation. Eur Radiol. 2003;13 suppl 4:L25–33.
139. Yabuuchi H, Fukuya T, Tajima T, et al. Salivary gland tumors: diagnostic value of gadolinium-enhanced dynamic MR imaging with histopathologic correlation. Radiology. 2003;226:345–54.
140. Chedid HM, Rapoport A, Aikawa KF, Menezes Ados S, Curioni OA. Warthin's tumor of the parotid gland: study of 70 cases. Rev Col Bras Cir. 2011;38:90–4.
141. Thoeny HC, De Keyzer F, Boesch C, et al. Diffusion-weighted imaging of the parotid gland: influence of the choice of b-values on the apparent diffusion coefficient value. J Magn Reson Imaging. 2004;20:786–90.
142. Habermann CR, Arndt C, Graessner J, et al. Diffusion-weighted echo-planar MR imaging of primary parotid gland tumors: is a prediction of different histologic subtypes possible? AJNR Am J Neuroradiol. 2009;30:591–6.
143. Triantafillidou K, Dimitrakopoulos J, Iordanidis F, Koufogiannis D. Mucoepidermoid carcinoma of minor salivary glands: a clinical study of 16 cases and review of the literature. Oral Dis. 2006;12(4):364–70.
144. Pires FR, Almeida OP, Araujo VC, Kowalski LP. Prognostic factors in head and neck mucoepidermoid carcinoma. Arch Otolaryngol Head Neck Surg. 2004;130:174–80.
145. Yuan JP, Liang BL, Xie BK, Song ZC, Zhong JL. Value of manifestations of magnetic resonance imaging (MRI) in diagnosis of parotid tumors and their pathological bases. Ai Zheng. 2003;22(5):514–9.
146. Weinberg MA, et al. Bisphosphonate-associated osteonecrosis of the jaws: impact on oral health. US Pharmacist; 2006.
147. Glanzmann C, Gratz KW. Radionecrosis of the mandibula: a retrospective analysis of the incidence and risk factors. Radiother Oncol. 1995;36(2):94–100.
148. Chiandussi S, Biasotto M, Dore F, Cavalli F, Cova MA, Di Lenarda R. Clinical and diagnostic imaging of bisphosphonate-associated osteonecrosis of the jaws. Dentomaxillofac Radiol. 2006;35:236–43.
149. Chang PC, Fischbein NJ, Holliday RA. Central skull base osteomyelitis in patients without otitis externa: imaging findings. AJNR Am J Neuroradiol. 2003;24(7):1310–6. The article provides multiple MRI examples of SBO including follow-up imaging.
150. Notani K, Yamazaki Y, Kitada H, et al. Management of mandibular osteoradionecrosis corresponding to the severity of osteoradionecrosis and the method of radiotherapy. Head Neck. 2003;25(3):181–6.
151. Schwartz HC, Kagan AR. Osteoradionecrosis of the mandible: scientific basis for clinical staging. Am J Clin Oncol. 2002;25(2):168–71.
152. Store G, Boysen M. Mandibular osteoradionecrosis: clinical behaviour and diagnostic aspects. Clin Otolaryngol Allied Sci. 2000;25(5):378–84.
153. Bou-Assaly W. Computed tomography imaging of acute neck inflammatory processes. World J Radiol. 2010;2(3):91.

Heart Diseases in Geriatric Patients

5

Anna Palmisano, Raffaele Ascione, Francesco De Cobelli, and Antonio Esposito

5.1 Introduction

In the United States (US), adults aged ≥75 years represent 6% of the entire population and the number of US citizens older than 80 years is expected to rise approximately by 25 million in the next 30 years.

Cardiovascular disease is the most frequent single cause of death in persons over 65 years of age, and more than 60% of myocardial infarctions occur in patients over 75 years of age [1]. The increase in life expectancy will likely cause an increase in myocardial infarction cases [2]. Cardiovascular diseases such as coronary artery disease, arrhythmias, heart failure and valve disease increase in incidence with increasing age [3]. Age itself affects cardiac physiology and remodelling, making challenge to distinguishing age-related changes to pathology. Main cardiovascular-related changes included increased diffuse fibrosis causing cardiovascular stiffness with reduced vascular compliance, ventricular diastolic and systolic dysfunction, and alteration in conduction system; increased lipid endothelial deposition with progressive atherosclerosis and fibrocalcific valve degeneration.

Cardiac Computed Tomography (CCT) and Magnetic Resonance Imaging (MRI) are able to provide a deep characterization of myocardial anatomy, function and remodelling, crucial for screening, diagnosis, risk stratification and therapy guidance. Furthermore, imaging has a pivotal role in planning of interventional procedures, rapidly developed in the last years aimed to safely treat more fragile patients

A. Palmisano · F. De Cobelli (✉) · A. Esposito
Clinical and Experimental Radiology Unit, Experimental Imaging Center, San Raffaele Scientific Institute, Milan, Italy

School of Medicine, Vita-Salute San Raffaele University, Milan, Italy
e-mail: palmisano.anna@hsr.it; decobelli.francesco@hsr.it; francesco.decobelli@hsr.it; esposito.antonio@hsr.it

R. Ascione
Department of Advanced Biomedical Sciences, University Federico II, Naples, Italy

G. Guglielmi, M. Maas (eds.), *Imaging in Geriatrics*, Practical Issues in Geriatrics, https://doi.org/10.1007/978-3-031-14877-4_5

[4]. The understanding of cardiac disease typically occurring in elderly and the potential value of each cardiac imaging modality may help to decide on the most suitable imaging modality and its timing [5]. This chapter provides an overview of cardiac imaging modalities for the most frequent cardiovascular diseases in the elderly population.

5.2 Coronary Artery Disease

5.2.1 Introduction

Coronary artery disease (CAD) constitutes one of the main causes of mortality in the Western world. Many important studies such as the NHANES (National Health and Nutrition Examination Survey), the FHS (Framingham Heart Study), MESA (Multi-Ethnic Study of Atherosclerosis) and the CHS (Cardiovascular Health Study) stated that the prevalence of CAD drastically increases in the elderly population with men affected more than women [6–8]. The development of an atherosclerotic plaque in the intima of the coronary arteries is the primary cause of the disease. The majority of coronary atherosclerotic plaques will not determine any symptoms; however, some can clinically manifest in various forms that are generally classified as chronic coronary syndrome (CCS) and acute coronary syndrome (ACS).

CCS include the so-called Stable Angina in which thoracic pain is exacerbated by the presence of an atherosclerotic plaque in the intima layer of the coronary arteries which induces significant stenosis of the coronary lumen and reduction of blood flow supply. This results in faster exhaustion of the coronary flow reserve and the subsequent insufficiency of oxygen supply to the myocardium, which typically occurs after physical exercise or in any situation with increased oxygen demand.

ACS is commonly triggered by the rupture or the erosion of the fibrous cap of an atherosclerotic plaque, which leads to rapid platelet aggregation and thrombus formation. This can determine a sudden variable degree of obstruction to the coronary blood flow with downstream myocardial damage, resulting in three different clinical manifestations: unstable angina, non-ST-elevation myocardial infarction (NSTEMI), or ST-elevation myocardial infarction (STEMI). In some cases, sudden arrhythmic death may be the first clinical manifestation of CAD.

5.2.2 CAD Pathophysiology

Atherosclerosis is a slow pathophysiological process that probably begins in the first stages of life and involves the deposition of lipids, fibrous tissue, smooth muscle cells, and calcium in the intimal layer of coronary arteries [9]. Atheroma generally forms in proximal coronary segments and vessel bifurcations [9, 10].

Acute coronary syndromes typically occur following the rupture or the erosion of a vulnerable plaque with subsequent thrombosis and occlusion of the vessel

lumen. Often, these plaques are not associated with relevant luminal stenosis and exhibit a thin, fibrous cap with a large necrotic core. Other typical features of vulnerability are plaque vascularization, high plaque volume, matrix metalloproteinase expression and collagenase activity, and macrophage infiltration of the fibrous cap [11].

Complete vessel occlusion can result in myocardial necrosis and subsequent STEMI or NSTEMI, whereas partial vessel occlusion can lead to ischemia without myocardial necrosis that clinically manifest as unstable angina [12].

However, the majority of atherosclerotic plaques remain clinically silent. These slow-growing plaques induce progressive vessel stenosis with flow-limiting condition, whose symptoms eliciting stable coronary artery disease became manifest during physical exercise and all condition requiring an increased oxygen demand for a mismatch between the myocardial oxygen demand and myocardial oxygen consumption. The reduction of coronary flow reserve is proportional to the degree of luminal narrowing; however, it is further worsened by the endothelial dysfunction, which typically occur in atherosclerosis causing impaired vasodilation independently by the degree of stenosis.

5.2.3 Multimodality Imaging with a Particular Focus on CT and MRI

Cardiac imaging can be used to unravel the coronary artery disease by either triggering the ischemic process or via the direct visualization of coronary artery stenoses [13].

The majority of coronary stenosis do not cause ischemia and consequently do not require revascularization. Ischemia was found in approximately 50% of patients with obstructive CAD (stenosis $\geq 50\%$); therefore, the functional significance of stenosis should be considered uncertain, and an imaging-based stress examination is frequently required to identify myocardial ischemia in the setting of CCS [14]. Ischemia can be triggered by physical exercise or pharmacologic stress [15]. Single-photon emission computed tomography (SPECT), positron emission tomography (PET) myocardial perfusion, stress echocardiography, stress computed tomography and stress magnetic resonance (MR) imaging are the most commonly used tests [16]. Recent studies stated that the Stress MRI and PET have similar accuracy and are suitable to rule out hemodynamically significant coronary artery diseases in a wide range of pre-test probability, while stress SPECT and echocardiography are less reliable [17]. Stress MRI has also the advantage, over PET, of combining a multiparametric characterization of the myocardium.

The direct visualization of coronary anatomy can be obtained invasively with coronary angiography (ICA) or non-invasively with coronary computed tomography angiography (CCTA). ICA offers the best spatial resolution and can be combined with the measurement of the fractional flow reserve (FFR) to quantify the stenosis significance and guide revascularization if its value is lower than 0.8 [16].

In the recent years, CCTA emerged has a valid alternative to ICA in patients with low-intermediate likelihood for CAD thanks to its negative predictive value close to 100% [13]. Despite CCTA is a pure anatomic method, the continuous technical and methodological development opened the possibility of a CT-based assessment of functional significance of stenosis using CT stress perfusion or non-invasive virtual FFR.

Each of the outlined strategies presents certain limitations. Ischemia testing has limited sensitivity and specificity, cannot identify where coronary plaques are located, and cannot perform stenosis grading and plaque characterization. Invasive coronary angiography is associated with potential complications for its invasiveness and high radiation exposure, as well as higher costs compared to non-invasive techniques. CCTA can suffer from poor image quality in patients with arrhythmias or tachycardia or can be misinterpreted determining false-positive results in case of a very high calcium burden [13].

For these reasons, choosing the best imaging strategy must take into account patient characteristics, pre-test probability, medical expertise and available technologies, preferring a non-invasive anatomical imaging strategy (CCTA) in case of no previous history of CAD, low to intermediate clinical likelihood and when information about the presence and the burden of coronary atherosclerosis is desired to tailor the patient management.

While the use of imaging is well established for diagnosing CAD in symptomatic patients, its role in primary prevention is still unclear. In asymptomatic individuals, traditional risk factors such as hypertension, diabetes mellitus, sex and family history are used to estimate the risk of future major cardiac events and the need for risk-lowering treatments. Non-enhanced cardiac CT has a crucial role in risk stratification via the evaluation of coronary calcium score and will be discussed in the following sections.

Non-invasive cardiac imaging has limited role in the setting of acute coronary obstruction [18, 19], but has gained a growing role in patients with low-risk acute chest pain or with a clinical-angiographic diagnosis of Myocardial Infarction with Non-Obstructed Coronary Arteries (MINOCA).

CCTA has rapidly gained a central role to rule out CAD in patients with acute chest pain and a relatively low pretest probability of ACS. However, it cannot exclude other important causes of acute chest pain with unobstructed coronaries, such as acute myocarditis, myocardial infarction with normal coronary arteries, and cardiomyopathies. A few recent studies showed the possibility to obtain information about myocardial scar and extracellular volume also in CT; however, these techniques still need experienced readers [20–22] and require large studies to define its generalizability.

Cardiac MRI is widely adopted in patients with non-obstructed coronary arteries at ICA, being able to provide differential diagnosis of ACS impacting on patients' treatment and management. Moreover, it plays a role in patients risk stratification and in the diagnosis of complications [18].

5.2.3.1 CCTA

Minimum technological requirement and patients' preparation are crucial to obtain a diagnostic image quality. 64-detector row CT is considered the minimum standard for CCTA.

Image quality improves substantially when the heart rate is regular and lower than 65 beats/min. In the absence of contraindication, the administration of beta-blockers and nitrates to lower the heart rhythm and to vasodilate coronary arteries is recommended to improve image quality and coronary evaluation. Different acquisition strategies are available to obtain the best image quality based on patient's heart rate, BMI and ability to breath-hold. In general, retrospective ECG-gated helical acquisition enables the reconstruction of image data sets at arbitrary time points during the cardiac cycle. This technique provides excellent flexibility for identifying the optimal cardiac phase without motion artefacts at the cost of higher radiation exposure. Prospective ECG-triggered acquisition substantially reduces radiation exposure but requires a lower and regular heart rate.

In the elderly population, considering the lower impact of radiation exposure, retrospective ECG-gated helical acquisition often represents a good choice, but the application of the tube-current modulation during the cardiac cycle to the retrospective ECG-gated helical acquisition is anyway recommended, in order to maintain radiation exposure at reasonable level.

Chronic kidney disease can represent an important limitation to the exam in this category of patients. However, dual energy acquisition offers the possibility to perform CCTA with very low dose of contrast agent.

Calcium Scoring

Calcium hydroxyapatite deposition in coronary arteries always occurs in the intima associated with coronary atherosclerotic plaque formation; here, inflammation triggers processes similar to osteogenesis. The majority of elderly patients presents with coronary calcium without any symptoms. Non-contrast cardiac CT is used to establish the coronary artery calcium score (CACS), also known as the Agatston score, considering each calcified plaque using dedicated software. Finally, scores for all detected lesions are summarized to obtain the total score. Non-contrast CT should be ECG-gated and acquired at 120 kVp; however, recent studies documented strong correlation with CACS measured from non ECG-gated non contrast CT scan and also from ECG-gated low dose (80 kVp) scan [23].

In asymptomatic individuals the presence and the extent of coronary calcium correlate to total atherosclerotic plaque burden and to the risk of future cardiovascular events [24]. Any coronary calcium, including a single focus of calcium, indicates increased atherosclerotic cardiovascular disease risk over the next 10–15 years, while its absence indicates less than 1% risk for atherosclerotic cardiovascular events in the next 10 years [25, 26].

Plaques and Stenosis Assessment

CCTA can unravel both calcified and non-calcified plaques [27].

Moreover, CCTA can identify plaque at high risk of rupture [28]. CCTA features of plaque vulnerability include positive remodelling, large plaque volume, low attenuation, spotty calcification, and napkin ring sign. In the case of rupture, subsequent thrombus appears as a low-density material within the coronary lumen that may completely occlude such lumen and is often associated with pronounced positive remodelling [29, 30].

The use of Coronary Artery Disease Reporting and Data System (CAD-RADS) [31] to report the results of a CCTA examination should be promoted to improve standardization and communications among physicians.

Bypass Graft and Stent Assessment

CCTA has a pivotal role in the follow-up after stent implantation and coronary artery bypass graft (CABG).

In-stent restenosis (ISR) is defined as a reduction >50% of the diameter of the coronary artery lumen inside or at the edges of the implanted stent (Fig. 5.1).

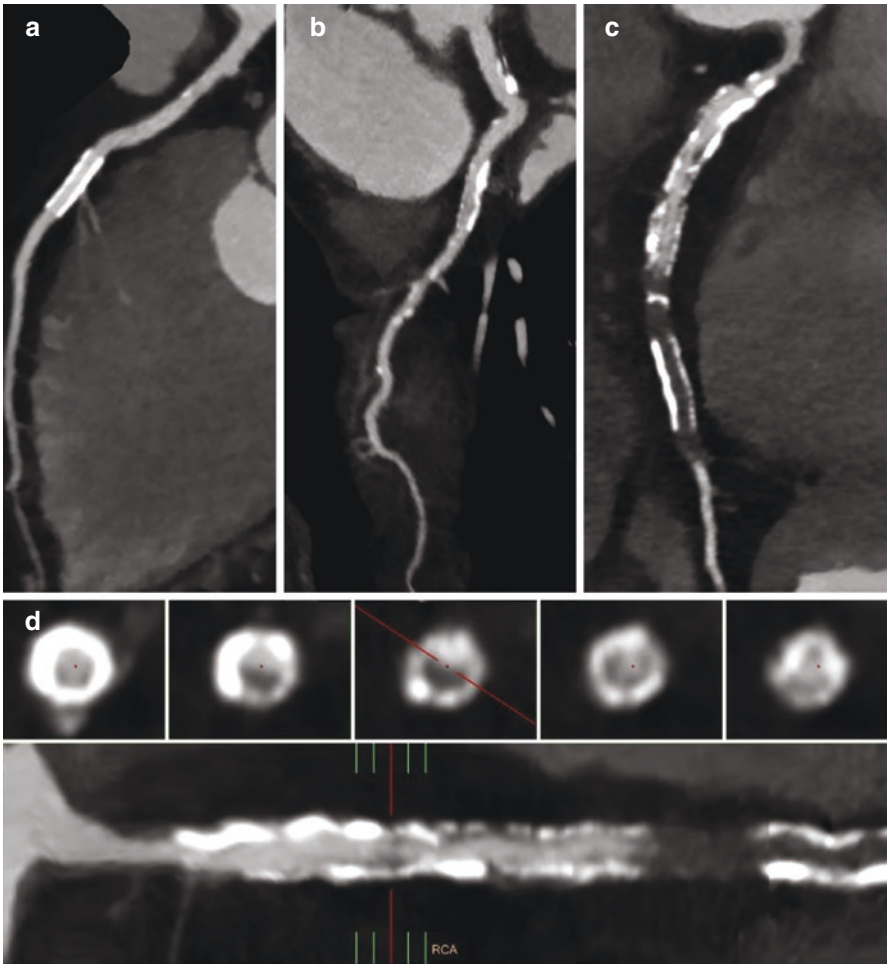

Fig. 5.1 (**a**–**d**) CCTA of a 77-year-old man with previous PCI on left anterior descending artery (**a**), circumflex (**b**) and right coronary artery (**c**). CCTA showed good patency of the coronary artery stent on left anterior descending artery (**a**) and circumflex artery (**b**), without signs of neo-intimal hyperplasia, differently from stents on the right coronary artery with evidence of intrastent stenosis >50% in the proximal and medium stent and total occlusion of the distal stent

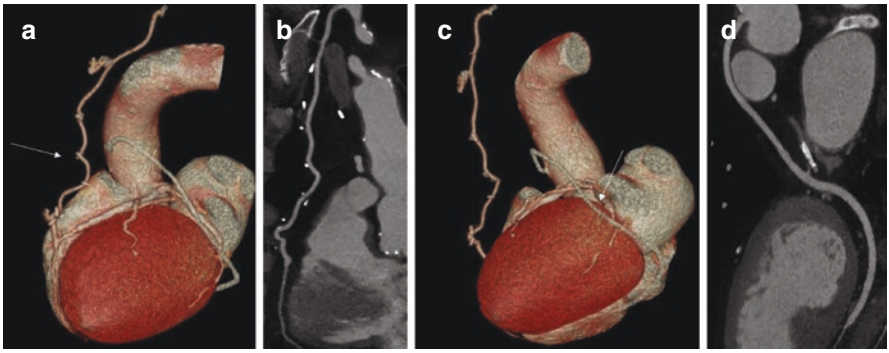

Fig. 5.2 (**a**–**d**) CCTA of a 78-year-old man with previous CABG: left internal mammary artery on left anterior descending artery (arrow in **a**), and a venous graft for the posterior descending artery (arrow in **c**). CCTA documented good patency of both grafts as showed in 3D volume rendering (**a** and **c**) and multiplanar reconstruction (**b** and **d**)

Identifying in-stent stenosis by coronary CTA is problematic and prone to inaccurate results, especially for stents with diameters <3.0 mm [32, 33].

CTA has excellent accuracy for the evaluation of coronary artery bypass grafts [34–36] patency in the early (<1 month) as well as late (>1 month) postoperative period (Fig. 5.2).

CT Tissue Characterization: Perfusion and Scar

CCTA alone is unable to accurately estimate the functional hemodynamic effect of a coronary stenosis. Stress perfusion CT can offer non-invasive functional information, which aids in selecting patients eligible for revascularization [37]. CT stress perfusion evaluates the attenuation differences induced in the myocardium by the first pass of the iodinated contrast material during pharmacological stress [38]. Stress can be obtained using adenosine or dipyridamole or regadenoson, which induces maximum vasodilation and steal effect [39]. Different protocols of CT stress perfusion are available. It can be performed in static or dynamic mode. Some centres prefer to acquire a stress scan followed by rest, while others acquire the rest scan first. Perfusion defects appear as a subendocardial or transmural hypoattenuating area in a coronary territory. The dynamic acquisition can be used to perform quantitative analysis to evaluate the myocardial blood flow (MBF) and the coronary flow reserve (CFR) that are used for the evaluation of epicardial disease and microvascular dysfunction [39].

Many studies confirmed that CTA pooled with CT stress perfusion has a high accuracy for predicting obstructive CAD (>50%) and has a high specificity and positive predictive value (PPV) [37, 40, 41]. However, CTP is generally not the first stress imaging test of choice, mainly because of the still very limited availability since CTP requires additional resources, top-class scanner and advanced expertise in using this technique and protocol.

Several studies showed the possibility to detect myocardial scar and quantify myocardial ECV with a delayed scan acquired at 10 min after the administration of

contrast media, with good accuracy compared to MRI [20–22]. Different scanning protocol were tested based on low kV single energy scan or dual energy acquisition [20–22].

5.2.3.2 MR Imaging

Cardiac Magnetic Resonance allows a complete morpho-functional and structural characterization of the myocardium; however, it requires long acquisition time, limiting its applicability in the emergency setting as well as in elderly patients with limited capability of collaboration. Geriatric patients generally have limited compliance because of the long exam time and difficulties to breath-hold. Therefore, faster cardiac protocols are highly desirable, especially for patients in unstable conditions or requiring acute care [42].

In the setting of ACS, cardiac MRI has a primary role when an advanced assessment of potential complications is required [43, 44]. If performed early (i.e., during the first 2 weeks after PCI), CMR with a standard protocol can accurately assess ventricular function, myocardial oedema and myocardial injury, detect early myocardial infarction complications [42] such as a free wall or interventricular septum rupture and detect thrombus or differentiating between aneurysm and pseudoaneurysm [45, 46]. Furthermore, it allows the depiction of other parameters such as microvascular obstruction (MVO), intramyocardial haemorrhage, the area at risk and the myocardial salvage index (MSI) [47] (Fig. 5.3). These biomarkers are increasingly used in the clinical trials designed to assess the effectiveness of new treatments in the setting of acute myocardial infarction.

T2 STIR imaging in at least two orthogonal planes is necessary to outline myocardial oedema, which represents a nonspecific response of the myocardium that is seen in patients with acute myocardial damage. It typically results in a hyperintensity of the injured myocardial area, and it is also very useful to differentiate acute from chronic myocardial infarction [48].

Cardiac LGE MRI has a primary role in the identification and quantification of myocardial necrosis [49]. The ischemic LGE pattern refers to subendocardial enhancement, with a variable transmural extent that follows a coronary artery territory distribution and allows the differential diagnosis with other pathologies that present with a non-ischemic LGE pattern [50, 51]. LGE imaging can also easily depict microvascular obstructions or intramyocardial haemorrhage, which are two critical prognostic markers. Furthermore, new advanced software allows an accurate automatic or semiautomatic quantification of scar burden, which is an essential predictor of LV remodelling and consequently of prognosis [43, 44, 52, 53].

Recently introduced, T1 and T2 mappings consist in parametric quantitative sequences that provide tissue-specific T1 and T2 values and allow an objective assessment of myocardial abnormalities. In acute ischemia settings, T1 mapping shows high native T1 and extracellular volumes of acutely infarcted and oedematous myocardium, while T2 mapping can quantitatively evaluate oedema and identify intramyocardial haemorrhage or MVO [54, 55].

In elderly patients, cardiac MRI can be useful late after PCI (i.e., within 1 month), especially in patients with anterior infarction, previous infarction or heart failure

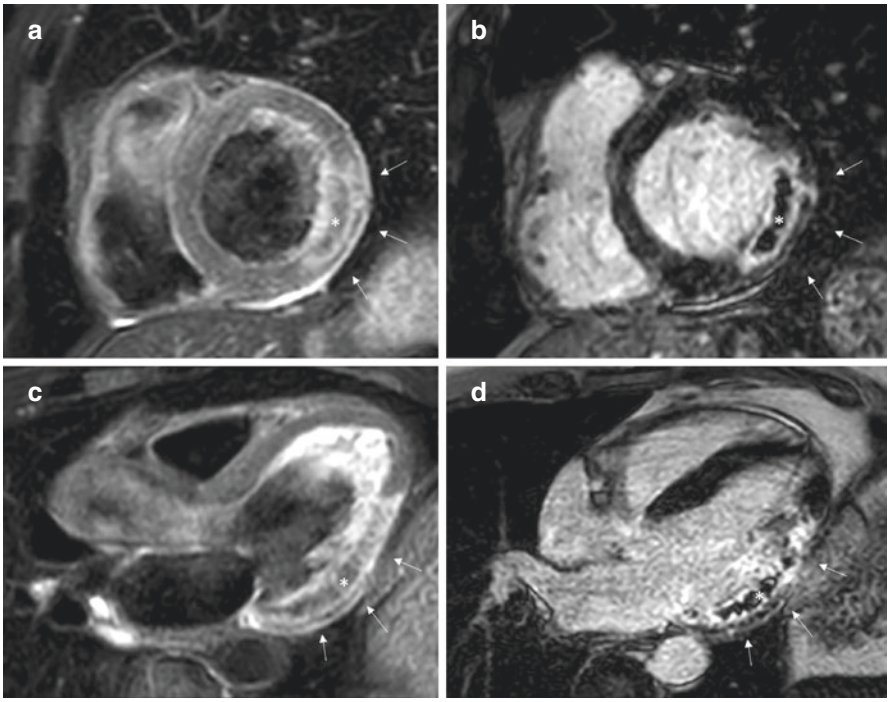

Fig. 5.3 (**a**–**d**) CMR images of a 45-year-old man with STEMI. CMR images were performed 6 days after STEMI due to culprit lesion on left circumflex artery, promptly treated with PCI. CMR showed oedema on the lateral mid-basal wall (**a** and **c**) involving 34% of myocardial mass associated with transmural post-ischemic LGE (**b** and **d**) involving 23% of myocardial mass. Endocardial hypointensity was recognizable in the endocardium of the injured myocardium both on STIR images (asterisks in **a** and **c**) and LGE images (asterisks in **b** and **d**) referrable to myocardial haemorrhage and microvascular obstruction respectively

[43, 56]. In this setting, imaging is indicated for the assessment of the LV ejection fraction before hospital discharge [47, 56] especially when echocardiography is suboptimal or inconclusive [47, 57].

Moreover, CMR represents a game-changer in all the cases of cTnT elevation of unknown origin, outlining the diagnosis of all the conditions that can mimic AMI, such as Takotsubo cardiomyopathy, myocarditis, and MINOCA. CMR is an important management tool in this setting since it has a crucial role in guiding therapy [42, 58].

In patients with chornic coronary syndrome with intermediate stenosis [59, 60], stress cardiac MRI is an effective imaging to identify myocardial ischemia and viability, resulting fundamental for guiding patients' revascularization. Inducible ischemia is detected as an area of myocardial hypointensity in a coronary territory, extending from the endocardium to the epicardium, recognizable during the first pass perfusion at the peak of myocardial enhancement, not visible at rest perfusion and in the absence of scar at LGE.

5.3 Heart Failure

5.3.1 Introduction

Heart failure (HF) is a clinical syndrome characterized by typical symptoms (e.g., dyspnoea, fatigue) and signs (e.g., peripheral oedema, jugular engorgement) due to a structural or functional cardiac anomalies which lead to a reduction of the stroke volume or an increase of the filling pressure. In this condition, the heart cannot guarantee an adequate volume of blood and oxygen to tissues [61]. Nowadays, around 23 million people are affected by HF worldwide, and these numbers are increasing. The majority of these patients are more than 70 years old, with men affected more than women, with an overall HF prevalence of ≥10%. Furthermore, HF is frequently underdiagnosed in this group of patients because of the lack of specific symptoms and the concomitant presence of many comorbidities that can lead to misdagnosis [1].

5.3.2 Aetiology and Pathophysiology of Heart Failure

Heart failure represents the latest stage of every cardiovascular disease. It is defined as ischemic heart failure if it is a consequence of CAD or as non-ischemic heart failure if it is due to other diseases (e.g., hypertension, idiopathic cardiomyopathies, valvular diseases, inflammation, auto-immune diseases, nutritional deficiency, infections, and drugs). These conditions can trigger two primary pathophysiological alterations: volume (i.e., valvular regurgitation) or pressure overload (i.e., hypertension, aortic stenosis) and systolic dysfunction (i.e., CAD, idiopathic cardiomyopathies) [62].

Clinically, it can manifest as left HF, whose symptoms are mainly due to low cardiac output with fatigue and syncope or pulmonary congestion with dyspnoea and pulmonary oedema. Instead, jugular vein engorgement, hepatic congestion, and peripheric oedema are the typical signs of right HF [63].

EF is an essential parameter in patients affected by HF, and European guidelines use EF to classify HF in three different categories: HF with preserved ejection fraction (HFpEF, >50%), HF with mid-range reduction of EF (HFmrEF, 40–49%), and HF with reduced ejection fraction (HFrEF, <40%). This classification is of paramount importance because it reflects aetiologies and comorbidities of HF, with an important impact on prognosis and therapy [61].

This classification also reflects the pathophysiological mechanism of HF, which can be distinguished in systolic and diastolic HF. In systolic dysfunction, there is a contractile insufficiency of the left ventricle that loses its capability to guarantee an expected cardiac output, leading to HFrEF (i.e., CAD, DCM) [61]. Dilated Cardiomyopathy (DCM) is a form of HFrEF and is defined as a left ventricular dilation and systolic dysfunction in the absence of coronary artery disease or abnormal loading conditions proportionate to the degree of LV impairment. It can be due to many causes, such as alcohol consumption, genetic aetiology (e.g., lamin A/C mutation or myotonic dystrophy), anthracycline therapy history, HIV infection,

persistent tachyarrhythmia (>100 beats/min), and inflammatory disease (e.g., sarcoidosis, giant cell myocarditis, or Lyme disease) [64].

In diastolic dysfunction, the left ventricle generally appears thickened, with a normal cavity but reduced left ventricular compliance, leading to abnormally increased filling pressures, which leads to a HFpEF. Even if counterintuitive, this form of HF appears to be very common in the elderly population [65]. Besides assessing EF, cardiac imaging can outline the pathological process of diastolic dysfunction generally caused by hypertensive cardiopathy, pericardial constriction, aortic stenosis and some infiltrative disorders, among which amyloidosis represents a significant cause in the geriatric population [66].

5.3.3 Multimodality Imaging with a Particular Focus on CT and MRI

Diagnosis of HF is typically based on clinical signs and symptoms, with echocardiography that represents a primary tool [61]. For the differential diagnosis between HFrEF and HFpEF, EF evaluation is obtained via TTE, and when it is suboptimal or inconclusive, CMR can be the exam of choice. As such, imaging plays a pivotal role in the diagnosis and the identification of HF aetiology [67]. Ischemia is the primary cause of HF and can be diagnosed through anatomical techniques such as CCTA or ICA, or with functional techniques such as stress echo and CMR, or nuclear medicine techniques [68].

Chest radiography is one of the first exams needed to study a patient with suspected HF in ED, mainly to exclude other causes of dyspnoea. Furthermore, it represents a straightforward methodology to monitor the response to therapy in acute settings.

Echocardiography is the pivotal technique for patients with HF of unknown origin. It can help to establish the aetiology and severity of HF as it can provide chamber dimensions, biventricular function, valvular diseases, and systolic/diastolic function (i.e., filling pressures and patterns). Given its ability to establish the EF value, echocardiography is the primary tool to diagnose a HF with preserved or reduced EF, providing preliminary insights into the diagnosis. Regional wall motion abnormalities may suggest an ischemic aetiology, while a homogeneous dilatation with diffuse motion abnormalities may be typical of a non-ischemic disease which can show other characteristic findings [61, 68].

5.3.3.1 CT Imaging

CCTA is a valuable tool for evaluating the coronary arteries, and it is primarily used to exclude CAD as a possible cause of HF of unknown origin. CTCA has been proposed as a gatekeeper to ICA for patients with new-onset HF [69]. Furthermore, many authors suggest that in these patients calcium score with an Agatston score of 0 has been shown to have a 100% sensitivity to exclude “high-risk CAD”, defined as left main coronary artery stenosis or stenosis in at least two major epicardial coronary arteries [70–72]. Thanks to the increase in temporal resolution of CT

scanner in the recent years, CCTA can accurately evaluate cardiac structure and function. Moreover, using Late Contrast Enhancement (LCE) scan, CT could also identify non-ischemic cardiac disease underlying HF and may provide a quantification of myocardial stiffness through the measurement of ECV with results comparable to CMR [73, 74].

5.3.3.2 MR Imaging

MR is the gold standard for volumetric analysis and cardiac function assessment, thanks to its high accuracy and reproducibility. Cine imaging can assess the severity and regionality of left ventricular dysfunction, volumes, and wall thickness. Moreover, it can evaluate myocardial perfusion, viability, and fibrosis, which can aid the evaluation of the aetiology of new-onset HF [75]. Recently introduced parametric techniques such as T1/T2 mapping and ECV can easily detect diffuse fibrosis earlier than older LGE sequences [76]. However, LGE imaging is the primary sequence for differentiation between ischemic and non-ischemic cardiomyopathies, based on the pattern, location and distribution of LGE. Ischemic pattern will always involve the subendocardium, whereas a non-ischemic pattern will always be limited to the mid- or epicardial wall sparing the subendocaridum [50, 77]. The absence of LGE in patients with a severe reduction of EF suggests non-ischemic cardiomyopathies such as idiopathic dilated, inflammatory, alcoholic, Takotsubo, and peripartum cardiomyopathies [78].

5.3.3.3 Indications and Planning for ICD and ICD-CRT

Cardiac imaging is also particularly useful to establish if and when devices such as implantable cardioverter-defibrillator (ICD) or cardiac resynchronization therapy (CRT) have to be implanted [79].

ICD represents the primary therapy to prevent sudden cardiac death in patients with EF <35%. Implant choice mainly depends on EF evaluation. When EF is lower than 35%, patients with HFrEF need to be implanted [80]. EF evaluation is mainly achieved through echocardiography, while CMR is indicated only if US is suboptimal or inconclusive. However, some authors suggest that echocardiography seems to overestimate EF in HFrEF patients, missing patients potentially eligible for ICD therapy. Moreover, many studies suggest that EF alone is insufficient to assess the risk of sudden cardiac death in HF patients. The integration of LGE CMR imaging can assess the presence, the distribution and the burden of myocardial scars, which represent the important risk-modifiers for the evaluation of defibrillator placement [79, 81]. For this reasons, CMR should always be applied in borderline cases.

CRT is a fundamental therapy for patients with refractory HF. Many studies have demonstrated that CRT can improve cardiac survival, decrease recurrent HF hospitalization and ameliorate the overall quality of life. Patients with specific characteristics such as wider QRS, left bundle branch block, female sex and non-ischemic cardiomyopathy are those who benefit the most from CRT [82]. A key factor seems to be ventricular dyssynchrony, which can be assessed via echocardiography through M mode, pulsed-wave Doppler imaging, tissue Doppler imaging (TDI),

speckle tracking, and real-time three-dimensional (RT3D) imaging [83]. Nevertheless, an important trial (PROSPECT) established that none of the many echocardiographic modalities is sensitive enough to be helpful in estimating response to CRT in clinical practice [84].

CMR can qualitatively or quantitatively assess interventricular and intraventricular dyssynchrony with different modalities such as myocardial tagging, strain-encoded MRI (SENC), phase-contrast MRI, and displacement encoding with stimulated echoes (DENSE). As for echocardiography, all these modalities have not yet proved to be useful.

On the other hand, the assessment of LGE at CMR imaging can provide valuable information in the prediction of response to CRT therapy [83] and may also help in improving the results of CRT therapy guiding the electrode implantation. LGE can evaluate three fundamental features that can predict a lower response to CRT:

1. The extent of the scar: if it is <15%, LGE can predict a good response to CRT [85].
2. The location of the myocardial scar: if it involves the postero-lateral wall, the myocardial scar is predictive of a lower response.
3. The presence of fibrosis in the site of LV lead placement, which may reduce the effectiveness of CRT [86].

Furthermore, some authors discovered that pacing in a site with <50% scar transmurality was associated with response to CRT [87].

In conclusion, CMR can provide a complete cardiac assessment for CRT, since it is the gold standard to evaluate the size and the function of the chambers, determine prognosis, and provide invaluable information about the probability of response to CRT via LGE.

5.3.4 Amyloidosis

As stated above, a common cause of HF in the elderly population is HFpEF. Imaging techniques are of fundamental importance not only for evaluating the EF, which is essential for the diagnosis, but also for the characterization of the pathological process that causes the underlying diastolic dysfunction.

Amyloidosis is a systemic infiltrative disease due to the presence of proteins with unstable structures that form aggregates and amyloid fibrils which can deposit in many different tissues. Immunoglobulin light chains (AL amyloidosis) and amyloid transthyretin (ATTR amyloidosis, hereditary, or wild type) are the most frequent variants determining cardiac amyloidosis (CA) and represent two CA subtypes with completely different prognosis and management [88]. The true prevalence of ATTR wild-type is unknown; autopsy studies revealed that 25% of the hearts of people aged 80 years or older contained wild-type fibrils regardless of the presence of symptoms [89].

The high accessibility and the ability to describe both cardiac structure and function make echocardiography the first-line tool in CA assessment. The typical echocardiographic findings in CA comprise a small left ventricle with concentric hypertrophy, a sparkling myocardial appearance, a biatrial enlargement with an increased atrial septum thickness, and a restrictive physiology [90].

Recent ultrasound techniques such as speckle tracking echocardiography were more sensitive than traditional echocardiography in detecting global and regional cardiac function changes. Several groups have shown the good sensitivity and specificity of basal to apical longitudinal strain ratio for differentiating CA from other cardiac pathologies [91, 92].

CMR is the imaging tool of choice to diagnose CA because of its tissue characterization capabilities [93]. LGE is historically the cornerstone of CMR to diagnose CA in patients whose kidney function allows contrast medium administration. The typical LGE pattern in CA is represented by diffuse and inhomogeneous myocardial hyperenhancement; sometimes, subendocardial circumferential hyperenhancement can be present in some patients while others can also show transmural hyperenhancement [94]. Some researchers suppose that these different LGE patterns are representative of different phases due to continuous amyloid deposition, with progression from no LGE to transmural LGE [95]. Another typical sign of amyloid deposition is the abnormal myocardial and blood-pool kinetics demonstrated in the inversion time scout sequence [96]. Native myocardial T1 mapping enables CA diagnosis without the need to administer gadolinium since very high T1 values are a typical feature of CA [97]. The integration of native T1 with post-contrast T1 values allows a non-invasive quantification of ECV [97]. High value of T1 mapping and ECV represent one of the earliest imaging signs for cardiac amyloid deposition (Fig. 5.4); they can be altered even when LGE is absent [98]. Instead, T2 mapping can show oedema in both types of amyloidosis, but this is generally larger in light chain CA [93]. While the integrated use of clinical findings, electrocardiography, echocardiography, and CMR makes the diagnosis of cardiac amyloidosis possible, these methodologies cannot accurately contribute to the characterization of the type of the underlying amyloid deposition. Myocardial scintigraphy with bone avid tracers has high sensitivity and specificity to diagnose ATTR CA; the ease of access, imaging simplicity, low cost and high specificity for ATTR CA are some of the advantages of this diagnostic tool [99–101]. In conclusion, cardiac imaging represents a critical tool for the diagnosis of CA. The stepwise use of various imaging modalities in conjunction with the clinical and laboratory data diagnose this pathology in most patients; therefore, cardiac biopsy, the gold standard diagnostic test to confirm and provide typization of amyloidosis, is no longer routinely performed in clinical practice due to its invasive nature and limited availability.

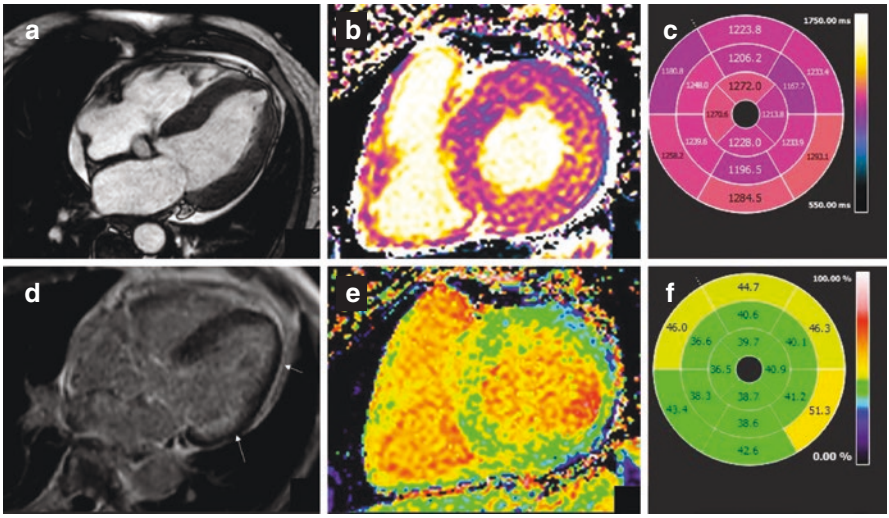

Fig. 5.4 CMR images of a 73-years-old man with cardiac amyloid. Cine SSFP image (**a**) shows a concentric myocardial hypertrophy (end-diastolic wall thickness of mid-basal septum: 19 mm; end-diastolic mass: 147 g) with slight diffuse edema (global T2 mapping: 58 ms; normal value <50 ms) and marked increase of native T1 mapping (**b**–**c**) with global T1: 1220 ms (normal value< 1045 ms) and of ECV values (**e**, **f**) with global ECV of 42% (normal value <27%) suggestive of a huge expansion of the extracellular space. LGE showed endocardial hyperitensity with a gradient from the bases to the apex (**d**). CMR findings were suggestive for cardiac amyloid

5.4 Valvular Heart Diseases

Valvular heart disease (VHD) increases in incidence at increasing age. Changing societal demographics with an ageing population, advances in imaging and the explosion of transcatheter interventional techniques have revolutionized the landscape of clinical management of these diseases. Multimodality imaging is essential in VHD for establishing diagnosis, monitoring disease, planning interventional and surgical procedures and follow-up.

5.4.1 Aortic Stenosis

5.4.1.1 Aetiology and Pathology

Aortic valve stenosis (AS) is the primary valve disease with the highest prevalence in western countries [102]; age-related degenerative calcific AS is now the most common aetiology of AS, followed by rheumatic stenosis and congenital stenosis [103]. Calcific AS is an active and progressive disease that shares similarities with atherosclerotic diseases such as inflammation, lipid infiltration and calcification [104].

5.4.1.2 Pathophysiology

A normal aortic valve has an opening area between 3 and 4 cm^2; a progressive reduction of the aortic valve area leads to a significant obstruction to the transvalvular flow and results in a transvalvular gradient. These haemodynamic changes cause an increase in pressure afterload and ventricular wall stress that stimulates hypertrophy of the left ventricular myocardium [105, 106]. In the early stages of the disease, left ventricular hypertrophy (LVH) reduces parietal stress and preserves the systolic function of the left ventricle; over time, LVH can be maladaptive with literature evidence that the hypertrophic myocardium represents an adverse prognostic marker in various clinical conditions [107–109]. LVH in patients with aortic valve stenosis is highly heterogeneous and is only weakly correlated with the extent of valve obstruction; it is more closely associated with age, male sex and obesity [110–115]. The heterogeneity of the myocardial response in terms of LVH has critical prognostic implications; it has been shown that with the same valvular obstruction, the finding of an inappropriate left ventricular mass significantly increases the mortality of patients with AS aortic [116]. The negative prognostic impact of an inappropriate left ventricular mass can be related to an increase in myocyte apoptosis and interstitial myocardial fibrosis deposition [117–119].

5.4.1.3 Multimodality Imaging

Echocadiography is the first-choice imaging technique to evaluate patients with AS and allows an accurate assessment of the severity of valvulopathy and of the systolic function of the left ventricle [120], in most of patients. Furthermore, by integrating the values of the valvular area, of the transvalvular gradient, and the left ventricle ejection fraction, it is possible to identify different phenotypes of AS with echocardiography. Such phenotypes are normal flow-high gradient, low-flow-low-gradient, paradoxical low flow-low gradient [120].

CT Imaging

CT with its high spatial resolution images of the aortic annuls and root represents a central modality for planning of transcatheter procedure of aortic valve replacement (TAVR/TAVI). In TAVI candidates, CT imaging provides a comprehensive assessment, including the analysis of the aortic annulus, the characterization of the valve anatomy (bicuspid or tricuspid), the burden of the aortic valve and aortic root calcification, and the evaluation of the peripheral vascular accesses [121, 122] (Fig. 5.5). The evaluation of aortic valve calcifications by CT has been proposed to estimate the severity of AS when the echocardiographic parameters are discordant: the cut-off value of AV calcifications associated with severe AS is ≥1274 AU in women and ≥2065 AU in men [123]. The evaluation of the aortic annulus anatomy is of paramount importance for a successful TAVI outcome. The annulus diameter dictates the aortic prosthetic size, making this measurement a critical point for procedural success; any error at this level could result in serious complications [124–126]. The aortic annulus has an oval shape with long and short diameters; CT is exceptionally accurate to obtain these measurements, as well as the perimeter and the area of the aortic annulus [127]. Another critical parameter determining the success of TAVI is

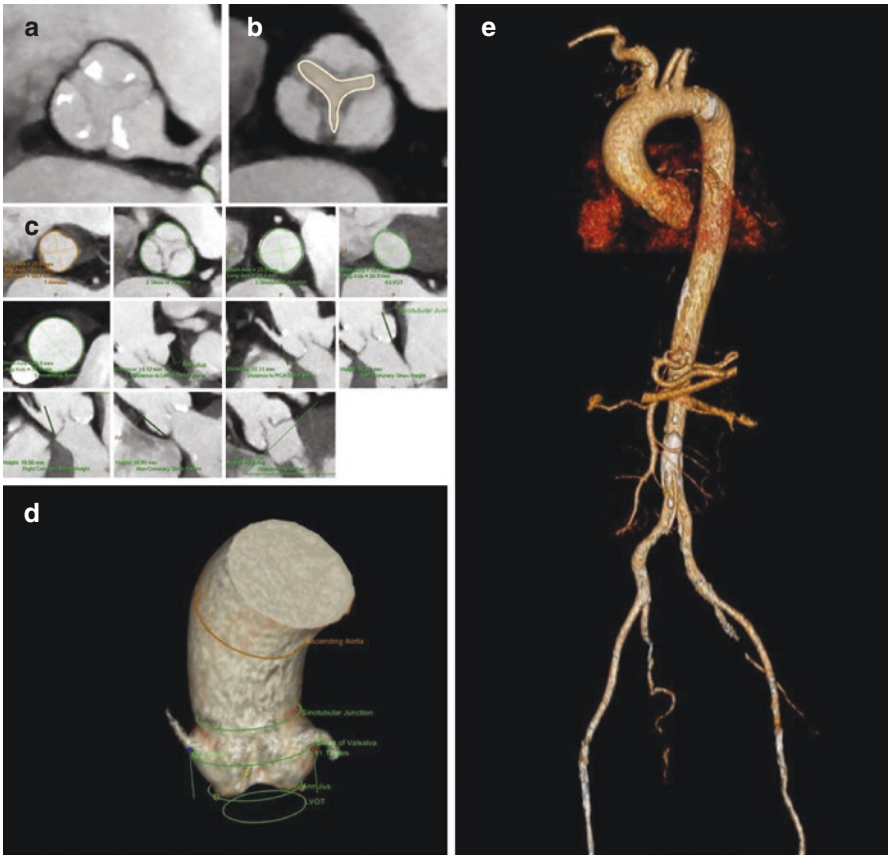

Fig. 5.5 CT angiography for planning of transcatheter aortic valve replacement in a 70-years-old woman. CT images shows a fibrocalcific degeneration of the aortic valve (**a**), with tricuspid morphology and moderate calcifications, characterized by severe stenosis with aortic valve planimetric area equal to 0.7 cm^2 (yellow area in **b**). CT images was used to characterize landing zone (multiplanar and 3D reconstruction of the aortic root in **c** and **d** respectively) and pheriperal accesses (**e**)

the height of the coronary ostia from the annulus plane, since the prosthetic valve or the native valve cusps displaced by the TAVI procedure, may cause coronary ostium obstruction and may impede the coronary ostial flow [128]. The recommended annulus-ostia length is >10–11 mm for the Edwards-Sapien valve, while there is no recommendation for Core Valve [128].

CMR Imaging

Cardiac magnetic resonance (CMR) is not routinely used in the diagnostic workflow of AS; the main reason for this is that AS traditionally has been considered as a disease of the valve while the myocardium has been largely ignored. On the contrary, recent studies documented a progressive myocardial remodelling in AS

from myocyte hypertrophy to increase of myocardial fibrosis till an irreversible stage. The identification of different stages of myocardial remodelling is of pivotal importance potentially impacting on the treatment success. CMR represents the standard of reference for the non-invasive evaluation of myocardial fibrosis. LGE CMR is the most accurate modality to visualize focal midwall myocardial fibrosis, which was found in up to 38% of patients with moderate or severe AS aortic and has been associated with an increase in mortality [129]. However, LGE is able to detect only replacement dense fibrosis, which is irreversible and associated with advanced stages of remodelling [130], differently from interstitial fibrosis which is reversible. The more recently introduced T1 mapping technique can quantify interstitial fibrosis throughout the measurement of the extracellular volume fraction (ECV), improving myocardial characterization also at the earliest stages [131]. ECV showed an excellent correlation with fibrosis at histology, and its alteration correlates with a symptomatic status [131–133]. In the future the assessment of the interstitial fibrosis could find a role in guiding the timing of AS interventional treatment.

5.4.2 Mitral Regurgitation

5.4.2.1 Introduction

Mitral regurgitation is the second most frequent valvular heart disease in western world [103]. Surgery is the first-choice in symptomatic patients with severe MR [120]; however, surgery is often denied to elderly patients because of their comorbidities [134]. The denial of surgical treatment to elderly patients with significant MR contributed to the tumultuous spread of percutaneous techniques in treating this pathology [135] with imaging playing a pivotal role in procedural planning and guiding.

5.4.2.2 Aetiology and Pathophysiology

MR could be primary or secondary based on the underlying pathophysiology with impact on therapy [120]. Secondary or functional MR is the most frequent form in the elderly population since it is commonly seen in patients with ischaemic and idiopathic cardiomyopathies. In secondary MR, the leaflets and chordae have a normal structure, and the regurgitation is due to an imbalance between closing and tethering forces on the valve which are consequences of alterations of left ventricle shape [136]. In primary MR, one or more elements of the mitral valve apparatus are directly affected, and the most frequent aetiology is degenerative, characterized primarily by mitral valve prolapse [137].

5.4.2.3 Multimodality Imaging

Echocardiography is the crucial examination in detecting MR [120]; it grades MR severity, establishes mechanism and aetiology, and provides a complete evaluation both of left ventricular systolic function and the degree of left atrium dilatation.

Furthermore, it quantifies pulmonary pressure and describes associated valve lesions. Transoesophageal echocardiography (TOE) provides a comprehensive description of the mitral valve, and it should always be performed when transthoracic echocardiography is inconclusive; furthermore, TOE is essential for guiding procedures in transcatheter valve interventions [138].

Echocardiographic assessment of the severity of mitral regurgitation can be qualitative, semiquantitative or quantitative; however, since no single parameter has proved to be more reliable than others, the evaluation is generally multi-parametric, mainly qualitative, although a quantitative approach is recommended when possible [139].

Quantitative severe MR is defined when the regurgitant volume is >60 mL, and the regurgitant fraction is around 50%, with an orifice area of >0.4 cm^2. Echocardiography plays a fundamental role in the selection of candidates for surgical treatment that generally happens when the patient affected by MR is symptomatic or asymptomatic but has less than 60% EF or a left ventricular end-systolic diameter (LVESD) >45 mm, or he is also affected by atrial fibrillation or pulmonary hypertension [120].

CT Imaging

Transcatheter mitral valve repair should be performed when the heart team evaluates a high surgical risk for the patient. In functional MR, TMVR is indicated in patients with severe MR where medical therapy and cardiac resynchronization therapy (CRT) are not effective [140]. In primary MR, TMVR is indicated in the presence of comorbidities such as CKD, COPB, advance age, and severe impairment of left ventricular function.

Two main transcatheter mitral valve repair strategies for severe MR include edge-to-edge repair (MitraClip) and annuloplasty rings (Cardioband) [141–143].

MitraClip is the selected treatment of moderate to severe degenerative and functional MR, while the Cardioband system consists of a percutaneous annuloplasty that can be used in settings of functional MR resulting from systolic dysfunction or annular dilatation. As mentioned above, echocardiography is an initial tool to assess mitral valve structure and disease; however, this can be challenging in patients with limited acoustic windows also considering the complexity of the mitral valve apparatus. In these cases, CCTA allows a full cardiac cycle acquisition, outlining similar morphologic findings to echocardiography and MRI such as mitral annulus geometry, dimensions and calcifications, morphology and mobility of valve and subvalve apparatus, with an improved spatial resolution. It can also be used to assess the anatomy of coronary arteries and of the aortic valve and interatrial septum, but it cannot assess the flow that can only be analysed via echocardiography or MRI [144, 145]. Furthermore, CTCA can easily exclude the presence of an atrial thrombus which would represent a contraindication to percutaneous mitral valve repair. Critical anatomic selection criteria for MitraClip device in functional MR are Coaptation length (≥2 mm), and depth (<11 mm). In contrast, Flail gap (<10 mm) and width (<15 mm) are the ones fundamental for MitraClip in primary MR

(prolapse) [146]. For Cardioband implantation, which is a percutaneous annuloplastry, CT planning must assess the location of the transeptal puncture and the relationship between left circumflex coronary artery anatomy [143].

MR Imaging

Even if echocardiography represents the main tool for diagnosis and follow-up of MR, MRI remains the gold standard for comprehensive assessment of the pathology and has shown higher accuracy than echocardiography to evaluate MR severity and guiding surgery. Phase contrast sequences can directly or indirectly quantify MR severity [147]. Tissue characterization with LGE and mapping may also help in the identification of the aetiology of secondary MRI and may provide information about myocardial remodelling.

5.5 Conclusion

Increase in life expectancy will lead to increased incidence of age-related cardiovascular disease.

Cardiovascular imaging has a fundamental role in the diagnosis, risk stratification, planning of treatment and monitoring of cardiac disease evolution in geriatric patients. However, imaging in elderly may be a challenge for reduced patient compliance and comorbidities. Recent advancement in technology allows an optimization of acquisition protocol with faster acquisition time and limited dose of contrast agent. However, more efforts and data are necessary to develop standardized protocols and to draw up guidelines and appropriate criteria for such specific population.

References

1. Mehta N, Chokshi NP, Kirkpatrick JN. Cardiac imaging in the geriatric population: what do we think we know, and what do we need to learn? Prog Cardiovasc Dis. 2014;57:204–14.
2. Pecer G. US bureau of the census: projections of the population of the United States, by age, sex, and race: 1988 to 2080. Current Population Reports, Series P-25, No. 1018. Washington, DC: US Government Printing Office; 1989.
3. Alexander KP, et al. Acute coronary care in the elderly, part I. Circulation. 2007;115:2549–69.
4. Zamorano JL, et al. EAE/ASE recommendations for the use of echocardiography in new transcatheter interventions for valvular heart disease. J Am Soc Echocardiogr. 2011;24:937–65.
5. Wong CY, Green P, Williams M. Decision-making in transcatheter aortic valve replacement: the impact of frailty in older adults with aortic stenosis. Expert Rev Cardiovasc Ther. 2013;11:761–72.
6. Kuller LH, et al. 10-Year follow-up of subclinical cardiovascular disease and risk of coronary heart disease in the cardiovascular health study. Arch Intern Med. 2006;166:71–8.
7. McClelland RL, Chung H, Detrano R, Post W, Kronmal RA. Distribution of coronary artery calcium by race, gender, and age: Results from the Multi-Ethnic Study of Atherosclerosis (MESA). Circulation. 2006;113:30–7.
8. Benjamin EJ, et al. Heart disease and stroke statistics' 2017 update: a report from the American Heart Association. Circulation. 2017;135(10):e146–603.

9. Narula J, et al. Histopathologic characteristics of atherosclerotic coronary disease and implications of the findings for the invasive and noninvasive detection of vulnerable plaques. J Am Coll Cardiol. 2013;61:1041–51.
10. Voros S, et al. Coronary atherosclerosis imaging by coronary CT angiography: current status, correlation with intravascular interrogation and meta-analysis. JACC Cardiovasc Imaging. 2011;4:537–48.
11. Falk E. Morphologic features of unstable atherothrombotic plaques underlying acute coronary syndromes. Am J Cardiol. 1989;63:114E–20E.
12. Gutstein DE, Fuster V. Pathophysiology and clinical significance of atherosclerotic plaque rupture. Cardiovasc Res. 1999;41:323–33.
13. Dowsley T, et al. The role of noninvasive imaging in coronary artery disease detection, prognosis, and clinical decision making. Can J Cardiol. 2013;29:285–96.
14. Fihn SD, et al. 2012 ACCF/AHA/ACP/AATS/PCNA/SCAI/STS guideline for the diagnosis and management of patients with stable ischemic heart disease. Circulation. 2012;126:3097–137.
15. De Jong MC, Genders TSS, Van Geuns RJ, Moelker A, Hunink MGM. Diagnostic performance of stress myocardial perfusion imaging for coronary artery disease: a systematic review and meta-analysis. Eur Radiol. 2012;22:1881–95.
16. Achenbach S, et al. CV imaging: what was new in 2012? JACC Cardiovasc Imaging. 2013;6:714–34.
17. Takx RAP, et al. Diagnostic accuracy of stress myocardial perfusion imaging compared to invasive coronary angiography with fractional flow reserve meta-analysis. Circ Cardiovasc Imaging. 2014;8:1–7.
18. Rybicki FJ, et al. 2015 ACR/ACC/AHA/AATS/ACEP/ASNC/NASCI/SAEM/SCCT/SCMR/SCPC/SNMMI/STR/STS appropriate utilization of cardiovascular imaging in emergency department patients with chest pain: a joint document of the American College of Radiology Appropriateness Criteria Committee and the American College of Cardiology Appropriate Use Criteria Task Force. J Am Coll Cardiol. 2016;67:853–79.
19. Bamberg F, et al. Imaging evaluation of acute chest pain: systematic review of evidence base and cost-effectiveness. J Thorac Imaging. 2012;27:289–95.
20. Esposito A, et al. Cardiac computed tomography in troponin-positive chest pain: sometimes the answer lies in the late iodine enhancement or extracellular volume fraction map. JACC Cardiovasc Imaging. 2019;12:745–8.
21. Palmisano A, et al. Late iodine enhancement cardiac computed tomography for detection of myocardial scars: impact of experience in the clinical practice. Radiol Med. 2020;125:128–36.
22. Sinitsyn V. Cardiac dual-energy CT with late iodine enhancement as an alternative to late gadolinium enhancement MRI. Radiology. 2018;288:692–3.
23. Hecht HS, et al. 2016 SCCT/STR guidelines for coronary artery calcium scoring of noncontrast noncardiac chest CT scans: a report of the Society of Cardiovascular Computed Tomography and Society of Thoracic Radiology. J Thorac Imaging. 2017;32:W54–66.
24. Budoff MJ, et al. Ten-year association of coronary artery calcium with atherosclerotic cardiovascular disease (ASCVD) events: the multi-ethnic study of atherosclerosis (MESA). Eur Heart J. 2018;39:2401b–8b.
25. Budoff MJ, et al. Cardiovascular events with absent or minimal coronary calcification: the Multi-Ethnic Study of Atherosclerosis (MESA). Am Heart J. 2009;158:554–61.
26. Lehmann N, et al. Value of progression of coronary artery calcification for risk prediction of coronary and cardiovascular events: result of the HNR study (Heinz Nixdorf Recall). Circulation. 2018;137:665–79.
27. Achenbach S, Raggi P. Imaging of coronary atherosclerosis by computed tomography. Eur Heart J. 2010;31:1442–8.
28. Ferencik M, et al. Use of high-risk coronary atherosclerotic plaque detection for risk stratification of patients with stable chest pain: a secondary analysis of the promise randomized clinical trial. JAMA Cardiol. 2018;3:144–52.

29. Tanaka A, et al. Non-invasive assessment of plaque rupture by 64-slice multidetector computed tomography—comparison with intravascular ultrasound. Circ J. 2008;72:1276–81.
30. Motoyama S, et al. Multislice computed tomographic characteristics of coronary lesions in acute coronary syndromes. J Am Coll Cardiol. 2007;50:319–26.
31. Leipsic J, et al. SCCT guidelines for the interpretation and reporting of coronary CT angiography: a report of the Society of Cardiovascular Computed Tomography Guidelines Committee. J Cardiovasc Comput Tomogr. 2014;8:342–58.
32. Andreini D, et al. Coronary in-stent restenosis: assessment with CT coronary angiography. Radiology. 2012;265:410–7.
33. Dai T, Wang JR, Hu PF. Diagnostic performance of computed tomography angiography in the detection of coronary artery in-stent restenosis: evidence from an updated meta-analysis. Eur Radiol. 2018;28:1373–82.
34. Chiurlia E, Menozzi M, Ratti C, Romagnoli R, Modena MG. Follow-up of coronary artery bypass graft patency by multislice computed tomography. Am J Cardiol. 2005;95:1094–7.
35. Chan M, et al. A systematic review and meta-analysis of multidetector computed tomography in the assessment of coronary artery bypass grafts. Int J Cardiol. 2016;221:898–905.
36. Frazier AA, et al. Coronary artery bypass grafts: assessment with multidetector CT in the early and late postoperative settings. Radiographics. 2005;25:881–96.
37. Celeng C, et al. Anatomical and functional computed tomography for diagnosing hemodynamically significant coronary artery disease: a meta-analysis. JACC Cardiovasc Imaging. 2019;12:1316–25.
38. Zhao R, Shan Y, Zou L, Zhao H, Zheng S. Solitary fibrous tumor of the seminal vesicle. Medicine (Baltimore). 2019;9:10–3.
39. Branch KR, et al. Myocardial computed tomography perfusion. Cardiovasc Diagn Ther. 2017;7:452–62.
40. Danad I, et al. Diagnostic performance of cardiac imaging methods to diagnose ischaemia-causing coronary artery disease when directly compared with fractional flow reserve as a reference standard: a meta-analysis. Eur Heart J. 2017;38:991–8.
41. Ko BS, et al. Computed tomography stress myocardial perfusion imaging in patients considered for revascularization: a comparison with fractional flow reserve. Eur Heart J. 2012;33:67–77.
42. Broncano J, et al. Cardiac MRI in patients with acute chest pain. Radiographics. 2021;41:8–31.
43. Bodi V, et al. Prognostic value of a comprehensive cardiac magnetic resonance assessment soon after a first ST-segment elevation myocardial infarction. JACC Cardiovasc Imaging. 2009;2:835–42.
44. Eitel I, et al. Comprehensive prognosis assessment by CMR imaging after ST-segment elevation myocardial infarction. J Am Coll Cardiol. 2014;64:1217–26.
45. Karamitsos TD, et al. Contained left ventricular rupture after acute myocardial infarction revealed by cardiovascular magnetic resonance imaging. Circulation. 2012;125:2278–80.
46. Sharma A, Kumar S. Overview of left ventricular outpouchings on cardiac magnetic resonance imaging. Cardiovasc Diagn Ther. 2015;5:464–70.
47. Ibanez B, et al. 2017 ESC guidelines for the management of acute myocardial infarction in patients presenting with ST-segment elevation. Eur Heart J. 2018;39:119–77.
48. McAlindon EJ, et al. Measurement of myocardium at risk with cardiovascular MR: comparison of techniques for edema imaging. Radiology. 2015;275:61–70.
49. Mahrholdt H, Wagner A, Judd RM, Sechtem U. Assessment of myocardial viability by cardiovascular magnetic resonance imaging. Eur Heart J. 2002;23:602–19.
50. McCrohon JA, et al. Differentiation of heart failure related to dilated cardiomyopathy and coronary artery disease using gadolinium-enhanced cardiovascular magnetic resonance. Circulation. 2003;108:54–9.
51. Rajiah P, Desai MY, Kwon D, Flamm SD. MR imaging of myocardial infarction. Radiographics. 2013;33:1383–412.
52. de Waha S, et al. Prognosis after ST-elevation myocardial infarction: a study on cardiac magnetic resonance imaging versus clinical routine. Trials. 2014;15:1–9.

53. Wu KC, et al. Prognostic significance of microvascular obstruction by magnetic resonance imaging in patients with acute myocardial infarction. Circulation. 1998;97:765–72.
54. Haaf P, et al. Cardiac T1 mapping and extracellular volume (ECV) in clinical practice: a comprehensive review. J Cardiovasc Magn Reson. 2016;18:1–12.
55. Bulluck H, Dharmakumar R, Arai AE, Berry C, Hausenloy DJ. Cardiovascular magnetic resonance in acute ST-segment-elevation myocardial infarction: recent advances, controversies, and future directions. Circulation. 2018;137:1949–64.
56. Jneid H, et al. 2012 ACCF/AHA focused update of the guideline for the management of patients with unstable angina/non-ST-elevation myocardial infarction (updating the 2007 guideline and replacing the 2011 focused update): a report of the American College of Cardiology Foundation/American Heart Association Task Force on practice guidelines. Circulation. 2012;126:875–910.
57. Thygesen K, et al. Fourth universal definition of myocardial infarction (2018). Eur Heart J. 2019;40:237–69.
58. Mukherjee D. Myocardial infarction with nonobstructive coronary arteries: a call for individualized treatment. J Am Heart Assoc. 2019;8:1–3.
59. Heitner JF, et al. Stress cardiac MR imaging compared with stress echocardiography in the early evaluation of patients who present to the emergency department with intermediate-risk chest pain. Radiology. 2014;271:56–64.
60. Ingkanisorn WP, et al. Prognosis of negative adenosine stress magnetic resonance in patients presenting to an emergency department with chest pain. J Am Coll Cardiol. 2006;47:1427–32.
61. Ponikowski P, et al. 2016 ESC guidelines for the diagnosis and treatment of acute and chronic heart failure. Eur Heart J. 2016;37:2129–200.
62. Tanai E, Frantz S. Pathophysiology of heart failure. Compr Physiol. 2016;6:187–214.
63. Schwinger RHG. Pathophysiology of heart failure. Cardiovasc Diagn Ther. 2021;11:263–76.
64. Japp AG, Gulati A, Cook SA, Cowie MR, Prasad SK. The diagnosis and evaluation of dilated cardiomyopathy. J Am Coll Cardiol. 2016;67:2996–3010.
65. Borlaug BA, Paulus WJ. Heart failure with preserved ejection fraction: pathophysiology, diagnosis, and treatment. Eur Heart J. 2011;32:670–9.
66. Rigolli M, Whalley GA. Heart failure with preserved ejection fraction. J Geriatr Cardiol. 2013;10:369–76.
67. Di Cesare E, et al. Multimodality imaging in chronic heart failure. Radiol Med. 2021;126:231–42.
68. White RD, et al. ACR Appropriateness Criteria ® suspected new-onset and known nonacute heart failure. J Am Coll Radiol. 2018;15:S418–31.
69. Ten Kate GJR, et al. Computed tomography coronary imaging as a gatekeeper for invasive coronary angiography in patients with newly diagnosed heart failure of unknown aetiology. Eur J Heart Fail. 2013;15:1028–34.
70. Abunassar JG, Yam Y, Chen L, D'Mello N, Chow BJW. Usefulness of the Agatston score = 0 to exclude ischemic cardiomyopathy in patients with heart failure. Am J Cardiol. 2011;107:428–32.
71. Budoff MJ, et al. Usefulness of electron beam computed tomography scanning for distinguishing ischemic from nonischemic cardiomyopathy. J Am Coll Cardiol. 1998;32:1173–8.
72. Sousa PA, et al. Role of cardiac multidetector computed tomography in the exclusion of ischemic etiology in heart failure patients. Rev Port Cardiol. 2014;33:629–36.
73. Ohta Y, et al. Myocardial delayed enhancement CT for the evaluation of heart failure: comparison to MRI. Radiology. 2018;288:682–91.
74. Oda S, et al. Myocardial late iodine enhancement and extracellular volume quantification with dual-layer spectral detector dual-energy cardiac CT. Radiol Cardiothorac Imaging. 2019;1:e180003.
75. Kim YJ, Kim RJ. The role of cardiac MR in new-onset heart failure. Curr Cardiol Rep. 2011;13:185–93.
76. Messroghli DR, et al. Clinical recommendations for cardiovascular magnetic resonance mapping of T1, T2, T2 and extracellular volume: a consensus statement by the Society for

Cardiovascular Magnetic Resonance (SCMR) endorsed by the European Association for Cardiovascular Imaging. J Cardiovasc Magn Reson. 2017;19:1–24.
77. Assomull RG, et al. Role of cardiovascular magnetic resonance as a gatekeeper to invasive coronary angiography in patients presenting with heart failure of unknown etiology. Circulation. 2011;124:1351–60.
78. Patel AR, Kramer CM. Role of cardiac magnetic resonance in the diagnosis and prognosis of nonischemic cardiomyopathy. JACC Cardiovasc Imaging. 2017;10:1180–93.
79. Laczay B, Patel D, Grimm R, Xu B. State-of-the-art narrative review: multimodality imaging in electrophysiology and cardiac device therapies. Cardiovasc Diagn Ther. 2021;11:881–95.
80. van der Bijl P, Delgado V, Bax JJ. Imaging for sudden cardiac death risk stratification: current perspective and future directions. Prog Cardiovasc Dis. 2019;62:205–11.
81. Al-Khatib SM, et al. 2017 AHA/ACC/HRS guideline for management of patients with ventricular arrhythmias and the prevention of sudden cardiac death: a report of the American College of Cardiology/American Heart Association Task Force on Clinical Practice Guidelines and the Heart Rhythm Society. Circulation. 2018;138:e272–391.
82. Brignole M, et al. 213 ESC guidelines on cardiac pacing and cardiac resynchronization therapy. Eur Heart J. 2013;34:2281–329.
83. Heydari B, Jerosch-Herold M, Kwong RY. Imaging for planning of cardiac resynchronization therapy. JACC Cardiovasc Imaging. 2012;5:93–110.
84. Chung ES, et al. Results of the predictors of response to CRT (PROSPECT) trial. Circulation. 2008;117:2608–16.
85. White JA, et al. Delayed enhancement magnetic resonance imaging predicts response to cardiac resynchronization therapy in patients with intraventricular dyssynchrony. J Am Coll Cardiol. 2006;48:1953–60.
86. Bleeker GB, et al. Effect of posterolateral scar tissue on clinical and echocardiographic improvement after cardiac resynchronization therapy. Circulation. 2006;113:969–76.
87. Chalil S, et al. Late gadolinium enhancement-cardiovascular magnetic resonance as a predictor of response to cardiac resynchronization therapy in patients with ischaemic cardiomyopathy. Europace. 2007;9:1031–7.
88. Maurer MS, Elliott P, Comenzo R, Semigran M, Rapezzi C. Addressing common questions encountered in the diagnosis and management of cardiac amyloidosis. Circulation. 2017;135:1357–77.
89. Tanskanen M, et al. Senile systemic amyloidosis affects 25% of the very aged and associates with genetic variation in alpha2-macroglobulin and tau: a population-based autopsy study. Ann Med. 2008;40:232–9.
90. Cueto-Garcia L, et al. Echocardiographic findings in systemic amyloidosis: spectrum of cardiac involvement and relation to survival. J Am Coll Cardiol. 1985;6:737–43.
91. Liu D, et al. Effect of combined systolic and diastolic functional parameter assessment for differentiation of cardiac amyloidosis from other causes of concentric left ventricular hypertrophy. Circ Cardiovasc Imaging. 2013;6:1066–72.
92. Phelan D, et al. Relative apical sparing of longitudinal strain using two-dimensional speckle-tracking echocardiography is both sensitive and specific for the diagnosis of cardiac amyloidosis. Heart. 2012;98:1442–8.
93. Kotecha T, et al. Myocardial edema and prognosis in amyloidosis. J Am Coll Cardiol. 2018;71:2919–31.
94. Karamitsos TD, Neubauer S. Detecting diffuse myocardial fibrosis with CMR: the future has only just begun. J Am Coll Cardiol Img. 2013;6:684–6.
95. Fontana M, et al. Prognostic value of late gadolinium enhancement cardiovascular magnetic resonance in cardiac amyloidosis. Circulation. 2015;132:1570–9.
96. White JA, et al. CMR imaging with rapid visual T1 assessment predicts mortality in patients suspected of cardiac amyloidosis. JACC Cardiovasc Imaging. 2014;7:143–56.
97. Baggiano A, et al. Noncontrast magnetic resonance for the diagnosis of cardiac amyloidosis. JACC Cardiovasc Imaging. 2020;13:69–80.

98. Lin L, et al. The prognostic value of T1 mapping and late gadolinium enhancement cardiovascular magnetic resonance imaging in patients with light chain amyloidosis. J Cardiovasc Magn Reson. 2018;20:2.
99. Rapezzi C, et al. Role of (99m)Tc-DPD scintigraphy in diagnosis and prognosis of hereditary transthyretin-related cardiac amyloidosis. JACC Cardiovasc Imaging. 2011;4:659–70.
100. Falk RH, Quarta CC, Dorbala S. How to image cardiac amyloidosis. Circ Cardiovasc Imaging. 2014;7:552–62.
101. Perugini E, et al. Noninvasive etiologic diagnosis of cardiac amyloidosis using 99mTc-3,3-diphosphono-1,2-propanodicarboxylic acid scintigraphy. J Am Coll Cardiol. 2005;46:1076–84.
102. Nkomo VT, et al. Burden of valvular heart diseases: a population-based study. Lancet. 2006;368:1005–11.
103. Iung B, et al. A prospective survey of patients with valvular heart disease in Europe: the Euro Heart Survey on valvular heart disease. Eur Heart J. 2003;24:1231–43.
104. Otto CM. Calcific aortic stenosis—time to look more closely at the valve. N Engl J Med. 2008;359:1395–8.
105. Grossman W, Jones D, McLaurin LP. Wall stress and patterns of hypertrophy in the human left ventricle. J Clin Invest. 1975;56:56–64.
106. Carabello BA. The relationship of left ventricular geometry and hypertrophy to left ventricular function in valvular heart disease. J Heart Valve Dis. 1995;4 Suppl 2:S132–8.; discussion S138–9.
107. Levy D, Garrison RJ, Savage DD, Kannel WB, Castelli WP. Prognostic implications of echocardiographically determined left ventricular mass in the Framingham Heart Study. N Engl J Med. 1990;322:1561–6.
108. Spirito P, et al. Magnitude of left ventricular hypertrophy and risk of sudden death in hypertrophic cardiomyopathy. N Engl J Med. 2000;342:1778–85.
109. Schillaci G, et al. Continuous relation between left ventricular mass and cardiovascular risk in essential hypertension. Hypertension. 2000;35:580–6.
110. Salcedo EE, et al. Determinants of left ventricular hypertrophy in patients with aortic stenosis. Cleve Clin J Med. 1989;56:590–6.
111. Kupari M, Turto H, Lommi J. Left ventricular hypertrophy in aortic valve stenosis: preventive or promotive of systolic dysfunction and heart failure? Eur Heart J. 2005;26:1790–6.
112. Lavie CJ, Milani RV, Patel D, Artham SM, Ventura HO. Disparate effects of obesity and left ventricular geometry on mortality in 8088 elderly patients with preserved systolic function. Postgrad Med. 2009;121:119–25.
113. Dweck MR, et al. Left ventricular remodeling and hypertrophy in patients with aortic stenosis: insights from cardiovascular magnetic resonance. J Cardiovasc Magn Reson Off J Soc Cardiovasc Magn Reson. 2012;14:50.
114. Gunther S, Grossman W. Determinants of ventricular function in pressure-overload hypertrophy in man. Circulation. 1979;59:679–88.
115. Orlowska-Baranowska E, et al. Influence of ACE I/D genotypes on left ventricular hypertrophy in aortic stenosis: gender-related differences. J Heart Valve Dis. 2004;13:574–81.
116. Cioffi G, et al. Prognostic effect of inappropriately high left ventricular mass in asymptomatic severe aortic stenosis. Heart. 2011;97:301–7.
117. Hein S, et al. Progression from compensated hypertrophy to failure in the pressure-overloaded human heart: structural deterioration and compensatory mechanisms. Circulation. 2003;107:984–91.
118. Bishopric NH, Andreka P, Slepak T, Webster KA. Molecular mechanisms of apoptosis in the cardiac myocyte. Curr Opin Pharmacol. 2001;1:141–50.
119. Cheng W, et al. Stretch-induced programmed myocyte cell death. J Clin Invest. 1995;96:2247–59.
120. Baumgartner H, et al. 2017 ESC/EACTS guidelines for the management of valvular heart disease. Eur Heart J. 2017;38:2739–91.

121. Salgado RA, et al. Preprocedural CT evaluation of transcatheter aortic valve replacement: what the radiologist needs to know. Radiographics. 2014;34:1491–514.
122. Tops LF, et al. Noninvasive evaluation of the aortic root with multislice computed tomography implications for transcatheter aortic valve replacement. JACC Cardiovasc Imaging. 2008;1:321–30.
123. Clavel M-A, et al. The complex nature of discordant severe calcified aortic valve disease grading: new insights from combined Doppler echocardiographic and computed tomographic study. J Am Coll Cardiol. 2013;62:2329–38.
124. Willson AB, et al. 3-dimensional aortic annular assessment by multidetector computed tomography predicts moderate or severe paravalvular regurgitation after transcatheter aortic valve replacement: a multicenter retrospective analysis. J Am Coll Cardiol. 2012;59:1287–94.
125. Barbanti M, et al. Anatomical and procedural features associated with aortic root rupture during balloon-expandable transcatheter aortic valve replacement. Circulation. 2013;128:244–53.
126. Blanke P, et al. Prosthesis oversizing in balloon-expandable transcatheter aortic valve implantation is associated with contained rupture of the aortic root. Circ Cardiovasc Interv. 2012;5:540–8.
127. Delgado V, et al. Automated assessment of the aortic root dimensions with multidetector row computed tomography. Ann Thorac Surg. 2011;91:716–23.
128. Ribeiro HB, et al. Coronary obstruction following transcatheter aortic valve implantation: a systematic review. JACC Cardiovasc Interv. 2013;6:452–61.
129. Dweck MR, et al. Midwall fibrosis is an independent predictor of mortality in patients with aortic stenosis. J Am Coll Cardiol. 2011;58:1271–9.
130. Krayenbuehl HP, et al. Left ventricular myocardial structure in aortic valve disease before, intermediate, and late after aortic valve replacement. Circulation. 1989;79:744–55.
131. Taylor AJ, Salerno M, Dharmakumar R, Jerosch-Herold M. T1 mapping basic techniques and clinical applications. JACC Cardiovasc Imaging. 2016;9:67–81.
132. Flett AS, et al. Diffuse myocardial fibrosis in severe aortic stenosis: an equilibrium contrast cardiovascular magnetic resonance study. Eur Hear journal Cardiovasc Imaging. 2012;13:819–26.
133. Flett AS, et al. Equilibrium contrast cardiovascular magnetic resonance for the measurement of diffuse myocardial fibrosis: preliminary validation in humans. Circulation. 2010;122:138–44.
134. Mirabel M, et al. What are the characteristics of patients with severe, symptomatic, mitral regurgitation who are denied surgery? Eur Heart J. 2007;28:1358–65.
135. Sala A, Alfieri O. Percutaneous treatment of mitral valve regurgitation: where do we stand? Int J Cardiol. 2019;288:137–9.
136. Levine RA, Schwammenthal E. Ischemic mitral regurgitation on the threshold of a solution: from paradoxes to unifying concepts. Circulation. 2005;112:745–58.
137. Enriquez-Sarano M, et al. Functional anatomy of mitral regurgitation: accuracy and outcome implications of transesophageal echocardiography. J Am Coll Cardiol. 1999;34:1129–36.
138. Dulgheru R, Bruls S, Lancellotti P. How I look at the regurgitant mitral valve—a stepwise echocardiographic assessment. Eur Hear journal Cardiovasc Imaging. 2021;22:491–3.
139. Lancellotti P, et al. Recommendations for the echocardiographic assessment of native valvular regurgitation: an executive summary from the European Association of Cardiovascular Imaging. Eur Heart J Cardiovasc Imaging. 2013;14:611–44.
140. Stone GW, et al. Transcatheter mitral-valve repair in patients with heart failure. N Engl J Med. 2018;379:2307–18.
141. Feldman T, Young A. Percutaneous approaches to valve repair for mitral regurgitation. J Am Coll Cardiol. 2014;63:2057–68.
142. Feldman T, et al. Percutaneous mitral repair with the MitraClip system: safety and midterm durability in the initial EVEREST (Endovascular Valve Edge-to-Edge REpair Study) cohort. J Am Coll Cardiol. 2009;54:686–94.

143. Maisano F, et al. Cardioband, a transcatheter surgical-like direct mitral valve annuloplasty system: early results of the feasibility trial. Eur Heart J. 2016;37:817–25.
144. Delgado V, et al. Assessment of mitral valve anatomy and geometry with multislice computed tomography. JACC Cardiovasc Imaging. 2009;2:556–65.
145. Alkadhi H, et al. Mitral annular shape, size, and motion in normals and in patients with cardiomyopathy: evaluation with computed tomography. Investig Radiol. 2009;44:218–25.
146. Feuchtner GM, et al. Cardiac CT angiography for the diagnosis of mitral valve prolapse: comparison with echocardiography1. Radiology. 2010;254:374–83.
147. Uretsky S, Argulian E, Narula J, Wolff SD. Use of cardiac magnetic resonance imaging in assessing mitral regurgitation: current evidence. J Am Coll Cardiol. 2018;71:547–63.

Vascular Diseases in Geriatric Patients

6

Gloria Caredda, Giuseppe Guglielmi, and Luca Saba

6.1 Introduction

Over time, the mean age of the population has progressively increased, with a large number of geriatric subjects. It is predicted that in 2030 they will represent the 19% of the general community in the USA, with about 19 millions of people over 85 years of age, with an increase of 22% of the geriatric population in 2050 and of 32% in 2100.

In this scenario, there has been a parallel increase in the number of the age-related diseases, thus it is possible to consider the presence of a concrete "demographic transition." In particular, the geriatric syndromes play a fundamental role, and they are generally related to a vascular chronic disease. More in depth, about 40 millions of people over 65 years of age are affected by a cardiovascular disease, which, together with other cerebrovascular conditions, represents the main cause of death in this age range, constituting an important healthcare, economic, and social issue.

Such a relative matter leads to the necessity of developing new prevention and treatment strategies, considering the vascular diseases at the base of a syndromic process, which might require a different patient management with respect to the single disease affecting a healthy subject. This is important, in particular, for the female patients, because, with aging and the hormone physiological changes, these diseases often occur with an insidious onset.

Generally, the aging process of the cardiovascular system is characterized by a stiffening of the vascular walls and the occurrence of atherosclerosis, affecting both the large vessels and the microvasculature, leading to organic systemic alterations.

G. Caredda · L. Saba (✉)
Department of Radiology, University of Cagliari, Cagliari, Italy

G. Guglielmi
Clinical and Experimental Medicine, University of Foggia, Foggia, Foggia, Italy
e-mail: giuseppe.guglielmi@unifg.it

G. Guglielmi, M. Maas (eds.), *Imaging in Geriatrics*, Practical Issues in Geriatrics, https://doi.org/10.1007/978-3-031-14877-4_6

The main risk factors related to vessel aging, which lead to vasculature system diseases, are represented by patient aging, smoking, other conditions such as diabetes mellitus, hypertension, hyperlipidemia, and other factors (some of them non-modifiable) like race, ethnicity (with an increased risk in African American and Hispanic subjects), chronic kidney disease, metabolic syndrome, high levels of C-reactive protein, β2-microglobulin, cystatin C, lipoprotein, and homocysteine. Among these factors, the main modifiable one is smoking, which increases the risk of peripheric vascular disease by about four times, with an onset that precedes by 10 years than that in non-smokers. Moreover, smoking patients usually have a worse prognosis.

Aside from these conditions, in geriatric patients, vascular trauma plays a key role. Their incidence is lower if compared to their young counterpart, but, at the same time, they are more severe. Indeed, in this age range, the mortality for vascular trauma (40% for falls) is higher than that of non-geriatric adults and, with respect to young people, death is more frequent in the emergency departments. The main cause is represented by car accidents, followed by falls (with an incidence of 32% in subjects over 75 years of age), with a predominance of abdominal and upper limbs harms, more frequent than in non-geriatric adults.

This is related to the physiological processes of this age range, with alterations affecting the nervous and the muscle-skeletal systems, which involve balance, making these patients more susceptible to falls. Furthermore, if multiple diseases are present, trauma management is more challenging, thus determining high morbidity and mortality [1–3].

6.2 Physiological Vascular Changes in Geriatric Population

In the geriatric population, some aging-related changes show an impact in the cardiovascular system, both as microscopic and as macroscopic alterations, leading to several organic diseases. In particular, the oxidative stress, caused by high levels of reactive oxygen species (ROS), has a crucial role in vasculature aging, reducing the production of the endothelium-derived nitric oxide (NO), thus leading to vascular stiffening, low parietal elasticity, and reduced tissue perfusion. Even aged dysfunctional mitochondria contribute to the production of ROS. Moreover, while in young subjects the result of ROS activity induces the activation of an antioxidant pathway, characterized by the production of Nrf2, the aging-related changes inactivate this process, making vasculature more sensible to ROS activity and more prone to inflammation, with an increase of endothelial apoptosis. This is also due to proinflammatory changes in gene expression in the endothelial and smooth muscle cells, which contribute to induce several conditions, from atherogenesis to microvasculature diseases and aneurysm formation, by promoting the production of proinflammatory cytokines, determining the “senescence-associated secretory phenotype.” Furthermore, senescent endothelial cells show a reduced angiogenetic and reparative ability.

Finally, other processes contribute to vasculature aging, in particular alterations in the balance between production and degradation of proteins, epigenetic modifications, and changes in the extracellular matrix, with a decreased vascular wall stability [3–5].

6.2.1 Peripheral Artery Disease

The expression "peripheral artery disease" (PAD) includes the conditions involving the arteries aside from the cranial and the cardiac territories. About 200 million people in the world are affected by PAD, with a similar prevalence between men and postmenopausal women. More frequently it is caused by atherosclerosis, which is considered the most important determinant, but it can be due to diabetes mellitus, smoking [6], vasculitis and other noninflammatory arteriopathies as well. This condition is usually combined with coronary artery disease (CAD) and cerebrovascular disease (CVD). An association between the lower extremity, the carotid, and the renal arterial territory disease is frequent as well [7].

Two forms of PAD can be distinguished, the proximal one, which affects the aortoiliac and the femoropopliteal tracts, and the distal subtype, involving the territories distal to the popliteal arteries. In some patients, the latter type is characterized by a calcification of the middle layer of the wall, leading to a poorly compressible vessel and a high mortality (Practice 2016).

6.3 Clinical Features

The most peculiar symptom is claudication, characterized by pain or cramps in the lower limb caused by moderate exercise, which is alleviated with rest [6].

In some patients, acute or chronic critical ischemia of the limb may also be observed, with pain in a rest state and ulcerations/gangrene in the distal region of the foot. Other patients may be asymptomatic as well (Practice 2016).

6.4 Clinical Diagnosis

PAD can be assessed by estimating the segmental blood pressure in different levels of the limb and evaluating the ankle-brachial index, the ratio between the systolic blood pressure measured in the ankle and the systolic blood pressure assessed in the arm, measured after 5–10 min of rest in a supine position [8]. The normal and pathologic values are reported in Table 6.1. In subjects with non-compressible arteries, instead, the toe-brachial index might be assessed. Even exercise testing may be valuable, using a treadmill or measuring the maximum walking times without symptoms. Finally, in cases of critical leg ischemia, the evaluation of transcutaneous oximetry provides the clinician with important information (Practice 2016).

Table 6.1 Ankle-brachial index (ABI)

ABI value	Indication
1.00–1.40	Normal
0.91–0.99	Borderline
<0.90	PAD
>1.40	Non-compressible arteries

PAD peripheral artery disease [8]

6.5 Imaging

6.5.1 Doppler Ultrasonography

The first-line technique for PAD evaluation is ultrasonography (US) with Doppler imaging. It is a noninvasive and highly available tool, able to assess the atherosclerotic plaque and monitor the patency of the revascularized vessels (Practice 2016). The typical flow pattern of arterial vessels is triphasic, due to the high resistance of muscle territory irroration, but it is lost in case of exercise or ischemia [9]. The severity of the disease varies according to the grade of stenosis and to the value of peak systolic velocity (PSV) and velocity ratio (VR), which are summarized in Table 6.2. In particular, a stenosis of 50–99% is hemodynamically significant when the PSV at the level of the lesion is double than that measured in a proximal arterial segment (>200 cm/s with turbulence) [9] (Трансплантати 2017).

In particular, Doppler US (DUS) is the first-line imaging technique for the assessment of the carotid territories, being able to distinguish patients with a high risk for ipsilateral ischemic stroke and identify those subjects who are candidate for endarterectomy or, on the other hand, for the only best medical treatment [8] (Fig. 6.1).

6.5.2 Computed Tomography Angiography

Computed tomography (CT) angiography has the advantage of providing, in a relatively short scanning time, high-resolution images which can be analyzed with the postprocessing three-dimensional reconstructions, including the multiplanar reconstruction (MPR), the maximum-intensity projections (MIP), the volume-rendering technique and the curved multiplanar reconstruction, providing information about the vessel stenosis and the plaques, and calcification of the arterial walls. On the other hand, it might furnish insufficient information about heavily calcified or very small vessels, not to mention the need for contrast agent administration, which might not be suitable for some patients. In addition, according to the cardiac output of the patient and considering the amount of time necessary for the contrasted blood to flow from the injection site to the peripheral arteries, a different acquisition and injection protocol should be adopted [10] (Practice 2016) (Figs. 6.2 and 6.3).

Table 6.2 Stenosis severity according to the degree of stenosis

Degree of arterial stenosis	Percentage of stenosis	PSV (cm/s)	VR
Normal	0%	<150	1.5:1
Stenosis	1–49%	150–200	1.5–2:1
Stenosis	50–99%	>200	>4:1
Complete occlusion	100%	–	–

PSV peak systolic velocity, *VR* velocity ratio [9] (Трансплантати 2017)

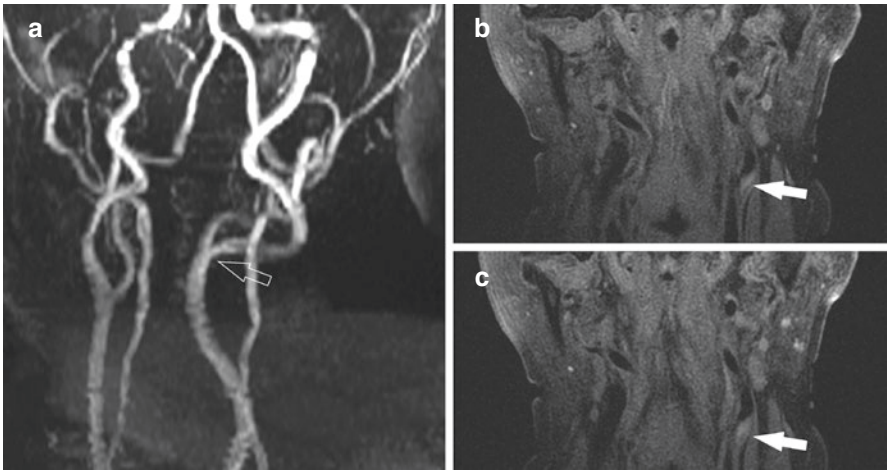

Fig. 6.1 (**a**–**c**) A 75-year-old male patient with left stroke. The MRI TOF shows the stenosis of 70% NASCET at the origin of the ICA (white open arrow). The FAT SAT MPRAGE shows the presence of hyperintese signal in the plaque due to the presence of IPH

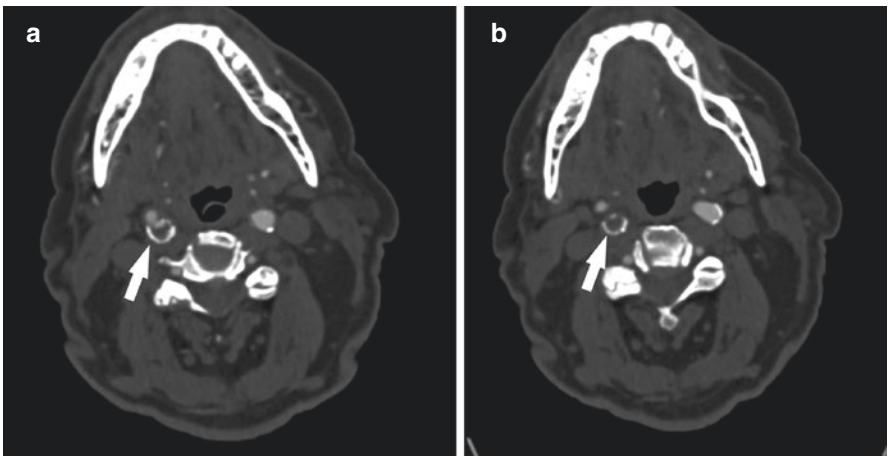

Fig. 6.2 (**a**, **b**) A 78-year-old male patient with right stroke. The CTA shows in the right ICA the presence of plaque in the ICA characterized by hypodense components and positive rim sign (white arrows)

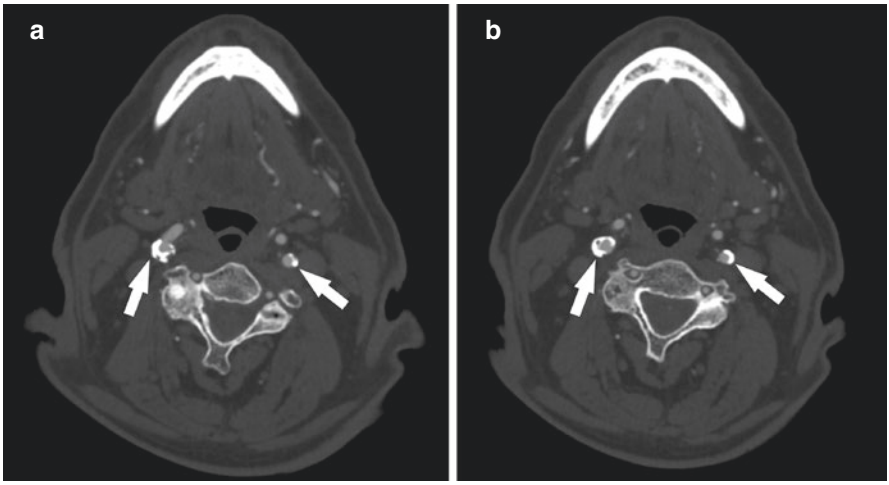

Fig. 6.3 (**a**, **b**) A 84-year-old female patient. The CTA shows bilateral calcified plaque

CT angiography is also the first-line method for the evaluation of patients with acute mesenteric ischemia and renal artery disease, providing a map of the arterial vessels and demonstrating the presence of vascular thrombi [8].

6.5.3 Magnetic Resonance Angiography

Besides, another important tool is magnetic resonance (MR) angiography. Although it cannot be performed in patients with metallic and non-MR safe devices, it provides information about large vascular territories without the use of radiations (Practice 2016).

MR angiography can be performed without the use of contrast agents, for instance with the acquisition of sequences such as time of flight (TOF), phase contrast, 3D half-Fourier fast spin echo (3D-FSE), balanced steady state free procession (b-SSFP), and quiescent-interval single-shot (QISS), providing information about arterial stenosis and wall plaque avoiding the risk of complications such as allergies or nephrogenic fibrosis. The acquisition of other sequences requires contrast administration, and it usually is the most frequently performed technique [11].

6.5.4 Digital Subtraction Angiography

Digital subtraction angiography (DSA) is generally performed in selected cases. In patients with carotid artery disease, it is required during the arterial stenting procedure or, less frequently, in case of discordances between other noninvasive methods.

In case of acute mesenteric ischemia, it has a pivotal role for a preoperative evaluation, although it cannot be performed in critical state patients. In subjects

with chronic mesenteric ischemia, it allows a therapeutic approach, besides a diagnostic evaluation.

In addition, it is a fundamental tool for assessing arterial territories distal to the knee, which are not well studied with other noninvasive techniques [8].

6.6 Features of Vulnerability of the Atherosclerotic Plaque

The atherosclerotic plaque may show some features that might increase the risk for stroke, which can be detected through diagnostic imaging evaluation. The presence of intraplaque hemorrhage, a lipid-rich necrotic core (LRNC) and the assessment of the fibrous cap is well evaluated with MRI. In particular, CT is able to detect the lipidic plaque components as well, but MRI better discriminates between LRNC and intraplaque hemorrhage. In addition, MRI also provides information about a thin or damaged fibrous cap.

Moreover, a plaque is considered active when intraplaque inflammation and neovascularization are detected, better estimated with a CT scan.

Other information about plaque vulnerability are obtained with the evaluation of plaque thickness and surface morphology, both well analyzed through DUS, CT, and MRI. In particular, among the three possible types of plaque surface (smooth, irregular, or ulcerated), the ulcerated form has the major risk for stroke.

Finally, it is useful to assess the volume of the plaque, with MRI providing better information about soft tissue contrast and CT allowing a better spatial resolution [12].

6.7 Treatment

The main therapeutic strategy is to remove the cardiovascular risk factors, through healthy life choices and medications. In addition, regular walking exercise is able to increase the development of the collateral circulation, improving the claudication pain. Finally, the last therapeutic approach is revascularization, performed in patients with critical ischemia (Practice 2016).

6.7.1 Aneurysms

Another condition, typical for old adults, is the development of aneurysms, found in the 3–4% of subjects older than 65 years of age, more frequently in the infrarenal aorta.

Aortic aneurysms are defined as a weakness of the aortic wall with the presence of an aortic diameter >30 mm and an increase of more than 50% with respect to the normal vessel, determining a dilatation with a saccular or fusiform morphology. The aneurysms with a diameter >55 mm in men and >50 mm in women are at risk of rupture.

Table 6.3 Determining agents for the development of aortic aneurysms

Determining factors for aortic aneurysms
Idiopathic
Genetic predisposition
Old age, male sex
Tobacco smoking
High DLD levels
Hypertension
Connective tissue disorders (Takayasu arteritis, Marfan syndrome)
Traumas
Infections (brucellosis, salmonellosis, tuberculosis)

LDL low-density lipoprotein [13]

Although mostly asymptomatic, in some patients they may lead to abdominal and back pain and other nonspecific symptoms before rupture, which is often fatal.

They are mostly determined by nonspecific causes, but, in other cases, they are induced by genetic predisposition, connective tissue disorders, infections, traumas, smoking, obesity, high levels of low-density lipoprotein (LDL), and other factors, which are summarized in Table 6.3 [13, 14].

Consequently, these causes lead to alterations of the elastic fibers of the extracellular matrix, because of the activation of elastolytic processes by means of metalloproteinases (MMP). Besides, a concurrent determinant is the presence of chronic parietal inflammation, with an infiltration of the arterial wall mostly by macrophages and lymphocytes [14, 15].

6.8 Diagnosis

In most cases, aneurysms are an incidental finding, casually noticed in other examinations or identified thanks to their typical calcifications pattern. In other subjects, they are clinically detected because of the presence of an abdominal palpable mass. However, more frequently aneurysms are recognized through diagnostic imaging. US, CT, and MR imaging (MRI) are the methods usually performed in order to obtain aneurysm's information such as its diameters [13–16]. The important measurements that should be evaluated when assessing an aortic aneurysm include the aneurysmal sac, the arterial portions proximal and distal to the dilatation, and the features of the vascular access that would be used in case of stent-graft positioning, in particular the ilio-femoral tract, including calcifications and thrombi [16].

6.8.1 Ultrasound

In patients with a non-ruptured aneurysm, US and DUS are the main techniques for disease screening and monitoring. Indeed, they are noninvasive methods which allow arterial diameter measurement with high reproducibility.

Besides, pulse-wave imaging (PWI) is able to identify the mechanical changes in the arterial wall, and the pulse-wave velocity (PWV) provides the clinician with important information about regional parietal changes.

Finally, the use of contrast agents in ultrasonography is a fundamental tool in the follow-up of patients treated with endovascular aneurysm repair (EVAR), especially in subjects who cannot undergo CT or MRI scans [14].

6.8.2 Computed Tomography

With 2D imaging, MIP and MPR images, CT angiography is able to assess the aneurysm's diameters, providing important information about the necessity for operative treatment.

Before contrast administration, a first scan is useful for identifying parietal calcifications in the aorto-iliac tract. An important pitfall that should be considered is represented by vascular tortuosity, which might lead to obtain an erroneous value of the vessel diameters, as well as their measurement in an axial plain.

In addition, CT has a pivotal role in examining the vascular anatomy for a proper procedural planning, identifying the correct device suitable for the single patient, by assessing the aorto-iliac length and the aneurysm's diameters.

Finally, CT has a higher sensitivity than conventional angiography in identifying the possibility of procedural and post-procedural complications, especially after EVAR, more frequently represented by endoleaks [14, 16].

6.8.3 Magnetic Resonance

MR angiography without contrast administration is a valuable option for patients who cannot undergo a CT examination, because of radiation exposure or risk for nephrogenic systemic fibrosis in subjects with chronic renal disease. Although it shows the same accuracy of CT in assessing the aortic diameters, it is not able to analyze small vascular structures such as accessory renal arteries, especially when their diameter is <2 mm, not to mention the impossibility for MRI to evaluate the parietal calcifications. For this reason, according to Picel and colleagues, CT scan without contrast agents should be performed in combination with an MRI examination [14, 16].

Moreover, MR angiography is able to recognize the presence of vascular endoleak in cases not identified with a CT scan [14].

6.8.4 Functional Imaging and Molecular Imaging

The last studies analyze the disease from a wider point of view, considering not only the vascular diameters but also the properties of the arterial wall. Indeed, a different risk of progression and rupture has been observed in aneurysms with similar

diameters. The use of particular tracers (i.e., radio-labeled blood cells) allows the localization of inflammatory and metabolic changes in the vascular walls. The main technique used for functional imaging is single-photon emission computed tomography (SPECT) with the employment of radioisotopes such as ^{99m}Tc, ^{111}In, ^{123}I, and ^{131}I. With this technique, the activity of the parietal thrombi can be evaluated, by detecting the focal activity of platelets and polymorphonucleates [14].

Several molecular probes are also used with techniques such as MRI, magnetic resonance spectroscopy (MRS), PET, optical bioluminescence, optical fluorescence, and targeted US. In the different stages of the disease, alterations in particular markers are detectable, providing important information that go beyond the measurement of the vascular diameter by itself. Indeed, an increment of the parietal activity is considered expression of wall inflammation, correlated with a major risk of rupture. Even modifications in extracellular components such as elastin and collagen are indicative for parietal instability, and thus increased risk of rupture [13, 14]. For instance, MRI images can be acquired using a particular probe, which consist in the ultrasmall superparamagnetic particles of iron oxide (USPIO), which marks areas of inflammation by detecting the activity of the macrophages. All of these information provided can be used as a guide for appropriate pre-procedural decision-making [15].

6.9 Treatment

If the aneurysm diameter is >5–5.5 cm or it increases >1 cm per year, a vascular reparation is necessary. In the past, an open repairing was performed, but nowadays an endovascular abdominal aneurysm repair (EVAR) is preferred, due to its post-procedure mortality rate of 4.7% compared to that (19.2%) of the open repair technique. A metallic stent secured at the proximal and the distal edges of the dilatation creates a preferential passage for the blood into the vessel, excluding the dilated portions [16].

In treated patients, imaging follow-up is necessary, with CT and CTA representing the gold standard. MRA is another surveillance option. US and nuclear imaging can be useful in some cases, the latter especially in case of endograft infection [17].

If the diameter of the aneurysm is >5.5–6.5 cm, the perioperative risk is increased and the same occurs for the risk of complications [16].

EVAR procedure is not free from complications. The most frequent one is the development of endoleaks, the presence of blood flow in the aneurysmal sac, which is not completely excluded by the endograft. It is present in about the 15–30% of patients, usually 30 days after EVAR. Five types of endoleaks might be recognized (see Table 6.4), types I and II being the most frequent (Figs. 6.4 and 6.5).

Endograft migration is another complication, named as the displacement of the endograft >5–10 mm. Endograft contamination (early occurrence) or colonization from a distant site of infection (later occurrence) may lead to endograft infection, which is characterized by a high mortality rate, usually due to septic shock.

Table 6.4 Types of endoleaks and causes of occurrence [17]

Type of endoleak	Cause
Type I	IA: anomaly in the adhesion of the proximal site of the graft IB: anomaly in the adhesion of the distal site of the graft
Type II	Patent aortic branches cause the presence of blood flow into the aneurysmal sac
Type III	Alteration in the graft structure
Type IV	Presence of pores in the endograft
Type V	Increasing dilatation of the aneurysmal sac without imaging signs of endoleak ("endotension" phenomenon)

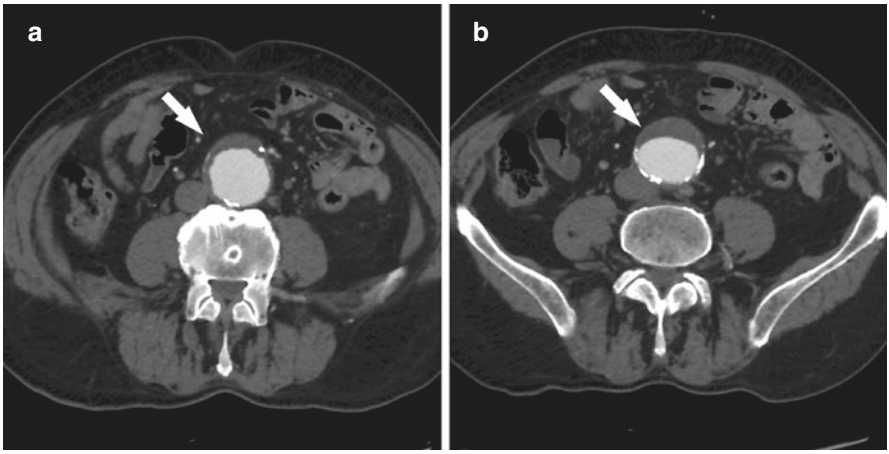

Fig. 6.4 (**a**, **b**) A 81-year-old male patient with AAA. The CTA shows the presence of infrarenal aneurysm with endoluminal moderate eccentric thrombus (white arrows)

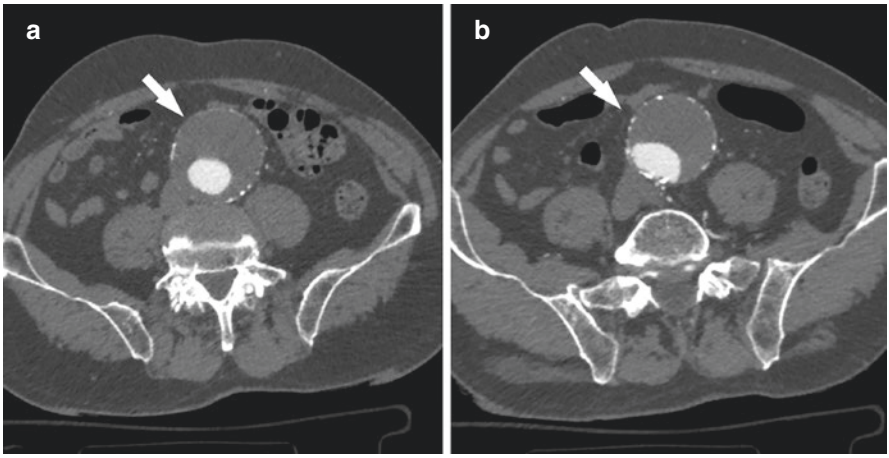

Fig. 6.5 (**a**, **b**) A 75-year-old male patient with AAA. The CTA shows the presence of infrarenal aneurysm with endoluminal severe eccentric thrombus (white arrows)

Other less frequent complications are represented by occlusion/kinking/collapse of the graft limbs and systemic complications, such as organs ischemia, cerebrovascular events, and post-implantation syndrome (an inflammatory/immune response as a reaction to the endograft's material, with systemic inflammation clinical signs and symptoms).

Finally, in some cases, an open surgical conversion may be necessary, i.e., in cases of symptomatic type V endoleaks or huge graft displacement [17].

References

1. Olin JW, Sealove BA. Peripheral artery disease: current insight into the disease and its diagnosis and management. Mayo Clin Proc. 2010;85(7):678–92. https://doi.org/10.4065/mcp.2010.0133.
2. Strandberg TE, Pitkälä KH, Tilvis RS, O'Neill D, Erkinjuntti TJ. Geriatric syndromes—vascular disorders? Ann Med. 2013;45(3):265–73. https://doi.org/10.3109/07853890.2012.727022.
3. Ungvari Z, Tarantini S, Donato AJ, Galvan V, Csiszar A. Mechanisms of vascular aging. Circ Res. 2018;123(7):849–67. https://doi.org/10.1161/CIRCRESAHA.118.311378.
4. Alvis BD, Hughes CG. Physiology considerations in geriatric patients. Anesthesiol Clin. 2015;33(3):447–56. https://doi.org/10.1016/j.anclin.2015.05.003.
5. Kovacic JC, Moreno P, Nabel EG, Hachinski V, Fuster V. Cellular senescence, vascular disease, and aging: part 2 of a 2-part review: clinical vascular disease in the elderly. Circulation. 2011;123(17):1900–10. https://doi.org/10.1161/CIRCULATIONAHA.110.009118.
6. Thiruvoipati T, Kielhorn CE, Armstrong EJ. Peripheral artery disease in patients with diabetes: epidemiology, mechanisms, and outcomes. World J Diabetes. 2015;6(7):961–9. https://doi.org/10.4239/wjd.v6.i7.961.
7. Imori Y, Akasaka T, Ochiai T, Oyama K, Tobita K, Shishido K, Nomura Y, Yamanaka F, Sugitatsu K, Okamura N, Mizuno S, Arima K, Suenaga H, Murakami M, Tanaka Y, Matsumi J, Takahashi S, Tanaka S, Takeshita S, Saito S. Co-existence of carotid artery disease, renal artery stenosis, and lower extremity peripheral arterial disease in patients with coronary artery disease. Am J Cardiol. 2014;113(1):30–5. https://doi.org/10.1016/j.amjcard.2013.09.015.
8. Vlachopoulos C, Georgakopoulos C, Tousoulis D. Diagnostic modalities in peripheral artery disease. Curr Opin Pharmacol. 2018;39:68–76.
9. Verim S, Taşçı I. Doppler ultrasonography in lower extremity peripheral arterial disease. Turk Kardiyol Dern Ars. 2013;41(3):248–55. https://doi.org/10.5543/tkda.2013.76429.
10. Lau JF, Weinberg MD, Olin JW. Peripheral artery disease. Part 1: clinical evaluation and noninvasive diagnosis. Nat Rev Cardiol. 2011;8(7):405–18. https://doi.org/10.1038/nrcardio.2011.66.
11. Mathew RC, Kramer CM. Recent advances in magnetic resonance imaging for peripheral artery disease. Vasc Med. 2018;23(2):143–52. https://doi.org/10.1177/1358863X18754694.
12. Saba L, Saam T, Jäger HR, Yuan C, Hatsukami TS, Saloner D, Wasserman BA, Bonati LH, Wintermark M. Imaging biomarkers of vulnerable carotid plaques for stroke risk prediction and their potential clinical implications. Lancet Neurol. 2019;18(6):559–72. https://doi.org/10.1016/S1474-4422(19)30035-3.
13. Brangsch J, Reimann C, Collettini F, Buchert R, Botnar RM, Makowski MR. Molecular imaging of abdominal aortic aneurysms. Trends Mol Med. 2017;23(2):150–64. https://doi.org/10.1016/j.molmed.2016.12.002.
14. Hong H, Yang Y, Liu B, Cai W. Imaging of abdominal aortic aneurysm: the present and the future. Curr Vasc Pharmacol. 2010;8(6):808–19. https://doi.org/10.2174/157016110793563898.
15. Jalalzadeh H, Indrakusuma R, Planken RN, Legemate DA, Koelemay MJ, Balm R. Inflammation as a predictor of abdominal aortic aneurysm growth and rupture: a systematic

review of imaging biomarkers. Eur J Vasc Endovasc Surg. 2016;52(3):333–42. https://doi.org/10.1016/j.ejvs.2016.05.002.
16. Picel AC, Kansal N. Essentials of endovascular abdominal aortic aneurysm repair imaging: preprocedural assessment. AJR Am J Roentgenol. 2014;203(4):W347–57. https://doi.org/10.2214/AJR.13.11735.
17. Daye D, Walker TG. Complications of endovascular aneurysm repair of the thoracic and abdominal aorta: evaluation and management. Cardiovasc Diagn Ther. 2018;8(Suppl 1):S138–56. https://doi.org/10.21037/cdt.2017.09.17.

Airway Diseases in Geriatric Patients

7

Maurizio Balbi, Roberta Eufrasia Ledda, Silvia Pamparino, Gianluca Milanese, Mario Silva, and Nicola Sverzellati

Abbreviations

B/A	Broncho-arterial
BAF	Bronchial anthracofibrosis
COPD	Chronic obstructive pulmonary disease
CT	Computed tomography
CXR	Chest radiography
DTS	Digital tomosynthesis
FEV_1	forced expiratory volume in 1 second
FVC	Force vital capacity
HRCT	High-resolution CT
HU	Hounsfield unit
ILD	Interstitial lung diseases
LAC	Large airway collapse
TD	Tracheal diverticula

M. Balbi · R. E. Ledda · G. Milanese · M. Silva · N. Sverzellati (✉)
Scienze Radiologiche, Department of Medicine and Surgery (DiMeC), University of Parma, Parma, Italy
e-mail: maurizio.balbi@unipr.it; robertaeufrasia.ledda@unipr.it; gianluca.milanese@unipr.it; mario.silva@unipr.it; nicola.sverzellati@unipr.it

S. Pamparino
Department of Health Sciences (DISSAL), Ospedale Policlinico San Martino, University of Genova, Genoa, Italy

G. Guglielmi, M. Maas (eds.), *Imaging in Geriatrics*, Practical Issues in Geriatrics, https://doi.org/10.1007/978-3-031-14877-4_7

7.1 Introduction

Lung development starts in utero and continues postnatally up to 25–30 years of age [1, 2]. From that point on, pulmonary function progressively declines, even in the absence of overt pulmonary disease [3]. The aging lung shows (1) a progressive decrease of alveolar surface area, (2) dilatation of airspaces, (3) reduced mucociliary clearance, and (4) decreased elasticity [4, 5]. These phenomena are sustained by cellular changes that impact structural, functional, and mechanical properties of the respiratory system, yet the precise underlying molecular mechanisms are poorly understood [6]. It has been suggested that the remodeling of the extracellular matrix, with the resulting degradation of elastin and collagen fibers, accounts for a major mechanism of the aging lung at the cellular level [7]. Furthermore, the aging process is well-known to be associated with a chronic, low-grade, systemic inflammation, referred to as "inflamm-aging," characterized by higher levels of several cytokines, including interleukins 1 and 6, and tumor necrosis factors alpha [6]. The number of airway neutrophils is higher in older individuals, regardless of the presence of airway diseases, and peripheral neutrophils show elevated primary granule release and neutrophil elastase activity, increasing the risk of airways wall damage [8].

As a consequence of such changes, the elderlies (>65 years of age) show lower pulmonary oxygenation and reduced exercise capacity as well as enhanced susceptibility to pulmonary diseases, both chronic, such as chronic obstructive pulmonary disease (COPD) and interstitial lung diseases (ILD), and acute/subacute, including pulmonary infections [5]. With greater life expectancy, understanding the imaging appearance of the healthy aging lung is of utmost importance to distinguish a disease state from age-related physiological changes [2–6, 9]. Most information about the effects of age on the respiratory system has come from histopathologic examination and pulmonary function testing, while the role of imaging in phenotyping the so-called senescent lung has been relatively marginal [10, 11]. As a result, the borderland between normal and abnormal airway imaging appearance in the elderly is, to some degree, still lined within a "gray area" [12].

Current evidence on radiological age-related normal and pathological changes of large and small airways will be discussed herein.

7.2 Imaging Techniques

A comprehensive discussion of the radiological techniques currently used in clinical practice for the evaluation of the airways and their current limitations goes beyond the scope of this chapter. In this paragraph, general considerations will be made, while detailed technical aspects pertaining to specific disorders will be treated in the following sections.

7.2.1 Chest Radiography (CXR)

Chest radiography (CXR) remains the first-line imaging for many thoracic diseases, showing a generally good performance as a screening evaluation [13]. If the accuracy of such modality is rather limited for evaluating small airways due to intrinsic limitations (i.e., limited resolution and superimposition of overlapping structures), large airway abnormalities can be relatively easily demonstrated on radiographic images, regardless of age [14]. Digital chest radiography has continuously and significantly improved over the last decades, with several processing tools being implemented to support radiologists in the detection of pathological findings, including digital tomosynthesis (DTS) and dual-energy subtraction techniques [15, 16]. DTS has been demonstrated to overcome conventional radiography in the assessment of central airways, improving their coronal view and thus facilitating the identification of a suspected either ingested or aspirated foreign body, which may be of value in geriatric patients [17]. Analogously to DTS, images obtained with dual-energy subtraction improve the detection of tracheal abnormalities. Tracheal stenosis and narrowing due to extrinsic compression can be, in fact, more easily demonstrated on soft-tissue-selective images [18].

Such techniques, however, are not free of limitations, including their relatively low availability, whereas chest CT, considered the imaging modality of choice, is much largely accessible.

7.2.2 High-Resolution Computed Tomography (HRCT)

Chest high-resolution CT (HRCT) is the current imaging modality of choice for the evaluation of airways. The two consistent components of HRCT include the use of thin sections ($\leq$1.5 mm) coupled with a high spatial frequency reconstruction algorithm [19]. Although there are no standardized HRCT protocols for the assessment of the airways, acquisition of volumetric scanning has several advantages compared to interspaced scanning (i.e., obtained with 10–20 mm intervals between axial scans), which is prone to miss focal abnormalities. Volumetric HRCT allows both the evaluation of the airways in a true cross-section using multiplanar reconstruction and application of post-processing techniques (e.g., minimum intensity projection and maximum intensity projection) as well as quantitative software [19, 20].

Technical parameters ought to be optimized to avoid motion artifacts, which deserve particular attention in the elderly. Possible strategies include caudocranial scanning, increased pitch, and faster rotation time [21]. The window setting used to interpret HRCT images is of utmost importance since it may significantly affect the apparent bronchial walls thickness, best assessed with window width centers between -250 and -750 HU and window width >1000 HU. Other settings, particularly window width <1000 HU, can lead to a substantial artificial thickening of bronchial walls [22].

Although a higher radiation exposure remains the major drawback of CT as compared to other techniques (i.e., CXR), it has been progressively overcome with continuous implementation of a variety of radiation dose reduction techniques [23, 24].

7.3 Normal Aging

7.3.1 Trachea and Main Bronchi

The trachea is considered to increase in size and become irregular in shape over time. Gibellino et al. observed a significant difference in tracheal diameters and cross-sectional area between a group of supposed healthy young men ($n = 18$; mean age, 21.1; mean coronal diameter, 1.79 cm; mean sagittal diameter 2.00 cm; mean cross-sectional area, 2.81 cm^2) and middle-age men ($n = 32$; mean age, 52.2; mean coronal diameter 1.91 cm; mean sagittal diameter 2.14 cm; mean cross-sectional area, 3.22 cm^2) [25]. However, neither patients greater than 61 years of age nor women were included in the analysis. Despite the small sample size and the relatively young subjects included, these results were in keeping with a previous study that observed a nearly steady increase in sagittal and coronal tracheal diameters from the third decade onward in 808 healthy subjects aged 10–79 years (430 males and 378 females) measured on radiographic images [26]. Collins et al. confirmed a significant positive correlation between age and radiographic tracheal size (r values between 0.324 and 0.603; $p < 0.01$) in 165 healthy nonsmokers (79 male and 86 females; mean age, 50 years) [27]. By means of computed tomography (CT), Sakai et al. demonstrated a significant positive correlation between tracheal area and age ($r = 0.37$; $p = 0.0006$) in 83 healthy male volunteers aged 21–83 years (mean age, 47.7 years) [28]. The same study also demonstrated that the trachea tends to become more irregular in shape with increasing age, as proven by a loss in its circularity ($r = -0.32$; $p = 0.003$) [28].

A more recent study, where 81 healthy volunteers aged 25–75 years (40 female and 41 male) underwent a chest CT at total lung capacity and during forced exhalation, showed that older men (mean age, 61.8 years) had 12% greater cross-sectional total area at total lung capacity than younger men (mean age, 32.2 years) ($p = 0.02$). However, no subjects aged >75 years were enrolled [29]. Most notably, men, but not women, showed a significant positive correlation between the percentage of airway collapse and age ($R^2 = 0.40$; $p < 0.001$) up to and exceeding the value of 50%, which represents the most reported threshold to define large airway collapse (LAC) [30]. These results have extended knowledge in the age-related changes of the trachea, suggesting that both age and sex should be considered in the diagnostic evaluation of expiratory dynamic airway collapse to not mistake a normal response to expiratory maneuvers for a disease state.

Tracheal cartilaginous rings can become calcific as an age effect. This finding is almost always incidental and does not have a recognized functional significance (Fig. 7.1). In a chest radiographic series, it was reported in 37% of patients aged 75 years or older [31]. Lloyd et al. described tracheobronchial calcification in 26%

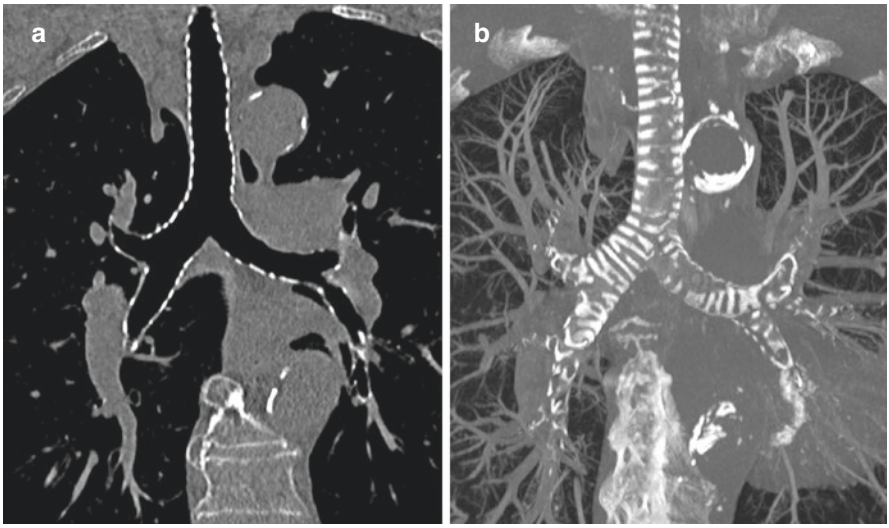

Fig. 7.1 (**a**, **b**) Coronal unenhanced CT images of a 79-year-old woman show tracheobronchial calcification rings. In (**b**), the calcifications are magnified by means of maximum-intensity-projection (MIP) reconstruction

of patients aged 40–45 years and in up to 65% of men and 40.5% of women aged 60–79 years undergoing chest CT for a wide range of suspected both mediastinal and pulmonary disorders [32]. Of note, tracheal calcification is not an exclusive manifestation of normal aging but has been associated with other conditions, including adrenogenital syndrome, diastrophic dysplasia, and a history of warfarin therapy [33]. When nodular in shape (8–10 mm) and adjacent to thickened tracheal cartilage, calcifications may result from a benign disorder called tracheobronchopathia osteochondroplastica. In this condition, however, the trachea appears much more irregular in shape than normal, making the diagnosis quite straightforward [34].

7.3.2 Airway Wall Thickness

Current evidence on age-related changes in airway wall thickness is somewhat conflicting. In a study by Matsuoka et al., no difference was observed in the ratio between the bronchial wall thickness and the bronchial total diameter measured on CT images of 85 healthy volunteers aged 21–90 years (mean age, 74 years) [35]. Conversely, using the accompanying pulmonary artery for comparison, Copley et al. found a higher frequency of bronchial wall thickening in older (>75 years) than younger (<55 years) asymptomatic subjects ($p < 0.001$) [36]. In these studies, CT scans were acquired using non-contiguous sections (see *High-Resolution CT* paragraph), and airway wall thickness was either measured manually [35] or evaluated by a point scale [36]. More recently, Telenga et al. found a significant ($p < 0.001$)

association between higher age and a lower airway wall thickness at an internal parameter of 10 mm (i.e., a standardized measurement of airway wall thickness obtained from the regression line between the square root of the airway wall area and the internal perimeter of the airway) in 99 healthy subjects (median age, 39 years; interquartile range, 22–54) [37]. Such measurements were performed using an automated software, potentially more reproducible and accurate than manual measurements [38]. These results are partly in keeping with those of Zach et al., who demonstrated a significant ($p = 0.006$) decrease of wall area percent (i.e., wall area/total bronchial area) and an increase of internal lumen area with age in a cohort of 92 healthy subjects aged 45–80 years [39].

It is worth emphasizing that no established criteria exist to define bronchial wall thickening, which remains a subjective diagnosis. Moreover, current CT metrics to evaluate bronchial wall thickness are affected by potential bias, such as lung volume, reconstruction parameters (i.e., see *High-Resolution CT* paragraph), underlying airway disease, and limited capability of CT of distinguishing bronchial wall from peribronchovascular interstitium [40, 41]. Of note, bronchial wall thickening can be underestimated when the bronchial diameter is used for comparison in patients with bronchial dilation (e.g., in case of bronchiectasis or suboptimal inflation). In contrast, thickening of the peribronchovascular interstitium may result in what appears to be bronchial wall thickening. Therefore, the effects of age on airway wall thickness are not easy to be ascertained.

7.3.3 Bronchial Caliber

The most used descriptive parameter to evaluate bronchial caliber is the bronchoarterial (B/A) ratio, which is obtained by dividing the diameter of the bronchus (most commonly the internal bronchial diameter) by the diameter of the adjacent pulmonary artery. As a rule of thumb, the B/A ratio is regarded as abnormal when it exceeds the value of 1, meeting the radiological definition of *bronchiectasis* [42]. There is evidence that the B/A ratio increases with age, reaching bronchiectatic dimensions in some cases (Fig. 7.2). Matsuoka et al. found a significant correlation between the B/A ratio and age ($r = 0.768$, $p < 0.0001$) in a group of 85 healthy subjects. The B/A ratio was greater than 1 in 41% of subjects aged >65 years and in 7% of subjects aged between 41 and 64 years but in no subjects aged between 21 and 40 years [35]. As stated above, Copley et al. observed that bronchial dilation was more prevalent in older (>75 years) than younger (<55 years) healthy subjects (60% vs. 6%; $p < 0.001$) [36]. Moreover, bronchial dilation was found to present a lesser extent in the younger than in the older group ($p < 0.001$), in which it also showed a lower lobe predominance (i.e., 80% of cases) [36].

Notably, an increase of the B/A ratio can be driven, at least to some extent, by a diameter reduction of the pulmonary arteries rather than a true bronchial dilation. This phenomenon can be due to a disease state (e.g., asthma) [43] but also found in healthy subjects, including those who live at high altitudes (exposed to hypoxia) [44] and never smokers [45]. Nevertheless, the lack of standardized age-specific reference values of

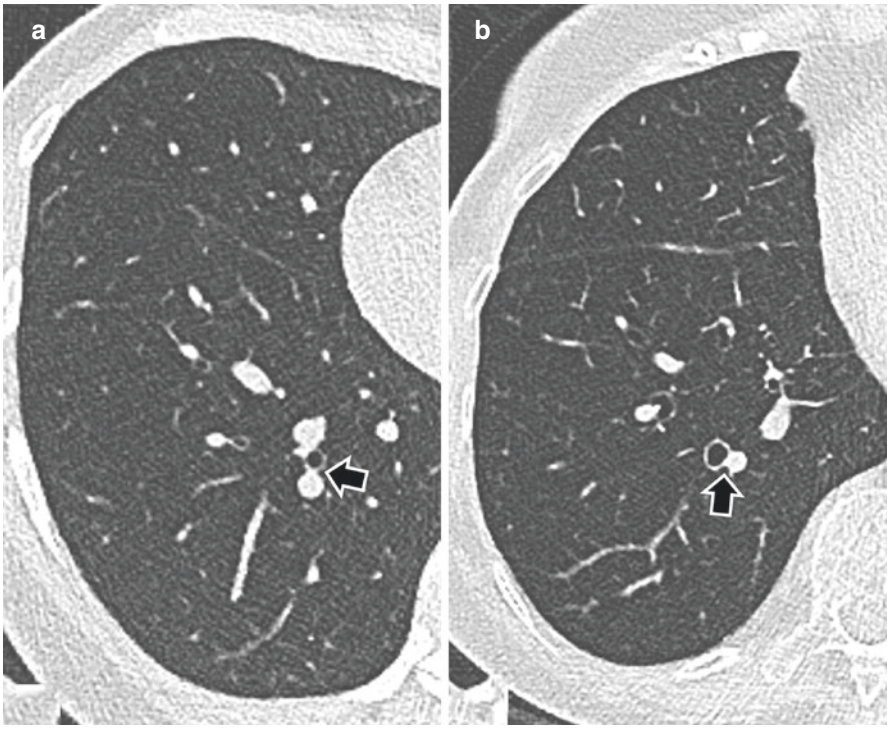

Fig. 7.2 (**a**) Axial unenhanced CT image of a healthy 23-year-old-man shows a broncho-arterial ratio <1 (arrow) at the right lower lobe posterior segment. (**b**) At the same level, the broncho-arterial ratio is >1 (arrow) in a 70-year-old-man with no history of cardiopulmonary disease. Recognition of an age-related increase of broncho-arterial ratio is essential to avoid a bronchiectasis overdiagnosis in otherwise healthy older individuals

airway and vessel size currently prevents understanding how they relate to each other with increasing age. Despite these well-known limitations, recognizing a B/A ratio greater than 1 as a possible age-related finding is essential to reduce the chance of a spurious diagnosis of "bronchiectasis" in an otherwise healthy old individual.

7.3.4 Small Airways

Given the limited resolution of CT in the visualization of airways <2 mm in diameter, the radiological evidence of small airways aging rests upon the evaluation of abnormal retention of air in the lung as a surrogate of obstruction, namely the *air trapping* [46]. This finding is demonstrated on CT expiratory scans as parenchymal areas with less than normal increase in attenuation and lack of volume reduction [47, 48]. Areas of air trapping can be seen in up to 80% of healthy subjects and with increasing frequency and extension over time, usually not exceeding 25% of the whole lung volume [49, 50]. In a study by Lee et al., air trapping was found in 3 out of 13 (23%) subjects

aged 21–30 years, 7 of 17 (41%) aged 41–50 years, 11 of 17 (65%) aged 51–60 years, and 13 of 17 (76%) aged 61 years or older [51]. The increase in the frequency of air trapping with age was found statistically significant ($p < 0.05$), as well as the correlation between air trapping extension and age ($r = 0.523$, $p < 0.001$) [51]. Thus, it was suggested that airway occlusion or luminal narrowing might occur with normal aging, although only a few over 75-year olds were included, and no histological sample was obtained. Subsequent work extended these findings by exploring a larger population of more advanced age and providing data from lung specimens. By means of parametric response mapping (i.e., a voxel-based image analysis that classifies lung by thresholding Hounsfield unit, HU, values from spatially aligned inspiratory/expiratory CT scans), Martinez et al. found that nonemphysematous air trapping increased by 2.7% per decade in a population of 580 never- and ever-smokers free from obstruction and respiratory symptoms (i.e., from 3.6%, if aged 40–50 years, to 12.7% when aged 70–80 years) [52]. Increasing air trapping was associated with increased force vital capacity (FVC) ($p = 0.004$) but unchanged forced expiratory volume in 1 second (FEV_1) ($p = 0.94$), yielding lower FEV_1/FVC ratios ($p < 0.001$) [52]. In keeping with these results, Verleden et al. demonstrated an age-dependent loss of terminal bronchioles in 32 never-smoker lung donors (age range 16–83 years) using a combination of ex vivo CT, whole lung micro-CT, and micro-CT of extracted cores. The loss of terminal bronchioles (i.e., about half of the total number of terminal bronchioles between 30 and 80 years of age) was corroborated by the association of the predicted pulmonary function with the total number of terminal bronchioles, suggesting that loss of small airways is a relevant structural component of age-related decline in pulmonary function of healthy individuals [53].

Of note, age-related changes in CT lung density are not exclusively attributable to a small airway involvement. Several studies have focused on the presumptive relationship between the physiological decrease in lung density with age (i.e., approximately 50 HU between 20 and 70 years of age) and the progressive enlargement of the airspaces over time, a phenomenon conventionally mislabeled as "senile emphysema" (despite the absence of destruction of alveolar walls, implicit in the word *emphysema*) [54–57]. In non-smoker elderlies, lung attenuation possibly approaches and even falls below the density thresholds commonly used to define emphysema (i.e., 910 HU or 950 HU), demanding caution when applying densitometry in aging lungs to avoid mistaking normal parenchyma for damage [57, 58]. Nevertheless, recent evidence suggests that age-related emphysematous changes may be of limited importance because of their low extent (i.e., <5% of the whole lung) and substantial stability over time (i.e., increase of about 0.1% per 10 years between the 50 and 80 years of age) [52].

7.4 Pathological Conditions

7.4.1 Chronic Obstructive Pulmonary Disease (COPD)

Chronic obstructive pulmonary disease (COPD) represents the fourth leading cause of death worldwide, with increasing prevalence in the elderly [3]. The estimated prevalence of COPD is more than 390 million people worldwide in 2030 [59]. To

date, various phenotypes of COPD have been described, with chronic bronchitis and emphysema accounting for the most common ones. The former is characterized by predominant airway-related changes (inflammation and airway wall thickening) with increased mucus production, whereas the latter by alveolar wall destruction and hyperinflation, resulting in impaired gas exchange [60]. Notably, it has been suggested that the small airway damage represents the *primum movens* of such heterogeneous disorder, even in the emphysematous phenotype [61].

Regardless of the phenotype, establishing the presence of COPD in the elderly can be quite challenging due to the significant morphological similarities between aged lung and COPD. The physiological airspace enlargement without the alveolar wall destruction observed in COPD is often erroneously labeled as "senile emphysema" [62, 63]. The risk of such misinterpretation is over-diagnosing COPD within the geriatric population, potentially leading to unnecessary investigations. Having said that, it is worth emphasizing that the diagnosis of COPD relies on both clinical and functional evidence of expiratory airflow obstruction [64], whereas imaging (mainly CT) normally serves the purpose of assessing the disease extent (emphysematous phenotype) and exacerbations (bronchitis phenotype). Measurement of emphysema severity by means of CT densitometry techniques has been established in the literature [65, 66], and different quantitative approaches—whose discussion would deserve a dedicated chapter—have been employed more recently [67–69]. Chronic bronchitis is demonstrated by a relative increase in bronchial wall thickness as compared to the bronchial lumen and with the diameter of adjacent pulmonary arteries, a rather subjective morphological feature, as discussed above, while poorly defined centrilobular nodules of ground-glass attenuation represent small airway inflammation [70].

Pulmonary cysts deserve special attention since they can be misinterpreted as bullous emphysema, although they represent an independent entity. The depiction of thin-walled air spaces on CT may help distinguish pulmonary cysts from emphysema [71].

7.4.2 Bronchiectasis

The term *bronchiectasis* refers to a clinico-radiological entity characterized by an irreversible abnormal dilatation of the bronchial tree, secondary to a combination of inflammation and obstruction/impaired clearance [72]. The most common clinical manifestations include chronic productive cough and dyspnea, whereas fatigue, hemoptysis, and thoracic pain are less common [73].

Although older bronchiectatic patients experience a worse quality of life and die more frequently during the 3-year follow-up as compared to younger affected subjects, no significant differences have been observed in terms of systemic inflammation levels and exacerbation rates across all age groups [72, 74], suggesting that comorbidities play a role in such a clinical and prognostic discrepancy.

It has been hypothesized that the bronchial dilation and bronchial wall thickening observed in the elderly population can be partly due to impaired large and small airway clearance mechanisms, secondary to a less effective mucociliary function and a decreased cough reflex, both contributing to mucus retention [75]. Recognized

etiologies of bronchiectasis include infections (25%), COPD (13%), connective tissue diseases (7.1%), and immunodeficiency (4.5%). Nevertheless, a non-negligible proportion of patients (36%) remains diagnosed with idiopathic bronchiectasis. If bronchiectasis related to asthma, inflammatory bowel disease, and ciliary dysfunction is more prevalent in younger adults, COPD-related bronchiectasis occurs more frequently in older adults and elderly patients [76, 77].

The gold standard imaging modality for diagnosing bronchiectasis remains chest HRCT [78]. The three most used radiological criteria to determine the presence of bronchiectasis are represented by (1) increased B/A ratio (a ratio >1–1.5 has been suggested to define bronchiectasis in adults) [78, 79], (2) lack of tapering, defined as unchanged airway diameter for 2 cm after branching, and (3) visualization of airways in the periphery of the lung, within 1 cm from the costal pleura or abutting mediastinal pleural [47, 80]. Although these CT features are usually of limited value to discriminate among different causes of bronchiectasis [81], the type of bronchiectasis (i.e., cylindric, varicose, or cystic) [82], their distribution within the lung regions, and concurrent ancillary findings might help narrow down the differential diagnoses. Associated findings include mucus retention/impaction, bronchial wall thickening, air trapping, and consolidation.

Bronchiectatic changes in the right middle lobe and lingula in older women deserve special consideration since they have a high predictive value for *Mycobacterium avium*–intracellulare complex (MAC) infection. When associated with centrilobular nodules, scarring, and volume loss of the affected lobes, these morphological abnormalities define the so-called Lady Windermere syndrome [83].

Traction bronchiectasis, secondary to pulmonary fibrosis, will not be discussed.

7.4.3 Large Airway Collapse (LAC)

LAC refers to an excessive inward movement of the trachea and/or main bronchi during expiration [30]. LAC comprises two entities: tracheomalacia, where there is softening of the cartilaginous rings, and excessive dynamic airway collapse, defined by an exaggerated forward displacement of the posterior tracheal membrane [30]. This nomenclature suffers from limited consistency throughout the literature; hence, the inclusive term of LAC will be used hereafter.

It is estimated that LAC affects about one out of ten patients undergoing bronchoscopy for pulmonary complaints and as many as a third of patients with COPD or severe asthma [30, 84, 85]. However, the true prevalence of this condition remains difficult to ascertain due to heterogeneous populations and the diagnostic methods of the available studies. LAC may go underrecognized because of associated respiratory diseases with overlapping symptoms, such as COPD, asthma, and bronchiectasis, which are regarded not only to mimic but even predispose to LAC [86, 87]. Other risk factors include prolonged intubation and longstanding extrinsic airway compression [87, 88]. Interestingly, although the degree of airways collapse appears to relate with age (in healthy male volunteers), a higher risk of developing LAC in the elderly has not been proven so far [29].

While dynamic bronchoscopy is still considered the diagnostic standard for LAC, in a recent meta-analysis, Mitropoulos et al. observed that CT had been the most reported modality to diagnose LAC over the past 30 years [30]. CT might serve as a complement or, especially in the elderly, an alternative to bronchoscopy, providing a rapid, noninvasive assessment of the central airways by means of inspiratory and expiratory acquisitions. Regardless of the investigation modality, there is still no agreement on what constitutes an "excessive" degree of collapse. At the time of its first definition, in 1965, Rayl et al. considered the airway collapse to be abnormal when the airway lumen decreased to at least half of its diameter during coughing, assessed on bronchography [89]. From that point on, such a threshold has been increasingly cited as "diagnostic" of LAC. However, when defined by >50% reduction of the airway lumen, LAC is over-diagnosed in about 17% of healthy subjects [30, 84, 88]. The adoption of higher thresholds of collapsibility (i.e., 70%) has shown promise in reducing the false-positive rate of LAC to about 2% [85]. Nevertheless, even when LAC approaches or exceeds this magnitude, it remains challenging to decipher the relationship between the degree of collapse with symptoms and flow limitation [90]. The diagnosis of LAC should, therefore, not rely on a mere imaging evaluation and be supported by the integration of data from bronchoscopy, clinical evaluation, and pulmonary function.

Normal tracheal morphology, either oval or round, is the most typically observed configuration on inspiratory CT images of patients with LAC. The inspiratory "lunate" trachea has the appearance of laterally splayed tracheal cartilage and excessive sagittal narrowing (i.e., coronal to sagittal diameter ratio >1), a configuration that is highly specific but low sensitive for LAC [91–93] (Fig. 7.3).

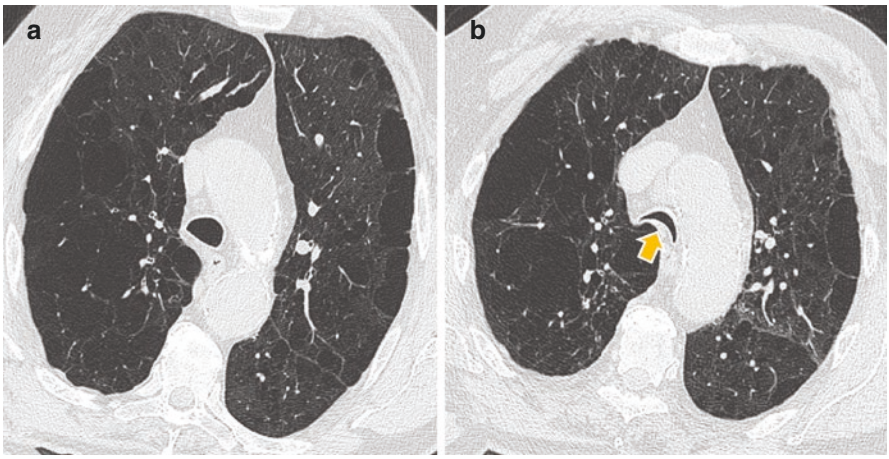

Fig. 7.3 Axial unenhanced CT images of a 76-year-old man show (**a**) increased ratio of coronal-to-sagittal tracheal diameters (i.e., lunate trachea) and (**b**) excessive collapse of the posterior tracheal wall (arrow) on expiration, highly suggestive of tracheomalacia. Advanced destructive emphysema and bronchial wall thickening, consistent with a COPD diagnosis, can also be appreciated

Expiratory airway collapse morphology includes: (1) an excessively bowed posterior wall that approximates the anterior wall's contour, resulting in the so-called frown sign; (2) a "saber-shape" type, characterized by distortion of the normal C-shape cartilage into an anteriorly elongated configuration with concomitant transverse narrowing (i.e., sagittal to coronal diameter ratio >2); and (3) circumferential narrowing, with a more isotropic reduction in airway cross-section [94]. This distinction is relevant since patients with an expiratory "frown-like" configuration are considered good candidates for tracheoplasty, a surgical technique for the treatment of LAC that involves reinforcement of the posterior membranous wall of the trachea [95, 96].

7.4.4 Broncholithiasis

The term *broncholithiasis* refers to calcified or ossified material, called *broncholith*, within the tracheobronchial tree, caused by either foreign body aspiration or calcified lymph nodes. The broncholiths, composed of calcium phosphate (85–90%) and calcium carbonate (10–15%) [97], are variable in size and usually irregular in shape. They can be classified into three different types: endobronchial, peribronchial, and transbronchial, based on their location within the tracheobronchial tree [98, 99]. In general, broncholiths tend to occur more frequently on the right side (upper and middle lobes in particular) due to the airway anatomy and intrathoracic lymph nodes distribution [97].

The incidence of broncholithiasis is higher in areas of endemic tuberculosis and/or histoplasmosis due to necrotizing granulomatous mediastinal lymphadenitis, but any focal process responsible for dystrophic calcification, including sarcoidosis, can potentially cause broncholithiasis [97, 100]. There is no established gender predilection, while the sixth and seventh decades of life seem to be the most affected [101].

Clinical manifestations range from nonproductive cough to massive hemoptysis and acute airway obstruction. Lithoptysis (expectoration of stones) is an almost pathognomonic symptom but relatively uncommon (seen in 6–26% of cases) [97, 102]. Most common complications include massive hemoptysis, secondary to bronchial irritation from the stone or rarely to vasculobronchial fistula, and obstructive pneumonia, whereas empyema, chronic lung abscess, mediastinal abscess, bronchoceles, and middle lobe syndrome account for less common ones [97].

Broncholithiasis can be easily depicted on CT when there is either an endobronchial or a peribronchial calcified nodule associated with features of bronchial obstruction, such as atelectasis, obstructive pneumonitis, or bronchiectasis (Fig. 7.4). Unsurprisingly, thin collimation helical CT is superior to conventional CT in determining whether a calcified nodule is endobronchial in position, overcoming volume-averaging artifacts [100, 102]. Bone or wide window CT settings are usually of help to confirm the presence of calcification/ossification and to better assess the morphology of a broncholith. Differential diagnoses include calcified fungus ball, calcified endobronchial tumors (e.g., carcinoid and hamartoma that can rarely occur

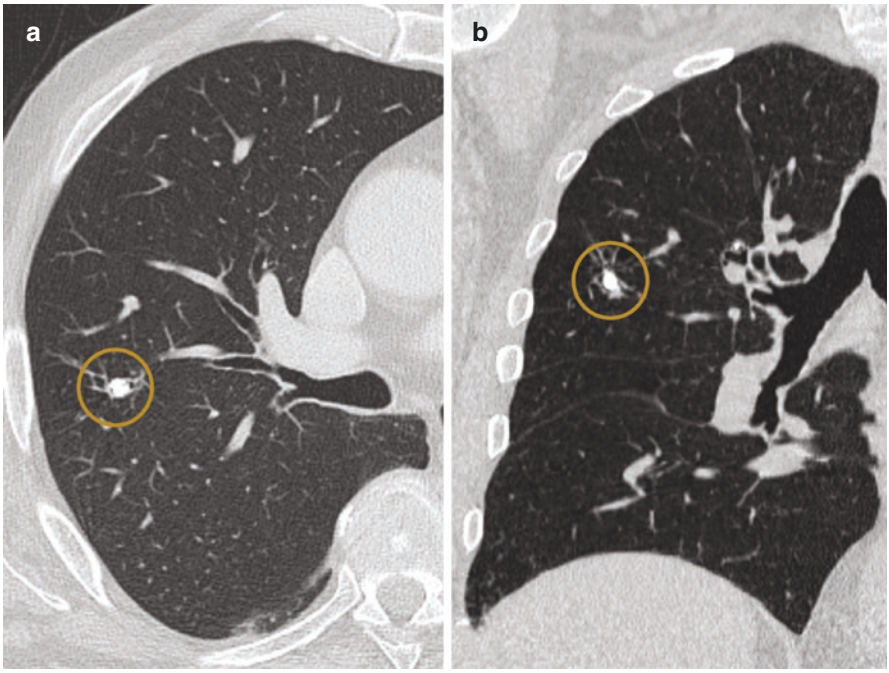

Fig. 7.4 Axial (**a**) and coronal (**b**) unenhanced CT images of a 70-year-old man presented with hemoptysis show a calcified nodule within a right upper lobe bronchus (empty circle), consistent with broncholithiasis

within the bronchi [103]), and rarer conditions such as tracheobronchial amyloidosis and tracheobronchopathia osteochondroplastica (*see above*) [102].

Surgical management is normally reserved for cases complicated by airway distortion, fistula formation, and massive hemoptysis, whereas a conservative approach seems to be an appropriate option for asymptomatic or minimally symptomatic subjects [97].

7.4.5 Tracheal Diverticula

Tracheal diverticula (TD) are outpouchings from the tracheal wall [104]. With the advent of CT and its continuous technical implementations (i.e., improvements in spatial resolution of multidetector CT and use of thin slices), the prevalence of such anatomical abnormality has been progressively increasing, ranging from 2% to 8% [105]. A gender predominance has not been demonstrated [104].

TD tend to involve the right posterolateral wall of the trachea at the level of T1–T3 vertebral bodies, an unprotected space compared to the contralateral side. TD are classified into congenital and acquired, with the latter normally encountered in the elderly population. Acquired TD are thought to be secondary to increased

intraluminal pressure that would cause out-bulging through a weak part of the tracheal wall or cystic distension of the mucous gland ducts [106, 107].

Although TD are usually asymptomatic, in some cases, they can be responsible of recurrent respiratory tract infections, acting as a reservoir for secretions and hemoptysis [106]. Larger diverticula (>30mm) have been reported to cause also painful neck swelling, cervical abscess, dysphagia, cough—secondary to compression of the vagus—and dysphonia due to compression of the recurrent laryngeal nerve [108].

CT generally shows small air bubbles connected to the tracheal lumen and surrounded by a very thin wall (Fig. 7.5). The communication with the trachea, however, is clearly appreciated in half of cases only, and usually with larger diverticula. These diverticula might also have a thicker wall and be multiloculated. It is worth emphasizing that when there is very little air within the diverticulum, it appears as a solid structure, often indistinguishable from a lymph node [104].

7.4.6 Bronchial Anthracofibrosis

Bronchial anthracofibrosis (BAF) represents a rather new pathological entity typically encountered in elderly females with a long-lasting biomass fuel smoke exposure [109, 110]. BAF can be associated with other clinical conditions, such as pulmonary tuberculosis (a coexistence as high as 50% has been reported), COPD, pneumonia, and malignancy [111]. The prevalence of such a rare condition is quite low in developed countries. Clinical presentation is nonspecific, including chronic productive cough and dyspnea, and depends on the associated diseases [111].

BAF diagnosis is established when bronchial bluish-black anthracotic pigmentation and narrowing/distortion of the affected bronchus are observed on bronchoscopy [112]. Nonetheless, CT evidence of multifocal bronchial narrowing along with peribronchial cuffing and mediastinal lymphadenopathy—either calcified or noncalcified—can raise the suspicion of BAF. Both segmental and lobar bronchi of the right upper and middle lobes are the most affected ones. Sparing of the trachea and

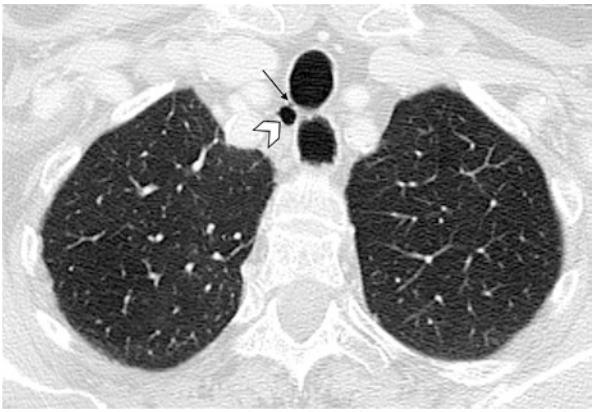

Fig. 7.5 Unenhanced CT image of a 70-year-old man depicts an air-filled right tracheal diverticulum (arrowhead). There is a thin communicating channel between the diverticulum and the tracheal lumen (arrow)

main bronchi is observed in most cases. Other CT features include collapse, consolidation, and mass lesions [113, 114].

7.5 Conclusions

Despite growing knowledge of cellular and molecular aging mechanisms, the borderland between normal and abnormal airway imaging in the elderly is still difficult to define. Distinguishing physiological age-related changes from a disease state remains quite challenging in a non-negligible proportion of the geriatric population. However, the role of imaging in the detection and stratification of airway diseases has been well-established, with chest HRCT being increasingly employed in clinical practice to support the management of patients suffering from airway disorders, including the elderlies.

References

1. Rojas M, Mora AL, Kapetanaki M, Weathington N, Gladwin M, Eickelberg O. Aging and lung disease. Clinical impact and cellular and molecular pathways. Ann Am Thorac Soc. 2015;12(12):S222–7.
2. Zank DC, Bueno M, Mora AL, Rojas M. Idiopathic pulmonary fibrosis: aging, mitochondrial dysfunction, and cellular bioenergetics. Front Med (Lausanne). 2018;5:10.
3. Brandsma CA, de Vries M, Costa R, Woldhuis RR, Konigshoff M, Timens W. Lung ageing and COPD: is there a role for ageing in abnormal tissue repair? Eur Respir Rev. 2017;26(146):170073.
4. Sharma G, Goodwin J. Effect of aging on respiratory system physiology and immunology. Clin Interv Aging. 2006;1(3):253–60.
5. Bowdish DME. The aging lung: is lung health good health for older adults? Chest. 2019;155(2):391–400.
6. Schneider JL, Rowe JH, Garcia-de-Alba C, Kim CF, Sharpe AH, Haigis MC. The aging lung: physiology, disease, and immunity. Cell. 2021;184(8):1990–2019.
7. Brandenberger C, Muhlfeld C. Mechanisms of lung aging. Cell Tissue Res. 2017;367(3):469–80.
8. Yoon YS, Jin M, Sin DD. Accelerated lung aging and chronic obstructive pulmonary disease. Expert Rev Respir Med. 2019;13(4):369–80.
9. Budinger GRS, Kohanski RA, Gan W, Kobor MS, Amaral LA, Armanios M, et al. The intersection of aging biology and the pathobiology of lung diseases: a joint NHLBI/NIA workshop. J Gerontol A Biol Sci Med Sci. 2017;72(11):1492–500.
10. Weibel ERGD. Architecture of the human lung. Use of quantitative methods establishes fundamental relations between size and number of lung structures. Science. 1962;137(3530):577–85.
11. Garcia-Rio F, Dorgham A, Pino JM, Villasante C, Garcia-Quero C, Alvarez-Sala R. Lung volume reference values for women and men 65 to 85 years of age. Am J Respir Crit Care Med. 2009;180(11):1083–91.
12. Hansell DM. Thin-section CT of the lungs: the Hinterland of normal. Radiology. 2010;256(3):695–711.
13. Levin DC, Parker L, Rao VM. Recent trends in imaging use in hospital settings: implications for future planning. J Am Coll Radiol. 2017;14(3):331–6.

14. Shepard JO, Flores EJ, Abbott GF. Imaging of the trachea. Ann Cardiothorac Surg. 2018;7(2):197–209.
15. Kuhlman JE, Collins J, Brooks GN, Yandow DR, Broderick LS. Dual-energy subtraction chest radiography: what to look for beyond calcified nodules. Radiographics. 2006;26(1):79–92.
16. Chou SH, Kicska GA, Pipavath SN, Reddy GP. Digital tomosynthesis of the chest: current and emerging applications. Radiographics. 2014;34(2):359–72.
17. Sone S, Kasuga T, Sakai F, Oguchi K, Itoh A, Li F, et al. Digital tomosynthesis imaging of the lung. Radiat Med. 1996;14(2):53–63.
18. Kamimura R, Takashima T. Clinical application of single dual-energy subtraction technique with digital storage-phosphor radiography. J Digit Imaging. 1995;8(1 Suppl 1):21–4.
19. Kazerooni EA. High-resolution CT of the lungs. AJR Am J Roentgenol. 2001;177(3):501–19.
20. ACR–STR practice parameter for the performance of high-resolution computed tomography (HRCT) of the lungs in adults. 2020. www.acr.org.
21. Gossner J, Nau R. Geriatric chest imaging: when and how to image the elderly lung, age-related changes, and common pathologies. Radiol Res Pract. 2013;2013:584793.
22. Bankier AA, Fleischmann D, Mallek R, Windisch A, Winkelbauer FW, Kontrus M, et al. Bronchial wall thickness: appropriate window settings for thin-section CT and radiologic-anatomic correlation. Radiology. 1996;199(3):831–6.
23. Kubo T. Vendor free basics of radiation dose reduction techniques for CT. Eur J Radiol. 2019;110:14–21.
24. Ohno Y, Koyama H, Seki S, Kishida Y, Yoshikawa T. Radiation dose reduction techniques for chest CT: principles and clinical results. Eur J Radiol. 2019;111:93–103.
25. Gibellino F, Osmanliev DP, Watson A, Pride NB. Increase in tracheal size with age. Implications for maximal expiratory flow. Am Rev Respir Dis. 1985;132(4):784–7.
26. Breatnach E, Abbott GC, Fraser RG. Dimensions of the normal human trachea. AJR Am J Roentgenol. 1984;142(5):903–6.
27. Collins DV, Cutillo AG, Armstrong JD, Crapo RO, Kanner RE, Tocino I, et al. Large airway size, lung size, and maximal expiratory flow in healthy nonsmokers. Am Rev Respir Dis. 1986;134(5):951–5.
28. Sakai H, Nakano Y, Muro S, Hirai T, Takubo Y, Oku Y, et al. Age-related changes in the trachea in healthy adults. Adv Exp Med Biol. 2010;662:115–20.
29. O'Donnell CR, Litmanovich D, Loring SH, Boiselle PM. Age and sex dependence of forced expiratory central airway collapse in healthy volunteers. Chest. 2012;142(1):168–74.
30. Mitropoulos A, Song WJ, Almaghlouth F, Kemp S, Polkey M, Hull JH. Detection and diagnosis of large airway collapse: a systematic review. ERJ Open Res. 2021;7(3).
31. Edge JR, Millard FJ, Reid L, Simon G. The radiographic appearances of the chest in persons of advanced age. Br J Radiol. 1964;37:769–74.
32. Lloyd DC, Taylor PM. Calcification of the intrathoracic trachea demonstrated by computed tomography. Br J Radiol. 1990;63(745):31–2.
33. Moncada RM, Venta LA, Venta ER, Fareed J, Walenga JM, Messmore HL. Tracheal and bronchial cartilaginous rings: warfarin sodium-induced calcification. Radiology. 1992;184(2):437–9.
34. Webb EM, Elicker BM, Webb WR. Using CT to diagnose nonneoplastic tracheal abnormalities: appearance of the tracheal wall. AJR Am J Roentgenol. 2000;174(5):1315–21.
35. Matsuoka S, Uchiyama K, Shima H, Ueno N, Oish S, Nojiri Y. Bronchoarterial ratio and bronchial wall thickness on high-resolution CT in asymptomatic subjects: correlation with age and smoking. AJR Am J Roentgenol. 2003;180(2):513–8.
36. Copley SJ, Wells AU, Hawtin KE, Gibson DJ, Hodson JM, Jacques AE, et al. Lung morphology in the elderly: comparative CT study of subjects over 75 years old versus those under 55 years old. Radiology. 2009;251(2):566–73.
37. Telenga ED, Oudkerk M, van Ooijen PM, Vliegenthart R, Ten Hacken NH, Postma DS, et al. Airway wall thickness on HRCT scans decreases with age and increases with smoking. BMC Pulm Med. 2017;17(1):27.

38. Reinhardt JM, D'Souza ND, Hoffman EA. Accurate measurement of intrathoracic airways. IEEE Trans Med Imaging. 1997;16(6):820–7.
39. Zach JA, Newell JD Jr, Schroeder J, Murphy JR, Curran-Everett D, Hoffman EA, et al. Quantitative computed tomography of the lungs and airways in healthy nonsmoking adults. Invest Radiol. 2012;47(10):596–602.
40. Castaner E, Gallardo X, Pallardo Y, Branera J, Cabezuelo MA, Mata JM. Diseases affecting the peribronchovascular interstitium: CT findings and pathologic correlation. Curr Probl Diagn Radiol. 2005;34(2):63–75.
41. Silva M, Milanese G, Seletti V, Ariani A, Sverzellati N. Pulmonary quantitative CT imaging in focal and diffuse disease: current research and clinical applications. Br J Radiol. 2018;91(1083):20170644.
42. Hansell DAP, Lynch DA, et al. Imaging of diseases of the chest. Amsterdam: Elsevier; 2005. p. 143–81.
43. Lynch DA, Newell JD, Tschomper BA, Cink TM, Newman LS, Bethel R. Uncomplicated asthma in adults: comparison of CT appearance of the lungs in asthmatic and healthy subjects. Radiology. 1993;188(3):829–33.
44. Kim JS, Muller NL, Park CS, Lynch DA, Newman LS, Grenier P, et al. Bronchoarterial ratio on thin section CT: comparison between high altitude and sea level. J Comput Assist Tomogr. 1997;21(2):306–11.
45. Diaz AA, Young TP, Maselli DJ, Martinez CH, Maclean ES, Yen A, et al. Bronchoarterial ratio in never-smokers adults: implications for bronchial dilation definition. Respirology. 2017;22(1):108–13.
46. Mohamed Hoesein FA, de Jong PA. Air trapping on computed tomography: regional versus diffuse. Eur Respir J. 2017;49(1).
47. Hansell DM, Bankier AA, MacMahon H, McLoud TC, Muller NL, Remy J. Fleischner Society: glossary of terms for thoracic imaging. Radiology. 2008;246(3):697–722.
48. Kligerman SJ, Henry T, Lin CT, Franks TJ, Galvin JR. Mosaic attenuation: etiology, methods of differentiation, and pitfalls. Radiographics. 2015;35(5):1360–80.
49. Mastora I, Remy-Jardin M, Sobaszek A, Boulenguez C, Remy J, Edme JL. Thin-section CT finding in 250 volunteers: assessment of the relationship of CT findings with smoking history and pulmonary function test results. Radiology. 2001;218(3):695–702.
50. Tanaka N, Matsumoto T, Miura G, Emoto T, Matsunaga N, Ueda K, et al. Air trapping at CT: high prevalence in asymptomatic subjects with normal pulmonary function. Radiology. 2003;227(3):776–85.
51. Lee KW, Chung SY, Yang I, Lee Y, Ko EY, Park MJ. Correlation of aging and smoking with air trapping at thin-section CT of the lung in asymptomatic subjects. Radiology. 2000;214(3):831–6.
52. Martinez CH, Diaz AA, Meldrum C, Curtis JL, Cooper CB, Pirozzi C, et al. Age and small airway imaging abnormalities in subjects with and without airflow obstruction in SPIROMICS. Am J Respir Crit Care Med. 2017;195(4):464–72.
53. Verleden SE, Kirby M, Everaerts S, Vanstapel A, McDonough JE, Verbeken EK, et al. Small airway loss in the physiologically ageing lung: a cross-sectional study in unused donor lungs. Lancet Respir Med. 2021;9(2):167–74.
54. Well DS, Meier JM, Mahne A, Houseni M, Hernandez-Pampaloni M, Mong A, et al. Detection of age-related changes in thoracic structure and function by computed tomography, magnetic resonance imaging, and positron emission tomography. Semin Nucl Med. 2007;37(2):103–19.
55. Soejima K, Yamaguchi K, Kohda E, Takeshita K, Ito Y, Mastubara H, et al. Longitudinal follow-up study of smoking-induced lung density changes by high-resolution computed tomography. Am J Respir Crit Care Med. 2000;161(4 Pt 1):1264–73.
56. Rosenblum LJ, Mauceri RA, Wellenstein DE, Thomas FD, Bassano DA, Raasch BN, et al. Density patterns in the normal lung as determined by computed tomography. Radiology. 1980;137(2):409–16.

57. Copley SJ, Giannarou S, Schmid VJ, Hansell DM, Wells AU, Yang GZ. Effect of aging on lung structure in vivo: assessment with densitometric and fractal analysis of high-resolution computed tomography data. J Thorac Imaging. 2012;27(6):366–71.
58. Marsh S, Aldington S, Williams MV, Nowitz MR, Kingzett-Taylor A, Weatherall M, et al. Utility of lung density measurements in the diagnosis of emphysema. Respir Med. 2007;101(7):1512–20.
59. Yang T, Chen C, Chen Z. The CT pulmonary vascular parameters and disease severity in COPD patients on acute exacerbation: a correlation analysis. BMC Pulm Med. 2021;21(1):34.
60. Miravitlles M, Calle M, Soler-Cataluna JJ. Clinical phenotypes of COPD: identification, definition and implications for guidelines. Arch Bronconeumol. 2012;48(3):86–98.
61. Mitzner W. Emphysema—a disease of small airways or lung parenchyma? N Engl J Med. 2011;365(17):1637–9.
62. Janssens JP, Pache JC, Nicod LP. Physiological changes in respiratory function associated with ageing. Eur Respir J. 1999;13(1):197–205.
63. Verbeken EK, Cauberghs M, Mertens I, Clement J, Lauweryns JM, Van de Woestijne KP. The senile lung. Comparison with normal and emphysematous lungs. 2. Functional aspects. Chest. 1992;101(3):800–9.
64. Rabe KF, Hurd S, Anzueto A, Barnes PJ, Buist SA, Calverley P, et al. Global strategy for the diagnosis, management, and prevention of chronic obstructive pulmonary disease: GOLD executive summary. Am J Respir Crit Care Med. 2007;176(6):532–55.
65. Gevenois PA, De Vuyst P, Sy M, Scillia P, Chaminade L, de Maertelaer V, et al. Pulmonary emphysema: quantitative CT during expiration. Radiology. 1996;199(3):825–9.
66. Cavigli E, Camiciottoli G, Diciotti S, Orlandi I, Spinelli C, Meoni E, et al. Whole-lung densitometry versus visual assessment of emphysema. Eur Radiol. 2009;19(7):1686–92.
67. Park J, Hobbs BD, Crapo JD, Make BJ, Regan EA, Humphries S, et al. Subtyping COPD by using visual and quantitative CT imaging features. Chest. 2020;157(1):47–60.
68. Occhipinti M, Paoletti M, Bartholmai BJ, Rajagopalan S, Karwoski RA, Nardi C, et al. Spirometric assessment of emphysema presence and severity as measured by quantitative CT and CT-based radiomics in COPD. Respir Res. 2019;20(1):101.
69. Gierada DS, Guniganti P, Newman BJ, Dransfield MT, Kvale PA, Lynch DA, et al. Quantitative CT assessment of emphysema and airways in relation to lung cancer risk. Radiology. 2011;261(3):950–9.
70. Lynch DA, Austin JH, Hogg JC, Grenier PA, Kauczor HU, Bankier AA, et al. CT-definable subtypes of chronic obstructive pulmonary disease: a statement of the Fleischner Society. Radiology. 2015;277(1):192–205.
71. Araki T, Nishino M, Gao W, Dupuis J, Putman RK, Washko GR, et al. Pulmonary cysts identified on chest CT: are they part of aging change or of clinical significance? Thorax. 2015;70(12):1156–62.
72. Polverino E, Goeminne PC, McDonnell MJ, Aliberti S, Marshall SE, Loebinger MR, et al. European Respiratory Society guidelines for the management of adult bronchiectasis. Eur Respir J. 2017;50(3).
73. Heidinger BH, Occhipinti M, Eisenberg RL, Bankier AA. Imaging of large airways disorders. AJR Am J Roentgenol. 2015;205(1):41–56.
74. Aliberti S, Lonni S, Dore S, McDonnell MJ, Goeminne PC, Dimakou K, et al. Clinical phenotypes in adult patients with bronchiectasis. Eur Respir J. 2016;47(4):1113–22.
75. Winter DH, Manzini M, Salge JM, Busse A, Jaluul O, Jacob Filho W, et al. Aging of the lungs in asymptomatic lifelong nonsmokers: findings on HRCT. Lung. 2015;193(2):283–90.
76. Cartier Y, Kavanagh PV, Johkoh T, Mason AC, Muller NL. Bronchiectasis: accuracy of high-resolution CT in the differentiation of specific diseases. AJR Am J Roentgenol. 1999;173(1):47–52.
77. Habesoglu MA, Ugurlu AO, Eyuboglu FO. Clinical, radiologic, and functional evaluation of 304 patients with bronchiectasis. Ann Thorac Med. 2011;6(3):131–6.
78. McGuinness G, Naidich DP. CT of airways disease and bronchiectasis. Radiol Clin North Am. 2002;40(1):1–19.

79. Naidich DP, McCauley DI, Khouri NF, Stitik FP, Siegelman SS. Computed tomography of bronchiectasis. J Comput Assist Tomogr. 1982;6(3):437–44.
80. Ooi GC, Khong PL, Chan-Yeung M, Ho JC, Chan PK, Lee JC, et al. High-resolution CT quantification of bronchiectasis: clinical and functional correlation. Radiology. 2002;225(3):663–72.
81. Reiff DB, Wells AU, Carr DH, Cole PJ, Hansell DM. CT findings in bronchiectasis: limited value in distinguishing between idiopathic and specific types. AJR Am J Roentgenol. 1995;165(2):261–7.
82. Singh A, Bhalla AS, Jana M. Bronchiectasis revisited: imaging-based pattern approach to diagnosis. Curr Probl Diagn Radiol. 2019;48(1):53–60.
83. Reich JM, Johnson RE. Mycobacterium avium complex pulmonary disease presenting as an isolated lingular or middle lobe pattern. The Lady Windermere syndrome. Chest. 1992;101(6):1605–9.
84. Leong P, Tran A, Rangaswamy J, Ruane LE, Fernando MW, MacDonald MI, et al. Expiratory central airway collapse in stable COPD and during exacerbations. Respir Res. 2017;18(1):163.
85. Dal Negro RW, Tognella S, Guerriero M, Micheletto C. Prevalence of tracheobronchomalacia and excessive dynamic airway collapse in bronchial asthma of different severity. Multidiscip Respir Med. 2013;8(1):32.
86. Nuutinen J. Acquired tracheobronchomalacia. Eur J Respir Dis. 1982;63(5):380–7.
87. Ridge CA, O'Donnell CR, Lee EY, Majid A, Boiselle PM. Tracheobronchomalacia: current concepts and controversies. J Thorac Imaging. 2011;26(4):278–89.
88. Feist JH, Johnson TH, Wilson RJ. Acquired tracheomalacia: etiology and differential diagnosis. Chest. 1975;68(3):340–5.
89. Rayl JE. Tracheobronchial collapse during cough. Radiology. 1965;85:87–92.
90. Boiselle PM, Michaud G, Roberts DH, Loring SH, Womble HM, Millett ME, et al. Dynamic expiratory tracheal collapse in COPD: correlation with clinical and physiologic parameters. Chest. 2012;142(6):1539–44.
91. Lomasney L, Bergin CJ, Lomasney J, Roggli V, Foster W. CT appearance of lunate trachea. J Comput Assist Tomogr. 1989;13(3):520–2.
92. Boiselle PM, Feller-Kopman D, Ashiku S, Weeks D, Ernst A. Tracheobronchomalacia: evolving role of dynamic multislice helical CT. Radiol Clin North Am. 2003;41(3):627–36.
93. Boiselle PM, Ernst A. Tracheal morphology in patients with tracheomalacia: prevalence of inspiratory lunate and expiratory "frown" shapes. J Thorac Imaging. 2006;21(3):190–6.
94. Leong P, Bardin PG, Lau KK. What's in a name? Expiratory tracheal narrowing in adults explained. Clin Radiol. 2013;68(12):1268–75.
95. Baroni RH, Feller-Kopman D, Nishino M, Hatabu H, Loring SH, Ernst A, et al. Tracheobronchomalacia: comparison between end-expiratory and dynamic expiratory CT for evaluation of central airway collapse. Radiology. 2005;235(2):635–41.
96. Wright CD. Tracheomalacia. Chest Surg Clin N Am. 2003;13(2):349–57, viii.
97. Alshabani K, Ghosh S, Arrossi AV, Mehta AC. Broncholithiasis: a review. Chest. 2019;156(3):445–55.
98. Jin YX, Jiang GN, Jiang L, Ding JA. Diagnosis and treatment evaluation of 48 cases of broncholithiasis. Thorac Cardiovasc Surg. 2016;64(5):450–5.
99. Cerfolio RJ, Bryant AS, Maniscalco L. Rigid bronchoscopy and surgical resection for broncholithiasis and calcified mediastinal lymph nodes. J Thorac Cardiovasc Surg. 2008;136(1):186–90.
100. Vix VA. Radiographic manifestations of broncholithiasis. Radiology. 1978;128(2):295–9.
101. Lim SY, Lee KJ, Jeon K, Koh WJ, Suh GY, Chung MP, et al. Classification of broncholiths and clinical outcomes. Respirology. 2013;18(4):637–42.
102. Seo JB, Song KS, Lee JS, Goo JM, Kim HY, Song JW, et al. Broncholithiasis: review of the causes with radiologic-pathologic correlation. Radiographics. 2002;22 Spec No:S199–213.
103. Ahn JM, Im JG, Seo JW, Han HS, Yoon HK, Kim WS, et al. Endobronchial hamartoma: CT findings in three patients. AJR Am J Roentgenol. 1994;163(1):49–50.
104. Gayer G. Tracheal diverticula. Semin Ultrasound CT MR. 2016;37(3):190–5.

105. Polat AV, Elmali M, Aydin R, Ozbay A, Celenk C, Murat N. Paratracheal air cysts: prevalence and correlation with lung diseases using multi-detector CT. J Med Imaging Radiat Oncol. 2014;58(2):144–8.
106. Shah M, Joshi JM. Tracheal diverticulum. Indian J Chest Dis Allied Sci. 2012;54(1):39–40.
107. Mackinnon D. Tracheal diverticula. J Pathol Bacteriol. 1953;65(2):513–7.
108. Caversaccio MD, Becker M, Zbaren P. Tracheal diverticulum presenting with recurrent laryngeal nerve paralysis. Ann Otol Rhinol Laryngol. 1998;107(4):362–4.
109. Gupta A, Shah A. Bronchial anthracofibrosis: an emerging pulmonary disease due to biomass fuel exposure. Int J Tuberc Lung Dis. 2011;15(5):602–12.
110. Pilaniya V, Kunal S, Shah A. Occurrence of bronchial anthracofibrosis in respiratory symptomatics with exposure to biomass fuel smoke. Adv Respir Med. 2017;85(3):127–35.
111. Kim YJ, Jung CY, Shin HW, Lee BK. Biomass smoke induced bronchial anthracofibrosis: presenting features and clinical course. Respir Med. 2009;103(5):757–65.
112. Shah A, Kunal S, Gothi R. Bronchial anthracofibrosis: the spectrum of radiological appearances. Indian J Radiol Imaging. 2018;28(3):333–41.
113. Kahkouee S, Pourghorban R, Bitarafan M, Najafizadeh K, Makki SS. Imaging findings of isolated bronchial anthracofibrosis: a computed tomography analysis of patients with bronchoscopic and histologic confirmation. Arch Bronconeumol. 2015;51(7):322–7.
114. Kim HY, Im JG, Goo JM, Kim JY, Han SK, Lee JK, et al. Bronchial anthracofibrosis (inflammatory bronchial stenosis with anthracotic pigmentation): CT findings. AJR Am J Roentgenol. 2000;174(2):523–7.

Neoplastic Diseases of the Respiratory System in Geriatric Patients

8

Zeno Falaschi, Francesco Filippone, Sergio Pansini, Stefano Tricca, Paola Basile, Sara Cesano, and Alessandro Carriero

8.1 Epidemiology

Lung cancer is the most common cancer in the world and the leading cause of cancer-related deaths in both Western countries and the United States, with the fastest-growing morbidity and mortality, especially in the elderly [1].

According to the latest statistics updated to 2020 of the American Cancer Society, there will be 235,760 estimated new cases of lung cancer in 2021, of which 119,100 cases in male and 116,660 in females; on the other hand, the age-adjusted death rate for lung cancer is higher for men (46.7 per 100,000 persons) than for women (31.9 per 100,000 persons). This means that more men are diagnosed with lung cancer each year, but more women live with the disease. In addition, these data also confirm that lung cancer is mostly a disease of the elderly, with a growing incidence from 0.6% (in the age range from 50 to 59 years), to 5.4% (from 70 years and older) [2].

Lung cancer refers to a histologically and clinically diverse group of malignancies arising in the respiratory tract, primarily but not exclusively in cells lining the airways of the lung. The four principal types, classified by light microscopy and special stains, are non-small-cell lung cancer (NSCLC), which is the most common type and it constitutes between 80% and 85% of all lung cancers, adenocarcinoma, small-cell carcinoma (SCLC), and squamous cell carcinoma. Unfortunately, at the time of diagnosis, the majority of patients already have metastatic disease, and a systemic, palliative treatment is the primary therapeutic option. More than 50% of advanced NSCLCs are diagnosed in patients older than age 65 years [3].

Z. Falaschi · F. Filippone · S. Pansini · S. Tricca · P. Basile · S. Cesano · A. Carriero (✉)
Department of Diagnosis and Treatment Services, Radiodiagnostics, Azienda Ospedaliero Universitaria Maggiore della Carità, Novara, Italy
e-mail: 20032825@studenti.uniupo.it; alessandro.carriero@med.uniupo.it

G. Guglielmi, M. Maas (eds.), *Imaging in Geriatrics*, Practical Issues in Geriatrics, https://doi.org/10.1007/978-3-031-14877-4_8

8.1.1 The Role of Aging

There is worldwide-accepted evidence of a population shift toward older ages: the current life expectancy in the United States is 78.7 years compared to 49 years in 1900. By the second half of this century, more than 20% of the population will be older than 65 years, and this increased life expectancy reflects, in part, a better understanding of the diseases, new interventions, and the success of public health programs [4].

The open question is what age cutoff should be used to define "elderly." In Europe and in the USA, an age greater than 70 years is accepted to define this variable. However, some authors define elderly patients in geriatric oncology as "old" when their clinical status starts to interfere with oncologic decision-making [5].

Clearly, this shift favors an increased risk of developing disorders that are more common at a more advanced age and lung cancer is one of them, since it is primarily a disease of older populations with less than 0.5% of lung cancer-related deaths registered at an age younger than 40 years [6].

Recent Surveillance, Epidemiology, and End Results data in the United States suggest that the median age at diagnosis of lung cancer is 70 years and, what is more, in the last decade, the incidence and the mortality from lung cancer have decreased among individuals aged 50 years and younger but have increased among those aged 70 years and older [7].

Aging is inextricably linked to physiologic changes in functional status, organ function, and drug pharmacokinetics. For example, it is associated with decreases in marrow reserve, drug clearance, and lean body mass. Furthermore, concomitant comorbidities that affect functional status, general health, and tumor symptoms are frequently present in this patient population and therefore the selection of their optimal treatment is daunted. This risk is also increased by one of the major problems in current practice, which is that the elderly are often excluded from participation in clinical trials and receive untested or inadequate treatment based on the long-held but completely unsubstantiated notion that cancer in older people is less aggressive and that older patients are inherently incapable of tolerating the exigencies of treatment, leading often to a substantial undertreatment of these patients [8].

8.1.2 Risk Factors

The rising incidence of lung cancer through the first half of the twentieth century prompted intensive epidemiologic investigations of the disease, resulting in the identification of a number of causal agents. Cigarette smoking is by far the largest cause of lung cancer, and the worldwide epidemic of lung cancer is largely attributable to smoking. However, occupational exposures, including asbestos, uranium, and coke (an important fuel in the manufacture of iron in smelters, blast furnaces, and foundries), have placed a number of worker groups at high risk, and some of these occupational agents are synergistic with smoking in increasing lung cancer risks [7].

In fact, nonsmoking asbestos workers are five times more likely to develop lung cancer than nonsmokers not exposed to asbestos; if they also smoke, the risk factor jumps to 50 or higher [9].

Furthermore there is some evidence that both indoor and outdoor air pollution also increases lung cancer risks, specifically exposure to radon is estimated to be the second-leading cause of lung cancer, accounting for an estimated 21,000 lung cancer deaths each year (range of 8000–45,000). Radon is a tasteless, colorless, and odorless gas that is produced by decaying uranium and occurs naturally in soil and rock. The majority of these deaths occur among smokers since there is a greater risk for lung cancer when smokers also are exposed to radon [7].

In addition, observational evidence showing a familial aggregation of lung cancer has suggested that genetic factors also may determine risks in smokers, but the specific genes remain under active investigation [8].

8.1.2.1 Smoke as the Main Risk Factor

Smoking has been shown to cause each of the major histologic types, although a dose–response relationship with the number of cigarettes smoked varies across types, being steepest for small cell carcinoma.

The causal link between smoking and lung cancer has been extensively investigated at the molecular and cellular levels, and there is nowadays a quickly expanding body of evidence that shows that the effects of tobacco smoke on cellular DNA are quite consistent with the current conceptual model of carcinogenesis—a multistep process of genetic change. Lung cancers have been estimated to have more than 10 and perhaps as many as 20 genetic changes before any individual clonal tumor emerges [10].

However, 40 years after smoking was first identified as a cause of lung cancer, it remains a leading cause of cancer and of death from cancer. During the 1990s deaths attributable to lung cancer declined significantly in men, while mortality rates in women continued to increase. These patterns of incidence and mortality reflect changes in smoking behaviors among US adults that occurred decades ago: (National Cancer Institute (NCI) 1997). The smoking habit declined faster among men than among women starting from the 1950s, and therefore the recent changes in lung cancer incidence rates reflect these previous smoking attitudes [11].

Prior reports have fully described the variation of lung cancer risk with aspects of smoking [12]. In smokers, the risk of lung cancer depends largely on the duration of smoking and the number of cigarettes smoked. The excess risks for smokers, compared with people who have never smoked, are remarkably high. Many studies provide RR estimates for developing lung cancer of 20 or higher for smokers compared with lifetime nonsmokers. What is more, a risk-free level of smoking has not been identified, and even involuntary exposure to tobacco smoke (second-hand smoke) increases lung cancer risks for nonsmokers. Instead, lung cancer risk decreases with successful cessation and maintained abstinence: in fact the data show that the RR for lung cancer among former smokers continues to decline as the duration of not smoking increases in comparison with the risk among continuing smokers, although it never reaches the level of risk of those

who have never smoked, even after 15–20 years of not smoking. Extensive data convincingly show how smoking cessation lowers lung cancer risks: using data from a 1990 case-control study, [13] estimated cumulative lung cancer risks for persons up to 75 years of age. The estimated lifetime risk of lung cancer deaths for men who continue to smoke, absent death from another cause, was 16%. Substantial reductions in this risk can be achieved by cessation at younger ages; even cessation at 60 years of age lowered the cumulative risk from 16% to about 10% [14].

Since the first research reports linking smoking to lung cancer and other diseases, the tobacco industry has continually changed the characteristics of the cigarette. These changes have included the addition of filter tips, perforation of the filter tips, use of reconstituted tobacco, and changes in the paper and in additives. Nevertheless, even though during the last 50 years characteristics of cigarettes have changed and yields of tar and nicotine have declined substantially, as assessed by the Federal Trade Commission's test protocol, the risk of lung cancer in smokers has not declined and the benefits are minimal in comparison with giving up cigarettes entirely [15].

The single most effective way to reduce hazards of smoking continues to be that of quitting entirely and the general pattern of this decline is the same for men and women, for smokers of filter-tipped and unfiltered cigarettes, and for all major histologic types of lung cancer [15].

In conclusion, despite the gains in understanding respiratory carcinogenesis and the potential of molecular and imaging techniques to screen for lung cancer, smoking prevention and cessation remain the fundamental strategies for controlling the lung cancer epidemic.

8.1.3 Clinical Symptoms of Lung Cancer

One of the biggest problems in lung cancer diagnosis is that the symptoms are shared with many benign pulmonary diseases and that they actually are more common in these pathologies.

As a matter of fact, lung cancer is usually asymptomatic in the early stages and this often leads to a delay in the diagnosis, that occurs when the tumor is already in an advanced stage.

Therefore, its symptoms are present only in a minority of the patients, are nonspecific, and appear only when the tumor has already spread.

Clinical presentation is heterogeneous, and it is caused by the local tumor growth, the intrathoracic spread, and the distant spreading. It also depends on the tumor type and its specific location and behavior. In fact, small-cell lung cancer (SCLC) generally arises in the central part of the lung, penetrates into the mediastinum, and consequently is more commonly associated with invasive symptoms. On the contrary, non-small-cell lung cancer (NSCLC) is usually located in the peripheral lung, and it is characterized by less specific symptoms [9].

For what concerns local growth-related lung cancer symptoms, they mainly consist of cough, dyspnea, wheeze, and hemoptysis.

Specifically, cough, which is caused by the obstruction of the airways, is the most common symptom. It is present in almost 50% of the patients, and it is more frequently associated with SCLC, since this tumor type is mainly located on larger bronchi. Although cough is not specific for this pathology, with no doubt a new and persistent cough in active or past smokers should raise concern for lung cancer. In addition, recurrent pneumonia in the same anatomic region as well as frequent exacerbation of chronic obstructive pulmonary disease should be considered as alarm signs [9].

On the other hand, hemoptysis is the most specific symptom, especially when associated with others. This also has a higher positive predictive value compared to the other symptoms. For this reason, every patient with hemoptysis should perform a chest X-ray.

For what concerns symptoms related to the intrathoracic spread, these are caused by the invasion of the tumor into the mediastinal structures and mainly consist of chest pain, vocal cord paralysis, superior vena cava syndrome (SVC), and dysphagia.

In particular, SVC syndrome is caused by the obstruction of the vena cava by the primary tumor or by enlarged lymph nodes or thrombus. It generally presents with edema of the upper body.

Instead, vocal cord paralysis and dysphagia are caused by the invasion of the recurrent laryngeal nerve and of the esophagus.

On the contrary, symptoms associated with the distant spreading of lung cancer have mostly the same frequency in SCLC and NSCLC [10].

The most common metastatic sites are brain, liver, adrenal gland, bones, and bone marrow. The central nervous system involvement frequently manifests with headache, seizure, altered mental status; while bone metastases present with bone pain, and liver metastases with anemia and weight loss.

In conclusion, lung cancer can also be associated with paraneoplastic syndromes with SCLC as the most common cause [16]. Among these conditions, the most frequent ones are syndrome of inappropriate antidiuresis, Cushing's syndrome, and hypercalcemia. In addition, SCLC can also be associated with neurologic syndromes such as Lambert-Eaton and Limbic encephalitis.

8.1.4 Lung Cancer Diagnosis: General Features

The diagnosis of lung cancer can be done through chest X-ray, computed tomography (CT) scans, magnetic resonance (MRI), positron emission tomography (PET), cytology sputum, and breath analysis.

All the available detection techniques of lung cancer have different detection levels and various markers. Nevertheless, it is often impossible to radiographically distinguish between the several histological lung cancer types.

8.1.4.1 Chest X-Ray

Lung cancer is relatively infrequently found on **chest X-rays** due to the combination of difficulty in visualizing small lesions. The diagnostic confidence is the greatest when the lesion is at least 8–10 mm [17].

Often it is impossible to radiographically distinguish between other histological lung cancer types.

The appearance is related to the location of the tumor. Central lesions may appear as a bulky hilum. Lobar collapse may be present when a bronchus is obstructed [18].

A more peripheral location may appear as a rounded or spiculated mass. Cavitation may be seen as an air-fluid level.

Pleural effusion may also be seen, and it might be caused by either tumor diffusion or venous obstruction [19].

8.1.4.2 Computed Tomography

The volumetric high-resolution CT (HRCT) is the gold standard for detecting and characterizing lung lesions, eventually followed by iodine contrast infusion [20].

The low-dose CT is currently performed in PET-CT studies, or in a screening setting.

Patients with suspected lung cancer should undergo a volumetric CT scan with HR reconstructions even if the X-ray is normal.

While CT is a very sensitive method for establishing a detailed lymph node map, its specificity is insufficient to determine whether the lymph nodes are malignant or benign. Therefore, PET-CT is the gold standard [20].

Typically, a benign solitary pulmonary nodule (SPN) is smaller than 20 mm, has regular contours, with low density values (e.g., fat or fluid), remains stable in dimensions after 2 years, and does not show significant contrast enhancement [21].

Signs of malignancy usually consist of large dimensions (more than 30 mm), irregular or spiculated contours with distortion of near vessels, peripheral ground glass opacity (halo sign), may contain diffuse and small calcifications, volume doubling time (VDT) of about 30–400 days, and show intense and rapid contrast enhancement [22].

A lung nodule is a rounded or irregular region of increased attenuation. The amount of attenuation can further classify the nodules as ground glass, subsolid, or solid [23, 24].

Some types of lung cancer can show peculiarities.

The *small-cell lung cancer (SCLC)* can be central (60–70%) or peripheric (30–40%). The latter is typically asymptomatic, has round shape and irregular contours with a pleural tail. The bigger ones show central necrosis and/or excavation.

The central tumors extend into the mediastinal space and are usually rapidly symptomatic. They show up as endo-bronchial masses with amorphous calcifications.

This tumor can rapidly spread through the lymphatic and hemic ways [16, 25].

The *carcinoid tumor* is usually central, endo-bronchial located, determining complete luminal-obstruction and lobar atelectasis or air trapping. It is often 2–5 cm large, has regular margins with micro-calcifications, highly vascularized

with intense contrast-enhancement. It has a slow growth so can reach very large dimensions and can spread through the extra-bronchial space. Rarely it is peripheric.

The *adenocarcinoma* may show different features based on the subtypes: the *pre-invasive* in situ *minimally invasive* adenocarcinoma and the invasive *lepidic predominant-adenocarcinoma* (formerly called bronchiolo-alveolar carcinoma, BAC) often consist of ground glass nodule or a subsolid nodule with a predominant ground glass component, while the remaining invasive subtypes of adenocarcinoma usually show up as a solid or subsolid nodule.

The invasive mucinous adenocarcinoma subtype (also formerly mucinous BAC) can have a variable appearance, including consolidation, air bronchograms, or multifocal subsolid nodules or masses [26].

Nuclear Medicine

FDG-PET/CT is essential for the lung cancer staging, since it can assess for the nodal and distant metastatic disease.

Adenocarcinoma in situ, low-grade adenocarcinomas and minimally invasive adenocarcinoma are commonly associated with PET false-negative results.

FDG PET/CT is recommended when assessing subsolid ground glass lung lesions that have a solid component measuring more than 8 mm [20].

8.2 Lung Cancer: Role of the Chest X-Ray

8.2.1 Chest X-Ray: Role in Screening and Diagnosis of Lung Cancer

Chest X-ray has a fundamental role in the diagnosis of many pulmonary diseases. Due to its low cost, availability, and low radiation, it is usually the first exam performed in order to diagnose lung pathologies. It is the first-line investigation in patients with suspected lung cancer.

Lung cancer diagnosis may occur because of an incidental finding in an asymptomatic patient that performs the exam for other reasons, in a symptomatic patient or as an unexpected evolution from pneumonia, atelectasis, or pleural effusion.

Chest X-ray is often the first performed exam, but it is not the most sensitive imaging technique. CT scan is considered the preferred exam to have a proper diagnosis and staging of the disease.

In fact chest X-ray sensitivity of lung nodule detection when it is <6 mm is very low, but it increases when the nodule is calcified. The sensitivity is about 50% when the nodule diameter is 6–10 mm [27].

Having an early diagnosis of lung cancer is associated with an improved survival; therefore, multiple studies have been performed to investigate the role of chest X-ray in screening. Unfortunately, no study has demonstrated a reduction in mortality connected to this exam. It has been shown that this technique fails to at least initially detect lung cancer in more than 20% of patients.

The missed diagnosis may be related to "observer error," to poor technique quality, but also to the dimension of the tumor. In fact, if it is less than 1 cm it can be easily not detected. In addition, the location of the tumor may play a role, especially when this is in the upper lobes where it can be masked by anatomical structures such as ribs and vessels.

For these reasons, CT scan is the preferred technique to diagnose this disease [20].

8.2.2 Radiological Characteristics Based on Cellular Type

Lung cancer may present in different ways on chest X-ray: as a nodule, a mass, an enlarged mediastinum, atelectasis, and pleural effusion.

Based on the cellular type of tumor, we can have different radiological characteristics. However the histological subtype cannot be correctly identified solely on the basis of chest X-ray, and a confirmative biopsy is always needed.

8.2.2.1 Adenocarcinoma

Adenocarcinoma is 31% of all lung cancers. It is usually peripherally located and measures less than 4 cm. It is associated with detection of hila and/or mediastinal enlargement on chest X-ray in 51% of cases.

8.2.2.2 Adenosquamous Carcinoma

This is only 2% of all lung cancers and normally presents as solitary and peripheral nodule. Cavitation may be seen.

8.2.2.3 Squamous Cell Carcinoma

Squamous cell carcinoma is 30% of all lung cancers and is usually centrally located, is often >4 cm and cavitation is frequently present.

8.2.2.4 Small-Cell Lung Cancer

It represents 18% of lung cancers and often present as bulky hila and mediastinal lymph node masses.

8.2.2.5 Carcinoid Tumor

It is 1% of all lung cancers, and it is usually <2.5 cm and often associated with obstructive pneumonia.

8.2.2.6 Large-Cell Lung Cancer

It is 9% of all lung cancers and is a histological diagnosis of exclusion [27].

8.2.3 Pulmonary Nodules and Masses

Pulmonary nodules are a very frequent finding on chest X-ray and their prevalence ranges from 0.09% to 0.2%.

A solitary nodule presents as a well-defined, rounded opacity that measures less or equal to 3 cm in diameter. Lesions larger than 3 cm are defined as masses. Solitary pulmonary nodules are benign in 60–70% of cases.

Of course when a lung nodule is detected the first thing to do is trying to understand whether this is benign or malignant. To do this, some parameters need to be evaluated: the velocity of growth, the margins, the dimensions, and the presence of cavitation and satellite nodules.

Benign lung tumors are not common, and the diagnosis often is histologically made. They include hamartomas, papillomas, lipomas, neurofibromas, and endometriosis [17].

8.2.3.1 Velocity of Growth

Benign tumors usually grow in years, active granulomas in weeks, whereas malignant nodules double their diameter in 2–18 months. We can say that a nodule has doubled when its diameter is increased by 1.25 times. For these reasons, comparison with precedent exams is essential during the evaluation of a pulmonary nodule [18].

8.2.3.2 Margins

The margin characteristics may give an indication of a nodule's nature. Regular and smooth margins are usually considered as suggestive of benign disease but in some cases may be present also in malignant nodules. Irregular, ill-defined, lobulated and spiculated margins are indicative of malignancy [21].

8.2.3.3 Dimensions and Cavitation

The dimensions of the nodule are helpful to predict malignancy. Nodules smaller than 5 mm are almost always benign, when they are more than 7 mm, they are malignant in 1% of cases, when less than 1 cm in 15%, and less than 2 cm in 40%. Masses more than 5 cm have a 95% chance of malignancy [20, 28].

Cavitation may be present in both benign and malignant tumors. Figure 8.1 shows two examples of pulmonary masses.

8.2.3.4 Differential Diagnosis

Lung cancer needs of course to be distinguished from different thoracic pathologies other than benign lung lesions such as mediastinal masses, metastases but also benign conditions.

It is not always easy to differentiate between a parenchymal mass and a mediastinal one. Some parameters may be helpful in performing differential diagnosis such as the location and the margins. A mass is usually located in the lung when it is surrounded by pulmonary tissue in the frontal and lateral projections. On the contrary, a mediastinal mass usually has sharper margins and often compresses, displaces, or obstructs mediastinal structures.

Primary lung cancers should also be distinguished from metastases. In fact, the lung is one of the most common sites of metastasis. The most common primary tumors that metastasize in the lungs are breast cancer, renal cell carcinoma, colon cancer, and seminoma.

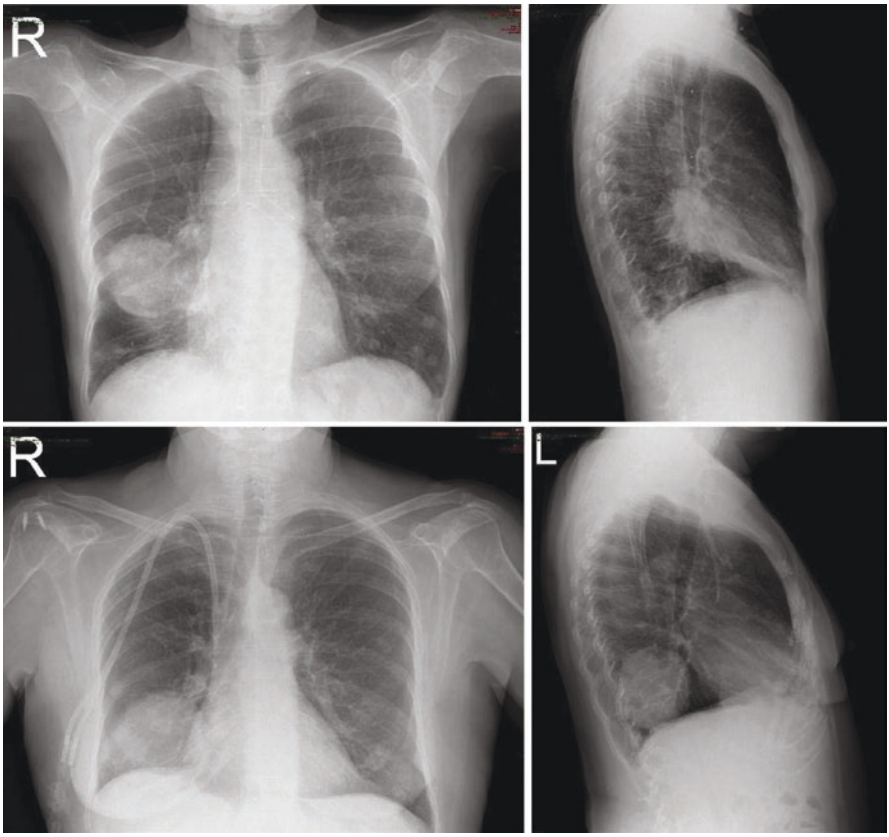

Fig. 8.1 Two examples of large pulmonary masses in the inferior right lobe in P-A and L-L projections

The lesion number can help us, in fact metastases are solitary only in a quarter of cases. Metastases also have sharp margins and do not contain cavitation.

A bronchogenic cyst may also be mistaken for lung cancer. This congenital defect is rare, and its location depends on the timing. It can be located in the mediastinum or intrapulmonary. On chest X-ray, it presents as a rounded opacity with smooth margins, usually in the lower lobes and can be filled with air or fluid.

8.2.4 Atelectasis

Lung cancer may also present as an area of atelectasis. This is defined as a loss of lung volume caused by the reduction in the content of air in the bronchi and in the alveolar spaces. Lungs that normally appear black become white when fluids or soft tissue substitutes air. So normally on the chest X-ray atelectasis appears as an opaque area. In the early phases this may not present as an opacity, but indirect signs

can be visible and be suggestive of its presence, for example, the reduction in lung volume.

Therefore in addition to the increased lung opacity, there are other signs. The first one is the shift of the interlobar fissures toward the area of atelectasis. When this is in the right and left upper lobes, both fissures move superiorly, as shown in Fig. 8.2. When it is in the middle lobe the oblique one moves upward and the horizontal one downward. If atelectasis is in the inferior lobes the oblique fissure moves downward and posteriorly.

A second sign is the upward displacement of the hemidiaphragm which is usually more evident when atelectasis involves the inferior lobes. In addition to this, the mobile mediastinal structures move toward the affected site. In case of upper lobes atelectasis, there is a displacement of trachea and the superior mediastinum. Trachea, which is normally in midline location, in correspondence with the spinous processes of the vertebral bodies, may shift toward the area of volume loss. When atelectasis involves the inferior lobes the heart and the inferior mediastinum usually move. When the heart shifts toward the left, there is an overlap between the right heart border and the spine. When it shifts toward right, the left heart border is almost in the midline.

The hila may also dislocate: superiorly if there is atelectasis of the upper lobes, downward if the inferior ones are affected. Of course it is important to remember that the left hilum in the majority of the population is located superior to the right one.

Another sign of atelectasis is the compensatory over inflation of the unaffected ipsilateral lobes or the contralateral lung. The bigger the atelectatic area the more evident the over inflation is.

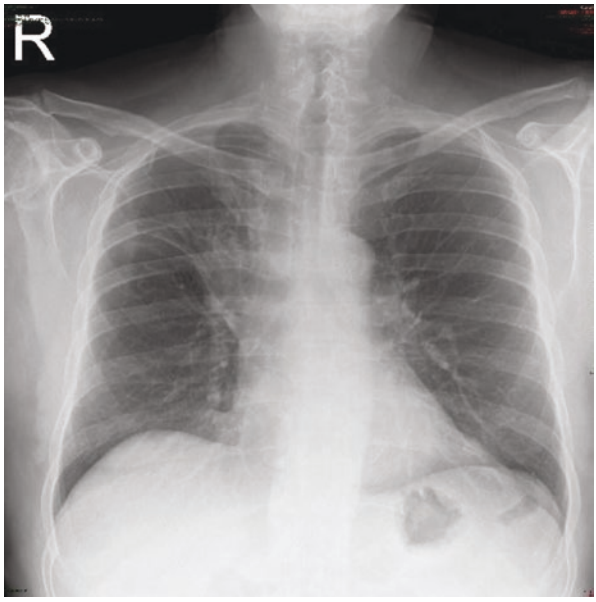

Fig. 8.2 This is a patient with lung cancer that presents with atelectasis: a parahilar opacity and an upward movement of the horizontal fissure

Of course there can be atelectasis of the whole lung and in this case the mediastinum is shifted toward the affected site so that the contralateral lung can cross the midline.

Atelectasis needs to be differentiated from a non-atelectatic parenchymal consolidation. The absence of air bronchogram may help us in doing this. In fact this does not occur in case of atelectasis because obstructed bronchi and bronchioles fill with secretions and appear radiopaque on the X-ray.

8.2.4.1 Types of Atelectasis

There are different types of atelectasis, and lung cancer is associated mainly with the obstructive and compressive ones.

Compressive Atelectasis

This type of atelectasis is caused by the passive compression of the lung that can be caused by a large pleural effusion, a pneumothorax or a space-occupying lesion such as a lung mass.

Obstructive Atelectasis

Obstructive atelectasis is caused by the absorption of air from the alveoli through the capillary bed distal to an obstructive lesion of the bronchial tree. This leads to the collapse of the affected segment or lobe, and since the pleurae remain in contact with each other, there is a pull on the mobile structures of the thorax toward the area of atelectasis. This can be caused by various etiologies such as bronchial carcinoma, mucus, and foreign bodies.

There are also cicatrization and band atelectasis. The first occurs due to fibrotic changes in the parenchyma caused by chronic inflammation that lead to lung volume reduction. The second presents as fine horizontal bands of atelectasis that occurs when the patient has decreased diaphragm mobility.

8.2.5 Pleural Effusion

Single-sided pleural effusion should always raise the suspect of lung cancer, as shown in Fig. 8.3. This is usually caused by the invasion of the pleural space by malignant cells, which may both cause a reactive increase in the reactive production of fluid and impair its reuptake by the pleura. Pleural effusion can be defined as an excessive accumulation of fluid in the space between the visceral and parietal pleura. The pleural space normally contains about 2–5 mL of fluid. This accumulates when the equilibrium between fluid formation and resorption is altered. This is the most common pleural finding documented on X-ray.

When the patient is in the upright position pleural fluid accumulates in the base of the thoracic cavity and we can only see it if it exceeds 250 mL. When the exam is performed in supine position, the fluid collects posteriorly and can demonstrate effusions as small as 15–20 mL. The whole hemithorax is opacified when 2 L of fluid is collected.

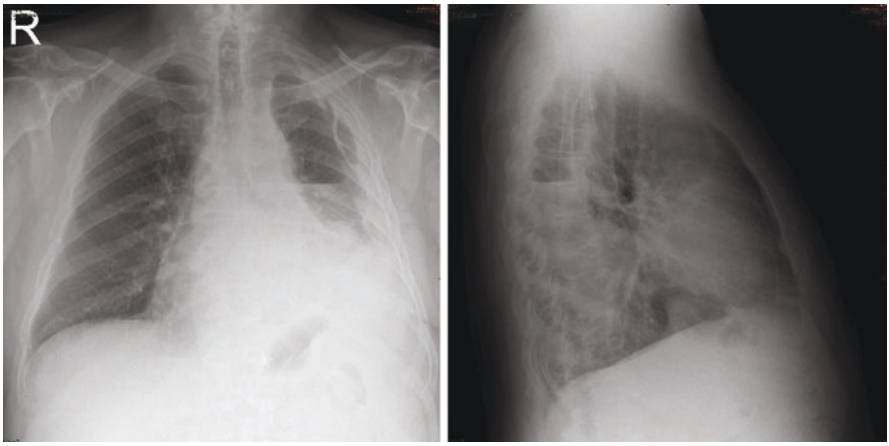

Fig. 8.3 This is an example of a patient with lung cancer that presents with pleural effusion

In some cases fluid may accumulate between the inferior surface of the lung and the hemidiaphragm and may simulate an elevation of the diaphragm.

Lung tumors should not be confused with pseudotumors which are also called vanishing tumors. These are fluid collections either between the layers of an interlobar pulmonary fissure or beneath it. Of course these disappear when the underlying condition is treated.

There are four types of pleural effusion: exudative, transudative, chylous, and hematic. The first two are the most common ones and differ for the protein content. Transudate contains less than 3 g/100 mL and occurs due to an increase in hydrostatic pressure or a decrease in oncotic pressure.

Exudate has more than 3 g/100 mL and is caused by an increased capillary permeability. The most common cause of exudative pleural effusion is malignancy. Other causes are infections, abdominal diseases, thromboembolism, and thoracic trauma.

The chylous effusion contains triglycerides or cholesterol and may occur for example due to the rupture of a great lymphatic vessel, whereas the hematic one may be caused by lung laceration or breaking of a vessel.

8.3 Role of CT in the Diagnosis of Lung Cancer in Older Patients

The most accurate technique nowadays in lung cancer detection and staging is CT imaging thanks to its high spatial and contrast resolution. In particular, thanks to the axial scan plane and the possibility of multiplanar reconstructions (MPR), it eliminates the overlapping of the various structures, solving the greater limit of traditional chest radiography (CXR) [23].

Moreover, the introduction and the utilization of high-resolution CT (HRCT) with thin sections has enabled radiologists to more accurately detect and determine the imaging characteristics of lung lesions, guiding the patient toward more precise therapeutic processes or further diagnostic exams (follow-up examinations, bioptic exams, CT-PET, etc.) [24].

The administration of iodinated organ contrast medium helps the staging of the disease, favoring the search for hilo-mediastinal adenopathies, metastases, and possible neoplastic embolisms [25].

Lung cancer can present as a nodule or a mass, two distinct entities based on a purely dimensional criterion. A pulmonary nodule is defined as a small (up to 30 mm) and well-defined opacity completely surrounded by normally ventilated lung parenchyma, while a mass is defined as an opacity measuring more than 30 mm, the latter is more likely to be neoplastic in nature [25].

8.3.1 Pulmonary Nodules

Pulmonary nodules are frequently found incidentally on chest CT exams performed for unrelated reasons.

The role of the radiologist is to distinguish between benign lesions and lesions with evolutionary characteristics, suggesting follow-up examinations or additional invasive imaging techniques.

To meet this need in 2017 updated Fleischner Society guidelines have been published to standardize the management of incidental pulmonary nodules and thereby reduce the number of unnecessary follow-up exams in patients with more than 35 years not belonging to specific high-risk groups (immunocompromised, with known primary cancers, etc.). As in these high-risk patients, treatment should be individualized relying on the specific clinical situation [26].

These guidelines suggest that CT with image thickness of 1.0–1.5 mm is necessary for the study, the characterization, and the correct measurement of pulmonary nodules. For the detection of micronodules, the reconstructions on the sagittal and coronal planes and the MIP (maximum intensity projections) images are very useful. Furthermore, follow-up imaging should use a low-radiation technique (average effective radiation dose 1.5 mSv) [24, 29].

These guidelines are based on risk stratifications of both patients and nodules. In particular, nodules are classified as solid or subsolid, besides specifically subsolid nodules can be subdivided into pure ground glass nodules (without solid component) and part-solid nodules as shown in Fig. 8.4.

Indeed, the two main factors determining the risk of a nodular lesion to be malignant are its size and morphology as shown in Tables 8.1 and 8.2.

Morphology refers specifically to attenuation characteristics (solid, part-solid, or purely ground glass) and to the margins (smooth, lobulated, or spiculated) of the nodule.

Size can be measured with a manual method based on the average of the long and short axes, rounded to the nearest millimeter or with nodule volumetry.

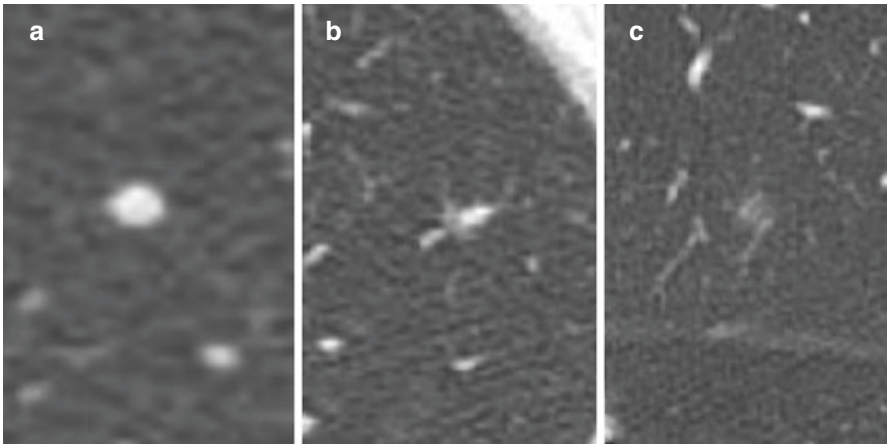

Fig. 8.4 Nodule types: (**a**) Solid, (**b**) Part solid and (**c**) Pure ground glass (GGO)

Table 8.1 2017 Fleischner Society Guidelines for management of incidental solid nodularities

Nodule type	Risk factors	<6 mm	6–8 mm	>8 mm
Solitary nodule	Low risk	No routine follow-up	CT at 6–12 months (consider at 18–24 months)	Consider CT, CT-PET or tissue biopsy at 3 months
Solitary nodule	High risk	Consider CT at 12 months	CT at 6–12 months and at 18–24 months	Consider CT, CT-PET or tissue biopsy at 3 months
Multiple nodules	Low risk	No routine follow-up	CT at 3–6 months (consider at 18–24 months)	CT at 3–6 months (consider at 18–24 months)
Multiple nodules	High risk	Consider CT at 12 months	CT at 3–6 months and at 18–24 months	CT at 3–6 months and at 18–24 months

Table 8.2 2017 Fleischner Society Guidelines for management of incidental subsolid nodularities

Nodule type	<6 mm	>6 mm
Solitary GGO nodule	No routine follow-up	CT at 6–12 months. If stable, CT every 2 years for a total of 5 years
Solitary part solid nodule	No routine follow-up	CT at 3–6 months. If stable, CT every year for 5 years
Multiple nodules	CT at 3–6 months. If stable, consider CT at 2 and 4 years	CT at 3–6 months. Subsequent management based on the most suspicious nodule(s)

Other factors to be evaluated in the characterization of pulmonary nodules are:

– Growth or stable size: A solid nodule that has been stable for 2 years or more on CT does not need any further investigations. In contrast, subsolid nodules could be attributable to a low-grade adenocarcinoma, which has slower growth average and an elevated VDT (volume doubling time), so it is considered likely to be benign only when stable for 5 or more years by CT.

– Margins: Usually, benign nodules present themselves with well-defined and smooth borders, while malignant lesions have spiculated or lobulated margins. However, this is a sensitive but not specific criterion, as some lesions with spiculated margins may nevertheless be benign. Furthermore, some malignant lesions, such as metastases, often present with clear margins.
– Fat and calcifications: The presence of fat density (between −30 and −150 HU) within a smooth bordered nodule is suggestive for pulmonary hamartoma. There are four patterns of calcification, which are central, diffuse, lamellated, and popcorn, that are mostly associated with granulomatous disease and hamartomas. Nevertheless, calcifications may also be present in malignant nodules especially if they are punctate or irregular.
– Location: Lung cancer is more frequent in the upper lobes, especially on the right side.
  Perifissural or adjacent nodules to the pleural surface usually represent intrapulmonary lymph nodes, especially if solid, homogeneous, and triangular-shaped. If they comply with these characteristics, even if they are larger than 6 mm, they do not require instrumental follow-up.
– Numerosity: The multiplicity of nodules is generally associated with benign conditions such as inflammatory diseases or granulomatous infections. The NELSON trial demonstrated an increased risk of malignancy if the number of nodules is between 1 and 4, if greater than 5 the risk is reduced [24].

8.3.2 Pulmonary Masses

The 2004 World Health Organization (WHO) classification divides lung cancers into two main histological categories: non-SCLC (NSCLC, 85% of all lung cancers) and small-cell lung carcinoma (SCLC, 15% of all lung cancers) [26, 30, 31].

The distinction between the various subtypes of lung cancer can help to evaluate the subsequent diagnostic and therapeutic process and can give the clinician information about a patient's prognosis.

However, although some morphological and metabolic characteristics may suggest the histotype of the detected lung cancer, the diagnosis of certainty is still histological and requires biopsy sampling.

8.3.2.1 Non-Small-Cell Lung Carcinoma (NSCLC)

NSCLC includes three main histological subtypes: squamous cell carcinoma, adenocarcinoma, and large-cell carcinoma.

– *Squamous cell carcinoma (SCC):*
  The term squamous refers to the flattened appearance of the neoplastic cells. This aspect is due to the chronic inflammation that develops and causes squamous metaplasia of the respiratory epithelium which then progresses into dysplasia and finally into a neoplastic lesion. From the histopathological point of view, it can be divided into four subtypes: papillary, clear cell, small cell, and basaloid.

SCC accounts for at least 20% of all bronchogenic cancers and is strongly associated with cigarette smoking.

In two-thirds of cases SCC has central location with intraluminal obstruction of the main, lobar, or segmental bronchus resulting in obstruction or atelectasis of the downstream parenchyma. Centrally located tumors therefore manifest themselves with symptoms such as chronic cough, superimposed infectious pneumonia, or hemoptysis and are usually reachable by endobronchial examinations. In the initial stages they therefore produce a thickening of the bronchial wall, subsequently they can manifest themselves with hilar or peri-hilar masses or they can be more subtle, manifesting mainly with indirect signs such as atelectasis [28].

SCC can also have peripheral localization usually manifesting itself as a mass with irregular borders. Peripheral cancer occurs later and is therefore diagnosed when it is larger with possible involvement of the chest wall or when it is metastatic. SCC is the most common histotype of Pancoast tumor, an example can be seen in Fig. 8.5.

Another feature frequently associated with SCC is cavitation, both in the primary lesion and in metastases with irregular and thick margins. Figure 8.6 shows an example of a big cavitated lesion, which has been proven to be a peripheral SCC [30, 32–34].

– *Adenocarcinoma:*

Histologically the term adenocarcinoma refers to an epithelial neoplasm with glandular differentiation or intracytoplasmic mucin production.

Adenocarcinoma is the most common histologic type of lung cancer, accounting for nearly 40% of lung cancers. Furthermore, adenocarcinoma is also the most common histologic group seen in women and nonsmokers, although there is a minimal association with cigarette smoking.

In 2011, the International Association for the Study of Lung Cancer (IASLC), American Thoracic Society (ATS), and European Respiratory Society (ERS) introduced a new classification of adenocarcinoma, which is now divided into four main categories: adenocarcinoma in situ (AIS), minimally invasive

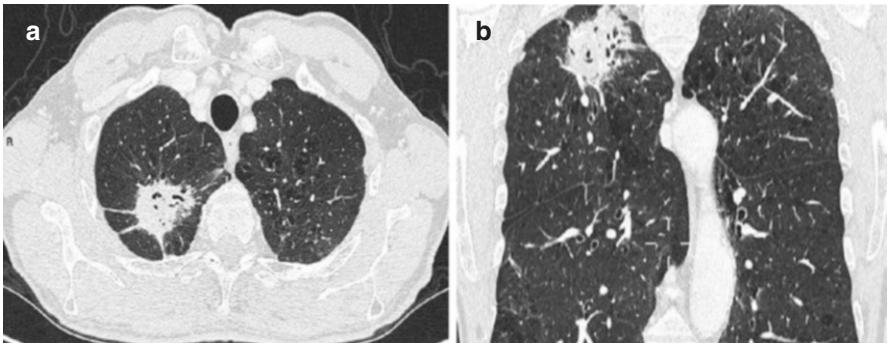

Fig. 8.5 (**a**) Axial CT scan of a 69-year-old man showing a Pancoast tumor in the right upper lobe. (**b**) Coronal view of the same CT

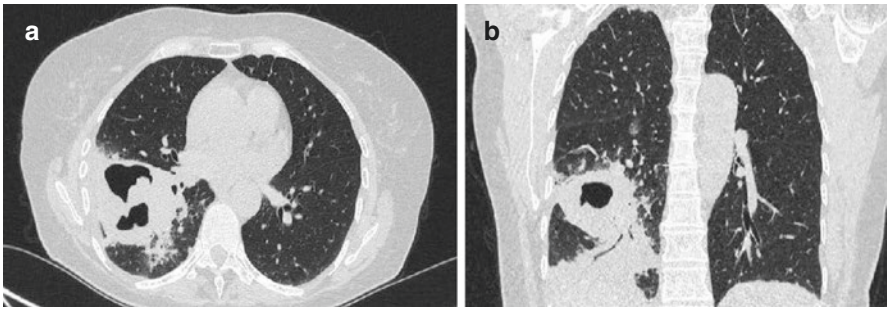

Fig. 8.6 (**a**) Axial CT scan of a 75-year-old man showing a cavitated mass in the right lower lobe. Histological examination proved to be an SCC. (**b**) Coronal view of the same CT

adenocarcinoma (MIA), lepidic predominant nonmucinous adenocarcinoma, and invasive mucinous adenocarcinoma [35].

Adenocarcinoma usually has peripheral localization; therefore, it is often paucisymptomatic and of occasional occurrence if small in size.

Moreover, it presents as a solid, partially solid, or ground glass nodule (GGN) or mass, and it may have well-defined, lobulated, irregular, or poorly defined margins.

In particular, the ground glass appearance suggests a lepidic growth pattern (growth of cancer cells along the alveoli without lymphovascular invasion), while solid lesions usually present invasive patterns.

In fact, in literature thick spiculations, thickened bronchovascular bundles, pleural retraction, concave notch and large size are reported as negative prognostic factors. While ground glass components, bubble-like lucencies, air bronchograms, and small size are associated with a better prognosis.

Since the imaging spectrum of lung adenocarcinoma has a good correlation to histologic findings AIS, MIA and lepidic predominant nonmucinous adenocarcinoma manifest as lesions with predominant ground glass components. Conversely, invasive mucinous adenocarcinoma usually presents as a lesion with an important solid component [28, 36–39].

In Fig. 8.7 we can see a peripheral solid mass with lobulated margins, which has been proven to be a case of adenocarcinoma.

– *Large-cell lung cancer (LCC):*

LCC is an undifferentiated neoplasm that lacks any features of squamous, glandular, and neuroendocrine differentiation in microscopy and immunohistochemistry; its diagnosis needs resection specimens. LCC is characterized by round/polygonal cells with large nucleoli and with a moderate amount of cytoplasm.

LCC currently accounts for about 2%–3% of all cases of bronchogenic carcinoma.

LCC is typically described as a large peripheral solid mass (usually >4 cm) with irregular or spiculated margins. It is an aggressive tumor that often presents focal necrosis, rapid growth, and early metastasis [28, 30, 39, 40].

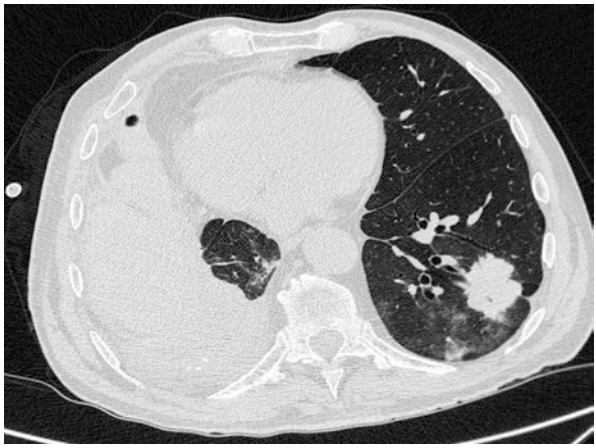

Fig. 8.7 Axial CT scan of an 82-year-old man showing a peripheral mass in the left lower lobe. Histological examination proved to be an adenocarcinoma. Some ground glass nodularities concomitant in the same lobe

8.3.2.2 Small-Cell Lung Carcinoma (SCLC)

SCLC is the third most common histologic type of lung cancer, accounting for approximately 15% of all bronchogenic carcinomas. In particular, SCLC is the most frequent primary pulmonary neuroendocrine neoplasm, and it is the histotype most linked to cigarette smoking.

SCLC is more aggressive than non-SCLC and is characterized by rapid growth, greater propensity for early development of widespread metastases (about 60%–70% of patients at diagnosis), and thus by a worse prognosis (despite high response rates to first-line chemotherapy, at least 80% develop recurrent or progressive disease) [31].

Over 90% of SCLCs are located centrally as they arise from the basal epithelium in a lobar or main bronchi. The mass often presents with central necrosis or hemorrhagic foci, intralesional calcifications are also present in 20% of cases. Administration of intravenous contrast medium can help to detect involvement of mediastinal structures [41, 42].

SCLCs frequently manifest as large hilar or peri-hilar masses with mediastinal or hilar lymphadenopathy (about 80%–90% of cases), as they rapidly involve regional lymph nodes. Occasionally, SCLCs can present as coalescent mediastinal enlarged lymph nodes without identification of the primary tumor, appearing similar to lymphoma [31, 42, 43].

Figure 8.8 shows an hilar mass indissociable from the bronchial branches and the vessels for the right lower lobe and some enlarged mediastinal lymph nodes. The mass has been proven to be an SCLC.

SCLCs are infiltrative tumors, in fact they often invade neighboring structures such as main bronchi, causing atelectasis or post-obstructive pneumonia and the pleura (about 40% of cases) causing effusion or thickening or pleural nodules. Moreover, SCLC of the lung is the most common cause of SCVS (superior vena cava syndrome), due to direct infiltration or compression/thrombosis.

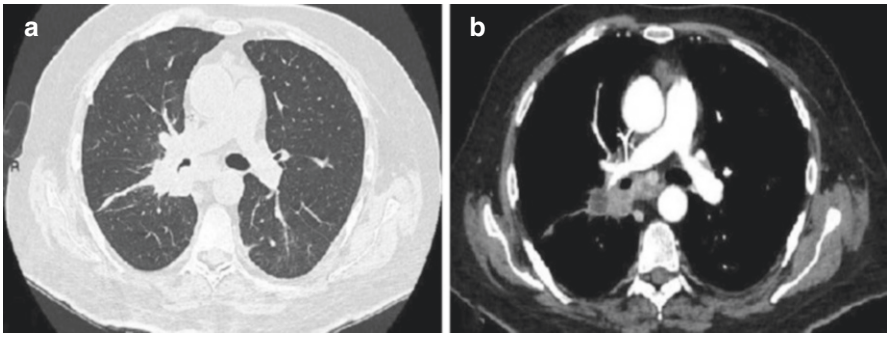

Fig. 8.8 (**a**) Axial CT scan of a 67-year-old man showing a peri-hilar mass in the right lower lobe. Histological examination proved to be an SCLC. (**b**) The same CT after administration of contrast medium that shows an indissociable mass from the bronchial branches and the vessels for the lower lobe. The mass has a central necrotic component. Some enlarged lymph nodes in the mediastinal area may also be observed

In addition to symptoms due to thoracic involvement, SCLC is the most frequent lung cancer associated with paraneoplastic syndromes, such as the syndrome of inappropriate antidiuretic hormone secretion.

8.3.3 Lung Cancer Staging

8.3.3.1 TNM Classification

In this section, we are going to expose the eighth edition of the TNM in lung cancer, which was issued by the international Association for the Study of Lung Cancer (IASLC) in 2017 [28].

T Component

The T component can be classified into five categories, as shown in Table 8.3. The tumor's greater dimension is the main variable when assessing this parameter, although the invasion of nearby anatomical structure plays a fundamental role. In particular, the invasion of mediastinal structures such as trachea, carina, or pericardium immediately leads to an increment of the T component. The infiltration of peripheral tissues such as the pleura or the chest wall also comports a T increment. If more than one neoplastic nodule is present, the location of such nodule respectively to the main mass determines T staging.

IASLC recommends that all tumors are measured in centimeters and to use the lung window in order to determine the greatest dimension, since using the mediastinal window can lead to an understaging.

N Component

Table 8.4 summarizes the N classification in the eighth edition of the TNM staging in lung cancer. Lymph nodes with a short axis >1 cm are to be considered

Table 8.3 T stage definition in the 8th edition of the TNM in lung cancer

T: Primary tumor	
Tx	Primary tumor cannot be assessed or tumor proven by presence of malignant cells in sputum or bronchial washings but not visualized by imaging or bronchoscopy
T0	No evidence of primary tumor
Tis	Carcinoma in situ
T1	Tumor ≤3 cm in greatest dimension surrounded by lung or visceral pleura without bronchoscopic evidence of invasion more proximal than the lobar bronchus (i.e., not in the main bronchus)
T1a (mi)	Minimally invasive adenocarcinoma
T1a	Tumor ≤1 cm in greatest dimension
T1b	Tumor >1 cm but ≤2 cm in greatest dimension
T1c	Tumor >2 cm but ≤3 cm in greatest dimension
T2	Tumor >3 cm but ≤5 cm or tumor with any of the following features: – Involves main bronchus regardless of distance from the carina but without involvement of the carina – Invades visceral pleura – Associated with atelectasis or obstructive pneumonitis that extends to the hilar region, involving part or all of the lung
T2a	Tumor >3 cm but ≤4 cm in greatest dimension
T2b	Tumor >4 cm but ≤5 cm in greatest dimension
T3	Tumor >5 cm but ≤7 cm in greatest dimension or associated with separate tumor nodule(s) in the same lobe as the primary tumor or directly invades any of the following structures: Chest wall (including the parietal pleura and superior sulcus tumors), phrenic nerve, parietal pericardium
T4	Tumor >7 cm in greatest dimension or associated with separate tumor nodule(s) in a different ipsilateral lobe than that of the primary tumor or invades any of the following structures: Diaphragm, mediastinum, heart, great vessels, trachea, recurrent laryngeal nerve, esophagus, vertebral body, and carina

Source: Goldstraw et al., The IASLC Lung Cancer Staging Project: Proposals for Revision of the TNM Stage Groupings in the Forthcoming (Eighth) Edition of the TNM Classification for Lung Cancer. https://doi.org/10.1016/j.jtho.2015.09.009. PMID: 26762738

malignant. The *N* parameter is determined primarily by the pathological nodes location. Direct extension of the primary tumor into a nodal station is considered pathologic nodal involvement.

M Component

Table 8.4 summarizes the M component. Nodules located in the pleura or in the pericardium, as well as pleural or pericardial effusion and contralateral or bilateral metastases in the lung parenchyma, are considered M1a. The M1b category identifies a tumor with a single extrathoracic metastasis, while the M1c category encompasses tumors with multiple extrathoracic metastases.

8.3.3.2 Lung Cancer Stages

Tables 8.5 and 8.6 describe the lung cancer stage groups suggested by the latest TNM edition, as well as the survival rates in different stages.

Table 8.4 N and M stage definitions in the eighth edition of the TNM in lung cancer

N: Regional lymph node involvement	
Nx	Regional lymph nodes cannot be assessed
N0	No regional lymph node metastasis
N1	Metastasis in ipsilateral peribronchial and/or ipsilateral hilar lymph nodes and intrapulmonary nodes, including involvement by direct extension
N2	Metastasis in ipsilateral mediastinal and/or subcarinal lymph node(s)
N3	Metastasis in contralateral mediastinal, contralateral hilar, ipsilateral or contralateral scalene, or supraclavicular lymph node(s)

M: Distant metastasis	
M0	No distant metastasis
M1	Distant metastasis present
M1a	Separate tumor nodule(s) in a contralateral lobe; tumor with pleural or pericardial nodule(s) or malignant pleural or pericardial effusion
M1b	Single extrathoracic metastasis
M1c	Multiple extrathoracic metastases in one or more organs

Source: Goldstraw et al., The IASLC Lung Cancer Staging Project: Proposals for Revision of the TNM Stage Groupings in the Forthcoming (Eighth) Edition of the TNM Classification for Lung Cancer. https://doi.org/10.1016/j.jtho.2015.09.009. PMID: 26762738

Table 8.5 Correspondence between lung cancer stages and TNM categories

T/M	Label	N0	N1	N2	N3
T1	T1a ≤ 1	IA1	IIB	IIIA	IIIB
	T1b > 1-2	IA2	IIB	IIIA	IIIB
	T1c > 2-3	IA3	IIB	IIIA	IIIB
T2	T2a Cent, PI	IB	IIB	IIIA	IIIB
	T2 a > 3-4	IB	IIB	IIIA	IIIB
	T2b > 4-5	IIA	IIB	IIIA	IIIB
T3	T3 > 5-7	IIB	IIIA	IIIB	IIIC
	T3 *Inv*	IIB	IIIA	IIIB	IIIC
	T3 *Saltell*	IIB	IIIA	IIIB	IIIC
T4	T4 > 7	IIIA	IIIA	IIIB	IIIC
	T4 *Inv*	IIIA	IIIA	IIIB	IIIC
	T4 *Ipsi Nod*	IIIA	IIIA	IIIB	IIIC
M1	M1a *Contr nod*	IVA	IVA	IVA	IVA
	M1a *Pl dissem*	IVA	IVA	IVA	IVA
	M1b *Single*	IVA	IVA	IVA	IVA
	M1c *Multi*	IVB	IVB	IVB	IVB

Source: Detterbeck et al., The Eighth Edition Lung Cancer Stage Classification. https://doi.org/10.1016/j.chest.2016.10.010

Table 8.6 Five-year survival rate for patients in different stages

Type	IA1	IA2	IA3	IB	IIA	IIB	IIIA	IIIB	IIIC	IVA	IVB
Clinical	92	83	77	68	60	53	36	26	13	10	0
Pathologic	90	85	80	73	65	56	41	24	12	–	–

Source: Detterbeck et al., The Eighth Edition Lung Cancer Stage Classification. https://doi.org/10.1016/j.chest.2016.10.010

Stage I: In this case the tumor is limited to the lungs and there is no nodal involvement.
Stage II: The neoplastic tissue is located in the lung and in the ipsilateral peribronchial or hilar nodes.
Stage III: The tumor is locally advanced and invades mediastinal nodes. In particular:
Stage IIIa: The neoplastic extension is only in ipsilateral mediastinal nodes.
Stage IIIb: The neoplastic extension is into contralateral mediastinal nodes or above the clavicle.
Stage IV: The tumor is diffused into both lungs, to the pleural fluid or any other body part [26].

8.4 Chest Characteristics in the Elderly Patient: Possible Difficulties and Overlapping of Diagnoses

In a global perspective, the improvement of general life conditions and the development of medical science have led to a stable increase in life expectancy worldwide. Therefore, the age profile of the society is changing; due to the longer life of the population and the combined reduction in fertility, we have seen a reduction of people of working age and an increase in the proportion of the elderly population, commonly referred to as people >65 years old, a phenomenon that is often referred to as "demographic aging." This trend, which first started in the richest countries in the world, has involved all developing countries and is expected to continue in the next couple of decades. These developments are likely to have profound implications, among others, in health and social care systems [44].

As we age, the human body is subjected to progressive decay due to physiological metabolic, hormonal, and anatomical changes. The respiratory system and the parenchymal, vascular, and osteo-cartilage structures that compose it are characterized by numerous physiological and pathological factors that determine a progressive remodeling over the years. It is mandatory for the radiologist to know the most important anatomical and physiological evolutionary characteristics of old age, first of all of the chest, so as to be able to establish the real limit between changes in the chest compatible with age and proper pathological pictures.

The constant aging of the general population, the condition of fragility and greater predisposition to the disease associated with the aging of the body, the constant improvement of the imaging technologies available to the radiologist, and the

increase in therapeutic options associated with greater expectations on the part of the of the patient are all factors for which diagnostic imaging plays a primary role in the elderly patient. The radiologist must know the main anatomical and physiological evolutionary characteristics of the chest in the elderly patient, so as to be able to establish the real limit between changes in the chest compatible with age and properly pathological pictures.

The thorax as a whole can undergo changes that may affect the rib cage, the thoracic wall, the lung, and the mediastinum. Imaging techniques are now able to objectify these changes, techniques that are an element of clarification for those clinical pictures that are often vague or difficult to interpret. In general, it can be said that traditional radiology, with the standard radiogram, is able to highlight most of the typical aspects of the senile chest and that computed tomography highlights them in a more analytical way by virtue of the advantages of reading the section image [45].

8.4.1 Age-Related Rib Cage Deformation

The thoracic cage represents the anatomical structure responsible for carrying out the function of "container" of the viscera of the thorax. It consists of the ribs, the sternum, the dorsal spine, the diaphragm, and the muscles of the anterior and posterior thoracic wall.

With aging, the skeleton of the rib cage undergoes a progressive stiffening, a consequence of the calcification of the costal cartilages and the arthritic-degenerative processes affecting the costo-vertebral joints. These events, which are associated with the progressive rarefaction of the bone matrix due to pathological condition commonly present in the elder (i.e., osteoporosis) and the physiological reduction of the tone of the parietal muscles, result in an increase in the fragility of the chest wall, which results in a greater predisposition to fractures and deformation of the bone components. Reduced thickness of intervertebral determinate worsening dorsal kyphosis and cause the onset of dorsal-lumbar scoliosis, which together with the factors listed above determine deformation and reduction of compliance of the rib cage. Other errors may be caused by frequent findings in the elderly such as rib compact islands, vertebral osteophytic bridges, costo-transverse arthritic hypertrophy, all situations that can simulate parenchymal nodular opacity [46].

Even the involutional aspects affecting the muscle tissue are a source of interpretation errors for the radiologist. In the elderly subject, there is a progressive replacement of muscle cells with fat cells, resulting in the progressive atrophy of the muscles of the chest wall. The atrophy of the muscle component, while not necessarily altering the thickness of the chest wall, in any case determines a significant alteration of the constitution. Such modifications may go unnoticed on a careful physical examination, but are always apparent on the examination performed using diagnostic imaging. On a standard chest radiographic examination, it is possible to observe widespread radiolucency of the thoracic resulting in the lower radio-attenuating capacity of the adipose component. This finding becomes even more

evident with the aid of the tomographic examination (CT) which allows a better definition through the acquisition of multiplanar sequences.

8.4.2 Mediastinum Deformation: Cardiomegaly, Aortic Ectasia

With aging, the cardiac organ undergoes various paraphysiological involutionary events, concerning the pericardium, myocardium, coronary arteries, and valve systems. The set of these paraphysiological alterations constitutes a commonly defined picture of the "senile heart."

The main pathophysiological characteristic of this condition consists in the imbalance that is created between the cardiac and respiratory pumps: the enlarged heart occupies a large part of the chest (which, as already mentioned, is relatively inexpensive), to the detriment of the lungs, so the respiratory excursions are reduced with alterations of the perfusion dynamics, as well as ventilatory ones [47].

The pericardial tissue undergoes the physiological process of adipose involution with an increase in the relative quantity of fat, more evident at the level of the cardio-phrenic angles which, consequently, present a greater "dullness" in the standard chest radiogram.

Furthermore, the volumetric increase in the heart chambers is appreciable, in particular in the left atrial cavity and especially in the left ventricle, where there is a significant increase in the ventricular myocardial mass, an aspect attributable to cardiac remodeling consequent to the state of typical systemic hypertension in the elderly patient (Fig. 8.9) [48].

The mediastinal image may appear enlarged as a whole or only in some points, generally without gross deformations. The main elements to be analyzed are the aorta, the trachea, and the heart. This aspect is accentuated with the patient's supine position (chest to bed) and can simulate an engagement of the superior mediastinum. Important elements to consider in order to exclude mediastinal pathology are the preservation of the normal radiolucency of the tracheal belt and the preservation of the normal thickness of the right paratracheal mediastinal line or "right

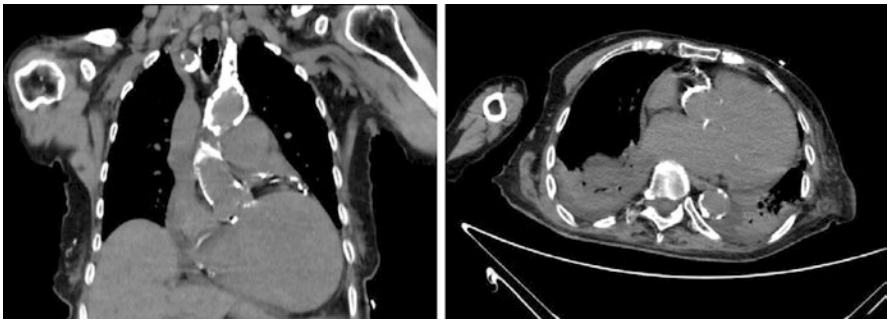

Fig. 8.9 Axial and coronal CT scan of a 83-year-old man with cardiomegalia. The volumetric increase in the heart chambers is appreciable, in particular in the left ventricle

paratracheal band." The frequent presence of catheters or tubes (CVC, SNG, PM electrodes, etc.) can facilitate the interpretation of mediastinal anomalies, offering important radiopaque landmarks [49].

These aspects are observable in the standard chest radiogram, appreciable as a rounding of the lower left cardiac arch and, in the lateral-lateral projection, in the protrusion by the cardiac shadow at the level of the clear retrocardiac space. In the more advanced stages, the picture of the cardiac lung presents additional elements: interstitial edema leads to the smoky appearance of the hila and vessels and leads to the formation of Kerley's striae, especially of type B. The trachea plays an important role in the radiological judgment of the mediastinum superior. In addition to the aspects previously analyzed, it can help in the evaluation of the hyper-transparency of the lung of the elderly (which, as we have seen, may not be attributable to a parenchymal pathology): for example, any "saber sheath" tracheal alteration can address toward a correct diagnosis of pulmonary emphysema (Fig. 8.10).

Further alterations come from the formation of calcified plaques The coronary arteries become twisted and are often home to calcific deposits and atherosclerotic plaques; moreover, at the level of the valvular apparatus, they form calcific deposits, especially at the level of the aortic valve and the mitral annulus. In these locations, any calcifications of the valve flaps and fibrous rings must therefore be sought in the radiogram, supplementing the study if necessary with a dynamic analysis of their kinetic behavior in radioscopy. The main radiological aspects (RT and CT) are the redistribution toward the apexes of the pulmonary pattern—"inverted distribution"—and a ratio of 1:1 between the caliber of the upper and lower vessels—"balanced distribution" (expressions of the increase in venous pressure in the small circle: 12–15 mmHg). The vessels generally become more tortuous and often increase in caliber, also contributing to the so-called dirty lung appearance.

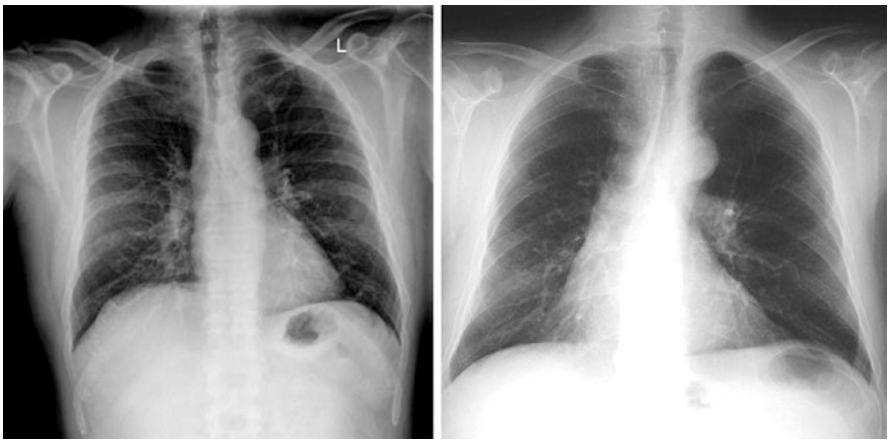

Fig. 8.10 Samples of standard chest radiograph in pulmonary emphysema with "saber sheath" trachea. It represents degeneration and ossification of the tracheal cartilage due to elevated intrathoracic pressure

Radiologic imaging of the chest is also of primary importance in the detection of aortic dilatation.

With increasing age, the aorta tends to acquire some characteristics that are mainly represented by vessel elongation, dilatation, and the deposition of calcium in the vessel walls. In particular, the aortic dilatation can represent a paraphysiological variable related to the increasing age. With older age the elastic tissue of the vessel walls can deteriorate and tends to be replaced with more rigid collagen tissue, leading to a dimensional increase in the diameter of the vessel. This dilatation can be pathologic when it increases over a certain dimension, moreover, when the dilatation is significant and reaches the appropriate measurement criteria, the term aortic aneurysm is utilized. Age is one of the main risk factors for the development of aortic aneurysm and for its subsequent rupture, leading to aortic dissection. Aortic ectasia is better identified with spiral CT scan technique, which permits to study all aorta districts, after the administration of contrast agent. However, it is possible to identify aortic ectasia also with chest X-ray, especially if there are parietal calcifications, typically observed in the geriatric patient, which facilitate the identification of the arterial profile (Fig. 8.11). In the evaluation of an aortic aneurysm, CT scan is able to determine the extension, the evaluation of the dimension of the lumen and the presence of thrombi [48].

8.4.3 COPD, Pneumonia

Chronic obstructive pulmonary diseases (COPD) essentially include, in the elderly, asthma, the emphysema-chronic bronchitis complex, bronchiectasis, and chronic inflammation of the small bronchi, and represent one of the main causes of morbidity and mortality in the elderly patient.

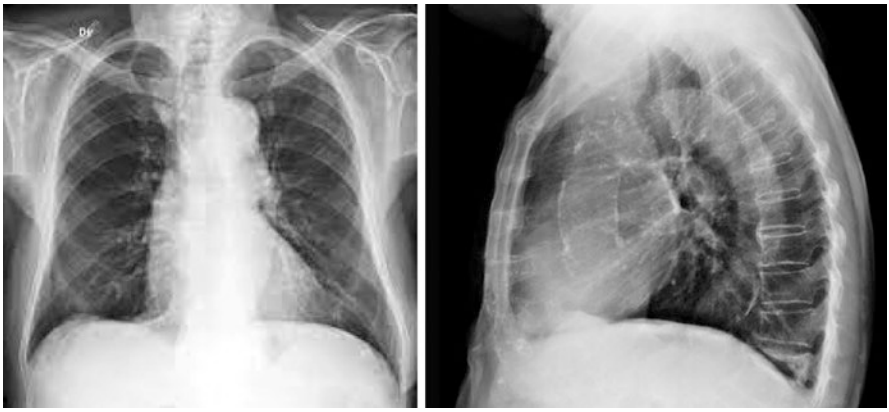

Fig. 8.11 Aortic ectasia in the ascendant and aortic arch in an 88-year-old male, observed as a prominent aortic knob

The findings of emphysema and chronic bronchitis in old age are the same as those found in younger subjects, but more difficult to interpret correctly given the frequent coexistence of alterations in other systems (cardiovascular, musculoskeletal) that can simulate them or mask the radiological manifestations. It is important for the radiologist to know the pathophysiological basis of the pathologies of the cardio-pulmonary circulation to avoid any misinterpretation of the image. For example, a common mistake for the radiologist is to confuse the radiolucency of the pulmonary fields resulting from the already described physiological involution of the muscular structures for a picture of senile emphysema, in the absence of those signs necessary to confirm a picture of hyperinsufflation, oligoemia, or of blisters that must be present to confirm the diagnosis of emphysema [50].

Furthermore, in the elderly patients, the worsening of the pathological state is often accompanied by nonspecific clinical manifestations such as asthenia, retrosternal pain, and deterioration of cognitive functions, thus leading to a late or inadequate diagnosis.

Both traditional radiology and computed tomography (CT) can provide an important help in giving an initial diagnostic address to the appearance of the first symptoms.

There are two classic radiological-clinical patterns that guide the physician in the diagnosis of emphysema/chronic bronchitis in the elderly: the first pattern, arterial deficiency, characterized by the rarefaction of the vascular pattern, corresponding to the prevalence of the emphysematous picture; the second pattern, increased markings, sees the accentuation of vascular landmarks characteristic of the prevalence of chronic bronchitis which is associated with secondary pulmonary arterial hypertension.

Among the radiographic alterations observable in COPD reported in the literature and may concern alterations of the diaphragm (widening of the costo-phrenic angles, lowering of the diaphragmatic dome, widening of the clear retrosternal space), parenchymal (presence of emphysematous bubbles, thickening of the bronchial walls, areas of opacity), cardiovascular alterations (heart drop, dilation of the pulmonary arteries with peripheral barrage), and alterations of the trachea (“saber sheath” trachea).

The principle can be stated that, even in the presence of multiple concomitant radiographic alterations, the standard X-ray is not very sensitive in the mild-moderate severity forms of COPD, it may also appear negative in patients with chronic bronchitis, while it acquires greater usefulness in the most advanced forms, although it is not possible to correctly quantify the extent or extent of functional or anatomical damage. It is generally used in the presence of acute onset of symptoms with fever to confirm the clinical suspicion of a bronchopneumonic outbreak, determining the presence of any complications, such as pleural effusion and bronchial obstructions. Moreover, it is often technically inadequate since it is carried out in nonoptimal conditions, with the patient in a semi-sitting position, insufficient inspiration, with portable equipment, which further reduces its already limited diagnostic value [51].

Finally, the chest X-ray can also detect, in asthmatic forms, nonspecific radiological signs, such as thickening of the bronchial walls and bronchopneumonic foci, or recognize the acute complications of an asthmatic event, such as pneumothorax or pneumomediastinum.

CT is more useful in this regard, which allows us to quantify with sufficient precision the extent of emphysema in HRCT and the severity of emphysematous damage even in the mildest forms; it is possible to demonstrate with HRCT the presence of emphysema in patients with impaired respiratory function and completely normal chest radiograph. In the pattern, increased markings are often observed in HRCT, in addition to the reduced parenchymal density, oligoemia, indicative of emphysema, thickening of the bronchial and bronchiolar walls and areas of ground glass opacity.

Finally, HRCT allows precise documentation of the type of prevailing emphysema:

- Centrilobular emphysema, the most common type usually associated with smoking, affects the centrilobular portion of the lung. Usually the upper lobes of the lungs are affected.
- Panlobular emphysema, also called **panacinar emphysema**, can involve the whole lung or mainly the lower lobes. Is commonly associated with alpha-1 antitrypsin deficiency (A1AD or AATD).
- Paraseptal emphysema, also called **distal acinar emphysema**, relates to emphysematous change next to a pleural surface. The cystic spaces known as blebs or bullae that form in paraseptal emphysema typically occur in just one layer beneath the pleura (Fig. 8.12).

In the forms of severe chronic asthma, HRCT, much better than the thoracic radiogram, is able to demonstrate and quantify the thickening of the bronchial walls due to the structural remodeling of the walls and can detect the frequent presence of bronchiolitis highlighting direct signs (branched opacities from commitment of the

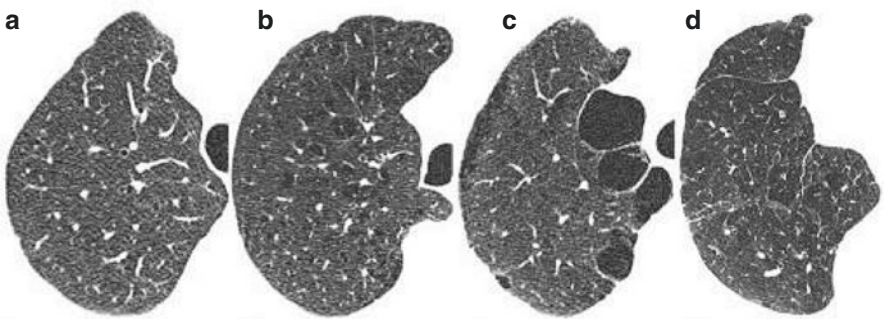

Fig. 8.12 Comparative images in axial computed tomography. (**a**) Absence of emphysema; (**b**) Centrilobular emphysema; (**c**) Paraseptal emphysema; (**d**) Panlobular emphysema

bronchial lumen, parietal thickening of the bronchioles with bronchiectasis) or indirect (expiratory air trapping) of anatomo-functional alteration of the small airways.

In elderly patients, however, the use of HRCT is often superfluous for a better morphological definition and for an accurate balance of extension of the emphasis, which in any case would have a limited therapeutic impact.

8.4.4 Pneumonia

Pneumonia represents the main causes of death from infection, especially in the elderly population where the immune system is often compromised due to an age-related decrease in immune activity, chronic use of medications altering immune function as the use of systemic corticosteroids in rheumatic disease.

Pneumonia can be divided into typical or atypical presentation, and in accordance to history in community acquired, nosocomial, or infections in the immunocompromised.

Conventional chest radiography plays a major role in diagnosing pneumonia, being able to detect or exclude infiltrates, show the extent of the disease, estimate possible complications, and show response to treatment. However, it is not indicated in the suspicion of pneumonia in an immunocompromised patient, where the image obtained is often normal.

Supported by clinical history and clinical laboratory data, chest radiography allows to limit the spectrum of possible pathogens and will guide the calculated use of antibiotics.

It is important to know the possible differential diagnoses in the presence of certain signs, such as the presence of persistent infiltrations, which can lead to a diagnosis of bronchoalveolar carcinoma. In the elderly patients, elimination of pulmonary infiltration usually takes longer. It was shown that 15% of elderly patients still showed radiographic abnormalities beyond 3 months. Delayed clearance may be related to existing comorbidity. For this reason, a minimum interval of 3 months for follow-up radiograph appears to be indicated to rule out previous malignant changes.

8.4.5 Conclusion

In the elderly, conventionally defined as individuals >65 years of age, it is often difficult to establish what is normal, due to the numerous anatomical and physiological changes that occur during the physiological process of aging. Knowing how to distinguish normal pictures from strictly pathological pictures is an important challenge for the radiologist today. Diagnostic imaging often offers borderline results to chest imaging, and it is essential to know how to distinguish a picture that is only apparently pathological from an image that may underlie the principle of pulmonary pathologies for which the elderly patient, due to the condition of fragility associated with aging, is particularly vulnerable.

8.5 Early Detection of Lung Cancer and Mortality Reduction with Low-Dose CT (LDCT)

Lung cancer is currently the leading cause of cancer-related mortality worldwide. Nevertheless, when diagnosed at the early stage (IA), it shows a survival rate of 75% at 5 years: it means that an early diagnosis is fundamental to reduce its mortality [52].

Low-dose CT (LDCT) is a low-dose radiation and rapid-execution imaging technique that has been largely studied as a screening method for lung cancer.

Two large randomized controlled trials of low-dose CT (LDCT)-based lung cancer screening in high-risk populations—the US National Lung Screening Trial (NLST) and NELSON—have provided evidence of a statistically significant mortality reduction in patients (20% for NLST, 24% in men and 33% in women for NELSON) LDCT-based screening programs for individuals at a high risk of lung cancer have already been implemented in the USA [53].

Following the US Preventive Services Task Force Recommendation Statement (USPSTF) guidelines, the annual screening for lung cancer with LDCT is recommended in adults aged 50–80 years who have a 20 pack-year smoking history and currently smoke or have quit within the past 15 years. Screening should be discontinued once a person has not smoked for 15 years or develops a health problem that substantially limits life expectancy or the ability to undergo curative lung surgery [54].

To better select the population at risk for lung cancer, they have introduced some risk-based prediction models (LLP and PLCO the most used) which include other risk factors like asbestos exposition, family history, cancer history, concomitant respiratory diseases, etc.

However, they yield modest additional life-years, increased overdiagnosis and poor benefit-to-harm ratio because of predominantly selecting older individuals. Efficient implementation of risk-based lung cancer screening requires careful consideration of life expectancy for determining optimal individual stopping ages. For example, in a recent study conducted in Germany as part of the German Lung Cancer Screening Intervention trial on 4052 long-term smokers, no significant reduction in lung cancer mortality was found among patients who underwent regular LDCTs. However, differential analyses by sex showed a significant reduction in lung cancer deaths among the screened women [55].

Effective risk stratification and management of detected lung nodules are crucial aspects for the success of any lung cancer screening programme. Many participants have a lung nodule detected at baseline which needs to be distinguished from a lung nodule developed within a known time frame.

Importantly, most lung nodules detected, either at baseline or thereafter, are small.

The assessment of nodule size has been based on the measurement of the longest diameter. However, nodules are rarely perfectly shaped, thus whenever possible, other means of size assessment such as volumetry estimation should be preferred.

Most nodules detected during lung cancer screening can be classified as low-risk or intermediate-risk nodules, involving decisions on additional follow-up screens (regular (1 year) or short-term (3 months)).

Regarding the screening frequency all countries recommend an annual screening interval; however, the outcomes of the NELSON study suggest that a sex-specific interval could be applied in the future because nodules tend to have a slower growth rate in women than in men.

Furthermore, analyzing the results from the Multicentric Italian Lung Detection (MILD) trial, it has been suggested that individuals with a negative baseline result might benefit from undergoing biennial instead of annual screening.

The debate on screening frequency is still ongoing (Table 8.7).

Numerous cost-effectiveness analyses have been conducted, some of them leading to both annual and biennial screening programmes potentially cost-effectiveness. Goffin et al. compared both strategies in a scenario using the NLST eligibility criteria, concluding that biennial screening used fewer resources and, although associated with lower gains of life-years, resulted in very similar quality-adjusted life-years gains over a time frame of 20 years.

The USA experience has shown only a fraction (<5%) of individuals at high risk of lung cancer who underwent through the screening programme, thus demonstrating the difficulties in the effective recruitment of participants in national screening programmes even when they are provided by most major medical societies.

The main reasons for low adherence most probably lay on the emotional involvement of the patient at high risk and on some limits of the method such as the high rate of false-positives and consequently the overdiagnosis: the NLST trial considered only two possible outcomes: positive or negative, with a 24% rate of FP.

However, in the NELSON trial, which has implemented the nodule-management protocols (introducing the "indeterminate" outcome) and risk-stratification algorithms, the false-positive rate was only 1.2% and the referral rate only 2.1%.

Challenges in the recruitment of high-risk and hard-to-reach individuals remain one of the major barriers to the implementation of lung cancer screening programmes. Even among the most efficient centers in terms of recruitment in ongoing UK implementation projects, few have a participation rate of >50%.

Table 8.7 Follow-up recommendations based on lung cancer nodule risk

Risk category	Lesions detected	Recommendation
Intermediate to high risk of lung cancer (<1%)	No baseline nodule; no new nodule at follow-up screening; solid baseline nodule <100 mm^3 or <5 mm; new solid nodule <30 mm^3 or <4 mm	Consider prolonged screening interval of up to 24 months
High risk of lung cancer (~3%)	Solid baseline nodule 100–300 mm^3 or 5–10 mm; new solid nodule 30–200 mm^3 or 4–8 mm; growing solid nodule with VDT of 400–600 days; subsolid nodule, baseline or new, of any size	Short-term follow-up (3 months); if negative: Annual screening
Very high risk of lung cancer (>15%)	Solid baseline nodule >300 mm^3 or >10 mm; new solid nodule >200 mm^3 or >8 mm; growing solid nodule with VDT <400 days; subsolid nodule that is growing or has an altered morphology	Referral to MDT for work-up; if negative: Annual screening

Source: Heuvelmans [56]. Appropriate screening intervals in low-dose CT lung cancer screening. Translational lung cancer research, 7(3), 281–287

During the COVID-19 pandemic, clinicians have been forced to balance the risk of delaying potentially necessary evaluation and management against the risks of exposing patients to the virus in hospital settings, or exposing healthcare workers to patients who may be asymptomatic carriers of the disease [57].

In this scenario, consensus statements were developed to guide clinicians managing lung cancer screening programs and patients with lung nodules during the COVID-19 pandemic, concluding that it is [58, 59] appropriate to defer enrollment in lung cancer screening and modify the evaluation of lung nodules due to the added risks from potential exposure. In particular more than 95% of the clinicians involved in the "CHEST expert panel" agreed to delay the evaluation of pulmonary nodules detected incidentally or by screening that have a low probability of cancer or are likely to be an indolent cancer [58, 60–67].

8.6 Therapy Response Evaluation in Lung Cancer Imaging

8.6.1 Post Surgery Imaging

8.6.1.1 Introduction

Lung cancers which fit into stage I (cT1N0 and cT2N0) or stage II (cT1N1, cT2N1 and cT3N0) can be eligible for surgery. Patients with a Stage IIIA neoplasia (cT3N1 and cT1–3N2) have a low probability of disease eradication by surgery alone, but they may be considered eligible after adjuvant therapy.

Up to 76% of lung cancer patients undergo some kind of surgery during their treatment journey. The commonly performed thoracic intervention on patients with lung cancer is the pulmonary resection. There are two main types of pulmonary resection: anatomical and non-anatomical. Anatomical resections are those which respect the scissures and/or the lung anatomical divisions, such as pneumonectomy, lobectomy, segmentectomy, or segmental resection. Two lobes in the right lung can also be removed in an upper lobectomy (excision of the upper and middle lobes) or in a lower lobectomy (excision of the lower and middle lobes). On the contrary, non-anatomical resections, which are also called atypical, usually remove a wedge-shaped portion of the lung parenchyma without respecting the anatomical boundaries.

Each procedure is subject to distinct postoperative complications, both early and delayed, which radiologists usually encounter in day-to-day practice.

8.6.1.2 Imaging Findings After Lung Resection

After the intervention the pleural space can be filled by air and/or fluid; one or more air-fluid levels may be present. If the resection does not involve the whole lung the pleural collection usually disappears in the following weeks-months, even if some chronic fluid accumulation may persist. If a radical pneumonectomy is carried out the affected hemithorax appears completely lucent in the X-rays performed immediately after the surgery and the mediastinum is slightly shifted toward the operated side. Fluid tends to gradually fill the pleural cavity in the days after surgery; complete filling may take as long as 30 days. Figure 8.13 shows an example of the chest

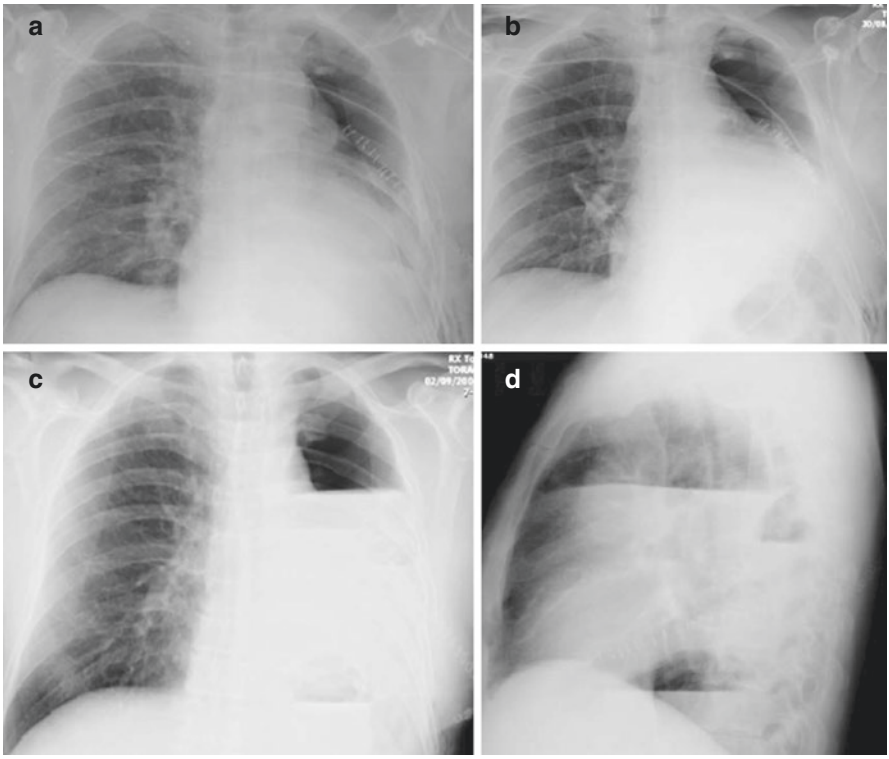

Fig. 8.13 (**a**) Chest X-ray obtained the first day after left pneumonectomy. (**b**) Chest X-ray obtained on the third day after the intervention in the same patient. (**c**, **d**) Postero-anterior and latero-lateral projections on the eighth day after the pneumonectomy. The images display how the left chest cavity is gradually filled with fluid and the mediastinum is shifted toward the operated side

cavity gradually filling with fluid. On the contrary, an increase in air component may indicate the presence of a perforation or a bronchopleural fistula. After the first month the residual lung tends to compensatory hyperinflation, while the mediastinal structures become furtherly shifted toward the operated side.

When an anatomical or an atypical partial resection is performed, volume loss is obviously expected. Pneumothorax may be present immediately after the surgery, as shown in Fig. 8.14. Surgical clips may be visible in the intervention site, where atelectasis or bleeding may also be found in the days after surgery. Muscle flaps are often used in order to obstruct the bronchi and prevent pneumothorax after lobectomy or pneumonectomy. Muscle tissue is commonly collected from the intercostal and from the serratus anterior; bone tissue may be present in the flap if periosteal tissue from the adjacent rib is included.

After the median longitudinal sternotomy, cerclage wires surrounding the sternal body are visible. If a traditional thoracotomy was performed a rib transection will be seen, while in case of an "en bloc" chest resection several consecutive ribs will

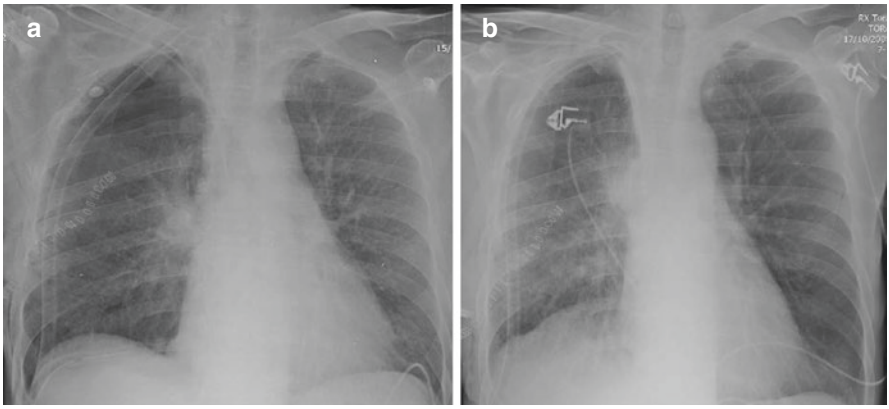

Fig. 8.14 (**a**) Chest X-ray performed the first day after a superior right lobectomy. The right diaphragm is elevated, subcutaneous edema and apical right pneumothorax are present. There is a basal drainage to collect pleural fluids and an apical drainage to collect air. (**b**) Chest X-ray performed on the same patient 3 days after the intervention. Resolution of the pneumothorax, no pleural effusion

be transected. Subcutaneous emphysema, seen as multiple parallel translucent lines in the subcutaneous tissue, is commonly seen after the surgery and usually reduces in subsequent radiographs.

8.6.1.3 Chest X-Ray

In the hours and days after the intervention, one or more chest radiographs are commonly performed in order to assess the position of lines and tubes in the patient's thorax cavity. More often than not these exams are performed in antero-posterior supine projection.

8.6.1.4 Chest CT

Patients with stage I or II lung cancer who were treated primarily with surgery should undergo a chest CT with intravenous contrast administration every 6 month for 2–3 years after the intervention according to the National Comprehensive Cancer Network (NCNN) guidelines. After that period of time, a noncontrast enhanced low-dose CT should be performed every year. On the other hand, patients with stage III lung cancer treated for curative and not palliative intent should undergo a contrast enhanced chest CT every 3–6 month for 3 years, followed by a contrast enhanced CT every 6 months for the subsequent 2 years and finally by a noncontrast enhanced low-dose CT performed annually.

8.6.1.5 Common Early Complications After Lung Cancer Resection

Bronchopleural Fistula: If the terminal airways are not correctly sealed after the intervention, a bronchopleural fistula may occur. On imaging, this is demonstrated by the postoperative pneumothorax failing to resolve or by the appearance of new air in the pleural space. A direct connection between the airway and the pleural

space may be demonstrated on chest CT, but not in every case. This complication often requires surgical intervention. Figure 8.15 shows an example of this complication.

Pneumonia: Aspiration, poor pain control, and mechanical ventilation may lead to pneumonia in the postoperative days. Radiological findings include ground glass opacities, consolidations, or cavitation that may be both peribronchial or subpleural. Pleural effusion may be present; an empyema may form following surgical contamination or preexisting infections. Pneumonectomy patients are the most affected.

Adult respiratory distress syndrome (ARDS): From 2 to 15% of patients undergoing thoracotomy develop a diffuse damage of the alveolar-capillary barrier resulting in acute lung injury (ALI). Clinically, respiratory failure and decreased PaO_2/FiO_2 ratio may be present. Findings on chest X-ray are nonspecific and are similar to those of typical pulmonary edema and pulmonary hemorrhage. On chest CT, the typical pattern involves bilateral dishomogeneous pulmonary opacifications that usually form a gravitational pattern, with lung consolidations in the most dependent areas and ground glass opacities in the superior regions. Additionally, bronchial dilatation in the ground glass areas and pulmonary cysts may be present. The prognosis is poor, with mortality that can be as high as 50%.

Pulmonary edema: This complication is more common after pneumonectomy. It is caused by augmented hydrostatic pressure and by altered alveolo-capillary barrier. Pulmonary edema is more common in patients who underwent abundant perioperative fluid resuscitations or plasma transfusions; even patients who suffer from arrhythmias are more affected. On chest X-ray common findings include interlobular septal thickening, Kerley B lines, and diffuse alveolar opacities. The most important differential diagnoses include pneumonia and ARDS.

Hemothorax: A damage to pulmonary or systemic vasculature can lead to a pleural space hematoma in up to 1.3% of operated patients. On X-rays a rapidly increasing pleural effusion may generate the suspicion of pleural hematoma and lead to further investigations. On chest CT, the pleural collection demonstrates diffusely high density values ranging from 40 to 90 Hounsfield units. A surgical reintervention to evacuate the collection is often needed.

Lung torsion: This is an infrequent complication with modern surgery techniques. However, a pulmonary lobe can undergo a torsion in the setting of pleural effusion and pneumothorax. The middle lobe is most commonly affected. On chest radiographs, the lobe appears diffusely radiopaque and reduced in dimensions, and also the lobar position can be unusual. On chest CT, the lobe appears diffusely hyperdense because of atelectasis and venous congestion; the airways and the vessels appear to be distorted and possibly occluded.

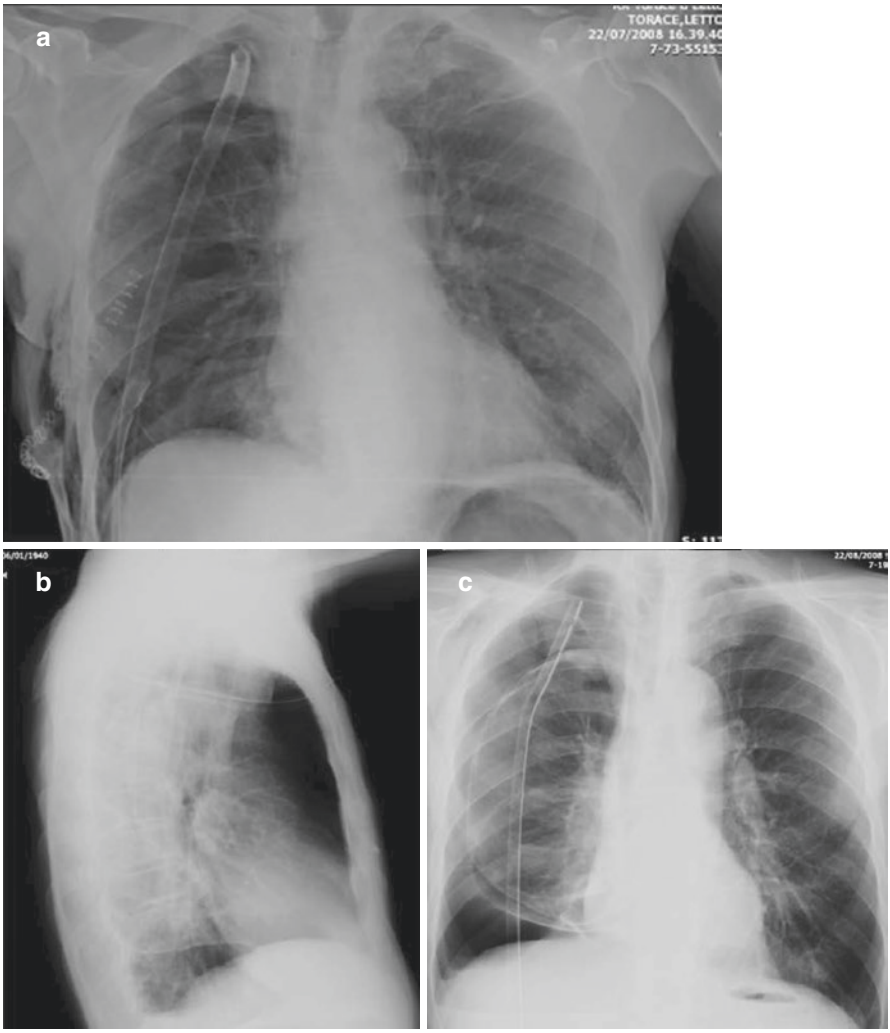

Fig. 8.15 (**a**) Chest X ray obtained the first day after right inferior lobectomy shows a large right pneumothorax. (**b**, **c**) The control X-ray obtained 30 days after the intervention shows how the pneumothorax fails to resolve. This raised the suspicion of bronchopleural fistula, which was subsequently confirmed via bronchoscopy

8.6.2 Response to Therapy Assessment: RECIST and iRECIST

8.6.2.1 Medical Therapy in Lung Cancer

In stage II and III lung cancer, adjuvant systemic chemotherapy can result in a 4 to 5% survival improvement at 5 years. In lower stages, the value of adjuvant therapy is more controversial: it was proved to result in a worse outcome in patients with

stage IA disease, while a limited survival benefit was demonstrated in patients with stage IB.

Neoadjuvant chemotherapy has not been so extensively evaluated; its use may however be beneficial since downstaging can be achieved, resulting in a less extensive resection.

Patients with locally advanced lung cancer (stage III) should undergo a contrast-enhanced total body CT to rule out distant metastases, followed by a PET/CT. A contrast enhanced brain MRI should also be performed to exclude intracranial localizations of the disease. Platinum based chemotherapy has proved to be effective in improving survival in stage III lung cancers, both in resectable and in unresectable tumors. Targeted immunotherapy agents have proven useful in the treatment of stage IV patients with specific mutations, such as EGFR and ALK. The role of immunotherapeutic agents in patients with stage I, II, and III lung cancer has not yet been evaluated properly, although several clinical trials are under way to assess the feasibility of targeted treatment in both the adjuvant and the neoadjuvant settings.

8.6.2.2 RECIST 1.1

Response evaluation criteria in solid tumors (RECIST) were first developed and published in 2000 but they have been extensively revised in 2009 when the updated RECIST came out. The objective of RECIST 1.1 guidelines is to simplify, optimize, and standardize the tumor burden response in solid tumors. Additionally, the guidelines give recommendations regarding the standard reporting in studies that utilize tumor reduction as primary endpoint.

RECIST 1.1 criteria dive the neoplastic lesions into *measurable* and *nonmeasurable*. Measurable lesions are those with a minimum size of 10 mm when measured with a CT scan or those with a minimum size of 20 mm when measured on chest X-rays. All other lesions are considered non measurable, including smaller lesions and truly unmeasurable lesions such as pleural effusion and neoplastic lymphangitis. Malignant lymph nodes are considered pathologically enlarged and measurable when their short axis assessed by CT scan is ≥15 mm. Only the short axis should be noted down at diagnosis and follow-up.

The initial neoplastic disease should be evaluated, establishing an *overall tumor burden at baseline*. In this occasion, the neoplastic disease localizations are to be divided into *target* and *nontarget* lesions. If more than a measurable lesion is present the radiologist should describe up to five target lesions, with a maximum of two target lesions for every organ. All target lesions must be measurable, and they should represent every involved organ; the choice of target lesions should take into account both the dimensions and the reproducibility of the measurement. That is, if the largest lesion does not lend itself to an accurate and reproducible dimensional assessment, the next biggest lesion should be chosen. A pathological lymph node can be a target lesion only if the short axis is ≥15 mm: only the short axis contributes to the tumor burden. All other lesions including other pathological lymph nodes are to be considered non target, but still correctly identified at baseline. The sum of all target lesions must be calculated: the short axis should be used for lymph nodes and the

biggest diameter should be used for all the other target lesions. This parameter is known as *baseline sum diameters*.

Target lesions response criteria:

- Complete response (CR): All target lesions are no longer visible, all pathological lymph nodes have a short axis <10 mm.
- Partial response (PR): A minimum decrease of 30% in the overall diameter of target lesions compared to the baseline sum diameters.
- Progressive disease (PD): An increase of the sum of the diameters of target lesion equal or superior to 20%, or the presentation of one or more new lesions.
- Stable disease (SD): Insufficient diameter reduction or increase to qualify either for PR or for PD.

Nontarget lesions response criteria:

- Complete response: all nontarget lesions are no longer visible, tumor markers are normal.
- Non-CR/non-PD: At least one nontarget lesion is still present or tumor markers levels are superior to the norm.
- Progressive disease: Categorical progression of preexisting nontarget lesions.

The response criteria of target and nontarget lesions are to be evaluated together, identifying the best overall response as shown in Table 8.8. Figures 8.16 and 8.17 show two clinical examples of partial response and progressive disease, respectively.

8.6.2.3 iRECIST

In recent years a new category of antineoplastic drugs has been developed, and it evolved into one of the most important in the treatment of aggressive tumors: immunomodulators. These highly specific pharmaceuticals act on specific intracellular pathways, such as CTLA 4, PD-1, and PD-L1, and agents active on those pathways have been marketed since 2011. Neoplastic diseases commonly treated with these agents include melanoma, bladder, kidney, lung, and head and neck cancers.

Table 8.8 Best overall response according to RECIST 1.1

Target lesions	Nontarget lesions	New lesions	Overall response
CR	CR	No	CR
CR	Non-CR/non-PD	No	PR
CR	Not evaluated	No	PR
PR	Non-PD or incompletely evaluated	No	PR
SD	Non-PD or incompletely evaluated	No	SD
Incompletely evaluated	Non-PD	No	NE
PD	Any	Yes or no	PD
Any	PD	Yes or no	PD
Any	Any	Yes	PD

CR complete response, *PR* partial response, *SD* stable disease, *PD* progressive disease, *NE* not evaluable

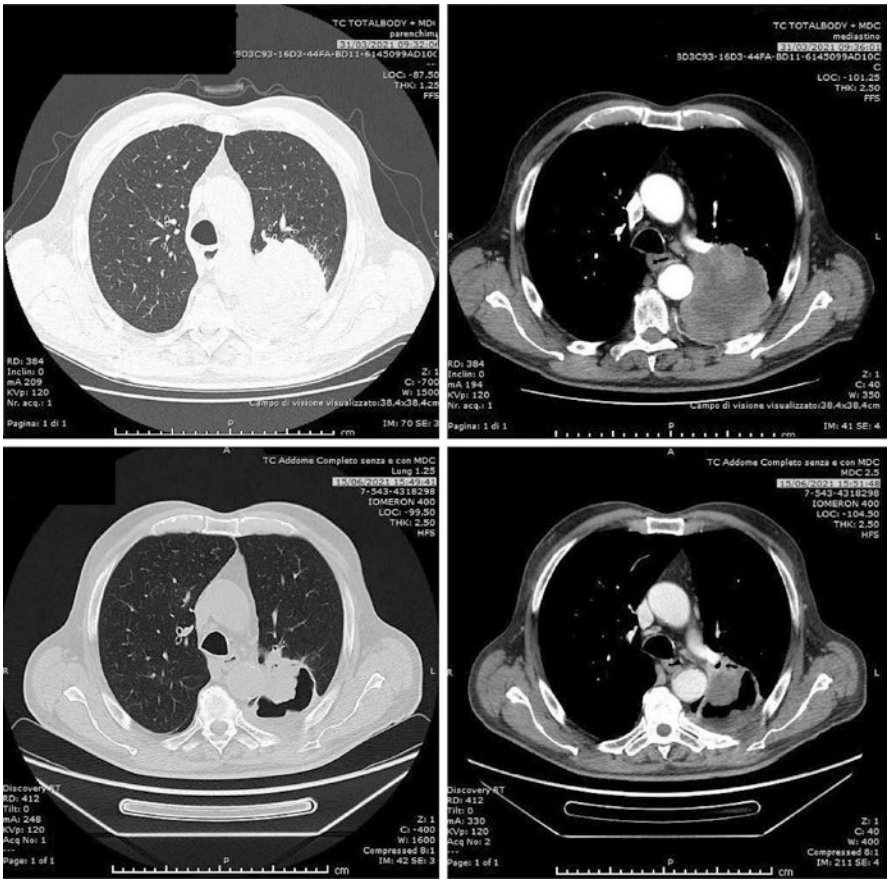

Fig. 8.16 Consecutive CT scans in a 71-year-old male patients. The images in the upper row are from the initial CT scan, while the lower pictures are from the follow-up CT scan obtained 3 months later, after 4 cycles of chemotherapy. The pulmonary mass shrinked from 8.7 to 6.1 cm; the pathological node's short axis reduced from 10 to 4 mm. This can be classified as partial response

Patients treated with these drugs can be a challenge for the radiologists, since immunomodulators can provoke an unusual pattern of response which resembles progressive disease. This concept has been known as *pseudoprogression*. From a histopathological point of view, the phenomenon of pseudoprogression seems to be correlated to the immune response stimulated by the drugs. The neoplastic tissue becomes infiltrated by T CD4+ and T CD8+ lymphocytes, and the inflammatory response may be accompanied by edema and hemorrhage. All these alterations can and often do result in a perceived increase of the tumoral mass, while the patient is actually responding to the therapy.

Given this response pattern, RECIST 1.1 felt inadequate to evaluate the therapy response in patients treated with immunomodulators, and new criteria had to be

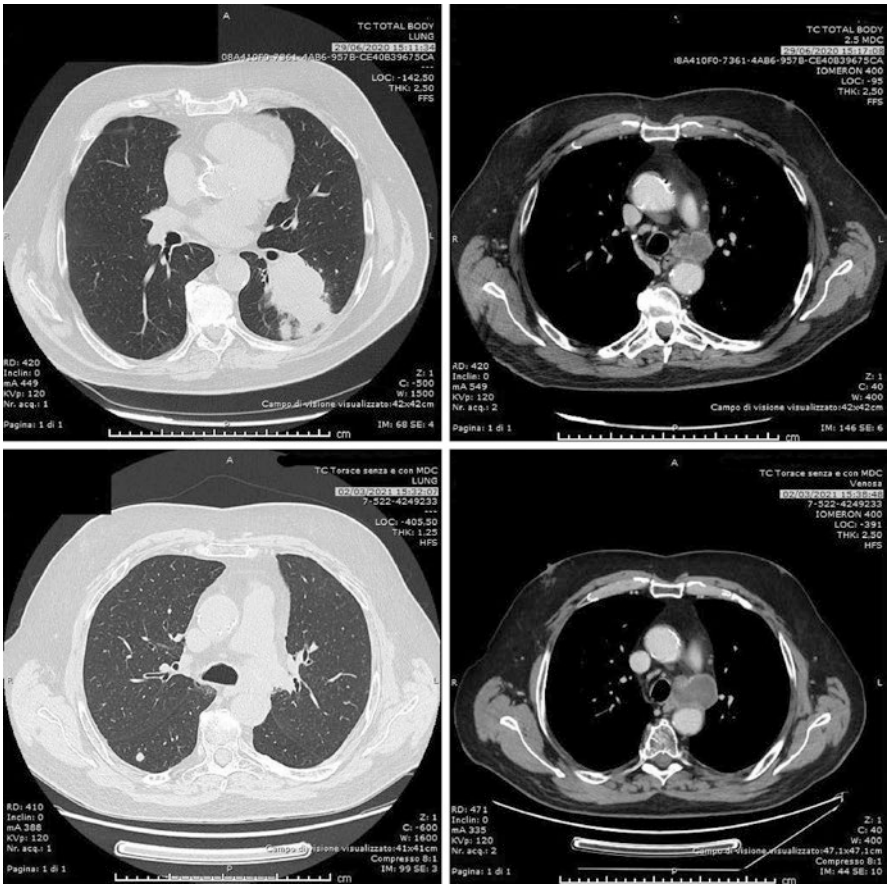

Fig. 8.17 Consecutive CT scans in a 74-year-old male patients. The images in the upper row are from the initial CT scan, while the lower pictures are from the follow-up CT scan obtained 9 months later, after chemotherapy treatment. A new lung nodule has appeared in the right lower lobe and the pathological node in the aorto-pulmonary window's short axis increased from 2.7 to 3.4 cm. This is progressive disease according to RECIST 1.1

developed by the RECIST working group itself. The new criteria, apart from adding the prefix "i" in front of the previous response evaluation classes (e.g., iCR, iPR), defined two new key concepts: unconfirmed progressive disease, **iUPD**, and confirmed progressive disease, **iCPD**.

iUPD is defined just like the progressive disease in RECIST 1.1, but it needs to be confirmed with a subsequent imaging evaluation obtained from 4 to 8 weeks after the first examination. The progression is confirmed only if there is a further increment of the previously reported lesions, or if there is dimensional expansion of previously stable localizations. If the progression is not confirmed, but instead the lesions show a volume decrease in comparison with baseline values compatible with iCR, iPR, or iSD, the bar is reset. In this case, iUPD has to manifest again and then to be confirmed in order to have a confirmed progressive disease (iCPD). As a

consequence iUPD can be assigned several times, as long as the progression is not confirmed in the following assessment. The appearance of new lesions results in iUPD, but the progression is confirmed only if other new lesions are present in the confirmatory evaluation or if the new lesions show dimensional increase. If iUPD was given only on the basis of target or nontarget lesions, then the progression *of the other category* in the confirmatory scan also brings to iCPD.

The principles for assigning the best overall response are similar to those described in RECIST 1.1, but the presence of iUPD makes things a little more intricate. In general, the best overall response in iRECIST (iBOR) is the best response to therapy recorded from the treatment start to its end, and all imaging evaluation must be taken into account. The assignment of an iUPD category will not nullify the following iBOR of iCR, IPR or iSD, as long as the requirements for iCPD are not met. A complete list of examples can be found in the iRECIST presentation article in the bibliography [51, 52, 68–77].

References

1. Parkin DM. Global cancer statistics in the year 2000. Lancet Oncol. 2001;2:533–43.
2. National Cancer Institute. Data sources: surveillance, epidemiology, and end results (SEER) 9 registries. National Cancer Institute; 2020.
3. Bravo-Iñiguez C, Perez Martinez M, Armstrong KW, et al. Surgical resection of lung cancer in the elderly. Thorac Surg Clin. 2014;24:371.
4. Kung HC, Hoyert DL, Xu J, Vincent GK, Velkoff VA. The next four decades-the older population in the United States: 2010 to 2050 Deaths: final data for 2005.
5. Mehta HJ, Ross C, Silvestri GA, et al. Evaluation and treatment of high-risk patients with early-stage lung cancer. Clin Chest Med. 2011;32:783.
6. Extermann M. Measuring comorbidity in older cancer patients. Eur J Cancer. 2000;36:453.
7. Smith PW, Jones DR. Biology and epidemiology of lung cancer. In: Patterson GA, Cooper JD, Deslauriers J, et al., editors. Pearson's thoracic and esophageal surgery. 3rd ed. Philadelphia, PA: Churchill Livingstone Elsevier; 2008.
8. Wingo PA, Cardinez CJ, Landis SH, et al. Long term trends in cancer mortality in the United States; 2003.
9. Hamilton W, Peters TJ, Round A, Sharp D. What are the clinical features of lung cancer before the diagnosis is made? A population based case-control study. Thorax. 2005;60(12):1059–65. https://doi.org/10.1136/thx.2005.045880.
10. Nasim F, Sabath BF, Eapen GA. Lung cancer. Med Clin N Am. 2019;103(3):463–73. https://doi.org/10.1016/j.mcna.2018.12.006.
11. Gridelli C, Perrone F, Gallo C, et al. Chemotherapy for elderly patients with advanced non small-cell lung cancer: the multicenter Italian lung cancer in the elderly study (MILES) phase III randomized trial. J Natl Cancer Inst. 2003;95:362–72.
12. National Center for Health Statistics: Health, United States, 7982. DHHS Pub. No. (PHS) 83–1232. Public Health Service. Washington: U.S. Government Printing Office; 1982.
13. Peto R, Darby S, Deo H, Silcocks P, Whitley E, Doll R. Smoking, smoking cessation, and lung cancer in the UK since 1950: combination of national statistics with two case-control studies. BMJ. 2000;321(7257):323–9.
14. Alberg AJ, Samet JM. Epidemiology of lung cancer. Chest. 2003;123:21S.
15. Ries LAG, Eisner MP, Kosary CL, et al. SEER Cancer Statistics Review 1975–2000.
16. Van Meerbeeck JP, Fennell DA, De Ruysscher DKM. Small-cell lung cancer. Lancet. 2011;378(9804):1741–55. https://doi.org/10.1016/S0140-6736(11)60165-7.

17. Bradley SH, Grice A, Neal RD, Abraham S, Rodriguez Lopez R, Shinkins B, Callister MEJ, Hamilton WT. Sensitivity of chest X-ray for detecting lung cancer in people presenting with symptoms: a systematic review. Br J Gen Pract. 2019;69(689):E827–35. https://doi.org/10.3399/bjgp19X706853.
18. Missrie I, Hochhegger B, Zanon M, Capobianco J, de Macedo C, Neto A, Maciel RP, Antunes VB, de Figueiredo CM, Szarf G, Meirelles G. Small low-risk pulmonary nodules on chest digital radiography: can we predict whether the nodule is benign? Clin Radiol. 2018;73(10):902–6. https://doi.org/10.1016/j.crad.2018.06.002.
19. William H. Learning radiology; n.d.
20. Vogl TJ, Reith W, Rummeny EJ. Diagnostic and interventional radiology. In: Diagnostic and interventional radiology; 2016. https://doi.org/10.1007/978-3-662-44037-7.
21. Hansell DM, Bankier AA, MacMahon H, McLoud TC, Müller NL, Remy J. Fleischner society: glossary of terms for thoracic imaging. Radiology. 2008;246(3):697–722. Epub 2008 Jan 14. PMID: 18195376. https://doi.org/10.1148/radiol.2462070712.
22. MacMahon H, Naidich DP, Goo JM, Lee KS, Leung ANC, Mayo JR, Mehta AC, Ohno Y, Powell CA, Prokop M, Rubin GD, Schaefer-Prokop CM, Travis WD, Van Schil PE, Bankier AA. Guidelines for management of incidental pulmonary nodules detected on CT images: from the Fleischner Society 2017. Radiology. 2017;284(1):228–43. Epub 2017 Feb 23. PMID: 28240562. https://doi.org/10.1148/radiol.2017161659.
23. Gruden JF, Ouanounou S, Tigges S, Norris SD, Klausner TS. Incremental benefit of maximum-intensity-projection images on observer detection of small pulmonary nodules revealed by multidetector CT. AJR Am J Roentgenol. 2002;179(1):149–57. PMID: 12076925. https://doi.org/10.2214/ajr.179.1.1790149.
24. Bueno J, Landeras L, Chung JH. Updated Fleischner society guidelines for managing incidental pulmonary nodules: common questions and challenging scenarios. Radiographics. 2018;38(5):1337–50. PMID: 30207935. https://doi.org/10.1148/rg.2018180017.
25. Hasegawa M, Sone S, Takashima S, Li F, Yang ZG, Maruyama Y, Watanabe T. Growth rate of small lung cancers detected on mass CT screening. Br J Radiol. 2000;73(876):1252–9. PMID: 11205667. https://doi.org/10.1259/bjr.73.876.11205667.
26. Detterbeck FC, Boffa DJ, Kim AW, Tanoue LT. The eighth edition lung cancer stage classification. Chest. 2017;151(1):193–203. Epub 2016 Oct 22. PMID: 27780786. https://doi.org/10.1016/j.chest.2016.10.010.
27. Cittadini G, Cittadini G, Sardarelli F. Cittadini—Diagnostica per immagini e radioterapia; n.d.
28. Goldstraw P, Chansky K, Crowley J, Rami-Porta R, Asamura H, Eberhardt WE, Nicholson AG, Groome P, Mitchell A, Bolejack V, International Association for the Study of Lung Cancer Staging and Prognostic Factors Committee, Advisory Boards, and Participating Institutions; International Association for the Study of Lung Cancer Staging and Prognostic Factors Committee Advisory Boards and Participating Institutions. The IASLC Lung Cancer Staging Project: Proposals for Revision of the TNM Stage Groupings in the Forthcoming (Eighth) Edition of the TNM Classification for Lung Cancer. J Thorac Oncol. 2016;11(1):39–51. 26762738. https://doi.org/10.1016/j.jtho.2015.09.009.
29. Carter BW, Lichtenberger JP 3rd, Benveniste MK, et al. Revisions to the TNM staging of lung cancer: rationale, significance, and clinical application. Radiographics. 2018;38(2):374–91. https://doi.org/10.1148/rg.2018170081.
30. Beasley MB, Brambilla E, Travis WD. The 2004 World Health Organization classification of lung tumors. Semin Roentgenol. 2005;40(2):90–7. PMID: 15898407. https://doi.org/10.1053/j.ro.2005.01.001.
31. Govindan R, Page N, Morgensztern D, Read W, Tierney R, Vlahiotis A, Spitznagel EL, Piccirillo J. Changing epidemiology of small-cell lung cancer in the United States over the last 30 years: analysis of the surveillance, epidemiologic, and end results database. J Clin Oncol. 2006;24(28):4539–44. PMID: 17008692. https://doi.org/10.1200/JCO.2005.04.4859.
32. Zhao YR, Heuvelmans MA, Dorrius MD, van Ooijen PM, Wang Y, de Bock GH, Oudkerk M, Vliegenthart R. Features of resolving and nonresolving indeterminate pulmonary nodules at

follow-up CT: the NELSON study. Radiology. 2014;270(3):872–9. Epub 2013 Nov 18. PMID: 24475806. https://doi.org/10.1148/radiol.13130332.
33. Rosado-de-Christenson ML, Templeton PA, Moran CA. Bronchogenic carcinoma: radiologic-pathologic correlation. Radiographics. 1994;14(2):429–46. quiz 447–8. PMID: 8190965. https://doi.org/10.1148/radiographics.14.2.8190965.
34. Hollings N, Shaw P. Diagnostic imaging of lung cancer. Eur Respir J. 2002;19(4):722–42. PMID: 11999004. https://doi.org/10.1183/09031936.02.00280002.
35. Austin JH, Garg K, Aberle D, Yankelevitz D, Kuriyama K, Lee HJ, Brambilla E, Travis WD. Radiologic implications of the 2011 classification of adenocarcinoma of the lung. Radiology. 2013;266(1):62–71. Epub 2012 Oct 15. PMID: 23070271. https://doi.org/10.1148/radiol.12120240.
36. Mets OM, Chung K, Scholten ET, Veldhuis WB, Prokop M, van Ginneken B, Schaefer-Prokop CM, de Jong PA. Incidental perifissural nodules on routine chest computed tomography: lung cancer or not? Eur Radiol. 2018;28(3):1095–101. Epub 2017 Oct 6. PMID: 28986629; PMCID: PMC5811588. https://doi.org/10.1007/s00330-017-5055-x.
37. Lambe G, Durand M, Buckley A, Nicholson S, McDermott R. Adenocarcinoma of the lung: from BAC to the future. Insights Imaging. 2020;11(1):69. PMID: 32430670; PMCID: PMC7237554. https://doi.org/10.1186/s13244-020-00875-6.
38. Aoki T, Nakata H, Watanabe H, Nakamura K, Kasai T, Hashimoto H, Yasumoto K, Kido M. Evolution of peripheral lung adenocarcinomas: CT findings correlated with histology and tumor doubling time. AJR Am J Roentgenol. 2000;174(3):763–8. PMID: 10701622. https://doi.org/10.2214/ajr.174.3.1740763.
39. Altmayer S, Verma N, Francisco MZ, Almeida RF, Mohammed TL, Hochhegger B. Classification and imaging findings of lung neoplasms. Semin Roentgenol. 2020;55(1):41–50. Epub 2019 Oct 25. PMID: 31964479. https://doi.org/10.1053/j.ro.2019.10.002.
40. Sholl LM. Large-cell carcinoma of the lung: a diagnostic category redefined by immunohistochemistry and genomics. Curr Opin Pulm Med. 2014;20(4):324–31. . PMID: 24811836. https://doi.org/10.1097/MCP.0000000000000068.
41. Carter BW, Glisson BS, Truong MT, Erasmus JJ. Small cell lung carcinoma: staging, imaging, and treatment considerations. Radiographics. 2014;34(6):1707–21. PMID: 25310425. https://doi.org/10.1148/rg.346140178.
42. Benson RE, Rosado-de-Christenson ML, Martínez-Jiménez S, Kunin JR, Pettavel PP. Spectrum of pulmonary neuroendocrine proliferations and neoplasms. Radiographics. 2013;33(6):1631–49. PMID: 24108555. https://doi.org/10.1148/rg.336135506.
43. Lee D, Rho JY, Kang S, Yoo KJ, Choi HJ. CT findings of small cell lung carcinoma: can recognizable features be found? Medicine (Baltimore). 2016;95(47):e5426. PMID: 27893684; PMCID: PMC5134877. https://doi.org/10.1097/MD.0000000000005426.
44. Sharma G, Goodwin J. Effect of aging on respiratory system physiology and immunology. Clin Interv Aging. 2006;1(3):253–60. https://doi.org/10.2147/ciia.2006.1.3.253.
45. Gossner J, Nau R. Geriatric chest imaging: when and how to image the elderly lung, age-related changes, and common pathologies. Radiol Res Pract. 2013;2013:584793. https://doi.org/10.1155/2013/584793.
46. Brandsma C-A, de Vries M, Costa R, Woldhuis RR, Königshoff M. Wim Timens lung ageing and COPD: is there a role for ageing in abnormal tissue repair? Eur Respir Rev. 2017;26(146):170073. https://doi.org/10.1183/16000617.0073-2017.
47. Groenink M, Langerak SE, Vanbavel E, van der Wall EE, Mulder BJ, van der Wal AC, Spaan JA. The influence of aging and aortic stiffness on permanent dilation and breaking stress of the thoracic descending aorta. Cardiovasc Res. 1999;43(2):471–80. https://doi.org/10.1016/S0008-6363(99)00095-4.
48. Freeman LM, Stein EG, Sprayregen S, Chamarthy M, Haramati LB. The current and continuing important role of ventilation-perfusion scintigraphy in evaluating patients with suspected pulmonary embolism. Semin Nucl Med. 2008;38(6):432–40.

49. Lowery EM, Brubaker AL, Kuhlmann E, Kovacs EJ. The aging lung. Clin Interv Aging. 2013;8:1489–96. https://doi.org/10.2147/CIA.S51152.
50. Copley SJ, Wells AU, Hawtin KE, et al. Lung morphology in the elderly: comparative CT study of subjects over 75 years old versus those under 55 years old. Radiology. 2009;251(2):566–73.
51. British Thoracic Society; Society of Cardiothoracic Surgeons of Great Britain and Ireland Working Party. BTS guidelines: guidelines on the selection of patients with lung cancer for surgery. Thorax. 2001;56(2):89–108. PMID: 11209097; PMCID: PMC1745996. https://doi.org/10.1136/thorax.56.2.89.
52. Cassidy A, Myles JP, et al. The LLP risk model: an individual risk prediction model for lung cancer. Br J Cancer. 2008;98:270–6.
53. de Koning HJ, van der Aalst CM, et al. Reduced lung-cancer mortality with volume CT screening in a randomized trial. N Engl J Med. 2020;382(6):503–13.
54. Goffin JR. Biennial lung cancer screening in Canada with smoking cessation-outcomes and cost-effectiveness. Lung Cancer. 2016;101:98–103.
55. Becker N, Motsch E, Trotter A, et al. Lung cancer mortality reduction by LDCT screening-results from the randomized German LUSI trial. Int J Cancer. 2020;146(6):1503–13. https://doi.org/10.1002/ijc.32486.
56. Heuvelmans MA. Appropriate screening intervals in low-dose CT lung cancer screening. Transl Lung Cancer Res. 2018;7(3):281–7.
57. Mazzone PJ. Management of Lung Nodules and Lung Cancer Screening during the COVID-19 pandemic: CHEST expert panel report. Chest. 2020;158(1):406–15.
58. Ten Haaf KT, Bastani M, et al. A comparative modeling analysis of risk-based lung cancer screening strategies. J Natl Cancer Inst. 2020;112:466–79.
59. US Preventive Services Task Force. Screening for Lung Cancer: US Preventive Services Task Force Recommendation Statement. JAMA. 2021;325:962–70.
60. National Lung Screening Trial Research Team. Reduced lung-cancer mortality with low-dose computed tomographic screening. N Engl J Med. 2011;365(5):395–409.
61. Oudkerk M, et al. European position statement on lung cancer screening. Lancet Oncol. 2017;18:e754–66.
62. Oudkerk ML, et al. Lung cancer LDCT screening and mortality reduction—evidence, pitfalls and future perspectives. Nat Rev Clin Oncol. 2021;18:135–51.
63. Pastorino US. Prolonged lung cancer screening reduced 10-year mortality in the MILD trial: new confirmation of lung cancer screening efficacy. Ann Oncol. 2019;30(7):1162–9.
64. Pham D, Bhandari S, et al. Lung cancer screening registry reveals low-dose CT screening remains heavily underutilized. Clin Lung Cancer. 2020;21:e206–11.
65. Radiology AC. Lung RADS version 1.1. 2019.
66. Rampinelli C, De Marco P, et al. Exposure to low-dose computed tomography for lung cancer screening and risk of cancer: secondary analysis of trial data and risk-benefit analysis. BMJ. 2017;356:j347.
67. Tammemägi MC, Haaf KT, et al. Development and validation of a multivariable lung cancer risk prediction model that includes low-dose computed tomography screening results: a secondary analysis of data from the National Lung Screening Trial. JAMA Netw Open. 2019;2:e190204.
68. Brunelli A, Charloux A, Bolliger CT, Rocco G, Sculier J-P, Varela G, Licker M, Ferguson MK, Faivre-Finn C, Huber RM, Clini EM, Win T, De Ruysscher D, Goldman L. ERS/ESTS clinical guidelines on fitness for radical therapy in lung cancer patients (surgery and chemoradiotherapy). Eur Respir J. 2009;34(1):17–41. https://doi.org/10.1183/09031936.00184308.
69. American Cancer Society. Cancer treatment and survivorship facts & figures 2014–2015. Atlanta: American Cancer Society; 2014.
70. Cardinale L, Priola AM, Priola SM, Boccuzzi F, Dervishi N, Lisi E, Veltri A, Ardissone F. Radiological contribution to the diagnosis of early postoperative complications after lung resection for primary tumor: a revisional study. J Thorac Dis. 2016;8(8):E643–52. PMID: 27621893; PMCID: PMC4999725. https://doi.org/10.21037/jtd.2016.07.02.

71. de Groot PM, Truong MT, Godoy MCB. Postoperative imaging and complications in resection of lung cancer. Semin Ultrasound CT MR. 2018;39(3):289–96. Epub 2018 Mar 1. PMID: 29807639. https://doi.org/10.1053/j.sult.2018.02.008.
72. Chae EJ, Seo JB, Kim SY, Do KH, Heo JN, Lee JS, Song KS, Song JW, Lim TH. Radiographic and CT findings of thoracic complications after pneumonectomy. Radiographics. 2006;26(5):1449–68. PMID: 16973775. https://doi.org/10.1148/rg.265055156.
73. Ettinger DS, Wood DE, Akerley W, Bazhenova LA, Borghaei H, Camidge DR, Cheney RT, Chirieac LR, D'Amico TA, Dilling TJ, Dobelbower MC, Govindan R, Hennon M, Horn L, Jahan TM, Komaki R, Lackner RP, Lanuti M, Lilenbaum R, Lin J, Loo BW Jr, Martins R, Otterson GA, Patel JD, Pisters KM, Reckamp K, Riely GJ, Schild SE, Shapiro TA, Sharma N, Stevenson J, Swanson SJ, Tauer K, Yang SC, Gregory K, Hughes M. NCCN Guidelines Insights: Non-Small Cell Lung Cancer, Version 4.2016. J Natl Compr Canc Netw. 2016;14(3):255–64. PMID: 26957612. https://doi.org/10.6004/jnccn.2016.0031.
74. Eisenhauer EA, Therasse P, Bogaerts J, Schwartz LH, Sargent D, Ford R, Dancey J, Arbuck S, Gwyther S, Mooney M, Rubinstein L, Shankar L, Dodd L, Kaplan R, Lacombe D, Verweij J. New response evaluation criteria in solid tumours: revised RECIST guideline (version 1.1). Eur J Cancer. 2009;45(2):228–47. PMID: 19097774. https://doi.org/10.1016/j.ejca.2008.10.026.
75. Seymour L, Bogaerts J, Perrone A, Ford R, Schwartz LH, Mandrekar S, Lin NU, Litière S, Dancey J, Chen A, Hodi FS, Therasse P, Hoekstra OS, Shankar LK, Wolchok JD, Ballinger M, Caramella C, de Vries EGE, RECIST Working Group. iRECIST: guidelines for response criteria for use in trials testing immunotherapeutics. Lancet Oncol. 2017;18(3):e143–52. Epub 2017 Mar 2. Erratum in: Lancet Oncol. 2019 May;20(5):e242. PMID: 28271869; PMCID: PMC5648544. https://doi.org/10.1016/S1470-2045(17)30074-8.
76. Postmus PE, Kerr KM, Oudkerk M, Senan S, Waller DA, Vansteenkiste J, Escriu C, Peters S, ESMO Guidelines Committee. Early and locally advanced non-small-cell lung cancer (NSCLC): ESMO Clinical Practice Guidelines for diagnosis, treatment and follow-up. Ann Oncol. 2017;28(suppl_4):iv1–iv21. PMID: 28881918. https://doi.org/10.1093/annonc/mdx222.
77. McWilliams A, Tammemagi MC, Mayo JR, Roberts H, Liu G, Soghrati K, Yasufuku K, Martel S, Laberge F, Gingras M, Atkar-Khattra S, Berg CD, Evans K, Finley R, Yee J, English J, Nasute P, Goffin J, Puksa S, Stewart L, Tsai S, Johnston MR, Manos D, Nicholas G, Goss GD, Seely JM, Amjadi K, Tremblay A, Burrowes P, MacEachern P, Bhatia R, Tsao MS, Lam S. Probability of cancer in pulmonary nodules detected on first screening CT. N Engl J Med. 2013;369(10):910–9. PMID: 24004118; PMCID: PMC3951177. https://doi.org/10.1056/NEJMoa1214726.

The Gastrointestinal System in Geriatric Patients

9

Damiano Caruso, Domenico De Santis,
Francesco Pucciarelli, and Andrea Laghi

9.1 Introduction

All organs and physiological processes of the human organism, including gastrointestinal system, are affected by aging [1]. Effect of aging of gastrointestinal system includes a reduction in sensory perceptions, salivation, oral health, the absorption of nutrients, and lactose tolerance. Although many of these age-related changes are primarily functional, there are other changes that can be detected with imaging techniques (e.g., pancreatic atrophy, lobulation, and fatty degeneration [2]). Functional changes can then result in organic alterations and therefore become visible by imaging, both directly and indirectly [3]. In this type of patient, diagnostic imaging acquires an increasingly important value, and constant technological innovations allow for a more accurate and early diagnosis.

One of the main problems of geriatric imaging is that patients might have multiple comorbidities, making it difficult for them to collaborate during the examination [4]. In fact, from the simplest of exams (such as X-ray) up to technically more complex examinations (such as MR-cholangiography), patient collaboration is a fundamental requirement in order to reduce artifacts and achieve reliable diagnostic quality.

This chapter will be focused on the main pathologies and problems related to the imaging of the elderly and the main strategies to solve them will be illustrated in the following paragraphs.

D. Caruso · D. De Santis · F. Pucciarelli · A. Laghi (✉)
Radiology Unit, Department of Medical Surgical Sciences and Translational Medicine, Sant'Andrea University Hospital, Sapienza—University of Rome, Rome, Italy
e-mail: andrea.laghi@uniroma1.it

G. Guglielmi, M. Maas (eds.), *Imaging in Geriatrics*, Practical Issues in Geriatrics, https://doi.org/10.1007/978-3-031-14877-4_9

9.2 Esophagus

9.2.1 Achalasia

Achalasia is an esophageal motility disorder characterized by the absence of primary peristalsis and impaired lower esophageal sphincter (LES) relaxation [5]. Achalasia can be primary (idiopathic) or secondary (pseudoachalasia), caused by malignant tumor at the gastroesophageal junction (GEJ) or, less commonly, by benign conditions such as Chagas' disease [6]. Achalasia is most frequently seen in middle and late adulthood with no gender predilection. Dysphagia is the main symptom, diagnosis is based on clinical findings and esophageal manometry [7].

9.2.1.1 Imaging Findings

Barium studies show a dilated non-peristaltic esophagus with smooth, tapered, symmetrical narrowing ("bird-beak narrowing") at the GEJ [6]. Computed tomography (CT) is useful for the evaluation of common complications (such as pneumomediastinum or pneumopericardium subsequent to esophageal perforation, either iatrogenic or not; aspiration pneumonia, and esophageal carcinoma) and for the evaluation of causes of secondary achalasia, such as the infiltration of esophageal plex by a pancreatic neoplasm [8, 9] (Figs. 9.1 and 9.2).

9.2.2 Hiatal Hernia

Hiatal hernia is a condition in which elements of the abdominal cavity herniates through the esophageal hiatus into the mediastinum; prevalence of hiatal hernia increases with age, with a slight female predilection. The organ most commonly involved is the stomach, and the most comprehensive classification of hiatal hernias divides them into four types: sliding (type I, the most common, >90%) and paraesophageal (type II, III, and IV). In sliding hernia, the GEJ is usually displaced >2 cm above the esophageal hiatus, due to a widening of hiatus itself. In paraesophageal hernia, the GEJ remains in its

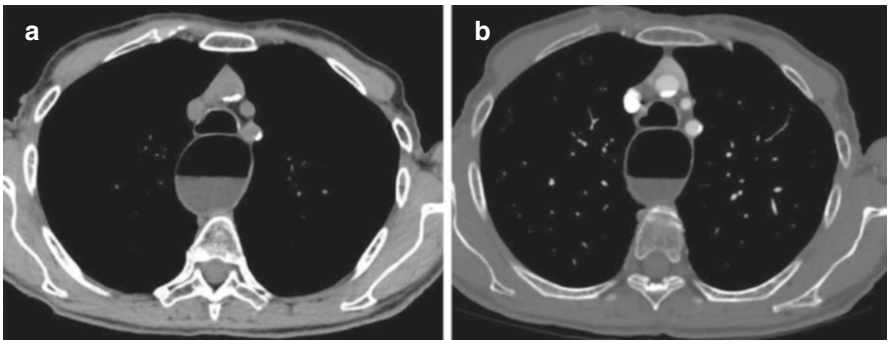

Fig. 9.1 Axial unenhanced CT (**a**) and portal venous phase (**b**) CT images of an 87-year-old woman with achalasia depicts a dilated and thin-walled esophagus containing air-fluid level

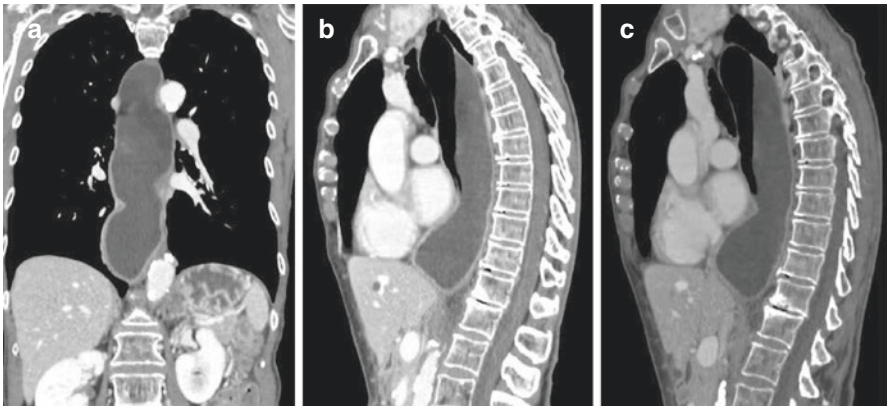

Fig. 9.2 Coronal (**a**) and sagittal reformatted (**b** and **c**) portal venous phase CT images of the same patient showing marked dilation of the entire esophagus, characterized by thin-wall and containing endoluminal air-fluid level

normal location while the fundus of the stomach herniates above the diaphragm through a defect in the phrenoesophageal membrane. Mixed hernias have also been described (type III), which simultaneously include components of type I and II. Type IV consists of mixed type with the association of herniation of other abdominal viscera. Hiatal hernia may be asymptomatic or cause nonspecific symptoms, such as chest pain or epigastric pain, nausea, and vomiting [10].

9.2.2.1 Imaging Findings

Chest X-ray is usually the imaging modality of first choice, especially in patients complaining chest pain. On standard chest X-ray typical sign is retrocardiac opacity with gas-fluid level. Contrast radiography under fluoroscopy is a useful modality for the identification of hiatal hernias, but it has some limitations in their classification (Fig. 9.3). The mobility of GEJ makes the "2 cm-rule" limiting, due to the esophagus shortening during swallowing of barium, which makes the measurement unreliable.

CT accurately identifies and classifies thoracic hernias, revealing a potential loss of integrity of the diaphragm, as well as the content of the hernia sac, especially using multiplanar reformatted images. CT imaging is also useful in the identification of compliances such as intestinal obstruction, highlighting dilated bowel tracts with air-fluid levels both in thorax and abdomen, and in the exclusion of other pathological conditions mimicking radiographic findings of hiatal hernia, such as epiphrenic esophageal diverticulum, retrocardiac lung abscess with concomitant air bubbles, and gastric pull-up surgery performed for esophageal tumors.

Ultrasound (US) and magnetic resonance (MRI) play a minor role. In particular transthoracic or transabdominal US examinations have some limitations due to gas-filled intrathoracic intestinal loops, aerated lungs, and acoustic shadowing from the ribs; this imaging modality is mostly used in pediatric cases. However, US can detect the hernia site and the integrity of diaphragm. The use of Echo Color Doppler (ECD) is helpful to directly visualize the vasculature of herniated organs [11]. Real-time MRI uses high spatiotemporal resolution sequences able to assess the dynamic

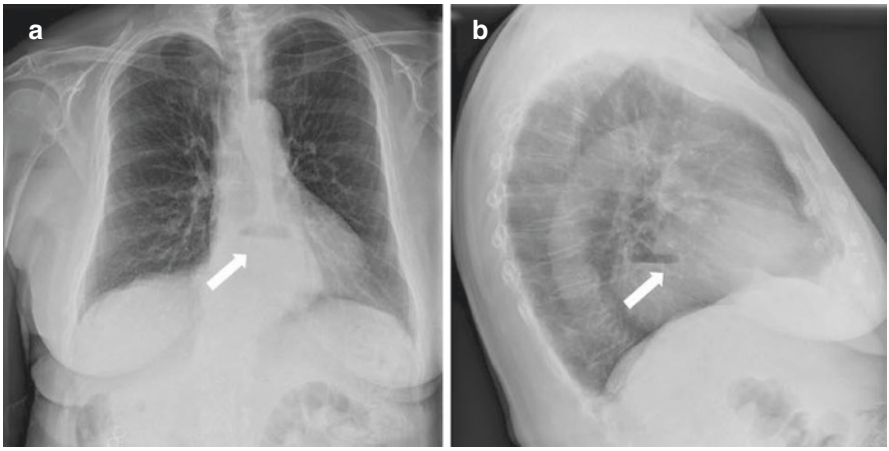

Fig. 9.3 Chest X-ray in posterior-anterior (**a**) and lateral view (**b**) of a 73-year-old woman with chest pain and dysphagia; a fluid-air level is present (arrows)

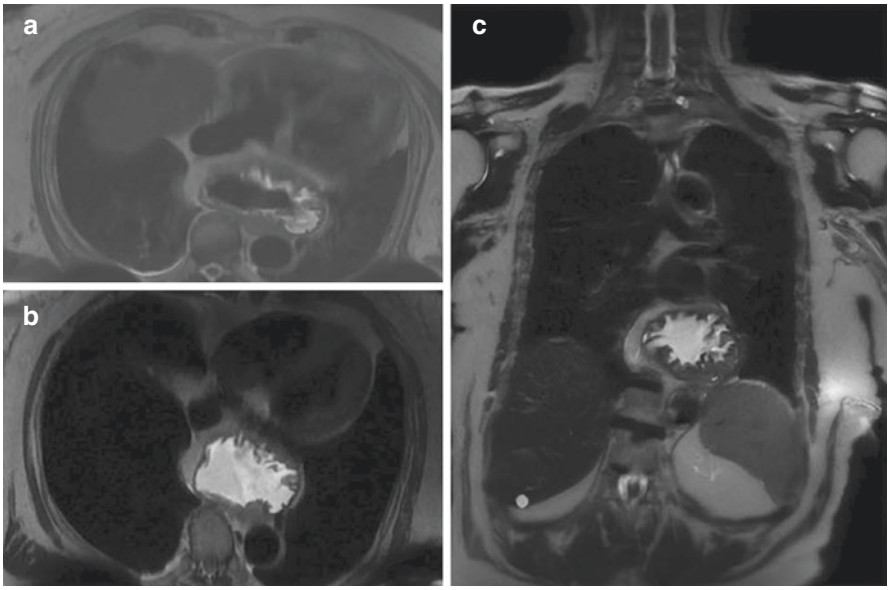

Fig. 9.4 MRI axial T2-weighted image without oral contrast (**a**), and axial and coronal T2-weighted images acquired after ingestion of oral contrast medium (**b** and **c**) of a 73-year-old woman with chest pain and dysphagia. A voluminous sliding hiatal hernia is confirmed

physiological process of swallowing but currently is not routinely performed. A recent study suggests the use of real-time MRI in patients with equivocal endoscopic results, preoperative assessment, and detection of surgical complications after fundoplication (Fig. 9.4) [12].

9.2.3 Ulcers

Esophageal ulcers are the complication of inflammatory pathologies affecting the esophagus. Common causes of esophagitis could be noninfectious (gastroesophageal reflux disease (GERD), post-actinic, drug-induced disease, etc.) or infectious (HIV, candida, etc.) [13]. GERD is very common in elderly individuals, with a prevalence of 14–20% [14].

9.2.3.1 Imaging Findings

Although endoscopy is the reference standard for evaluating esophageal mucosal pathology, radiology also plays an important role [13]. Superficial ulcers and erosions associated with reflux esophagitis can be seen on double-contrast studies such as tiny collections of barium at or near the gastroesophageal junction [13]. A minor role is played by CT, which is less sensitive and nonspecific [15].

9.2.4 Esophageal Cancer

Esophageal cancer is an uncommon cause of cancers, and its incidence increases rapidly after the age of 40 years; mortality of esophageal cancer before the age of 45 years is also relatively low and increases rapidly after the age of 50 years, peaking between the ages of 80 and 85 years [16]. The most common type of esophageal cancer is squamous cell carcinoma (81–90%), followed by adenocarcinoma (4–19%); alcohol, smoking, and Barret esophagus are some of the most common predisposing factors [17]. Clinical presentation is often nonspecific (dysphagia is one of the most frequent symptoms), and further symptoms may be related to both locoregional and distant disease dissemination.

9.2.4.1 Imaging Findings

Imaging methods are especially useful for disease staging, as the reference standard for diagnosis is endoscopy. Chest X-ray may show mostly indirect signs (irregularities of the esophageal lumen, signs of compression of the lesion, etc.).

CT not only allows the identification of signs related to the primary lesion, such as eccentric or circumferential wall thickening, but is also able to accurately assess locoregional dissemination (such as peri-esophageal soft tissue and fat stranding, tracheobronchial or aortic invasion) and the presence of distant metastases [17] (Fig. 9.5).

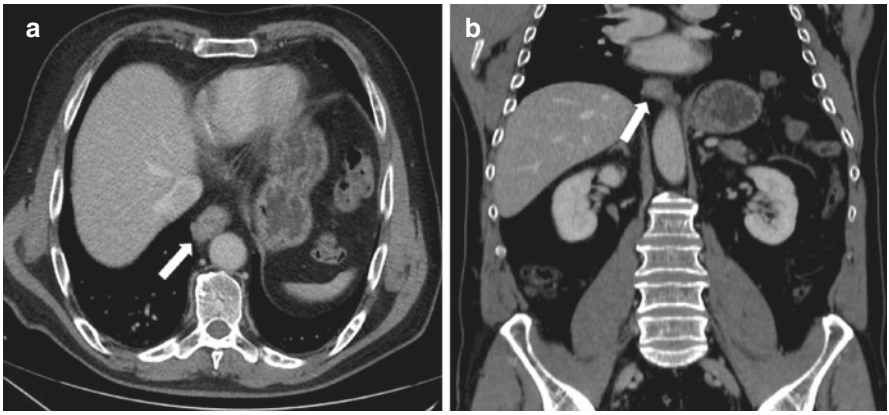

Fig. 9.5 Axial (**a**) and coronal (**b**) portal venous phase CT images of a 71-year-old man with distal esophagus cancer, showing circumferential irregular wall thickening (>5 mm; arrows)

9.3 Stomach and Duodenum

9.3.1 Peptic Ulcers

Peptic ulcers are the consequence of increased gastric acid secretion. *Helicobacter pylori* infection is the main cause of peptic ulcers, although other etiologies have been also recognized, such as stress and the use of nonsteroidal anti-inflammatory drugs and corticosteroids [18]. Although its incidence is showing a trend of decrease, peptic ulcer disease still represent a global problem, with a lifetime risk of development ranging from 5% to 10% [19]. Duodenal ulcers are four times more common than gastric ulcers; affected patients are often asymptomatic or present with nonspecific symptoms (epigastric pain, nausea, etc.) or with signs and symptoms related to complications (bleeding, perforation, etc.) [18].

9.3.1.1 Imaging Findings

The reference standard for diagnosis is gastroscopy; however, imaging is crucial for the assessment of complications. Gastric and duodenal peptic ulcers have similar features on double-contrast barium upper GI series, appearing as radiopaque outpouchings of the bowel wall when barium fills the ulcer crater [20]. CT plays a role in the detection of complications, in particular it can detect signs of perforation (pneumoperitoneum) and bleeding [21].

9.3.2 Duodenal Diverticulum

Duodenal diverticula are outpouching from the duodenal wall. They are usually located near the ampulla of Vater and often asymptomatic. If present, symptoms

are related to complications such as hemorrhage, inflammation (diverticulitis), jaundice, cholangitis, or perforation [22]. The presence of symptoms is correlated to the size of the diverticula: large diverticula might cause relatively high pressure upon the distal part of the common bile duct, reducing its caliber and causing functional bile stasis or reflux of duodenal content, including bacterial agents, which can ultimately lead to cholangitis, gallstones formation, and chronic pancreatitis [23, 24].

9.3.2.1 Imaging Findings

CT is the imaging technique of choice in the diagnosis of diverticula and their complications. Diverticula are identifiable as saccular outpouchings arising from the duodenum that may contain gas, fluid, contrast, food debris, or any combination of these. They often contain a gas-fluid or gas-contrast level [25].

MR cholangiography (MRC) can also evaluate the relationship between diverticula and the common bile duct. Highly T2-weighted sequences are crucial to detect high signal intensity structures, such as biliary fluid content. Small-sized duodenal diverticula can be overlooked, while the large ones are usually easily detected due to their fluid content [24].

9.3.3 Gastric and Duodenal Cancer

Gastric cancer is the fifth most commonly diagnosed cancer in the world, and the seventh most prevalent [26]; the cumulative risk of developing gastric cancer from birth to 74 years of age is 1.87% in males and 0.79% in females worldwide. The most common gastric malignancy is adenocarcinoma (95% of malignant tumors of the stomach); there is a strong association with *Helicobacter pylori* infection; and other risk factors are represented by smoking, pernicious anemia, anthropic gastritis, and adenomatous polyposis [27].

9.3.3.1 Imaging Findings

CT is the staging imaging modality of choice, capable of diagnosing primary tumor, assessing the locoregional spread, and detecting nodal involvement and distant metastases [28] (Figs. 9.6 and 9.7). Lesion detection is facilitated by ingestion of negative contrast agents (water or gas); typical findings depend on the morphology of lesions and includes a polypoid mass with or without ulceration, focal wall thickening with mucosal irregularity, or focal infiltration of the wall and ulcerations. Infiltrating carcinoma is typically characterized by wall thickening and loss of normal rugal fold pattern [29]. Comparable findings are found in duodenal cancer [30].

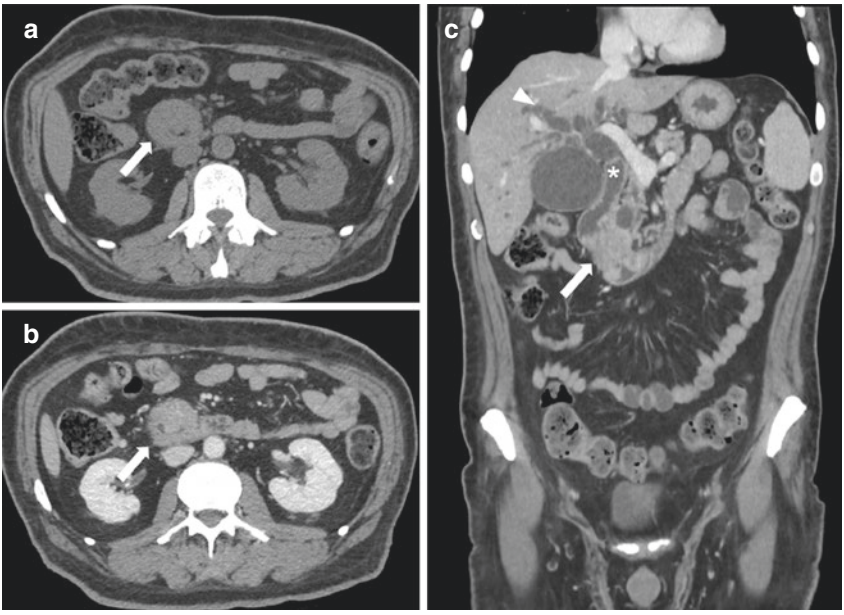

Fig. 9.6 Axial (**a**, **b**) and coronal (**c**) portal venous phase CT images of a 79-year-old man with duodenal cancer. Note the diffuse duodenal wall thickening (arrows) causing dilation of the main biliary duct (asterisk) and the intrahepatic biliary tree (arrowhead)

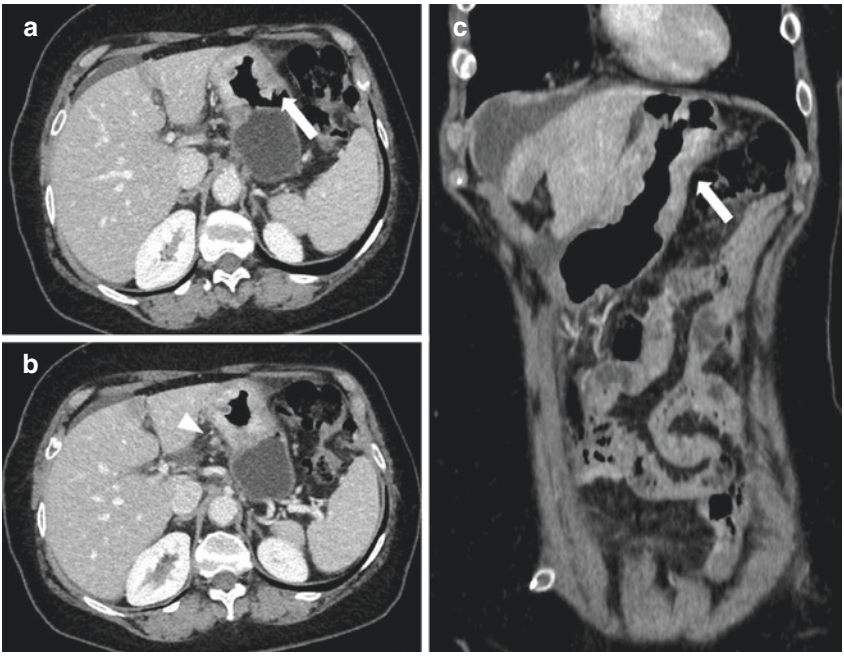

Fig. 9.7 Axial (**a**, **b**) and coronal (**c**) portal venous phase CT images of a 72-year-old woman with gastric cancer demonstrates extensive, circumferential, and irregular gastric wall thickening (arrow) and enlarged nodes in the lesser sac (arrowhead)

9.4 Small Bowel

9.4.1 Small Bowel Cancer

Primary neoplasms of the small bowel are rare, 60% of these tumors are malignant. Peak incidence occurs in the fifth and sixth decades, clinical manifestations are nonspecific and can include nausea, vomiting, abdominal pain, weight loss, and melena [31].

9.4.1.1 Imaging Findings

Small bowel imaging is challenging due to motion artifacts caused by bowel peristalsis and respiratory motion. Due to widespread availability and high diagnostic accuracy, CT and MR have become the imaging methods of choice for the assessment of the small bowel. CT enterography and MR enterography, characterized by oral ingestion of contras medium, provide excellent evaluation of small bowel tumors [32]. Furthermore, these techniques are also capable to identify peritoneal disease involvement (peritoneal carcinomatosis). Benign tumors can be directly visualized as well-circumscribed masses with smooth margins growing within the bowel lumen, their complications are represented by obstruction, intussusception, or bleeding. Malignant lesions are characterized by irregular margins and invasive locoregional growth; among malignant types, carcinoids are characterized by increased serotonin production, invasive growth, and pronounced perifocal fibrotic reaction (desmoplastic reaction). Typical imaging findings include muscularis propria thickening, puckering, wall retraction, serosal invasion, and mesenteric metastases.

9.5 Large Bowel

9.5.1 Colonic Diverticulosis

Colonic diverticulosis is a disease characterized by the presence of multiple diverticula; they are usually located at the mesenteric side of the colonic lumen, especially in the sigmoid colon and, to a lesser extent, in the descending colon, with a size range from a few millimeters to few centimeters [33, 34]. Chronic constipation is considered to be the main risk factor. Disease prevalence increases substantially with age, up to 50–66% in patients older than age 80 years. Diverticula are usually asymptomatic; when present, symptoms are related to complications like inflammation (diverticulitis) and perforation [35].

9.5.1.1 Imaging Findings

The imaging modality of choice in the assessment of colonic diverticula is CT, allowing precise evaluation of diverticula number, size, and location. CT is also able to identify complications and related inflammatory changes [36]. Imaging finding of inflammation include pericolic stranding, often disproportionately prominent

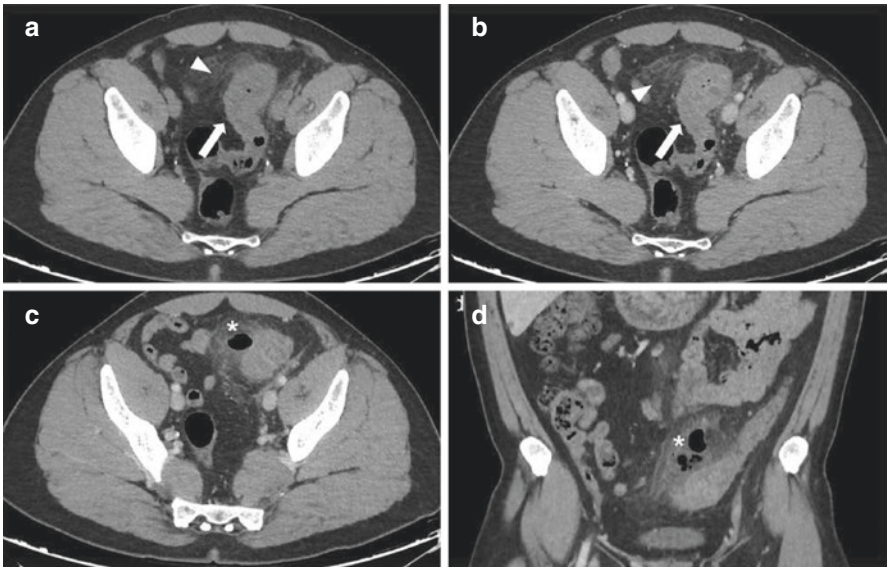

Fig. 9.8 Axial unenhanced phase (**a**), axial (**b**, **c**), and coronal reformatted (**d**) portal venous phase CT images of a 66-year-old man with acute diverticulitis, complicated with perforation. Note the pericolic stranding (arrowheads) and the segmental bowel wall thickening (arrows). Perforation is demonstrated by the presence of extra-intestinal air bubbles (asterisks)

compared to the amount of bowel wall thickening, segmental thickening, and colonic wall enhancement (Fig. 9.8). The latter is usually characterized by inner and outer high-attenuation layers with a thick middle layer of low attenuation. Complications include perforation, abscess formation (seen in up to 30% of cases) and fistulization (usually a long-term complication) [34].

9.5.2 Polyps

Polyps are wall protrusions and can be sessile or pedunculated. Mostly asymptomatic, they can cause symptoms in case of malignant transformation or in case of excessive growth [37].

9.5.2.1 Imaging Findings

Reference Standard for Diagnosis Is Represented by Colonoscopy; However, CT Colonography Is Playing an Increasing Role in Polyp Detection [38]

9.5.3 Colorectal Cancer

Colorectal cancer (CRC) is the third deadliest and fourth most commonly diagnosed cancer in the world [39]. Incidence of CRC is expected to rise worldwide, since the

risk of developing CRC increases with age, and most countries have an ever-growing aging population [40]. Adenocarcinoma is the most common type (98%) and, in the vast majority of cases, arises from pre-existing colonic adenomas (neoplastic polyps), which progressively undergo a malignant transformation [41].

CRC is usually asymptomatic at early stages, eventually causing symptoms due to excessive growth or complications (bleeding, perforation, and obstruction).

9.5.3.1 Imaging Findings

Although endoscopy is the reference standard for diagnosis, CT is the staging modality of choice due to its ability in diagnosing primary tumor, assessing the local spread, and detecting nodal involvement and distant metastases [42]. Most colorectal cancers are identifiable as soft tissue masses with irregular margins narrowing the bowel lumen; ulcerations are common in larger masses (Fig. 9.9). Occasionally low-density masses with low-density lymph nodes are seen in mucinous adenocarcinomas, due to most of the tumor being composed of extracellular mucin; psammomatous calcifications in mucinous adenocarcinoma can also be present. Complications include fistulae, obstruction, intussusception, and perforation. Extracolic spread is also suggested by loss of fat planes between the colon and adjacent organs. Liver is the predominant organ to be involved in case of metastatic dissemination. With CT, hepatic metastases usually appear as inhomogeneous hypoattenuating masses, best visualized in portal venous phase. Other common sites of metastases from colon cancer include the lungs, adrenal glands, and bones [42].

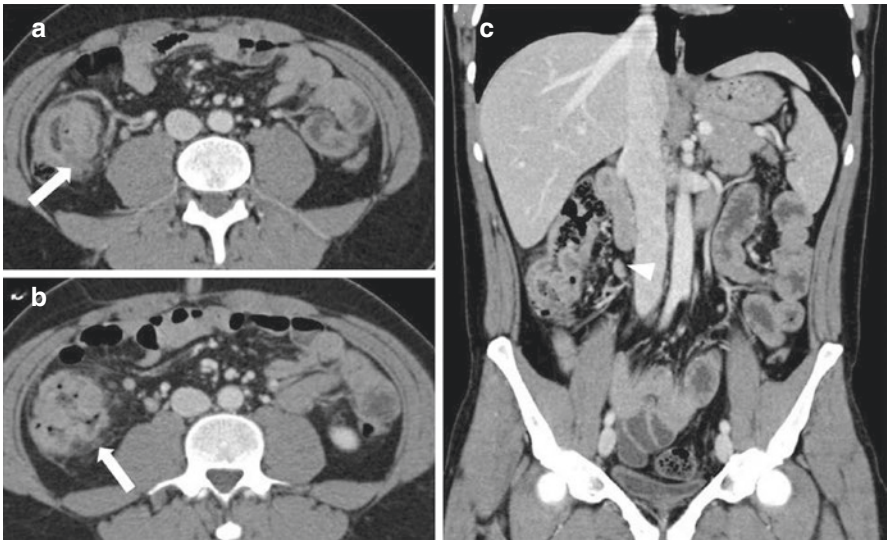

Fig. 9.9 Axial (**a**, **b**) and reformatted coronal (**c**) portal venous phase CT images of a 78-year-old man with adenocarcinoma of the ascending colon. Note the irregular wall thickening with adjacent fat stranding (arrows) and enlarged locoregional nodes (arrowhead)

9.6 Abdominal Emergencies in Geriatric Patients

Abdominal pain is a common cause of access to emergency, hospitalization, and surgery among older patients. Elderly people are more often susceptible to complications compared to a younger patient for the same disease, due to their fragility, the atypical disease presentations, the delays in care seeking, and the presence of comorbidities; as a consequence, they generally have a worse prognosis [43].

9.6.1 Acute Cholecystitis

Biliary tract disease, specifically acute cholecystitis (AC), is a frequent abdominal emergency in elderly patients. The clinical presentation is usually atypical, with right upper abdominal quadrant pain without fever, nausea, or vomiting.

9.6.1.1 Imaging Findings

US is considered the diagnostic modality of choice in the initial diagnosis of AC. Typical findings are the presence of cholelithiasis in combination with the sonographic Murphy sign. Both gallbladder wall thickening (>3 mm) and pericholecystic fluid are secondary findings. The atypical clinical presentation and the high incidences of comorbidities and associated complications (perforation, cholangitis, and emphysematous cholecystitis) make relevant the use of CT [44]. CT and MRI findings include the identification gallstones, thickened gallbladder wall, pericholecystic fluid collections, and subserosal edema (Figs. 9.10 and 9.11).

9.6.2 Acute Appendicitis

Acute appendicitis refers to inflammation of the appendix. The classical presentation consists of periumbilical pain (referred) which within a day or later shifts to McBurney point, with associated fever, nausea, and vomiting. Although it is a pathology most commonly seen on the second to third decades of life, older patients [45] generally has an atypical presentation, without fever and with late onset of symptoms; abdominal pain is usually generalized.

9.6.2.1 Imaging Findings

US findings supportive of the diagnosis of appendicitis include: aperistaltic, noncompressible, dilated appendix (>6 mm outer diameter), hyperechoic appendicolith with posterior acoustic shadowing, distinct appendiceal wall layers, periappendiceal fluid, and periappendiceal reactive nodal prominence/enlargement [46].

A contrast-enhanced CT should be performed in order to get to a tempestive diagnosis: due to its highly sensitivity (94–98%) and specificity (up to 97%) for the diagnosis of acute appendicitis; additionally, CT allows for alternative causes of abdominal pain to be ruled out [47]. Typical CT findings include appendiceal

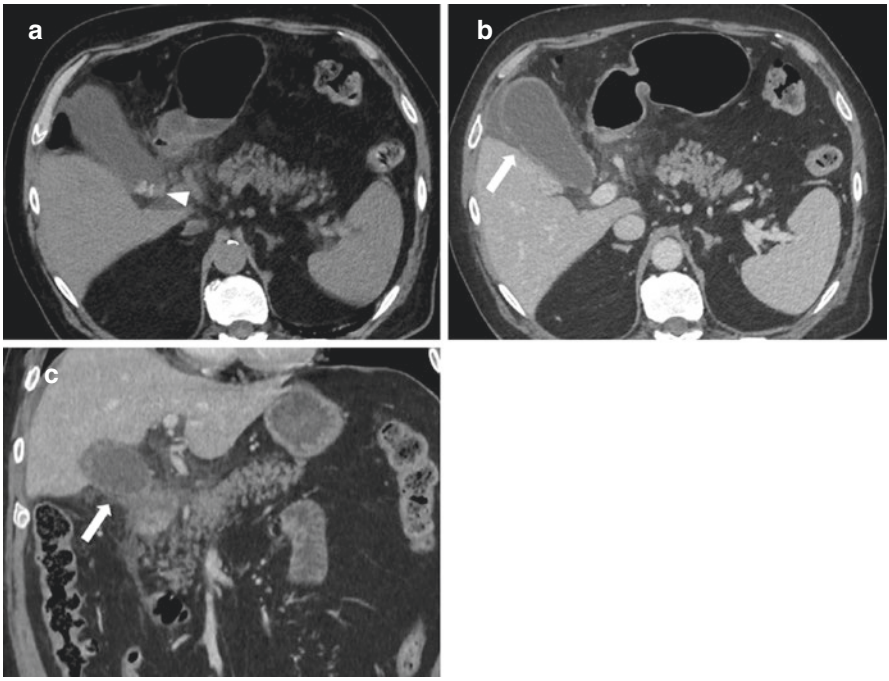

Fig. 9.10 Axial unenhanced CT (**a**), axial (**b**), and coronal (**c**) portal venous phase CT of a 73-year-old man with acute cholecystitis. Note the thickened and enhancing gallbladder wall surrounded by fluid and adjacent fat stranding (arrows). Unenhanced CT depicts also hyperdense gallbladder stones in the infundibulum (arrowhead)

dilatation (>6 mm diameter), wall thickening (>3 mm), periappendiceal inflammation (fat stranding, thickening of the lateroconal fascia, mesoappendix extraluminal fluid phlegmon, and abscess) [48].

9.6.3 Bowel Obstruction

Surgical adhesions and hernias are the main causes of small bowel obstruction, while malignancy is the most frequent cause of large bowel obstruction.

9.6.3.1 Imaging Findings

A plain radiograph is the first imaging modality usually performed when a small or large bowel obstruction is suspected. It can show bowel distention, air-fluid levels, and a reduced bowel air in the segment downstream the obstruction. CT examination can nearly always detect the point of obstruction and its cause (Fig. 9.12). The addiction of water-soluble contrast can be helpful in distinguishing complete from incomplete small bowel obstruction [49].

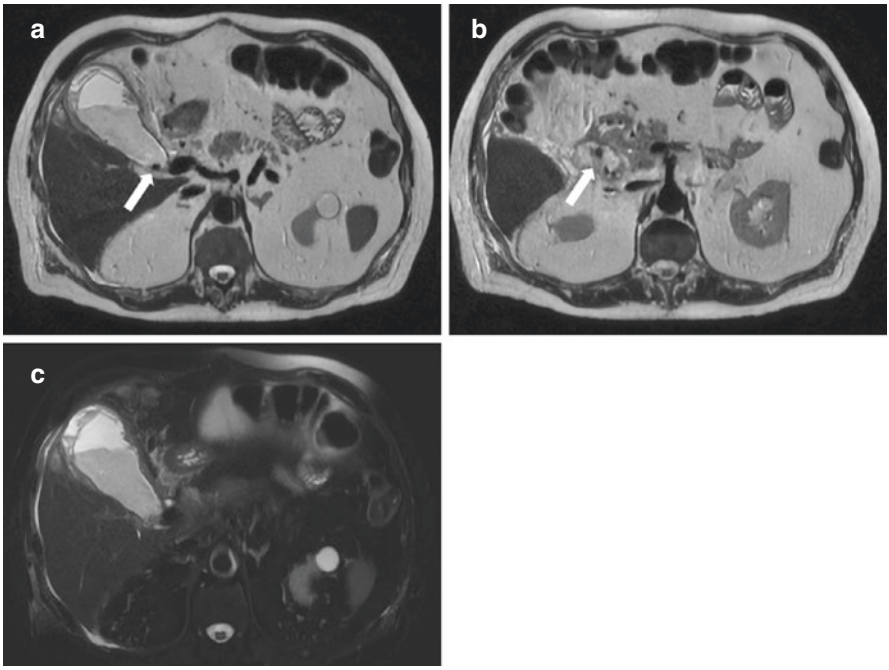

Fig. 9.11 Axial T2-weighted (**a**, **b**) and T2-weighted fat saturated (**c**) MR images of a 73-year-old man with acute cholecystitis. MR images confirm the presence of gallstones in the gallbladder infundibulum and show dilation of in the main biliary duct (arrows)

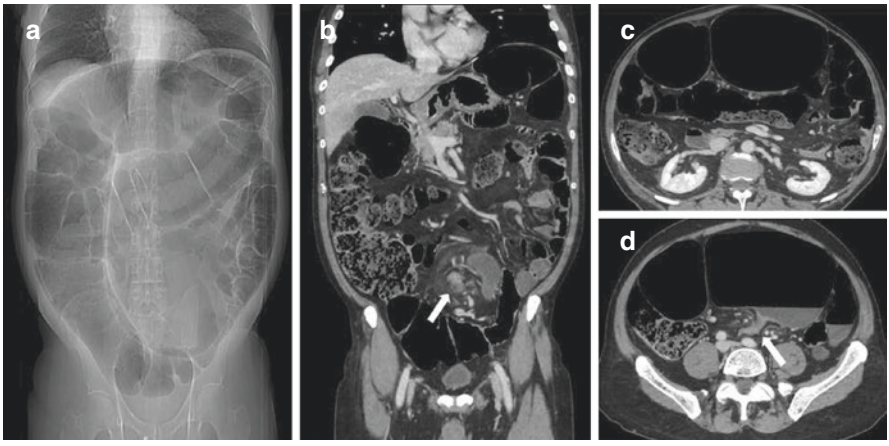

Fig. 9.12 CT scout image (**a**), coronal (**b**), and axial (**c** and **d**) portal venous phase CT images of a 79-year-old man with volvulus. Note the "whirlpool sign" (arrows) and the dilated proximal bowel loops filled with air

9.6.4 Acute Pancreatitis

Acute pancreatitis is an acute inflammation of the pancreatic gland, mostly caused by gallstones, characterized by abdominal pain, usually radiating to the back, nausea, vomiting, and high level of serum amylase. The risk of necrotizing pancreatitis is significantly higher in patients older than 80 years [50].

9.6.4.1 Imaging Findings

Although diagnosis is based mainly on clinical data, imaging plays an important role. In particular CT typical findings include focal or diffuse parenchymal enlargement, density reduction due to edema, and indistinct pancreatic margins owing to inflammation and surrounding retroperitoneal fat stranding; complications include pancreatic fluid collections and necrosis, pseudocyst, and vascular complications [51] (Fig. 9.13).

9.6.5 Acute Mesenteric Ischemia

Postprandial pain, nausea, and vomiting can be symptoms of an acute mesenteric ischemia, with a peak of incidence in the elderly. Etiology is mainly due to embolic and thrombotic causes, other causes include nonocclusive mesenteric ischemia, veno-occlusive mesenteric ischemia, and strangulating bowel obstruction [52].

9.6.5.1 Imaging Findings

Contrast-enhanced CT is the technique of choice for the diagnosis of acute mesenteric ischemia. Typical CT findings are related to bowel wall necrosis and perforation and include pneumatosis intestinalis (gas in intestinal wall), hepatic portal venous gas, pneumoperitoneum, and variable amounts of free fluid. The intravenous contrast medium administration is crucial to detect the vascular cause [53] (Figs. 9.14 and 9.15).

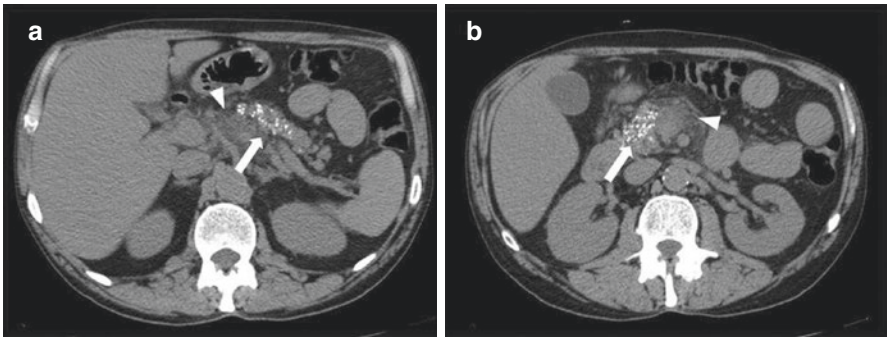

Fig. 9.13 Axial unenhanced CT (**a**, **b**) of a 71-year-old man with acute pancreatitis. Indistinct pancreatic margins, surrounding retroperitoneal fat stranding (arrowhead), and diffuse pancreatic calcifications (arrows) are showed

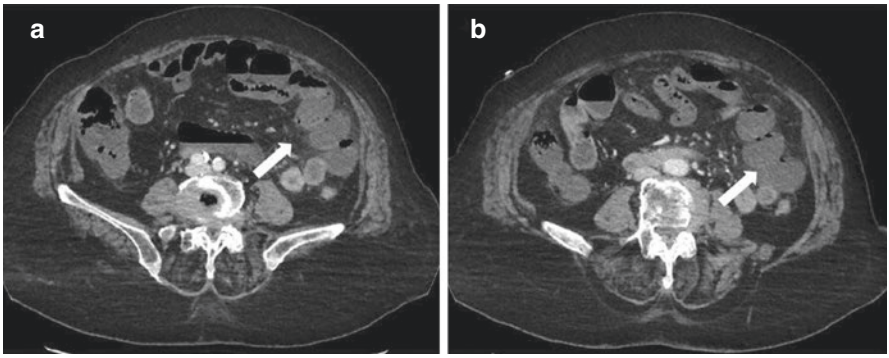

Fig. 9.14 Axial portal venous phase CT images (**a**, **b**) of a 67-year-old woman with mesenteric ischemia. Note the intramural bowel gas and adjacent fat stranding adjacent to bowel loops in left hypochondrium (arrows)

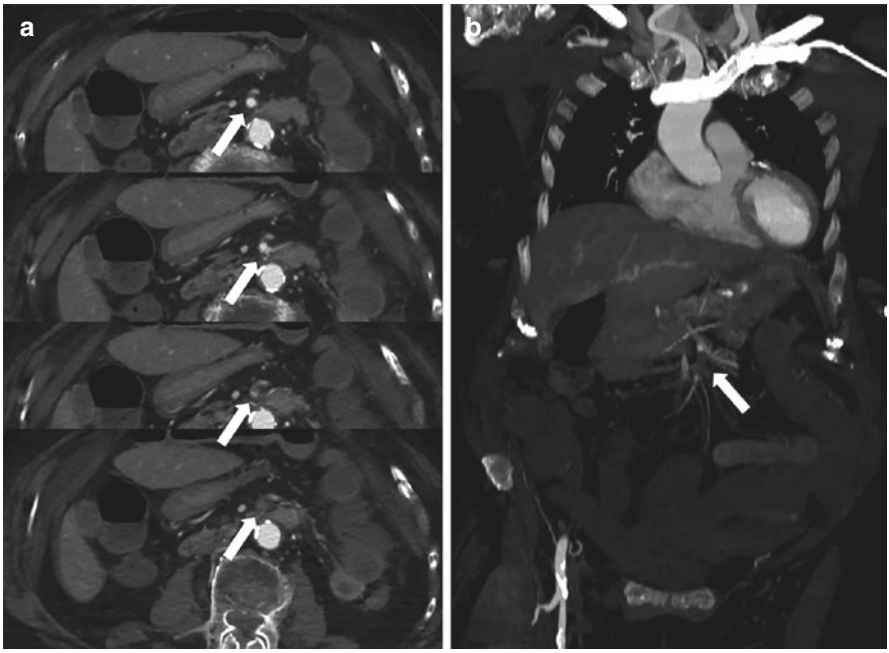

Fig. 9.15 Multiple axial arterial phase images (**a**) and coronal maximum intensity projection CT images (**b**) of a 67-year-old woman with mesenteric ischemia, depicting obstructed superior mesenteric artery (arrows)

References

1. Rémond D, et al. Understanding the gastrointestinal tract of the elderly to develop dietary solutions that prevent malnutrition. Oncotarget. 2015;6(16):13858–98.
2. Sato T, et al. Age-related changes in normal adult pancreas: MR imaging evaluation. Eur J Radiol. 2012;81(9):2093–8.
3. Dumic I, et al. Gastrointestinal tract disorders in older age. Can J Gastroenterol Hepatol. 2019;2019:6757524.
4. Mohammed S, Rosenkrantz AB. Providing compassionate care for the elderly patient in radiology. Curr Probl Diagn Radiol. 2020;49(2):67–9.
5. Achem SR, Gerson LB. Distal esophageal spasm: an update. Curr Gastroenterol Rep. 2013;15(9):325.
6. Woodfield CA, et al. Diagnosis of primary versus secondary achalasia: reassessment of clinical and radiographic criteria. AJR Am J Roentgenol. 2000;175(3):727–31.
7. Gupta P, et al. Primary versus secondary achalasia: new signs on barium esophagogram. Indian J Radiol Imaging. 2015;25(3):288–95.
8. Akaishi T, et al. Clinical usefulness of endoscopy, barium fluoroscopy, and chest computed tomography for the correct diagnosis of achalasia. Intern Med. 2020;59(3):323–8.
9. Rabushka LS, Fishman EK, Kuhlman JE. CT evaluation of achalasia. J Comput Assist Tomogr. 1991;15(3):434–9.
10. Kahrilas PJ, Kim HC, Pandolfino JE. Approaches to the diagnosis and grading of hiatal hernia. Best Pract Res Clin Gastroenterol. 2008;22(4):601–16.
11. Cakmakci E, et al. Accuracy of ultrasonography in the diagnosis of sliding hiatal hernias. Acad Radiol. 2013;20(4):453–6.
12. Chaturvedi A, et al. Imaging of thoracic hernias: types and complications. Insights Imaging. 2018;9(6):989–1005.
13. Levine MS. Radiologic imaging of gastroesophageal reflux disease. Berlin: Springer. p. 235–53.
14. Adanir H, et al. Endoscopic findings of gastro-esophageal reflux disease in elderly and younger age groups. Front Med (Lausanne). 2021;8:606205.
15. Berkovich GY, Levine MS, Miller WT. CT findings in patients with esophagitis. AJR Am J Roentgenol. 2000;175(5):1431–4.
16. Liang H, Fan JH, Qiao YL. Epidemiology, etiology, and prevention of esophageal squamous cell carcinoma in China. Cancer Biol Med. 2017;14(1):33–41.
17. Charles TR, Jobe BA, Hunter JG, et al. Esophageal cancer: principles and practice. New York: Demos Medical.
18. Malik TF, Gnanapandithan K, Singh K. Peptic ulcer disease. In: StatPearls [Internet]. Treasure Island, FL: StatPearls; 2022. https://www.ncbi.nlm.nih.gov/books/NBK534792/. Accessed 29 Jul 2021.
19. Snowden FM. Emerging and reemerging diseases: a historical perspective. Immunol Rev. 2008;225:9–26.
20. Baghdanian AH, et al. Imaging manifestations of peptic ulcer disease on computed tomography. Semin Ultrasound CT MR. 2018;39(2):183–92.
21. Guniganti P, et al. CT of gastric emergencies. Radiographics. 2015;35(7):1909–21.
22. Moysidis M, et al. The challenging diagnosis and treatment of duodenal diverticulum perforation: a report of two cases. BMC Gastroenterol. 2020;20(1):5.
23. Castilho Netto JM, Speranzini MB. Ampullary duodenal diverticulum and cholangitis. Sao Paulo Med J. 2003;121(4):173–5.
24. Tsitouridis I, et al. MR cholangiography in the evaluation of patients with duodenal periampullary diverticulum. Eur J Radiol. 2003;47(2):154–60.
25. Bittle MM, et al. Imaging of duodenal diverticula and their complications. Curr Probl Diagn Radiol. 2012;41(1):20–9.
26. Rawla P, Barsouk A. Epidemiology of gastric cancer: global trends, risk factors and prevention. Prz Gastroenterol. 2019;14(1):26–38.

27. Weissleder R, Wittenberg J, Harisinghani MMGH, et al. Primer of diagnostic imaging. Philadelphia, PA: Mosby.
28. Horton KM, Fishman EK. Current role of CT in imaging of the stomach. Radiographics. 2003;23(1):75–87.
29. Federle MP, Jeffrey RB, Woodward PJ, et al. Diagnostic imaging: abdomen. Salt Lake City, UT: Amirsys.
30. Jayaraman MV, et al. CT of the duodenum: an overlooked segment gets its due. Radiographics. 2001;21:S147–60.
31. Rummeny EJ, Reimer P, Heindel W. MR imaging of the body. New York, NY: Thieme Medical.
32. Jasti R, Carucci LR. Small bowel neoplasms: a pictorial review. Radiographics. 2020;40(4):1020–38.
33. McPhee S, Tierney L, Papadakis M. Current medical diagnosis & treatment. New York, NY: McGraw Hill Medical.
34. Horton KM, Corl FM, Fishman EK. CT evaluation of the colon: inflammatory disease. Radiographics. 2000;20(2):399–418.
35. Matrana MR, Margolin DA. Epidemiology and pathophysiology of diverticular disease. Clin Colon Rectal Surg. 2009;22(3):141–6.
36. Flor N, et al. The current role of radiologic and endoscopic imaging in the diagnosis and follow-up of colonic diverticular disease. AJR Am J Roentgenol. 2016;207(1):15–24.
37. Øines M, et al. Epidemiology and risk factors of colorectal polyps. Best Pract Res Clin Gastroenterol. 2017;31(4):419–24.
38. Pickhardt PJ, et al. Colorectal cancer: CT colonography and colonoscopy for detection—systematic review and meta-analysis. Radiology. 2011;259(2):393–405.
39. Rawla P, Sunkara T, Barsouk A. Epidemiology of colorectal cancer: incidence, mortality, survival, and risk factors. Prz Gastroenterol. 2019;14(2):89–103.
40. Pitchumoni CS, Broder A. Chapter 2—Epidemiology of colorectal cancer. In: Floch MH, editor. Colorectal neoplasia and the colorectal microbiome. San Diego, CA: Academic Press; 2020. p. 5–33.
41. Kumar V, Robbins SL, Abbas AK, et al. Robbins and Cotran pathologic basis of disease. Philadelphia: Saunders.
42. Horton KM, Abrams RA, Fishman EK. Spiral CT of colon cancer: imaging features and role in management. Radiographics. 2000;20(2):419–30.
43. Lyon C, Clark DC. Diagnosis of acute abdominal pain in older patients. Am Fam Physician. 2006;74(9):1537–44.
44. McGillicuddy EA, et al. Acute cholecystitis in the elderly: use of computed tomography and correlation with ultrasonography. Am J Surg. 2011;202(5):524–7.
45. Callahan MJ, Rodriguez DP, Taylor GA. CT of appendicitis in children. Radiology. 2002;224(2):325–32.
46. Puylaert JB. Acute appendicitis: US evaluation using graded compression. Radiology. 1986;158(2):355–60.
47. Spangler R, et al. Abdominal emergencies in the geriatric patient. Int J Emerg Med. 2014;7:43.
48. Pereira JM, et al. Disproportionate fat stranding: a helpful CT sign in patients with acute abdominal pain. Radiographics. 2004;24(3):703–15.
49. Ozturk E, et al. Small bowel obstruction in the elderly: a plea for comprehensive acute geriatric care. World J Emerg Surg. 2018;13:48.
50. Banks PA, et al. Classification of acute pancreatitis—2012: revision of the Atlanta classification and definitions by international consensus. Gut. 2013;62(1):102–11.
51. Koo BC, Chinogureyi A, Shaw AS. Imaging acute pancreatitis. Br J Radiol. 2010;83(986):104–12.
52. Fitzpatrick LA, et al. Pearls, pitfalls, and conditions that mimic mesenteric ischemia at CT. Radiographics. 2020;40(2):545–61.
53. Rha SE, et al. CT and MR imaging findings of bowel ischemia from various primary causes. Radiographics. 2000;20(1):29–42.

The Male Urogenital System in Geriatric Patients

10

Emilio Quaia and Filippo Crimí

Population aging is taking place throughout the world, and about 13% of the 76 million persons in the USA were aged 65 years and older [1]. In Europe, there is the oldest population in the world, with almost 25% of European projected to be aged 65 years or older by 2030. In particular, Italy and Germany are estimated to have the oldest population in Europe. The progressive increase in the proportion of a population that is elderly depends on changes in the survival of older persons and in the birth rate [1]. The increasingly greater life expectancy of the population has been mainly determined by reduced mortality at older ages. The five leading causes of death, including heart disease, cancer, stroke, chronic lower respiratory tract disease, and Alzheimer's disease, account for 69.5% of all death [1]. The renal causes of death account only for 2% of all deaths and for 4% of chronic conditions in persons aged >65 years, even though these represent an important cause of disability and comorbidity in older patients.

Due to the progressive increase in the mean age of the population, it is very important to know the morphologic changes of the kidney according to aging. As a matter of fact, older individuals, often with a compromised renal reserve and substantial comorbidities, are the norm in the hospitalized population [2]. The functional alterations of the aged kidney are characterized principally by a progressive reduction of renal blood flow from about 600 to 300 mL/min/1.73 m^2 and of glomerular filtration rate (GFR) from 130 to 60–80 mL/min. An accurate quantitation of the GFR should always be performed in elderly patients before injection of iodinated and gadolinium-based contrast agents. Moreover, when exposed to iodinated

E. Quaia (✉)
Institute of Radiology, Padova University Hospital, Padova, Italy

Department of Medicine-DIMED, University of Padova, Padova, Italy
e-mail: emilio.quaia@unipd.it

F. Crimí
Institute of Radiology, Padova University Hospital, Padova, Italy
e-mail: filippo.crimi@unipd.it

G. Guglielmi, M. Maas (eds.), *Imaging in Geriatrics*, Practical Issues in Geriatrics, https://doi.org/10.1007/978-3-031-14877-4_10

contrast agents, non-steroidal anti-inflammatory drugs, aminoglycosides, or hemodynamic challenges (e.g., surgery and anesthesia, sepsis, volume depletion), this at-risk patient population often develops an abrupt decline in GFR.

The kidneys undergo involutional changes with age. There is a gradual decline in kidney weight starting after the age of 50 years, with the most marked decrease occurring between the seventh and eighth decade. The progressive loss of kidney mass appears to affect the renal cortex more than the renal medulla [3]. Microscopically, there is a reduction in the number of glomeruli and an increase in glomerular sclerosis with increasing age [4]. The glomerular sclerosis in the elderly is different from diabetic intercapillary diffuse sclerosis and focal glomerulosclerosis and corresponds to a progressive glomerular hyalinization, such that glomeruli become shrunken, eosinophilic, and hypocellular masses.

The increase in the percentage of sclerotic glomeruli has been attributed to the protein-rich diet characteristic of modern society which probably determines a state of chronic glomerular hyperfiltration and hyperperfusion. A further cause would be glomerular ischemia secondary to the changes in the renal blood flow occurring with ages. The presence of atherosclerosis increases the incidence of glomerular sclerosis, raising the possibility that glomerular sclerosis in the elderly is nothing other than a reflection of vascular disease and thus should be considered a secondary phenomenon. On electron microscopic analysis, there is an increase in focal thickening of both glomerular and tubular basement membranes, probably due to the accumulation of type IV collagen [3]. The loss of glomerular mass is proportional to the loss of tubular mass, so that the tubular balance is well preserved. The outer cortical glomeruli are more extensively involved than the deeper glomeruli. Moreover, in addition to glomerular sclerosis, there is a gradual increase in the interstitial fibrosis.

Although most would agree that there is a decrease in the total number of glomeruli, there is a very wide scatter in the data, and many elderly people seem to retain the same number of glomeruli as expected in younger persons [4]. The average thickness of the glomerular basement membrane increases with age, but this does not appear to be associated with any change in function. The volume of the mesangium increases, but as this is accompanied by a decrease in glomerular volume, it is difficult to draw any significant conclusion. The most significant changes appear in the juxtamedullary glomeruli. Changes also take place in the tubules where there may be irregular thickening of the basement membrane and, particularly in the distal tubule, the formation of diverticula. There is overall reduction in the tubular volume, and this seems to parallel the reduction in glomerular volume. The interstitium may contain areas of tubular atrophy and fibrosis. Renal arteries develop intimal thickening and reduplication of the elastic lamina. Increasing tortuosity and tapering of the interlobular arteries have been reported. Changes have been recognized in the afferent arterioles, and there is evidence that there are differences between those arterioles supplying the juxtaglomerular glomeruli and more cortical glomeruli. It would appear that with increasing age, shunts develop between the

afferent and efferent arterioles in the juxtamedullary glomeruli, whereas in the cortical glomeruli the vessels become obliterated. The significance of these findings is unclear, as it is difficult to separate out changes which may have been engendered by hypertension and those due to aging alone [4].

BPH is an "age-dependent" disease with a reported prevalence in patients older than 60 years of 50% that increases to 90% in patients older than 85 years. Half of these patients show lower urinary tract symptoms and, therefore, should undergo medical or surgical therapy. Imaging by US and MRI plays a fundamental role in the detection of this condition and in the clinical decision-making for treatment. Prostate cancer is the second most common cancer affecting men worldwide and the risk of prostate cancer increases with age, it has been reported that the median age of symptoms onset is 72 years. US was the most used technique to identify prostate cancer but in the last years, thanks to the PI-RADS standardized reporting system, MRI has progressively become the gold standard for the detection of prostate cancer. Prostatitis is also quite common in old men, especially chronic prostatitis, and is pivotal to correctly identify this infection that in some cases can be misdiagnosed as prostate cancer both at US and MRI.

10.1 Morphologic Alterations in the Kidney of an Elderly Patient

Aging induces in the kidney a progressive, functional, and anatomic decay that does not have a particular clinical impact. The fundamental alterations of renal morphology in elderly patients include size reduction, parenchymal thickness reduction, margin irregularities, and increased corticomedullary differentiation. In particular, the most important morphologic alteration of the aged kidney is the volume reduction, approximately 20–30% in 80-year-old men, and a loss of weight that decreases from 250–270 to 180–200 g after age 65 [5].

In elderly patients, the kidneys appear frequently reduced in their largest dimension (within the range of 9–9.5 cm) on grayscale US, with reduction in the renal parenchymal thickness due to chronic reduction of the renal parenchymal perfusion from nephroangiosclerosis. The renal capsule becomes thicker and there is an increase of the renal sinus fatty tissue, in particular at the level of the renal hilum (Fig. 10.1). Typically, there is evidence of irregular margins (Fig. 10.2a), frequently with a pseudolobular appearance (Fig. 10.2b) and/or coexisting with renal parenchymal scars due to previous renal cortical infarctions (Fig. 10.2b). The corticomedullary differentiation appears usually increased due to the relative higher echogenicity of the renal cortex compared to the medulla due to nephroangiosclerosis. Anyway, less frequently, the corticomedullary differentiation may also be reduced. On color/power Doppler US, the renal peripheral vessels are usually not visualized in the subcapsular renal parenchyma (Fig. 10.3).

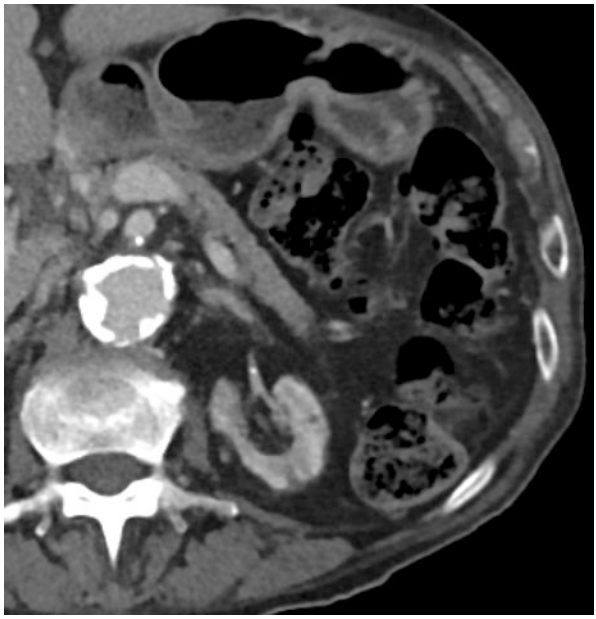

Fig. 10.1 Kidney in an 80-year-old patient. Contrast-enhanced CT, transverse plane. Reduction of renal cortical thickness and increase of the renal sinus fatty tissue at the renal hilum

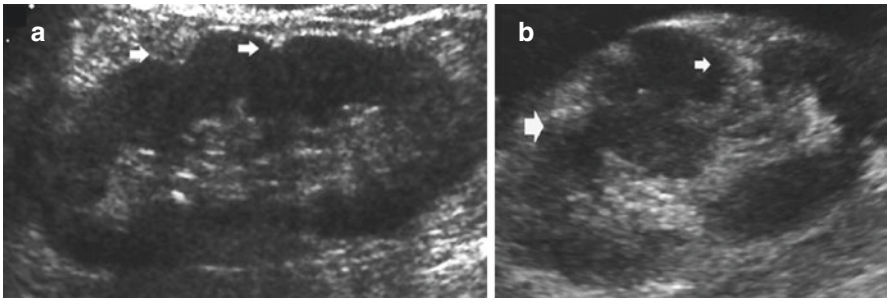

Fig. 10.2 (**a**, **b**) Different grades of renal margin irregularities. Longitudinal grayscale US scan. (**a**) Reduction of the renal parenchymal thickness with renal contour irregularities (*arrows*) and increased corticomedullary differentiation. (**b**) Diffuse renal margin irregularities also with evidence of renal parenchymal scars (*arrows*) due to previous regional infarctions. The interposed renal parenchyma presents a pseudolobar appearance

On contrast-enhanced CT a typical diffuse irregularity of margins is identified, often associated with a reduced cortical thickness or renal parenchymal scarring due to previous renal infarcts (Fig. 10.4). Renal parenchymal retention cysts (Fig. 10.5a) and renal sinus cysts (Fig. 10.5b) are frequently identified and probably develop because of inflammatory reactions and infections that occur in the distal tract of the tubuli [6]. On CT urography these fundamental morphologic changes are frequently associated with calyceal alterations with narrowing of the first-order calyces and multiple cysts of the renal sinus.

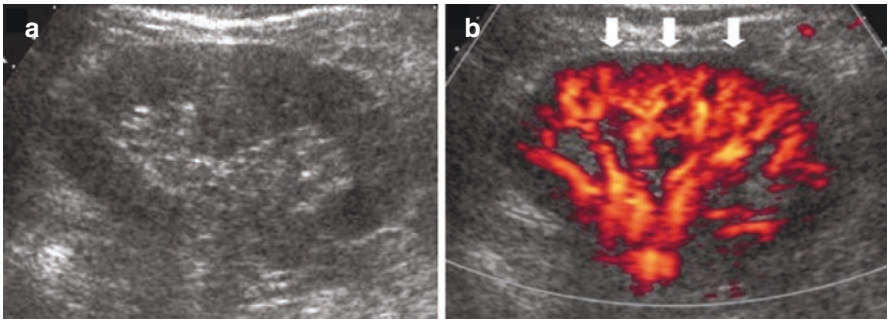

Fig. 10.3 (**a**, **b**) Fundamental morphologic alterations of the kidney in the elderly patient. (**a**) Grayscale US. Increased echogenicity of the renal parenchyma with reduced corticomedullary differentiation. (**b**) Power Doppler US. Reduced renal parenchymal vascularization at the level of the subcapsular region (*arrows*)

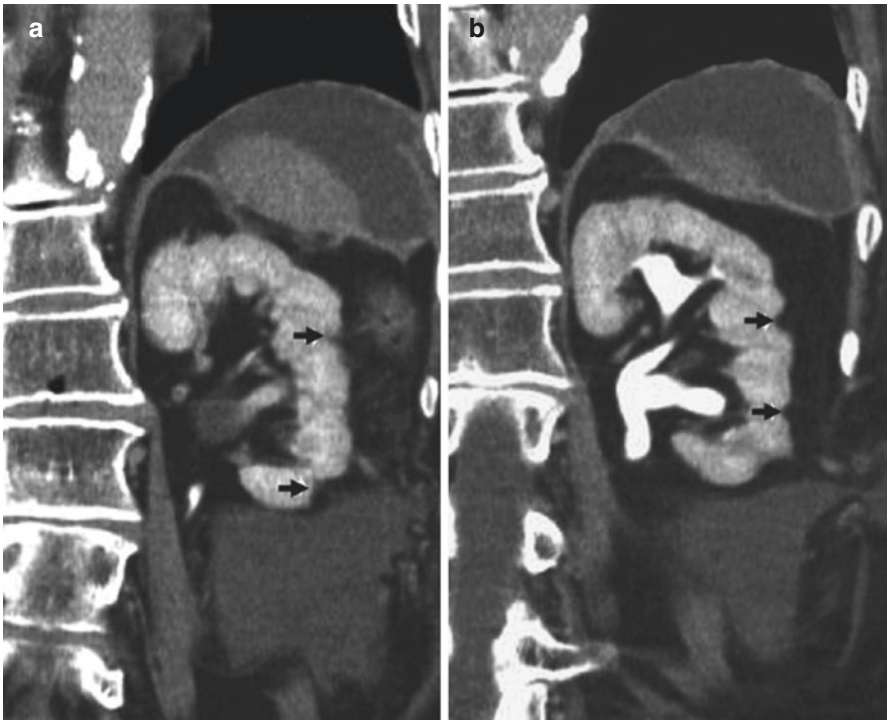

Fig. 10.4 (**a**, **b**) Fundamental morphologic alterations of the kidney in the elderly patient. Contrast-enhanced CT, excretory phase. Coronal reformation. Diffuse reduction of the renal cortical thickness with overt focal irregularities of renal margins (*arrows*)

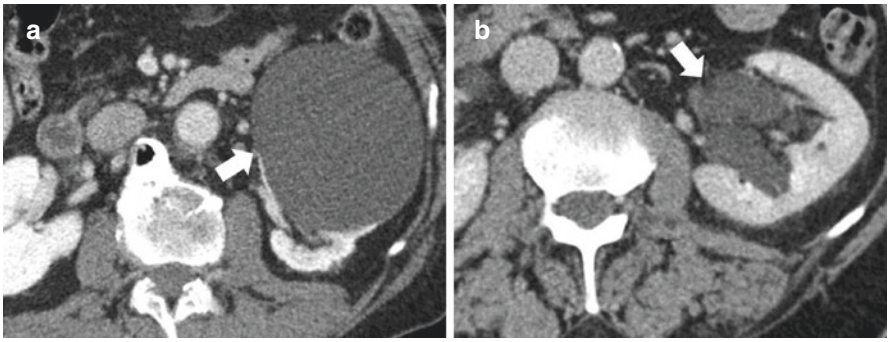

Fig. 10.5 (**a**, **b**) Contrast-enhanced CT showing a large renal parenchymal retention cysts (**a**) and renal sinus cysts (**b**)

10.2 Nephrosclerosis

Nephrosclerosis is the term used for the renal pathology associated with sclerosis of renal arterioles and small arteries due to medial and intimal thickening as a response to hemodynamic changes, aging, genetic defects, or some combination of these and to hyaline deposition in arterioles [7]. The resultant effect is focal ischemia of the renal parenchyma supplied by vessels with thickened walls and consequent narrowed lumen [7]. Some degree of nephrosclerosis is present at autopsy with increasing age preceding or in the absence of hypertension. Hypertension and diabetes mellitus increase the incidence and severity of the lesions. In nephrosclerosis, there is a general hardening of the kidney due to overgrowth and contraction of interstitial connective tissue. Nephrosclerosis may be compared to the arteriosclerosis of the small renal arteries, and it is due to renovascular disease, mainly chronic hypertension. The renal vascular alterations of hypertension depend on the severity of the blood pressure elevation and whether the process accelerates to malignant hypertension. Arteriolosclerosis of small cortical renal arteries, interlobar, arcuate, and interlobular is a common feature of the kidney in patients with systemic arterial hypertension and particularly in elderly patients [8].

In nephroangiosclerosis, both kidneys are usually symmetrically reduced in their diameters with cortical scars. Cortical echogenicity is increased with increased or reduced corticomedullary differentiation according to the grade of echogenicity of the renal medulla. Color and power Doppler US reveal nonspecific reduction of vascularization (Fig. 10.6). If compared to the younger population, renal RIs are typically increased (>0.7 and frequently around 0.8) (Fig. 10.7). Renal perforating arteries and veins [9] are much more visible in the kidneys of nephroangiosclerotic patients in comparison with normal subjects since they enlarge in nephroangiosclerosis and present normally directed flows from the kidney toward the renal capsule.

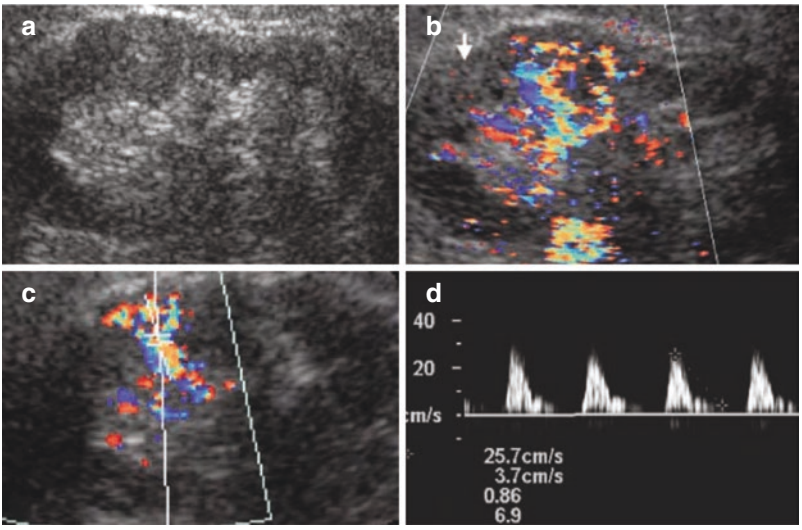

Fig. 10.6 (**a**–**d**) Fundamental morphologic alterations of the kidney in the elderly patient. Reduction of the renal parenchymal thickness, margin irregularities, and increased corticomedullary differentiation are evident on grayscale US (**a**). (**b**) Color Doppler US, longitudinal scan. Reduction of renal cortical vascularization. (**c**, **d**) Doppler interrogation of the intrarenal segmental arteries with increased arterial resistive indices

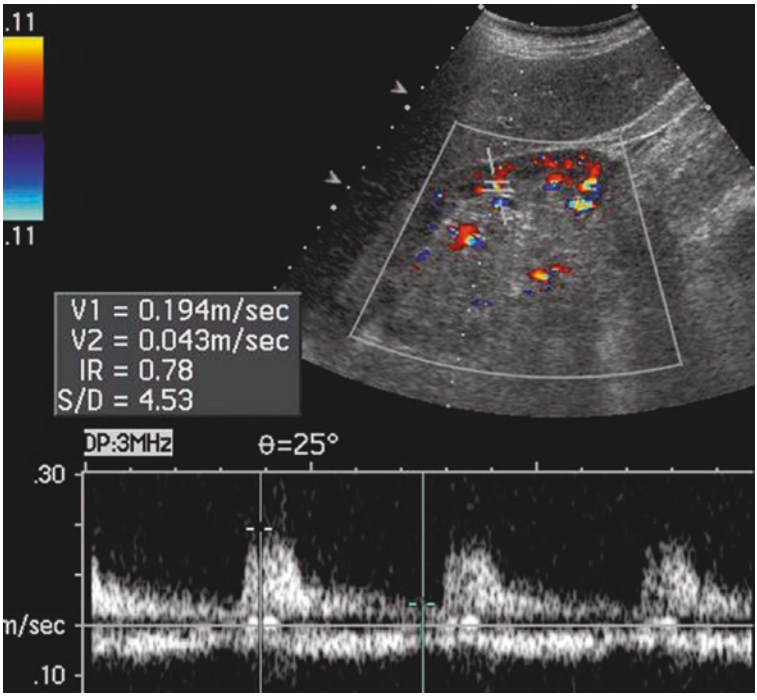

Fig. 10.7 Fundamental morphologic alterations of the kidney in the elderly patient. Color Doppler US with Doppler interrogation of renal segmental artery. Increased arterial resistive index measured at the level of one renal segmental artery of the lower renal pole

10.3 Renovascular Disease

The geriatric population is affected by many vascular diseases since the incidence of atherosclerosis increases with age. Generally, the imaging of vascular diseases in the elderly is complicated by the presence of coexisting diseases, while the image quality is degraded due to obesity and limited patient compliance. Renovascular hypertension accounts for 0.5–5% of patients who have hypertension. The renovascular disease may manifest as asymptomatic renal artery stenosis, intractable or uncontrollable hypertension requiring multiple medications, or ischemic nephropathy with progressive loss of renal function [10]. In young patients, the most common cause of renovascular hypertension is fibromuscular dysplasia, while in the elderly the most common cause is atherosclerosis mainly localized in the ostial or proximal tract of the renal artery. Color Doppler US, helical computed tomographic (CT) angiography, angiotensin converting enzyme (ACE) inhibitor scintigraphy with captopril, and magnetic resonance (MR) angiography have been assessed in the diagnosis of renal artery stenosis. Digital subtraction angiography remains the gold standard for the diagnosis of renal artery stenosis, and it is part of any endovascular intervention. Contrast-enhanced CT and MR imaging angiographic techniques have improved in their detection of renal artery stenosis, and MR angiography is generally considered more sensitive for renal artery stenosis than US [11]. Anyway, kidney disease limits the use of contrast agents during CT and MR imaging examinations, and this is particularly true in elderly patients. Moreover, coexistent cardiopulmonary diseases, such as congestive heart failure, arrhythmias, and chronic obstructive lung diseases, limit the ability of the elderly to hold breath during image acquisition [10]. Additionally, cardiopulmonary diseases may preclude the use of some of the imaging modalities because of the inherent contraindications, such as pacemakers in MR examinations. Consequently, color Doppler US is the principal imaging technique employed in the elderly for renovascular disease diagnosis.

The velocimetric analysis of Doppler trace derived from renal arteries is of primary importance to identify renal artery stenosis. Direct Doppler criteria have been proposed for the detection of renal artery stenosis, including an increased peak systolic velocity (>150–180 cm/s) (Fig. 10.8) and end-diastolic velocity at the level of the stenosis [12, 13], a poststenotic flow disturbance resulting in spectral broadening and reversed flow [12], an increased ratio (≥3.5) of peak systolic velocity in the renal artery and aorta (renal-aortic ratio), and the presence of turbulence within the renal artery [14, 15]. Although this technique is easy to perform, its accuracy is questionable because the lack of an early systolic peak has a low sensitivity for

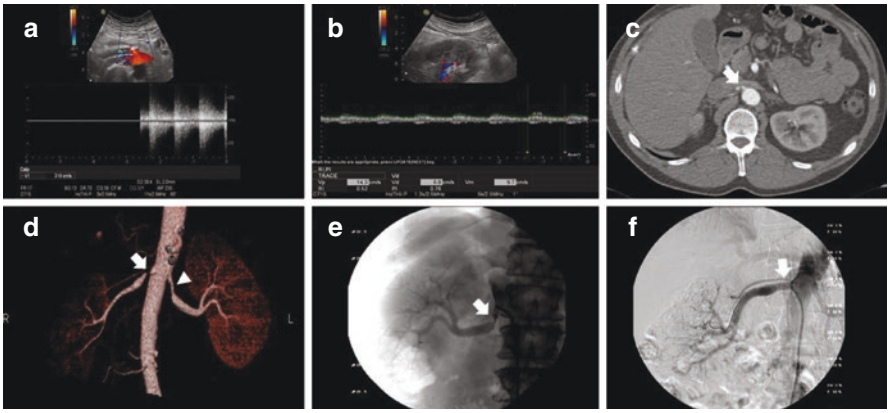

Fig. 10.8 (**a**–**f**) Renal artery stenosis in a 75-year-old male patient. Worsening renal function was precipitated by the treatment of hypertension with angiotensin converting enzyme (ACE) inhibitors. (**a**) Doppler interrogation revealed aliasing at the level of the proximal tract of the right renal artery with spectral broadening of the Doppler trace and increase of the peak systolic velocity. (**b**) "tardus et parvus" profile of the waveform at intrarenal arteries. (**c**, **d**) CT angiography (CTA). Severe stenosis of the right renal artery is confirmed (*arrow*) and a moderate stenosis of the left renal artery (*arrowhead*). (**e**, **f**) angiography confirmed the stenosis that was treated with a stent

moderate stenoses, and the waveform is dependent on the maintenance of vessel compliance, which limits its effectiveness in elderly patients and patients with atherosclerosis [16, 17].

Downstream hemodynamic repercussions of renal artery stenosis in the distal intrarenal arterial bed may be identified by Doppler US and may provide an indirect diagnosis of renal artery stenosis. Numerous parameters are still debated [12], except in cases of critical stenosis (>80%). In fact, even though intraparenchymal arterial examination is technically easier than the evaluation of the main renal artery, Doppler US findings in interlobar-arcuate renal cortical arteries are less reliable than Doppler US findings on stenotic site since downstream repercussions are absent in 20% of principal renal artery tight stenosis (>80%), for a well-developed collateral blood supply. In the presence of a hemodynamically significant renal artery stenosis, the Doppler trace reveals a "tardus et parvus" profile at poststenotic or intrarenal tract of the renal artery [18, 16], consisting of an increased time to reach the peak of the trace (acceleration time >70 ms) with loss of early systolic peak and decreased acceleration index (<300 cm/s^2). Poststenotic pulsus tardus is caused by the compliance of the poststenotic vessel wall in conjunction with the stenosis, which produces the tardus effect by damping the high-frequency

components of the arterial waveform. This information allows to identify those conditions, which may produce false-positive or false-negative results when the tardus phenomenon is used to predict hemodynamically significant upstream stenosis [16]. This is the case of the loss of vascular compliance in severe diffuse atherosclerosis of elderly patients, which may prevent the tardus-parvus phenomenon decreasing the sensitivity of color Doppler US [13]. Other findings that may be observed in the intraparenchymal arteries in the presence of renal artery stenosis are decreased resistive indices in interlobar-arcuate renal cortical arteries with increased side difference higher than 10% [12].

Contrast-enhanced CT angiography (CTA) and MR imaging angiography (MRA) are also very sensitive and specific for the demonstration of renal artery occlusion. Additional views provided by CTA allow for display of the renal arteries in multiple planes and projections, often necessary for the depiction of stenosis (Fig. 10.8). Calcified plaques limit the CT evaluation of luminal narrowing. In particular, in cases with extensive calcification, as is frequently observed in elderly patients, renal artery stenosis can be obscured by MIP technique and requires careful evaluation of the volume-rendered images. CTA can also depict secondary signs of renal artery stenosis, including poststenotic dilatation and renal parenchymal changes of atrophy and decreased cortical enhancement. CTA is also very helpful in the post-treatment evaluation of renal stent grafts and can usually delineate between the highly attenuating graft material and the intraluminal contrast material.

MRA is well suited for the evaluation of renal artery stenosis in the elderly. Calcified atheromatous plaques do not hamper the assessment of the arterial lumen. MR angiography provides information about the size of the kidney, collateral vessels, and poststenotic dilatation. Contrast-enhanced axial MR imaging can directly show the narrowing of the stenosis, and reformatted multiplanar imaging is often used. Both MIP and volume rendering are useful and complimentary in the evaluation of renal artery stenosis. Axial images alone are not sufficient for the evaluation of renal artery stenosis because the renal arteries often have a tortuous course, especially in elderly patients. Multiplanar reformations are very useful, in particular to show renal artery occlusion.

10.4 Renal Infarction

Nontraumatic acute renal infarction is quite common in elderly patients, and it may present the same symptoms of stone colic or acute pyelonephritis. Renal infarction may be caused by tight stenosis or occlusion of segmental or of the main renal artery or by renal artery embolization due to renal angioplasty, atrial fibrillation, and cardiac valvular defects. Other causes of renal infarction are vasculitis, systemic lupus erythematosus, drug-induced vasculitis, paraneoplastic syndrome, hypercoagulable state, or acute venous occlusion [19]. Both CT and angiography are reference imaging techniques in renal infarct detection, whereas US presents a lower sensitivity. Even though large renal infarcts may be hypoechoic in comparison with the viable renal parenchyma, segmental renal infarcts are usually isoechoic or rarely hyperechoic if hemorrhagic component is present.

Renal infarcts often reveal a wedge shape with capsular base. Even though baseline color Doppler US and power Doppler US present overt limitations to detect renal perfusion defects due to the low sensitivity to low-velocity and low-amplitude flow states, they may increase diagnostic capabilities of US in detecting renal infarcts, especially in elderly or obese patients and in patients with renal diseases. In renal infarct, color Doppler US and power Doppler US reveal absolute absence of renal cortical flows, even though it is very difficult to differentiate renal segmental infarct from areas which appear poorly perfused due to underlying parenchymal disease, deep renal position, and artifacts. Moreover, color Doppler US presents a low accuracy in the detection of small renal infarcts in the subcapsular region for limited spatial resolution and in the superior renal pole for the high Doppler angle and for the depth position [20].

Recent advances in microbubble-based contrast agents, and dedicated contrast-specific modes, have determined the achievement of increased image contrast in tissues. By transmitting at the fundamental frequency and receiving selectively harmonic frequencies, the background signal from stationary tissues is markedly suppressed resulting in a greater signal-to-noise ratio and a better visibility of renal infarcts. Blooming and flash artifacts are eliminated, shadowing artifacts are lessened, both spatial and temporal resolutions are improved, and the brightness of grayscale pixel does not depend on angle-dependent frequency shift estimates. Differently from iodinated contrast agent and gadolinium-based contrast agents, microbubbles are pure intravascular agents which are not excreted in renal tubules and may be safely employed in patients with advanced chronic renal failure, which is frequently observed in the elderly. Microbubble-based contrast agents and contrast-specific imaging techniques improve significantly the diagnostic confidence level in identifying nonperfused renal parenchymal zones and allow a reliable depiction of renal perfusion defects (Fig. 10.9). Renal perfusion defects due to renal parenchymal infarction appear as single or multiple focal wedge-shaped areas of absent, diminished, or delayed contrast enhancement in comparison to the adjacent renal parenchyma after microbubble injection [21].

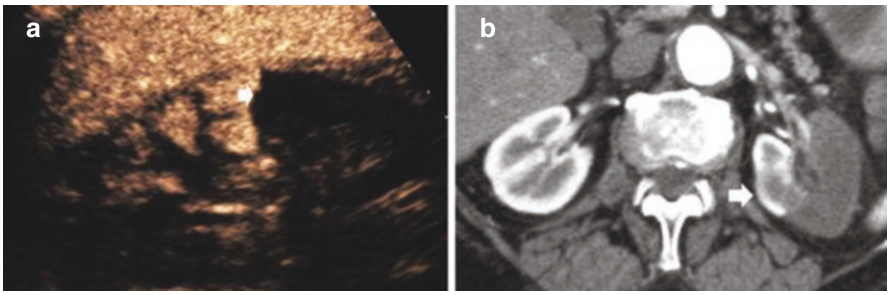

Fig. 10.9 (**a**) Contrast-enhanced US after sulfur hexafluoride-filled microbubble injection. (**b**) Contrast-enhanced CTA, corticomedullary phase. The left kidney shows partial parenchymal infarction (*arrow*) in a 72-year-old woman with atrial fibrillation

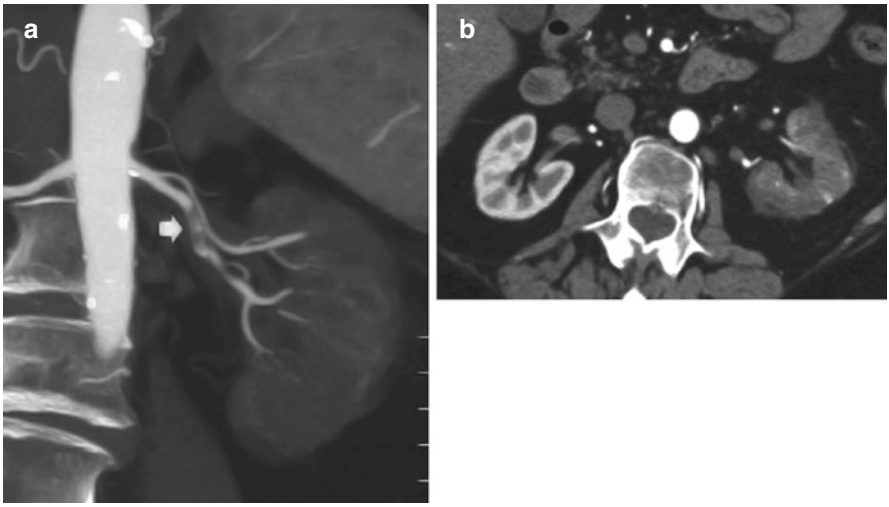

Fig. 10.10 (**a**, **b**) Renal artery thrombosis in a 75-year-old male patient. (**a**) Contrast-enhanced CTA. Coronal reformation. The left renal artery is occluded by a complex thrombus (*arrow*) with relative avascularity of the left kidney. (**b**) Contrast-enhanced CT. Corticomedullary phase shows a complete renal infarction

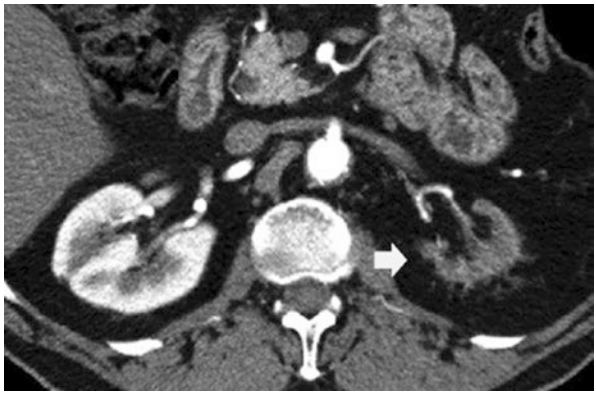

Fig. 10.11 Renal shrinkage due to chronic vascular hypoperfusion due to the tight stenosis of the left renal artery. Contrast-enhanced CT. Corticomedullary phase. The left kidney (*arrow*) appears small and without any sign of function (contrast excretion)

Contrast-enhanced CT is the reference imaging technique in renal infarct detection. The parenchymal appearance of renal perfusion defects depends on the site of arterial occlusion, if segmental (Fig. 10.9) or the main renal artery is involved (Fig. 10.10), and on thrombus age [19]. Contrast material-enhanced CT shows the absence of enhancement in the affected renal tissue. Acute renal infarctions typically appear as wedge-shaped areas of decreased attenuation, while after the acute phase of renal infarction, atrophy begins and the infarcted tissue contracts, leaving a cortical scar. Chronic renal artery stenosis with persistent renal parenchymal hypoperfusion leads to progressive shrinkage of the parenchyma with absent residual function (Fig. 10.11).

10.5 Atheroembolic Renal Disease

Atheroembolic renal disease (renal artery atheroembolization) is a complication of severe ulcerative atheromatosis of the abdominal aorta [22] or may be due to renal angioplasty, atrial fibrillation, and cardiac valvular defects. Atheroemboli localizes in vessels smaller than the interlobular arteries, so that renal infarction does not occur and clinical picture is frequently bland [22] even though acute renal failure is the mode of presentation in most cases. Atheroembolic renal disease with acute renal failure may develop during or immediately after intravascular surgical intervention, intravascular interventional procedures (e.g., renal angioplasty), or anticoagulation due to atheroemboli detached from the renal artery wall. The most common clinical manifestation is the sudden onset of flank or back pain with or without hematuria, proteinuria, fever, and leukocytosis.

Color and power Doppler US is a first-line imaging procedure to detect renal perfusion defect but presents clear limitations due to the relative insensitivity to low-velocity and low-amplitude flow states [23]. Coley et al. [24] found a global accuracy of color Doppler US for the detection of partial renal infarction of 20%. Contrast-enhanced color and power Doppler US are limited by blooming and flash artifacts, which may be attenuated by reducing the instrument gain settings, also diminishing the detection of focal abnormalities in renal blood flow [23]. Contrast-enhanced CT (Fig. 10.12) is the reference imaging technique to identify renal perfusion defects [19]. Contrast-enhanced US (Fig. 10.13) represents a very sensitive and reliable imaging technique in revealing the renal parenchymal perfusion defects due to renal artery embolization [21]. Renal perfusion defects may appear as multiple focal wedge-shaped areas of absent, diminished, or delayed contrast enhancement in comparison to the adjacent renal parenchyma after microbubble injection [21].

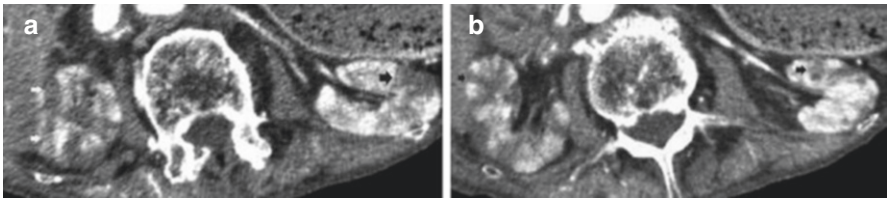

Fig. 10.12 (**a**, **b**) Contrast-enhanced CT. Multiple renal parenchymal perfusion defects (*arrows*) due to diffuse septic embolization are evident on both kidneys of an 85-year-old patient

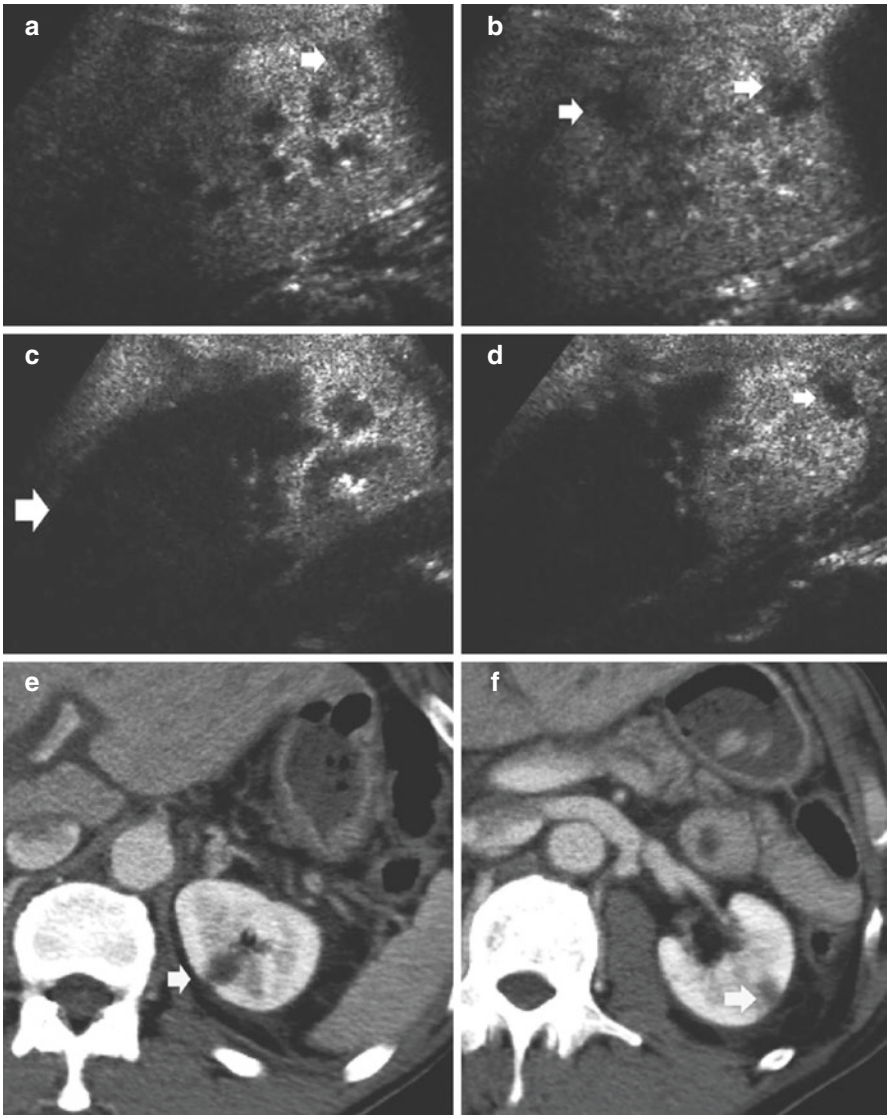

Fig. 10.13 (**a**–**h**) Renal artery embolization in an 82-year-old male patient presenting at the emergency unit with acute flank pain on the right side. (**a**–**d**) Contrast-enhanced US after sulfur hexafluoride-filled microbubble injection. (**e**–**h**) Contrast-enhanced CT, nephrographic phase. Multiple bilateral renal parenchymal perfusion defects (*arrows*), involving mainly the right kidney, due to embolization of an ulcerated plaque of the thoracic aorta

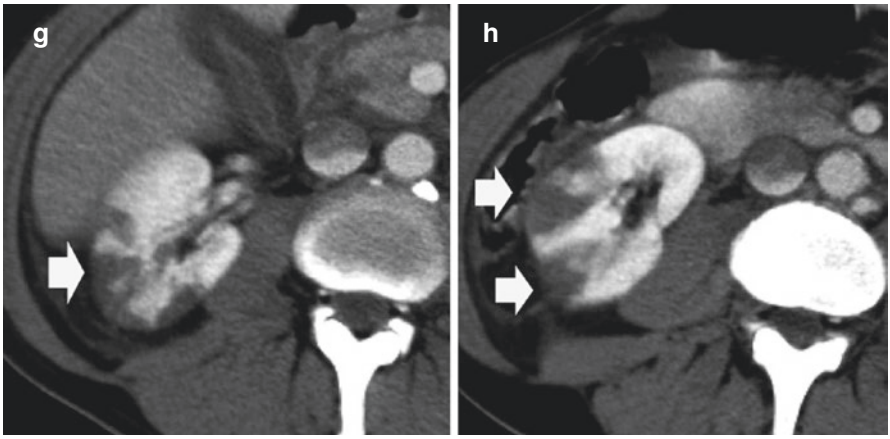

Fig. 10.13 (continued)

10.6 Renal Vein Thrombosis

Renal vein thrombosis in elderly patients, as in adults and differently from infants, is typically of insidious onset and is almost always overimposed on an established disease [22]. Causes of renal vein thrombosis in elderly patients include idiopathic nephrotic syndrome, especially that due to membranous glomerulonephritis, volume loss due to dehydration (often aggravated by diuretic therapy) with altered renal blood flow, hypercoagulable states (malignancy), renal cell carcinoma, or extrinsic compression of the renal vein (retroperitoneal fibrosis, lymphoma, etc.). The process may progress without any clinical sign. Mild abdominal or back pain may be present, but severe pain is uncommon. Pulmonary emboli occur during the course of approximately 50% of patients with chronic renal vein thrombosis and are frequently the first manifestation of this condition [22].

Diagnosis of renal vein thrombosis relies on the visualization of an echogenic thrombus within a dilated renal vein devoid of flow signals on CD corticomedullary differentiation on grayscale US. Doppler spectral analysis of renal arteries may reveal slightly increased RIs and normal parenchymal venous flows, since collateral venous supplies open after renal vein thrombosis. Absent or reversed end-diastolic flow in renal interlobar–arcuate arteries has been described in transplanted kidney which lacks collateral venous supply. US contrast agents facilitate identification of renal vein patency and thrombosis in cases of technical failure and enhance detection of collateral venous blood supply. A mass is evident in the renal vein with renal enlargement and delayed renal function.

CTA and MRA show complete occlusion of the renal vein [19] which appears dilated and heterogeneous, while the infracted kidney appears enlarged and with a diffuse alteration of the nephrographic phase (Fig. 10.14). Renal vein involvement by tumor (Fig. 10.15) is frequently identified in elderly patients and it is crucial in the determination of surgical options for removing a renal tumor. The renal veins are well depicted on CT during the corticomedullary or nephrographic phase of contrast enhancement.

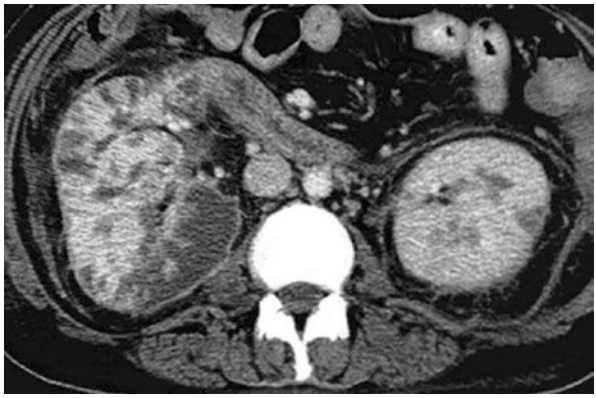

Fig. 10.14 Thrombosis of the right renal vein. Contrast-enhanced CT. Nephrographic phase. The renal vein appears dilated and heterogeneous, while the right kidney appears enlarged and with diffuse alteration of the nephrographic phase

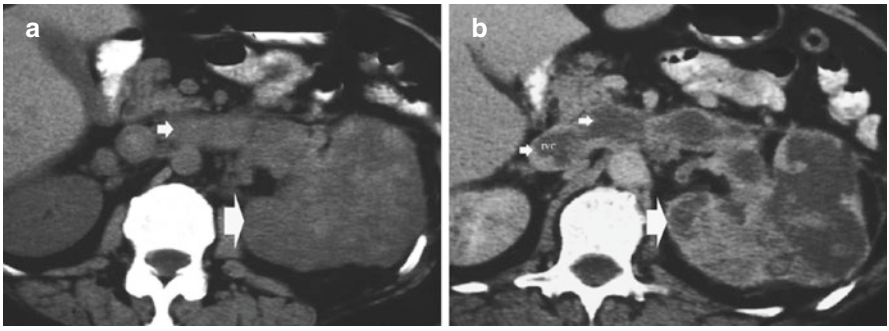

Fig. 10.15 (**a**, **b**) Thrombosis of the left renal vein due to infiltrating papillary renal cell carcinoma. (**a**) Unenhanced CT. (**b**) Contrast-enhanced CT. Contrast-enhanced CT. Nephrographic phase. The renal vein appears dilated and heterogeneous (*small arrow*), while the left kidney (*large arrow*) appears enlarged and with diffuse alteration of the nephrographic phase. The inferior vena cava (*IVC*) is also involved and appears occluded by a tumoral thrombus

10.7 Renal Failure

10.7.1 Acute Renal Failure

In the elderly, the kidneys are more vulnerable when other pathologies occur, in particular, atherosclerosis, arterial hypertension, diabetes mellitus, bacterial infections, and malnutrition. Most cases of acute renal failure in elderly patients are caused by drugs or are secondary to dehydration, especially in patients with hypertensive intrarenal nephrosclerosis. In elderly patients, the differentiation between renal and prerenal cause of acute renal failure may be difficult because the RIs are usually elevated for the preexisting renal parenchymal disease. Moreover, an elderly patient with severe and prolonged prerenal acute renal failure leading to acute tubular necrosis may present increased RIs.

Acute renal failure is a common complication of hypertensive nephrosclerosis in elderly patients with mild chronic renal failure [25]. Worsening renal function may be precipitated by the treatment of hypertension, mainly with ACE inhibitors, or by other causes such as nephrotoxic drug or dehydration. The evidence of acute renal failure without an apparent cause following therapy with ACE inhibitors highly suggests renal artery stenosis in well-hydrated elderly patients. Other possible causes of acute renal failure in these patients are renal artery thrombosis and atheroembolic renal disease. Doppler US examination is the first imaging modality to be employed in these patients to rule out renal artery stenosis. Identification of the kidneys of two different sizes is suggestive of ischemic disease.

The demonstration of increased flow velocity at the level of renal artery stenosis is diagnostic. Anyway, the Doppler evaluation of intrarenal and renal perforating arteries can be useful in these patients since the direct assessment of the main renal artery may be difficult due to bowel gas interposition and incomplete patient compliance. The intrarenal vessels may show an altered waveform with a pattern corresponding to pulsus tardus and parvus. Perforating arteries are vessels connecting the capsular plexus with the interlobar and interlobular arteries, which became hypertrophic in those pathologic conditions that reduce the blood flow through the renal artery. Perforating arteries with flow toward the kidney have been detected and interrogated in about 60% of kidneys with renal artery stenosis of hypertensive elderly patients with acute renal failure. Conversely, in the kidneys with no ischemic arterial lesions, only perforating arteries with flow toward the renal capsule were identified [9].

Acute cortical necrosis is a rare cause of acute renal failure, usually occurring in extremely ill individuals, often as a result of obstetric complications, hemorrhagic shock, disseminated intravascular coagulation, severe trauma, sepsis, shock, or burns. Contrast-enhanced US or CT (Fig. 10.16) has been shown to be diagnostic of acute cortical necrosis showing necrosis of the renal cortex with sparing of the renal medulla appearing as enhancing renal medulla, nonenhancing renal cortex and a thin rim of subcapsular tissue, and absent renal excretion of iodinated contrast agent [26]. Necrosis results from constriction of small intracortical blood vessels with preferential flow of blood away from the renal cortex. The likelihood that normal renal function will return is low. Usually, the involved kidney becomes shrunken and scarred. Cortical nephrocalcinosis may then develop [27].

Cholesteric renal embolization represents an acute diffuse renal vessel embolization, frequently manifesting with acute renal failure. Clinical diagnosis includes the presence of livedo reticularis due to distal embolization in the lower extremities and cholesterol crystals on the eye fundus examination. Color Doppler US examination is not useful to diagnose this pathologic entity due to the small size of renal perfusion defects. In cholesteric renal embolization, the identification of small renal perfusion defects in the renal subcapsular region is penalized by the limited spatial resolution of US which cannot identify renal perfusion defects smaller than 5 mm since in this clinical situation the renal perfusion defects are often very small to be detected by contrast-enhanced US. Anyway, if larger or equal to 5 mm, renal perfusions defects may be identified on contrast-enhanced US after microbubble injection (Fig. 10.17). Microbubble-based agents should be always employed to exclude

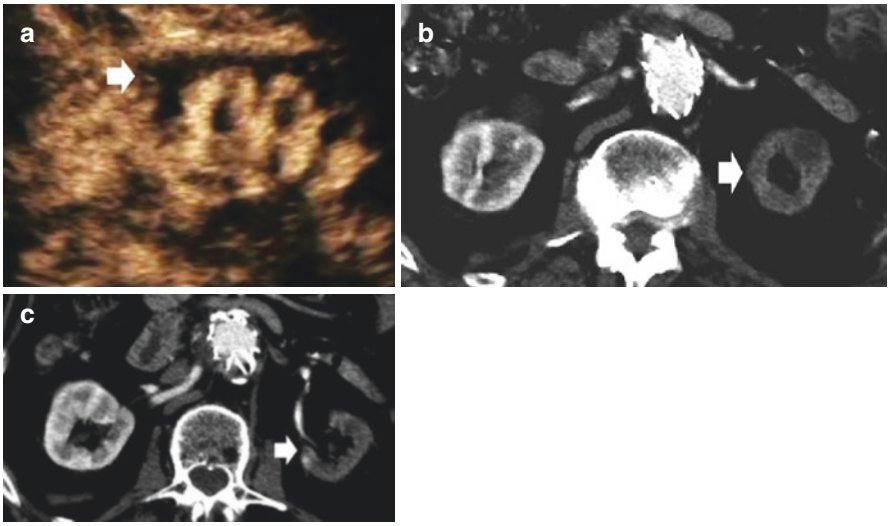

Fig. 10.16 (**a**–**c**) Renal acute cortical necrosis. An 80-year-old patient with aortic endoprosthesis was admitted to the emergency unit with acute renal failure. The absence of contrast enhancement in the superficial cortex of the left kidney (*arrow*) is identified after microbubble injection (**a**). (**b**, **c**) Contrast-enhanced CT confirmed the existence of diffuse renal cortical necrosis in the left kidney (*arrow*)

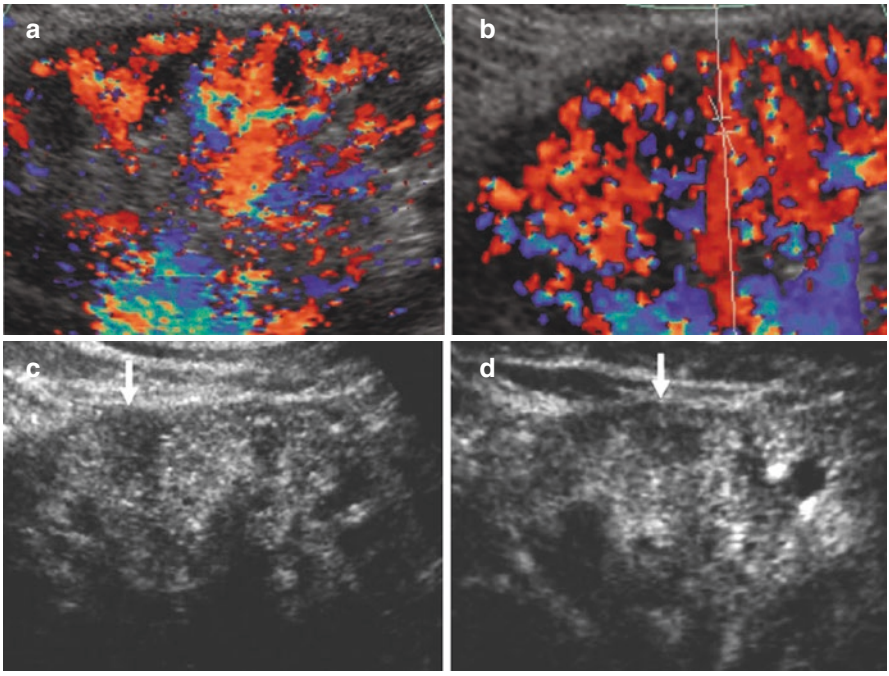

Fig. 10.17 (**a**–**d**) Cholesteric renal embolization in a 70-year-old female patient presenting with acute renal failure. Baseline color Doppler US (**a**, **b**) does not allow the identification of renal perfusion defects. Contrast-enhanced US (**c**, **d**) allows a reliable depiction of renal perfusion defect (*arrow*)

renal infarcts in every old patient presenting with a renal colic-like pain in the flank region.

10.7.2 Chronic Renal Failure

The proportion of elderly individuals is growing rapidly in all societies, and the incidence of chronic kidney disease among elderly people increases constantly [28]. Therefore, the accurate monitoring of kidney function, that is GFR, in elderly people is of considerable clinical interest in order to detect individuals who are at risk for developing chronic kidney disease. The management of end-stage renal failure in the elderly should not be significantly different from that in younger patients and should be based on the capacity for rehabilitation.

Chronic kidney disease is an important problem in the elderly and is associated with a high risk of kidney failure, cardiovascular disease, and death [29]. The disorder is indicated either by a GFR of less than 60 mL/min/1.73 m^2 of body surface area or by the presence of kidney damage, assessed most commonly by the finding of albuminuria for 3 or more consecutive months [30–32]. In persons 70 years of age or older, the percentage of people with a chronic kidney disease is around 30% [29].

Risk factors for chronic kidney disease include an age of more than 60 years, hypertension, diabetes, cardiovascular disease, and a family history of the disease. According to a recent series, diabetic nephropathy, obstructive uropathy, and hypertensive nephrosclerosis were the major causes of chronic renal failure and accounted for 80% of total chronic renal failure in the elderly [33].

Recommendations for evaluating people at increased risk are to measure urine albumin to assess kidney damage and to estimate the GFR with an equation based on the level of serum creatinine [32]. Older adults who suffer an acute injury to the kidneys—from trauma, surgery, or illness—are at dramatically increased risk of later end-stage renal disease.

Special care should be used in patients with chronic renal failure when the IV injection of iodinated or gadolinium-based agents is planned. Iodinated contrast agents should be employed in patients with chronic renal failure only before and after proper hydration, while gadolinium-based contrast agents should not be employed in patients with a GFR value below 30 mL/min. Differently from iodinated contrast agent and gadolinium-based contrast agents, microbubbles may be safely employed in patients with advanced chronic renal failure, especially in the evaluation of renal masses and perfusion defects.

US reveals reduced renal length and cortical thickness and a hyperechoic renal parenchyma with a poor visibility of renal pyramids and of renal sinus. Doppler US reveals a reduced parenchymal perfusion and increased resistive index (RI) values. In elderly patients with mild chronic renal failure, acute renal failure represents a

common complication of hypertensive nephrosclerosis [25]. Worsening renal function may be precipitated by the treatment of hypertension, mainly with ACE inhibitors, or by other causes such as nephrotoxic drug or dehydration.

The evidence of acute renal failure without an apparent cause following therapy with ACE inhibitors highly suggests renal artery stenosis in well-hydrated patients. Doppler US examination is the first imaging modality to be employed in these patients to rule out renal artery stenosis. Other possible causes of acute renal failure in patients with mild chronic renal failure are renal artery thrombosis and atheroembolic renal disease. Many urological interventions can precipitate or exacerbate chronic kidney disease, most notably radical nephrectomy.

10.8 Obstructive Uropathy

In elderly patients, acute urinary tract obstruction can occur anywhere in the urinary tract from the renal papilla to the urethral meatus and may be determined by a plenty of causes. As in some patients, obstruction may be completely asymptomatic even though, most frequently, it manifests with clear clinical symptoms.

Hydronephrosis may also be absent in the acute obstruction of the urinary tract principally due to hypovolemia, dehydration, or nephrosclerosis. The most important causes of urinary tract obstruction in elderly patients are urinary stones, tumors of the urinary tract and ureter, and benign prostatic hyperplasia (Fig. 10.18).

The obstruction of the urinary tract, if not treated, usually determines a progressive atrophy of the renal parenchyma which is frequently observed in elderly patients.

Chronic obstructive uropathy (Fig. 10.19) may be determined by the tumoral infiltration of the ureteral wall or by chronic incomplete obstruction of the ureter, which may be suddenly complicated by an acute event such as infection.

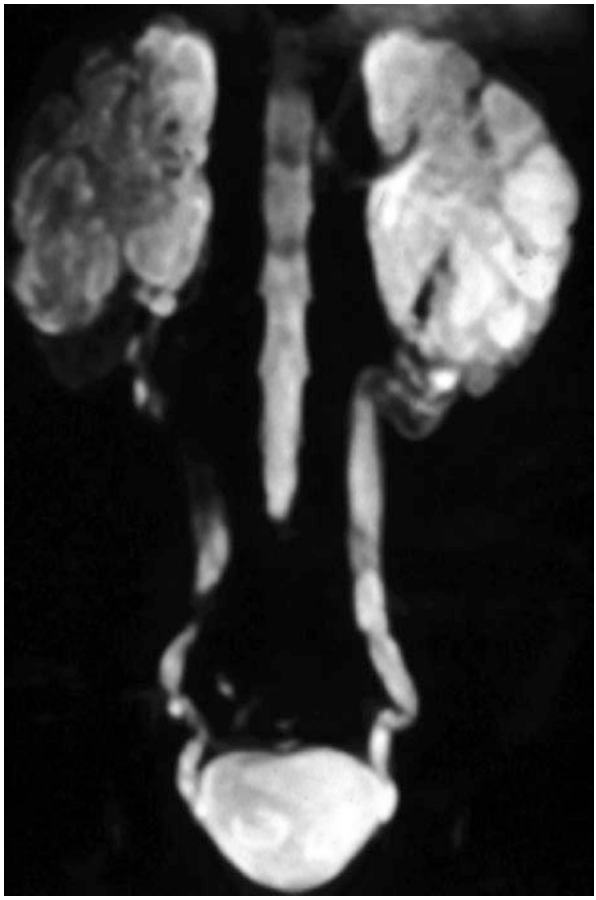

Fig. 10.18 Static-fluid MR urography in an 85-year-old man patient with benign prostatic hyperplasia. Bilateral fourth-grade hydronephrosis

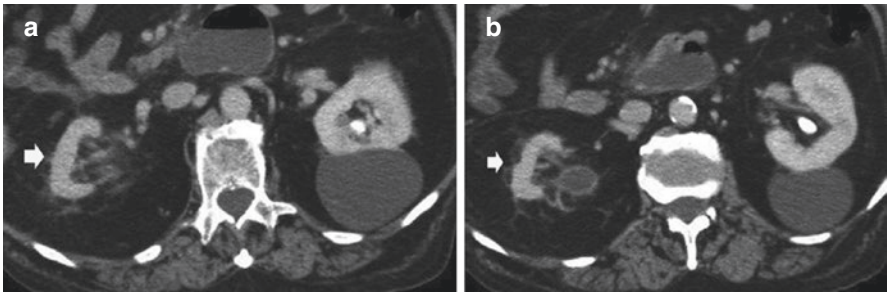

Fig. 10.19 (**a**, **b**) Contrast-enhanced CT, excretory phase. Chronic urinary tract obstruction of the right kidney (*arrow*) due to tissue scarring of the lower ureter. The kidney appears small and without any sign of function (contrast excretion). Perirenal strands with dilatation and wall thickening of the renal pelvis are also evident on the right kidney

10.9 Renal Infections

Acute pyelonephritis is an infectious disease involving both renal parenchyma and renal pelvis mucosa which can be diffuse or focal. Diffuse pyelonephritis is an infection involving the entire kidney, even though the severity of the process may vary in extension (in one or both kidneys). Focal pyelonephritis is a localized infection of the kidney appearing as a wedge- or round-shaped parenchymal lesion, which can regress if well treated or evolve to a collection extending toward the peri- and pararenal spaces. Focal and diffuse pyelonephritis may resolve with the evidence of normal renal parenchyma or scarring or may evolve with liquefaction and formation of nephric or perinephric abscesses.

Pyelonephritis is the most common cause of gram-negative bacteremia in elderly patients admitted to a community hospital. Acute pyelonephritis can be severe in the elderly as in people who are diabetic or immunosuppressed with frequent evidence of renal abscesses (Fig. 10.20). Appropriate antibiotic therapy and, of equal importance, a lack of serious associated medical illnesses contributed to the 97% survival. An increased incidence of bacteremia and septic shock distinguishes acute, symptomatic, and bacterial pyelonephritis in the elderly from that in young patients and particularly in women [34].

Pyonephrosis is the most common complication of pyelonephritis in elderly patient when ureteral obstruction is present. Urinary tract obstruction due to a urinary stone is the most common cause of pyonephrosis (Fig. 10.21).

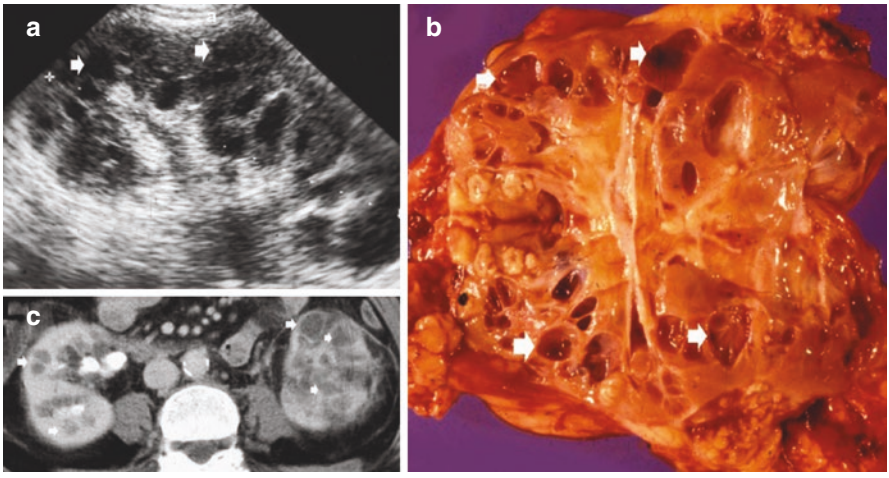

Fig. 10.20 Pyelonephritis with diffuse abscessual evolution in a 70-year-old diabetic woman presenting with septic shock (**a**) Grayscale US. Longitudinal scan. The left kidney appears increased in dimension with multiple cystic lesions (*arrows*). (**b**) Contrast-enhanced CT during the nephrographic phase after iodinated contrast injection. Both kidneys appear involved by multiple abscessual lesions (*arrows*). (**c**) Gross autopsy specimen confirming multiple renal abscesses (*arrows*)

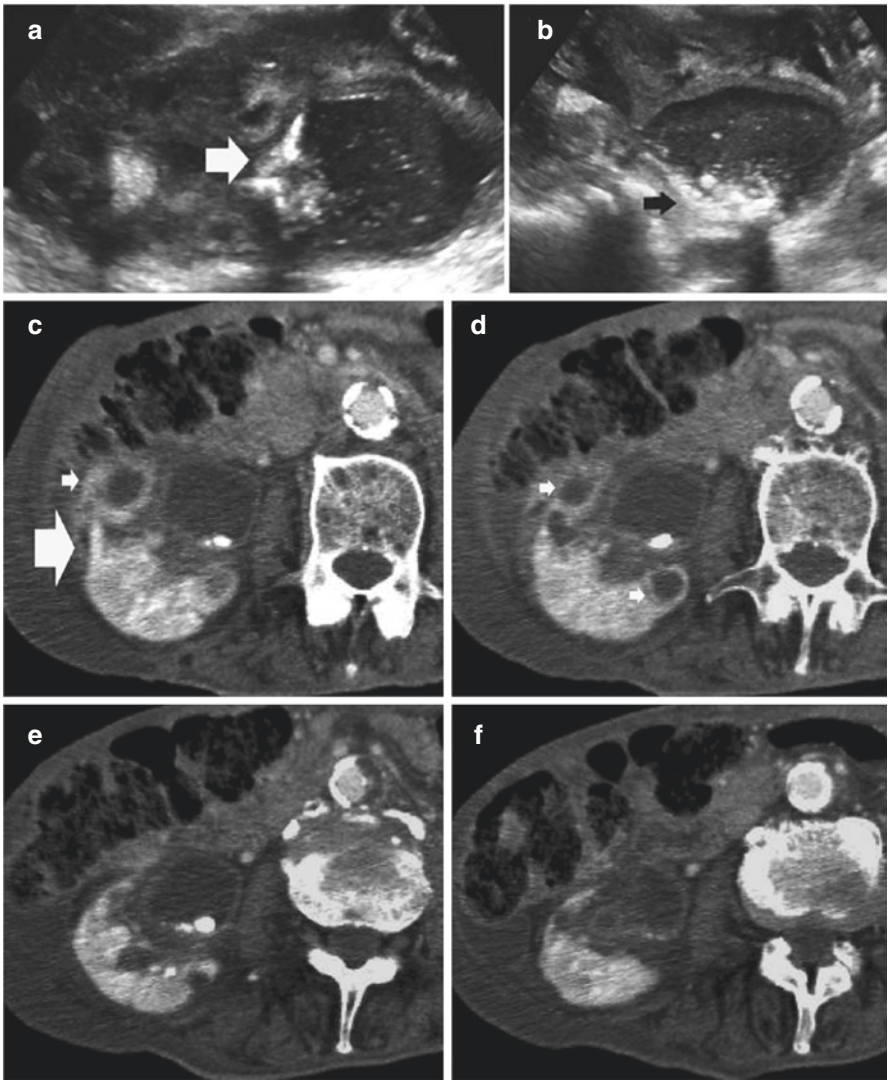

Fig. 10.21 (**a**–**f**) Pyonephrosis in an 82-year-old woman presenting with acute right flank pain. Grayscale US, longitudinal (**a**) and transverse scan (**b**). The right kidney presents dilatation of the intrarenal urinary tract (*white arrow*) with diffuse corpuscular echogenic content and evidence of renal stones (*black arrow*) lying in the renal pelvis with posterior acoustic shadowing. (**c**–**f**) Contrast-enhanced CT, nephrographic phase. The right kidney (*large arrow*) presents increased dimensions, multiple renal stones lying in the renal pelvis, and dilatation and diffuse thickening of the renal pelvis. Renal parenchyma presents also some abscesses (*small arrows*) due to infection diffusion

10.10 Neoplastic Pathologies

Frequently, urologists are confronted with an elderly patient (≥75 years of age) with a renal mass seeking treatment. As the population ages, comorbidities become more confounding in predicting patient outcome to therapy and may influence the application of surgical therapy with curative intent to elderly patients [35]. Epidemiological studies show an increasing incidence of renal cell carcinoma over the past two decades, and interestingly, this increase has included a larger proportion of elderly people. The presentation of renal cancer has evolved. There has been an increase in the incidence of cases in the USA and several European countries and, at the same time, a shift to incidentally diagnosed, smaller, localized tumors in a slightly older population [36].

Generally, in elderly patients there is an increase in neoplastic disorders including clear cell-type renal carcinoma and transitional cell carcinoma (TCC). The median age of presentation of renal cell carcinoma is in the sixth decade of life. Conversely, transitional cell carcinoma of the upper urinary tract is commonly seen in older patients, usually between the sixth and eighth decade of life. This increased incidence is mainly due to the more widespread use of imaging technology [37]. Most renal tumors are completely asymptomatic and are found incidentally in elderly patients during imaging of the upper abdomen mainly by US (Fig. 10.22). There is a great variance of growth rate with the majority of small renal tumors (≤3 cm in diameter) in the elderly, with a prevalence of low growth rate (0.35 cm/year with a median range of 0–10 cm), and a low incidence of distant metastases [38]. Conversely, the majority of larger renal tumors usually present local invasiveness (Figs. 10.23 and 10.24) and distant metastases (Fig. 10.25). A "wait and see" observational approach for renal masses 1.5 cm or smaller in the elderly can be suggested [39].

TCCs are relatively rare tumors of the kidney, while they are commonly seen in older patients usually between the sixth and eighth decade of life with a mean age

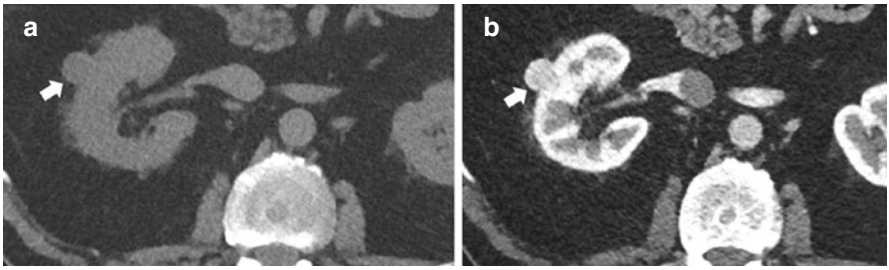

Fig. 10.22 (**a**, **b**) Small renal tumor incidentally found in a 75-year-old male patient during US examination of the abdomen. Unenhanced CT scan (**a**) showed a solid exophytic mass (*arrow*) with enhancement after contrast injection in arterial phase (**b**). Clear cell-type renal cell carcinoma is identified after partial nephrectomy

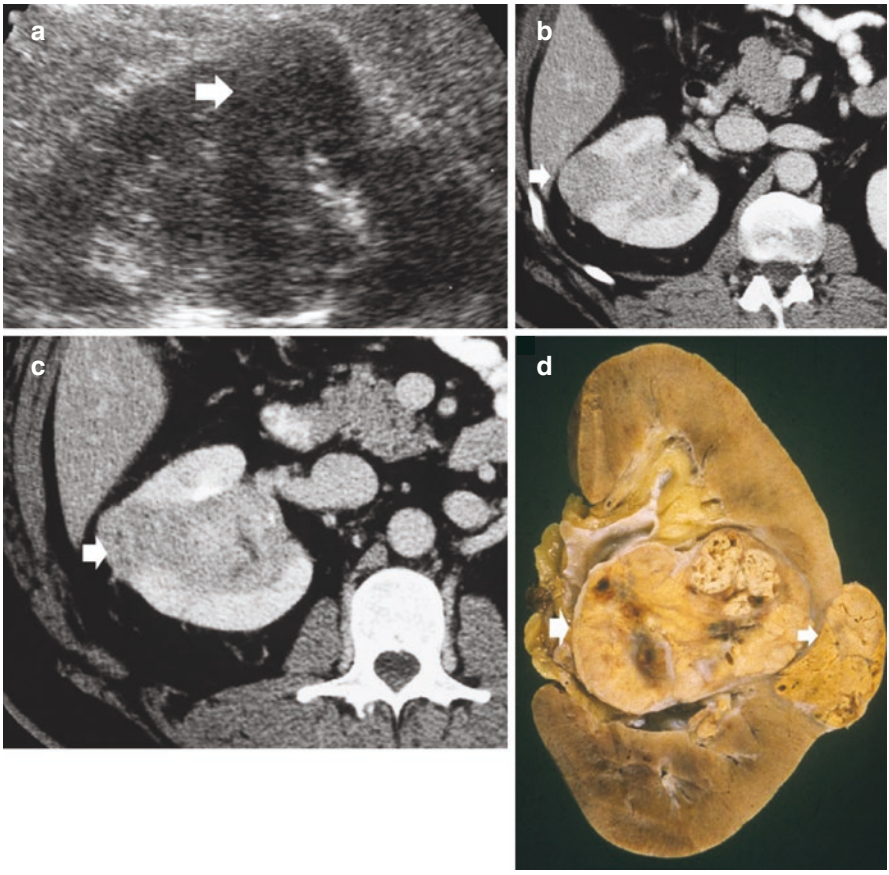

Fig. 10.23 (**a**–**d**) Clear cell-type renal cell carcinoma in a 75-year-old man with hematuria. Local tumoral invasiveness. (**a**) Grayscale US. A solid renal mass (*arrow*) is identified on the right kidney. (**b**, **c**) Contrast-enhanced CT. Nephrographic phase shows a renal mass (*arrow*) on the right kidney with invasion of the renal pelvis. (**d**) Photograph of gross specimen. Evidence of invasion of the renal pelvis which justified the presenting symptom hematuria

of 65 years. TCCs of the renal pelvis or calices present an incidence of 5–15% of all malignant tumors of the kidney [40, 41]. The incidence in men exceeds that in women and the usual sex ratio is between 2:1 and 4:1 [41]. Over 85–90% of upper urinary tract tumors are TCCs, with the renal pelvis (Fig. 10.26) being more commonly involved than the ureter [42]. Renal lymphoma occurs in all age groups, even though the disease usually affects adults (average age, 60 years) and frequently elderly patients. Renal involvement with lymphoma occurs much more commonly with non-Hodgkin disease, the majority of patients having intermediate- or

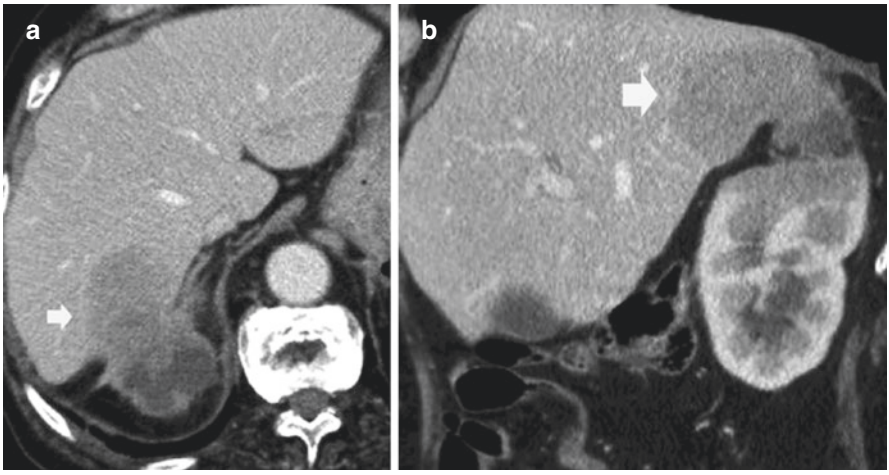

Fig. 10.24 (**a**, **b**) Clear cell-type renal cell carcinoma in an 82-year-old man. Local tumoral invasiveness. Contrast-enhanced CT. (**a**) Transverse plane. (**b**) Sagittal plane. Corticomedullary phase shows a large solid renal mass of the right kidney invading the adjacent liver parenchyma (*arrow*)

high-grade lymphomas including Burkitt and histiocytic types [43]. Lymphoma that is isolated to the kidney as a primary site of involvement is quite rare, whereas additional sites of extranodal involvement are common and are seen in most patients at the time of diagnosis. Lymphoma typically involves the kidney in one of the several recognizable patterns including multiple renal masses, solitary masses, diffuse renal infiltration, renal invasion from contiguous retroperitoneal disease (Fig. 10.27), perirenal disease, or atypical patterns of renal involvement with invasion of the renal pelvis.

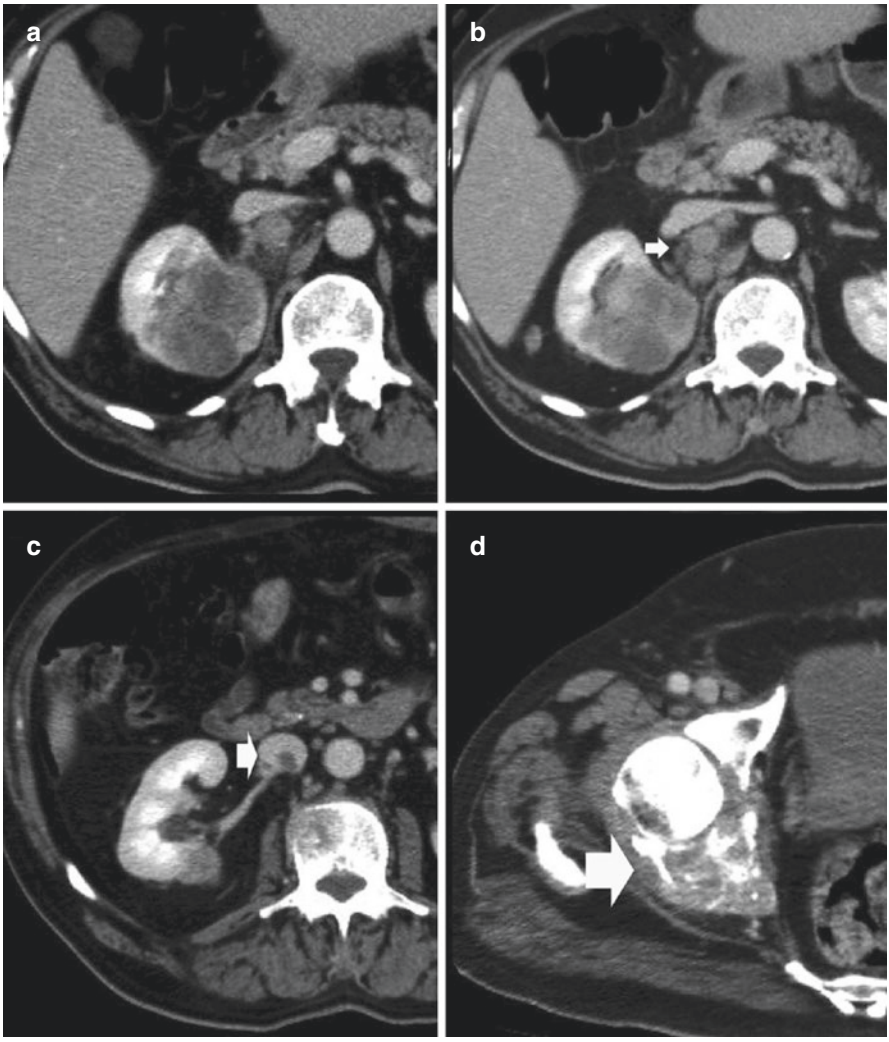

Fig. 10.25 (**a**–**d**) Clear cell-type renal cell carcinoma in a 77-year-old man. (**a**) Contrast-enhanced CT. Nephrographic phase shows a heterogeneous large renal mass on the lower pole of the right kidney. (**a**, **b**) Multiple enlarged lymph nodes (*small white arrow*) are identified in the retrocaval nodal site. (**c**) Floating thrombus (*large white arrow*) in the inferior vena cava is also present. (**d**) Distant bone metastasis is visualized on the right acetabulum (*large arrow*)

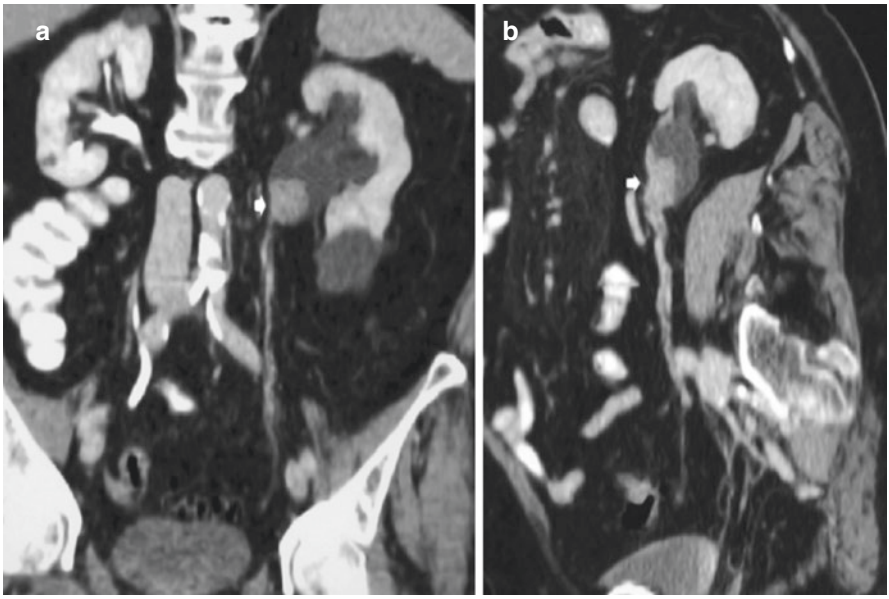

Fig. 10.26 (**a**, **b**) Transitional renal cell carcinoma in a 70-year-old man with hematuria. (**a**) Contrast-enhanced CT. Coronal (**a**) and sagittal reformations (**b**). A solid endoluminal tumor (*arrow*) in the left kidney pelvis

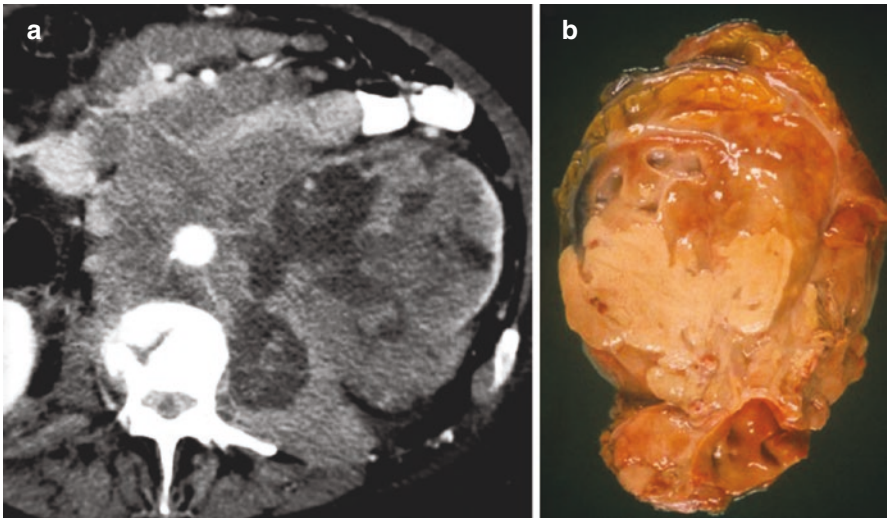

Fig. 10.27 (**a**, **b**) Renal lymphoma in a 67-year-old male patient with a known non-Hodgkin disease retroperitoneal disease. (**a**) Contrast-enhanced CT, transverse plane. Direct and extensive renal parenchymal invasion from contiguous retroperitoneal disease. (**b**) Photograph of gross specimen from autopsy. Gross pathologic examination reveals yellow/gray tumor with extensive renal parenchymal invasion

10.11 Prostate

10.11.1 Benign Prostatic Hyperplasia (BPH)

In elderly patients it is common to find a condition of BPH, since it is an "age-dependent" disease with a reported prevalence in patients older than 60 years of 50% that increases to 90% in patients older than 85 years [44]. Up to 50% of these patients show lower urinary tract symptoms that include obstructive symptoms, such as incomplete emptying, intermittent voiding, weak stream, and straining, and irritative urinary symptoms, such as frequent voiding, urgency, and nocturia [44–46]. A clinical questionnaire, the International Prostate Symptom Score, divides the patients in those with mild, moderate, or severe symptoms [47]. Men showing moderate or severe symptoms are addressed to medical therapy, with α-blockers or 5α-reductase inhibitors, or minimally invasive surgical interventions to reduce prostate volume and improve the symptoms [48]. Anatomically, the prostate is divided into a stromal zone, named fibromuscular stroma, and four glandular zones that are, respectively, periurethral, transition, central, and peripheral zone [44, 49]. Posteriorly to the preprostatic urethra is located a zone of glandular tissue, named periurethral glands [44, 49]. The first signs of BPH can be detected in the periurethral glands, while later the glandular tissue of the transition zone is affected by the pathology, producing consequently a hyperplasia of the surrounding fibromuscular stroma. The progression of the hyperplastic glandular growth brings an increase in the gland volume directed toward the bladder neck [44, 50]. Since hyperplasia affects both the glandular and stromal tissue, there are two main mechanisms that produce the symptoms and signs of urinary obstruction: the first is a compressive narrowing of the urethra and bladder neck due to glandular hypertrophy and the second is an increased tone of the muscles of the stroma around the urethra [44, 50]. Imaging is indicated in case of hematuria, abnormal findings at digital rectal examination, increased prostate-specific antigen (PSA), increased serum creatinine or urinary retention [44]. Ultrasound (US) is the most common imaging technique used for prostate examination. On US the BPH appears first ad spherical hypoechoic areas antero-laterally and cranially to the verumontanum and, later, as multinodular isoechoic nodules on a hypoechoic background in the transition zone [44, 51]. The US examination can be transrectal, transabdominal, and transperineal and is crucial to correctly evaluate the prostate volume and bladder voiding [52]. The total volume can be calculated by measuring length, height, and width of the prostate, multiplying the product by $\pi/6$ (Fig. 10.28); the dimensional cut-off that is generally used to identify a BPH is 25 cm^3 [44, 53]. In magnetic resonance imaging (MRI) examination the same formula can be used to calculate the prostate volume, allowing a better definition of the intra-glandular anatomy and of the morphological changes caused by BPH (Fig. 10.29) [48, 53].

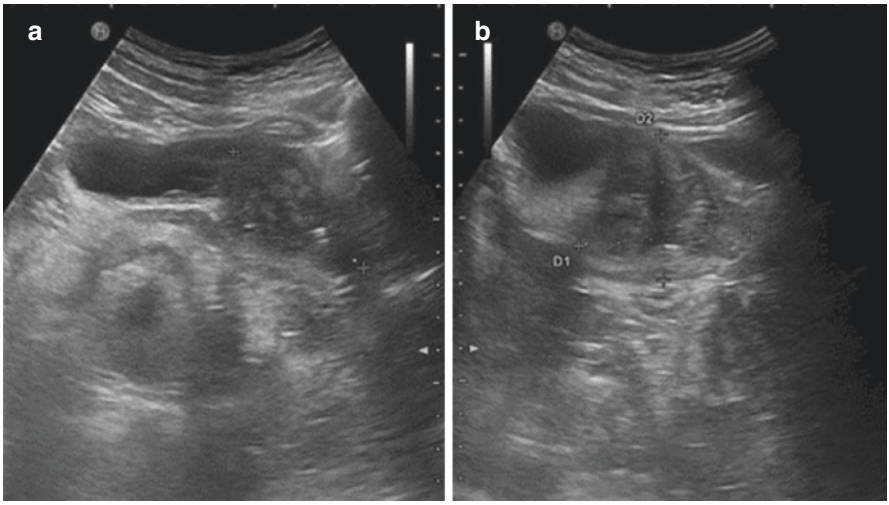

Fig. 10.28 (**a**, **b**) Benign prostatic hyperplasia (BPH) at ultrasound in sagittal (**a**) and transverse plane (**b**). The calculated volume of the prostate is 65 cm^3. Multiple isoechoic nodules on a hypoechoic background are detected in the transition zone

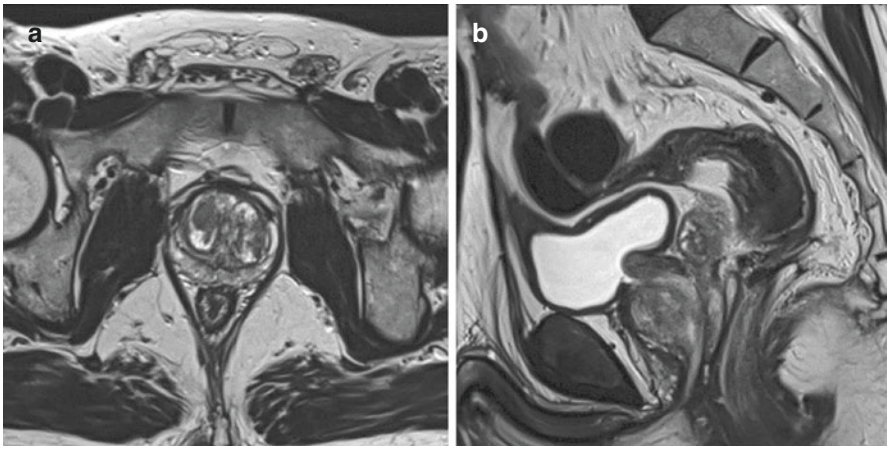

Fig. 10.29 (**a**, **b**) Benign prostatic hyperplasia (BPH) at MRI in transverse (**a**) and sagittal plane (**b**). The calculated volume of the prostate is 52 cm^3. Multiple typical encapsulated nodules of the BPH can be appreciated in the transition zone

10.11.2 Prostatic Cancer

Prostate cancer is the second most common cancer affecting men worldwide, with an estimated number in 2020 of 1,400,000 new cases and 375,000 deaths [54]. The vast majority of tumors arising from the prostate are carcinomas of epithelial origin [55]. Prostate cancer originates mainly from the peripheral zone that is located posteriorly and constitutes the main glandular component, nevertheless among one-fourth of the tumors originate from the transition zone that is located more anteriorly [56]. The risk of prostate cancer increases with age: foci of prostate cancer have been identified in 30–40% of men aged 60 years or older and the median age of symptoms onset is 72 years [57, 58]. Hence, it is fundamental to have screening procedures performed, especially in elderly patients. The screening tests are two: the first is the physical examination with the digital rectal examination (DRE) and the second one is the serum prostate-specific antigen (PSA) measurement that is more reliable and widely used [59]. Anomalous findings in DRE or increased PSA levels bring the suspect of prostate cancer and, therefore, imaging and eventually biopsies are required to confirm the diagnosis. Since a few years ago, endorectal US was the main imaging modality to verify the presence of prostate cancer [60]. At US prostate cancer in around 60–70% of cases is detected as a hypoechoic nodule in the gland, although the remaining 30–40% are iso or hyperechoic; anyway, the reported accuracy of this technique is low, around 50–60% [60]. The accuracy of the transrectal US has been reported to improve with the use of color/power Doppler techniques, with the use of microbubble contrast agents and with elastography [60]. Nevertheless, in the last 10 years MRI has increasingly been used for the detection of prostate cancer and its risk stratification. The first standardized system to report MRI results was published in 2013, the Prostate Imaging Reporting and Data System (PI-RADS), that was later updated in 2015 and now is currently used with the 2.1 version published in 2019 [61–63]. The PI-RADS system assigns a score to the lesions found by MRI in the prostate from PI-RADS 1 (very low risk of prostate cancer) to PI-RADS 5 (very high risk of prostate cancer). The MRI characterization of the lesion changes in the peripheral zone compared to the transition zone, in the first one is mainly based on diffusion weighted imaging (DWI) signal of the nodule, while in the second one on T2-weighed signal of the lesion [63]. For the peripheral zone, the characteristics of the lesions are the following that are based mainly on diffusion weighted imaging (DWI): PI-RADS 1 normal signal in DWI without alteration at the apparent diffusion coefficient (ADC) map; PI-RADS 2 mild hypointensity in the ADC map but not focal hyperintensity in high *b* value DWI images; PI-RADS 3 focal mild or moderate hypointensity in ADC map and mild hyperintensity in high *b* value DWI images; PI-RADS 4 focal and marked hypointensity on the ADC map with marked hyperintensity in high *b* value DWI images. <1.5 cm; PI-RADS 5 same as 4 but ≥1.5 cm in greatest dimension or definite extraprostatic extension/invasive behavior [63]. The contrast enhancement pattern plays a role in this scale since PI-RADS 3 lesions with hypervascularization in arterial phase should be classified as PI-RADS 4 [63] (Fig. 10.30).

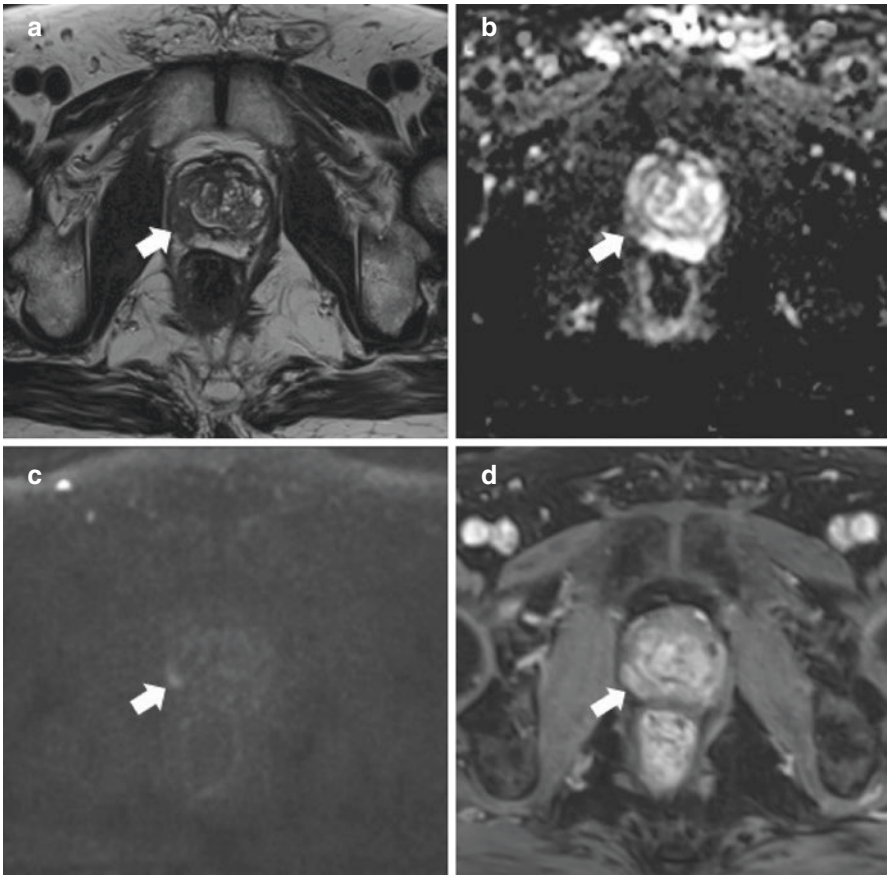

Fig. 10.30 (**a–d**) Prostate MRI in a 72 years-old patient with PSA elevation. (**a**) **T2-weighted image** showing a hypointense lesion (*arrow*) of the peripheral zone with a maximum diameter of 14 mm and without extracapsular extension; (**b**) focal and marked hypointensity of the lesion on the ADC map (*arrow*); (**c**) marked hyperintensity of the lesion (*arrow*) in 1500 *b* value DWI images; (**d**) contrast enhancement of the nodule after contrast injection (*arrow*). The lesion was scored as a PI-RADS 4 nodule and targeted biopsies revealed a Gleason 7 prostate adenocarcinoma

In the transition zone, the grading is based on the T2-wighted signal of the lesion: PI-RADS 1 normal appearing transition zone (rare) or a round, completely encapsulated nodule; PI-RADS 2 a mostly encapsulated nodule or a homogeneous circumscribed nodule without encapsulation ("atypical nodule"), or a homogeneous mildly hypointense area between nodules; PI-RADS 3 heterogeneous signal intensity with obscured margins; includes others that do not qualify as PI-RADS 2, 4, or 5; PI-RADS 4 lenticular or non-circumscribed, homogeneous, moderately hypointense, and <1.5 cm in greatest dimension; PI-RADS 5 same as 4 but ≥1.5 cm in greatest dimension or definite extraprostatic extension/invasive behavior [63]. If a

PI-RADS 3 lesion ≥1.5 cm shows marked hypointensity on the ADC map and marked hyperintensity in high *b* value DWI images, it should be classified as PI-RADS 4 [63].

The PI-RADS system divides the prostate into 39 sectors/regions for three parts of the prostate, the apex, the mid prostate, and the base of the prostate [63].

Multi-parametric MRI results allow to identify the suspicious lesions in the prostate and to target the biopsies on them [64]. There are three techniques of MRI guidance to perform a targeted prostate biopsy: the first is the cognitive fusion in which the US operator performs the biopsy aiming in the prostate area where the MRI results showed a lesion, the second is the direct MRI-guided biopsy that is a biopsy performed directly in the MRI tube and guided by the images acquired during the procedure and finally using device for images fusion where there is a co-registration of stored MR images with real-time US scan [64].

MRI and contrast-enhanced CT can also identify loco-regional lymph node metastases, at MRI or CT nodes with a short axis ≥1 cm, or ≥0.8 cm if round shaped, are suspect for metastatic involvement [65]. A better accuracy for nodal metastases detection has been reported for choline-PET/CT and prostate-specific membrane antigen (PSMA)-PET/CT compared to CT and MRI [66].

For distant metastases contrast-enhanced CT is routinely used but MRI, choline-PET/CT, PSMA-PET, and NaF-PET/CT showed a better accuracy, especially in detection of bone metastases [66].

10.11.3 Prostatitis

The bacterial prostatitis can be acute or chronic, with an estimated prevalence around 10% [67]. Acute infections are most common in young men, while chronic prostatitis often occurs in elderly patient with obstruction of the lower urinary tract, even in absence of prior history of acute prostatitis [68]. The prostatitis can be focal or diffuse, the peripheral zone is most frequently involved than the transition zone and the most frequent cause is an ascending urethral infection from urine infected by Escherichia Coli [68, 69]. During bacterial prostatitis, US shows a hypoechoic rim around the gland with an increased flow at color Doppler, while MRI features are low T2 signal intensity with increased contrast enhancement in arterial phase and mild/moderate signal restriction in DWI sequences, due to infiltration of the glandular tissue by inflammatory cells [68, 69]. Acute prostatitis could progress in intraprostatic abscesses that at US and MRI examination appears as a fluid collection with thick irregular walls that present increased flow at color Doppler and contrast enhancement at MRI [68, 69]. In case of granulomatous prostatitis that can be idiopathic, infective, iatrogenic, malacoplakia, or associated with systemic granulomatous disease, the US and MRI signal is very similar to prostate cancer., hence, it is fundamental to collect a correct clinical history in order to avoid unnecessary biopsies [68].

References

1. Ferrucci L, Giallauria F, Guralnik JM. Epidemiology of aging. Radiol Clin North Am. 2008;46:643–52.
2. Dagher PR, Herget-Rosenthal S, Ruehm SG, et al. Newly developed techniques to study and diagnose acute renal failure. J Am Soc Nephrol. 2003;14:2188–98.
3. Faubert PF, Porush JG. Renal disease in the elderly. 2nd ed. Basel: Marcel Decker; 1998.
4. Davison AM. Renal disease in the elderly. Nephron. 1998;80:6–16.
5. Mulder WJ, Hillen HF. Renal function and renal disease in the elderly: part I. Eur J Intern Med. 2001;12(4):327–33.
6. Pozzi Mucelli R, Faccioli N, Manfredi R. Imaging findings of genitourinary tumors in the elderly. Radiol Clin North Am. 2008;46:773–84.
7. Alpers CE. The kidney. In: Kumar V, Abbas AK, Fausto N, editors. Robbins and Cotran pathologic basis of disease. Philadelphia: Elsevier Saunders; 2005. p. 955–1021.
8. Quaia E, Bertolotto M. Renal parenchymal diseases: is characterization feasible with ultrasound? Eur Radiol. 2002;12:2006–20.
9. Bertolotto M, Quaia E, Galli G, et al. Color Doppler sonographic appearance of renal perforating vessels in subjects with normal and impaired renal function. J Clin Ultrasound. 2000;28:267–76.
10. Kalva SP, Mueller PR. Vascular imaging in the elderly. Radiol Clin North Am. 2008;46:663–83.
11. Zhang H, Prince MR. Renal MR angiography. Magn Reson Imaging Clin N Am. 2004;12:487–503.
12. Correas JM, Helenon O, Moreau JF. Contrast enhanced ultrasonography of native and transplant kidney diseases. Eur Radiol. 1999;9(Suppl 3):394–400.
13. Grant EG, Melany ML. Ultrasound contrast agents in the evaluation of the renal arteries. In: Goldberg BB, Raichlen JS, Forsberg F, editors. Ultrasound contrast agents. Basic principles and clinical applications. 2nd ed. London: Martin Dunitz; 2001. p. 289–95.
14. Desberg AL, Paushter DM, Lammert GK, et al. Renal artery stenosis: evaluation with color Doppler flow imaging. Radiology. 1990;177:749–53.
15. Helenon O, Rody EL, Correas JM, et al. Color Doppler US of renovascular disease in native kidneys. Radiographics. 1995;15:833–54.
16. Bude RO, Rubin JM, Platt JF, et al. Pulsus tardus: its cause and potential limitations in detection of arterial stenosis. Radiology. 1994;190:779–84.
17. Bude RO, Rubin JM. Detection of renal artery stenosis with Doppler sonography: it is more complicated than originally thought (editorial). Radiology. 1995;196:612–3.
18. Stavros AT, Parker SH, Yakes WF, et al. Segmental stenosis of the renal artery: pattern recognition of tardus and parvus abnormalities with duplex sonography. Radiology. 1992;184:487–92.
19. Kawashima A, Sandler CM, Ernst RD, et al. CT evaluation of renovascular disease. Radiographics. 2000;20:1321–40.
20. Correas JM, Claudon M, Tranquart F, et al. Contrast-enhanced ultrasonography: renal applications. J Radiol. 2003;84:2041–54.
21. Bertolotto M, Martegani A, Aiani L, et al. Value of contrast-enhanced ultrasonography for detecting renal infarcts proven by contrast-enhanced CT. A feasibility study. Eur Radiol. 2008;18(2):376–83.
22. Cohen JJ. Vascular disorders of the kidney. In: Wyngaarden JB, Smith LH, Bennett JC, editors. Cecil textbook of medicine. Philadelphia: Saunders; 1992. p. 598–9.
23. Taylor GA, Ecklund K, Dunning PS. Renal cortical perfusion in rabbits: visualization with color amplitude imaging and an experimental microbubble-based US contrast agent. Radiology. 1996;201:125–9.
24. Coley BD, Mattrey RF, Roberts A, et al. Potential role of PFOB enhanced sonography of the kidney. II. Detection of partial infarction. Kidney Int. 1991;39:740–5.
25. Pozzi Mucelli R, Bertolotto M, Quaia E. Imaging techniques in acute renal failure. In: Ronco C, Bellomo R, La Greca G, editors. Blood purification in intensive care. Basel: Karger; 2001. p. 76–91.

26. Jordan J, Low R, Jeffrey RB. CT findings in acute renal cortical necrosis. J Comput Assist Tomogr. 1990;14(1):155–6.
27. Cohan RH, Cowan NC, Ellis JH. Unknown ESUR cases 2004. Abdom Imaging. 2006;31:141–53.
28. Fliser D. Assessment of renal function in elderly patients. Curr Opin Nephrol Hypertens. 2008;17(6):604–8.
29. Stevens LA, Levey AS. Chronic kidney disease in the elderly—how to assess risk. N Engl J Med. 2005;352:2122–4.
30. National Kidney Foundation. K/DOQI clinical practice guide-lines for chronic kidney disease: evaluation, classification, and stratification. Am J Kidney Dis. 2002;39(Suppl 1):S1–S266.
31. Levey AS, Eckardt KU, Tsukamoto Y, et al. Definition and classification of chronic kidney disease: a position statement from kidney disease: improving global outcomes (KDIGO). Kidney Int. 2005;67:2089–100.
32. Stevens LA, Coresh J, Greene T, et al. Assessing kidney function—measured and estimated glomerular filtration rate. N Engl J Med. 2006;354:2473–83.
33. Prakash J, Saxena RK, Sharma OP. Spectrum of renal disease in the elderly: single center experience from a developing country. Int Urol Nephrol. 2001;33(2):227–33.
34. Gleckman R, Blagg N, Hibert D, et al. Acute pyelonephritis in the elderly. South Med J. 1982;75(5):551–4.
35. Berdjis N, Hakenberg OW, Novotny V, et al. Treating renal cancer in the elderly. BJU Int. 2006;97:703–5.
36. Linehan JA, Nguyen MM. Kidney cancer: the new landscape. Curr Opin Urol. 2009;19(2):133–7.
37. Jayson M, Sanders H. Increased incidence of serendipitously discovered renal cell carcinoma. Urology. 1998;51:203–5.
38. Bosniak MA, Birnbaum BA, Krinsky GA, et al. Small renal parenchymal neoplasms: further observations on growth. Radiology. 1995;197(3):589–97.
39. Silverman SG, Israel GM, Herts BR, et al. Management of the incidental renal mass. Radiology. 2008;249:16–31.
40. Grabstald H, Whitmore WF, Melamed MR. Renal pelvic tumors. JAMA. 1971;218:845–54.
41. Nocks BN, Heney NM, Daly JJ, et al. Transitional cell carcinoma of the renal pelvis. Urology. 1982;19:472–7.
42. Wong-You-Cheong JJ, Wagner BJ, Davis CJ. Transitional cell carcinoma of the urinary tract: radiologic-pathologic correlation. Radiographics. 1998;18:123–42.
43. Urban BA, Fishman EK. Renal lymphoma: CT patterns with emphasis on helical CT. Radiographics. 2000;20:197–212.
44. Wasserman NF. Benign prostatic hyperplasia: a review and ultrasound classification. Radiol Clin North Am. 2006;44(5):689–710, viii. https://doi.org/10.1016/j.rcl.2006.07.005.
45. Guneyli S, Ward E, Peng Y, Nehal Yousuf A, Trilisky I, Westin C, Antic T, Oto A. MRI evaluation of benign prostatic hyperplasia: correlation with international prostate symptom score. J Magn Reson Imaging. 2017;45(3):917–25. Epub 2016 Aug 3. https://doi.org/10.1002/jmri.25418.
46. Grossfeld GD, Coakley FV. Benign prostatic hyperplasia: clinical overview and value of diagnostic imaging. Radiol Clin North Am. 2000;38:31–47.
47. Park YJ, Bae KH, Jin BS, Jung HJ, Park JS. Is increased prostatic urethral angle related to lower urinary tract symptoms in males with benign prostatic hyperplasia/lower urinary tract symptoms? Korean J Urol. 2012;53:410–3.
48. Wasserman NF, Spilseth B, Golzarian J, Metzger GJ. Use of MRI for lobar classification of benign prostatic hyperplasia: potential phenotypic biomarkers for research on treatment strategies. AJR Am J Roentgenol. 2015;20:564–71.
49. McNeal JE. Normal histology of the prostate. Am J Surg Pathol. 1988;12:619–33.
50. Marks LS, Treiger B, Dorey FJ, et al. Morphology of the prostate: distribution of tissue components in hyperplastic glands. Urology. 1996;44:486–92.

51. Hasegawa Y, Sakamoto N, Gotoh K. Relationship of ultrasonic and histologic findings in benign prostatic hyperplasia. Prostate. 1996;28:111–6.
52. Aprikian S, Luz M, Brimo F, Scarlata E, Hamel L, Cury FL, Tanguay S, Aprikian AG, Kassouf W, Chevalier S. Improving ultrasound-based prostate volume estimation. BMC Urol. 2019;19(1):68. https://doi.org/10.1186/s12894-019-0492-2.
53. Lee JS, Chung BH. Transrectal ultrasound versus magnetic resonance imaging in the estimation of prostate volume as compared with radical prostatectomy specimens. Urol Int. 2007;78(4):323–7.
54. Sung H, Ferlay J, Siegel RL, Laversanne M, Soerjomataram I, Jemal A, Bray F. Global cancer statistics 2020: GLOBOCAN estimates of incidence and mortality worldwide for 36 cancers in 185 countries. CA Cancer J Clin. 2021;71(3):209–49. Epub 2021 Feb 4. https://doi.org/10.3322/caac.21660.
55. Humphrey PA. Histopathology of prostate cancer. Cold Spring Harb Perspect Med. 2017;7(10):a030411. https://doi.org/10.1101/cshperspect.a030411.
56. McNeal JE, Redwine EA, Freiha FS, Stamey TA. Zonal distribution of prostatic adenocarcinoma. Correlation with histologic pattern and direction of spread. Am J Surg Pathol. 1988;12(12):897–906.
57. Whitmore WF Jr. Localised prostatic cancer: management and detection issues. Lancet. 1994;343(8908):1263–7. https://doi.org/10.1016/s0140-6736(94)92156-3.
58. Meikle AW, Smith JA. Epidemiology of prostate cancer. Urol Clin North Am. 1990;17(4):709–18.
59. Frankel S, Smith GD, Donovan J, Neal D. Screening for prostate cancer. Lancet. 2003;361(9363):1122–8. https://doi.org/10.1016/S0140-6736(03)12890-5.
60. Harvey CJ, Pilcher J, Richenberg J, Patel U, Frauscher F. Applications of transrectal ultrasound in prostate cancer. Br J Radiol. 2012;85 Spec No 1(Spec Iss 1):S3–S17. Epub 2012 Jul 27. https://doi.org/10.1259/bjr/56357549.
61. Rosenkrantz AB, Kim S, Lim RP, et-al. Prostate cancer localization using multiparametric MR imaging: comparison of prostate imaging reporting and data system (PI-RADS) and Likert scales. Radiology. 2013;269(2):482–92.
62. Weinreb JC, Barentsz JO, Choyke PL, Cornud F, Haider MA, Macura KJ, Margolis D, Schnall MD, Shtern F, Tempany CM, Thoeny HC, Verma S. PI-RADS prostate imaging—reporting and data system: 2015, version 2. Eur Urol. 2016;69(1):16–40. Epub 2015 Oct 1. https://doi.org/10.1016/j.eururo.2015.08.052.
63. Turkbey B, Rosenkrantz AB, Haider MA, Padhani AR, Villeirs G, Macura KJ, Tempany CM, Choyke PL, Cornud F, Margolis DJ, Thoeny HC, Verma S, Barentsz J, Weinreb JC. Prostate imaging reporting and data system version 2.1: 2019 update of prostate imaging reporting and data system version 2. Eur Urol. 2019;76(3):340–51. Epub 2019 Mar 18. https://doi.org/10.1016/j.eururo.2019.02.033.
64. Marks L, Young S, Natarajan S. MRI-ultrasound fusion for guidance of targeted prostate biopsy. Curr Opin Urol. 2013;23(1):43–50. https://doi.org/10.1097/MOU.0b013e32835ad3ee.
65. Zarzour JG, Galgano S, McConathy J, Thomas JV, Rais-Bahrami S. Lymph node imaging in initial staging of prostate cancer: an overview and update. World J Radiol. 2017;9(10):389–99. Published online 2017 Oct 28. https://doi.org/10.4329/wjr.v9.i10.389.
66. Turpin A, Girard E, Baillet C, Pasquier D, Olivier J, Villers A, Puech P, Penel N. Imaging for metastasis in prostate cancer: a review of the literature. Front Oncol. 2020;10:55. https://doi.org/10.3389/fonc.2020.00055.eCollection.2020.
67. Ramakrishnan K, Salinas RC. Prostatitis: acute and chronic. Prim Care. 2010;37(3):547–63, viii–ix.
68. Kitzing YX, Prando A, Varol C, Karczmar GS, Maclean F, Oto A. Benign conditions that mimic prostate carcinoma: MR imaging features with histopathologic correlation. Radiographics. 2016;36(1):162–75. Epub 2015 Nov 20. https://doi.org/10.1148/rg.2016150030.
69. Mitterberger M, Horninger W, Aigner F, Pinggera GM, Steppan I, Rehder P, Frauscherb F. Ultrasound of the prostate. Cancer Imaging. 2010;10(1):40–8. https://doi.org/10.1102/1470-7330.2010.0004.

The Female Urogenital System in Geriatric Patients

11

Maria Assunta Cova, Lorella Bottaro, Cristina Marrocchio, and Alessandro Marco Bozzato

11.1 Techniques of Imaging and Normal Anatomy

The female genital system includes the ovaries, fallopian tubes, uterus and cervix, and vagina. The imaging appearance of the female genital system changes significantly during a woman's lifespan, reflecting the influence of hormones. After menopause, hormonal levels diminish, leading to a progressive involution of the uterus, cervix, ovaries, and vagina. The observed genital diseases also change in the elderlies, with increased incidence of neoplastic processes and of organ prolapse due to laxity of the pelvic floor musculature and less frequent ovarian functional disorders [1, 2].

Common indications for imaging the pelvis of a post-menopausal patient include post-menopausal bleeding, pelvic pain or pressure, history of ovarian cysts, increasing abdominal girth, or adnexal masses. Knowing the anatomy and normal imaging appearance of the female pelvis in the post-menopausal woman is fundamental since findings that can be normal in the reproductive years can be pathological when

M. A. Cova (✉)
Department of Medicine, Surgery and Health Sciences, University of Trieste, Azienda Sanitaria Universitaria Giuliano Isontina, Trieste, Italy

Department of Radiology, Azienda Sanitaria Universitaria Giuliano Isontina, Cattinara Hospital, Trieste, Italy
e-mail: m.cova@fmc.units.it

L. Bottaro
Department of Radiology, Azienda Sanitaria Universitaria Giuliano Isontina, Cattinara Hospital, Trieste, Italy
e-mail: lorella.bottaro@asugi.sanita.fvg.it

C. Marrocchio · A. M. Bozzato
Department of Medicine, Surgery and Health Sciences, University of Trieste, Azienda Sanitaria Universitaria Giuliano Isontina, Trieste, Italy
e-mail: cristina.marrocchio@studenti.units.it; alessandromarco.bozzato@studenti.units.it

G. Guglielmi, M. Maas (eds.), *Imaging in Geriatrics*, Practical Issues in Geriatrics, https://doi.org/10.1007/978-3-031-14877-4_11

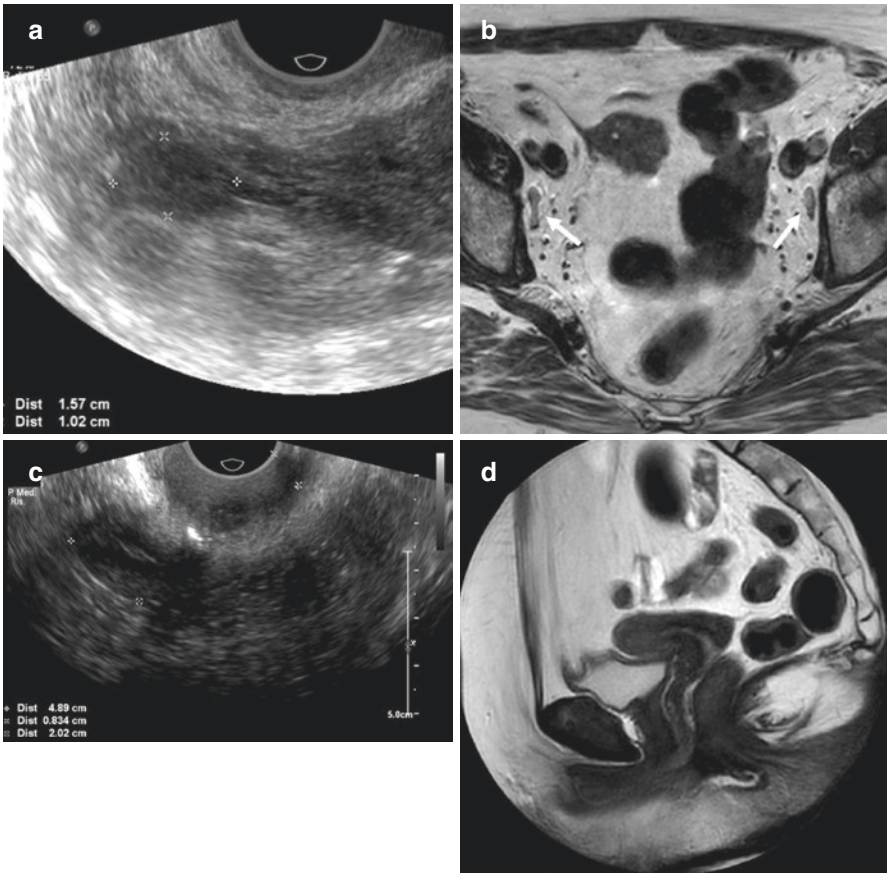

Fig. 11.1 Normal anatomy. (**a**) Normal US anatomy of the ovaries after menopause, appearing small and homogeneously hypoechoic due to the lack of follicles *(between calipers*). (**b**) MR appearance of the involuted ovaries, which have a decreased volume and a homogeneous intermediate signal intensity on T2-weighted images (*arrows)*. (**c**) US appearance of the uterus after menopause, decreased in size *(between calipers*). (**d**) Sagittal T2-weighted imaging showing an involuted uterus, decreased in dimension and with less defined anatomical layers

observed in this age, and, conversely, physiological post-menopausal changes should not be interpreted as pathological findings (Fig. 11.1).

11.1.1 Ultrasound

The first imaging modality is commonly a pelvic ultrasound since it is a widely available, low-cost technique that does not use ionizing radiation. The transabdominal US allows the assessment of the uterus, the higher part of the cervical canal, and the ovaries and should be performed with a full bladder. It provides a wider field of view that can be useful to assess large pelvic masses, or in case the transvaginal

approach does not allow an adequate assessment because of its smaller field of view, e.g., in case of large uterine size or ovaries or other lesions located high in the pelvis. Transvaginal ultrasound (TVUS) is performed after bladder voiding and using high-frequency probes. This approach has higher resolution in assessing the uterus, the cervix, and the adnexa [3]. This is particularly true in older patients, in whom decreased urinary bladder capacity, increased body habitus, and involution of the organs to be studied may decrease the diagnostic accuracy of the transabdominal approach [3].

The ovaries are generally identified by knowing their location with respect to the uterus and recognizing the broad ligaments on whom posterior aspect they are attached; however, they can be difficult to assess after menopause for their reduction in volume and reduced number or absence of follicles [4]. The normal ovarian volume starts decreasing after 30 years, passing from 6.6 cm^3 in women younger than 30 years to 2.6 cm^3 in women 50–59 years old, and can continue decreasing during menopause [5]. The mean post-menopausal volumes range from 1.2 to 5.8 cm^3, and a volume greater than 8 cm^3 is always considered abnormal [3, 6, 7]. The post-menopausal ovaries appear more hypoechoic and homogeneous because of the fewer or absent follicles. Small echogenic foci, 1–3 mm in size, with no associated soft-tissue component, may be recognized, generally at the periphery. These may be related to dystrophic calcifications in atretic follicles, epithelial inclusion cysts, or millimetric cysts causing reverberation artifacts [3]. The fallopian tubes are not normally seen unless abnormal or surrounded by fluid. When recognized, the normal tubes appear as elongated echogenic structures, directed posterolaterally from the uterine horns, with echogenic fingerlike projections (fimbriae), and about 10–12 cm in length and 1–4 mm in diameter [8]. The appearance and the size of the uterus vary depending on the woman's age [3, 9]. The uterine size in young women ranges from 5 to 9 cm, while it decreases after menopause, varying from 3.5 to 7.5 cm in length and from 1.2 to 3.3 cm in the anteroposterior diameter. On TVUS, a hyperechoic thin endometrium and a myometrium with coarse, speckled echotexture can often be seen [3]. Free peritoneal fluid, when small and simple, can be normal in early menopause, but in late menopause its presence is always abnormal and can be related to gynecological and non-gynecological diseases [3].

11.1.2 Magnetic Resonance Imaging

Magnetic resonance imaging (MRI) is a panoramic imaging modality with high contrast resolution. It provides an excellent assessment of the female pelvis as a second-line imaging modality after US or as a primary imaging modality when US is not feasible [3]. MRI can be performed on both 1.5 T and 3 T and pelvic phased array coils are recommended at both 1.5 T and 3.0 T to increase signal-to-noise ratio (SNR), with anterior and superior saturation bands. Antiperistaltic agents can be optionally used to minimize artifact caused by bowel movement or contraction. The exam is usually performed with the patient in the supine position. The acquisition protocol will depend on the specific pathology and organ to study; the standard protocol should

include: T2-weighted images, which provide the most information, fat-saturated T1-weighted sequences, useful to differentiate fat from hemorrhage in lesions with high T1 signal intensity, diffusion-weighted images, and fat-saturated sequences after the intravenous administration of gadolinium-based contrast medium [10].

The normal ovaries in the elderly patient can be difficult to recognize on MRI. After menopause, the relative increase of stromal cells and reduction of follicular cells within the cortex results in a decreased T2-signal intensity and a homogeneous intermediate to low T1-signal intensity. Moreover ovaries show an enhancement less or equal than the uterine myometrium, after contrast administration [3, 11]. Usually, the normal fallopian tubes are not visible on cross-sectional imaging. If ascites are present, they may be outlined as serpiginous structures near the uterus, and their course within the pelvis helps to differentiate them from the broad ligament.

The uterus usually has intermediate or low signal intensity on T1-weighted sequences [12, 13], while, on T2-weighted images, it has three layers with different signal intensities: the inner one, corresponding to the endometrium, is hyperintense, the intermediate one, the junctional zone, is hypointense, whereas the outer one, i.e., the myometrium, has intermediate signal intensity [3, 14]. This uterine zonal anatomy may not be present in older women [3]. The endometrium is characterized by the presence of glands, and its thickness usually ranges from 1 to 2 mm in old patients [3]. The junctional zone can be hardly recognizable after menopause, and its thickness must not be greater than 12 mm [3, 15, 16]. On post-contrast T1-weighted sequences, the endometrium presents later and lower enhancement than myometrium, which is characterized by high signal intensity in the early phases [9]. A study with a small sample size has also reported that zonal fractional anisotropy and ADC values of endometrium and myometrium in women after menopause are lower compared to those in women before menopause [17].

On T2-weighted sequences, the cervix has three layers with different signal intensities: the hyperintense innermost one, the so-called central zone, consists of mucus and palmate folds; the hypointense middle one is the innermost part of the fibromuscular stroma and is in continuity with the uterine junctional zone; the outer one, i.e., the outermost part of the fibromuscular stroma, has intermediate signal intensity [3, 9, 18, 19]. On post-contrast T1-weighted sequences, the middle zone presents earlier enhancement than the other ones [9].

The vagina is a fibromuscular structure about 7 cm to 9 cm long, located posteriorly to the urethra and vesical trigone and anteriorly to the rectum [20]. It can be divided anatomically into a lower third, below the level of the bladder base, a middle third, at the level of the bladder base, and an upper third, at the level of the vaginal fornices [20]. The division is important for tumor staging and because of the different lymphatic drainage, which is into the internal and external iliac lymph nodes for the upper two-thirds, and the superficial inguinal nodes for the lower third [20]. The vaginal mucosa appears as a T1-hypointense and T2-hyperintense thin layer with enhancement after contrast administration. The mucosal layer appears to be thinner in menopausal patients unless they are on hormonal replacement therapy [20–22]. External to the mucosa, the vaginal wall appears hypointense on both T1- and T2-weighted images, corresponding to the submucosal layer, consisting of

collagen and elastic fibers, and the muscular layer, composed of smooth muscle cells organized in an inner circular and outer longitudinal layer. Most externally, there is the adventitia layer, in which a serpiginous T2-high-signal intensity can be recognized, corresponding to the vaginal venous plexus [20, 21].

The vulva includes the mons pubis, labia majora and labia minora, clitoris, and vestibule. It has low-to-intermediate signal intensity on T1-weighted images and slightly high signal intensity on T2-weighted images [20].

11.1.3 Computed Tomography

The role of computed tomography (CT) in studying the female pelvis is limited and is generally reserved to acute settings or for pelvic malignancies systemic staging.

When recognizable, the ovaries appear as small, roughly triangular structures of soft-tissue density, often near the iliac vessels or uterus [3]. The gonadal vessels may be an important anatomical landmark for their identification. On non-contrast CT, the uterus appears as a uniform hypoattenuating formation, with a central zone of lower attenuation representing the endometrial canal [9]. The vaginal mucosa, which in fertile women is hyper-enhancing, becomes of similar density to that of the vaginal wall in the post-menopausal age. The vaginal wall shows poor enhancement after contrast administration [20]. Vaginal pathologies may be difficult to assess at CT because of the similar density with the adjacent soft-tissue structures. The vulva is identified as a triangular soft-tissue density structure within the perineum, posterior to the symphysis pubis and anterior to the anal sphincter [23].

11.2 Ovaries

11.2.1 Endometriosis

Endometriosis results from the presence of aberrant endometrial tissue outside the uterine cavity [24]. It is a common occurrence in the female population, with an estimated 5 to 10% of women in the reproductive age being affected [25].

The pathogenesis of endometriosis is complex, particularly after menopause, when it is unclear if it is a continuation or a reactivation of a previously existing disease or a de novo condition. Estrogen exposure appears to have a key role; indeed, due to the decreased estrogen levels after menopause, endometriotic lesions in most cases regress in this age group [26] (Fig. 11.2).

Although endometriosis in post-menopausal patients is relatively uncommon, it is estimated that about 2 to 5% of post-menopausal women are affected [27], and it should be considered as a possible diagnosis. Hormone replacement therapy, especially estrogen-only treatments without progestin, and Tamoxifen use have been associated with post-menopausal endometriosis [28–30]. Other risk factors include a history of symptoms before menopause suggestive of endometriosis and conditions that may raise the level of serum estrogens, such as obesity [28].

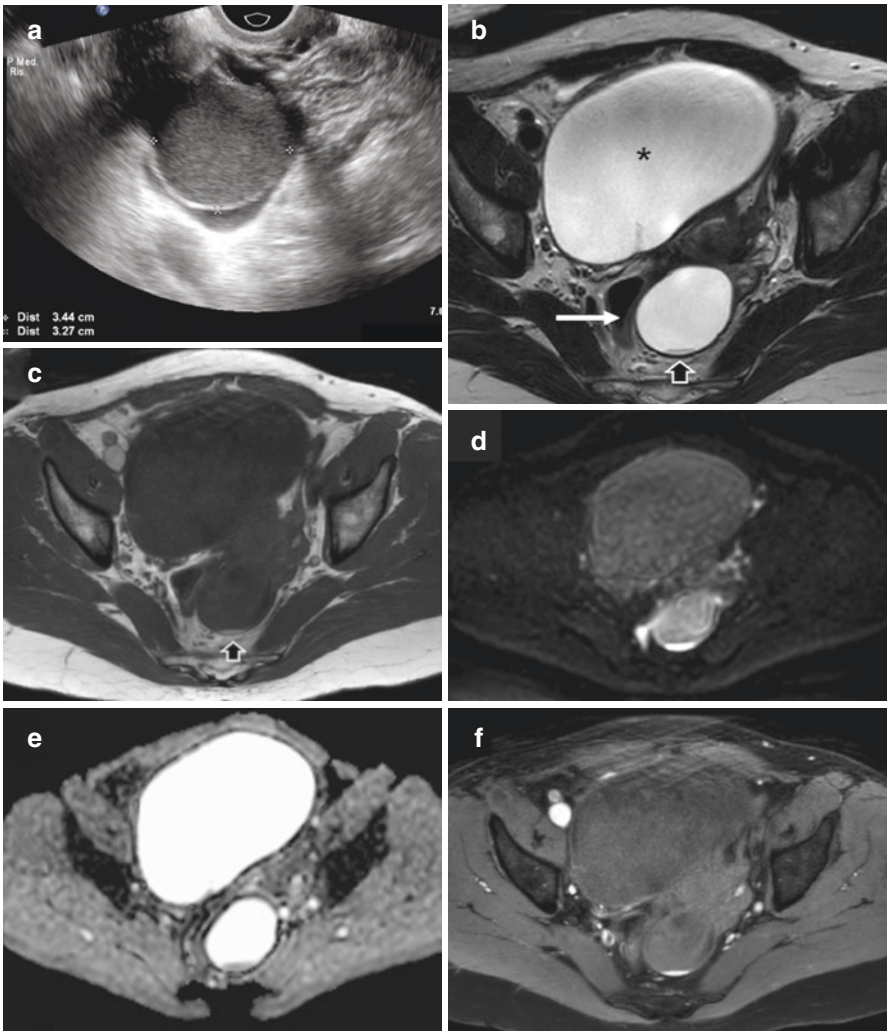

Fig. 11.2 Endometriosis. (**a**) TVUS showing a unilocular lesion in the right ovary, with a homogeneous hypoechoic content and diffuse low-level internal echoes, the so-called ground glass appearance (*between calipers*). (**b**–**f**) MRI of a different patient showing an endometrioid cyst in the left ovary. Axial T2-weighted image (**b**) showing an ovoid mass with regular margins (*white arrow*). The mass is characterized by a mostly cystic T2-hyperintense (**b**) and T1-hypointense (**c**) content, and a hematic component in the dependent regions, separated by a fluid-fluid level. The hematic component is in the subacute phase, showing T1-hyperintensity and T2-hypointensity (*black arrows)*, with restricted diffusion on DWI (**d**), as confirmed on the ADC map (**e**). In the presence of a T1-hyperintense cystic content, it is always important to obtain fat-suppressed T1-weighted images (**f**) to exclude the presence of fat. Note the large simple cystic mass in the right ovary (*asterisk,* **b**)

The identification of endometriosis in older patients may be an incidental finding during imaging or surgery performed for other reasons. If symptoms occur, they are non-specific and include pelvic pain, dyspareunia, dyschezia, and abnormal vaginal bleeding. Symptoms can also be related to the specific organ involved, which may be outside the pelvis [30].

Endometriosis is associated with an increased risk of ovarian cancer, particularly the clear cell, endometrioid, and low-grade serous types [31–33]. The risk of malignant degeneration of an endometrioma is estimated to be about 1% [34, 35]. In the post-menopausal patient, the risk of malignancy is further increased because of the older age and the long-standing history of ovarian endometriosis [35]. Therefore, it is important to identify endometriosis in post-menopausal patients and carefully assess the lesions to identify any suspicious features.

11.2.1.1 Imaging Findings

Endometriosis is characterized by endometrial implants, endometrial cysts, called endometriomas, and adhesions [36]. The endometrial implants can be superficial peritoneal deposits or deep infiltrating implants or nodules at least 5 mm in depth [37]; extra-pelvic implants can also occur. Endometriomas, also called "chocolate cysts" for their appearance, result from repeated cyclic hemorrhages within a deep implant. The small endometrial implants, when active, may cause an inflammatory response that ultimately leads to fibrosis and adhesions.

The most common localization of the endometrial foci are the ovaries, followed by the uterine ligaments, posterior cul-de-sac, pelvic peritoneum, fallopian tubes, sigmoid and rectal serosa, anterior cul-de-sac, and bladder [10]. In general, endometriotic lesions after menopause seem to be less active and less extensive than in pre-menopausal women [38].

Laparoscopy is the gold standard for the diagnosis of endometriosis [39]. Imaging is indicated when there is a clinical suspicion of endometriosis but equivocal clinical history and examination. MRI is indicated as a second-line imaging modality after US, if the lesions remain undetermined at US, before surgery for optimal preoperative staging, or if there is a clinical suspicion of malignant degeneration [10, 40, 41].

US Findings

US is the most common modality used in the suspect of endometriosis. Particular attention should be paid to the evaluation of the ovaries and the cul-de-sac, common sites involved [39].

The US appearance of endometrial cysts is highly variable. The most common one is a unilocular cystic lesion with a homogeneous hypoechoic content, with diffuse low-level internal echoes, sometimes referred to as "ground glass" [39, 42]. Rarely, they may be completely anechoic, similar to a functional cyst [39].

Endometriomas may also appear as multilocular complex lesions, with thick walls and septa, wall nodularity, and echogenic foci within the cyst wall [43, 44]. These echogenic foci are thought to be related to cholesterol deposits in the endometrial wall and should be differentiated from wall nodules, which usually appear

larger and less echogenic [39]. Also, the multilocularity may in some cases be due to multiple adjacent separate cysts [39]. Malignancy should always be suspected in the presence of a solid mural nodule; an increasing size of the cyst is another less reliable signs of degeneration [45].

The heterogeneous appearance of the endometrioid cysts results in a broad range of differential diagnoses, including functional cysts, tubo-ovarian abscesses, dermoid cysts, and benign or malignant lesions [41]. The stability or minimal growth at follow-up represents an important distinguishing feature from functional cysts, in particular hemorrhagic ones, which may be very similar in appearance but generally have a more acute onset and resolve in 4–6 weeks [39].

MRI Findings

Endometrial cysts have two typical patterns of presentation. In the early subacute bleeding phase, they will be T1-hyperintense and T2-hypointense. In the later subacute phase, they will be hyperintense on both T1 and T2 weighted images [39, 46, 47]. The shading sign, i.e., loss of signal within the lesion that can be seen on T2-weighted images, is an important sign of endometriomas. This is due to the presence of hematic products in different stages of degeneration because of repeated bleedings [39]. After contrast administration, subtraction images help detect any enhancing tissue if there is a concern of malignant degeneration [37]. The differential diagnosis of endometriomas includes dermoid cysts, hemorrhagic cysts, mucinous cystic neoplasms, and an ovarian carcinoma with internal hemorrhage. The absence of signal loss on fat-suppressed T1-weighted images confirms the hematic content and rules out fat-containing lesions such as dermoid cysts [39, 48]. T1-weighted images help in the differential with mucinous cystic neoplasms, which will show a high signal intensity but less than fat or blood. Differentiating an endometrioma from a hemorrhagic corpus luteum can be more difficult; hemorrhagic cysts are usually unilocular (while endometriomas are often multilocular and bilateral), do not show the T2-shading sign, and mostly disappear at follow-up. An ovarian carcinoma with internal hemorrhage will have features suggestive of malignancies such as solid components, larger dimensions, and septations [39].

Endometrial implants will have variable signal intensities. They may have low T1 signal intensity and high T2 signal intensity, similar to the normal endometrium, or they can be hyperintense or hypointense on both T1- and T2-weighted images [39].

Adherences will appear as spiculated hypointense bands between organs, with or without anatomical distortion, that in advanced disease may result in the so-called kissing ovaries configuration, i.e., the ovaries displaced posteriorly and medially toward one another [49].

Imaging features of endometriosis-associated malignancy are similar to the other malignancies not related to endometriosis. On MRI, it will often have an intermediate T2 signal intensity, with avid enhancement and restricted diffusion. Enhancing mural nodules and septations will be best appreciated on post-contrast T1-weighted images with fat suppression and subtraction [30]. Restricted diffusion may also occur in benign endometriomas due to the presence of blood products [50]. Another non-specific sign is the loss of T2 shading [51]. Extra-ovarian malignancy

associated with endometriosis may have an infiltrative appearance, and benign variants, e.g., polypoid endometriosis, may mimic features of malignancy [30].

11.2.2 Ovarian Masses

11.2.2.1 Imaging Approach to Adnexal Masses

The first imaging modality in women with a suspected ovarian mass is usually TVUS [52]. US can provide important information on adnexal masses, including their dimension, walls, margins, content (liquid or solid), presence of any septation, and any associated finding such as the presence of free fluid in the pelvis. The color Doppler can also provide important information on their vascularization.

Numerous scoring systems and algorithms have been proposed to develop more objective US-based approaches to differentiate benign from malignant adnexal lesions, among them, more recently, an Ovarian-Adnexal Reporting and Data System for Ultrasound (O-RADS US) and for MRI (O-RADS MRI) [53–60].

The International Ovarian Tumor Analysis (IOTA) group published a consensus paper to standardize the terms and definitions used when reporting an ovarian mass at US [58]. According to their paper, when approaching an ovarian mass, its dimension, its morphologic features (presence of septa, solid components, solid papillary projections, a regular or irregular internal wall), and its content (anechoic, low-level echogenic, ground glass, hemorrhagic, or mixed echogenic) should be noted. Based on these features, adnexal lesions can be classified qualitatively into one of the six categories: unilocular cyst (unilocular cyst without septa and without solid parts or papillary structures), multilocular cyst (at least one septum but no measurable solid components or papillary structures), unilocular-solid cyst or multilocular-solid cyst (unilocular or multilocular cyst with measurable solid component or at least one papillary structure, respectively), solid tumor (solid component constituting 80% or more of the tumor when assessed on two-dimensional section), or not classifiable because of poor visualization. They also described the scoring for a subjective semiquantitative assessment of flow on color Doppler imaging, ranging from a score of 1, in which the lesion has no blood flow, to a score of 4, in which the lesion is highly vascular with marked blood flow. The IOTA "Simple Rules" can be used to classify an adnexal mass as benign, malignant, or indeterminate and are applicable to about 80% of ovarian masses [52, 61]. The IOTA "Easy Descriptors," four for features typical of common benign lesions and two suggestive of malignancy, can also help recognize those lesions with typical characteristics of benignity or malignancy; these descriptors are applicable to about 43% of adnexal masses [57].

Even using the IOTA Simple Rules, 22% of lesions remain indeterminate on US [62]. As most of these turn out to be benign lesions, such as fibromas, MRI is indicated in sonographically indeterminate masses, as their characterization has an important impact on the therapeutic management of the patient [63]. In particular, MRI is useful to further characterize a solid adnexal mass, or a complex adnexal mass with equivocal features of malignancy, or to determine the organ of origin in case of large pelvic masses or a mass adjacent to the uterus but whose origin cannot

be clearly assessed [63]. Features that indicate a uterine origin are the presence of a pedicle between the lesion and the uterus; the "bridging vessel sign" on contrast-enhanced T1-weighted images (i.e., the presence of vascular structures going from the uterus to the lesion as it receives its blood supply from uterine vessels); and, in case of uterine leiomyomas, the normal uterine tissue may be draped around the lesion like a "claw" [46, 63]. Suggestive of an ovarian origin is the "ovarian beak sign," i.e., the presence of sharp angles between the lesion and the ovary [64]; also, an ovarian fibroma will be separate from the uterus [63]. According to current guidelines, the MRI protocol should include a sagittal T2-weighted sequence of the pelvis, a T1- and T2-weighted sequences in the same orthogonal plane (axial or coronal) and with the same slice thickness covering the mass, a DWI sequence, and dynamic contrast-enhanced T1-weighted sequences [63]. If the lesion shows high signal intensity on T1-weighted images, an axial fast spin-echo (FSE) T1-weighted sequence with fat suppression needs to be acquired. If doubt exists on whether the lesion belongs to the uterus or the ovary, 3D T1-weighted or FSE T1-weighted sequences with fat suppression or FSE T2-weighted sequences may be acquired on the axial plane of the ovary, which corresponds to the parallel plane of the endometrial cavity [10].

11.2.2.2 Ovarian Tumors

Ovarian cancer accounts for only 3% of female cancer, but it is the fifth most common cause of cancer-related mortality in women. The vast majority of ovarian cancers are detected at an advanced stage, with a poor prognosis. The strongest risk factors for ovarian cancer are a familiar history of ovarian cancer and increasing age, with an incidence steeply increasing after menopause [65]. In the early stages, the tumor is often asymptomatic, while symptoms, such as bloating, pelvic or abdominal pain, urinary symptoms, and palpation of an adnexal mass at physical examination, are most frequent in an advanced disease [66]. US and MRI are used to identify and further characterize adnexal masses, while contrast-enhanced CT, MRI, and PET/CT are used for staging and follow-up [10]. MRI, in particular when using DWI sequences, has a higher per-lesion sensitivity, especially for implants smaller than 1 cm, smaller peritoneal implants, and involvement of adjacent organs [10].

Epithelial Tumors

Epithelial tumors constitute 60% of all ovarian tumors and 85% of malignant ones [67]. Their incidence increases with age, peaking in the sixth to seventh decade [68]. They include serous, mucinous, seromucinous, endometrioid, clear cell, Brenner tumors, and undifferentiated carcinoma [69].

Serous and Mucinous Tumors

Serous and mucinous tumors may be benign or malignant. Features suspicious for malignancy include presence of solid tissue and papillary vegetations within mostly multilocular cystic lesions, dimensions superior to 4 cm, thick (>3 mm) and irregular walls and thick septa, and large soft-tissue parts with necrotic foci [67, 70]

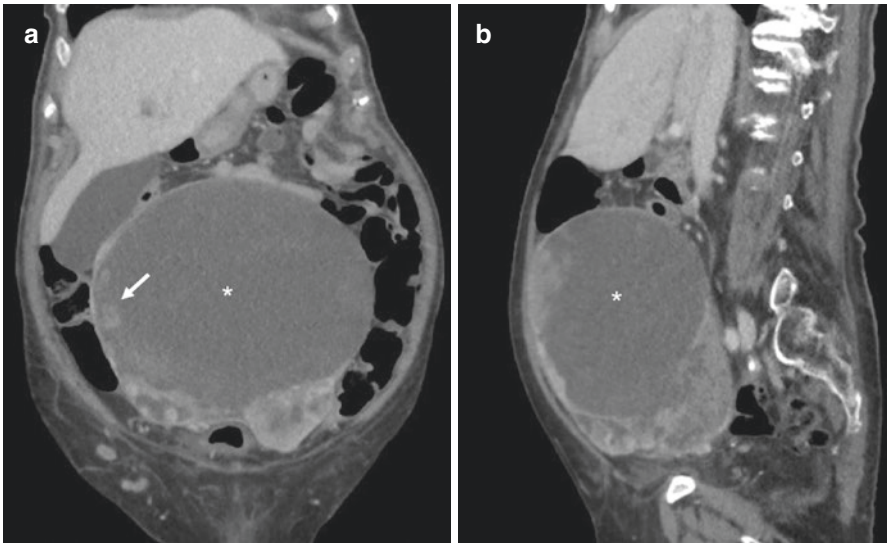

Fig. 11.3 Ovarian cystadenoma with features of malignancy. Coronal (**a**) and sagittal (**b**) CT scan reconstructions showing a large abdominal multilocular cystic lesion (*) with the presence of thick, irregular walls and septa, papillary projections within the lumen (*arrow*) and enhancing soft-tissue components with necrotic foci

(Fig. 11.3). The solid tissue will have intermediate signal intensity on T1- and intermediate on T2-weighted images [70, 71]. The signal intensity of the papillary vegetations reflects their tissue architecture, composed of a stromal core lined by neoplastic cells. They will appear as structures of intermediate signal intensity on T1-weighted images and with a hypointense core lined by a hyperintense neoplastic epithelium on T2-weighted images [67, 72]. Malignant lesions tend to have a faster and more intense enhancement than benign lesions after contrast administration [73]. Malignancy is also associated with ascites, lymphadenopathies, invasion of pelvic organs, and peritoneal and omental implants, whose identification can be helped by the DWI sequence, especially if small in dimensions [70, 71].

Serous cystadenomas appear as mostly unilocular cystic mass, with a thin wall or septum and no vegetations. They have a homogeneous low signal intensity on T1-weighted images and high signal intensity on T2-weighted images, with no enhancement or enhancement of the thin walls alone after contrast administration [67, 74, 75]. Serous cystadenocarcinoma can have discrete dimensions, are bilateral in two-thirds of cases, and have malignant features at imaging [68].

Mucinous cystadenomas are multilocular cystic masses with thin walls or septa and no vegetations, usually larger than serous cystadenomas [67, 71]. The signal intensity will depend on mucin concentration, with T1 hypointensity and T2 hyperintensity with higher water content, and T1 hyperintensity and T2 hypointensity with thicker mucin [70]. Sometimes, multiple locules with variable signal intensities can be observed, in an appearance referred to as “stained-glass” [76] (Figs. 11.4 and 11.5).

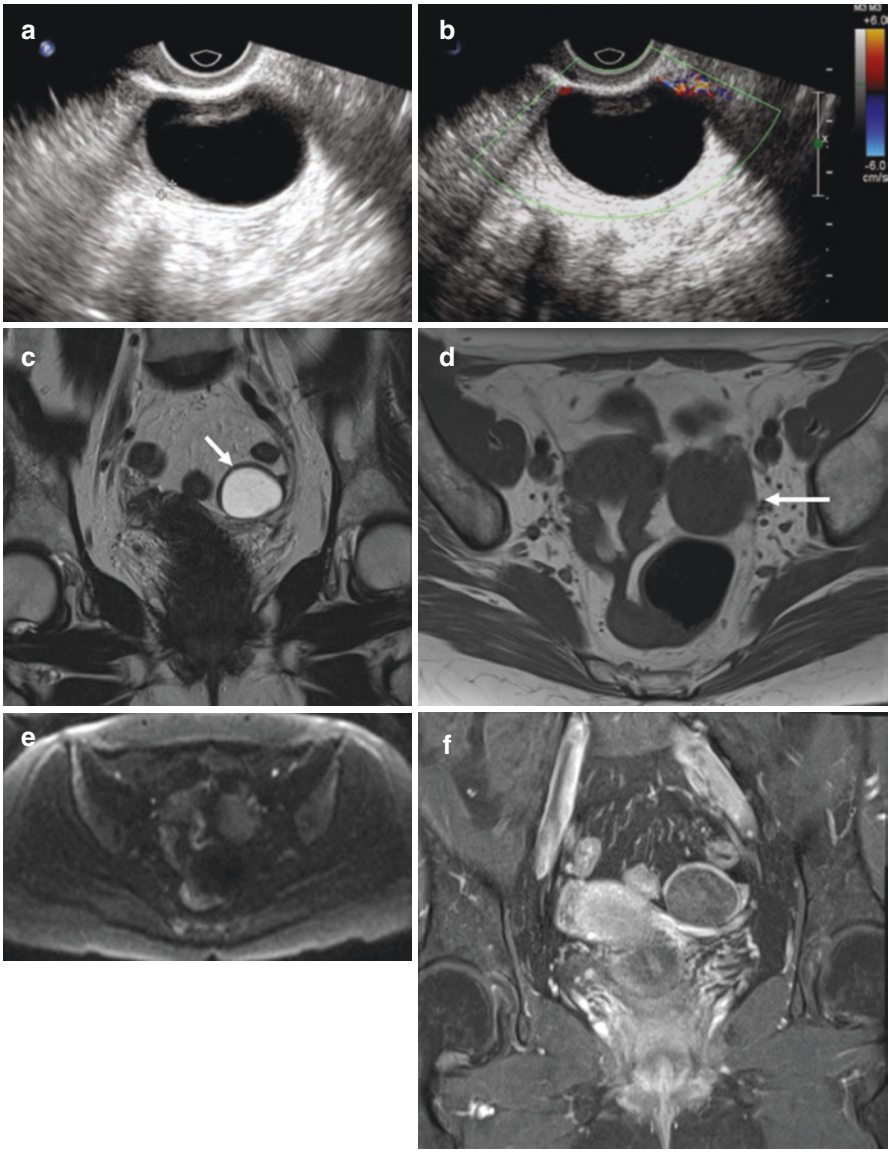

Fig. 11.4 Ovarian cystadenoma. (**a**, **b**) TVUS showing an ovoid mass with regular margins and minimally thickened wall (3 mm) (*between calipers,* **a**), with a finely corpuscular content. At the color Doppler analysis, neither the mass nor its thickened wall exhibit any significant vascularization (**b**). (**c**–**f**) MRI exam of the same patient showing a mass in the left ovary with minimally thickened wall, well appreciated on the coronal T2-weighted sequence (*arrow,* **c**), and a content with high signal intensity on T2-weighted images and slightly low signal intensity on T1-weighted images (*arrow,* **d**). There is no restricted diffusion (**e**) and only the wall shows enhancement (**f**). The mass has no aggressive features

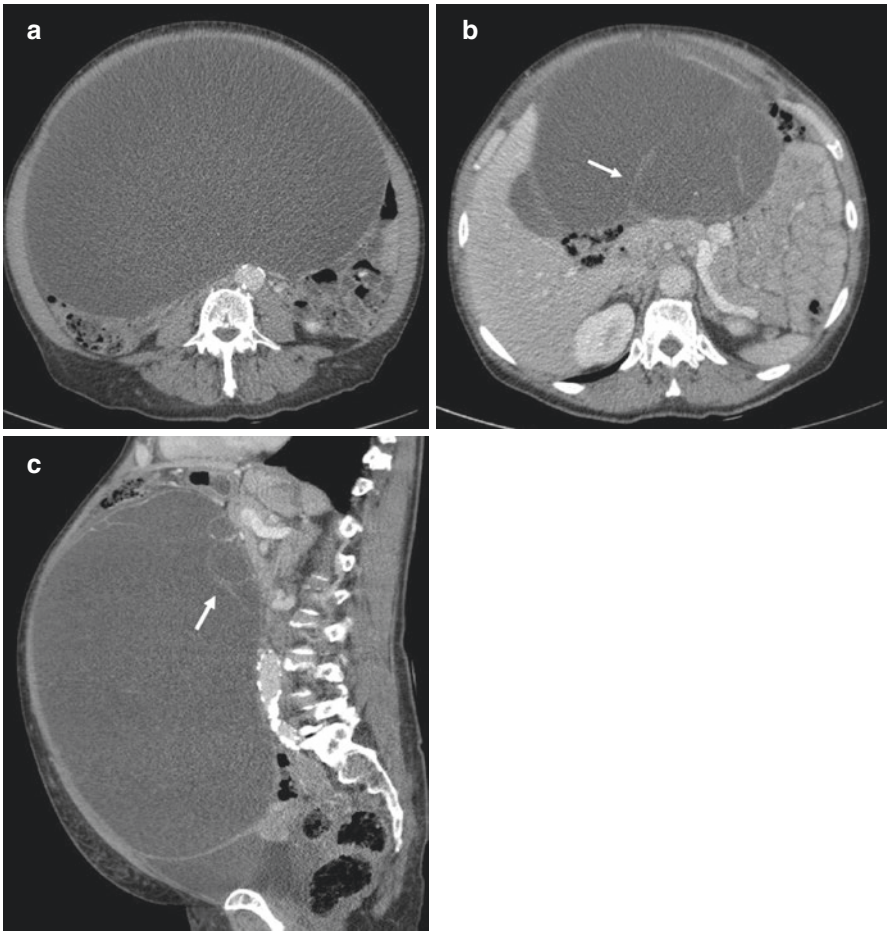

Fig. 11.5 Mucinous cystadenoma. Axial contrast-enhanced CT scan (**a**, **b**) and sagittal reconstructions (**c**) showing a cystic mass of significant dimensions within the abdomen, with thin, minimally enhancing wall and septa (*arrows),* and no vegetations. The mass dislocates the abdominal organs posteriorly

Mucinous cystadenocarcinoma is a large multilocular cystic mass and can be associated with pseudomyxoma peritonei, due to rupture of the cyst or peritoneal metaplasia [68, 74, 77].

Cystadenofibromas are uncommon epithelial neoplasms that are partly fibrotic. The fibrotic component will have a low signal intensity on T2-weighted images and the differential diagnosis with malignant solid neoplasms may be difficult [68, 78].

Non-Serous Non-Mucinous Epithelial Ovarian Tumors

Endometrioid carcinoma (Fig. 11.6) accounts for 10–15% of ovarian tumors. It may occur in the setting of endometriosis, and in up to 33% of cases endometrial

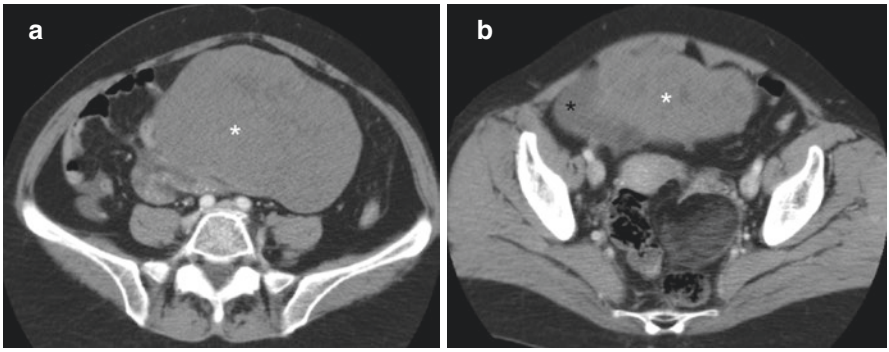

Fig. 11.6 Endometrioid carcinoma. (**a**, **b**) Axial contrast-enhanced CT scan at different levels of a patient admitted to the emergency room for left flank pain. In the abdomen, there is a hypodense voluminous solid mass (*white asterisks*, **a**, **b**), slightly heterogeneous in density and with no enhancement after contrast administration (unenhanced CT not shown). A small amount of fluid in its most caudal region is also present (*black asterisk*, **b**). The patient underwent surgery, and this was confirmed to be an endometrioid carcinoma

hyperplasia or synchronous endometrial carcinoma are also present [24, 63, 79]. The tumor appears as a complex cyst with solid components, with the solid component having an intermediate or heterogeneous signal intensity and enhancement after contrast administration [67, 80]. The involvement is bilateral in about 40% of cases, and this frequently indicates the spread of the disease beyond the genital tract [24].

Clear cell carcinomas (Fig. 11.7) represent about 5% of ovarian tumors and may be solid or cystic [67, 68]. The usual MR appearance is a unilocular cyst with solid protrusions into the lumen, with very variable T1 signal intensity [67].

Brenner tumors are rarely malignant and constitute 2–3% of ovarian tumors. They are associated with other ovarian tumors in 30% of cases, and the large majority are unilateral [67]. There is a cystic and a solid variant [24]. They appear as multilocular cystic masses with a solid component that is T2-hypointense and has at least a moderate enhancement after contrast administration. Amorphous calcifications may be present [46, 67].

Germ Cell Tumors

Germ cell tumors comprise about 20% of ovarian tumors and 2–5% of all ovarian malignancies [81, 82]. They include mature teratomas (also called dermoid cyst), immature teratomas, dysgerminomas, endodermal sinus (yolk sac) tumors, embryonal carcinoma, choriocarcinoma, and mixed germ cell tumors [69]. Ovarian germ cell tumors arise primarily in young patients, between 10 and 30 years of age, representing 70% of ovarian neoplasms in this age group [83]; after menopause, malignant ovarian germ cell tumors are very rare, while mature teratomas are uncommonly seen [82, 84].

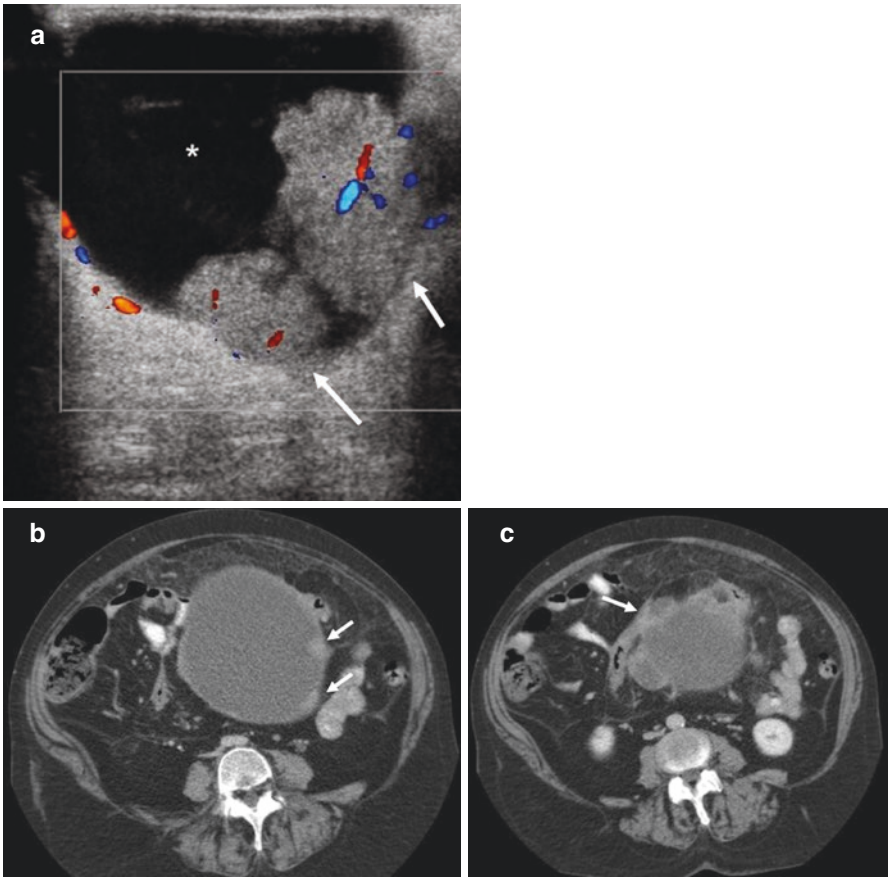

Fig. 11.7 Clear cell ovarian carcinoma. (**a**) Color Doppler US showing a unilocular cyst (*) with solid protrusions (*arrows*) into the lumen, demonstrating high signal. (**b**, **c**) Axial contrast-enhanced CT showing enhancing nodules (*arrows,* **b**) and the infiltration of the sigma (*arrow,* **c**)

- Benign cystic mature teratomas are the most common germ cell tumor of the ovary, composed of mature tissue of ectodermal, mesodermal, and endodermal origin [48]. Therefore, hairs, skin glands, bone, cartilage, fat, and muscles may be present within the mass. Monodermal tumors of the ovary, such as struma ovarii or carcinoid tumors, also exist [48]. The US appearance is usually non-specific, appearing as a predominantly cystic, solid, or complex mass with reflections and shadowing. Findings vary from the classic presence of a so-called Rokitansky nodule (cystic lesion with a densely echogenic tubercle projecting into the cyst lumen), to an atypical diffusely or partially echogenic mass with sound attenuation, due to the presence of sebaceous material and hair within the cavity, to multiple thin echogenic bands due to hairs. Fluid-fluid levels can result from the separation of the sebum, which appears more hypoechoic than the fluid layer. Shadowing may be present due to calcific or tooth components [48, 85]. At MRI,

the tumor appears heterogeneous, with the sebaceous component being T1-hyperintense, with a signal intensity similar to retroperitoneal fat and a T2 signal intensity similar to fat in most cases The lesion will show signal loss on fat-saturated T1-weighted images or in the out-of-phase chemical shift sequence [75], which allows the differential diagnosis with other lesions having high T1 and T2 signal intensities (hemorrhagic cysts or endometriomas) [48, 65]. Calcifications will show low signal intensity on T1- and T2-weighted images (Fig. 11.8). At CT, fat can be easily recognized; wall calcifications or dermoid plug may also be present [75] (Fig. 11.9). Complications of ovarian teratomas may be torsion, rupture, or degeneration [86]. Mature teratomas can undergo malignant degeneration in 1–2% of cases [86], although this rate increases in post-menopausal women, with a study reviewing 20 cases of mature cystic teratomas in post-menopausal women reporting an incidence of malignant change of 15% [87]. Contrast enhancement of a Rokitansky nodule raises the possibility of malign transformation; however, this finding does not always indicate malignancy [88].

Sex-Cord Stromal Tumors

Sex-cord stromal tumors can affect patients from a broad range of ages [89]. They account for about 8% of ovarian tumors, are mostly confined to the ovary at the time of diagnosis, and may have hormonal activity [89]. They include pure stromal tumors (e.g., thecomas, fibromas, fibrothecomas, and sclerosing stromal tumors), pure sex-cord tumors (e.g., granulosa cell tumor), and mixed sex cord-stromal tumors (e.g., Sertoli–Leydig cell tumor) [69]. Sclerosing stromal tumors and Sertoli–Leydig cell tumors are rare and occur predominantly in patients of a younger age [67].

- Granulosa cell tumors are the most common ovarian tumors to produce estrogens and the most common malignant sex cord-stromal tumor [90]. The adult form represents 95% of them and occurs mostly in perimenopausal and post-menopausal patients [89], with an incidence peaking at 50–55 years [91]. The imaging characteristics are non-specific, as they may appear as a solid mass, a tumor with hemorrhagic or fibrous components, or may be multilocular cystic or entirely cystic tumors [67]. The multilocular cystic pattern with solid components is the most common one, often resulting in a typical sponge-like appearance on T2-weighted sequences [89]. For their hormonal production, endometrial hyperplasia, endometrial polyps, or endometrial carcinoma can co-occur in 3–25% of cases [90]. Peritoneal dissemination is not frequent [67].
- Fibromas, fibrothecomas, and thecomas are a spectrum of benign tumors ranging from purely fibrotic to lipid-rich tumors generally occurring in peri- and post-menopausal patients [89, 92]. Due to their fibrotic component, fibromas have a

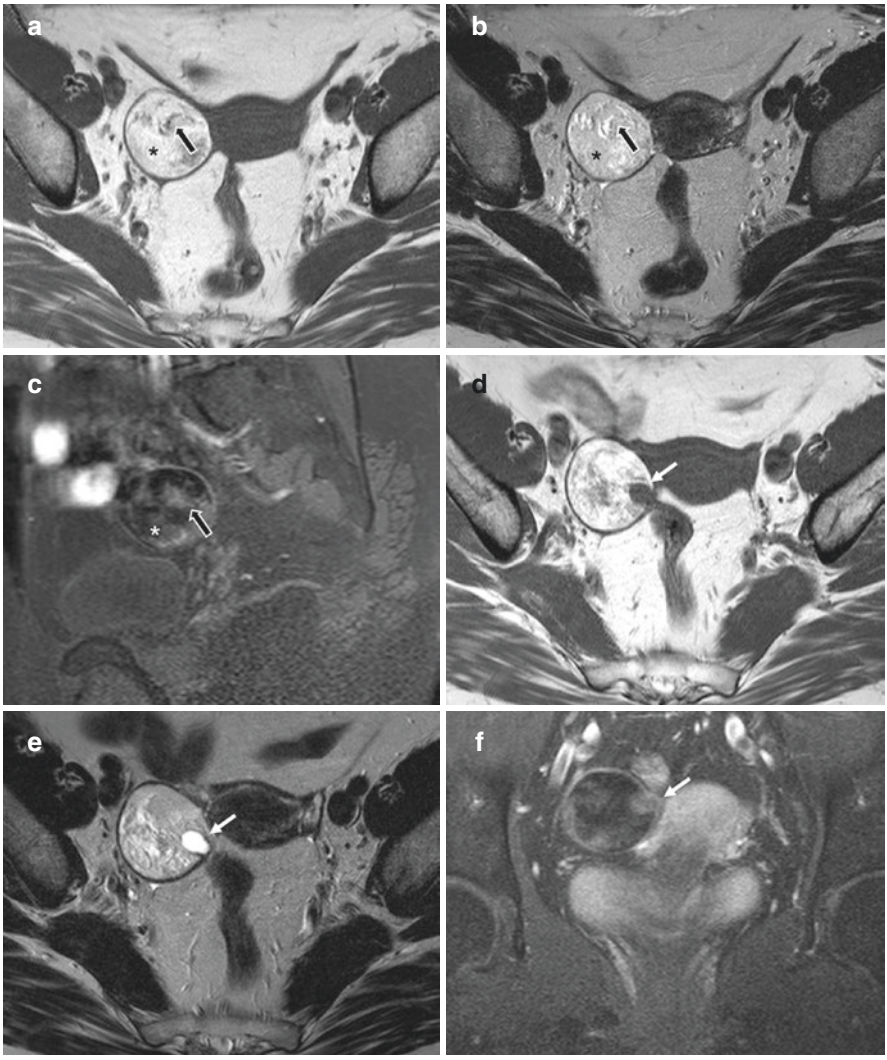

Fig. 11.8 Teratoma. On T1-weighted (**a**) and T2-weighted images (**b**)**,** the tumor (*) appears heterogeneously hyperintense, with a signal intensity similar to retroperitoneal fat, and it contains T2-hyperintense and T1-hypointense septa (*black arrows*). The lesion shows loss of signal on fat-saturated T1-weighted imaging (**c**). On the T1-weighted (**d**) and T2-weighted images (**e**) on a different plane, the so-called Rokitansky nodule (*white arrows*) can be appreciated. It appears T1-hypointense and T2-hyperintense, with mild enhancement on fat-saturated contrast-enhanced T1-weighted images (**f**, *coronal plane*)

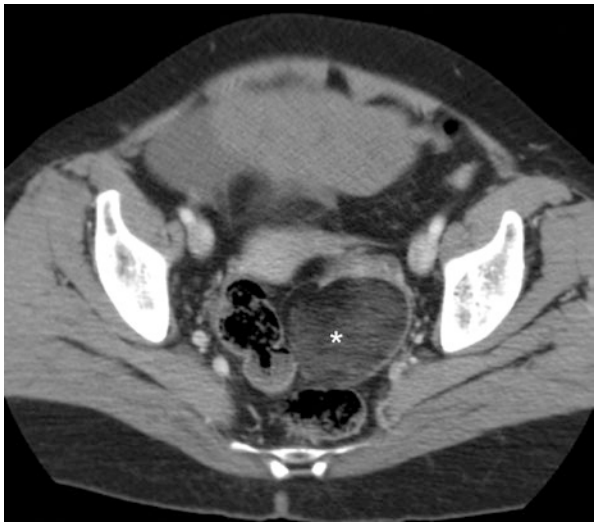

Fig. 11.9 Teratoma. Axial CT scan showing a solid, heterogeneous, ovoid mass in the left adnexa, with adipose density (*asterisk*)

homogenous solid appearance with delayed enhancement on CT [67] and have low T1 and very low T2 signal intensity on MRI, with high-intensity areas due to edema and cystic degeneration that may be present [67, 75, 93]. They have low signal intensity on DWI sequence and only minimal enhancement after contrast administration [65, 71, 75] (Fig. 11.10). At US, they appear as hypoechoic masses with sound attenuation; however, findings are variable and sometimes they can be seen as hyperechoic masses with increased through transmission [70]. Uncommonly, they are associated with Meigs' syndrome (ovarian tumor, ascites, pleural effusion) [92]. The imaging appearance of thecomas is not specific and, especially if the fibrotic component is not prominent, they can be similar to malignant tumors [71, 89]. The differential diagnosis of these tumors includes other fibrous-rich ovarian lesions (Brenner tumors, cystadenofibroma) and pedunculated uterine leiomyomas [46].

11.2.3 Adnexal Torsion

Adnexal torsion is the twisting of an ovary, and often the fallopian tube, on their ligamentous support, that may result in compromised blood flow [94]. It constitutes a gynecological emergency requiring surgery, presenting with acute onset, intense, and progressive pain, which in post-menopausal women may be continuous and dull rather than acute and sharp [95, 96]. Adnexal torsion frequently is a complication of ovarian cysts and tumors [97], and most cases occur in pre-menopausal patients because of the increased frequency of benign cysts and teratomas. It may occur after menopause, although the incidence is low [95]. While the rate of malignancy in younger patients is believed to be low, in post-menopausal patients, torsion is more frequently associated with a malignant mass, but this occurs in a relative minority of cases [95, 98].

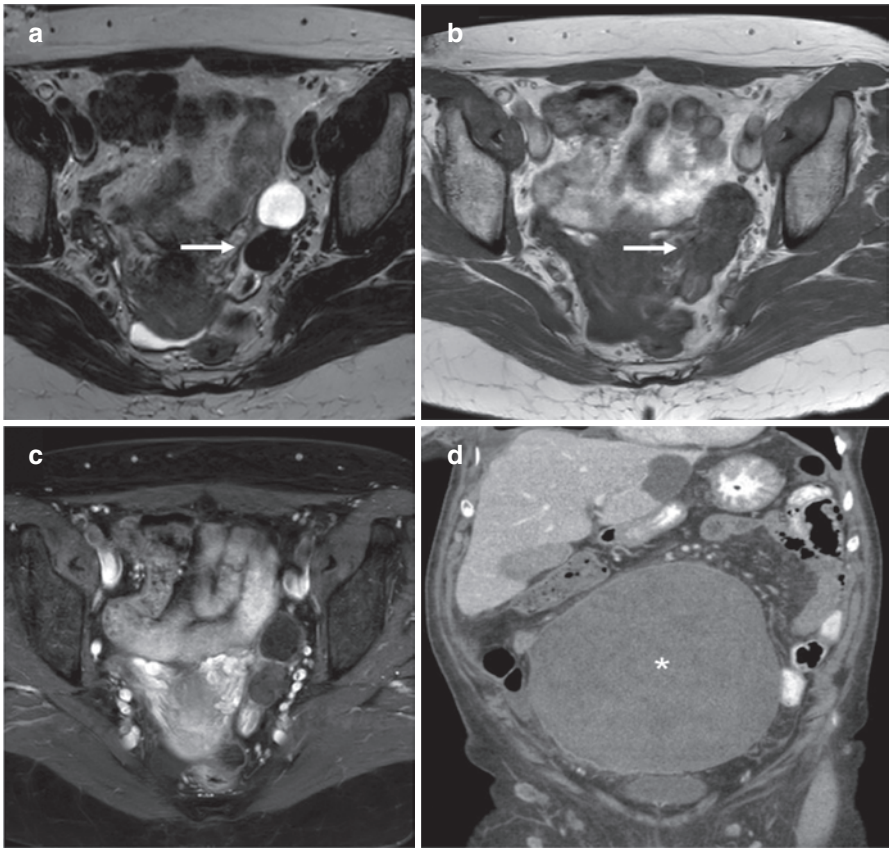

Fig. 11.10 Ovarian fibroma. *(***a**–**c***)* MRI showing a roundish mass in the left ovary, with very low signal intensity on T2-weighted image (*arrow,* **a**) and low signal intensity on T1-weighted image (*arrow,* **b**), with only mild enhancement after contrast administration (**c**), compatible with an ovarian fibroma. (**d**) CT scan of a different patient showing a large solid abdominal mass with mild enhancement and heterogeneous density (*), confirmed to be a fibroma after surgical excision

Imaging findings of ovarian torsion common to all modalities are an enlarged ovary displaced supero-medially, a uterus displaced toward the affected side, a thickened and twisted pedicle, a thickened tube, inflammatory changes surrounding the involved adnexa with free pelvic fluid, and eventually a benign lead mass [98]. US is commonly the first imaging study performed and shows an enlarged, edematous ovary in which the follicles are displaced peripherally [94]. The twisted pedicle appears as a thickened tubular structure near the uterus and may show the "whirlpool sign," that is, the twisting of the hypoechoic vessels, with or without a color Doppler signal [98]. The findings of color Doppler analysis are variable: although abnormal or reduced blood flow is a sensitive sign of torsion [99], normal vascularity can be maintained until relatively late and should not exclude the diagnosis [98]. On CT and MRI, it appears as a mass located superiorly to the uterus and near the midline [98]. Edema is seen as a hyperintensity of the central medulla on T2-weighted images [98]. Features suggesting nonviability include hemorrhagic foci, which will

appear hyperdense on CT and hyperintense on T1-weighted images and absent enhancement [98]. Contrast-enhanced dynamic subtraction MRI can confirm the absence of blood flow [100]. When the lead mass is a cyst, a smooth concentric cyst wall thickening suggests simple edema, while an irregular or eccentric thickening may indicate hemorrhagic infarction [97, 101].

11.2.4 Inflammatory Conditions of the Ovary

11.2.4.1 Tubo-Ovarian Abscess

Pelvic inflammatory disease is an uncommon condition in post-menopausal women, and when it occurs it is usually polymicrobial and associated with the formation of a tubo-ovarian abscess (TOA) [102]. US is the primary imaging modality for the assessment of TOA, showing a cystic, solid, or complex mass in the adnexal or cul-de-sac region, with adjacent fluid. Indistinct uterine margins and loss of midline endometrial echoes may also be present [103]. CT can be useful to assess the extent of the disease, presence of complications, and in case patients do not respond to antibiotic therapy. Findings include a thick-walled hypodense adnexal mass with internal septations and thickening of the uterosacral ligaments [104]. The pus-dilated tubes can be recognized as fluid-filled serpiginous structures with thick enhancing walls. Internal gas bubbles are a specific sign of TOA but are rarely observed. The rectosigmoid colon and ureter can be involved by the inflammatory process [105]. On MRI, it appears as a mass heterogeneously hyperintense on T2-weighted images and hypointense on T1-weighted images if the content is fluid, but the imaging appearance depends on the hemorrhagic content and protein concentration. Fat-suppressed T2-weighted images are used to assess parametrial inflammation, which appears as a hyperintense edematous area [105–107]. Contrast-enhanced fat-suppressed T1-weighted sequences are used to assess the extension of inflammation and may show peritoneal enhancement [106]. Fibrosis and adhesions may be present, appearing as T2-hypointense meshlike strands in the adjacent fat with contrast enhancement [107]. There is considerable overlap in the imaging appearance of TOA with that of other complex cystic masses, including neoplasms and abscesses of non-gynecological origin [105].

11.3 Uterus and Cervix

11.3.1 Nabothian Cysts

A nabothian cyst is a mucus-filled cyst located usually on the surface of the cervix [3]. On TVUS, it usually appears as an anechoic well-defined cystic lesion, with no signal on color Doppler imaging [108], whereas, on non-contrast CT, it may appear as a low attenuation formation. It is usually hyperintense on T2-weighted images, while on T1-weighted images it appears as an intermediate or hyperintense lesion because of its proteinaceous component and does not show enhancement after contrast administration [109, 110] (Fig. 11.11).

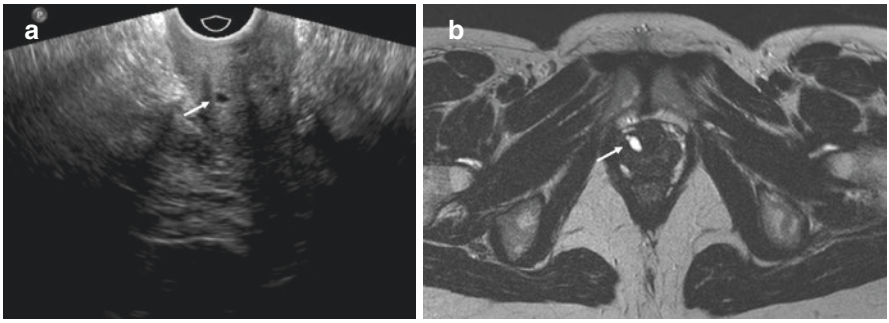

Fig. 11.11 Nabothian cyst (*arrows*). On gray-scale TVUS (**a**), a Nabothian cyst appears as an anechoic well-defined cystic lesion, whereas it appears hyperintense on the axial T2-weighted MR image (**b**)

11.3.2 Adenomyosis

Adenomyosis is defined as the ectopic presence of endometrial stroma and glands within the myometrium, associated with surrounding hyperplasia and hypertrophy of the myometrium. It can appear as a diffuse form, if less than 25% of the lesion is surrounded by normal myometrium, or as a focal form (adenomyoma), if more than 25% of the lesion is surrounded by normal myometrium [111, 112]. Although the histological exam is the gold standard for the diagnosis of adenomyosis, a non-invasive diagnosis can also be possible with TVUS and MRI. On TVUS, seven items should be evaluated for the assessment of adenomyosis:

- its presence, according to the MUSA (Morphological Uterus Sonographic Assessment) criteria: enlarged globular uterus, asymmetrical thickening of the myometrium, myometrial cysts, echogenic subendometrial lines and buds, hyperechogenic islands, fan-shaped shadowing, interruption of the junctional zone, and high signal intensity on color Doppler imaging may be present because of an increased vascularity,
- its location (anterior, posterior, lateral left, lateral right, or fundal), evaluated in the sagittal and transverse plane,
- the differentiation between focal and diffuse disease,
- the evaluation of non-cystic or cystic adenomyosis, if there is at least a cyst with largest diameter of more than 2 mm,
- the evaluation of myometrial involvement and serosa,
- the disease extension (mild, if less than 25% of the uterus is affected; moderate, if between 50% and 75% of the uterus is affected; severe, if more than 50% of the uterus is affected),
- the size of the lesion [111, 113].

On MRI, the diffuse form and the focal form of adenomyosis can be also evaluated. The former presents itself with increased uterine dimensions (Fig. 11.12a). On T2-weighted images, ill-defined hypointense foci, because of muscular hyperplasia

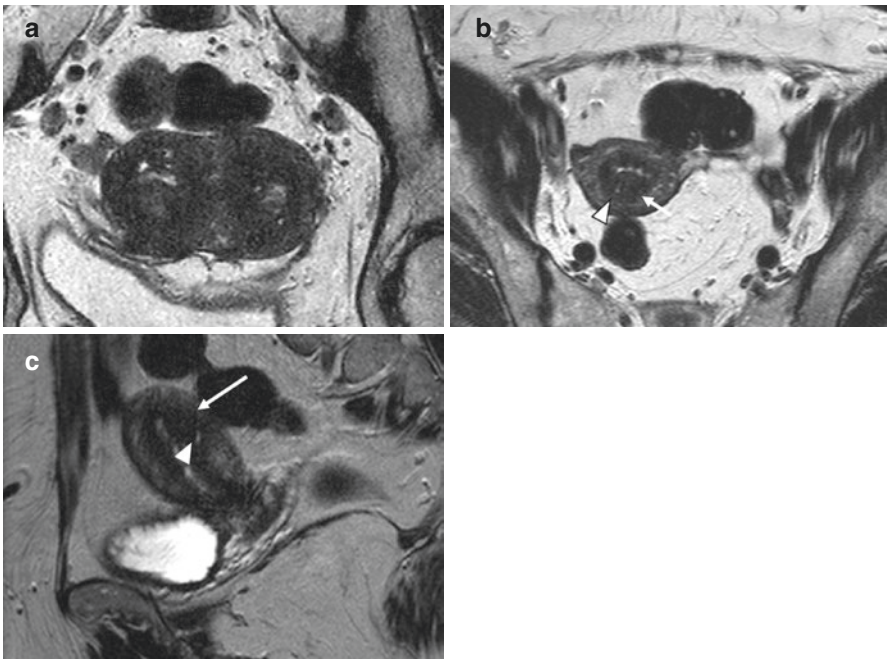

Fig. 11.12 Diffuse form of adenomyosis in a bicornuate uterus (**a**) and focal form of adenomyosis (**b**, **c**). (**a**) Axial T2-weighted image showing increased uterine dimensions, ill-defined hypointense areas, due to muscular hyperplasia and hypertrophy, mildly hyperintense foci consisting of ectopic endometrium, and markedly hyperintense cystic foci. Less than 25% of the lesion is surrounded by normal myometrium. (**b**, **c**) In a different patient, axial (**b**) and sagittal (**c**) T2-weighted images showing a hypointense mass-like formation (*arrows*) in the myometrium with hyperintense cystic area (*arrowheads*). More than 25% of the lesion is surrounded by normal myometrium

and hypertrophy, and multiple hyperintense foci, consisting of ectopic endometrium, can be seen. On T1-weighted images, the areas of adenomyosis have the same signal intensity compared to the surrounding myometrium, but sometimes hyperintense hemorrhagic areas can be present in zones with ectopic presence of endometrial stroma and glands [110, 114–116]. The focal form appears as a hypointense mass-like formation in the myometrium on T2-weighted images, and hyperintense areas can also be present [110] (Fig. 11.12b, c).

Sometimes the differential diagnosis between adenomyosis and leiomyomas may be difficult; nevertheless, the latter usually have well-defined margins, a pseudocapsule, and greater mass effect than the former [114, 117, 118].

11.3.3 Polyps

Polyps are benign lesions occurring in both perimenopausal and post-menopausal women [110, 119]. They consist of endometrial glands, fibrotic components, and vessels and can be sessile or pedunculated, usually located in the uterine fundus [120]. On TVUS, a polyp may appear hypoechoic or hyperechoic [121] (Fig. 11.13),

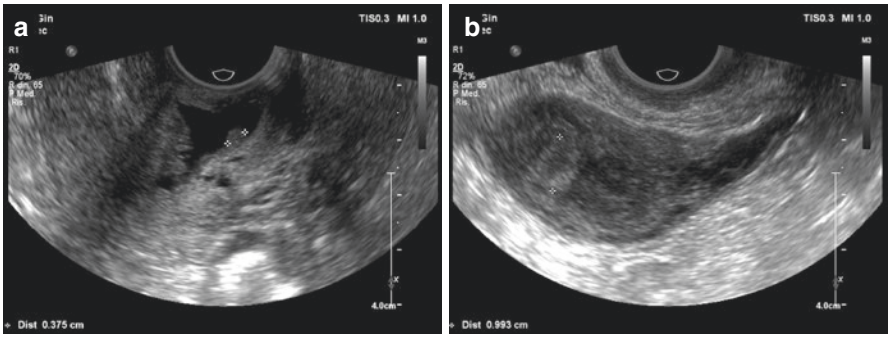

Fig. 11.13 Cervical (**a**) and endometrial (**b**) polyps. (**a**) Gray-scale TVUS showing a hypoechoic pedunculated cervical polyp (*between calipers*). (**b**) Gray-scale TVUS showing a mildly hypoechoic endometrial polyp with hyperechoic periphery (*between calipers*)

whereas, on T2-weighted MR images, it appears slightly hypointense compared to the endometrium and may have a hypointense fibrous core [117]. It also shows higher ADC values compared to endometrial carcinoma [122]. Sometimes the differential diagnosis between a polyp and a submucosal leiomyoma may be difficult; nevertheless, the latter usually originates from the myometrium and has lower signal intensity on T2-weighted images [110, 119].

11.3.4 Leiomyomas

Leiomyomas are the most frequent uterine benign disease, occurring in about 20–30% of young women, usually regressing in post-menopausal women [64, 123]. Leiomyomas, generally affecting the body of the uterus and more rarely the cervix, are uterine smooth muscle benign neoplasms that may also contain connective tissue and have a pseudocapsule [119, 123]. They can be divided depending on their location into: submucosal (in the subendometrial zone), intramural (within the myometrium), subserosal (in the subserosal zone), or cervical (in the cervix) [110, 123]. On TVUS, leiomyomas may appear as well-defined lesions hyperechoic or hypoechoic compared to the myometrium; they may show shadowing near and within the formation, and calcifications with distal shadowing may also be present (Fig. 11.14a). On MRI, leiomyomas can be appreciated as solid roundish formations with sharp borders [124]. Besides standard T1-weighted and T2-weighted sequences of the female pelvis, additional coronal and axial oblique perpendicular to the long axis of the uterus T2-weighted sequences are helpful to accurately localize the lesions and to confirm their uterine origin. On T1-weighted sequences, they can be hardly distinguished because they show intermediate signal intensity similar to myometrium [119, 123], whereas, on T2-weighted images, they usually show low signal intensity or slightly high signal intensity in case of high cellularity and may have a hyperintense pseudocapsule [123] (Fig. 11.14b). When fat is present, leiomyomas are called lipoleiomyomas, and they appear as high signal intensity lesions on both T1 and T2-weighted images [110] (Fig. 11.15). After contrast

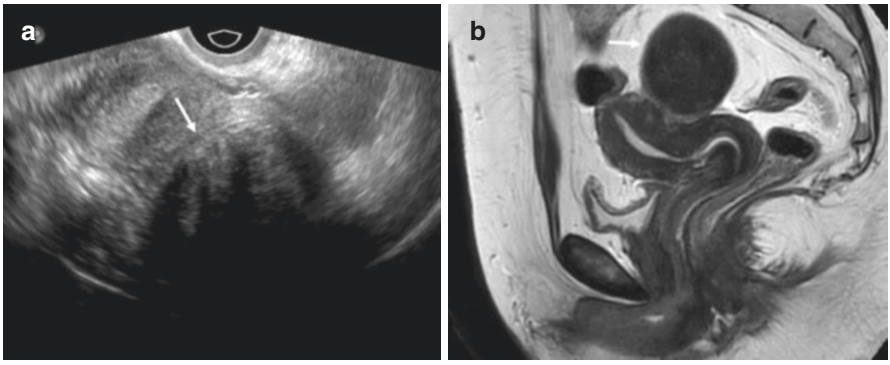

Fig. 11.14 Leiomyoma. (**a**) Gray-scale TVUS showing a large, well-defined subserosal leiomyoma (*arrow*). (**b**) Sagittal T2-weighted MR image in the same patient confirming the leiomyoma (*arrow*), showing the typical hypointense signal

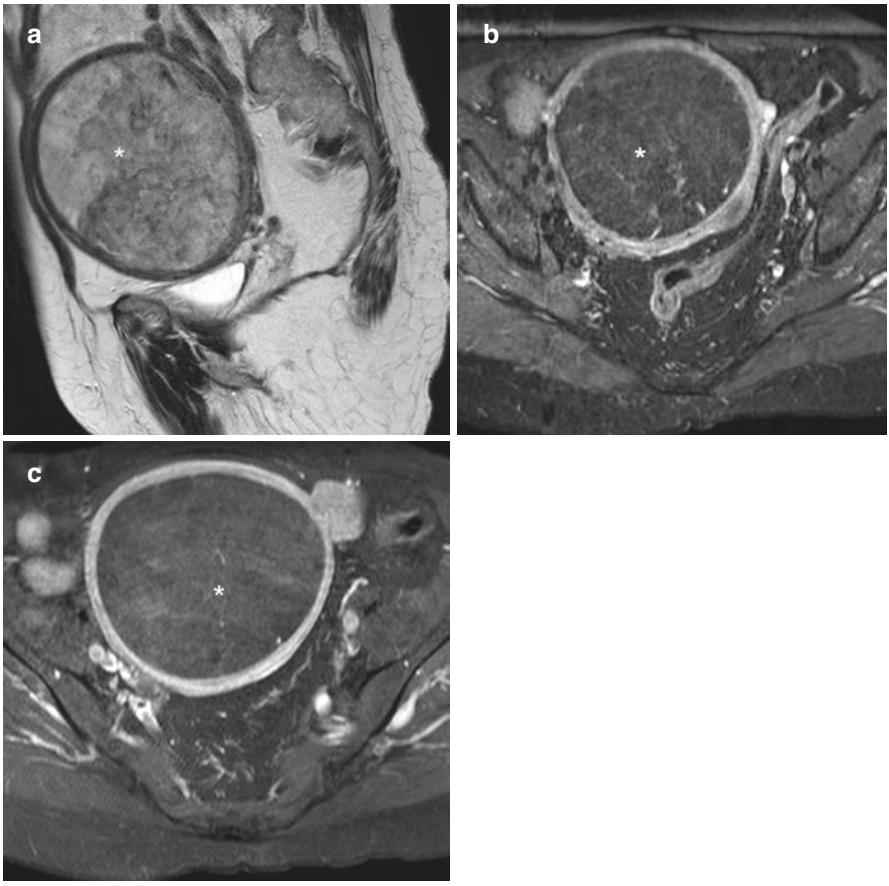

Fig. 11.15 Lipoleiomyoma (*). It appears hyperintense on T2-weighted image (**a**) and on T1-weighted image (not shown). The lesion shows loss of signal on fat-saturated T1-weighted image (**b**) and no enhancement on fat-saturated T1-weighted image after contrast administration (**c**)

administration, their behavior may vary depending on their cellularity [125]. Leiomyomas, particularly if large, may undergo degeneration, showing different appearances depending on the type of degeneration: red, cystic, myxoid, hyaline, or calcific [110, 123, 126]. Red degeneration shows T1-hyperintensity and variable signal intensity on T2-weighted images, while cystic degeneration is characterized by high signal intensity on T2-weighted sequences. Both types do not usually show enhancement, differently from myxoid degeneration, which also appears hyperintense on T2-weighted images and hypointense on T1-weighted images [64, 110]. Hyaline degeneration is characterized by low signal intensity on T2-weighted sequences and intermediate signal intensity on T1-weighted sequences [110]. Moreover, in the end-stage, leiomyomas may undergo calcific degeneration, showing signal void in all sequences [126] (Fig. 11.16).

Malignant evolution is quite rare and has to be suspected in case of a leiomyoma increasing rapidly in size or with irregular borders [125, 127, 128]. When the tumor shows an aggressive behavior, MRI can be used to assess the involvement of the surrounding organs and lymph nodes [129]. However, it is not possible to certainly differentiate large degenerated leiomyomas from leiomyosarcomas based on the signal characteristics on MRI [123] (Fig. 11.17). Leiomyosarcomas usually show low signal intensity on T1-weighted images and intermediate/high signal intensity on T2-weighted images; the diagnosis of leiomyosarcoma may be suggested by nodular borders, hemorrhage, T2-weighted dark areas, and central foci without enhancement [64]. The solid components of the lesion are associated with necrosis, showing high signal intensity on T2-weighted sequences, and are usually characterized by early enhancement after contrast administration. In addition, leiomyosarcoma usually shows high signal intensity on DWI and low signal intensity on ADC. Nevertheless, restricted diffusion on DWI may not help in the differential diagnosis with leiomyomas, which also can show restricted diffusion on DWI because of their high cellularity [126, 129].

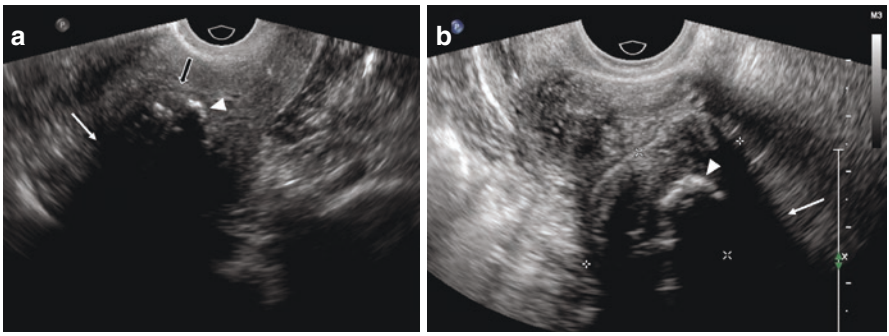

Fig. 11.16 Calcific leiomyoma. Gray-scale TVUS showing an end-stage leiomyoma (*black arrow,* **a** and *between calipers,* **b**) with calcific degeneration (*arrowheads*) and distal shadowing (*white arrows*)

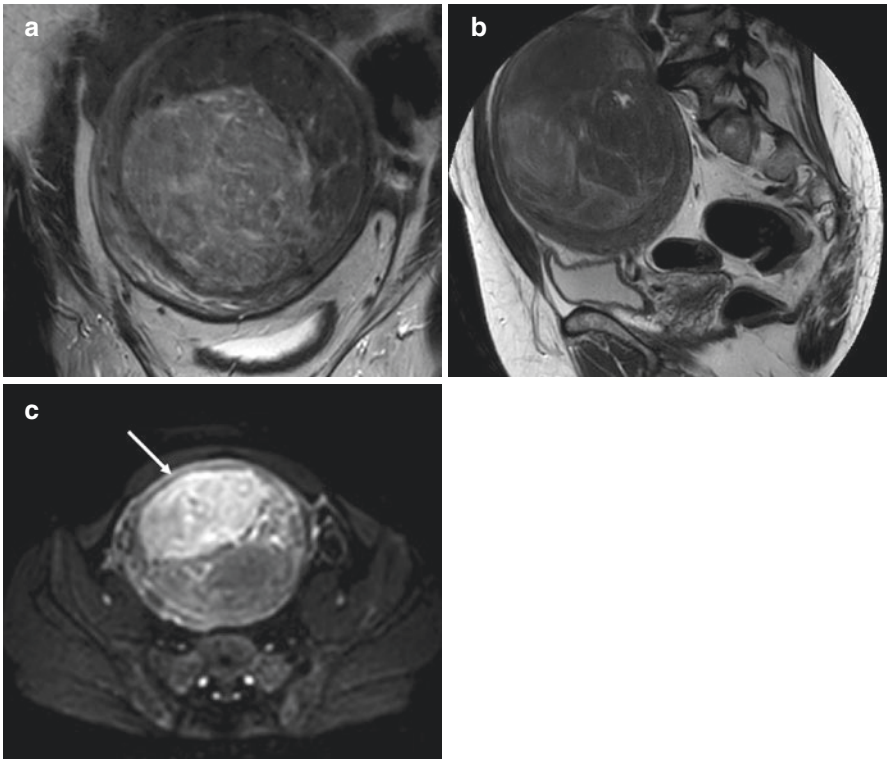

Fig. 11.17 Large degenerated leiomyoma. Coronal (**a**) and sagittal (**b**) T2-weighted images showing a large degenerated intramural leiomyoma. Some components show high signal on DWI (*arrow,* **c**). In this case, it is not possible to certainly differentiate this large degenerated leiomyoma from leiomyosarcoma based on MR imaging. Nevertheless, the absence of nodular borders, hemorrhage, T2-weighted dark areas, and central foci without enhancement is suggestive of a large degenerated leiomyoma

11.3.5 Endometrial Carcinoma

Endometrial carcinoma (EC) is estimated to be the most common gynecologic malignancy in western countries, ranging from 4 to 8%, with a maximal incidence in post-menopausal women [130].

EC arises from endometrial glands and can be focal or diffuse [131]. It can be divided into two types: type I (grade 1 and 2 endometrioid carcinoma), usually affecting perimenopausal women, is characterized by estrogen dependency and good prognosis, while type II (grade 3 endometrioid carcinoma and cancers of non-endometrioid histology), occurring in post-menopausal women, is characterized by non-estrogen dependency and poor prognosis [122, 132, 133]. The most common risk factors of EC are nulliparity, obesity, diabetes, hypertension, polycystic ovary, older age, late-onset menopause, early menarche [130, 134, 135]. The most frequent presenting symptom is abnormal uterine bleeding [130].

TVUS should be the first imaging choice in older women with abnormal bleeding to measure the endometrial thickness. An upper threshold of 5 or 4 mm is considered as the cut-off of normality in these patients [133].

Although the staging of EC, which follows the International Federation of Gynecology and Obstetrics (FIGO) criteria [132], depends on surgical and histopathological findings, MRI, thanks to its contrast resolution, can be an important tool in the preoperative staging of the EC [122, 136].

According to current guidelines, the dedicated MRI protocol should include an axial oblique perpendicular to uterus corpus T2-weighted sequence for an accurate evaluation of the depth of myometrial invasion, an axial oblique DWI sequence to match the T2-weighted sequence, and a T1- or T2-weighted sequence up to the renal hilum for lymph nodes and hydronephrosis. In case of grade 3 endometrioid adenocarcinoma or non-endometrioid carcinomas, an axial DWI sequence to match the sequence for lymph nodes and hydronephrosis should be added. In addition, contrast-enhanced images acquired after two and a half minutes should be usually performed [10].

EC is stage IA (Fig. 11.18) in case of a tumor confined to less than half of the myometrium, whereas it becomes stage IB (Fig. 11.19) in case of involvement of

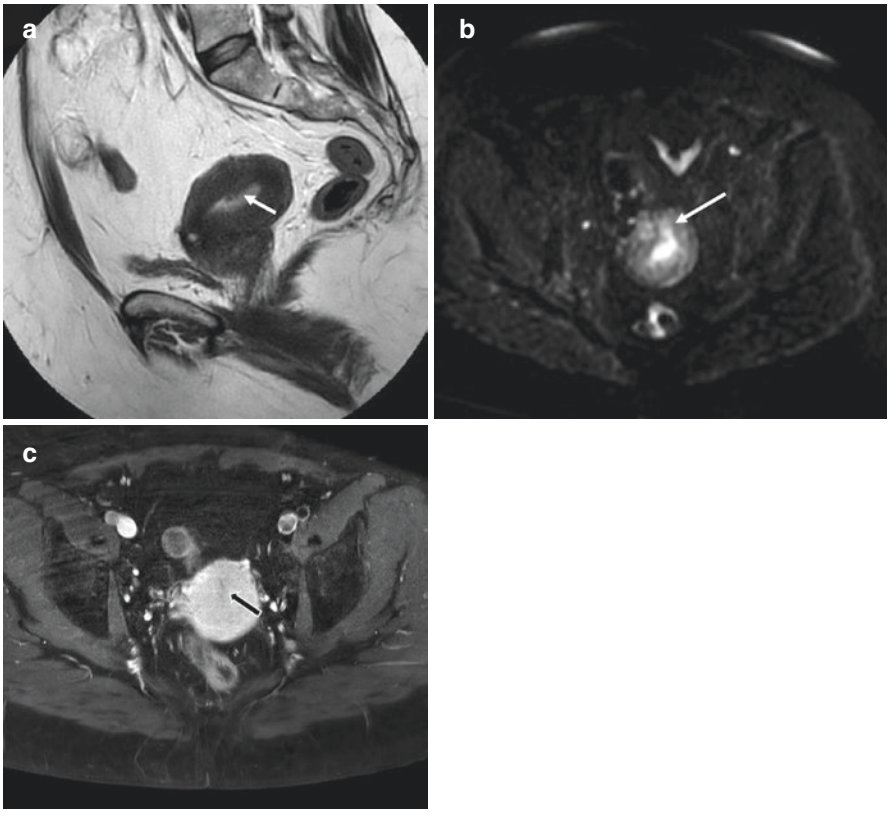

Fig. 11.18 Endometrial cancer, FIGO stage IA: A tumor (*arrow*) confined to less than half of the myometrium can be appreciated on the sagittal T2-weighted image (**a**), DWI image (**b**), and fat-suppressed T1-weighted contrast-enhanced image, on which it appears hypointense, being hypovascular compared to the normal myometrium (**c**)

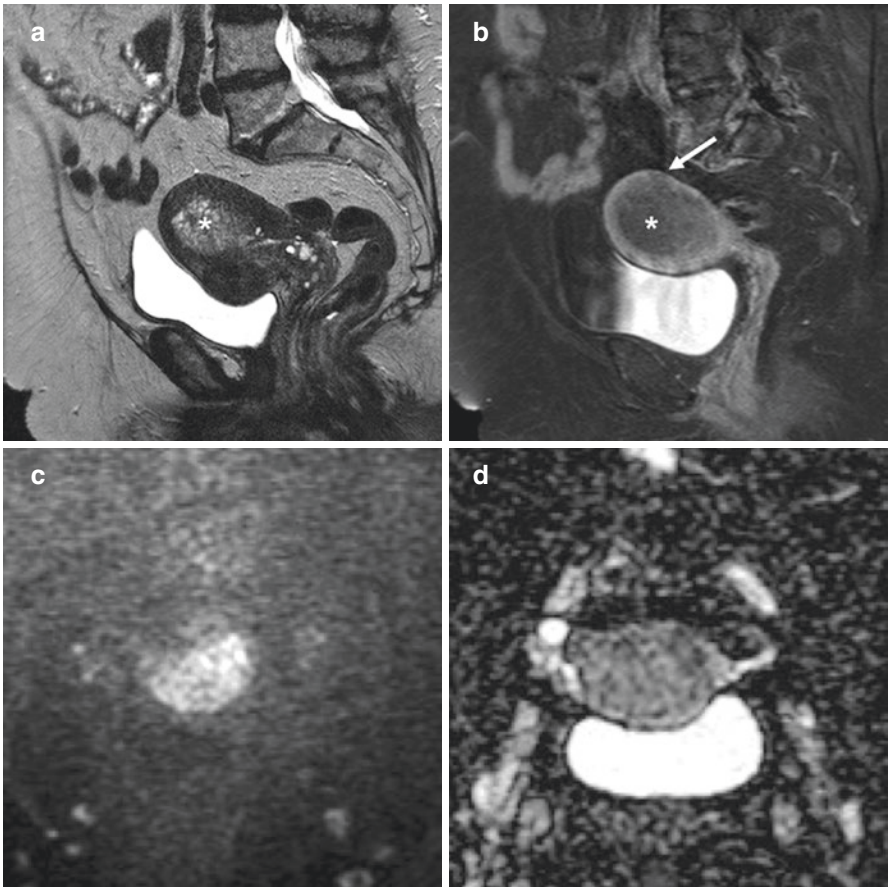

Fig. 11.19 Endometrial cancer, FIGO stage IB. A tumor (*asterisk*) within the uterine lumen, hyperintense on T2-weighted image (**a**) and hypointense being hypovascular compared to the myometrium on the contrast-enhanced image with fat suppression (**b**), involving more than half of the myometrium (*arrow,* **b**), can be appreciated. The lesion shows restricted diffusion, with high signal intensity on DWI (**c**) and low signal on the ADC map (**d**)

more than half of the myometrium [136, 137]. Stage II EC is a tumor involving the hypointense stroma of the cervix. A dynamic contrast-enhanced T1-weighted sequence may be useful in the evaluation of difficult cases; indeed, if the enhancement of the cervical mucosa is conserved in the delayed phase, the presence of stromal infiltration can be excluded [136]. EC is stage III if the lesion interrupts the outer contour of the uterus; EC in this stage remains confined to the true pelvis [136, 137]. EC is stage IVA in case of invasion of the vesical or rectal mucosa. This can be excluded with high accuracy in case of preservation of the fat planes between the lesion and bladder or rectum. When distant metastases are present, EC becomes stage IVB [122, 136, 137] (Fig. 11.20).

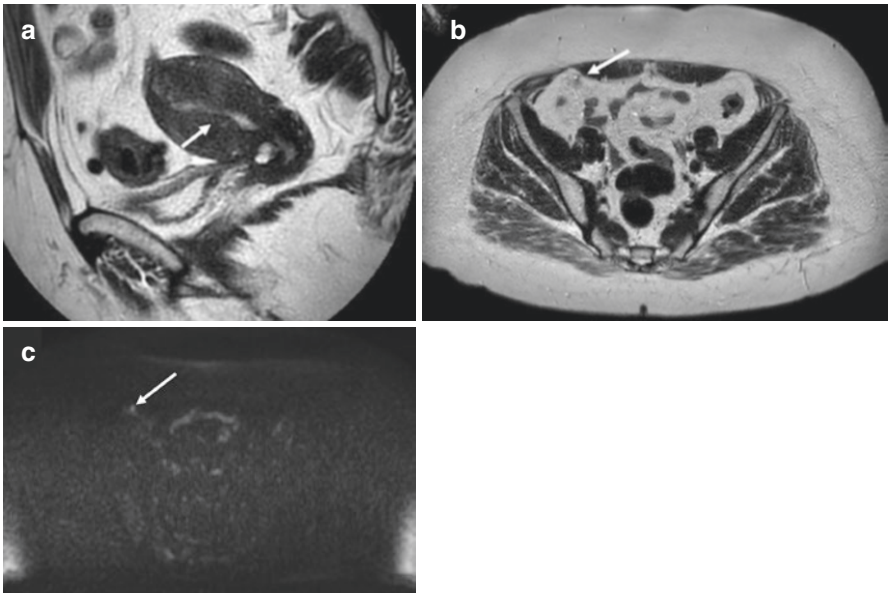

Fig. 11.20 Endometrial cancer, FIGO stage IVB. A tumor involving less than half of the myometrium can be appreciated on the sagittal T2-weighted image (*arrow,* **a**). Axial T2-weighted imaging (**b**) shows a peritoneal metastasis in the right iliac fossa (*white arrow,* **b** *and* **c**), which has high signal intensity on DWI (**c**). The staging was histologically confirmed after hysterectomy

MRI can also be useful in the evaluation of myometrial and cervical stromal invasion [136]. On T1-weighted sequences, EC usually appears as a lesion isointense to the myometrium [137], whereas, on T2-weighted images, it appears as a diffuse or well-delineated mass with heterogeneous intermediate signal intensity, higher than the hyperintense endometrium and lower than the hypointense myometrium [122, 136].

On post-contrast T1-weighted images, the lesion shows an early enhancement compared to the surrounding endometrium and slow enhancement compared to the myometrium, appearing hypointense compared to the myometrium in the late phase [122]. Post-contrast T1-weighted sequences can play a key role in the evaluation of the infiltration of the cervical stroma and the myometrium. In case of EC confined to the endometrium, a continuous enhancement of the subendometrial zone can be seen, whereas a disruption of this zone can be present in case of myometrial invasion [136].

EC shows restricted diffusion on DWI due to increased cellularity. Indeed, DWI increases the capability of detecting EC, in particular smaller ones, and can be useful in the assessment of the infiltration of the myometrium and the cervical stroma; DWI also improves the identification of metastases in the vagina, cervix, adnexa, and peritoneum [122, 136, 137].

DWI is sensitive but not specific for the identification of malignant lymph nodes because reactive lymph nodes also show high signal intensity on this sequence. Therefore, a size threshold of 10 mm in short axis diameter for para-aortic nodes and 8 mm for pelvic ones is used to define neoplastic infiltration. Round shape, spiculated margins, heterogeneous signal intensity, or necrosis are other morphologic patterns suggesting tumor involvement [122, 136, 137].

After therapy, diffusion-weighted and post-contrast T1-weighted sequences can also be used to differentiate the inflammation after radiotherapy from recurrence [122].

Sometimes the differential diagnosis between EC and uterine polyps or endometrial hyperplasia can be difficult: DWI may be a useful tool in these cases because the ADC value of normal endometrium and polyps is significantly higher than EC. Nevertheless, also hyperplastic endometrium may show low ADC values like EC. Blood products may also show low ADC values; a careful evaluation of T1-weighted images is important to confirm this finding. In addition, the evaluation of T2-weighted images can be useful for the differential diagnosis between EC and a leiomyoma mimicking an endometrial thickening because leiomyomas appear hypointense on this sequence [112].

11.3.6 Squamous Cell Carcinoma of the Uterine Cervix

Cervical cancer (CC) is the fourth most frequent neoplasm in women, with an average age of 53 years at diagnosis [138]. Patients usually present with vaginal bleeding and discharge [139, 140]. Various risk factors are associated with CC, including young age at first sexual intercourse, multiple sexual partners, sexually transmitted viral infections (HPV, HSV2), and multiparity [140–142]. CC usually arises from the transformation zone, between the ectocervix and the endocervix [143]. The most common cancer histotypes are adenocarcinoma and squamous cell carcinoma (up to 89% of cases) [140]. Dysplasia, which can be divided into mild, moderate, and severe, precedes the development of neoplasia, which is defined as preinvasive (cervical intraepithelial neoplasia, CIN) if the basement membrane is not involved, and as invasive in case of penetration of the basement membrane and involvement of stroma of the cervix.

Staging is obtained according to the FIGO system [132]. While TVUS is an important tool for the initial evaluation of EC, evidence supporting its use in CC is weak because the parametrial involvement cannot be surely assessed on

transvaginal ultrasonography. CT is a rapidly acquired exam with high spatial resolution, but it has lower soft-tissue contrast than MRI and it is usually not adequate for the differentiation between CC and normal cervical stroma or parametria. In contrast, MRI is the imaging method of choice for staging and restaging CC because of its high soft-tissue contrast on T2-weighted images [139, 144]. On this sequence, CC appears as an intermediate/high signal intensity mass within the hypointense cervical stroma [137]. The most adequate plan to evaluate enhancement in the cervix is the sagittal one [10]. On post-contrast T1-weighted sequences, small CC usually shows an early homogeneous enhancement, while large ones show a heterogeneous enhancement because of necrotic components [145]. Nevertheless, there is no consensus in the literature about the use of intravenous contrast agents for CC staging [137, 144].

DWI images may be useful in detecting small tumors because CC usually shows high signal intensity on DWI and low signal intensity on ADC; indeed, CC reveals statistically significant lower ADC values compared to the normal cervix [137].

CC is stage IA in case of a tumor not detectable on MRI [146], while it is stage IB if an intermediate/high signal intensity lesion is seen within the hypointense stroma of the cervix on T2-weighted images. CC is a stage IIA tumor if it involves the low signal intensity of the upper two-thirds of the vagina, whereas it is stage IIB if there is infiltration of the parametria, appearing as a disruption of the hypointense cervical stroma ring [122, 137]. In this case, an evaluation in the oblique plane perpendicular to the endocervical canal longitudinal axis is mandatory to detect parametrial invasion. On this plane, a T2-weighted sequence and a late phase acquisition after contrast should be usually done. In stage IIIA, CC involves the lower third of the vagina, and in stage IIIB, it infiltrates the pelvic wall or the ureters. CC is stage IV when it has extended beyond the true pelvis or has involved the rectal or bladder mucosa (Fig. 11.21). On T2-weighted images, the organ involvement appears as a focal disruption of the hypointense muscular layer of the bladder or rectum by the hyperintense CC. Also post-contrast T1-weighted sequences can be useful in evaluating tumor infiltration because CC usually shows stronger enhancement than the muscular layer [139].

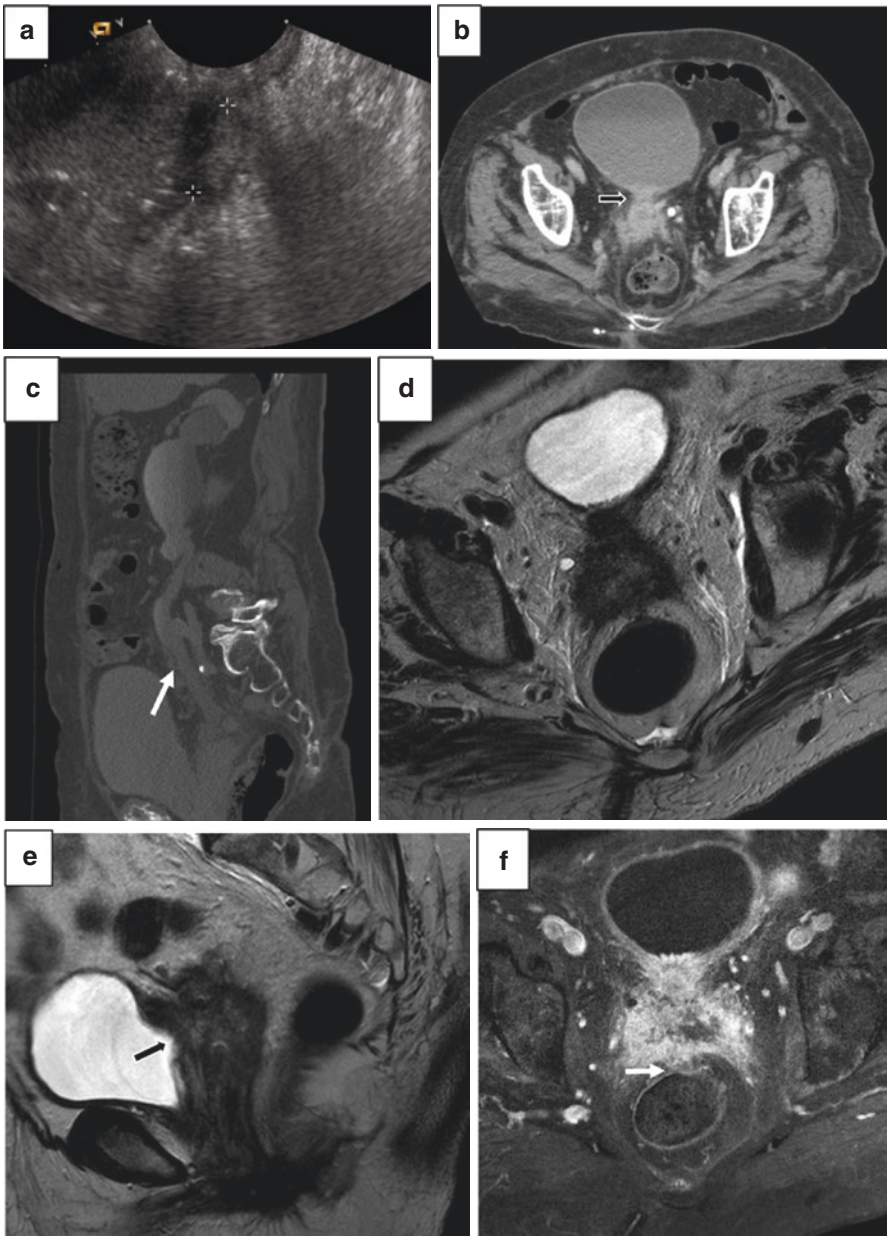

Fig. 11.21 Cervical cancer, FIGO stage IV. Gray-scale TVUS (**a**) showing a hypoechoic cervical lesion (*between calipers*). Contrast-enhanced axial CT scan (**b**) showing the cervical cancer involving the posterior wall of the bladder (*black arrow*). Note the dilation of the right ureter, better shown on curvilinear sagittal reconstructions (*white arrow,* **c**), secondary to the infiltration of the right ureteral meatus. Axial (**d**) and sagittal (**e**) T2-weighted images showing the cervical cancer involving the bladder; the organ involvement appears as a focal disruption of the hypointense muscular layer of the bladder (*arrow,* **e**). The post-contrast axial T1-weighted sequence (**f**) is useful in the evaluation of tumor infiltration because the lesion usually shows stronger enhancement than the muscular layer; note also the involvement of the anterior wall of the rectum (*arrow, **f***)

11.4 Vagina and Vulva

11.4.1 Malignant Tumors of the Vagina

11.4.1.1 Primary Tumors

For a tumor to be considered a primary vaginal cancer, it must originate from the vagina, with no involvement of the external os superiorly and the vulva inferiorly, and with no clinical or histological evidence of cervical or vulvar cancer or a prior history of these tumors within 5 years [147]. Tumors that extend to the external os are classified as cervical cancer, and vaginal tumors occurring within 5 years from a malignant cervical or vulvar cancer are considered recurrences of these tumors rather than a new primary malignancy [148, 149].

Primary vaginal cancer is a rare entity, constituting about 10% of vaginal cancers and 1–2% of gynecological malignancies [150]. The incidence of the disease increases with age, with about 50% of patients presenting after 70 years of age [151]. The most common cancer histotype is squamous cell carcinoma (90%), which is typical of an older age and is frequently associated with HPV; other risk factors are a history of previous cervical or vulvar carcinoma [152]. Adenocarcinoma (9%) is not typical of post-menopausal patients, occurring in much younger women (mean age 19 years) [151]. The remaining primary vaginal cancers are melanomas, sarcomas, and lymphomas [148].

Patients may be asymptomatic or may present with painless vaginal bleeding, vaginal discharge, urinary tract symptoms, pelvic pain, or a pelvic mass [153]. At clinical examination, it may appear as an ulcerating lesion, a fungating mass, or an annular constricting mass [152].

Imaging Findings of Vaginal Squamous Cell Carcinoma

The diagnosis of primary vaginal cancer is obtained clinically by biopsy. Staging is clinical as well and follows the American Joint Committee on Cancer TNM staging and the FIGO system [154, 155].

Imaging should not be used to change the clinical staging; however, FIGO recommends cross-sectional studies to better define the tumor volume and extension of the disease, in order to guide management. Specifically, MRI is more sensitive in detecting the tumor size and the paravaginal and parametrial involvement and can also be used in individual cases when the clinical assessment of the tumor is difficult [148]. MRI is also useful to evaluate for local recurrences after therapy. Contrast-enhanced CT is used to detect distant metastases and lymph node spread. US can be used to evaluate inguinal nodes and to guide biopsy, if necessary [10].

The MRI protocol to study vaginal cancer should include at least T2-weighted images of the pelvis in the axial, sagittal, and axial oblique (perpendicular to the long axis of the vagina) plane and axial T1-weighted and DWI sequences of the pelvis. The use of endovaginal gel and obtaining axial pre- and dynamic contrast-enhanced T1-weighted fat-saturated images of the pelvis and sagittal contrast-enhanced T1-weighted fat-saturated sequences are optional [10].

The squamous cell vaginal carcinoma occurs more commonly in the upper third of the vagina, on the posterior wall, and can appear as a diffuse mass with ill-defined and irregular margins, as a well-defined lobulated mass, or as a circumferential thickening [152, 156]. The tumor is best assessed on T2-weighted images, on which it shows an intermediate signal intensity, which is distinguished from the low intensity of the vaginal wall. On T1-weighted images, it is isointense to muscles and can be identified only when large enough to alter the contour of the vagina [152].

Vaginal cancer spreads by direct extension to the surrounding pelvic organs, including paravaginal tissue, parametria, urethra, bladder, and rectum [148]. If the T2-hypointensity of the outer layer of the vaginal wall is preserved, the tumor is limited to the mucosa and is a stage I; when the wall hypointensity is disrupted, the tumor has extended to the paravaginal tissues and is stage II. The extension through the vaginal wall is best assessed on the oblique axial plane. A stage III tumor involves the pelvic sidewalls, which are best assessed on axial and coronal planes, and it is seen as a higher T2-signal intensity within the muscles due to edema or direct tumor invasion. In stage IVA, the cancer involves the mucosa of the rectum or bladder, and direct infiltration with loss of the normal hypointensity of the bladder and rectal walls as well as loss of the vesicovaginal fat plane or rectovaginal septum is appreciated. Bullous edema may be difficult to differentiate from tumor infiltration and may result in overstaging. A stage IVB tumor spreads to distant organs, and lungs, liver, and bones are commonly involved sites [151, 152, 155] (Fig. 11.22).

The lymphatic spread of the tumor is complex and is often present, even in earlier stages (6–14% in stage I, 26–32% in stage II) [156, 157]. In general, upper vaginal tumors drain to pelvic lymph nodes, including obturator, internal and external iliac lymph nodes; involvement of para-aortic nodes is rare. The lower vagina drains to inguinal and femoral lymph nodes. The middle third of the vagina can follow either route. Posterior wall lymphatics drain to the inferior gluteal, sacral, and rectal nodes [148, 152].

After treatment, recurrences are most commonly seen within the first 2 years. Tumors of the upper third tend to recur locally, while lower tumors are more often associated with pelvic sidewalls invasion or distant recurrences [151, 152]. MRI is useful in differentiating residual tumor from post-treatment changes although it may be difficult, especially in the few months after treatment, when T2-hyperintense edema is also present. In time, the scar tissue appears T2 hypointense, while the tumor has T2-intermediate to high signal intensity and enhances avidly [151].

Complications after treatment generally occur within 5 years, but they may be as late as 20 years and are due to radiation-induced bladder, vaginal, and rectal toxicity. They include cystitis, proctitis, bowel stricture and perforation, bone osteonecrosis, and stress fractures [151, 158]. Common complications are rectovaginal and vesicovaginal fistulas, best demonstrated on axial or sagittal high-resolution T2-weighted or short tau inversion recovery (STIR) sequences, where they appear as a tract with fluid hyperintensity and air hypointensity [151, 152].

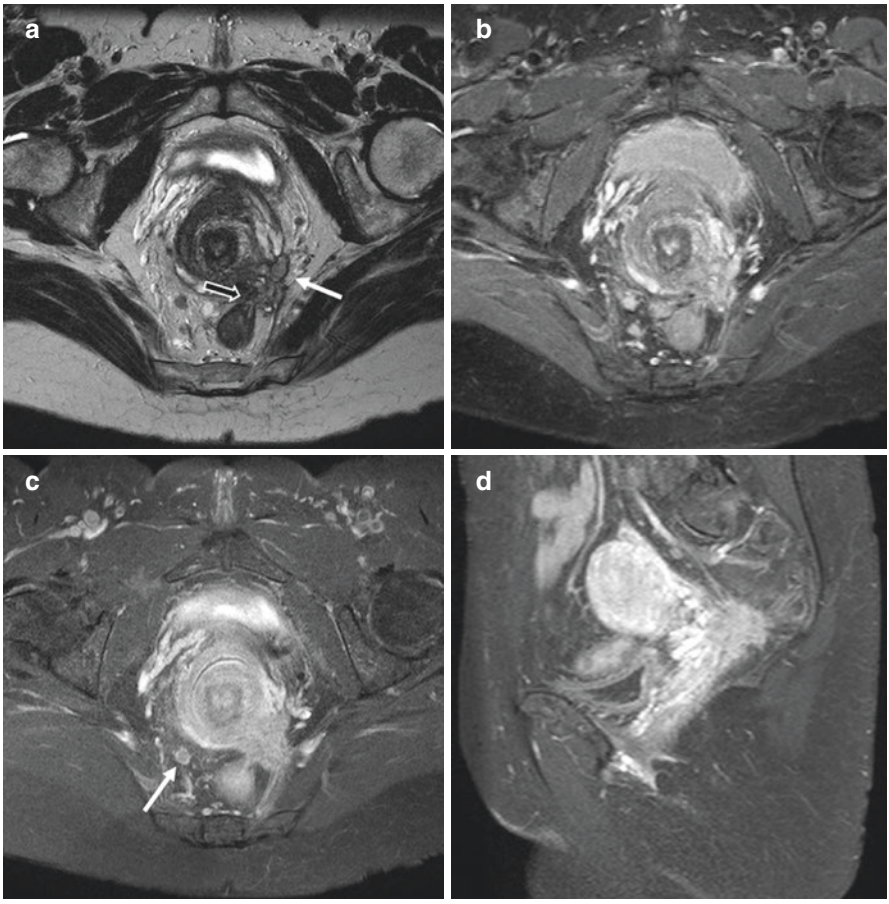

Fig. 11.22 Vaginal cancer. Axial T2-weighted sequence (**a**), axial fat-suppressed sequence (**b**), and fat-suppressed contrast-enhanced T1-weighted sequences on the axial (**c**) and sagittal (**d**) plane, showing a prevalently exophytic mass (*white arrow,* **a**) with spiculated margins, involving the postero-lateral fornix and the postero-lateral region of the cervix on the left. The mass infiltrates the adjacent adipose tissue and the left uterosacral ligament, and it infiltrates the rectal serosa at 2 o' clock (*black arrow,* **a**). Note the right presacral small lymph node with irregular margins (*arrow,* **c**). According to FIGO staging, this is a stage IV tumor

11.4.1.2 Secondary Tumors

Most vaginal malignancies are secondary tumors, accounting for more than 80% of vaginal cancers [148]. Most malignant tumors of the vagina are due to secondary involvement by adjacent tumors, but lymphatic or hematogenous metastatic spread from distant cancers can also occur. The primary tumors most frequently metastasizing to the vagina are ovarian, cervical, endometrial, and rectal cancer, but also vulvar and bladder carcinoma can involve the vagina. Only very rarely vaginal metastases from other extra-genital cancers, e.g., colon, breast, pancreas, small

bowel, occur [152]. In general, the MR features of vaginal metastases mimic the primary tumor [152].

11.5 Vulva

11.5.1 Malignant Tumors of the Vulva

Vulvar cancer accounts for 2% to 5% of gynecological malignancies peaking in the seventh decade, with about 66% of cases occurring after the age of 70 years; however, the mean age of occurrence is decreasing in the last years due to an increased rate of HPV infection [20, 159]. The most common vulvar cancer is squamous cell carcinoma (90%), followed by melanoma (5–10%) and basal cell carcinoma (2–4%). Rarer occurrences are Paget's disease (1–2%), affecting mainly postmenopausal women of a median age of 72 years, sarcoma, adenocarcinoma, and Bartholin gland carcinoma. Metastases from other primary cancers constitute 5–8% of vulvar malignancies [160].

In pre-menopausal women, vulvar squamous carcinoma is more likely to be associated with HPV infection, while older patients often have vulvar dermatoses, like lichen sclerosis. Clinically, many patients are asymptomatic; when symptoms are present, they include pruritus, burning, pain, abnormal bleeding or discharge, or the occurrence of a lump or an ulcer. It can appear as a warty or polypoid mass or a raised, flat ulcerated plaque-like lesion at clinical examination.

11.5.1.1 Imaging Findings of Vulvar Squamous Cell Carcinoma

Diagnosis of vulvar cancer is usually made by clinical examination and biopsy [159]. Imaging, and in particular CT and MRI, has a role especially in locally advanced disease to identify the local extent of the tumor and the infiltration of adjacent structures, to evaluate lymphadenopathies and distal metastases, and to aid in surgical planning [159]. US may be useful to evaluate nodal involvement and to guide biopsies. On US, the tumor appears as a soft-tissue mass with internal vascularity [161, 162]. CT is not useful for local staging because of its low contrast resolution, but it may identify the bladder or rectum involvement and can detect distant metastases [163]. On CT, the tumor appears as a non-specific vulvar thickening or mass with soft-tissue density [162].

Vulvar squamous cell carcinoma is staged according to the American Joint Committee on Cancer TNM staging and the FIGO system. The FIGO staging was

revised in 2009 and can be applied to most vulvar cancer except melanoma [159]. MRI is preferred for local staging. The exam is performed after bladder emptying, and ultrasound gel may be used to distend the vagina to better assess vaginal wall infiltration and possibly to identify smaller vulvar lesions. The protocol should include axial T1-weighted FSE images with a large FOV to evaluate lymphadenopathies and bone marrow abnormalities; axial and coronal high-resolution T2-weighted FSE sequences to evaluate the primary tumor; and sagittal dynamic fat-saturated contrast-enhanced T1-weighted images with a small FOV for the extent of tumor involvement. High-resolution axial T2-weighted FSE sequences with a small FOV and 3-mm thick sections can be obtained through the perineum. The tumor may be better appreciated on T2-weighted images with fat suppression than non-fat saturated images, and contrast-enhanced sequences can help identify small tumors and assess invasion of the urethra, anus, and vagina. Diffusion-weighted sequences can also be useful to assess the primary tumor and lymphadenopathies [163].

On MRI, the tumor has low signal intensity on T1-weighted images and intermediate-to-high signal intensity on T2-weighted images [20]. In two-thirds of cases, the labia are involved, with the clitoris and Bartholin glands [20] (Fig. 11.23). Small stage I cancers may be missed and stage I or II tumors with an "en-plaque" aspect may also be difficult to identity on MRI [164]. The urethra, anorectum, vagina, perineal muscles, and the bladder should be carefully assessed for signs of infiltration, which will appear as a tissue of intermediate signal intensity, in continuity with the primary tumor, within the hypointense muscular walls of the urethra, vagina, and anorectum. T2-weighted images in the sagittal and coronal planes could be helpful to assess the whole tumor if deep infiltration is suspected [164].

The tumor spreads mainly by local invasion, followed by lymphatic spread and hematogenous spread to distant organs (lung, liver, bone) [161]. Inguinal and femoral lymph nodes are the first to be involved, followed by pelvic nodes [165]. Lymph node involvement can be uni- or bilateral, depending on tumor size and its closeness to the middle line [159].

The most important prognostic factors in vulvar cancer are tumor size, depth of infiltration, and particularly the presence of lymph node metastases. Recurrences can be local or distant and are generally seen within 2 years after initial treatment [20] (Fig. 11.24).

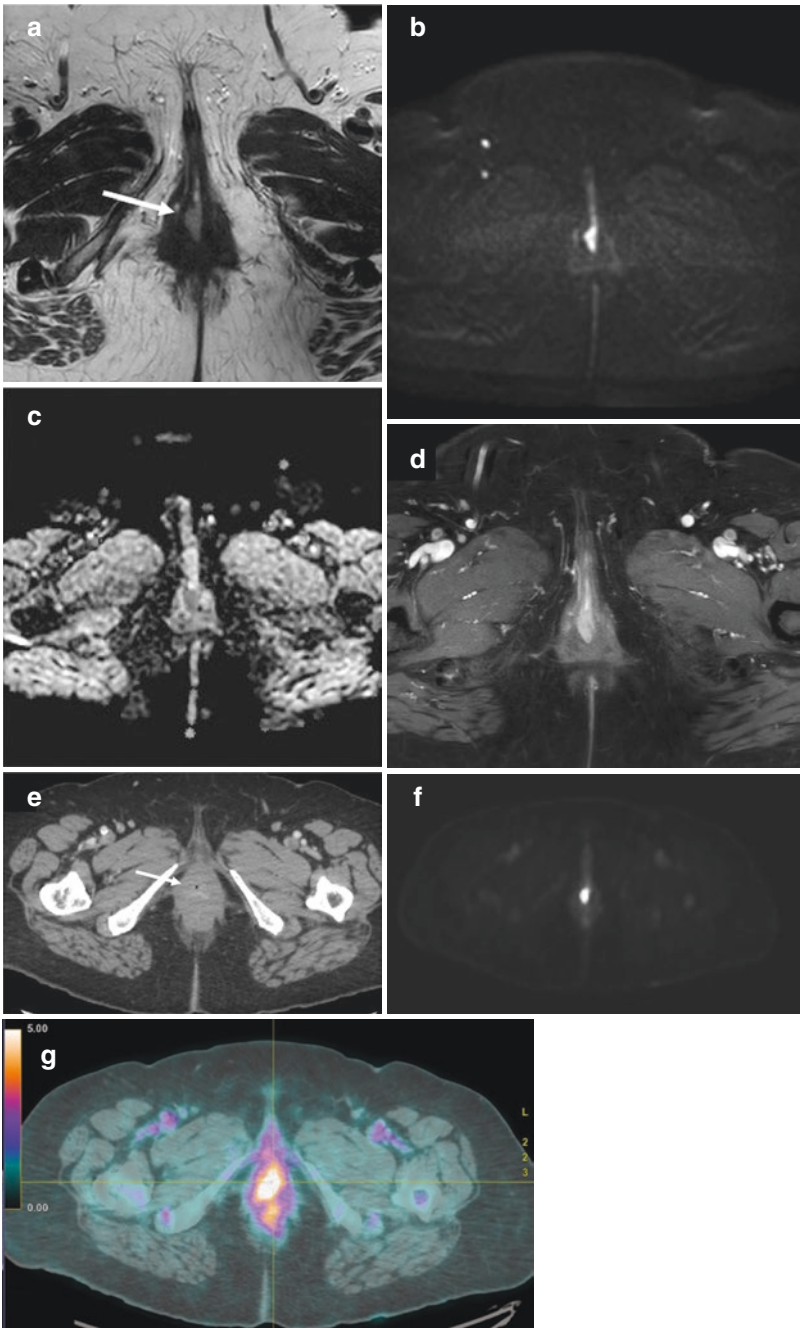

Fig. 11.23 Vulvar cancer. At the vaginal introitus, on the right side, there is a vulvar lesion (*arrow,* **a**), with intermediate T2 signal intensity (**a**), restricted diffusion (**b**, **c**), and enhancement after contrast administration (**d**). At the PET/CT (**e**–**g**), on the unenhanced CT, a paravaginal hypodense tissue in the perineum can be recognized (*arrow,* **e**), and it shows an intense uptake of the [18F]-fluorodeoxyglucose tracer (**f**), well-shown on the fusion imaging (**g**)

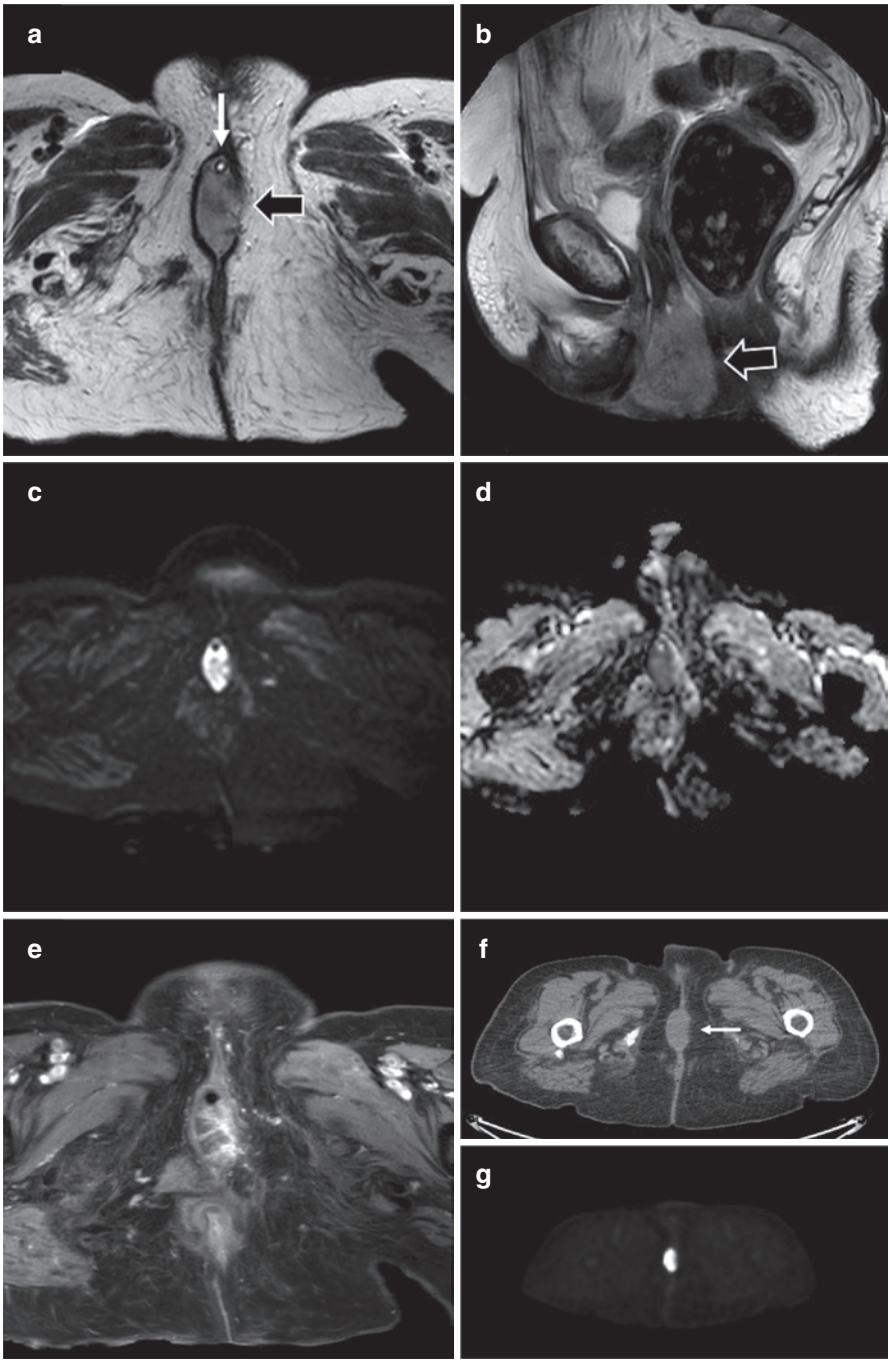
a
b
c
d
e
f
g

Fig. 11.24 Locoregional recurrence of vulvar cancer. Patient with previous vulvectomy performed 5 years before and a urinary catheter in place. At the vaginal introitus, there is a solid lesion (*black arrow,* **a**), heterogeneously hypointense on T2-weighted sequences (**a**, **b**), that involves the full thickness of the vaginal wall, extending cranially up to the middle vaginal third (**b**), and surrounding the urethra in its inferior two-thirds (*white arrow,* **a**). The lesion shows restricted diffusion (**c**, **d**) and a heterogeneous enhancement for the presence of central necrotic areas (**e**). At the PET/CT scan, the lesion can be seen as a solid mass on the unenhanced CT images (*arrow*, **f**), with an intense uptake of the [18F]-fluorodeoxyglucose tracer (**g**)

11.6 Pelvic Organ Prolapse

Functional disorders of the pelvic floor refer to a group of medical conditions affecting the ligaments, fasciae, and muscles, supporting the pelvic organs [166]. These conditions are relatively common and predominantly affect older women [167].

The appearance of the pelvic organs can be evaluated on MRI at rest and during active contraction, the so-called Valsalva maneuver. A state-of-the-art MRI protocol includes axial, coronal, and sagittal rapid half-Fourier T2-weighted imaging sequences at rest; successively, six to eight rapid T2-weighted images are also acquired during the Valsalva maneuver [168].

The pelvic floor can be divided into three anatomic compartments: the anterior, the middle, and the posterior. In the anterior compartment there are the bladder and the urethra, in the middle one the uterus, the cervix, and the vagina, in the posterior one the rectum, the anus, and the anal sphincter. This paragraph will be focused on the pathology of the middle compartment, while the pathology of the anterior and the posterior ones will not be included in this chapter.

In the pelvic middle compartment, disorders include uterine or cervical prolapse. Pelvic organ prolapse is the abnormal descent or herniation of the pelvic organs through their respective hiatus due to failure of support structures and perineal hiatal weakening. Uterine prolapse is the uterine herniation beyond the vagina, caused by a failure of the ligamentous and fascial supports (the pubocervical ligaments, parametrium and paracolpium, uterosacral ligaments, rectovaginal fascia, and perineal body). The laxity of the uterosacral ligaments contributes to an anterior movement of the cervix with progressive uterine retroversion, causing the prolapse [168, 169]. Cervical prolapse can be seen as a bulging mass outside the external genitalia [168].

On MR defecography, it can be diagnosed when the cervix is located 1 cm below the pubococcygeal line (PCL), a straight line connecting the inferior border of the pubic symphysis to the last coccygeal joint [167]. The distance between the PCL and the most anterior and inferior aspect of the cervix is used as reference for grading: a prolapse is considered small when the distance is less than 3 cm, moderate if 3 to 6 cm, and severe if over 6 cm [166]. In case of previous hysterectomy, the vaginal apex should be at least 1 cm above the PCL line, using the most posterior and superior aspect of the vaginal vault [166]. Vaginal vault prolapse is generally associated with other pelvic prolapses, most commonly an enterocele [170].

References

1. Permuth-Wey J, Sellers TA. Epidemiology of ovarian cancer. In: Verma M, editor. Cancer. Epidemiology: modifiable factors. Totowa, NJ: Humana Press; 2009. p. 413–37.
2. Tinelli A, Malvasi A, Rahimi S, Negro R, Vergara D, Martignago R, Pellegrino M, Cavallotti C. Age-related pelvic floor modifications and prolapse risk factors in postmenopausal women. Menopause. 2010;17:204–12.
3. Langer JE, Oliver ER, Lev-Toaff AS, Coleman BG. Imaging of the female pelvis through the life cycle. Radiographics. 2012;32:1575–97.
4. Hall DA, McCarthy KA, Kopans DB. Sonographic visualization of the normal postmenopausal ovary. J Ultrasound Med. 1986;5:9–11.
5. Pavlik EJ, DePriest PD, Gallion HH, Ueland FR, Reedy MB, Kryscio RJ, van Nagell JR. Ovarian volume related to age. Gynecol Oncol. 2000;77:410–2.
6. Cohen HL, Tice HM, Mandel FS. Ovarian volumes measured by US: bigger than we think. Radiology. 1990;177:189–92.
7. Aviram R, Gassner G, Markovitch O, Cohen I, Fishman A, Tepper R. Volumes of normal ovaries, ovaries with benign lesions, and ovaries with cancer in menopausal women: is there an optimal cut-off value to predict malignancy? J Clin Ultrasound. 2008;36:1–5.
8. Revzin MV, Moshiri M, Katz DS, Pellerito JS, Mankowski Gettle L, Menias CO. Imaging evaluation of fallopian tubes and related disease: a primer for radiologists. Radiographics. 2020;40:1473–501.
9. Yitta S, Hecht EM, Mausner EV, Bennett GL. Normal or abnormal? Demystifying uterine and cervical contrast enhancement at multidetector CT. Radiographics. 2011;31:647–61.
10. ESUR Female Pelvis Imaging Working Group. ESUR quick guide to female pelvis imaging, 1.0. Vienna: European Society of Urogenital Radiology; 2019.
11. Outwater EK, Mitchell DG. Normal ovaries and functional cysts: MR appearance. Radiology. 1996;198:397–402.
12. Bartoli JM, Moulin G, Delannoy L, Chagnaud C, Kasbarian M. The normal uterus on magnetic resonance imaging and variations associated with the hormonal state. Surg Radiol Anat. 1991;13:213–20.
13. Hricak H, Alpers C, Crooks LE, Sheldon PE. Magnetic resonance imaging of the female pelvis: initial experience. AJR Am J Roentgenol. 1983;141:1119–28.
14. Takeuchi M, Matsuzaki K, Nishitani H. Manifestations of the female reproductive organs on MR images: changes induced by various physiologic states. Radiographics. 2010;30:1147.
15. Brown HK, Stoll BS, Nicosia SV, Fiorica JV, Hambley PS, Clarke LP, Silbiger ML. Uterine junctional zone: correlation between histologic findings and MR imaging. Radiology. 1991;179:409–13.
16. Meylaerts LJ, Wijnen L, Grieten M, Palmers Y, Ombelet W, Vandersteen M. Junctional zone thickness in young nulliparous women according to menstrual cycle and hormonal contraception use. Reprod Biomed Online. 2017;34:212–20.
17. Kılıçkesmez Ö, Fırat Z, Oygen A, Bozkurt DK, Güzelbey T, Gürses B, Taşdelen N. Diffusion tensor imaging of the uterine zones related to the menstrual cycle and menopausal status at 3 tesla MRI. Balkan Med J. 2016;33:607–13.
18. deSouza NM, Hawley IC, Schwieso JE, Gilderdale DJ, Soutter WP. The uterine cervix on in vitro and in vivo MR images: a study of zonal anatomy and vascularity using an enveloping cervical coil. AJR Am J Roentgenol. 1994;163:607–12.
19. Togashi K, Nakai A, Sugimura K. Anatomy and physiology of the female pelvis: MR imaging revisited. J Magn Reson Imaging. 2001;13:842–9.
20. Tsili AC. Vagina and vulva. In: Forstner R, Cunha TM, Hamm B, editors. MRI CT female pelvis. Cham: Springer International; 2019. p. 343–68.
21. Landes CJ, Blair JC. Normal growth and puberty. In: Imaging of gynecological disorders in infants and children. Berlin: Springer; 2011. p. 81–113.

22. Walker DK, Salibian RA, Salibian AD, Belen KM, Palmer SL. Overlooked diseases of the vagina: a directed anatomic-pathologic approach for imaging assessment. Radiographics. 2011;31:1583–98.
23. Grant LA, Sala E, Griffin N. Congenital and acquired conditions of the vulva and vagina on magnetic resonance imaging: a pictorial review. Semin Ultrasound CT MR. 2010;31:347–62.
24. Ellenson LH, Pirog EC. The female genital tract. In: Robbins and Cotran pathologic basis of disease. Amsterdam: Elsevier; 2014. p. 991–1042.
25. Bulun SE. Endometriosis. N Engl J Med. 2009;360:268–79.
26. Secosan C, Balulescu L, Brasoveanu S, Balint O, Pirtea P, Dorin G, Pirtea L. Endometriosis in menopause-renewed attention on a controversial disease. Diagnostics (Basel). 2020;10:E134.
27. Punnonen R, Klemi PJ, Nikkanen V. Postmenopausal endometriosis. Eur J Obstet Gynecol Reprod Biol. 1980;11:195–200.
28. Bendon CL, Becker CM. Potential mechanisms of postmenopausal endometriosis. Maturitas. 2012;72:214–9.
29. Gemmell LC, Webster KE, Kirtley S, Vincent K, Zondervan KT, Becker CM. The management of menopause in women with a history of endometriosis: a systematic review. Hum Reprod Update. 2017;23:481–500.
30. Cope AG, VanBuren WM, Sheedy SP. Endometriosis in the postmenopausal female: clinical presentation, imaging features, and management. Abdom Radiol. 2020;45:1790–9.
31. Streuli I, Gaitzsch H, Wenger J-M, Petignat P. Endometriosis after menopause: physiopathology and management of an uncommon condition. Climacteric. 2017;20:138–43.
32. Li J, Liu R, Tang S, et al. Impact of endometriosis on risk of ovarian, endometrial and cervical cancers: a meta-analysis. Arch Gynecol Obstet. 2019;299:35–46.
33. Pearce CL, Templeman C, Rossing MA, et al. Association between endometriosis and risk of histological subtypes of ovarian cancer: a pooled analysis of case-control studies. Lancet Oncol. 2012;13:385–94.
34. Stern RC, Dash R, Bentley RC, Snyder MJ, Haney AF, Robboy SJ. Malignancy in endometriosis: frequency and comparison of ovarian and extraovarian types. Int J Gynecol Pathol. 2001;20:133–9.
35. Melin A, Sparén P, Persson I, Bergqvist A. Endometriosis and the risk of cancer with special emphasis on ovarian cancer. Hum Reprod. 2006;21:1237–42.
36. Gougoutas CA, Siegelman ES, Hunt J, Outwater EK. Pelvic endometriosis: various manifestations and MR imaging findings. AJR Am J Roentgenol. 2000;175:353–8.
37. Siegelman ES, Oliver ER. MR imaging of endometriosis: ten imaging pearls. Radiographics. 2012;32:1675–91.
38. Cumiskey J, Whyte P, Kelehan P, Gibbons D. A detailed morphologic and immunohistochemical comparison of pre- and postmenopausal endometriosis. J Clin Pathol. 2008;61:455–9.
39. Woodward PJ, Sohaey R, Mezzetti TP. Endometriosis: radiologic-pathologic correlation. Radiographics. 2001;21:193–216; questionnaire 288-294.
40. Bazot M, Bharwani N, Huchon C, et al. European society of urogenital radiology (ESUR) guidelines: MR imaging of pelvic endometriosis. Eur Radiol. 2017;27:2765–75.
41. Schreiter V, Kinkel K. Endometriosis. In: Forstner R, Cunha TM, Hamm B, editors. MRI CT female pelvis. Cham: Springer International; 2019. p. 325–41.
42. Jung SI. Ultrasonography of ovarian masses using a pattern recognition approach. Ultrasonography. 2015;34:173–82.
43. Patel MD, Feldstein VA, Chen DC, Lipson SD, Filly RA. Endometriomas: diagnostic performance of US. Radiology. 1999;210:739–45.
44. Jain KA. Prospective evaluation of adnexal masses with endovaginal gray-scale and duplex and color Doppler US: correlation with pathologic findings. Radiology. 1994;191:63–7.
45. McDermott S, Oei TN, Iyer VR, Lee SI. MR imaging of malignancies arising in endometriomas and extraovarian endometriosis. Radiographics. 2012;32:845–63.
46. Khashper A, Addley HC, Abourokbah N, Nougaret S, Sala E, Reinhold C. T2-hypointense adnexal lesions: an imaging algorithm. Radiographics. 2012;32:1047–64.
47. Vargas HA, Barrett T, Sala E. MRI of ovarian masses. J Magn Reson Imaging. 2013;37:265–81.

48. Outwater EK, Siegelman ES, Hunt JL. Ovarian teratomas: tumor types and imaging characteristics. Radiographics. 2001;21:475–90.
49. Foti PV, Farina R, Palmucci S, et al. Endometriosis: clinical features, MR imaging findings and pathologic correlation. Insights Imaging. 2018;9:149–72.
50. Dhanda S, Thakur M, Kerkar R, Jagmohan P. Diffusion-weighted imaging of gynecologic tumors: diagnostic pearls and potential pitfalls. Radiographics. 2014;34:1393–416.
51. Tanaka YO, Okada S, Yagi T, Satoh T, Oki A, Tsunoda H, Yoshikawa H. MRI of endometriotic cysts in association with ovarian carcinoma. AJR Am J Roentgenol. 2010;194:355–61.
52. Timmerman D, Planchamp F, Bourne T, et al. ESGO/ISUOG/IOTA/ESGE consensus statement on preoperative diagnosis of ovarian tumors. Ultrasound Obstet Gynecol. 2021;58:148–68.
53. Jacobs I, Oram D, Fairbanks J, Turner J, Frost C, Grudzinskas JG. A risk of malignancy index incorporating CA 125, ultrasound and menopausal status for the accurate preoperative diagnosis of ovarian cancer. Br J Obstet Gynaecol. 1990;97:922–9.
54. Moore RG, Brown AK, Miller MC, et al. The use of multiple novel tumor biomarkers for the detection of ovarian carcinoma in patients with a pelvic mass. Gynecol Oncol. 2008;108:402–8.
55. Amor F, Vaccaro H, Alcázar JL, León M, Craig JM, Martinez J. Gynecologic imaging reporting and data system: a new proposal for classifying adnexal masses on the basis of sonographic findings. J Ultrasound Med. 2009;28:285–91.
56. Andreotti RF, Timmerman D, Benacerraf BR, et al. Ovarian-adnexal reporting lexicon for ultrasound: a white paper of the ACR ovarian-adnexal reporting and data system committee. J Am Coll Radiol. 2018;15:1415–29.
57. Ameye L, Timmerman D, Valentin L, et al. Clinically oriented three-step strategy for assessment of adnexal pathology. Ultrasound Obstet Gynecol. 2012;40:582–91.
58. Timmerman D, Valentin L, Bourne TH, Collins WP, Verrelst H, Vergote I, International Ovarian Tumor Analysis (IOTA) Group. Terms, definitions and measurements to describe the sonographic features of adnexal tumors: a consensus opinion from the International Ovarian Tumor Analysis (IOTA) Group. Ultrasound Obstet Gynecol. 2000;16:500–5.
59. Van Calster B, Van Hoorde K, Valentin L, et al. Evaluating the risk of ovarian cancer before surgery using the ADNEX model to differentiate between benign, borderline, early and advanced stage invasive, and secondary metastatic tumours: prospective multicentre diagnostic study. BMJ. 2014;349:g5920.
60. Thomassin-Naggara I, Poncelet E, Jalaguier-Coudray A, et al. Ovarian-adnexal reporting data system magnetic resonance imaging (O-RADS MRI) score for risk stratification of sonographically indeterminate adnexal masses. JAMA Netw Open. 2020;3:e1919896.
61. Timmerman D, Testa AC, Bourne T, et al. Simple ultrasound-based rules for the diagnosis of ovarian cancer. Ultrasound Obstet Gynecol. 2008;31:681–90.
62. Timmerman D, Ameye L, Fischerova D, et al. Simple ultrasound rules to distinguish between benign and malignant adnexal masses before surgery: prospective validation by IOTA group. BMJ. 2010;341:c6839.
63. Forstner R, Thomassin-Naggara I, Cunha TM, Kinkel K, Masselli G, Kubik-Huch R, Spencer JA, Rockall A. ESUR recommendations for MR imaging of the sonographically indeterminate adnexal mass: an update. Eur Radiol. 2017;27:2248–57.
64. Kubik-Huch RA, Weston M, Nougaret S, Leonhardt H, Thomassin-Naggara I, Horta M, Cunha TM, Maciel C, Rockall A, Forstner R. European Society of Urogenital Radiology (ESUR) guidelines: MR imaging of leiomyomas. Eur Radiol. 2018;28:3125–37.
65. Forstner R. CT and MRI in ovarian carcinoma. In: Forstner R, Cunha TM, Hamm B, editors. MRI CT female pelvis. Cham: Springer International; 2019. p. 287–323.
66. Hennessy BT, Coleman RL, Markman M. Ovarian Cancer Lancet. 2009;374:1371–82.
67. Jung SE, Lee JM, Rha SE, Byun JY, Jung JI, Hahn ST. CT and MR imaging of ovarian tumors with emphasis on differential diagnosis. Radiographics. 2002;22:1305–25.
68. Seidman JD, Ronnett BM, Shih I-M, Cho KR, Kurman RJ. Epithelial tumors of the ovary. In: Kurman RJ, Hedrick Ellenson L, Ronnett BM, editors. Blaustein's pathology of the female genital tract. Cham: Springer International; 2019. p. 841–966.

69. Kurman RJ, International Agency for Research on Cancer, World Health Organization, editors. WHO classification of tumours of female reproductive organs. 4th ed. Lyon: International Agency for Research on Cancer; 2014.
70. Jeong YY, Outwater EK, Kang HK. Imaging evaluation of ovarian masses. Radiographics. 2000;20:1445–70.
71. Foti PV, Attinà G, Spadola S, et al. MR imaging of ovarian masses: classification and differential diagnosis. Insights Imaging. 2016;7:21–41.
72. Outwater EK, Huang AB, Dunton CJ, Talerman A, Capuzzi DM. Papillary projections in ovarian neoplasms: appearance on MRI. J Magn Reson Imaging. 1997;7:689–95.
73. Thomassin-Naggara I, Daraï E, Cuenod CA, Rouzier R, Callard P, Bazot M. Dynamic contrast-enhanced magnetic resonance imaging: a useful tool for characterizing ovarian epithelial tumors. J Magn Reson Imaging. 2008;28:111–20.
74. Wasnik AP, Menias CO, Platt JF, Lalchandani UR, Bedi DG, Elsayes KM. Multimodality imaging of ovarian cystic lesions: review with an imaging based algorithmic approach. World J Radiol. 2013;5:113–25.
75. Schlattau A, Cunha TM, Forstner R. Adnexal masses: benign ovarian lesions and characterization. In: Forstner R, Cunha TM, Hamm B, editors. MRI CT female pelvis. Cham: Springer International; 2019. p. 241–71.
76. Laurent P-E, Thomassin-Piana J, Jalaguier-Coudray A. Mucin-producing tumors of the ovary: MR imaging appearance. Diagn Interv Imaging. 2015;96:1125–32.
77. Shen DH, Ng TY, Khoo US, Xue WC, Cheung AN. Pseudomyxoma peritonei—a heterogenous disease. Int J Gynaecol Obstet. 1998;62:173–82.
78. Tang YZ, Liyanage S, Narayanan P, Sahdev A, Sohaib A, Singh N, Rockall A. The MRI features of histologically proven ovarian cystadenofibromas-an assessment of the morphological and enhancement patterns. Eur Radiol. 2013;23:48–56.
79. Tanaka YO, Yoshizako T, Nishida M, Yamaguchi M, Sugimura K, Itai Y. Ovarian carcinoma in patients with endometriosis: MR imaging findings. AJR Am J Roentgenol. 2000;175:1423–30.
80. Shaaban AM. Ovarian endometrioid carcinoma. Diagn Imaging Gynecol. 2014.
81. Maniar KP, Vang R. Germ cell tumors of the ovary. In: Kurman RJ, Hedrick Ellenson L, Ronnett BM, editors. Blaustein's pathology of the female genital tract. Cham: Springer International; 2019. p. 1047–124.
82. Boussios S, Attygalle A, Hazell S, Moschetta M, McLachlan J, Okines A, Banerjee S. Malignant ovarian germ cell tumors in postmenopausal patients: the Royal Marsden Experience and literature review. Anticancer Res. 2015;35:6713–22.
83. Smith HO, Berwick M, Verschraegen CF, Wiggins C, Lansing L, Muller CY, Qualls CR. Incidence and survival rates for female malignant germ cell tumors. Obstet Gynecol. 2006;107:1075–85.
84. Ozgur T, Atik E, Silfeler DB, Toprak S. Mature cystic teratomas in our series with review of the literature and retrospective analysis. Arch Gynecol Obstet. 2012;285:1099–101.
85. Saba L, Guerriero S, Sulcis R, Virgilio B, Melis G, Mallarini G. Mature and immature ovarian teratomas: CT, US and MR imaging characteristics. Eur J Radiol. 2009;72:454–63.
86. Tamai K, Koyama T, Saga T, Kido A, Kataoka M, Umeoka S, Fujii S, Togashi K. MR features of physiologic and benign conditions of the ovary. Eur Radiol. 2006;16:2700–11.
87. Wei F, Jiang Z, Yan C. Analysis of 20 mature ovarian cystic teratoma cases in postmenopausal women. Chin Med J (Engl). 2001;114:137–8.
88. Park SB, Kim JK, Kim K-R, Cho K-S. Imaging findings of complications and unusual manifestations of ovarian teratomas. Radiographics. 2008;28:969–83.
89. Outwater EK, Wagner BJ, Mannion C, McLarney JK, Kim B. Sex cord-stromal and steroid cell tumors of the ovary. Radiographics. 1998;18:1523–46.
90. Jung SE, Rha SE, Lee JM, Park SY, Oh SN, Cho KS, Lee EJ, Byun JY, Hahn ST. CT and MRI findings of sex cord-stromal tumor of the ovary. AJR Am J Roentgenol. 2005;185:207–15.
91. Schumer ST, Cannistra SA. Granulosa cell tumor of the ovary. J Clin Oncol Off J Am Soc Clin Oncol. 2003;21:1180–9.

92. Staats PN, Young RH. Sex cord-stromal, steroid cell, and other ovarian tumors with endocrine, paraendocrine, and paraneoplastic manifestations. In: Kurman RJ, Hedrick Ellenson L, Ronnett BM, editors. Blaustein's pathology of the female genital tract. Cham: Springer International; 2019. p. 967–1045.
93. Troiano RN, Lazzarini KM, Scoutt LM, Lange RC, Flynn SD, McCarthy S. Fibroma and fibrothecoma of the ovary: MR imaging findings. Radiology. 1997;204:795–8.
94. Chang HC, Bhatt S, Dogra VS. Pearls and pitfalls in diagnosis of ovarian torsion. Radiographics. 2008;28:1355–68.
95. Cohen A, Solomon N, Almog B, Cohen Y, Tsafrir Z, Rimon E, Levin I. Adnexal torsion in postmenopausal women: clinical presentation and risk of ovarian malignancy. J Minim Invasive Gynecol. 2017;24:94–7.
96. Baines PA, Allen GM. Pelvic pain and menstrual related illnesses. Emerg Med Clin North Am. 2001;19:763–80.
97. Rha SE, Byun JY, Jung SE, Jung JI, Choi BG, Kim BS, Kim H, Lee JM. CT and MR imaging features of adnexal torsion. Radiographics. 2002;22:283–94.
98. Dawood MT, Naik M, Bharwani N, Sudderuddin SA, Rockall AG, Stewart VR. Adnexal torsion: review of radiologic appearances. Radiographics. 2021;41:609–24.
99. Mashiach R, Melamed N, Gilad N, Ben-Shitrit G, Meizner I. Sonographic diagnosis of ovarian torsion: accuracy and predictive factors. J Ultrasound Med. 2011;30:1205–10.
100. Vandermeer FQ, Wong-You-Cheong JJ. Imaging of acute pelvic pain. Clin Obstet Gynecol. 2009;52:2–20.
101. Moribata Y, Kido A, Yamaoka T, Mikami Y, Himoto Y, Kataoka M, Fujimoto K, Konishi I, Togashi K. MR imaging findings of ovarian torsion correlate with pathological hemorrhagic infarction. J Obstet Gynaecol Res. 2015;41:1433–9.
102. Jackson SL, Soper DE. Pelvic inflammatory disease in the postmenopausal woman. Infect Dis Obstet Gynecol. 1999;7:248–52.
103. Wilbur AC, Aizenstein RI, Napp TE. CT findings in tuboovarian abscess. AJR Am J Roentgenol. 1992;158:575–9.
104. Bennett GL, Slywotzky CM, Giovanniello G. Gynecologic causes of acute pelvic pain: spectrum of CT findings. Radiographics. 2002;22:785–801.
105. Kim SH, Kim SH, Yang DM, Kim KA. Unusual causes of tubo-ovarian abscess: CT and MR imaging findings. Radiographics. 2004;24:1575–89.
106. Dohke M, Watanabe Y, Okumura A, Amoh Y, Hayashi T, Yoshizako T, Yasui M, Nakashita S, Nakanishi J, Dodo Y. Comprehensive MR imaging of acute gynecologic diseases. Radiographics. 2000;20:1551–66.
107. Rezvani M, Shaaban AM. Fallopian tube disease in the nonpregnant patient. Radiographics. 2011;31:527–48.
108. Fogel SR, Slasky BS. Sonography of Nabothian cysts. AJR Am J Roentgenol. 1982;138:927–30.
109. Kier R. Nonovarian gynecologic cysts: MR imaging findings. AJR Am J Roentgenol. 1992;158:1265–9.
110. Sudderuddin S, Helbren E, Telesca M, Williamson R, Rockall A. MRI appearances of benign uterine disease. Clin Radiol. 2014;69:1095–104.
111. Van den Bosch T, de Bruijn AM, de Leeuw RA, Dueholm M, Exacoustos C, Valentin L, Bourne T, Timmerman D, Huirne J. Sonographic classification and reporting system for diagnosing adenomyosis. Ultrasound Obstet Gynecol. 2019;53:576–82.
112. Cova MA, Marrocchio C, Bozzato AM. Female genital system. MRI Abdomen Tech. Imaging Find; 2021.
113. Kröncke TJ. Benign uterine lesions. In: Hamm B, Forstner R, editors. MRI CT female pelvis. Berlin, Heidelberg: Springer; 2007. p. 61–100.
114. Agostinho L, Cruz R, Osório F, Alves J, Setúbal A, Guerra A. MRI for adenomyosis: a pictorial review. Insights Imaging. 2017;8:549–56.
115. Takeuchi M, Matsuzaki K. Adenomyosis: usual and unusual imaging manifestations, pitfalls, and problem-solving MR imaging techniques. Radiographics. 2011;31:99–115.

116. Reinhold C, Tafazoli F, Wang L. Imaging features of adenomyosis. Hum Reprod Update. 1998;4:337–49.
117. Kinkel K, Ascher SM, Reinhold C. Benign disease of the uterus. In: Diseases of the abdomen and pelvis 2018-2021: diagnostic imaging—IDKD book. Cham: Springer; 2018.
118. Reinhold C, Tafazoli F, Mehio A, Wang L, Atri M, Siegelman ES, Rohoman L. Uterine adenomyosis: endovaginal US and MR imaging features with histopathologic correlation. Radiographics. 1999;19:S147–60.
119. Kröncke TJ. Benign uterine lesions. In: Forstner R, Cunha TM, Hamm B, editors. MRI CT female pelvis. Cham: Springer International; 2017. p. 77–116.
120. Peterson M, Dabbs DJ, Weidner N. Uterus. In: Modern surgical pathology. Philadelphia: WB Saunders; 2009. p. 1295–340.
121. Robertson M, Scott P, Ellwood DA, Low S. Endocervical polyp in pregnancy: gray scale and color Doppler images and essential considerations in pregnancy. Ultrasound Obstet Gynecol. 2005;26:583–4.
122. Otero-García MM, Mesa-Álvarez A, Nikolic O, Blanco-Lobato P, Basta-Nikolic M, de Llano-Ortega RM, Paredes-Velázquez L, Nikolic N, Szewczyk-Bieda M. Role of MRI in staging and follow-up of endometrial and cervical cancer: pitfalls and mimickers. Insights Imaging. 2019;10:19.
123. Deshmukh SP, Gonsalves CF, Guglielmo FF, Mitchell DG. Role of MR imaging of uterine leiomyomas before and after embolization. Radiographics. 2012;32:E251–81.
124. Wilde S, Scott-Barrett S. Radiological appearances of uterine fibroids. Indian J Radiol Imaging. 2009;19:222–31.
125. DeMulder D, Ascher SM. Uterine Leiomyosarcoma: can MRI differentiate Leiomyosarcoma from benign leiomyoma before treatment? AJR Am J Roentgenol. 2018;211:1405–15.
126. Nougaret S, Sbarra M, Robbins J. Imaging Spectrum of benign uterine disease and treatment options. Radiol Clin North Am. 2020;58:239–56.
127. Bharambe BM, Deshpande KA, Surase SG, Ajmera AP. Malignant transformation of leiomyoma of uterus to leiomyosarcoma with metastasis to ovary. J Obstet Gynaecol India. 2014;64:68–9.
128. Leibsohn S, d'Ablaing G, Mishell DR, Schlaerth JB. Leiomyosarcoma in a series of hysterectomies performed for presumed uterine leiomyomas. Am J Obstet Gynecol. 1990;162:968–74; discussion 974–976.
129. Santos P, Cunha TM. Uterine sarcomas: clinical presentation and MRI features. Diagn Interv Radiol Ank Turk. 2015;21:4–9.
130. Morice P, Leary A, Creutzberg C, Abu-Rustum N, Darai E. Endometrial cancer. Lancet. 2016;387:1094–108.
131. Hedrick Ellenson L, Ronnett BM, Soslow RA, Lastra RR, Kurman RJ. Endometrial carcinoma. In: Kurman RJ, Hedrick Ellenson L, Ronnett BM, editors. Blaustein's pathology of the female genital tract. Cham: Springer International; 2019. p. 473–533.
132. Amant F, Mirza MR, Koskas M, Creutzberg CL. Cancer of the corpus uteri. Int J Gynaecol Obstet. 2018;143(Suppl 2):37–50.
133. Horta M, Cunha TM. Endometrial cancer. In: Forstner R, Cunha TM, Hamm B, editors. MRI CT female pelvis. Cham: Springer International; 2017. p. 179–208.
134. Aune D, Sen A, Vatten LJ. Hypertension and the risk of endometrial cancer: a systematic review and meta-analysis of case-control and cohort studies. Sci Rep. 2017;7:44808.
135. McCartney CR, Marshall JC. Polycystic ovary syndrome. N Engl J Med. 2016;375:1398–9.
136. Nougaret S, Horta M, Sala E, et al. Endometrial cancer MRI staging: updated guidelines of the European Society of Urogenital Radiology. Eur Radiol. 2019;29:792–805.
137. Freeman SJ, Aly AM, Kataoka MY, Addley HC, Reinhold C, Sala E. The revised FIGO staging system for uterine malignancies: implications for MR imaging. Radiographics. 2012;32:1805–27.
138. Arbyn M, Weiderpass E, Bruni L, de Sanjosé S, Saraiya M, Ferlay J, Bray F. Estimates of incidence and mortality of cervical cancer in 2018: a worldwide analysis. Lancet Glob Health. 2020;8:e191–203.

139. Collettini F, Hamm B. Cervical cancer. In: Forstner R, Cunha TM, Hamm B, editors. MRI CT female pelvis. Cham: Springer International; 2019. p. 117–77.
140. Pirog EC, Wright TC, Ronnett BM, Kurman RJ. Carcinoma and other tumors of the cervix. In: Kurman RJ, Hedrick Ellenson L, Ronnett BM, editors. Blaustein's pathology of the female genital tract. Cham: Springer International; 2019. p. 315–74.
141. Hinkula M, Pukkala E, Kyyrönen P, Laukkanen P, Koskela P, Paavonen J, Lehtinen M, Kauppila A. A population-based study on the risk of cervical cancer and cervical intraepithelial neoplasia among grand multiparous women in Finland. Br J Cancer. 2004;90:1025–9.
142. Li S, Wen X. Seropositivity to herpes simplex virus type 2, but not type 1 is associated with cervical cancer: NHANES (1999-2014). BMC Cancer. 2017;17:726.
143. Burghardt E, Ostör AG. Site and origin of squamous cervical cancer: a histomorphologic study. Obstet Gynecol. 1983;62:117–27.
144. Balleyguier C, Sala E, Da Cunha T, et al. Staging of uterine cervical cancer with MRI: guidelines of the European Society of Urogenital Radiology. Eur Radiol. 2011;21:1102–10.
145. Haldorsen IS, Lura N, Blaakær J, Fischerova D, Werner HMJ. What is the role of imaging at primary diagnostic work-up in uterine cervical cancer? Curr Oncol Rep. 2019;21:77.
146. Bhatla N, Berek JS, Cuello Fredes M, et al. Revised FIGO staging for carcinoma of the cervix uteri. Int J Gynaecol Obstet. 2019;145:129–35.
147. Edge SB, Compton CC. The American joint committee on cancer: the 7th edition of the AJCC cancer staging manual and the future of TNM. Ann Surg Oncol. 2010;17:1471–4.
148. Adams TS, Rogers LJ, Cuello MA. Cancer of the vagina: 2021 update. Int J Gynaecol Obstet. 2021;155(Suppl 1):19–27.
149. Hacker NF, Eifel PJ, van der Velden J. Cancer of the vagina. Int J Gynaecol Obstet. 2012;119(Suppl 2):S97–9.
150. Adhikari P, Vietje P, Mount S. Premalignant and malignant lesions of the vagina. Diagn Histopathol. 2017;23:28–34.
151. Gardner CS, Sunil J, Klopp AH, Devine CE, Sagebiel T, Viswanathan C, Bhosale PR. Primary vaginal cancer: role of MRI in diagnosis, staging and treatment. Br J Radiol. 2015;88:20150033.
152. Parikh JH, Barton DPJ, Ind TEJ, Sohaib SA. MR imaging features of vaginal malignancies. Radiographics. 2008;28:49–63; quiz 322.
153. Dixit S, Singhal S, Baboo HA. Squamous cell carcinoma of the vagina: a review of 70 cases. Gynecol Oncol. 1993;48:80–7.
154. Amin MB, American Joint Committee on Cancer, American Cancer Society. In: Amin MB, Edge SB, Gress DM, Meyer LR, editors. AJCC cancer staging manual. 8th ed. Chicago IL: American Joint Committee on Cancer, Springer; 2017.
155. FIGO Committee on Gynecologic Oncology. Current FIGO staging for cancer of the vagina, fallopian tube, ovary, and gestational trophoblastic neoplasia. Int J Gynaecol Obstet. 2009;105:3–4.
156. Al-Kurdi M, Monaghan JM. Thirty-two years experience in management of primary tumours of the vagina. Br J Obstet Gynaecol. 1981;88:1145–50.
157. Davis KP, Stanhope CR, Garton GR, Atkinson EJ, O'Brien PC. Invasive vaginal carcinoma: analysis of early-stage disease. Gynecol Oncol. 1991;42:131–6.
158. Chyle V, Zagars GK, Wheeler JA, Wharton JT, Delclos L. Definitive radiotherapy for carcinoma of the vagina: outcome and prognostic factors. Int J Radiat Oncol Biol Phys. 1996;35:891–905.
159. Rogers LJ, Cuello MA. Cancer of the vulva. Int J Gynaecol Obstet. 2018;143(Suppl 2):4–13.
160. Tan A, Bieber AK, Stein JA, Pomeranz MK. Diagnosis and management of vulvar cancer: a review. J Am Acad Dermatol. 2019;81:1387–96.
161. Alkatout I, Schubert M, Garbrecht N, Weigel MT, Jonat W, Mundhenke C, Günther V. Vulvar cancer: epidemiology, clinical presentation, and management options. Int J Womens Health. 2015;7:305–13.
162. Serrado MA, Horta M, Cunha TM. State of the art in vulvar cancer imaging. Radiol Bras. 2019;52:316–24.

163. Viswanathan C, Kirschner K, Truong M, Balachandran A, Devine C, Bhosale P. Multimodality imaging of vulvar cancer: staging, therapeutic response, and complications. AJR Am J Roentgenol. 2013;200:1387–400.
164. Buy JN, Ghossain M. Premalignant and malignant tumors of the vulva. In: Buy JN, Ghossain M, editors. Gynaecological imaging: a reference guide to diagnosis. Berlin Heidelberg: Springer; 2013. p. 801–7.
165. Griffin N, Grant LA, Sala E. Magnetic resonance imaging of vaginal and vulval pathology. Eur Radiol. 2008;18:1269–80.
166. García del Salto L, de Miguel CJ, Aguilera del Hoyo LF, Gutiérrez Velasco L, Fraga Rivas P, Manzano Paradela M, Vacas MI, Marco Sanz AG, Fraile Moreno E. MR imaging-based assessment of the female pelvic floor. Radiographics. 2014;34:1417–39.
167. Salvador JC, Coutinho MP, Venâncio JM, Viamonte B. Dynamic magnetic resonance imaging of the female pelvic floor-a pictorial review. Insights Imaging. 2019;10:4.
168. Boyadzhyan L, Raman SS, Raz S. Role of static and dynamic MR imaging in surgical pelvic floor dysfunction. Radiographics. 2008;28:949–67.
169. Doshani A, Teo REC, Mayne CJ, Tincello DG. Uterine prolapse. BMJ. 2007;335:819–23.
170. Maglinte DDT, Bartram CI, Hale DA, Park J, Kohli MD, Robb BW, Romano S, Lappas JC. Functional imaging of the pelvic floor. Radiology. 2011;258:23–39.

Osteoarthritis in Axial Skeleton in Geriatric Patients

12

Francesca Serpi, Salvatore Gitto, and Luca Maria Sconfienza

12.1 Degenerative Pathology

With the increase in life expectancy, degenerative pathologies of the spine are becoming more and more common during clinical practice, with a high medical and socioeconomic impact.

Degenerative changes in the spine are usually associated with back pain and/or symptoms of neural structure compression, caused by anatomical and biomechanical alterations.

Imaging the degenerative spine might be quite challenging. In fact, the presence of symptoms and pain does not always correspond to abnormal findings at imaging, as well as the presence of degenerative imaging changes does not necessarily correlate with the presence and the severity of pain. In addition, sometimes it is not easy to discriminate between imaging findings of normal aging and degenerative pathology.

The spine is a multiarticular structure, which enables motions in different directions and absorbs multidirectional loads. Specifically, two adjacent vertebrae, the intervertebral disc, spinal ligaments, and facet joints between them constitute a *functional spinal unit* [1].

The main functions of the spine are to provide structural support, enable trunk movement, and protect the neural elements [2].

Approximately 70% of applied axial compression is transmitted by the vertebral body and the intervertebral disc, with the remaining 30% of the load being distributed through the facet joints (Fig. 12.1) [3].

F. Serpi · S. Gitto · L. M. Sconfienza (✉)
Unit of Diagnostic and Interventional Radiology, IRCCS Ospedale Galeazzi-Sant'Ambrogio, Milan, Italy

Department of Biomedical Sciences for Health, Università degli Studi di Milano, Milan, Italy
e-mail: io@lucasconfienza.it

G. Guglielmi, M. Maas (eds.), *Imaging in Geriatrics*, Practical Issues in Geriatrics, https://doi.org/10.1007/978-3-031-14877-4_12

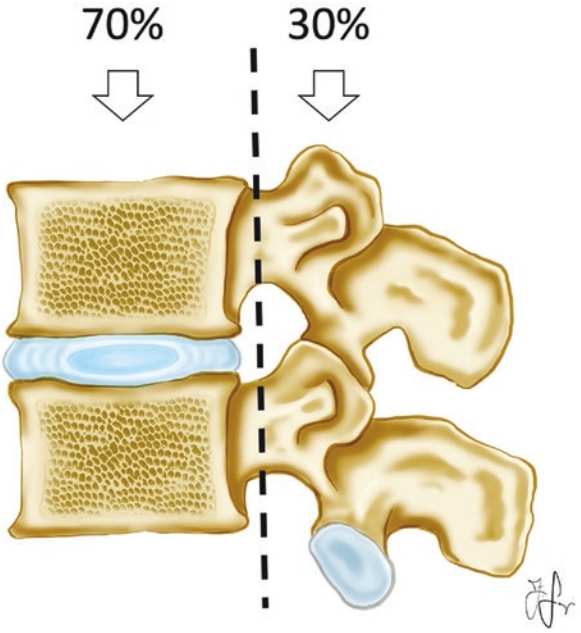

Fig. 12.1 Schematic representation of a functional spinal unit. Axial compression is transmitted 70% by vertebral body and the intervertebral disc, 30% of load is distributed through the facet joints

Degenerative changes are considered an adaptive response to insults, such as mechanical (micro or macro-insults) or metabolic injuries (chondrosis or mucopolysaccharidoses), rather than a true disease [4].

In the majority of cases, degenerative changes are related to mechanic causes, such as chronic micro-insults, trauma, and vertebral fractures or load redistribution that occurs after spinal surgery.

It is important to notice that the pathogenesis of the degenerative process represents a biomechanically related continuum of anatomical alterations that evolves over time [3]. A good knowledge of the pathophysiology of these biomechanical changes in the spine is essential for radiologists to characterize radiological abnormalities. Therefore, degenerative changes should not be considered as an isolated event or reported as a random finding. All elements of the spine, including the intervertebral discs, facet joints, ligaments, and bony structures, may undergo morphological changes that can be classified as degenerative. However, in the majority of cases the degenerative process starts within the nucleus pulposus and progresses to the other elements of the functional spinal unit (horizontal or segmental degeneration) [5–7], such as the annulus fibrosus, endplates, and bone marrow of the adjacent vertebral bodies. Advanced degeneration may eventually lead to facet joint osteoarthrosis, ligamentum flavum hypertrophy, and spinal canal stenosis [3].

Degenerative changes can also alter the entire biomechanics of the spine, including the adjacent functional spinal units (adjacent segment disease) [8, 9].

12.2 Functional Spinal Unit

12.2.1 Intervertebral Disc

12.2.1.1 Anatomy and Pathophysiology

Intervertebral discs are located between adjacent vertebral bodies, acting as shock absorbers. They are complex structures composed of nucleus pulposus, annulus fibrosus, cartilaginous endplates, and vertebral body ring apophyseal attachments of the annulus [10]. The intervertebral disc is mainly avascular and supplied by passive diffusion from the vertebral endplates. The L4/L5 disc space is the largest avascular structure in the body. Therefore, all structural changes are usually irreversible as adult discs have limited healing potential [3]. A normal nucleus pulposus is a gelatinous structure with high viscosity and elasticity, comprised of proteoglycans and intermolecular water (up to 80%), which acts hydrostatically by transmitting mechanical forces evenly to the annulus fibrosus and endplates in every direction. Abnormal mechanical axial stress impairs nucleus biochemical turnover and composition. As degeneration progresses, the nucleus pulposus becomes dehydrated and results in reduced intradiscal pressure, thus passing the mechanical load to the annulus fibrosus which acts like a fibrous solid to resist compression directly [3].

Each annulus fibrosus comprises 15–20 collagenous laminae running obliquely from the edge of one vertebra down to the edge of the vertebra below and merging anteriorly and posteriorly with longitudinal ligaments. Increased stress on the annulus fibrosus may lead to cracks and cavities in the fibers, subsequently progresses with clefts and fissures [11]. Inhomogeneous mechanical stress on the annulus fibrosus and on their insertion on the vertebral body can produce hyperplastic changes at the edges of the vertebral body with osteophytes formation [3]. Moreover, this loss of fibers structural integrity of the annulus fibrosus may favorite disc herniation and failure to maintain anatomical alignment and vertebral position, leading to instability and/or spondylolisthesis [3].

12.2.1.2 Imaging

At imaging, normal nucleus pulposus has a hyperintense signal on T2-weighed images (WI), which directly correlates with proteoglycan and subsequently water concentration. **Disc dehydration** corresponds to progressive signal loss on T2-WI and loss of disc height [12].

Pfirrmann et al. developed a grading system for lumbar disc degeneration according to magnetic resonance imaging (MRI) T2-WI, discal structure, distinction between nucleus pulposus and annulus fibrosus and disc height (Table 12.1) [13].

Other imaging signs that can be associated with disc degenerations are: the **vacuum phenomenon** (Fig. 12.2), accumulation of nitrogen within the disc, which can be visible both on X-ray and computed tomography (CT) as the presence of gas within the disc and represented as a signal void on both T1 and T2-WI at MRI [14, 15]; **intradiscal fluid accumulation**, with hyperintense signal at T2-WI, which can be associated with endplates degeneration, mimicking early spondylodiscitis [15]; **intradiscal calcification** (Fig. 12.2), which frequently involves the annulus fibrosus and is located in the lower part of the thoracic spine [16].

Table 12.1 Classification of disc degeneration at MRI

Grade	Structure	Distinction of nucleus and anulus	Signal intensity	Height of intervertebral disc
I	Homogeneous, bright white	Clear	Hyperintense, isointense to cerebrospinal fluid	Normal
II	Inhomogeneous with or without horizontal bands	Clear	Hyperintense, isointense to cerebrospinal fluid	Normal
III	Inhomogeneous, gray	Unclear	Intermediate	Normal to slightly decreased
IV	Inhomogeneous, gray to black	Lost	Intermediate to hypointense	Normal to moderately decreased
V	Inhomogeneous, black	Lost	Hypointense	Collapsed disc space

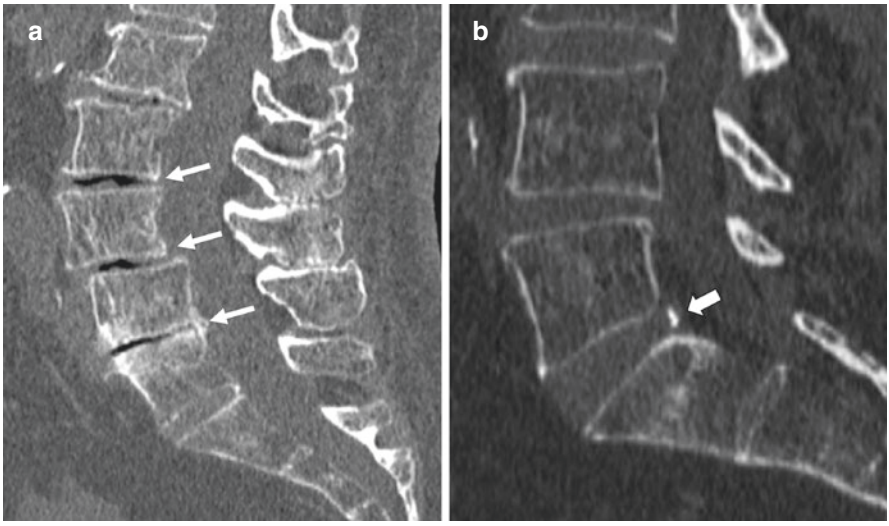

Fig. 12.2 Signs of disc degeneration. The vacuum phenomenon is due to the accumulation of nitrogen within the disc (arrows), represented as air density within the disc in CT (**a**). Intradiscal calcification typically involve the annulus fibrosus, as in this picture (arrow) at the level of the posterior fibers of the intervertebral disc L5-S1 (**b**)

A normal annulus fibrosus has a hypointense signal in all MR sequences. **Annulus fissures** can be located within the fibers or can either involve the fibers at their insertions on the adjacent endplates. The term "annular tear" should be discouraged because it might be misunderstood as an injury [10].

A small amount of fluid interposes in the annular fissure, corresponding to T2-weighted MRI scans of localized high intensity zones (HIZ) within the annulus [10]. Annulus fibrosus fissures can be circumferential, radial, or peripheral [3] or concentric, radial, or transversal, according to another classification system [10].

A *circumferential* or *concentric fissure* (Fig. 12.3) is a separation or delamination of annular transverse fibers parallel to the peripheral contour of the disc. A *radial fissure* is a vertically, horizontally, or obliquely oriented separation of annular fibers that extends from the nucleus peripherally to or through the annulus. A *peripheral* or *transverse fissure* is a horizontally oriented radial fissure, usually limited to the peripheral annulus that disrupts Sharpey's fibers (Fig. 12.4) [3, 10].

Acute fissure can be associated with pain, although the MRI appearance does not change over time, thus it is not possible to discriminate between acute and chronic fissures at imaging [3, 17].

An HIZ itself may represent the actual annular fissure or alternatively may represent vascularized fibrous tissue (granulation tissue repair) within the substance of the disc in an area adjacent to a fissure, with a positive Gadolinium contrast uptake on MRI. Therefore, visualization of an HIZ does not imply a traumatic etiology or that the disc is a source of pain [10].

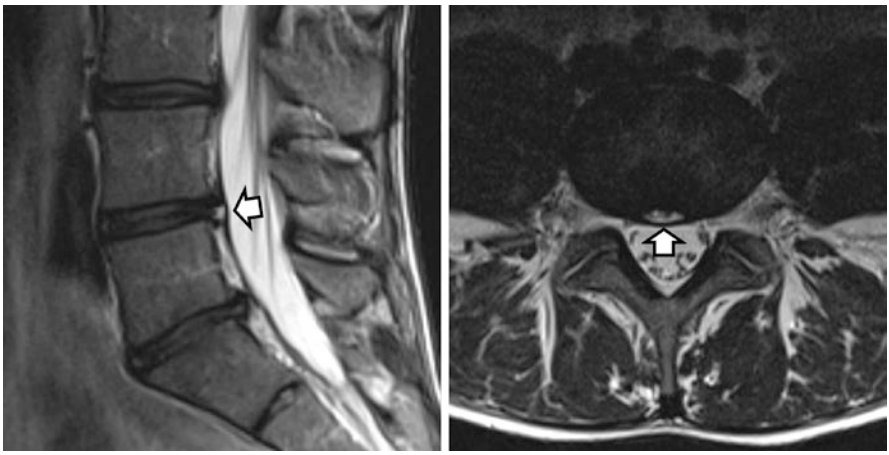

Fig. 12.3 Circumferential fissure of the posterior annular fibers at L4-L5. It consists of the separation or delamination of annular transverse fibers parallel to the peripheral contour of the disc (arrows)

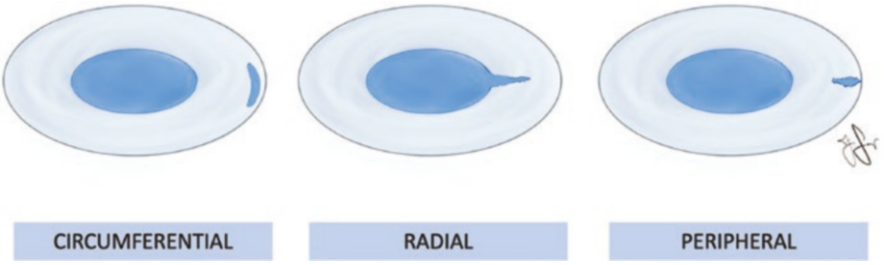

Fig. 12.4 A circumferential or concentric fissure is a separation or delamination of annular transverse fibers parallel to the peripheral contour of the disc. A radial fissure is a vertically, horizontally, or obliquely oriented separation of annular fibers that extends from the nucleus peripherally to or through the annulus. A peripheral or transverse fissure is a horizontally oriented radial fissure, usually limited to the peripheral annulus that disrupts Sharpey's fibers

12.2.1.3 Disc Displacement

Displacement of disc material beyond the normal margins of intervertebral disc space can be either diffuse ("bulging") or focal. According to the nomenclature of the combined task forces of the North American Spine Society (NASS), the American Society of Spine Radiology (ASSR), and the American Society of Neuroradiology (ASNR), the presence of disc tissue extending beyond the edges of the ring apophyses (exclusion of the osteophyte formation), throughout the circumference of the disc, is called "**bulging**" and is not considered a form of herniation [10]. On axial plane it involves more than 25% of the circumference of the disc and typically extends a relatively short distance, usually less than 3 mm, beyond the edges of the apophyses (Fig. 12.5). A bulging can be either symmetric or asymmetric. Asymmetric bulging is defined as the presence of more than 25% of the outer annulus beyond the perimeter of the adjacent vertebrae, more evident in one section of the periphery of the disc than another, but not sufficiently focal to be characterized as a protrusion [10]. Asymmetrical bulging is often seen as an adaptation to adjacent deformity, such as scoliosis.

Focal displacement, instead, refers to the extension of the disc material less than 25% of the periphery of the disc as viewed in the axial plane and it is called **disc herniation**. The herniated material may be nucleus, cartilage, fragmented apophyseal bone, annular tissue, or any combination of them (Fig. 12.6) [10].

Herniated disc can be further classified according to:

- *Shape* of the herniated material: protruded or extruded (Fig. 12.7). **Protrusion** is present when the distance between the edges of the disc herniation is less than the distance between the edges of the base. **Extrusion** is present when, at least in one plane, any distance between the edges of the disc material is greater than the

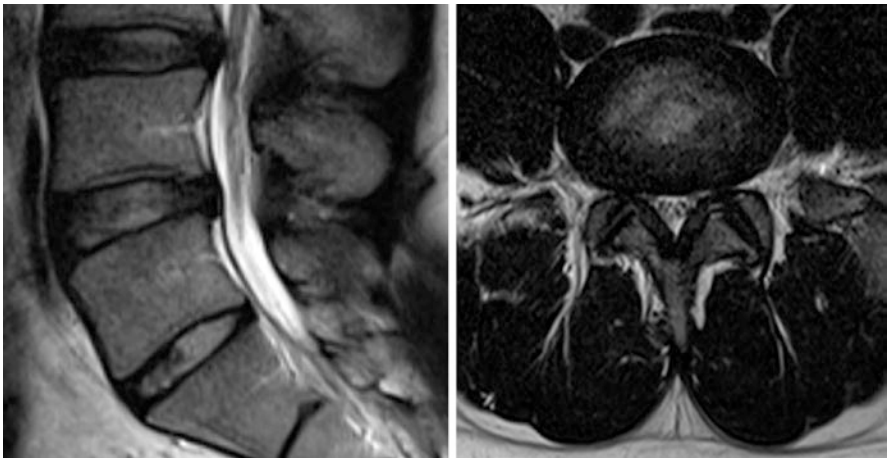

Fig. 12.5 Bulging L4-L5. A bulging refers to the presence of disc tissue extending beyond the edges of the ring apophyses, involving more than 25% of the circumference of the disc on axial plane and typically extending a relatively short distance

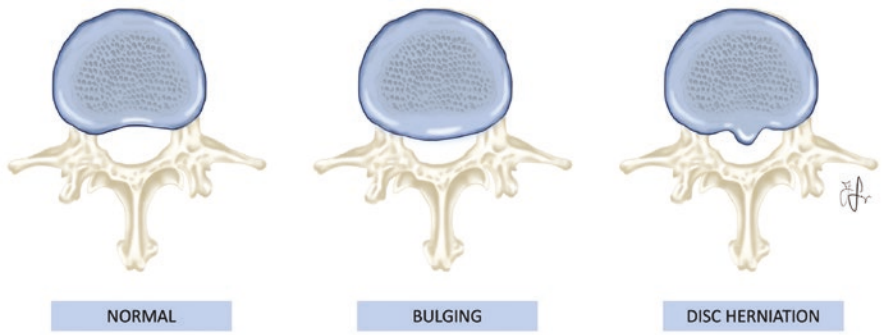

Fig. 12.6 A bulging is the presence of disc tissue extending beyond the edges of the ring apophyses more than 25% of the circumference of the disc and typically extends a relatively short distance. Disc herniation refers to the extension of disc material less than 25% of the circumference of the disc

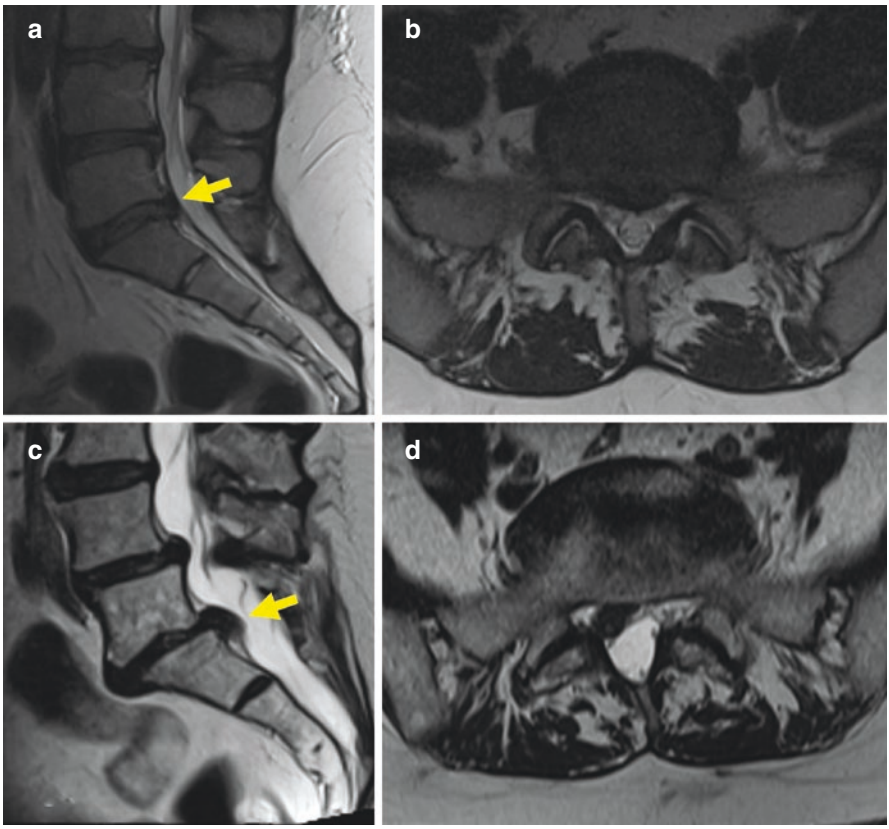

Fig. 12.7 Protrusion L5-S1 (arrow), the distance between the edges of the disc herniation is less than the distance between the edges of the base (**a**, **b**). Extrusion L5-S1 (arrow), the distance between the edges of the disc material is greater than the distance at the base, extending in the right subarticular space with possible conflict with the nerve root of S1 (**c**, **d**)

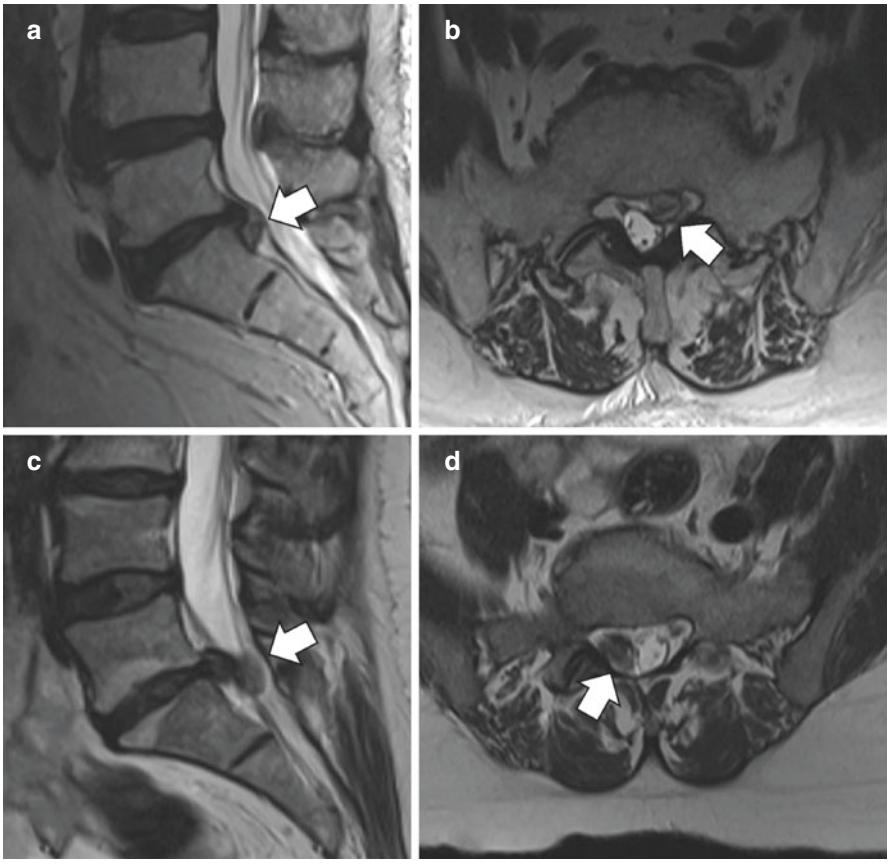

Fig. 12.8 Contained left subarticular hernia at L5-S1. L5-S1 (arrows), without transligament involvement (**a**, **b**). Uncontained right subarticular hernia at L5-S1 (arrows), with transligament caudal migration (**c**, **d**)

distance at the base [10]. Extruded hernia on the sagittal plane sometimes causes the posterior longitudinal ligament to tent, which often causes neurological symptoms and pain [3].

- *Containment*: contained or uncontained (Fig. 12.8). A hernia is **contained** if the displaced portion is covered by outer annulus fibers and/or the posterior longitudinal ligament, or **uncontained** in the absence of posterior covering. Referring specifically to the posterior longitudinal ligament, some authors have distinguished displaced disc material as subligamentous, extraligamentous, transligamentous, or perforated. The term subligamentous is favored as an equivalent to contained [10]. Due to limitation of CT and MRI, it is not always possible to discriminate between contained and uncontained herniation. Nevertheless, if the posterior margin of the herniated disc is smooth on axial plane, it is likely contained, whereas if the margins are irregular, it is likely uncontained. CT discography does not always allow to distinguish whether the herniated components of

a disc are contained, but only whether there is a communication between the disc space and the vertebral canal [10].

- *Continuity*: Extruded discs in which all continuity with the disc of origin is lost may be further characterized as "**sequestrated**." A sequestrated hernia can be either contained (subligamentous) or not. More generally, disc material displaced away from the site of extrusion, in either sagittal or axial plane, may be characterized as "**migrated**." Migration refers to the position of the displaced disc material, rather than to its continuity with the disc of origin; therefore, it is not synonymous with sequestration. A migrated disc can be sequestrated or not (Fig. 12.9) [10].
- *Volume and Composition*: Due to anatomical interindividual differences, there is no universal classification to assess spinal canal involvement. A simple scheme is to assess spinal canal compromission on axial plane. Less than one-third is considered "mild," from one- to two-third "moderate," and more than two-third "severe" [10]. Acute disc herniation has usually high water content with hyperintense signal on T2-WI and tends to dehydrated and shrink over time, which leads to progressively volume decrease and loss of signal in T2-WI.

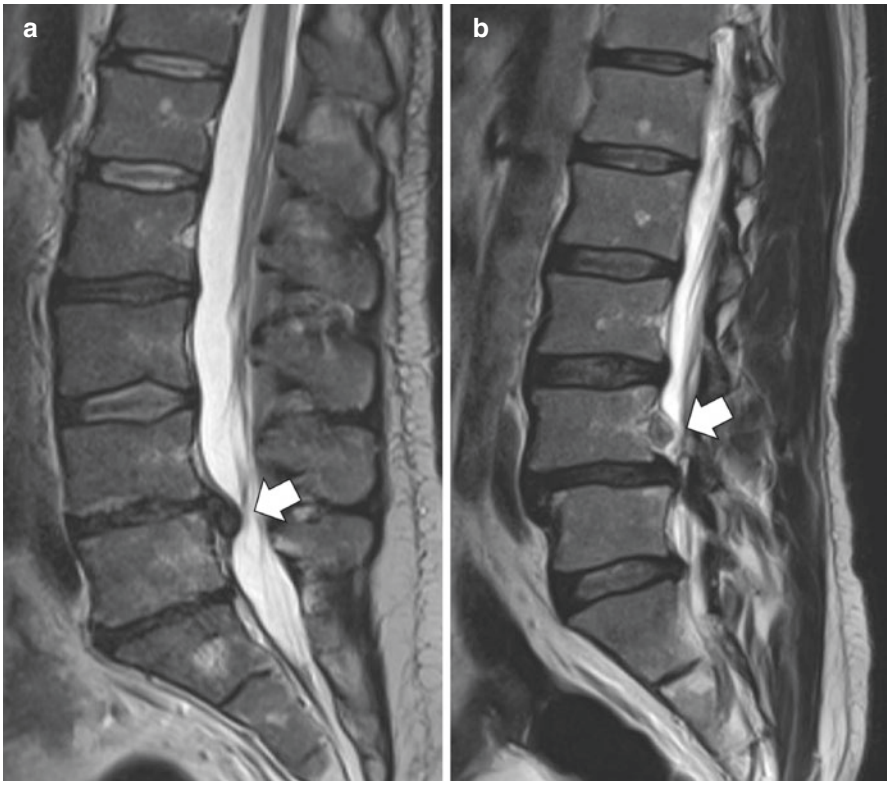

Fig. 12.9 L4-L5 hernia (arrow), caudally migrated without sequestrum (**a**). L4-L5 hernia, cranially migrated with sequestrum (arrow). The extruded material has lost the continuity with the disc of origin (**b**)

- *Location*: Based on the position of the herniation compared to anatomical landmarks, hernias can be classified on axial plane (Fig. 12.10) as central, right/left subarticular, right/left foraminal, right/left extraforaminal, or anterior. On sagittal plane (Fig. 12.11) they can be classified as discal, infrapedicular, pedicular, or suprapedicular.

Principal disc displacement characteristics and classification are summarized in Table 12.2.

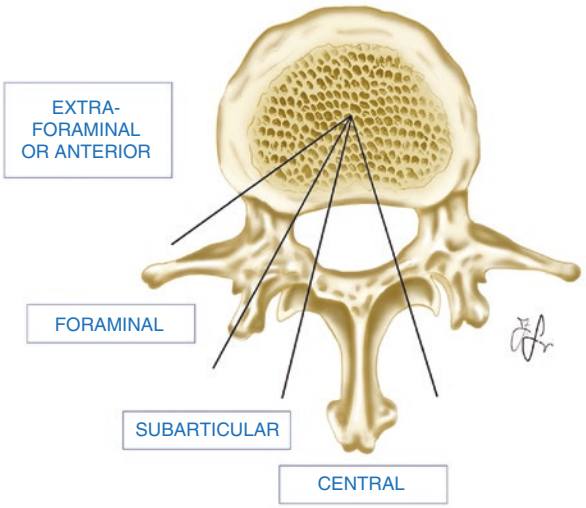

Fig. 12.10 Location of hernias classified on axial plane

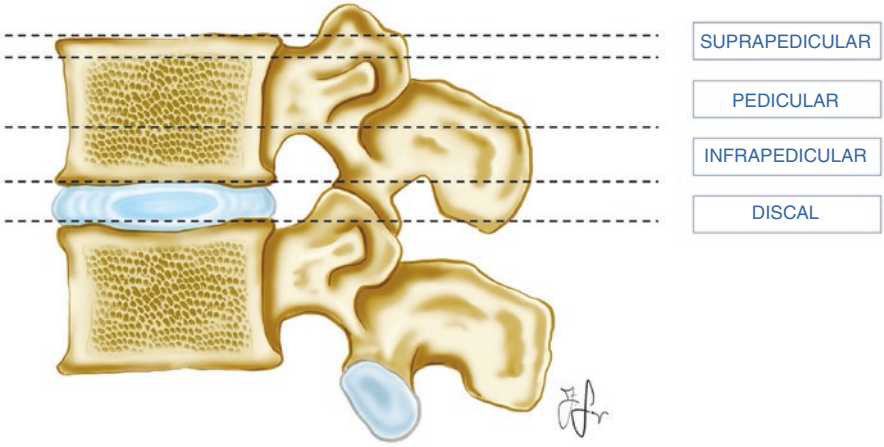

Fig. 12.11 Location of hernias classified on sagittal plane

Table 12.2 Summary of principal disc displacement characteristics and classification

Disc displacement		
Bulging (>25%)	Symmetric/ asymmetric	Asymmetric bulging: more evident in one section of the periphery of the disc than another
Hernia (<25%)	Protrusion/ extrusion	Protrusion, when the distance between the edges of the disc herniation is less than the distance between the edges of the base. Extrusion, when, at least in one plane, any distance between the edges of the disc material is greater than the distance at the base
	Contained/ uncontained	Contained, if the displaced portion is covered by outer annulus fibers and/or the posterior longitudinal ligament
		Uncontained, absence of posterior covering
	Sequestrated/ migrated	Sequestrated, extruded hernia in which all continuity with the disc of origin is lost
		Migrated disc material displaced away from the site of extrusion, independently from continuity
	Volume	Based on spinal canal compromission on axial plane: mild (<1/3), moderate (1/3–2/3), severe (>2/3)
	Composition	Acute disc herniation: high water content, hyperintense signal on T2 WI MRI
		Chronic disc herniation: dehydrated, progressively volume decreased, and loss of signal in T2 WI MRI
	Location	Axial plane: central, right left subarticular, right/left foraminal, right/left extraforaminal or anterior
		Sagittal plane: discal, infrapedicular, pedicular, or suprapedicular

12.2.1.4 Symptoms and Complications

- **Neurological complications**: Pain is usually associated with posterior/foraminal spinal cord or neural compression. Annular fissure and acute disc herniation involving the anterior aspect of the disc can also be responsible for back pain. According to pathogenesis, nerve compression is not only related to disc herniation, but it can also be caused by other etiologies, such as hypertrophic joint facet osteoarthritis or facet cysts. Indirect signs for nerve root compression are enlargement of the nerve root (pre- and post-compression) and nerve root enhancement after intravenous Gadolinium administration. The underlying mechanism for nerve enlargement and enhancement may relate to inflammation and alteration of the blood/nerve barrier [18]. In the lumbar spine, nerve roots in the intervertebral foramen are located superior to the intervertebral discs. Therefore, a foraminal herniation does not necessarily affect the nerve root. Symptoms caused by neural compression at the lumbar level has often a multifactorial etiology (disc herniation, dorsal spondylophytes, flavum ligament hypertrophy, and osteoarthritis of the facet joint). Complete absence of fat around the nerve root in the intervertebral foramen is consistent with nerve root compression in the lumbar spine [19]. In contrast, in the cervical spine the nerve roots at the intervertebral foramen are located at the same level or slightly below the interverbal discs. Therefore, a small protrusion might already cause symptoms. Fat visibility around the nerve root in the intervertebral foramen is an unreliable sign in the cervical spine [19].

  There is no universally accepted radiological definition to distinguish between acute, subacute, and chronic disc herniations. From a neurological point of view,

patients with symptoms and pain can be divided into acute (up to 4 weeks), subacute (between 4 and 12 weeks), and chronic (more than 12 weeks) [20].

- **Vascular complications:** They develop secondary to acute or chronic compression of the vertebral artery or medullary segmental arteries feeding the spinal cord (large cervical radiculomedullary at C5–C7; dominant radiculomedullary artery at T4–T5; the artery of Adamkiewicz located at T10 and the additional radiculomedullary artery of Desproges-Gotteron arises at L4–L5), which may cause a severe neurological deficit and also may require intervention [3].
- **Focal complications:** They can occur because of chronic persistent inflammation, such as epidural scarring, which may limit nerve roots passage through foramina and may cause nerve root tethering. This process is virtually impossible to identify at imaging [3]. Intradural herniation (very rare) and epidural vein varicosis are other possible focal complications [3].

12.2.2 Endplate Changes

Endplates play a crucial role to maintain the mechanical environment as well as the proper nutrition of avascular discs. With aging, spinal bodies endplates undergo changes which comprehend thinning of the endplates, focal endplate defect, and somatomarginal osteophytes, all without alteration of signal of subchondral bone marrow on MRI. On the contrary, abnormal load and stress affect vertebral endplates bone marrow, leading to histological degenerative changes. According to the Modic classification (Fig. 12.12), type I change corresponds to bone marrow edema and vascularized fibrous tissues (decreased signal intensity on T1-WI, increased signal intensity on T2-WI, and enhancement after contrast administration), type II reflects the presence of yellow marrow (increased on T1-WI, iso/hyperintense on T2-WI without contrast enhancement), and type III represents sclerotic reaction (decreased on both T1- and T2-WI). Type I is strongly associated with unspecific lumbar pain and can slowly progress to type II; however, reverse reconversion has also been reported [21]. Type I is related either to biomechanical or biochemical factor. In fact, the uneven distribution of loads due to disc degeneration creates fissures and microfractures of the endplates. Moreover, the intravertebral migration of the nucleus pulposus with high concentration of inflammatory substances results in local bone marrow inflammatory reaction [3]. Type III is stable and almost always asymptomatic [22]. Modic type I may sometimes mimic a vertebral infection. Diffusion weighted imaging (DWI) is useful for differentiating degenerative and infectious endplates bone marrow abnormalities. Modic I shows the so-called claw sign on DWI, which is a linear, well-marginated, typically paired region of restricted diffusion, situated within the adjoining vertebral bodies, at boundaries between normal marrow and vascularized endplates marrow. Typically, a slow progressive degenerative disease produces a well-defined border response. Conversely, an infection process can develop very

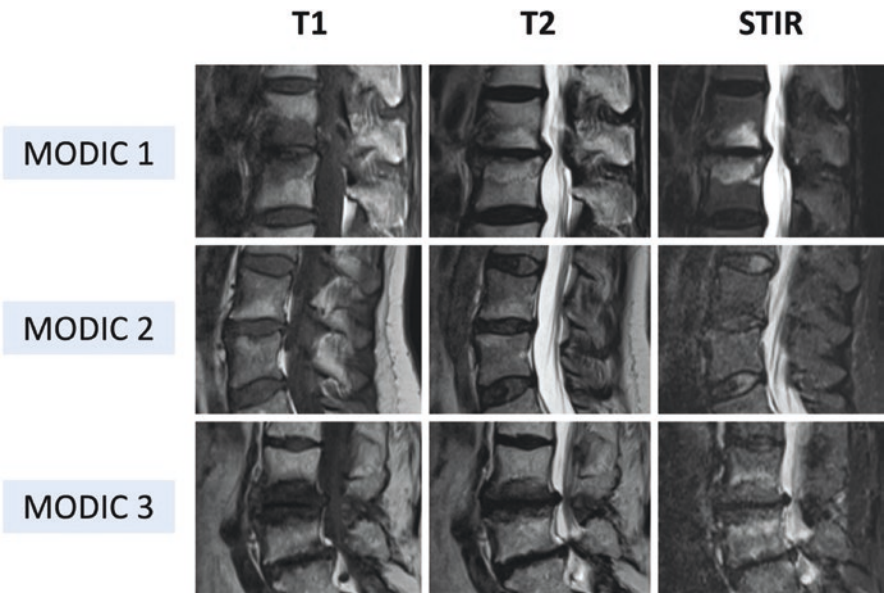

Fig. 12.12 Modic classification of endplates degenerative changes. Modic I: bone marrow edema and vascularized fibrous tissue; Modic II: yellow marrow metaplasia; Modic III: sclerotic reaction

quickly, with diffuse infiltrate of pathogens and edema of the marrow, without a well-defined border and a claw sign [3, 23, 24].

12.2.3 Facet Joints

Facet joints are true synovial joints, presented at every intervertebral level, except at C1-C2. They contribute to spinal movement and, as any other synovial articulation, they can be subjected to degenerative disease. Although facet joint osteoarthritis may occur independently and could be a source of pain on its own, it typically represents a secondary process that is associated with disc degeneration and loss of disc height [3]. The consequently altered motion and increased stress on the facet joint result in arthrosis, osteophytes, synovial cysts, and craniocaudal subluxation (Fig. 12.13) [3]. Moreover, with aging, paraspinal muscles mass decreases, which contributes to facet joint osteoarthrosis by allowing poorly controlled segmental motion [25]. Joint osteoarthrosis can be classified based on osteophytes formation and joint space narrowing [3, 26].

Degenerative synovial changes can also produce synovial cysts (Fig. 12.14), with the majority located at the lumbar (L4-L5) level. They are usually hyperintense on T2-WI but can also be hyperintense at T1-WI if they contain hemorrhagic or proteinaceous components [3]. Clinically speaking, hypertrophic facet joint osteoarthritis can determine stenosis of the canal and of the preforaminal or foraminal space, leading to symptoms related also to neural elements compression. Moreover, facet joint osteoarthritis plays an important role in spinal instability and anterior

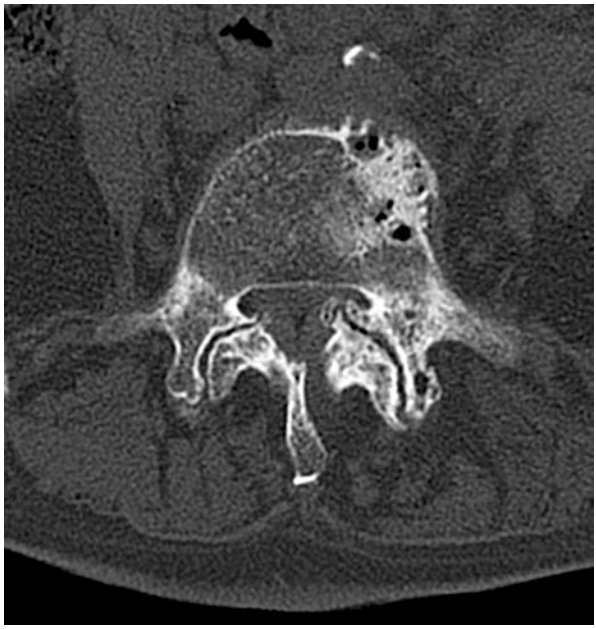

Fig. 12.13 Facet joint osteoarthritis. Severe narrowing and almost total loss of joint space, sclerosis and osteophyte formation

degenerative spondylolisthesis (Fig. 12.15). The different orientation of joint facets influences facet joints subluxation, which is more common at L4-L5, due to sagittal orientation of facet joints, rather than L5-S1, where facet joints have a coronal-oblique orientation, thus preventing forward displacement [27].

12.2.4 Ligamentum Flavum

Ligamentum flavum is also called yellow ligament, due to the high content of yellow elastin. It is composed of two adjacent laminae, extending from the second cervical vertebra to the first sacral vertebra, forming the posterior boundary of the spinal canal [3]. Degenerative disc alterations and herniation, together with facet joint osteoarthritis, determine abnormal movements and instability, which is a potential trigger for ligamentum flavum thickening (Fig. 12.16). The term "hypertrophy" should be discouraged because the degenerative process is not characterized by an enlargement of cellular elements, but by a degeneration of elastic fibers and an accumulation of collagen due to chronic inflammation; this process determines corrugation of the ligament and predisposes to calcification (Fig. 12.17) [28]. However, this can contribute to reduction of the diameter of the spinal canal and represents one of the elements that can participate in the spinal canal stenosis [3].

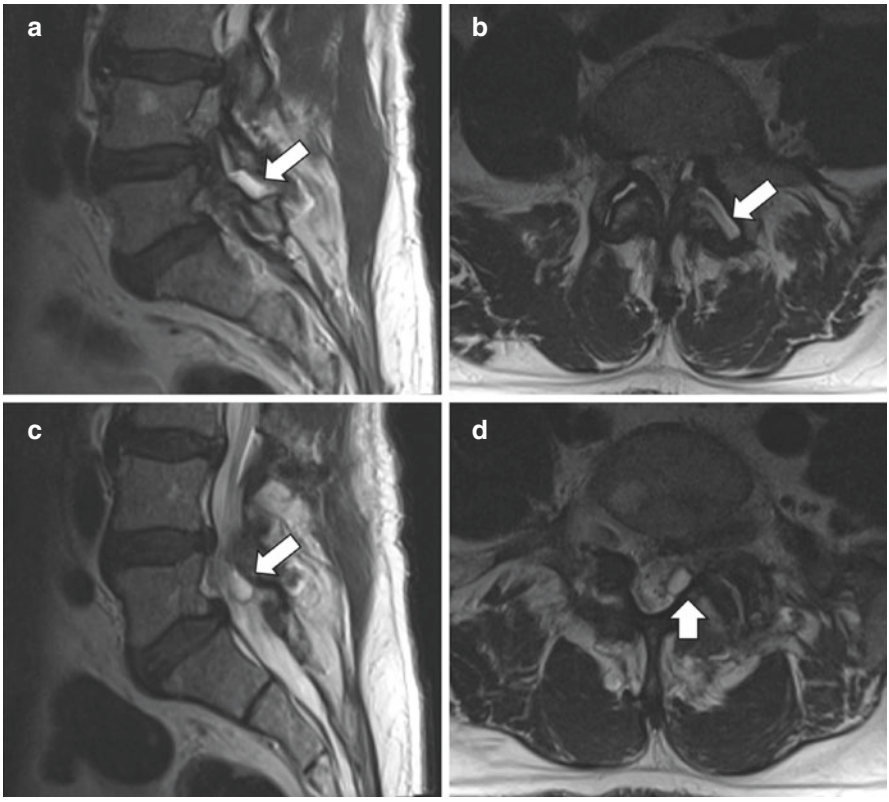

Fig. 12.14 Left facet joint fluid accumulation at L4-L5, arrows (**a**, **b**), with initial formation of a synovial cyst. In the axial plane, facet fluid is also accumulated on the right side (**b**) but in less quantity. Left facet joint synovial cyst at L4-L5 (**c**, **d**), extending in the spinal canal (arrows)

12.2.5 Interspinous Processes

Degenerative changes of the interspinous processes, also known as Baastrup disease or "kissing spine," are less common than facet joint osteoarthrosis and predominately located in the lumbar spine. They are characterized by interspinous space reduction, with marginal sclerosis, osteophytes, bony erosions, and the presence of a neosynovial joint or interspinous bursitis, visible on MRI as a concave up liquid signal between consecutive spinous processes (Figs. 12.18 and 12.19) [29]. Clinically, it is associated with lower back pain that increases with extension or after pressing the spinous processes and that is relieved in flexion [29].

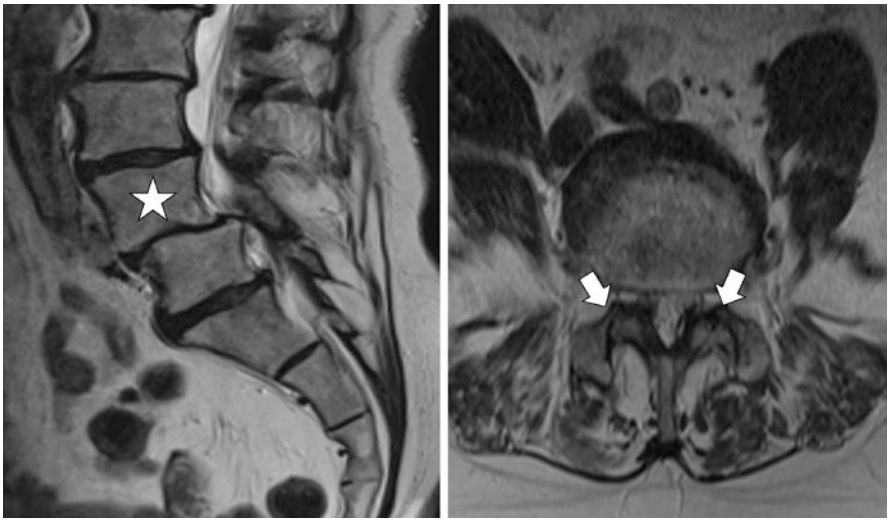

Fig. 12.15 L4-L5 anterior degenerative spondylolisthesis (star) with facet joints sublux-ation (arrow)

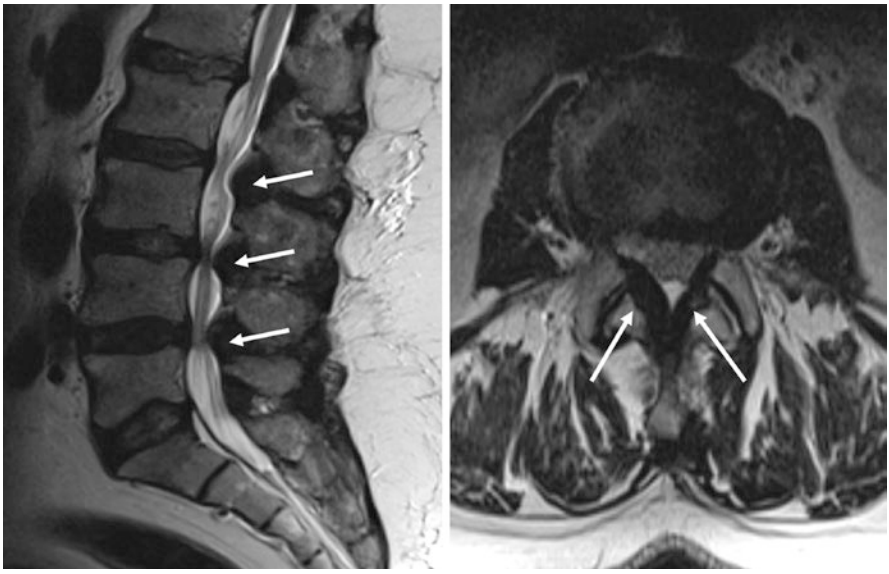

Fig. 12.16 Ligamentum flavum thickening (arrows). This contributes to the reduction of spinal canal size

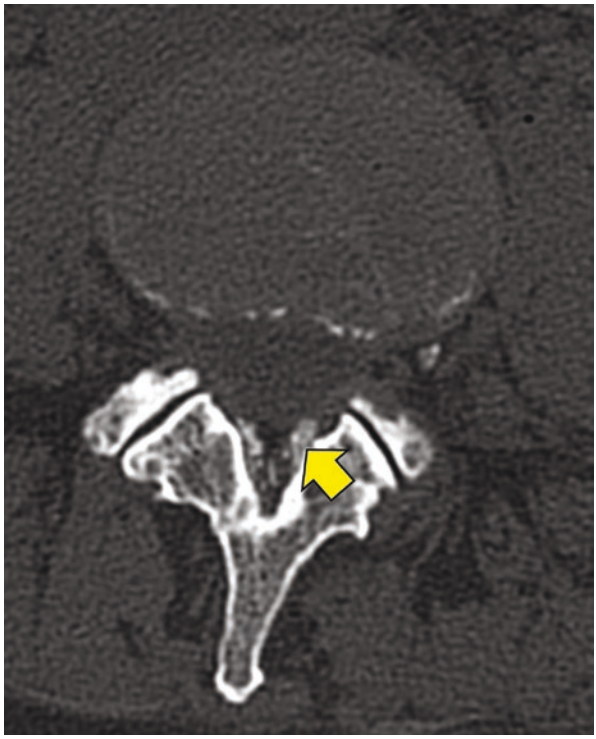

Fig. 12.17 Chronic inflammation predisposes to ligamentum flavum calcification (arrow)

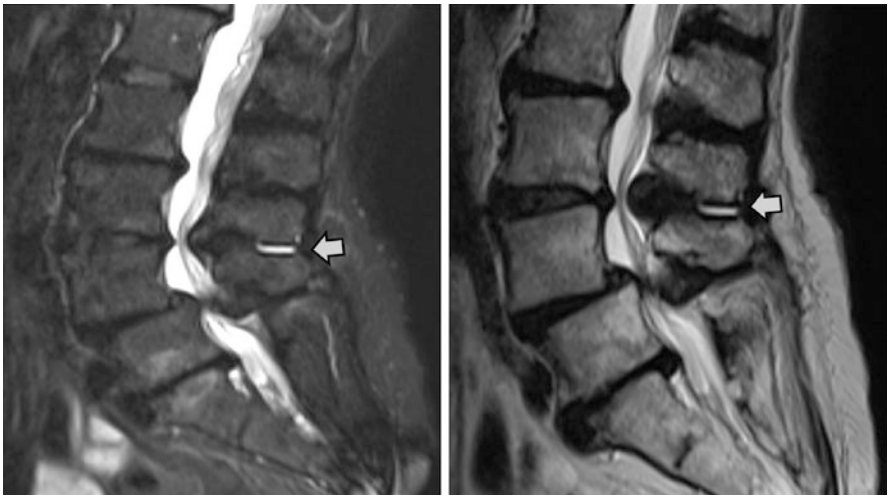

Fig. 12.18 Degenerative changes of the interspinous processes: interspinous bursitis. L3-L4 small fluid collection both on STIR sequence of the left and T2 weighted sequence on the right (arrows)

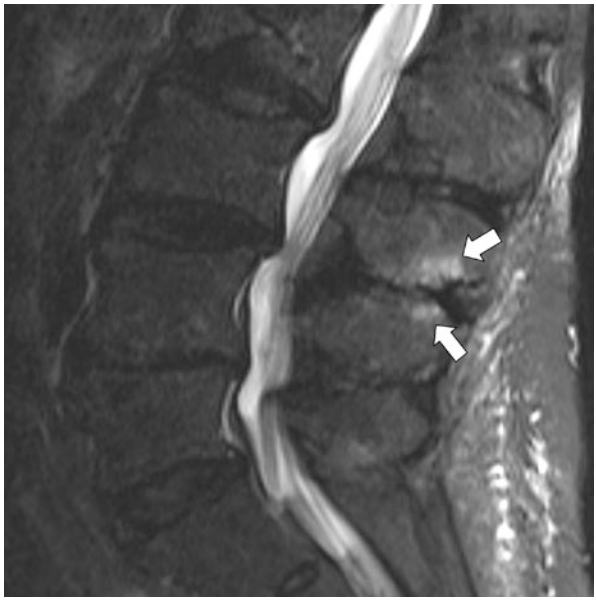

Fig. 12.19 Degenerative changes of the interspinous processes: space reduction with bone erosion and bone edema the opposed spinous processes, also known as "kissing spine" (arrows)

12.2.6 Instability, Spondylolisthesis, Spinal Canal, and Nerve Foramina Stenosis

Due to degenerative changes of the disc, facet joints, and ligamentous apparatus, the ability to maintain the anatomical alignment of the functional spinal unit, at static position and/or during movements, decreases. This results in functional instability and degenerative spondylolisthesis. It typically occurs at lumbar or cervical levels and is virtually absent in the thoracic spine, thanks to costovertebral joints which act as a further stabilizer.

Instability can be defined as an abnormal response to applied loads characterized kinematically by abnormal movement beyond normal constraints [30]. Spondylolisthesis refers to forward slippage of a vertebra on the subjacent one in the sagittal plane. Backward vertebral slippage, a type of spondylolisthesis, has been called retrolisthesis [14].

The process of degenerative instability is divided into three phases: early dysfunction, instability, and stabilization [31]. The first phase (early dysfunction) is characterized by initial and reversible anatomical modifications induced by altered axial load. In the second phase (instability), anatomical changes progress with disc height reduction, capsule-ligament laxity, and facet joint osteoarthrosis. Finally, in the third phase (stabilization), new biomechanical constraints occur induced by anatomical changes, such as osteophytes and intervertebral space reduction, which lead to a new spinal mechanical stabilization, however at the cost of movement reduction [32]. In the third stage sometimes spondylolisthesis has already occurred. In fact, the radiologic observation of degenerative spondylolisthesis does not necessarily imply intervertebral instability at the time of imaging because a new stabilization

may have already occurred [14]. Degenerative instability consists of pure motion dysfunctional syndrome with no or minimal anatomical changes, undetectable on imaging (microinstability), or overt instability, which can be radiologically detectable [33]. As persistent uni- or multisegmental instability progresses, it leads to rotational and translational vertebral subluxation, resulting in degenerative spondylolisthesis, which may be stable or unstable [3].

Conventional MRI and CT performed in the prone position provides limited information on the functional status of the affected segment as spondylolisthesis with instability may "self-reduce" without a normal axial load [3]. Therefore, diagnosis is based both on direct and indirect signs of instability, such as joint facets

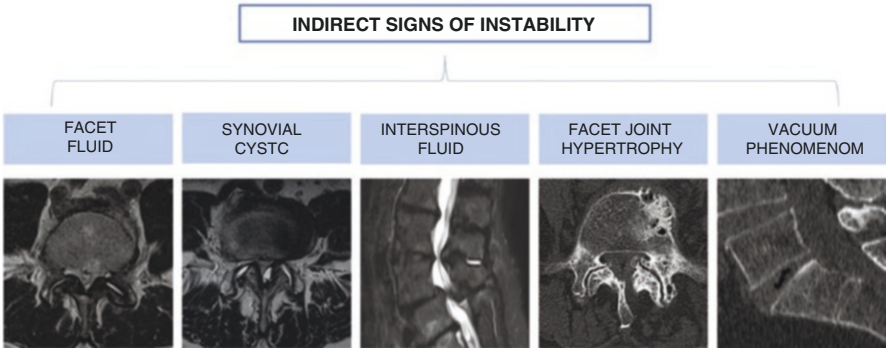

Fig. 12.20 Major indirect signs of instability

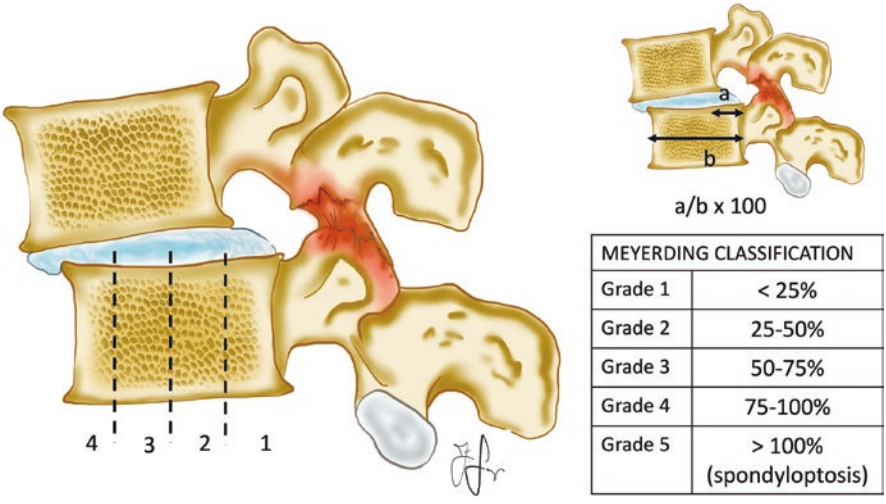

Fig. 12.21 Meyerding classification of spine spondylolisthesis

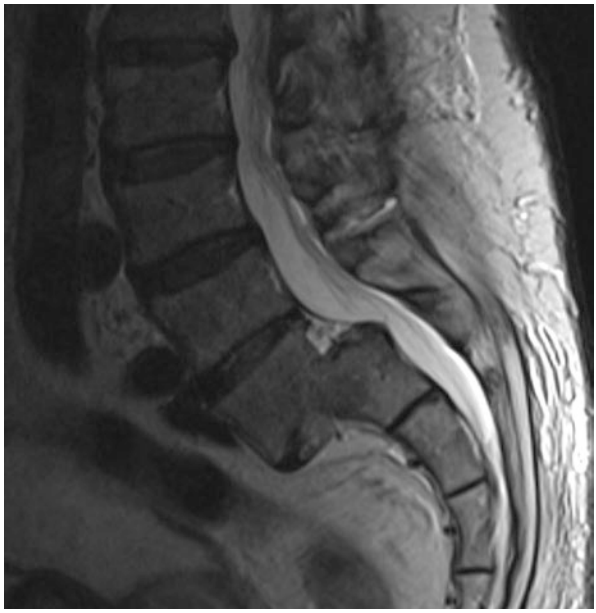

Fig. 12.22 Grade III of spondylolisthesis according to Meyerding classification

fluid, facet synovial cysts, interspinous fluid, facet joints hypertrophy, and intradiscal vacuum phenomenon (Fig. 12.20) [3].

Functional flexion/extension radiographs are considered the gold standard for diagnosing the presence of degenerative instability in the setting of spondylolisthesis [34]. For lumbar spine spondylolisthesis, the Meyerding classification is a common method for grading anterior vertebral spondylolisthesis, based on the ratio of the overhanging part of the superior vertebral body to the anteroposterior length of the adjacent inferior vertebral body (Figs. 12.21 and 12.22).

For the lumbar spine, on flexion-extension radiographs, values of 10° for sagittal rotation and 4 mm for sagittal translation are typically used to infer instability [14]. For the cervical spine, a slippage of 3 mm on functional radiographs is considered a reliable cut-off [3].

Degenerative spondylolisthesis is an important factor that can contribute to spinal canal stenosis, which is defined as a decrease in the area that can affect the spinal canal, the lateral recesses, or neural foramina, compressing neural and vascular structure, thus resulting in various degrees of clinical disabilities [3, 16].

Degenerative spinal canal stenosis is considered a multifactorial condition, rather than an answer to a single insult. In fact, there are four major factors that can contribute to spinal canal stenosis that should be always checked carefully: disc herniation, hypertrophic facet joint osteoarthrosis, ligamentum flavum hypertrophy, and spondylolisthesis (Fig. 12.23) [3].

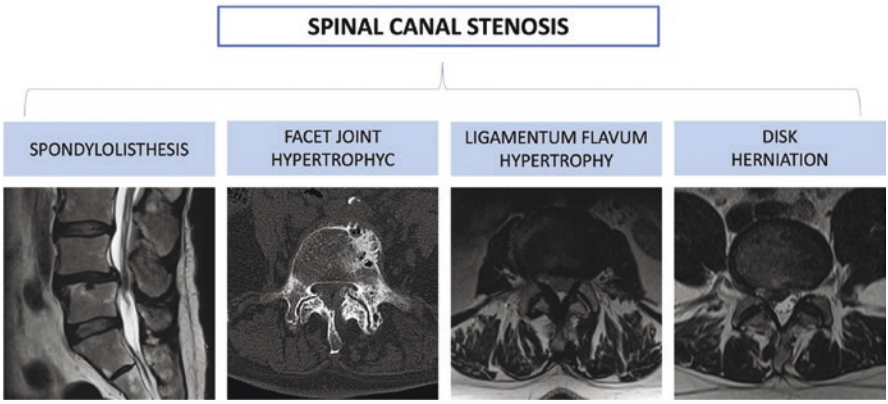

Fig. 12.23 Major factors that contribute to spinal canal stenosis, which is usually the result of a multifactorial condition

Grading systems based on spinal canal measurements appear impractical; therefore, qualitative assessment of the relationships between the anatomical structures plays a major role in establishing the presence of spinal canal stenosis [3].

According to the combined task forces of the North American Spine Society (NASS), the American Society of Spine Radiology (ASSR), and the American Society of Neuroradiology (ASNR), canal compromise less than one-third is considered "mild" between one-third and two-third "moderate," and more than two-third "severe." The same grading can be applied to neuroforaminal involvement [10].

Other lumbar spine stenosis classification systems, based on MR imaging, are Lee and Schizas classification. The **Lee system** is a 4-grade classification system based on the obliteration of cerebrospinal fluid (CSF) space in front of the cauda equina in the dural sac and the separation degree of the cauda equina on T2-W axial MRI. Grade 0, no lumbar central canal stenosis (LCCS), refers to no obliteration of the anterior cerebrospinal fluid (CSF) space. Grade 1, mild LCCS, refers to mild obliteration of the anterior CSF space but all elements of the cauda equina clearly separated from each other. Grade 2, moderate LCCS, refers to moderate obliteration of the anterior CSF space and some cauda equina aggregation where it is impossible to identify each other visually. Grade 3, severe LCCS, refers to severe obliteration of the anterior CSF space, marked compression of the dural sac and the entire cauda equina appearing as one bundle [35].

The **Schizas system** is a 7-grade classification system based on the morphology of the dural sac on T2-W axial MRI with the rootlet/CSF fluid ratio taken into account. Grade A, no or minor stenosis, refers to clearly visible CSF inside the dural sac within homogeneous distribution. Grade A1 refers to the condition where the rootlets lie dorsally and occupy less than half of the dural sac area. Grade A2 refers to cases where the rootlets lie dorsally, in contact with the dura but in a horseshoe configuration. Grade A3 refers to rootlets lying dorsally and occupying more than half of the dural sac area. Grade A4 refers to cases where the rootlets lie centrally

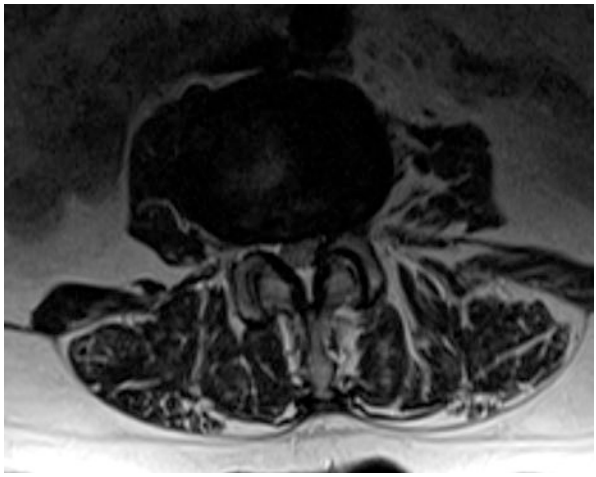

Fig. 12.24 Grade C stenosis (Schizas classification)

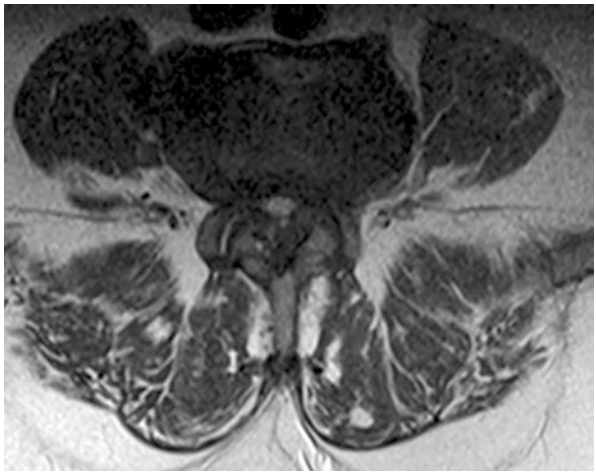

Fig. 12.25 Grade D stenosis (Schizas classification)

and occupy the majority of the dural sac area. Grade B, moderate stenosis, includes cases where the rootlets occupy the entire dural sac, but can still be individualized. Grade C (Fig. 12.24), severe stenosis, refers to cases where no rootlets can be recognized, with the dural sac demonstrating a homogeneous gray signal with no visible CSF signal, but epidural fat present posteriorly. Grade D (Fig. 12.25), extreme stenosis, refers to no rootlets being recognizable and no epidural fat posteriorly [36].

12.3 A Focus on Imaging Techniques and Their Role in the Assessment of the Degenerative Spine

Conventional radiography usually represents the first level examination for the spine, allowing a good assessment of spinal alignment, vertebral bodies morphologies, calcifications, and the vacuum phenomenon. However, it has a marginal role due to technical limitations, mostly due to air and other structures overlap and the impossibility to study bone marrow, neural structures, and soft tissue. The standard projections are the anteroposterior and latero-lateral view. In addition, the oblique view is used for the assessment of foramens and, eventually, spondylolysis (scotty dog sign) [32]. Moreover, functional flexion/extension radiographs are considered the gold standard for diagnosing the presence of degenerative instability in the setting of spondylolisthesis [34].

Computed tomography has a better accuracy in the assessment of bone margins and osteophytes, and it represents the reference standard for spondylolysis. Thanks to its high resolution for small bone alteration of the posterior arch, it is useful for the evaluation of the spinal canal and neural foramina [32]. However, like traditional radiography, it has a limited role in the assessment of soft tissue and neural structures.

MRI is the first-choice technique for the study of discs and ligaments changes. MRI of the spine is generally performed with the patient in supine position. Upright MRI is also feasible and favored by some groups due to the plausible explanation that axial loads on the intervertebral disc are reduced in supine position. However, upright MRI is limited by poor resolution, very limited availability, increased motion artifacts, and high false-positive findings [37, 38].

The standard MRI protocol typically includes two-dimensional (2D) sagittal T1-W fast spin-echo (FSE), sagittal T2-W FSE, and axial T2-W FSE images. Most institutions add a short tau inversion recovery (STIR) sequence, a gradient echo sequence (particularly in the cervical spine), and coronal proton density weighted (PDw), T2-W or T1-W sequence. High-resolution three-dimensional (3D) sequences with secondary reconstruction are particularly helpful in the cervical spine. In fact, secondary reformatted images can be better oriented along the oblique sagittal plane to show the foramen and higher resolution allows better assessment of the relatively small cervical nerve roots. The sagittal images are used to evaluate the vertebral bodies, intervertebral discs, ligaments, facet joints, spinal canal, spinal cord and/or sac and intervertebral foramen. The STIR images are usually performed in the sagittal plane and are useful to identify bone marrow edema. Axial images are useful for confirmation and evaluation of central canal stenosis, cord signal change, disc herniations, spinal cord compression, and nerve root compression. The facet joints are best assessed on axial images for the presence of arthrosis, synovitis, and indirectly for segmental instability. The coronal images, if performed, are particularly helpful

for identification and classification of lumbosacral transitional vertebra, for an overview of the extent of scoliosis and for detection of extraforaminal herniations. Gradient echo sequences may be used to evaluate calcification and ossification of the ligaments and to identify posterior endplate ridges, particularly in the cervical spine. The use of contrast can be helpful in the postoperative setting. Contrast administration is useful to discriminate between disc material and fibrosis. There is a diffuse contrast-media uptake in epidural fibrosis/granulation tissue, while there is only rim-enhancement in disc tissue. Further, partially healed chronic annular tears may demonstrate enhancement due to the presence of granulation tissue, not identified in normal T2-W non-contrast MR images. MR neurography including diffusion tensor imaging (DTI) techniques for the spinal cord and nerve roots are currently only used for specific questions (e.g., in patients with neurofibromatosis) and for research purpose, but not yet used in standard protocols. Novel functional imaging techniques, such as T2/T2* mapping, T1ρ calculation, T2 relaxation time measurement, diffusion quantitative imaging, chemical exchange saturation transfer, delayed contrast-enhanced MRI of cartilage, sodium-MRI and MR spectroscopy, are promising tools that may allow the evaluation of early disc degeneration [3, 19].

However, independently from the imaging technique, it is important to keep in mind that the presence of degenerative change is not itself an indicator of symptoms. In fact, altered radiological findings do not always have corresponding clinical symptoms and pain and, conversely, clinical pain does not always correlate to the presence and severity of radiological changes. Therefore, determination of the relationship between imaging anatomical changes and its symptoms remains challenging. Moreover, some anatomical changes encompass the normal spectrum of aging and are not associated with degenerative pathology. Further, the majority of standard examinations are usually performed in supine position, in the absence of axial load, and in static conditions, possibly increasing the number of false negative exams.

When patients with degenerative spine diseases are referred for imaging, the important task is to identify the main cause of the patient's pain or neurological symptoms, keeping in mind that degenerative pathology is a biomechanical continuum of anatomical alterations and that a degenerative finding should not be considered an isolated event or reported as a random finding. This interpretation, associated with the detection of direct and indirect signs of instability, is useful to guide the referring physician to choose a targeted treatment option [3].

References

1. Dupré DA, Cook DJ, Brad Bellotte J, Oh MY, Whiting D, Cheng BC. Disc nucleus fortification for lumbar degenerative disc disease: a biomechanical study. J Neurosurg Spine. 2016;24:708–14.
2. Oxland TR. Fundamental biomechanics of the spine--what we have learned in the past 25 years and future directions. J Biomech. 2016;49:817–32.
3. Kushchayev SV, Glushko T, Jarraya M, Schuleri KH, Preul MC, Brooks ML, Teytelboym OM. ABCs of the degenerative spine. Insights Imag. 2018;9:253–74.

4. Bogduk N. Degenerative joint disease of the spine. Radiol Clin N Am. 2012;50:613–28.
5. Inoue N, Espinoza Orías AA. Biomechanics of intervertebral disk degeneration. Orthop Clin North Am. 2011;42:487–99, vii.
6. Niosi CA, Oxland TR. Degenerative mechanics of the lumbar spine. Spine J. 2004;4:202S–8S.
7. Horst M, Brinckmann P. 1980 Volvo award in biomechanics. Measurement of the distribution of axial stress on the end-plate of the vertebral body. Spine. 1981;6:217–32.
8. Virk SS, Niedermeier S, Yu E, Khan SN. Adjacent segment disease. Orthopedics. 2014;37:547–55.
9. Rousseau M-A, Lazennec J-Y. Degenerative disease supra- and infra-jacent to fused lumbar and lumbo-sacral levels. Orthop Traumatol Surg Res. 2016;102:S1–8.
10. Fardon DF, Williams AL, Dohring EJ, Murtagh FR, Gabriel Rothman SL, Sze GK. Lumbar disc nomenclature: version 2.0: recommendations of the combined task forces of the North American Spine Society, the American Society of Spine Radiology and the American Society of Neuroradiology. Spine J. 2014;14:2525–45.
11. Ferguson SJ, Steffen T. Biomechanics of the aging spine. Eur Spine J. 2003;12(Suppl 2):S97–S103.
12. Modic MT, Masaryk TJ, Ross JS, Carter JR. Imaging of degenerative disk disease. Radiology. 1988;168:177–86.
13. Pfirrmann CW, Metzdorf A, Zanetti M, Hodler J, Boos N. Magnetic resonance classification of lumbar intervertebral disc degeneration. Spine. 2001;26:1873–8.
14. Leone A, Guglielmi G, Cassar-Pullicino VN, Bonomo L. Lumbar intervertebral instability: a review. Radiology. 2007;245:62–77.
15. D'Anastasi M, Birkenmaier C, Schmidt GP, Wegener B, Reiser MF, Baur-Melnyk A. Correlation between vacuum phenomenon on CT and fluid on MRI in degenerative disks. AJR Am J Roentgenol. 2011;197:1182–9.
16. Chanchairujira K, Chung CB, Kim JY, Papakonstantinou O, Lee MH, Clopton P, Resnick D. Intervertebral disk calcification of the spine in an elderly population: radiographic prevalence, location, and distribution and correlation with spinal degeneration. Radiology. 2004;230:499–503.
17. Munter FM, Wasserman BA, Wu H-M, Yousem DM. Serial MR imaging of annular tears in lumbar intervertebral disks. AJNR Am J Neuroradiol. 2002;23:1105–9.
18. Kobayashi S, Yoshizawa H, Yamada S. Pathology of lumbar nerve root compression. Part 1: Intraradicular inflammatory changes induced by mechanical compression. J Orthop Res. 2004;22:170–9.
19. Farshad-Amacker NA, Farshad M, Winklehner A, Andreisek G. MR imaging of degenerative disc disease. Eur J Radiol. 2015;84:1768–76.
20. Qaseem A, Wilt TJ, McLean RM, Forciea MA, Clinical Guidelines Committee of the American College of Physicians. Noninvasive treatments for acute, subacute, and chronic low back pain: a clinical practice guideline from the American College of Physicians. Ann Intern Med. 2017;166:514–30.
21. Kerttula L, Luoma K, Vehmas T, Grönblad M, Kääpä E. Modic type I change may predict rapid progressive, deforming disc degeneration: a prospective 1-year follow-up study. Eur Spine J. 2012;21:1135–42.
22. Modic MT, Ross JS. Lumbar degenerative disk disease. Radiology. 2007;245:43–61.
23. Patel KB, Poplawski MM, Pawha PS, Naidich TP, Tanenbaum LN. Diffusion-weighted MRI "claw sign" improves differentiation of infectious from degenerative modic type 1 signal changes of the spine. AJNR Am J Neuroradiol. 2014;35:1647–52.
24. Eguchi Y, Ohtori S, Yamashita M, et al. Diffusion magnetic resonance imaging to differentiate degenerative from infectious endplate abnormalities in the lumbar spine. Spine. 2011;36:E198–202.
25. Gellhorn AC, Katz JN, Suri P. Osteoarthritis of the spine: the facet joints. Nat Rev Rheumatol. 2013;9:216–24.
26. Pathria M, Sartoris DJ, Resnick D. Osteoarthritis of the facet joints: accuracy of oblique radiographic assessment. Radiology. 1987;164:227–30.

27. Guglielmi G, Schiavon F, Cammarota T. Radiologia geriatrica. Milan: Springer Milan; 2006. https://doi.org/10.1007/88-470-0486-1.
28. Pizzini FB, Poletti M, Beltramello A, et al. Degenerative spine disease: Italian position paper on acquisition, interpretation and reporting of magnetic resonance imaging. Insights Imag. 2021;12:14.
29. Clarençon F, Law-Ye B, Bienvenot P, Cormier É, Chiras J. The degenerative spine. Magn Reson Imaging Clin N Am. 2016;24:495–513.
30. Frymoyer JW, Selby DK. Segmental instability. Rationale for treatment. Spine. 1985;10:280–6.
31. Izzo R, Popolizio T, D'Aprile P, Muto M. Spinal pain. Eur J Radiol. 2015;84:746–56.
32. Leone A, Martino F. Imaging del rachide. Milan: Springer Milan; 2008. https://doi.org/10.1007/978-88-470-0836-6.
33. Manfrè L. Spinal instability. Milan: Springer Milan; 2015. https://doi.org/10.1007/978-3-319-12901-3.
34. Even JL, Chen AF, Lee JY. Imaging characteristics of "dynamic" versus "static" spondylolisthesis: analysis using magnetic resonance imaging and flexion/extension films. Spine J. 2014;14:1965–9.
35. Lee GY, Guen YL, Lee JW, Joon WL, Choi HS, Hee SC, Oh K-J, Kyoung-Jin O, Kang HS, Heung SK. A new grading system of lumbar central canal stenosis on MRI: an easy and reliable method. Skelet Radiol. 2011;40:1033–9.
36. Schizas C, Theumann N, Burn A, Tansey R, Wardlaw D, Smith FW, Kulik G. Qualitative grading of severity of lumbar spinal stenosis based on the morphology of the dural sac on magnetic resonance images. Spine. 2010;35:1919–24.
37. Khalil JG, Nassr A, Maus TP. Physiologic imaging of the spine. Radiol Clin N Am. 2012;50:599–611.
38. Tarantino U, Fanucci E, Iundusi R, Celi M, Altobelli S, Gasbarra E, Simonetti G, Manenti G. Lumbar spine MRI in upright position for diagnosing acute and chronic low back pain: statistical analysis of morphological changes. J Orthop Traumatol. 2013;14:15–22.

Osteoarthritis in Appendicular Skeleton in Geriatric Patients

13

Antonio Barile, Riccardo Monti, Federico Bruno, Julia Daffinà, Francesco Arrigoni, and Carlo Masciocchi

13.1 Introduction

Osteoarthritis (OA) is the most common form of arthritis and is the third leading cause of disease burden in developed countries with significant social and health impact. As the average age and life expectancy are increasing, this form of arthritis is expected to increase in the incoming decades. OA commonly affects weight-bearing joints such as the knee, which is most commonly affected, and the main clinical features are pain and stiffness. The gravity of this disease leads to a progressive decline in physical functioning. Imaging plays a vital role in initial diagnosis, staging, and monitoring of longitudinal progression and provides indications for conservative, minimally invasive, or surgical treatment. Although the primary focus of imaging lies in bone alterations, osteoarthritis should be framed as a whole organ disease, and multimodal instrumental evaluation is essential to highlight the various joint components involved and their alterations.

13.2 Shoulder Osteoarthritis

Compared to other appendicular joints, the glenohumeral joint is one of the least commonly affected by osteoarthritis. The estimated radiographic prevalence is in the range of 16–20% in an elderly population. The main risk factor for glenohumeral osteoarthritis is age. Other factors that increase the likelihood risk of developing shoulder osteoarthritis include female gender, obesity, Caucasians, previous trauma, rotator cuff tears, glenohumeral instability, and crystalline arthropathy. In

A. Barile (✉) · R. Monti · F. Bruno · J. Daffinà · F. Arrigoni · C. Masciocchi
Department of Biotechnological and Applied Clinical Sciences, University of L'Aquila, L'Aquila, Italy
e-mail: antonio.barile@univaq.it; carlo.masciocchi@univaq.it

G. Guglielmi, M. Maas (eds.), *Imaging in Geriatrics*, Practical Issues in Geriatrics, https://doi.org/10.1007/978-3-031-14877-4_13

addition to idiopathic origin, further causes of glenohumeral osteoarthritis are the presence of prior trauma, glenohumeral dislocation, proximal humeral fractures, shoulder osteonecrosis, inflammatory arthritis, septic arthritis, hemochromatosis, hemophilia, and iatrogenic causes such as multiple injections of intra-articular steroids [1].

Symptoms are usually slowly progressive, characterized by posterior or deep localized shoulder pain associated with limited range of motion and stiffness. Other symptoms include blockage, grinding, and joint instability. As in other diarthrodial joints, glenohumeral osteoarthritis is associated with the thickening of the subchondral bone plate and the formation of marginal osteophytes, which can usually be seen both on the posterior glenoid rim and on the central part of the humeral head. The soft tissue changes associated with this condition are the capsular thickening and contraction, potentially leading to a deficit of internal rotation, and the further eccentric erosion of the posterior glenoid [2].

As with other joint OA involvements, general imaging hallmarks comprehend osteophyte formation, joint space narrowing, and subchondral bone plate sclerosis, whereas subchondral cyst formation and joint surface remodeling or deformity are seen in later stages.

13.2.1 Conventional Radiography (CR)

To assess the presence and degree of arthritis in the glenohumeral joint the first step is conventional radiography. Standard projections include an anteroposterior view, a Grashey view (AP oblique internal rotation), and a further axillary view. These views allow grant the assessment of the presence, type, and degree of arthritis and rule out other conditions, including fractures, dislocations, and bone injuries [3].

To determine the extent of osteoarthritis of the glenohumeral joint various radiographic classifications were established. The most widely adopted is the Samilson-Prieto classification. This classification acknowledges grade 0 is normal, grade 1 is mild with osteophytes smaller than 3 mm on the humeral head, grade 2 is moderate with osteophytes between 3 and 7 mm on the humeral head or glenoid rim, and grade 3 is severe with osteophytes over 7 mm, with or without contextual joint incongruity. The state of the rotator cuff can be inferred from the radiographic evaluation of Grashey's view. This view is accessed from a lateral oblique projection at 30°, tangential to the glenohumeral joint, to obtain an image parallel to the glenoid face in order to reveal any degenerative modifications [4].

For the rotator cuff the radiographic classification used integrity is the Hamada–Fukuda classification, a radiographic morphological description of the natural course of massive rotator cuff tear assessing the height of the acromiohumeral space. There are five distinctions within this classification:

- Type 1: Normal joint morphology and acromiohumeral distance bigger than 6 mm
- Type 2: Acromiohumeral distance smaller than 5 mm

- Type 3: Type 2 plus the acetabularization (i.e., exaggerated undersurface concavity) of the acromion
- Type 4: Types 2 and 3 plus the narrowing of the glenohumeral joint space
- Type 5: Types 2, 3, and 4 plus the humeral head collapse

Finally, an axillary view is essential in preoperative planning. It allows the assessment of the posterior glenoid wear and deficiency, which has ramifications on the glenoid preparation (concentric reaming) necessary to center the glenoid-based implant [5].

13.2.2 Computed Tomography (CT)

For an effective preoperative planning and to assess the humeral and glenoid bone condition, computed tomography (CT) provides greater bony detail compared to radiographs. If there are concerns regarding the glenoid's bone loss, the presence of cyst, or retroversion on standard radiographs, CT should be suggested as it may influence both the type of arthroplasty choice and the location of the glenoid component. The CT study of the affected shoulder is necessary to estimate the glenoid bone loss, which may require preoperative planning before eccentric reaming, augmentation of bone graft, use of augmented glenoid components, or consideration of total reverse shoulder arthroplasty. Therefore, CT evaluation should be considered mandatory in all patients undergoing an arthroplasty procedure that requires glenoid resurfacing (e.g., total shoulder arthroplasty and total reverse shoulder arthroplasty) as it allows the quantification of the glenoid border and recognition of different forms of glenoid bone loss such as cyst that can alter implant fixation and placement [6].

13.2.3 Magnetic Resonance Imaging (MRI)

Besides visualizing the glenoid and humeral head morphology, MRI can help detect the underlying etiology. Thanks to MRI, the evaluation of various tissue abnormalities, regarding cartilage, labrum, and glenohumeral ligaments can be assessed. However, the capacity of detecting cartilage lesions is limited by the comparison with to other joints. Additionally, magnetic imaging provides valuable information for the rotator cuff evaluation, which forms an integral part of surgical planning. Shoulder MRI is suggested in patients with rotator cuff deficiency doubts on clinical examination. Indeed, an intact rotator cuff is required for both hemiarthroplasty and total shoulder arthroplasty. Therefore, the integrity of the rotator cuff is a crucial factor in determining whether the patient is a candidate for total anatomical shoulder arthroplasty, hemiarthroplasty, or conversely to total reverse shoulder arthroplasty [7, 8]. MRI shows soft tissues with an excellent detail, it can also add information on rotator cuff tears and on the presence and degree of muscle atrophy.

The Goutallier Grading Scale of Fat Infiltration of Rotator Cuff Muscles was initially described using CT to assess the degree of fat infiltration of individual rotator cuff muscles. Goutallier's classification consists of: grade 0 is normal muscle, grade 1 is some fat streaks, grade 2 is less than 50% fat muscle atrophy, grade 3 is 50% fat muscle atrophy, and grade 4 is greater than 50% of fat muscle atrophy. The importance of this classification scale is its implication in the reparability of the rotator cuff: a degree of Goutallier fat infiltration of 3 or greater (i.e., fat infiltration equal to or greater than 50% of muscle mass) has a 50–70% tear rate [9].

13.3 Acromioclavicular Osteoarthritis

Although AC osteoarthritis is less common than other locations such as the knee or the hip, it is differently much more frequent than glenohumeral osteoarthritis. Around 54–57% of elderly patients have an X-ray evidence of degenerative changes in the AC joint. On the other hand, clinically relevant AC osteoarthritis is uncommon, although it is more frequently related to other pathologies, such as the CR upper impingement syndrome [10]. Primary osteoarthritis is strongly age-related, as a matter of fact the degenerative process begins in early adulthood. Secondary osteoarthritis, mainly following trauma such as joint sprains or distal clavicular fractures, appears to be even more prevailing than primary osteoarthritis. The clinical picture is pain in the anterior/superior aspect of the shoulder, sometimes radiating to the base of the neck/trapezius muscle. Daily movements or activities that involve overhead or transverse movements increment pain. Local tenderness can be caused by AC joint palpation. This range of symptoms is not specific and is also reported in cervical spine disease and CR impingement syndromes, which, as aforementioned, are predominant causes of shoulder pain. The direct intra-articular injection of anesthetics can grant a differential diagnosis. The imaging evaluation of the AC joint begins with an X-ray. This joint can be studied with average AP views of the shoulder. However, the best option according to literature is the Zanca view (a cephalad inclination of 10–15° with a 50% reduction in exposure compared to standard AP view shoulder). Imaging findings are typical of degenerative diseases: sclerosis, osteophytes, subchondral cysts, and joint space narrowing [11]. Bone modifications seen on X-rays are evidenced more precisely on CT scan. At the same time, MRI is more useful for evaluating changes in capsuloligamentous structures, bone edema, and abnormalities in surrounding soft tissues (e.g., effusion of bursal or tendon pathology) [12]. The AC joint can only be partially evaluated with US. Still, it should be a part of routine shoulder examination, as AC joint osteoarthritis can sometimes mimic rotator cuff tendinopathy and may cause anterosuperior impingement. AC osteophytes are found in 50% of patients with rotator cuff tears but also in 14% of patients without rotator cuff tears. By placing the high-frequency linear probe on a coronal plane at the level of the joint, the evaluation of the two articular ends of the acromion and clavicle is possible. The superior AC ligament is clearly seen as a banded arch echo structure that overstays the bones; below it, the joint space can vary in size and echogenicity with movements. In case

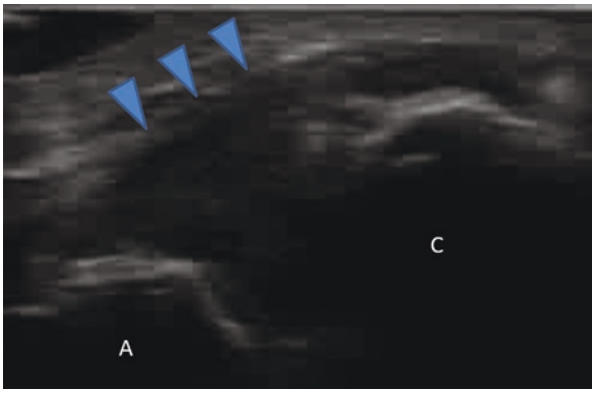

Fig. 13.1 US scan of the acromioclavicular joint showing capsular distension with effusion (arrowheads). A: acromion; C: clavicle

of AC joint osteoarthritis, US can help evaluate superficial bone irregularities and osteophytes, capsular hypertrophy, joint space narrowing, and joint effusion or synovial hypertrophy (Fig. 13.1). Bilateral evaluation of the AC joint is always suggested to evaluate capsular hypertrophy and joint space narrowing with increased sensitivity. US AC joint findings should always be correlated with rotator cuff and bursa findings and clinical picture. AC joint arthrosis-related shoulder pain can only be diagnosed in the absence of RC abnormalities and with radiological proof showing this condition. Besides, US signs of acromioclavicular osteoarthritis and rotator cuff or bursal pathology are frequently connected; in this case, the joint injection test can be a valuable diagnostic tool. Another frequent finding in US is an AC joint cyst whose pathogenesis is still debated. They are however more commonly related to full-thickness RC tears. Tendon tears cause the cranial migration of the humeral head and damage the inferior AC joint capsule, creating a connection between the glenohumeral joint and the AC joint [13].

13.4 Hand Osteoarthritis

Despite the high prevalence, hand OA generally receives less attention compared to OA of the weight-bearing joints. It typically affects the distal interphalangeal (DIP) joints and the thumb base and, less frequently, the proximal interphalangeal (PIP) joints. Patients with hand OA can experience considerable pain, stiffness, and disability with a high impact on health-related quality of life. Outcome measures in OA usually include evaluation of pain and disability and structural changes in the joint can be studied with outcome [14].

13.4.1 Conventional Radiography (CR)

Currently the cheapest, most feasible, and available imaging modality for morphological assessment of the structural features of the OA hand is conventional

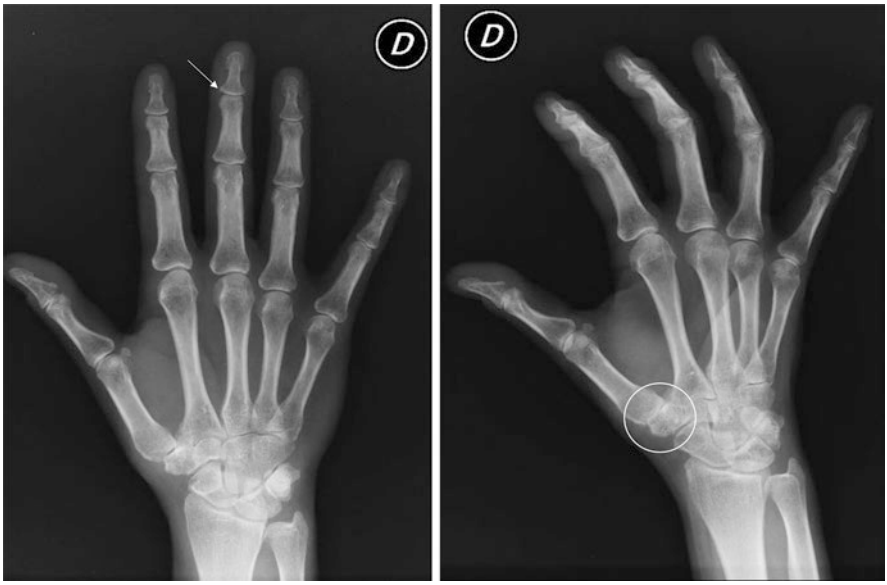

Fig. 13.2 AP and oblique radiographic view showing initial osteoarthritis changes at the level of the DIP with joint space narrowing and sclerosis (arrow). More advanced OA changes of the trapeziometacarpal joint (circle)

radiography (CR). At present, there is no established gold standard for the definition of radiographic hand OA. Studies also differ in classification systems most commonly used and in the radiographic definitions of radiographic.

CR provides a two-dimensional picture of bone modifications, such as osteophytes, erosions, cysts, and sclerosis and joint space narrowing (JSN) as an indirect measure of cartilage loss (Fig. 13.2). Osteophytes can be divided into "true" intra-articular osteophytes and traction spurs. "True" intra-articular osteophytes are found at joint margins and can be easily seen on CR with a traditional posteroanterior view. Traction spurs are differently located at the extensor tendon insertion or on the central shaft and are most easily seen on CR with an oblique or lateral view. Whether these enthesophytic changes are related to OA is not entirely clear, previous studies have suggested that they are mainly related to age and local biomechanical factors and not to systemic enthesopathy [15].

Since cartilage is indirectly evaluated by the inter-osseous distance, the radiographic measurement of JSN is currently recommended as an imaging endpoint for clinical trials of disease-modifying OA drugs. The radiological assessment may be affected by the hand positioning (e.g., flexion deformity) and is further complicated by erosive development in the fingers joints, which can lead to increased joint space width (JSW) (pseudo-enlargement) despite the worsening of the disease. Radiographic erosions in hands with OA are seen as bone damage in the central part

of the joints with a typical gull-wing configuration. These erosions typically occur in the DIP and PIP joints, but they have been described in the joints of the base of the thumb as well. Longitudinal studies have shown that JSN precedes erosive development, suggesting that local biomechanical factors are important for erosive development. These findings may suggest that erosive hand OA represents severe hand OA rather than a different disease entity. Whereas cysts are identified by the loss of trabecular structure, sclerosis gives an increased density in the CR. Both features can be related to bone remodeling [16].

At present, there is no consensus on the preferred grading scale. The first proposed radiographic scoring system was the Kellgren and Lawrence (K&L) scale which is the most widely used so far. The K&L scale classifies OA over a range from 0 to 4 points (where grade of at least 2 is OA) based on different factors. These include: the presence/severity of osteophytes, JSN, sclerosis, pseudocystic areas, and altered shape of the bony ends. In spite of different grading descriptions for various joint groups and difference between publications, there is general confusion in the way of interpreting the various grades. Furthermore the K&L scale is criticized for the emphasis given to osteophytes; however, sclerotic joints cannot be classified as OA unless osteophytes are present. Therefore, several studies used modified K&L scales to overcome these limitations. The evaluation of individual characteristics instead of using a global score can optimize the joint assessment, hence the OARSI (Osteoarthritis Research Society International) atlas is more frequently used. With this atlas as a reference, the presence and severity of individual characteristics (osteophyte, JSN, malalignment, erosion, subchondral sclerosis, subchondral cysts) are assessed on semi-quantitative scales at the level of DIP, PIP, first CMC, thumb and trapezionavicular joint. However, scoring individual features can take longer [17].

Standard radiographs to characterize the basal thumb joint include PA, lateral and oblique views of the hand or wrist. Arthritis of the basal joint of the thumb is most commonly described using the Eaton-Littler classification which was first proposed in 1973 and modified in 1987 by Eaton and Glickel. In this classification, stage I is given by normal joint contours with mild joint widening (secondary to synovitis, ligamentous laxity, or effusion), while stage II shows mild joint space narrowing (<2 mm), mild sclerosis, subchondral cysts, and/or periarticular debris. Stage III follows with noticeable joint space narrowing, prominent sclerosis, subchondral cysts, and periarticular debris. Finally, stage IV concerns the scaphotrapezius joint, plus the narrowing's worsening, increased sclerosis, and the presence of subchondral cysts. In the clinical examination, CMC subluxation, metacarpal adduction, and MCP hyperextension are seen. However, the Eaton-Littler classification has its flaws, including only moderate compatibility with clinical presentations, morphological findings and therapeutic recommendations, and sub-optimal inter- and intra-observer variability. Although some authors underline the convenience of transverse imaging (e.g., MRI, ultrasound, CT) in basal thumb joint arthritis diagnosing, there is currently no recommended role for advanced imaging [18].

13.4.2 Ultrasonography (US)

In recent years, ultrasonography has been acknowledged as a useful tool for finger joints' inflammation evaluation in patients with rheumatoid arthritis. Recently, the prevalence, validity, and reliability of US characteristics have also been studied in patients with hand OA. By scanning the joint in both longitudinal and transverse projection we can obtain conditions regarding the dorsal appearance with the joint in full flexion, while volar aspects are studied with the joints in a neutral position. US allows visualization of a broad spectrum of OA features of the hand, including osteophytes, marginal erosions, and synovitis (Fig. 13.3). It may also be considered a feasible and prompt tool for visualizing inflammation in patients with hand OA. Conversely, one of the US disadvantages is the inability of the beam to penetrate the cortex. Because of joint anatomy, the visualization of the cartilage and bone damage is mainly limited to its peripheral parts. Overlying osteophytes, which interfere with the acoustic window, further complicate the assessment. In severely damaged joints, it may be difficult to determine where an erosion begins and an osteophyte ends. Most US studies of patients with hand OA reported a high prevalence of grayscale synovitis, while potency Doppler activity was less frequent. In erosive OA, often called "inflammatory" OA, a greater power Doppler activity, synovial hypertrophy, and joint effusion compared to patients with non-erosive radiographic OA joints can be found. Synovitis appears to be more prevalent in joints with active erosions, while the prevalence is lower in joints that have been remodeled [19, 20].

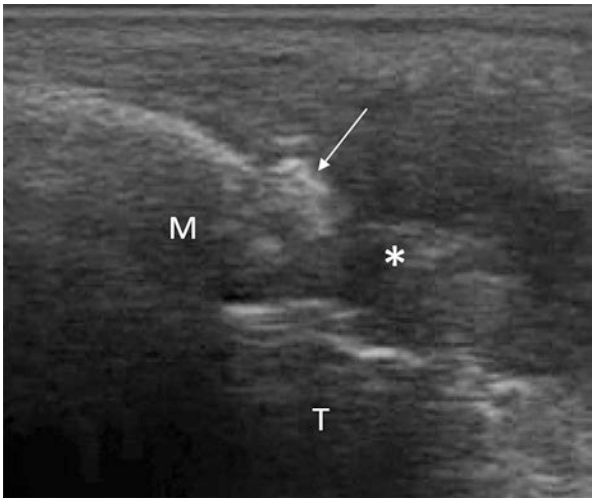

Fig. 13.3 US scan of the first carpometacarpal joint (M: metacarpal bone, T: trapezius) showing capsular distension with effusion (asterisk), osteophyte and periarticular calcifications (arrow)

13.4.3 Magnetic Resonance Imaging (MRI)

With the use of MRI, OA is now recognized as a disease that affects the entire joint. Currently, only limited research is available on the prevalence, reliability, and validity of pathology defined by MRI in hand OA. Common features of hand osteoarthritis MRI can provide a multiplane image of all joint components, including structural features such as osteophytes, cartilage, erosions/cysts, misalignment, and inflammatory features such as synovitis and tenosynovitis (Fig. 13.4). MRI is the only technique capable of showing bone marrow's injury, which is an important feature of structural progression and nonetheless, a source of pain. The prevalence of MRI pathology in patients with hand OA has been studied in several cohorts, founding a high prevalence of synovitis based on gadolinium enhancement. Synovitis was also widespread in joints without radiographic OA, and this is in line with previous observations in knee OA. However, minimal gadolinium enhancement can also occur in the population without OA, and therefore synovitis cannot be seen unless there is an accompanying thickness of the synovium. In the joints of the little fingers, it is also important to be aware of partial volume artifacts that can mimic BMLs [21].

Haugen et al. recently proposed an extensive preliminary MRI scoring system with an accompanying atlas for hand OA, validated with good intra- and inter-reader reliability. Their system includes osteophytes evaluation, JSN, erosions, cysts, misalignment, synovitis, flexor tenosynovitis, BML, and collateral ligament pathology such as absence/discontinuity at insertion sites. The scoring was developed for the DIP and PIP joints, and future studies need to confirm whether it can be further applied to the metacarpophalangeal (MCP) and base of the thumb joints [22].

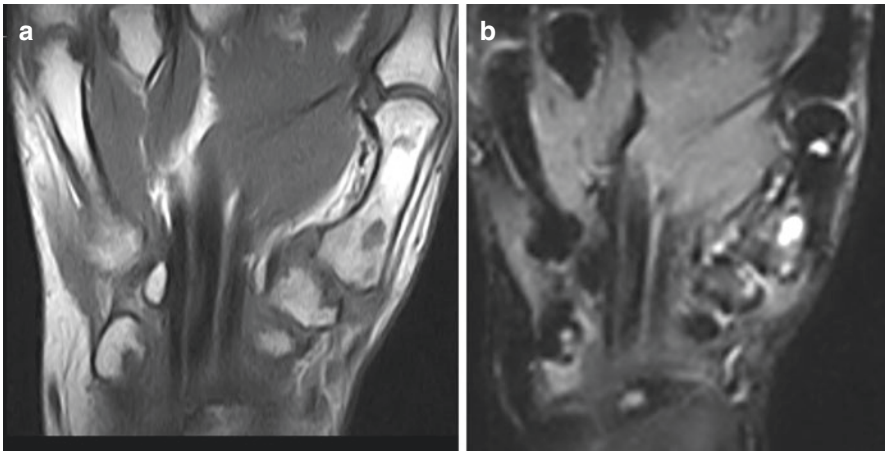

Fig. 13.4 Coronal T1 (**a**) and STIR (**b**) slices of the hand showing advanced trapeziometacarpal joint osteoarthritis changes with joint space narrowing, joint capsule thickening, and reactive bone marrow edema

13.5 Knee Osteoarthritis

Knee OA is the most common joint disease in the elderly and, overall, is very common. It is estimated to affect ~12.5% of patients >45 years. The medial femorotibial joint district is more commonly affected and is usually more severe than the lateral one.

13.5.1 Conventional Radiography (CR)

The hallmarks of knee OA are like the aforementioned for other joints, This includes joint space narrowing which is usually asymmetric, typically regarding the medial tibiofemoral and/or the patellofemoral region. JSN <3 mm on weight-bearing knee radiographs is considered a finding of absolute joint space narrowing with a normal joint space >5 mm (Fig. 13.5). Compared to non-weight-bearing radiographs, weight-bearing radiographs evidence a bigger joint space narrowing, hence affecting the radiographic severity.

Plain radiographs are the imaging flagships including follow-up, although there is a poor correlation between radiographic findings and clinical symptoms. The initial study of a patient with knee OA suspect should include a Rosenberg view, a PA radiograph with weight-bearing, and 45° flexion, which is more sensitive in detecting joint space narrowing [23].

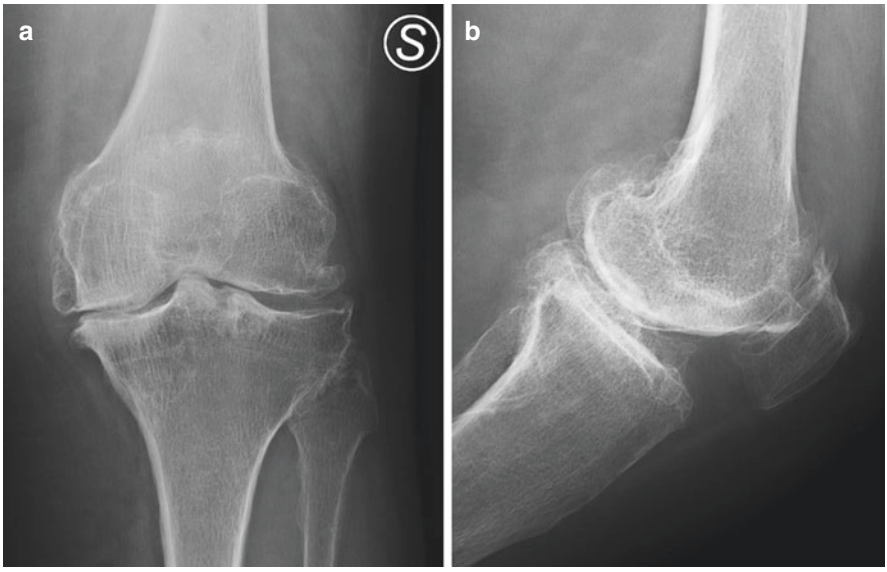

Fig. 13.5 Frontal (**a**) and lateral (**b**) plain film view in a patient with knee osteoarthritis showing marked medial joint space narrowing, subchondral bone sclerosis, and osteophytes

Kellgren and Lawrence first described a grading system in 1957 which was later adopted as the standard measure for assessing radiographic OA by the World Health Organization in 1961. The original description was graded as follows:

- Grade 0 (none): absence of X-ray osteoarthritic changes
- Grade 1 (doubtful): doubtful joint space narrowing and possible osteophytic lipping
- Grade 2 (minimal): osteophytes and possible joint space narrowing
- Grade 3 (moderate): moderate multiple osteophytes, definite narrowing of joint space and some sclerosis, and possible deformity of bone ends
- Grade 4 (severe): large osteophytes, marked narrowing of joint space, severe sclerosis, and definite deformity of bone ends

Subsequently, methods were used to classify OA individual aspects, such as osteophytes, JSN, and subchondral sclerosis. However, there are several limitations associated with both these classifications. Firstly, they predominantly include ordinal measures, with only a limited number of categories. Secondly, the osteophytes' role is unclear, although their presence is crucial in the classification systems. For example, despite being related to the presence of pain, osteophytes are not related to severity and do not seem associated with disease progression. The underlying use of JSN is the hypothesis that longitudinal joint space reduction is a valid measure of a reduction in joint cartilage volume [24].

13.5.2 Magnetic Resonance Imaging (MRI)

For OA assessment, standard MR sequences allow morphological and qualitative evaluation of articular cartilage and other joint structures. In the last years, several advanced MR imaging sequences and techniques were developed to provide a global, sensitive, and specific assessment of the joint degenerative processes with semi-quantitative, quantitative, and compositional analysis methods [25].

Semi-quantitative MR scoring systems are based on the global morphological evaluation of pathological changes (e.g., alterations of articular cartilage, subchondral bone, fibrocartilages) that affect the functional and structural integrity of the joint and determine the severity of the disease. These scoring systems are used with standard morphological MR sequences, especially T2 and PD fat saturated sequences. Four scoring systems were established for the knee: the Whole Organ Magnetic Resonance Score (WORMS), the Knee Osteoarthritis Scoring System (KOSS), the Boston-Leeds Osteoarthritis Knee Scoring (BLOKS), and the MOAKS (MRI Osteoarthritis Knee Score). Equivalent scores were also created for other peripheral joints, such as the Oslo Hand OA MRI Score (OHOA-MRI), the Hip Osteoarthritis MRI Scoring System (HOAMS), and the Scoring Hip Osteoarthritis with MRI (SHOMRI). Concerning the methodology, in brief, the joint is divided into several articular compartments/subregions (e.g., medial and lateral tibia, medial

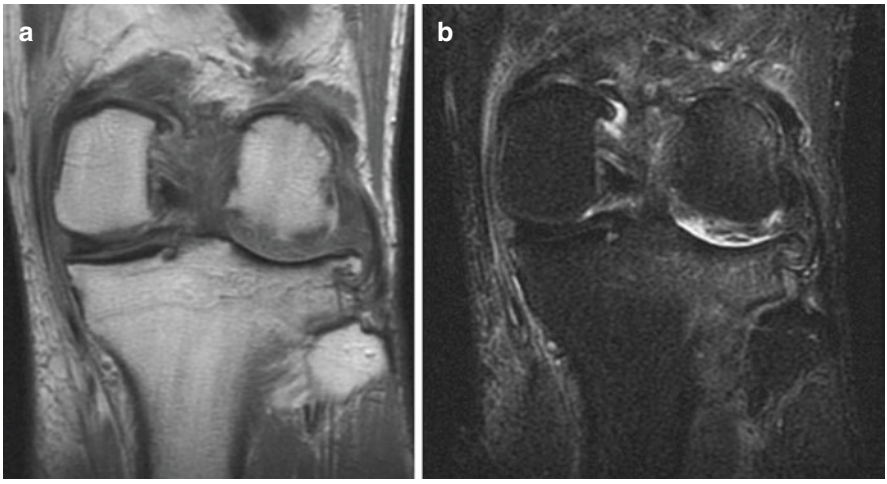

Fig. 13.6 Coronal T1 (**a**) and STIR (**b**) knee MR images depicting high-grade lateral femoral condyle and tibial plateau chondropathy

and lateral femoral condyle), and several joint features (e.g., cartilage signal and morphology, synovitis, subchondral bone) are analyzed and scored according to the severity of the involvement (Fig. 13.6). Numerous studies validated the reproducibility of these scoring systems; the MOAKS is currently the most used one for the knee, bringing together the advantages of these scoring systems. The clinical assessment of semi-quantitative analysis was demonstrated by the presence of some specific alterations (such as Hoffa synovitis, joint effusion, medial meniscus lesions) associated with an increased risk of OA radiographic progression. Other studies, using these transversal and longitudinal comparisons methods of disease evolution, highlighted how the presence of cartilage damage and the presence of subchondral edema correlate with an increased risk of prosthetic surgery necessity.

Quantitative MRI assessment provides a more sensitive and specific evaluation of cartilage's degeneration degree and it is superior to semi-quantitative techniques in evaluating structural changes. Three-dimensional (3D), high-resolution sequences are required to image the bone–cartilage interface and the cartilage surface with adequate contrast. After image acquisition, the post-processing analysis involves automatic or manual segmentation of the articular cartilage (that is, the separation of the cartilage from the underlying bone and adjacent tissues). This data sets and image reconstructions allow the evaluation of several quantitative features (e.g., cartilage thickness, area, volume) as continuous variables. Studies on quantitative cartilage evaluation showed good inter-operator reproducibility at different degrees of cartilage degeneration and excellent correlation with the surgical and histological findings. Quantitative methods have a good correlation with semi-quantitative results, even if more sensitive and specific in predicting cartilage loss (especially in small widespread defects using regional analysis); therefore, some authors suggest a combined use of these techniques. Modifications in the cartilage's volume and

thickness were used as an outcome parameter in observational studies regarding pharmacological treatments (e.g., chondroitin sulfate), physical therapy and rehabilitation, and surgical treatment trials. These assessments have become new quantitative metric parameters that can be considered as biomarkers, to improve the prognostic value of conventional disease progression assessments. The necessity of a dedicated software and the tedious analysis can be considered as a major disadvantage to ordinary clinical application.

Articular cartilage is made of chondrocytes which spread within a matrix composed of water and a highly organized reticulum of collagen proteoglycans (PGs) and glycosaminoglycans (GAGs). Collagen fibers orientation varies from the surface to the deepest calcified zone. In OA, before cartilage fissuration, there is a progressive disruption of the matrix's architecture with GAGs and collagen loss and a consequent increase of water content. Noticeably, these matrix modifications in the early stages of OA development are not discernible in standard morphological MRI sequences. Based on the known pathogenesis of joint degenerative processes, we can appreciate the histological level of biochemical changes in cartilage ultrastructure, including the reduction of proteoglycans (PGs) and glycosaminoglycans (GAGs) and the increase in water content, anticipate morphological changes. Advanced imaging technologies provide information on the ultrastructural and biochemical composition of cartilage to detect and monitor the initial stages of the joint degenerative processes. MR imaging techniques are in fact based on the cartilaginous ultrastructural components modification (e.g., GAG, PG). In particular, we consider relaxation times measurements (T2 and T1ρ mapping), sodium imaging, delayed gadolinium enhancement MRI of cartilage (dGEMRIC) imaging, chemical exchange saturation transfer imaging of GAG (gagCEST), and imaging and diffusion imaging (DWI and DTI).

T2 and T1ρ mapping: These sequences measure the T1 and T2 relaxation times (expressed in ms) of molecules present in the tissue. Briefly, T2 relaxation time reflects the ease of protonic water molecules movement within the matrix. In the articular cartilage, T2 relaxation times mainly depend on the collagen content of the extracellular matrix and the orientation of collagen fibers, and higher relaxation times are correlated with an increased deterioration of the cartilage matrix. The T2 relaxation time is measured as a function of the signal measured in multi-echo SE and FSE T2-weighted images with mono- or multi-exponential decay curve at the different echo times (TE). T1ρ mapping is a compositional approach which is sensitive to regional changes in cartilage matrix proteoglycans characterized by continuous resonance RF pulse. Water molecules protons associated with different macromolecules such as PGs dissipate energy faster than protons of free water molecules, therefore long T1ρ relaxation times correlate with GAG depletion. The main disadvantages are given by issues related to the high SAR (due to the application of long-lasting RF pulses) and long acquisition times. A fundamental advantage of relaxation mapping sequences is that contrast medium administration is not necessary. Both T1ρ and T2 mapping can be assessed both qualitatively with colorimetric scale and quantitatively by ROI positioning. Fibrocartilages (e.g., menisci) can be studied using T1ρ and T2 mapping since they are composed of collagen,

proteoglycans, and water as well. Ultrashort time echo (UTE) T1 and T2 mapping sequences can be used to analyze low intrinsic relaxation time tissues such as menisci, tendons, deep layers of cartilage, deep cartilage areas where non-UTE imaging is not sensitive enough.

Sodium imaging (23Na): This compositional imaging technique is based on the detection of sodium, the positive cation linked to the negatively charged glycosaminoglycan (GAG) of the cartilage's matrix. More specifically, the sodium concentration within the cartilage matrix is directly correlated to the concentration of GAG and hence to proteoglycans. The main strength of sodium (23Na) MRI is in fact the high specificity to proteoglycan. As in relaxometry and diffusion imaging, exogenous contrast medium administration is not required to obtain sufficient tissue contrast. However, in vivo sodium imaging of cartilage limits includes low intrinsic SNR, caused by the low 23Na MRI signal compared to the one from protons.

Delayed gadolinium enhancement MRI of cartilage (dGEMRIC): Contrast medium (gadolinium), injected intravenously is necessary for this imaging method. The scan is performed 60–90 min after injection, to allow diffusion of the contrast medium into the cartilage matrix. Gadolinium is negatively charged and is rejected by positively charged GAGs in cartilage, while in case of cartilage matrix degradation, the amount of contrast in cartilage tissue will be increased in an inversely related manner. The dGEMRIC technique showed high sensitivity and specificity; the routine clinical use is limited by the need for high doses of gadolinium.

Chemical exchange saturation transfer imaging of GAG (gagCEST): This sequence is based on the constant labile protons transfer between solutes (in the case of cartilage, GAGs) and water. The difference between water–water transfer and water–GAG transfer is measured as the magnetic transfer ratio. The signal obtained from the energy transferred after radiofrequency proton saturation is proportional to the concentration of GAG in the tissue. Unfortunately, strong magnetic fields (7 T scanners) are required to obtain sufficient signal, thus widespread use, even in the research field, is currently limited.

Compositional MRI sequences were widely explored in literature for the assessment of cartilage, menisci, and tendons in degenerative osteoarthropathies of peripheral joint, mostly the results concerning the use of T2 mapping on knee articular cartilage. The most important results were obtained by longitudinal studies on disease progression, demonstrating the association and the predictive value of compositional cartilage changes with potential risk factors such as age, sex, BMI, sport, injuries, surgery. Imaging with advanced MRI sequences is becoming increasingly important in cartilage's degeneration studies. Because of the recent widespread development of disease-modifying drugs and regenerative therapies (e.g., platelet-rich plasma, hyaluronic acid, chondrocyte implantation), MRI is also crucial in assessing new therapies for OA prevention or for approaches to avoid progression. As the efficacy is closely connected with early treatment, their use requires suitable biomarkers to provide an early diagnosis and detect signs of progression during treatment. Advanced MRI findings can represent, in this scenario, a powerful tool to understand how to better treat and manage OA and this will possibly allow the creation of a "target-based therapy" for every single component of the cartilage matrix [26].

13.6 Hip Osteoarthritis

The hip is the third most common joint affected by osteoarthritis after the knee and the hand. Women are more commonly affected than men. The reported prevalence varies in different studies and is also subject to geographic distribution. The risk of symptomatic hip osteoarthritis in people reaching the age of 85 is estimated up to 25% in some regions. Attributes, characteristics, or exposures that increase the likelihood of developing hip osteoarthritis are advanced age, obesity, genetics, repetitive stress and mechanical overload, acetabular dysplasia, femoroacetabular impingement, epiphysis capital femoral slip, Perthes disease, and trauma.

Patients usually experience slowly progressive hip pain or hip-related groin pain that radiates into the thigh, gluteus, or knee. Pain can be worse at night, during rest, or after strenuous activity, reducing motion and limiting the walking distance. It can be associated with morning stiffness or after rest. Other symptoms include joint locking, grinding and instability, fatigue, and pain-related psychological distress. Occasionally, a striking discrepancy is observed between radiological findings and clinical symptoms, in fact, patients with pronounced radiological changes have only mild symptoms, while patients with minor radiographic findings complain of acute pain. Therefore, OA diagnosis and, above all, the therapeutic indication, should be made only after both radiological and clinical evaluation [27].

13.6.1 Conventional Radiography (CR)

Plain hip radiographs are inexpensive, widely available, and readily obtainable, and they allow a prompt OA assessment.

For hip osteoarthritis definition, an anteroposterior radiograph of the hip and a lateral cross or lateral view of the frog leg are crucial. As for other joints, reliable radiological indicators are joint space narrowing, subchondral sclerosis, subchondral cysts, and the formation of osteophytes. Narrowing of the hip joint space $\leq$2 mm or <2.5 mm or the combination of joint space narrowing and the presence of osteophytes, especially in the absence of elevated inflammatory markers (e.g., ESR < 20 mm/h), can be used as an indicator of osteoarthritis [28]. In addition, loose bodies (<10), joint deformities, and subluxations can be observed. In advanced stages of OA, the head of the femur is deformed assuming a cylindrical or mushroom-shaped form. The classic radiological sign of osteoarthritis is the joint space narrowing, particularly seen on anteroposterior radiographs taken while the patient is standing (Fig. 13.7). When joint space and cartilage narrowing occurs, the femoral head changes its position relatively to the socket. Femoral head migration is primarily cranial (combined with anterolateral or anteromedial motion) but occasionally axial or medial. This description of the migration is based on what can be observed in the anteroposterior X-ray image. Radiographic signs of medial-caudal migration of the femoral head are the joint space narrowing in the medial joint with subchondral sclerosis and the osteophytes formation in case of laterocranial joint space enlargement. The orthopedic surgeon gives joint replacement indication without

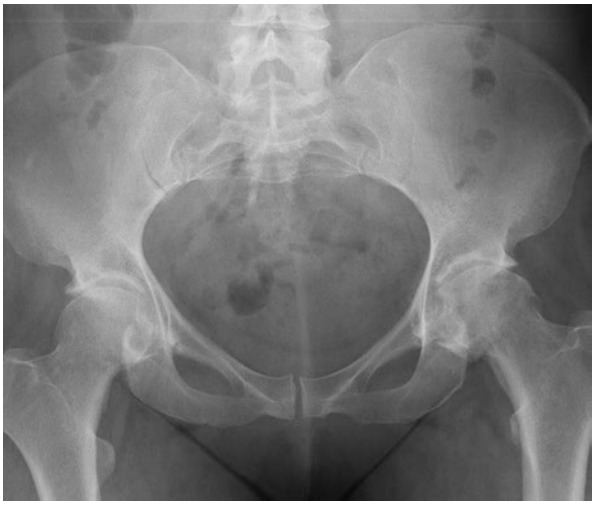

Fig. 13.7 Radiographic findings in a patient with bilateral hip osteoarthritis, with joint space narrowing, subchondral sclerosis, and acetabular osteophytes

regard to the migration's direction. However, as various types of migration lead to leverage ratios modifications, geometric hip joint reconstruction using endoprosthetics goals include center of rotation normalization, anatomical offset reconstruction, and equalization of the leg length [29].

The radiological classification systems most commonly used for hip osteoarthritis assessment are: the Kellgren and Lawrence score, the Croft score, and the Tönnis classification. Although they are all affected by subjectivity, the Kellgren and Lawrence score is apparently the most reliable.

Another semi-quantitative method, which does not provide a grade definition of OA, but classifies several features such as the formation of femoral and acetabular osteophytes and the narrowing of the superior and medial joint space is the OARSI atlas. According to this atlas, a score from 0 to 3 is attributed to the presence and quantity of marginal osteophytes at the level of the upper acetabular side, upper femur, and lower femur, and to the presence or absence of osteophytes on the lower acetabular side.

The narrowing of the joint space is marked 0–3 points on both the superior and medial side. Additional scores (presence/absence) are used for the evaluation of acetabular subchondral cysts, subchondral femoral cysts, femoral subchondral sclerosis, flattening of the femoral head, and thickening of the medial femoral calcar (buttress).

13.6.2 Computed Tomography (CT)

CT exams with multiplane and three-dimensional reconstructions have now replaced most of X-ray views and can easily be used even in patients with limited range of motion. The representation of subchondral sclerosis, cyst formation, and small osteophytes or also the evidence of loose bodies is more accurate than projection

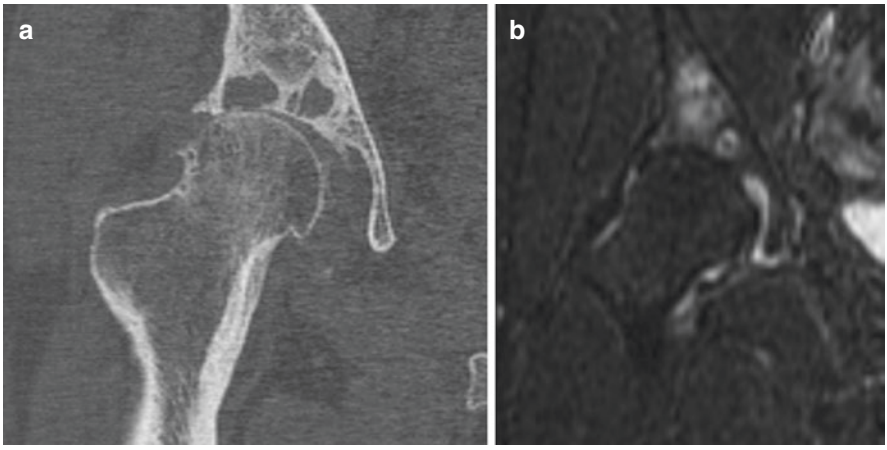

Fig. 13.8 CT (**a**) and STIR MRI (**b**) of the hip joint showing osteoarthritis changes with subchondral geodes, bone marrow edema, and joint effusion

radiography (Fig. 13.8). Another common CT indication is the preoperative diagnosis of hip socket abnormalities or post-traumatic conditions in presence of metal devices which is done by assessing the amount of acetabular bone stock and checking for misalignment or deformity of the proximal femur. The orthopedic surgeon requests the available bone stock localization which allows a safe endoprosthetic anchoring of the implant components. For example, for dysplastic osteoarthritis with high femoral head dislocation and neo-joint, the question will be how large the original acetabulum is and whether there is enough sized bone stock available to firmly anchor the planned socket. In case of axial misalignment and deformity of the proximal femur (e.g., after corrective osteotomy on the proximal femur), three-dimensional CT imaging is essential in planning the multiplane corrective osteotomy if needed. The objective of this procedure is to anchor the shaft components in the femur with a correct alignment and with a sufficient anchoring surface [30].

13.6.3 Magnetic Resonance Imaging (MRI)

MRI is most commonly indicated for the evaluation for surgery where there is a large discrepancy between clinical symptoms and osteoarthritis degree of severity in X-ray images. The orthopedic surgeon examines the MRI to judge the labral and cartilage damage, the presence of effusion/synovitis, and of subchondral and paralabral cysts. When there is hip joint OA, the primary significance of MRI is to show both early signs of arthritis (joint cartilage, labrum) and active signs of osteoarthritis. Additionally, MRI is also capable of showing any associated muscle atrophy. Further indications are to evidence active osteoarthritis (bone marrow edema, synovitis, effusion), as well as assessing the cartilage prior to hip arthroscopy (or the use of endoprostheses). On selected patients MRI is suggested for preoperative

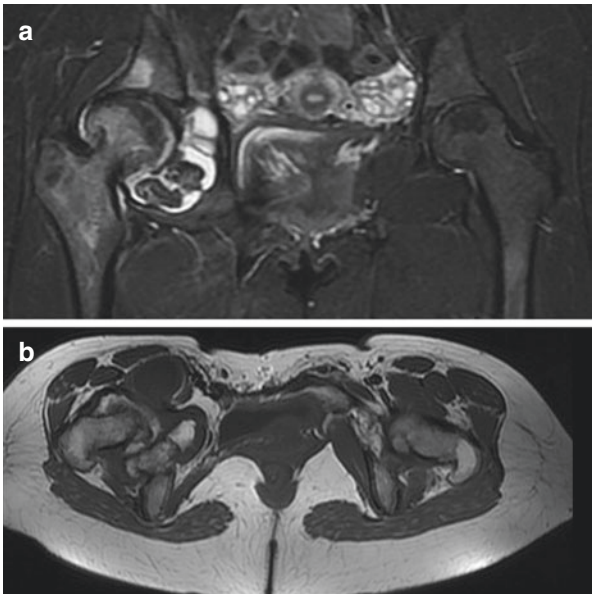

Fig. 13.9 STIR coronal (**a**) and T1-W axial (**b**) MRI images in a patient with right hip osteoarthritis showing the presence of fluid joint distension and synovial chondromatosis

evaluation of actual cartilage damage in joint-preserving periacetabular osteotomy. In addition to the 3D visualization of the acetabular and femoral head-neck morphology, MRI allows the evaluation of a large variety of tissue abnormalities not only of the cartilage and acetabular labrum but also of the bone marrow, ligaments, and synovium. Loose bodies in the form of cartilage and bone peeling are also a typical sign of osteoarthritis and are easier to detect with MRI than on X-rays (Fig. 13.9) [31].

Images should be acquired in sagittal and oblique coronal axial planes. Radial and axial images are of additional utility for femoral head-neck junction and acetabular anatomy evaluation in the case of femoroacetabular impingement associated with cam and/or pincer morphology. For simplified acquisition, 3D imaging and secondary oblique and radial reconstructions are recommended.

The semi-quantitative scoring systems based on MRI most commonly used are the HOAMS, HIMRISS, and SHOMRI scores. The HOAMS evaluates a variety of hip joint characteristics such as condral lesions, bone marrow lesions, subchondral cysts, osteophytes, labral lesions, synovitis, and joint effusion, as well as friction, dysplasia, intra-articular bodies, labral hypertrophy, paralabral cysts, femoral hernia fossa, insertional tendonitis, and/or bursitis. The SHOMRI score evaluates fewer features including: condral loss, bone marrow edema pattern, subchondral cysts, labral anomalies and cysts, intra-articular loose bodies, joint effusion or synovitis, and ligament abnormalities. For the evaluation of active disease, HIMRISS (hip inflammation MRI scoring system) was described, which focuses on the active inflammatory aspects of osteoarthritis and measures only three characteristics of the disease, namely bone marrow injury, effusion, and synovitis [32].

13.7 Foot and Ankle Osteoarthritis

About 1% of the world's adult population is affected by OA of the ankle, which results in pain, dysfunction, and reduced mobility. The mental and physical disability associated with end-stage ankle OA is at least as severe as that associated with end-stage hip OA. While the etiology of OA of the hip and knee is well understood and highlighted in numerous clinical studies, research relating to OA of the ankle is limited. Knowledge and analysis of the underlying etiology are important in selecting the best treatment strategy and are critical to achieving long-term satisfactory results and avoiding postoperative complications. Unlike the hip and knee, the ankle joint is rarely affected by primary OA. Numerous clinical and epidemiological studies have identified prior trauma as the most common cause of OA in the ankle instead. Patients with post-traumatic OA are generally younger patients than the ones with the primary form. An epidemiological study of patients with disabling OA of the hip, knee, and ankle showed that 1.6% of patients with hip OA, 9.8% of patients with knee OA, and 79.5% of patients with ankle OA had a verified history of 1 or more joint injuries. Saltzman and his colleagues evaluated 639 patients with end-stage painful OA in the ankle (Kellgren grade 3 or 4), founding that 70% of patients had post-traumatic OA, 12% had rheumatoid OA, and 7% had primary OA. While rotational ankle fractures were identified as the most common reason for post-traumatic ankle OA, previous ligament injuries have also been found to be a cause of ankle OA. Secondary OA has also been associated with a variety of underlying diseases or disorders, such as rheumatoid disease, hemochromatosis, hemophilia, gout, neuropathic diseases, avascular talus necrosis, osteochondral lesions, and postinfectious arthritis [33, 34].

A 4-film series of conventional radiographs including anteroposterior and lateral views of the foot, mortise view of the ankle, and Saltzman view of the hindfoot can be routinely performed for radiographic evaluation of the ankle and foot OA. Only foot and ankle X-rays are acceptable because non-weight bearing X-rays are often misleading. Additionally, standing views can help standardize radiographic techniques, allowing for more reliable comparison of inter and intra-individual radiographs. Ankle alignment must be analyzed on all 3 levels: supra-malleolar, intra-articular, and infra-malleolar. Supra-malleolar alignment of the ankle should be assessed in the coronal and sagittal planes by measuring the distal medial tibial angle and the anterior distal tibial angle, respectively. Measurement of the distal medial tibial angle depends on the radiographic technique. Saltzman's view should be used to assess infra-malleolar alignment. Several measurement techniques can be applied to quantify the infra-malleolar hindfoot alignment. Firstly, the angle between the longitudinal axis of the tibia and the heel axis can be measured as suggested by Cobey and Reilingh. Takakura and colleagues used weight-bearing radiographs to classify OA of the ankle into four stages. For clinical use, investigators simplified this classification, describing stage 1 as early, stages 2 and 3 as intermediate, and stage 4 as late [35].

13.8 Interventional Radiology in Osteoarthritis

Interventional radiology can offer a wide range of therapeutic procedures also in musculoskeletal pathology through ultrasound, CT, and MRI guidance. Based on the above evidence, the synovium—that is synovial inflammation—has become one of the main therapeutic targets not only for inflammatory arthropathies but also in degenerative arthrosis. Corticosteroids are arguably the most widely used anti-inflammatory drugs. The possibility, through image guidance, of direct intra-articular injection of drugs is the key to maximizing therapeutic effects while minimizing known systemic side effects. In addition to intra-articular administration, ultrasound imaging guidance is useful for intra-bursal and peri-tendinous assessment, where corticosteroids may have an anti-inflammatory action on synovial tissue. The imaging guide also helps minimize other risks of unguided corticosteroid infiltration, such as tendon ruptures. Injection of hyaluronic acid (HA) is another interventional procedure that can be suggested for degenerative joint disease (i.e., osteoarthritis) but mainly for the synovium. Hyaluronic acid is a glycosaminoglycan consisting of highly hydrophilic chains of D-glucuronic acid and *N*-acetylglucosamine. There are numerous types of hyaluronic acid on the market, which are distinguished mainly by their molecular weight. Hyaluronic acid with low molecular weight, able to bind to binding proteins (hyaladerin) and to the CD44 receptor, acts mainly with a biological effect of viscoinduction (i.e., by stimulating the endogenous production of HA). Those with high molecular weight, however, have a lower biological effect while carrying out a powerful viscous supplementation action, thanks to their rheological properties. Although the meta-analysis highlights the available studies heterogeneity, intra-articular injections of HA appear to be effective in the treatment of arthritic pain (mild to moderate OA) in both the knee and the hip. The size of the results on pain resolution varies between studies, peaking at 8 weeks (superior to corticosteroids). Cross-linked (high molecular weight) products have greater pain efficacy than linear HA and there is evidence to support the efficacy of HA also regarding functional improvement (level 1B). In all guidelines, use is recommended for osteoarthritis management of second-line treatment in symptomatic patients after conservative therapy (NSAIDs). Injection of platelet-rich plasma is another therapeutic tool that we can consider. This product, consisting of a platelet ultrafiltrate, carries out its action through various growth factors (PDGF, TGF-B, EGF, CTGF) released with their anti-inflammatory and trophic action on various joint tissues. There are several in vitro and clinical evidence that intra-articular injection of PRP can exert a positive influence in patients with knee cartilage degeneration and OA and that it may have greater and longer efficacy than HA in improving pain and joint function [36, 37].

References

1. Kobayashi T, Takagishi K, Shitara H, Ichinose T, Shimoyama D, Yamamoto A, et al. Prevalence of and risk factors for shoulder osteoarthritis in Japanese middle-aged and elderly populations. J Shoulder Elb Surg. 2014;23(5):613–9.
2. Mehl J, Imhoff AB, Beitzel K. [Osteoarthritis of the shoulder: pathogenesis, diagnostics and conservative treatment options]. Orthopade. 2018;47(5):368–76.
3. Tauber M, Martetschlager F. [Shoulder Osteoarthritis-pathogenesis, classification, diagnostics and treatment]. Orthopade. 2019;48(9):795–808.
4. Thomas M, Bidwai A, Rangan A, Rees JL, Brownson P, Tennent D, et al. Glenohumeral osteoarthritis. Should Elb. 2016;8(3):203–14.
5. Dekker TJ, Steele JR, Vinson EV, Garrigues GE. Current peri-operative imaging concepts surrounding shoulder arthroplasty. Skelet Radiol. 2019;48(10):1485–97.
6. Bercik MJ, Kruse K II, Yalizis M, Gauci MO, Chaoui J, Walch G. A modification to the Walch classification of the glenoid in primary glenohumeral osteoarthritis using three-dimensional imaging. J Shoulder Elb Surg. 2016;25(10):1601–6.
7. Choate WS, Shanley E, Washburn R, Tolan SJ, Salim TI, Tadlock J, et al. The incidence and effect of fatty atrophy, positive tangent sign, and rotator cuff tears on outcomes after total shoulder arthroplasty. J Shoulder Elb Surg. 2017;26(12):2110–6.
8. Barreto RPG, Braman JP, Ludewig PM, Ribeiro LP, Camargo PR. Bilateral magnetic resonance imaging findings in individuals with unilateral shoulder pain. J Shoulder Elb Surg. 2019;28(9):1699–706.
9. Davis DL, Gilotra MN, Calderon R, Roberts A, Hasan SA. Reliability of supraspinatus intramuscular fatty infiltration estimates on T1-weighted MRI in potential candidates for rotator cuff repair surgery: full-thickness tear versus high-grade partial-thickness tear. Skelet Radiol. 2021;50(11):2233–43.
10. McDonald S, Hopper MA. Acromioclavicular joint disease. Semin Musculoskelet Radiol. 2015;19(3):300–6.
11. Krill MK, Rosas S, Kwon K, Dakkak A, Nwachukwu BU, McCormick F. A concise evidence-based physical examination for diagnosis of acromioclavicular joint pathology: a systematic review. Phys Sportsmed. 2018;46(1):98–104.
12. Veen EJD, Donders CM, Westerbeek RE, Derks RPH, Landman EBM, Koorevaar CT. Predictive findings on magnetic resonance imaging in patients with symptomatic acromioclavicular osteoarthritis. J Shoulder Elb Surg. 2018;27(8):e252–e8.
13. Precerutti M, Formica M, Bonardi M, Peroni C, Calciati F. Acromioclavicular osteoarthritis and shoulder pain: a review of the role of ultrasonography. J Ultrasound. 2020;23(3):317–25.
14. Kalichman L, Hernandez-Molina G. Hand osteoarthritis: an epidemiological perspective. Semin Arthritis Rheum. 2010;39(6):465–76.
15. Leung GJ, Rainsford KD, Kean WF. Osteoarthritis of the hand I: aetiology and pathogenesis, risk factors, investigation and diagnosis. J Pharm Pharmacol. 2014;66(3):339–46.
16. Haugen IK, Boyesen P. Imaging modalities in hand osteoarthritis--and perspectives of conventional radiography, magnetic resonance imaging, and ultrasonography. Arthritis Res Ther. 2011;13(6):248.
17. Marshall M, van der Windt D, Nicholls E, Myers H, Hay E, Dziedzic K. Radiographic hand osteoarthritis: patterns and associations with hand pain and function in a community-dwelling sample. Osteoarthr Cartil. 2009;17(11):1440–7.
18. Weiss AC, Goodman AD. Thumb basal joint arthritis. J Am Acad Orthop Surg. 2018;26(16):562–71.

19. Sivakumaran P, Hussain S, Ciurtin C. Comparison between several ultrasound hand joint scores and conventional radiography in diagnosing hand osteoarthritis. Ultrasound Med Biol. 2018;44(3):544–50.
20. Fjellstad CM, Mathiessen A, Slatkowsky-Christensen B, Kvien TK, Hammer HB, Haugen IK. Associations between ultrasound-detected synovitis, pain, and function in interphalangeal and thumb base osteoarthritis: data from the nor-hand cohort. Arthritis Care Res. 2020;72(11):1530–5.
21. Marshall M, Watt FE, Vincent TL, Dziedzic K. Hand osteoarthritis: clinical phenotypes, molecular mechanisms and disease management. Nat Rev Rheumatol. 2018;14(11):641–56.
22. Saltzherr MS, Muradin GSR, Haugen IK, Selles RW, van Neck JW, Coert JH, et al. Cartilage evaluation in finger joints in healthy controls and early hand osteoarthritis patients using high-resolution MRI. Osteoarthr Cartil. 2019;27(8):1148–51.
23. Teichtahl AJ, Wluka AE, Davies-Tuck ML, Cicuttini FM. Imaging of knee osteoarthritis. Best Pract Res Clin Rheumatol. 2008;22(6):1061–74.
24. Jacobson JA, Girish G, Jiang Y, Sabb BJ. Radiographic evaluation of arthritis: degenerative joint disease and variations. Radiology. 2008;248(3):737–47.
25. Kornaat PR, Bloem JL, Ceulemans RY, Riyazi N, Rosendaal FR, Nelissen RG, et al. Osteoarthritis of the knee: association between clinical features and MR imaging findings. Radiology. 2006;239(3):811–7.
26. Bruno F, Arrigoni F, Palumbo P, Natella R, Maggialetti N, Reginelli A, et al. New advances in MRI diagnosis of degenerative osteoarthropathy of the peripheral joints. Radiol Med. 2019;124(11):1121–7.
27. Aresti N, Kassam J, Nicholas N, Achan P. Hip osteoarthritis. BMJ. 2016;354:i3405.
28. Nilsdotter A, Bremander A. Measures of hip function and symptoms: Harris Hip Score (HHS), Hip Disability and Osteoarthritis Outcome Score (HOOS), Oxford Hip Score (OHS), Lequesne Index of Severity for Osteoarthritis of the Hip (LISOH), and American Academy of Orthopedic Surgeons (AAOS) Hip and Knee Questionnaire. Arthritis Care Res. 2011;63(Suppl 11):S200–7.
29. Weber MA, Merle C, Rehnitz C, Gotterbarm T. Modern radiological imaging of osteoarthritis of the hip joint with consideration of predisposing conditions. RöFo. 2016;188(7):635–51.
30. Gold GE, Cicuttini F, Crema MD, Eckstein F, Guermazi A, Kijowski R, et al. OARSI clinical trials recommendations: hip imaging in clinical trials in osteoarthritis. Osteoarthr Cartil. 2015;23(5):716–31.
31. Jaremko JL, Lambert RG, Zubler V, Weber U, Loeuille D, Roemer FW, et al. Methodologies for semiquantitative evaluation of hip osteoarthritis by magnetic resonance imaging: approaches based on the whole organ and focused on active lesions. J Rheumatol. 2014;41(2):359–69.
32. Huang BK, Tan W, Scherer KF, Rennie W, Chung CB, Bancroft LW. Standard and advanced imaging of hip osteoarthritis. What the radiologist should know. Semin Musculoskelet Radiol. 2019;23(3):289–303.
33. Barg A, Pagenstert GI, Hugle T, Gloyer M, Wiewiorski M, Henninger HB, et al. Ankle osteoarthritis: etiology, diagnostics, and classification. Foot Ankle Clin. 2013;18(3):411–26.
34. Kraus VB, Kilfoil TM, Hash TW II, McDaniel G, Renner JB, Carrino JA, et al. Atlas of radiographic features of osteoarthritis of the ankle and hindfoot. Osteoarthr Cartil. 2015;23(12):2059–85.
35. Wilkinson VH, Rowbotham EL, Grainger AJ. Imaging in foot and ankle arthritis. Semin Musculoskelet Radiol. 2016;20(2):167–74.
36. Acanfora C, Bruno F, Palumbo P, Arrigoni F, Natella R, Mazzei MA, et al. Diagnostic and interventional radiology fundamentals of synovial pathology. Acta Biomed. 2020;91(8-S):107–15.
37. Barile A, La Marra A, Arrigoni F, Mariani S, Zugaro L, Splendiani A, et al. Anaesthetics, steroids and platelet-rich plasma (PRP) in ultrasound-guided musculoskeletal procedures. Br J Radiol. 2016;89(1065):20150355.

Metabolic Bone Disease in Geriatric Patients

14

Maria Pilar Aparisi Gómez, Francisco Aparisi, Giuseppe Guglielmi, and Alberto Bazzocchi

14.1 Introduction

As humans age, the lean components of the organism such as total body water, organ mass, mineral bone, and skeletal muscle decrease, while total body fat increases, with an associated redistribution: it becomes more abundant in the abdominal region than in peripheral locations [1].

The process of aging involves endocrine and metabolic alterations, but besides, an increasingly sedentary lifestyle generates a positive imbalance between intake and use of energy [2, 3]. Aging is characterized by a low-grade chronic inflammatory status known as "inflammaging" [4].

Due to the role fat has as an endocrine organ, the increase in body fat and the redistribution of the fat in geriatric population have been demonstrated to be associated with risk factors for non-insulin-dependent diabetes and cardiovascular disease [5].

M. P. Aparisi Gómez
Department of Radiology, Auckland City Hospital, Auckland, New Zealand

Department of Radiology, IMSKE, Valencia, Spain
e-mail: pilara@adhb.govt.nz

F. Aparisi
Department of Radiology, Hospital Nueve de Octubre, Valencia, Spain

G. Guglielmi
Clinical and Experimental Medicine, University of Foggia, Foggia, Foggia, Italy
e-mail: giuseppe.guglielmi@unifg.it

A. Bazzocchi (✉)
Diagnostic and Interventional Radiology, IRCCS Istituto Ortopedico Rizzoli, Bologna, Italy
e-mail: abazzo@inwind.it

G. Guglielmi, M. Maas (eds.), *Imaging in Geriatrics*, Practical Issues in Geriatrics, https://doi.org/10.1007/978-3-031-14877-4_14

The loss of mineral contents in bone and structural changes are a major risk for morbidity, need for institutionalization, and mortality. Sarcopenia, with a decrease in muscle mass and function, has been associated with impaired immunity and functional status [6, 7].

The three tissues (fat, muscle, and bone) have a very close relationship, and therefore analysis and evaluation should be approached in a combined way.

Osteoporosis is described as a systemic bone disease characterized by low bone mass and microarchitectural deterioration of bone tissue, with a consequent increase in bone fragility and susceptibility to fracture [8].

Osteoporosis as an entity may result either from defective skeletal development leading to a start point of low bone mass and quality, or from an imbalance in coupling, with an increase in the resorption of bone, exceeding formation.

The most prevalent cause for osteoporosis and therefore statistically the most common cause for fragility fractures is postmenopausal osteoporosis, which is inherently linked to aging in women; however, any situation where there is osteoporosis, either primary or secondary to several conditions, in both genders, increases the risk of occurrence of a fragility fracture. Postmenopausal osteoporosis develops after a decrease in estrogen levels following menopause.

Senile osteoporosis is another primary cause for osteoporosis and affects both genders. This is age related, occurring in individuals older than 75 years. Bone formation is impaired through a mechanism of decreased renal production of 1,25 dihydroxyvitamin D with a subsequent drop in calcium absorption from the diet that results in secondary hyperparathyroidism [9].

The most prevalent type of fragility/insufficiency fracture is the vertebral compression fracture, but the effect of osteoporosis on the skeleton is systemic, and there is increased risk of almost all types of fractures. Other frequent locations for insufficiency fractures are the pelvic girdle and the proximal femur. Locations such as the femoral diaphysis, tibia, fibula, and calcaneus and metatarsal bones are less frequent and can represent a diagnostic challenge [10].

In the bone, the aging process is characterized by a progressive accumulation of adipose cells within the bone marrow (BM). The role of marrow adipose tissue (MAT) as a component of the BM microenvironment has been thoroughly investigated in the last few years. A growing amount of evidence shows that there is an inverse association between MAT content and both bone mineral density (BMD) and bone integrity [11].

In this chapter, we aim to summarize the current knowledge on changes in bone metabolism occurring in the elderly and review the possibilities of assessment that each one of the imaging techniques offers for the adequate assessment of bone mineral density in the geriatric population.

The contents of this chapter need to be taken into consideration together with the chapter on body composition in geriatric patients. The effects of aging on fat and muscle are extensively reviewed in a dedicated chapter, but it is important to acknowledge the close relationship and interrelation existing between all components.

14.2 Changes in Bone with Aging

14.2.1 Menopause

Estrogen has a very important role in normal physiologic remodeling, and its deficiency after menopause results in remodeling imbalance with an increase in bone turnover. The imbalance leads to a progressive loss of trabecular bone first (most metabolically active) and then progressively cortical bone [9].

Menopause is defined by the World Health Organization (WHO) as the "permanent cessation of menstruation resulting from the loss of ovarian follicular activity," initiated by the decline in estrogen and progesterone production and by increasing follicle stimulating hormone (FSH) and luteinizing hormone (LH) levels. Twelve months of consecutive amenorrhea are necessary to establish the onset of menopause. The perimenopausal stage is defined as the time elapsed from the commencement of the first clinical signs (cycle irregularity, known as "menopause transition") and a year after the last period. Elevation of early follicular phase FSH is a clinical marker of reduced ovarian reserve and decreased response of the ovary to ovulation induction.

The endocrinology of menopause is complex and results from changes in the pituitary-ovarian axis with age in regularly cycling women. The decline in follicle numbers results in a decline in ovarian hormone production, which alters the pituitary feedback.

The rise in serum FSH is accompanied by minimal changes in circulating levels of LH. Concentrations of androgens appear to be lower in the postmenopausal status, it is thought that this happens as a function of increasing age during the reproductive years as opposed to a consequence of menopause as such. By 12–24 months after menopause, the levels of estradiol in serum are normally <80 pm/L, compared with mean values of approximately 550 pm/L in premenopausal stage. The levels of FSH are 10–15 times higher than the levels that would be usual in earlier follicular phases in young women. LH levels are approximately 3 times higher. Plasma testosterone levels decrease from ~1 to 0.6 nmol/L. There is an approximately 40% decrease in the ovarian androstenedione production, dehydroepiandrosterone sulfate (DHEAS) production declines in a linear fashion with age, not related to postmenopausal status as such [12].

The decrease in estradiol levels has different systemic effects and can contribute to the development of different disorders: osteoporosis, cardiovascular risk, changes in mood, and mental health.

14.2.2 Calcitriol

Senile osteoporosis is another primary cause for osteoporosis and affects both genders. This is age related, occurring in individuals older than 75 years. Bone formation is impaired through an alteration in the metabolism of vitamin D. In this context the cortical as well as the trabecular bone is affected [9].

Vitamin D, as its major metabolite, 1,25-dihydroxyvitamin D or calcitriol, plays a role in the homeostasis of bone, muscle, and adipose tissue through life, not only during growth, but also in aging.

In the elderly, levels may be impaired, due to various reasons, which include reduced intake, decreased skin production of cholecalciferol (first precursor of active vitamin D), possibly due to lower sun exposure, decrease in the activity of liver hydroxylases with a drop in the conversion to calcidiol, and (25-hydroxyvitamin D) and decrease in the activity of renal hydroxylases with a drop in the conversion to calcitriol [13].

Calcitriol is relevant in the function of proteins that transport calcium, and as a result of its decrease, calcium absorption is decreased.

There is a strong correlation between low calcidiol concentrations and increasing levels of obesity [14].

Obese individuals, even when controlling for sunlight exposure, are significantly more likely to have low concentrations of calcidiol, which reflects inadequate vitamin D status [15].

Inadequate vitamin D status can increase adipogenesis by promoting higher parathyroid hormone (PTH) secretion, which increases the influx of extracellular calcium into adipocytes, promoting adipogenesis. In a similar way, low calcium in serum may promote an increase in the circulating calcitriol and PTH, with the same increased adipogenesis result [16, 17].

Calcitriol is essential for normal bone turnover and maintenance, as well as for the metabolism of calcium, phosphorus, and magnesium [14]. A decrease in calcitriol disturbs calcium homeostasis and impairs bone health, which leads to an increase in fracture incidence [18]. Despite this, the recommendations for vitamin intake and adequate serum concentrations of calcidiol are still controversial [19].

Inadequate levels of vitamin D have also been associated with sarcopenia, decreased grip strength, and impaired functionality in older adults [20, 21].

Studies have demonstrated that the inverse relationship between vitamin D status and PTH concentration is associated with compromised muscle mass and strength, as well as diminished physical function [20, 21].

A study in the elderly demonstrated that low calcidiol and high PTH increase the risk of sarcopenia, reflexed in low muscle mass and reduced hand grip strength [22].

Another study has found that patients with insufficient calcidiol and low BMD are also more likely to develop sarcopenia [20].

14.3 Interaction Among Bone, Muscle, and Fat

In the past, it was believed that obesity had a protective role in bone and in muscle, providing mechanical load and therefore stimulus for their maintenance. Fat is as well a source of estrogens, which are beneficial to maintain bone health, reducing bone resorption, contributing to muscle repair and regeneration and reducing adipogenesis [23–25].

However, some concepts have shifted. Fat has been seen to act as an endocrine organ, releasing hormones such as leptin and releasing cytokines, which are proinflammatory agents [26]. In particular, visceral fat (VAT) has a negative impact on bone and muscle [27]. VAT secretes proinflammatory cytokines such as tumor necrosis factor-alpha (TNF α), interleukin 1 and 6 (IL-1 and IL-6), and even C-reactive protein in high inflammatory status [28]. These factors promote and sustain low-grade chronic inflammation, which in turn causes derangement of all three tissues simultaneously and causes more fat deposition, perpetuating the problem [27, 28].

Weight gain in older adults leads to greater visceral fat accumulation and long term impairments in bone and muscle as a consequence.

A study performed in 500 healthy women demonstrated that body fat higher than 33% was negatively correlated to femoral neck bone mineral density (BMD), and if this increased to 38%, it was negatively correlated to BMD in the lumbar spine and total-body BMD [29].

Another study identified a cut off of 38.3% body fat as the inflection point where the slope of the relation between visceral fat and percent body fat increases significantly [30]. This disputes the concept that obesity is protective for bone health, especially for women, but the relationship between obesity and bone is ultimately of complex nature [31], and more research is needed to determine the threshold in which body fat becomes harmful for bones and muscle [29], as we will review when addressing the topic of frailty.

The amount of bone marrow adipose tissue (MAT) increases with aging, in obesity and osteoporosis. MAT appears to reduce osteoblast and osteoclast activity, slowing down bone turnover (which may be beneficial in some cases like menopause) and decreasing the rate of bone accrual [32]. A negative correlation between MAT and BMD has been proven [33]. However, it is still confusing whether the relationship between MAT and osteoporosis is causative or correlative [32].

It is clear that MAT has a role in bone health, through its paracrine and endocrine interaction with the other components of bone. There is evidence that the bone marrow stem cells (precursors of adipocytes and osteoblasts) may favor adipogenic differentiation in the presence of excessive adiposity, and this is one of the reasons osteoporosis has been labeled as the "obesity of bone" [34] and increased adipogenesis in the marrow "osteosteatosis" [35].

The MAT–bone interaction is a fertile area of research. The development of imaging, and more especially MR based techniques has unlocked numerous pathways to assess and quantify MAT and thus set the ground to carry out studies to further elucidate the implications of MAT in physiologic and pathologic conditions [36].

A prospective study in a population of Korean women demonstrated that postmenopausal women with higher VAT levels lost significantly more lean mass over a period of 27 months than women with lower VAT levels. The decrease in VAT did not result in a parallel change in BMI, which suggested that fat was replacing the lost muscle tissue and possibly infiltrating it [27, 37].

Aging in skeletal muscle involves fat deposit, in the form of intra- and extramyocellular adipocytes, known as myosteatosis. This is seen in older women, even if they are not obese [38], but can also be seen in younger individuals [39]. Myosteatosis has been considered the "obesity of muscle" [35].

The role of proinflammatory cytokines such as TNF α and IL-6 in muscle wasting and their elevated serum concentration in sarcopenia and sarcopenic obesity has been established [40]. Additionally, muscle mass is the main determinant of resting metabolic rate, and loss of muscle would in turn also promote weight gain and fat accumulation.

In this way, it is easy to see how muscle and bone loss and accumulation of VAT with aging, aggravated by overall excess of adiposity are part of a cycle where increased inflammation from visceral fat favors sarcopenia and osteopenia, promotes obesity and as a consequence, greater fat accumulation.

Although fat infiltration of bone and muscle is a part of normal aging, its elevation in an obesogenic environment exacerbates loss of bone and muscle. The increase in MAT and myosteatosis, combined with the age related loss of bone and muscle mass contributes even more to loss of bone and muscle and therefore strength and overall functionality [38, 41].

Loss of functionality and mobility increases the risk for falls and fractures. Besides, processes like myosteatosis lead to the development of disorders like diabetes, in which the risk of falls is increased, secondary to impaired vision or neuropathy [11, 38].

All this explains the increased risk of frailty in older adults, in cases of osteosarcopenic obesity and of osteopenic obesity and sarcopenic obesity [42, 43].

Older women suffering from any of these conditions were inferior in several functional performance measures to only obese counterparts and those suffering from osteosarcopenic obesity showed significantly poorer performance in hand grip strength, balance, and walking speed, compared to each one of the other groups [43].

Chung et al. found in a study on older adults that sarcopenic obesity put them at greater risk of osteoporosis, and the physical decline from sarcopenia appeared to promote greater loss of bone [44]. The physical decline from any of the conditions may easily aggravate other declines, ultimately leading to osteosarcopenic obesity.

Overall changes in body composition, leading to impairments in bone, muscle, and fat tissues have to be taken into consideration when evaluating the health of the elderly.

14.4 Bone as Endocrine Organ

Osteoblasts secrete osteocalcin (bone gamma-carboxyglutamic acid (Gla) protein), which is largely incorporated into the extracellular bone matrix (hydroxyapatite), but a small amount remains in serum and is used as an indicator of bone formation [45].

Most of the osteocalcin is carboxylated with vitamin K dependent enzymes and as a result of this process it can bind calcium within the hydroxyapatite matrix and stabilize the bone [45]. In cases in which activity of the enzyme is impaired, as in

low vitamin K status, often present in the elderly, there will be an excess of undercarboxylated osteocalcin which will not bind to hydroxyapatite and therefore less bone stabilization, resulting in bone loss. Osteocalcin also stimulates the secretion of adiponectin from fat cells. Some studies demonstrated that adiponectin had a negative impact on bone mass by decreasing osteoblast proliferation [46, 47] but other studies showed that through the same pathway, adiponectin inhibited osteoclastogenesis [48, 49].

Undercarboxylated osteocalcin in serum was shown to stimulate pancreatic beta cell proliferation and insulin secretion and thus positively contribute to modulate energy metabolism [50].

Mounting evidence on systemic hormonal actions of osteocalcin have gained it the consideration of an osteokine [26].

14.5 Consequences of the Changes in Bone with Aging

14.5.1 Fragility Fractures

Hip, vertebral, and wrist fractures are the most frequent fractures associated with osteoporosis. The effect of osteoporosis is systemic, though, so there is increased risk for almost all types of fractures.

The combined lifetime risk for a hip, forearm, and vertebral fracture is approximately 40%, which is equivalent to the risk of developing cardiovascular disease [51].

Fragility fractures due to osteoporosis are one of the most substantial challenges to public health. The World Health Organization considers osteoporosis to be second to cardiovascular risk as a critical health problem.

Approximately 1 in 3 women and 1 in 5 men over the age of 50 will have a fragility fracture in their remaining lifetime, as per data in Caucasian populations, from the International Osteoporosis Foundation [52].

In 2000 there were an estimated nine million new osteoporosis fractures, of which 1.6 million were at the hip, 1.7 million were at the forearm, and 1.4 million were clinical vertebral fractures. Europe and the Americas accounted for 51% of all these fractures, while most of the remainder occurred in the Western Pacific region and Southeast Asia.

In 2006 it was estimated that osteoporosis caused more than 8.9 million fractures annually worldwide, resulting in an osteoporosis fracture every 3 s [53].

In patients with a hip fracture, it is estimated that up to 20% will die within the following year due to associated morbidity, with a mortality at 5 years 20% greater than expected, and approximately 20% will require permanent care [54] (Fig. 14.1).

Patients with vertebral fractures have less severe complications, but these are more frequent, and approximately only 30% of them come to clinical attention [55]. In these cases there is substantial disability from pain and generally increased thoracic kyphosis.

Vertebral fractures have a prevalence of about 35–50% among women over 50 years of age (postmenopausal status) [56], frequently occur in absence of a major

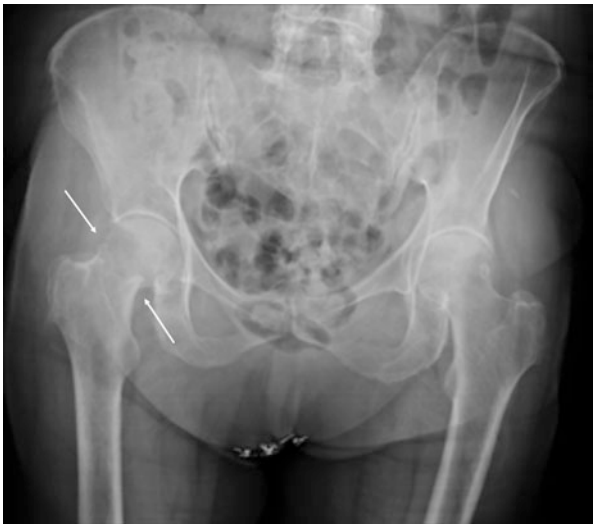

Fig. 14.1 Subcapital femoral neck fracture of the right hip. These fractures normally result from a fall from height in the context of osteopenia or osteoporosis. In patients with a hip fracture, it is estimated that up to 20% will die within the following year due to associated morbidity, with a mortality at 5 years 20% greater than expected, and approximately 20% will require permanent care. The main radiographic features of osteoporosis consist of increased bone radiolucency, cortical thinning, and changes in the trabecular pattern, all visible on this radiograph

trauma and may be asymptomatic [57], and increase the risk of a new incidental VF and other fragility fractures. Individuals with a pre-existing VF have a four- to five-fold increase in risk of sustaining a new VF, the risk increases with the number of prevalent fractures at baseline and is BMD-independent [56]. Conventional radiography and DXA represent the techniques of choice for VFs detection [57].

Wrist fractures increase almost twofold the risk of subsequent hip or vertebral fractures, but also the risk of a new forearm fracture is increased by 3.3 times, and other skeletal fractures by 2.4 times [58].

Humeral fractures, which are the third most common type of fracture in people over 65 years, have been associated with a higher risk of hip fractures more than 5 times in the following year [59].

Fractures at the foot or ribs were seen to double the risk of hip, vertebral, forearm, and other types [58].

The existence of an insufficiency fracture is an indication for treatment of osteoporosis.

14.5.2 Frailty

Physical frailty is recognized as a geriatric syndrome, which has become a relevant concern in public health worldwide, with global population aging [60, 61]. The most widely used definition of frailty includes the presence of three of the following

indicators: muscle strength loss, slowness, fatigue, low physical activity, and body weight loss [62].

Frail older adults are at increased risk of falls, hip fracture, disability, and mortality [63]. Evidence that body weight is positively associated with bone health in older adults is increasing [25]; there is also evidence that lean and fat masses, constituting 95% of body weight, might have a different relationship with bone mass [64].

The potential consequences of body-composition change in frail older persons should be put both in the context of bone health and with regard to risks of osteoporotic fractures. Frail people have lower muscle mass and higher fat mass than non-frail people, but osteoporosis is highly prevalent in the elderly population. Derangements in inflammatory, endocrine, coagulation, and metabolic systems should be individually assessed in frail adults and not allow for generalization in comparison with non-frail aging populations [65, 66]. Zaslavsky et al. demonstrated that adiposity in the context of frailty has a different impact on survival than the one that can be observed in non-frail population [67]. A recent study from the same group showed that appendicular, trunk, and total body fat, as well as lean mass indexes, are significant determinants of total hip BMD in frail women. Higher lean and fat mass indexes are associated with lower risks of hip fractures, and whole-body fat is the only index to retain indirect association, independently of total hip BMD. Change over time in body-composition indexes was not a significant determinant of bone health in older women with frailty [68]. These data confirm previous studies showing an association between whole-body and abdominal fat mass measures and lower risks of hip fracture. The association was independent of BMD, indicating that central adiposity might be informative in predicting fractures over and beyond BMD [69]. In summary, central adiposity may have some benefits for bone health in the context of frailty, and this should be put in the balance with the risks of cardiovascular disease.

In studies that included men and women, higher lean mass was not significantly correlated with hip fractures in models adjusted for total hip BMD [38, 68] which seems contradictory, given that the association of low BMD and low lean mass on increasing fracture risk has also been proven [70]. The positive impact of lean mass on hip fracture risk might thus be channeled through anabolic processes on the bone.

Using the pool of patients from the Women's Health Initiative, with sample size of over 120,000 postmenopausal women, Harris et al. concluded that women with low BMD (T-score <-1), with and without sarcopenia, had a higher risk of fracture than women with isolated sarcopenia and those considered normal. These results suggest that sarcopenia does not carry additional risk for fracture in women [71]. The study was limited to fractures around the hip; although women with the combination of low BMD and sarcopenia had a higher risk of fracture, whereas sarcopenia alone was not an independent risk factor for fracture in women, the fact that adding sarcopenia to low BMD resulted in a greater risk suggests that there is communication between muscle and bone at this site, associated with frailty [72]. The interaction may be mediated by mechanical stimuli, genetic factors, hormonal influences, and body composition. Total bone mineral content is associated more closely with

lean tissue than with fat tissue mass, and regional BMD is predicted by changes in fat tissue mass [73].

A number of mechanisms for the fat–bone relationship in older adults have been proposed. These include the effect of soft tissue mass on skeletal loading, the association of fat mass with the pancreatic beta cell, and adipocyte secretion of hormones involved in bone metabolism [25]. Additionally, weight reduction may lead to accelerated rates of bone loss in postmenopausal women. In a large study that also used data across the Women's Health Initiative, postmenopausal women who lost more than 5% of their baseline weight within 3 years of follow-up had 65% higher rate of hip fractures as compared with women with stable weight (<5% change). This confirms that body weight is positively associated with bone health [74].

Frail women are at increased risk of recurrent falls compared with non-frail women [75], and most hip fractures are secondary to falls [76]. A lower muscle mass may lead to accidents or falls [77], with secondary fractures, but falls could also be a confounding factor, indicative of poor general health [78]. Conversely, higher fat mass might be protective during falls by fat cushioning [69].

14.6 Diagnosis of Metabolic Bone Disease Applied to the Elderly

14.6.1 Radiography

Findings suggestive of osteoporosis can be frequently found on radiographs. The main radiographic features of osteoporosis consist of increased bone radiolucency, cortical thinning, and changes in the trabecular pattern [79]. The first sign results from the decline in BMC and deterioration of the trabecular microarchitecture; this feature is detectable only in the advanced stages of the disease, when the amount of bone loss reaches at least 30% [80] (Fig. 14.1).

Cortical thinning results from the reabsorption of the periosteal, intracortical, and endosteal layers. When this happens in the vertebral bodies concomitantly to the increase in bone radiolucency, the vertebrae acquire a "picture frame" appearance, also known as "ghost vertebra" [80] (Fig. 14.2). In the early stages of osteoporosis, this cortical thinning appears as scalloping in the inner margin of the cortex (endosteal scalloping).

The alteration in trabecular pattern happens because trabeculae offer a greater surface area for resorption processes and respond faster to metabolic changes than cortical bone. Trabeculae are more abundant in the axial skeleton and at the ends of the long bones. Secondary trabeculae, which are not primarily involved in weight bearing function, are lost first, while the primary trabeculae become more prominent and disappear at later stages. Using this predictable sequence of resorptive processes, some authors developed semiquantitative indexes for the diagnosis and grading of osteoporosis. The most widely used are those proposed by Singh et al., for the proximal femur, and Jhamaria et al., for the calcaneus [81–83]. These indexes

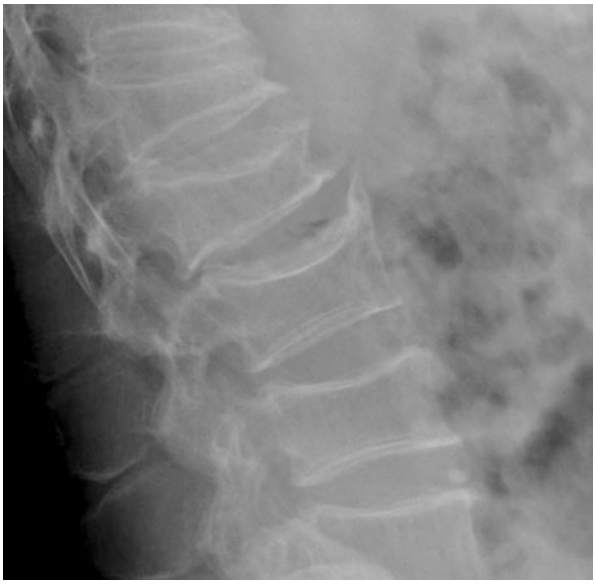

Fig. 14.2 Multiple vertebral insufficiency fractures in the thoracolumbar transition, with different morphology and severity. Based on Genant's method vertebral deformities are graded according to shape and severity. Cortical thinning results from the reabsorption of the periosteal, intracortical, and endosteal layers. When this happens in the vertebral bodies concomitantly to the increase in bone radiolucency, the vertebrae acquire a "picture frame" appearance, also known as "ghost vertebra"

have a great inter-observer variation and are dependent on the quality of radiographs and superimposition of soft tissues.

Radiographic absorptiometry (RA) (method comparing densities) and metacarpal radiogrammetry (evaluation of cortical changes—ratios using radiographs of metacarpals) were developed from radiography for quantitative purposes. Metacarpal radiogrammetry has evolved into digital X-ray radiogrammetry (DXR), in which automated measurements obtained from three metacarpal bones (instead of one in conventional radiogrammetry) provide more accuracy and precision, through the calculation of a "bone volume per projected area" (VPA) from which BMD is derived via a geometrical operation [84]. A significant correlation exists between DXR-derived BMD (DXR-BMD) at the three mid-metacarpals and DXA-derived BMD at the spine, total hip, and distal radius [85].

Radiographs are also important for the diagnosis of vertebral fractures. The existence of an insufficiency fracture is an indication for treatment of osteoporosis.

Several radiograph-based methods have been developed to identify and score VFs. Quantitative morphometry (QM), the visual semiquantitative (SQ) method, and an "algorithm-based qualitative" (ABQ) method [86] are now available, the most commonly used being the visual SQ method proposed by Genant et al. [87]. This method has been extensively validated and according to the ISCD official positions it represents the technique of choice to characterize VFs [57, 88]. Based on

Genant's method vertebral deformities are graded according to shape and severity. Readers are asked to estimate the percentage of height and/or area reduction semi-quantitatively—without a direct measurement (Fig. 14.2). The deformity is classified based on the location (anterior—wedge, middle—biconcave, or posterior and anterior loss—crush) and on severity of height loss (normal: 0, mild 20–25%: 1, moderate 25–40%: 2, and severe >40%: 3, plus grade 0.5 for uncertain or questionable vertebrae). A spinal fracture index can be calculated by adding the individual vertebral body scores. This allows a quantification of the extent of deformation [57].

An important remark about radiographs is that they represent an opportunistic method to diagnose vertebral fractures. Fractures can be incidentally found in a number of methods and examinations performed for other clinical purposes (e.g. chest or abdominal radiographs) [89–91].

These fractures are currently underreported by radiologists, probably because the main focus is set on evaluating different pathology [92]. Lastly, vertebral fractures can occur as pathological fractures in the context of malignancy. In some cases radiographs will be able to give enough information to provide unsuspected diagnoses.

Artificial Intelligence applied to imaging is an evolving field and will be fundamental for this task [93].

14.6.2 Dual Energy X-ray Absorptiometry (DXA)

Dual energy X-ray absorptiometry (DXA) represents the most widely used technique for the assessment of BMD, thanks to its availability, the very low radiation dose, and its low cost. It represents the standard for diagnosis and monitoring of osteoporosis and conditions involving low bone mass. It is normally the first clinical imaging tool used to diagnose osteoporosis.

DXA is based on the use of two X-ray beams of different energy. The ratio between the degree of attenuation of the lower energy and the higher energy beam is the "*R* value" and is specific for each tissue. From the *R* value, using complex algorithms, it is possible to obtain the amount of BMC in pixels containing bone. BMD is then calculated as the ratio BMC/area (in g/cm^2) [79]. The DXA measurement of BMD is an areal measurement [areal-BMD (a-BMD)], as opposed to a true "density" (per volume).

BMD is expressed in terms of standard deviation (SD) comparing individual BMD measurement to a reference range obtained from a population of healthy young adults (*T*-score) and from an age-matched population of the same gender and ethnic group (*Z*-score). In postmenopausal women and in men older than 50, osteoporosis is defined by a *T*-score ≤ -2.5 SD at the lumbar spine (from L1 to L4), femoral neck, or total hip [68]; BMD ≥ -1 SD is considered normal, while BMD in the range between -1 and -2.5 SD is in the range of osteopenia (Fig. 14.3). BMD measured by DXA accounts only for 60–70% of variation in bone strength (other factors such as bone architecture are also contributory) and the majority of

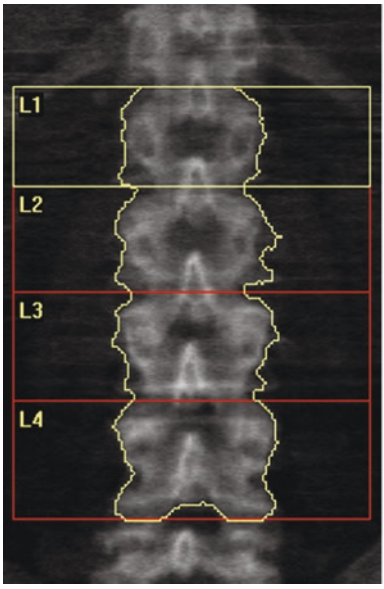

Regione	Area (cm²)	BMC (g)	BMD (g/cm²)	T-score	Z-score
L1	13.82	12.38	0.896	-0.9	1.2
L2	15.73	15.55	0.989	-0.4	1.9
L3	16.28	17.84	1.096	0.1	2.5
L4	18.10	17.86	0.987	-0.7	1.8
Totale	63.92	63.62	0.995	-0.5	1.8

Fig. 14.3 DXA, lumbar spine. Woman, 73 years old, 67 kg. *T*-score is within the normal range (above −1 SD)

osteoporotic fractures occur in people whose BMD is in the non-osteoporotic range [94]. DXA performed at the forearm (focused on the distal one-third of the radius—or the 33% distal radius—of the non-dominant forearm for diagnosis) is chosen when the femur and/or spine cannot be accurately assessed (e.g. previous fractures, surgery, dysplasia, severe osteoarthritis, etc.) in patients with hyperparathyroidism and very obese patients (over the weight limit for DXA table) (Figs. 14.4 and 14.5).

Quality assurance and cross-calibration of DXA are paramount [95].

Trabecular bone score (TBS) is a gray-scale textural analysis technique which gives extra information on bone microstructure and strength. TBS can be obtained from a previously acquired lumbar spine DXA scan (same regions of interest, ROIs) (Fig. 14.6). The major advantages of TBS are simplicity and low cost [96]. A dedicated software is used to measure the level of variation among pixels in gray scale within the 2D DXA image and differentiate between bone structures with similar areal-BMD (a-BMD) but different bone microstructures [97] (Fig. 14.7).

TBS does not directly assess bone microarchitecture, but its results have been associated with vertebral, hip, and major osteoporotic fracture risk in postmenopausal women and with hip and major osteoporotic fracture risk in men aged over 50 [98, 99]. TBS gives lower values in postmenopausal women and in men with previous fragility fractures than their nonfractured counterparts. TBS results are lower in women who have sustained a fragility fracture but in whom DXA does not indicate osteoporosis or even osteopenia [100] (Fig. 14.8).

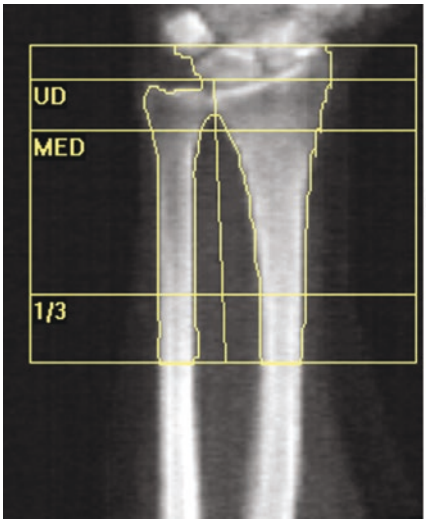

Radio + Ulna	Area (cm^2)	BMC (g)	BMD (g/cm^2)	T-score	Z-score
UD	6.29	2.09	0.332	-1.6	-0.1
MED	11.52	5.34	0.464	-2.3	-0.3
1/3	4.32	2.52	0.583	-1.7	0.3
Totale	22.13	9.94	0.449	-2.2	-0.3

Fig. 14.4 DXA of the forearm. Typically, when a central site, lumbar spine and/or proximal femora, cannot be reliably assessed in patients investigated for osteoporosis, and in specific clinical scenarios, the forearm is scanned

Other non-BMD measures from DXA scans focused on hip geometry measures, including hip structural analysis, hip axis length (HAL), and neck-shaft angle, can be performed, with limited value in clinical practice. HAL derived from DXA is associated with hip fracture risk in postmenopausal women [101].

DXA and conventional radiography are the techniques of choice for the detection of vertebral fractures [57] (Fig. 14.9). This is because of the possibility to perform panoramic views, the lower radiation exposure, the timing (the patient can be scanned for both BMD and VFs in the same session), the integrated morphometric tool advantages of DXA, and the spatial resolution and better qualitative assessment advantage of radiography. Quantitative morphometry as a scoring method remains a useful tool in specific settings [102].

Lateral spine imaging with standard radiography or densitometric VFA is indicated when *T*-score is <-1.0 and of one or more of the following is present: Women age $\geq$70 years or men $\geq$ age 80 years; historical height loss >4 cm (>1.5 in.); self-reported but undocumented prior vertebral fracture; glucocorticoid therapy equivalent to $\geq$5 mg of prednisone or equivalent per day for $\geq$3 months [ISCD 2019 guidelines].

14.6.3 Quantitative Ultrasound (QUS)

QUS is based on the interaction and the propagation of ultrasounds (mechanical waves) through cortical and trabecular bone. Parameters on QUS reflect the structural anisotropy of bone, allowing inference of its mechanical properties [103].

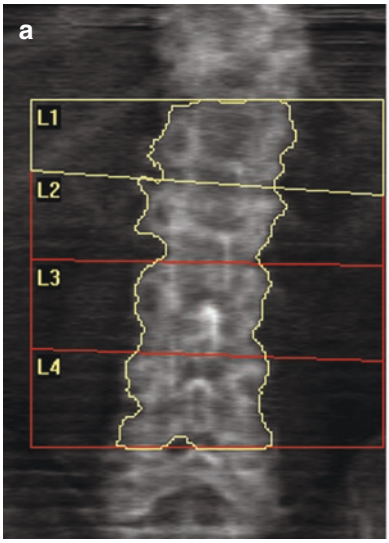

Regione	Area (cm²)	BMC (g)	BMD (g/cm²)	T-score	Z-score
L1	11.51	8.21	0.714	-2.5	-0.6
L2	10.78	9.69	0.899	-1.2	1.0
L3	12.43	11.23	0.904	-1.6	0.7
L4	13.86	11.39	0.822	-2.2	0.2
Totale	48.57	40.53	0.834	-1.9	0.3

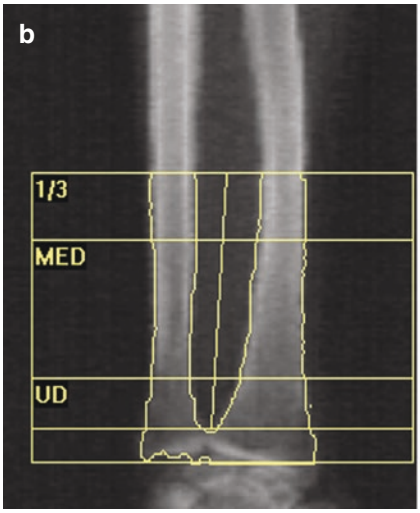

Radio + Ulna	Area (cm²)	BMC (g)	BMD (g/cm²)	T-score	Z-score
1/3	4.86	2.34	0.481	-3.5	-1.2
MED	9.37	3.34	0.356	-4.4	-2.0
UD	4.94	0.89	0.180	-4.5	-2.8
Totale	19.17	6.57	0.342	-4.3	-2.0

Fig. 14.5 A 71 years old female patient presented with multiple vertebral fractures (including more than two levels at L1-L4) (**a**), previous fractures and surgical fixation at both proximal femurs, and post-traumatic changes at the non-dominant forearm. The site for BMD analysis was the dominant wrist, which confirmed a status of osteoporosis, with a *T*-score = −3.5 SD (**b**)

QUS is a non-expensive, portable technique that involves no ionizing radiation. However, the reproducibility of the results, due to the diversity of available devices and calibration, is suboptimal and can be misleading. For this reason, according to the ISCD official positions, results from different devices cannot be directly compared [104].

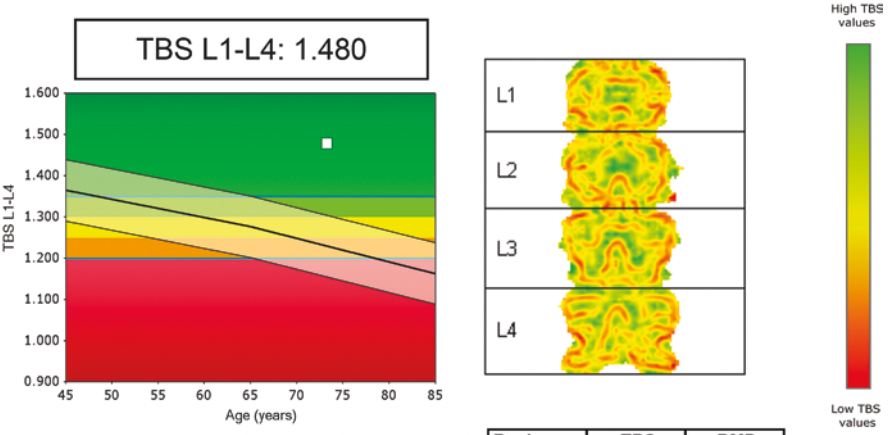

Region	TBS	BMD
L1	1.408	0.896
L2	1.517	0.989
L3	1.541	1.096
L4	1.454	0.987
L1-L4	1.480	0.992
L1-L3	1.489	0.993
L1-L2	1.462	0.942
L2-L4	1.504	1.024
L2-L3	1.529	1.042
L3-L4	1.498	1.041

Fig. 14.6 TBS analysis (explanation of software). Same patient as in Fig. 14.3. TBS shows a normal bone structure

The main parameters assessed by QUS include speed of sound (SoS), a parameter closely related to bone mineralization, and broadband ultrasound attenuation (BUA), closely related to the structural characteristics of trabecular bone [105]. There is a strong level of correlation between trabecular transmission parameters (SoS and BUA) in the heel and BMD derived by DXA at lumbar spine and femoral neck. Validated heel QUS devices have been demonstrated to predict fragility fractures in postmenopausal women (hip, vertebral, and global fracture risk) and in men over 65 (hip and all non-VFs), independently of central DXA BMD [104].

QUS is usually performed in the distal metaphysis of the phalanx, calcaneus, radius, and tibia. It is important to emphasize that the only validated measurement site in the context of osteoporosis diagnosis and management is the heel. In the study of osteoporosis, DXA remains the method of choice in clinical practice for therapeutic decisions, but if a DXA scan cannot be performed, pharmacologic treatment can be initiated on the basis of a sufficient high fracture probability, assessed by heel QUS (using device specific thresholds) in conjunction with clinical risk factors (according to ISCD position) [104].

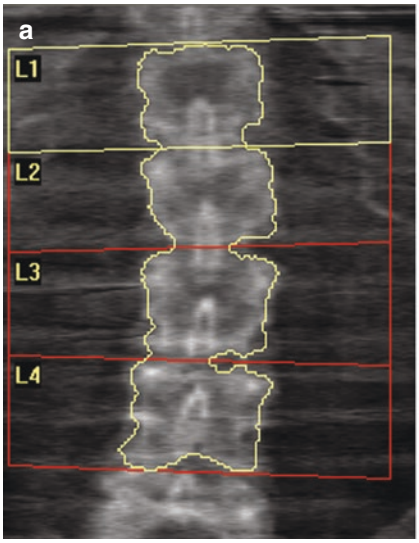

Regione	Area (cm²)	BMC (g)	BMD (g/cm²)	T-score	Z-score
L1	10.65	4.51	0.423	-5.2	-3.2
L2	10.64	5.39	0.507	-4.7	-2.6
L3	12.02	6.02	0.501	-5.3	-3.0
L4	12.21	6.18	0.506	-5.0	-2.7
Totale	45.51	22.09	0.485	-5.1	-2.9

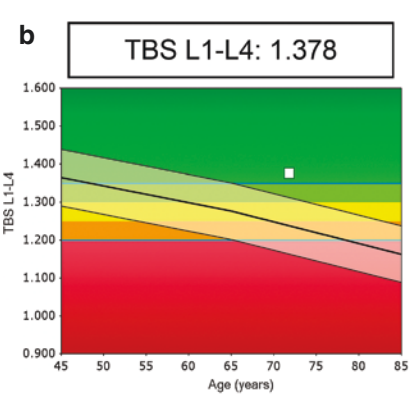

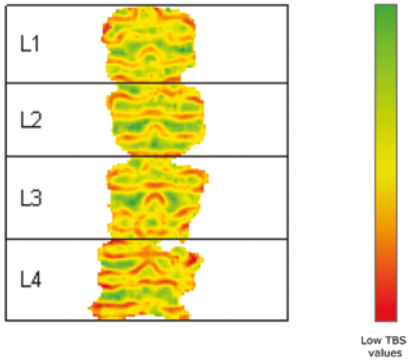

Region	TBS	BMD
L1	1.410	0.417
L2	1.512	0.512
L3	1.374	0.506
L4	1.215	0.511
L1-L4	1.378	0.487
L1-L3	1.432	0.478
L1-L2	1.461	0.465
L2-L4	1.367	0.510
L2-L3	1.443	0.509
L3-L4	1.294	0.508

Fig. 14.7 Woman, 71 years old, 42 kg. DXA shows very low aBMD values (*T*-score in the range of osteoporosis according to WHO criteria) (**a**), TBS has values within the normal limits (**b**)

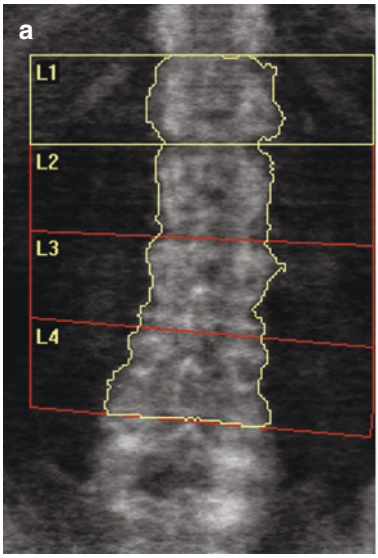

Regione	Area (cm²)	BMC (g)	BMD (g/cm²)	T-score	Z-score
L1	12.23	12.10	0.990	0.0	2.0
L2	12.18	11.86	0.974	-0.5	1.8
L3	12.90	14.09	1.092	0.1	2.5
L4	14.69	14.75	1.004	-0.5	1.9
Totale	52.00	52.80	1.015	-0.3	2.0

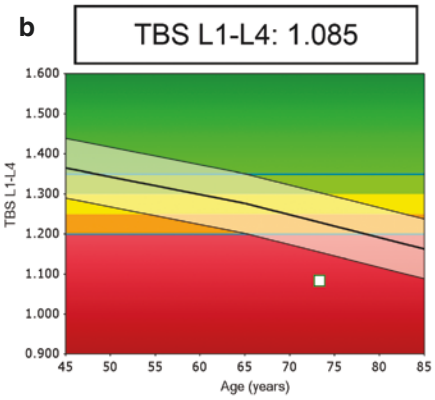

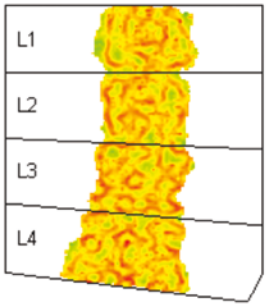

Region	TBS	BMD
L1	1.176	0.987
L2	1.100	0.972
L3	0.997	1.093
L4	1.066	1.008
L1-L4	1.085	1.015
L1-L3	1.091	1.018
L1-L2	1.138	0.980
L2-L4	1.055	1.024
L2-L3	1.049	1.033
L3-L4	1.032	1.050

Fig. 14.8 Woman, 73 years old, 92 kg. DXA shows a *T*-score in the normal according to WHO criteria (**a**). TBS deonstrates low values - abnormal bone structure (**b**)

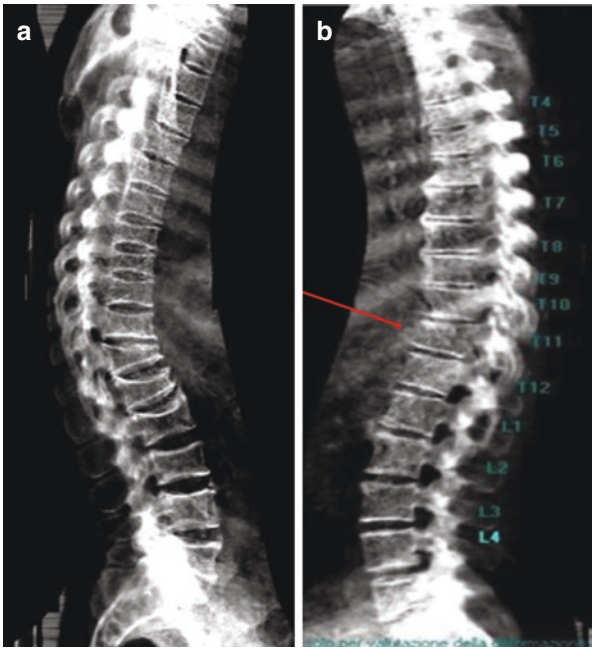

Fig. 14.9 DXA scan for vertebral fracture assessment in an aging patients with multiple vertebral fractures (**a**) and in a patient with a mild vertebral deformity (**b**) (fracture—red arrow) and osteoarthritis changes

14.6.4 Computed Tomography (CT)

CT technology has evolved to offer quantitative imaging modalities to study bone and muscle. Quantitative CT (QCT) and peripheral quantitative CT (pQCT) were originally designed to assess bone parameters, respectively, at central and peripheral sites. Currently they are also used for the quantification of muscle mass and fat distribution.

The usefulness of QCT in the study of osteoporosis is related to its ability to measure BMD in a chosen volume [volumetric-BMD (v-BMD)], with no interference from other tissues and the possibility of studying cortical and trabecular bone separately [106].

QCT-derived v-BMD represents a true density measure expressed in g/cm^3, instead of an areal density as measured by DXA. This avoids the DXA overestimation of BMD resulting from spinal degenerative changes, vascular calcifications, and other sclerotic lesions in the surrounding soft tissues [107] (Fig. 14.10). QCT, compared to DXA, provides a measure of purely trabecular bone, which is more metabolically active and may be primarily affected by metabolic bone diseases, thus allowing for better sensitivity to detect osteoporosis [108]. QCT-derived *T*-scores are however not equivalent to those obtained from DXA and therefore cannot be used according to the WHO diagnostic classification [109]. However, the American College of Radiology (ACR) introduced guidelines for evaluating QCT studies

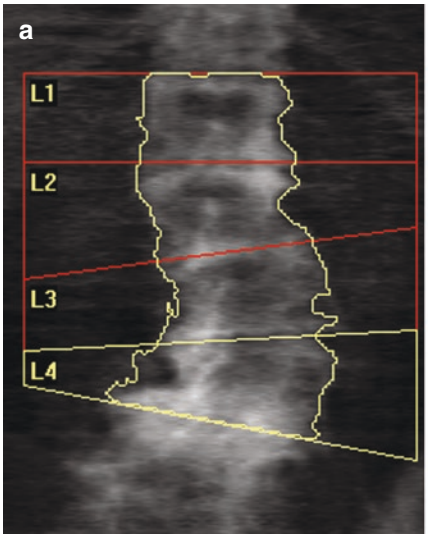

Regione	Area (cm²)	BMC (g)	BMD (g/cm²)	T-score	Z-score
L1	11.07	9.55	0.862	-1.2	1.1
L2	11.82	11.95	1.012	-0.1	2.4
L3	12.08	11.07	0.916	-1.5	1.1
L4	14.14	19.15	1.354	2.7	5.4
Totale	49.11	51.73	1.053	0.1	2.6

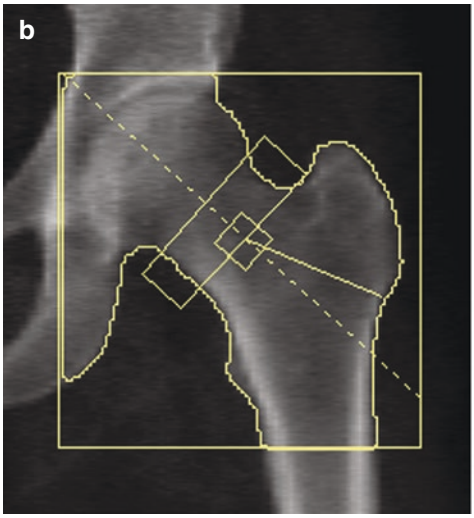

Regione	Area (cm²)	BMC (g)	BMD (g/cm²)	T-score	Z-score
Collo	4.92	2.91	0.590	-2.3	-0.1
Troc	9.99	5.58	0.559	-1.4	0.2
Inter	17.57	15.55	0.885	-1.4	0.3
Totale	32.48	24.04	0.740	-1.7	0.3
di Ward	1.26	0.62	0.494	-2.0	0.9

Fig. 14.10 DXA scan of the lumbar spine and of the non-dominant proximal femur. With aging, osteoarthritic (OA) changes increase and particularly affect lumbar spine assessment of BMD. Calcified ateromatosis, scoliosis, sequelae of vertebral fractures, and other conditions also significantly impact the assessment. In the patient scanned and presented in this figure (Woman, 77 years old, 60 kg), lumbar spine shows inaccurate values due to OA changes and scoliosis (**a**), while the proximal femur (**b**) can reliably depict a status of osteopenia (*T*-score −2.3 SD at the femoral neck, not far from osteoporosis)

including diagnostic cut-off points that may be used for assigning a spine QCT diagnostic category equivalent to the WHO guidelines (The ACR introduced guidelines for evaluating QCT studies [https://www.acr.org//media/ACR/Files/Practice-Parameters/qct.pdf]) (Fig. 14.11).

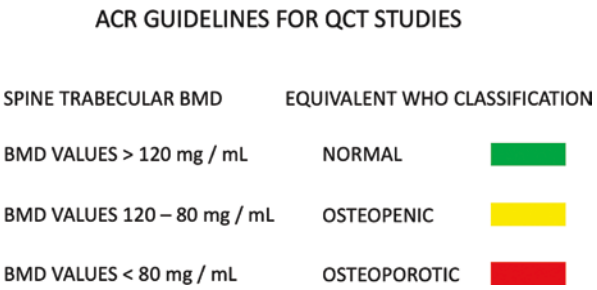

Fig. 14.11 American College of Radiology guidelines for QCT studies

The region of interest for QCT is the lumbar spine. Other measurement sites commonly include the proximal femur, forearm, and tibia [109]. In clinical application, spine and proximal femur are analyzed using standard whole-body CT scanners equipped with dedicated software for the analysis. Multiple studies have evaluated the clinical utility of QCT in fracture prediction and in longitudinal studies: the ability of spinal trabecular BMD obtained by QCT to predict spinal fractures in postmenopausal women is comparable to or better than that of lumbar spine BMD obtained by DXA; sufficient evidence to support this statement in men is still necessary [110]. Total femur trabecular BMD obtained by QCT has the capability to predict hip fractures as well as hip BMD obtained by DXA in both menopausal woman and older men [111].

QCT has also been extensively tested in monitoring age-, disease-, and treatment-related BMD changes [110, 111]. However, DXA should be favored for therapeutic decisions and in clinical practice to limit radiation exposure, unless QCT can provide superior information [111].

Also CT offers the possibility of opportunistic screening. BMD can be potentially calculated from a pre-existing acquisition in patients at increased risk of fracture, without need for any additional DXA scan. However, the absence of in-scan calibration phantom and the lack of a standardized acquisition protocol are common problems. According to the ISCD official positions (last version 2019), the identification of patients with high fracture risk (according to low BMD or strength measures derived by CT at the spine or proximal femur) is possible with conventional CT scan only if machine-specific cut-off values and scanner stability have been established [110].

Multidetector spiral CT (MDCT) of the thorax and abdomen is one of the most useful tools for opportunistic diagnosis of vertebral fractures in postmenopausal women. On the midline-sagittal CT plane, the central area of the vertebral body end plate (the site where vertebral fractures appear) can be very accurately analyzed. Axial images are not very sensitive, but coronal and sagittal reconstructions are now widely used and these may easily demonstrate fractures. The initial localizer views of CT (scout) are suitable for detection of incidental vertebral fractures [112]. Intra- and inter-observer agreement based on a semiquantitative method is fair to good. Mild degrees of fracture and fractures located in levels T4 to T9 represent the main sources of error [113].

Several studies have stated that incidental osteoporotic fractures are underreported and that sagittal CT reformations provide additional information and should be a part of standard CT analyses, to improve detection rate [92]. Clinical studies have demonstrated that MDCT structure measurements at the proximal femur and spine improve differentiation between osteoporotic patients with proximal femur fractures or spine fractures and healthy control patients [114]. Besides, it has been proven useful in monitoring treatment with teriparatide [115]. Data obtained with MDCT are useful for final element analysis (FEA), which has been used to study bone strength and monitor changes after the administration of treatment. Using conversion factors, reliable measurements can be calculated from the spine and hip from routine abdominal and pelvic MDCT scans [116].

Dedicated pQCT scanners (peripheral scanners) are used to evaluate v-BMD and bone microarchitecture at the distal radius and tibia. The use of high-resolution peripheral scanners (HR-pQCT) is currently limited to research. Its use is yielding important information on bone deterioration in secondary osteoporosis and related bone diseases [117]. HR-pQCT can assess BMD, microstructural, and mechanical parameters of both cortical and trabecular bone separately at the distal radius and tibia with a very low effective dose, in a very localized field. HR-pQCT is limited to the appendicular skeleton, but a good correlation has been proven between density (a-BMD and v-BMD), geometry through cross-sectional area (CSA) and stiffness parameters measured peripherally and those derived by QCT at lumbar spine and proximal femur, the sites where the vast majority of osteoporotic fractures occur.

Using HR-pQCT at the distal radius and tibia, a relatively recent study documented that postmenopausal women with primary hyperparathyroidism (PHPT) demonstrated thinner cortices, reduced trabecular BMD and cortical BMD in comparison with healthy controls; in the PHPT group, analysis of the microarchitecture (individual trabecular segmentation) documented a large heterogeneity in the distribution of the trabeculae and a depletion of plate-like trabeculae, with a lower trabecular plate-to-rod ratio [118].

In postmenopausal women with type 2 DM and history of fragility fractures HR-pQCT has shown that both cortical bone porosity and pore volume are increased at the distal radius and distal tibia [119]. The increased cortical porosity and the impaired trabecular microarchitecture among type 2 DM patients could explain, at least in part, the high incidence of fragility fractures, even though these patients display a normal or even elevated BMD in DXA examination [120].

14.6.5 Magnetic Resonance Imaging (MRI)

On MRI, the cortical bone is dark (void of signal) because of the small number of mobile protons and the very short T2 relaxation time. The trabecular bone is also void of signal, but the surrounding bone marrow has high signal, with intensity proportional to the amount of fatty content [106].

High-resolution MRI depicts trabecular bone density and structure in vitro and in vivo with a high spatial resolution, however at resolutions similar to individual

trabeculae dimension, partial volume effects may arise. MRI is time-consuming and technically challenging. Since QCT and HR-pQCT can directly depict the trabecular network, they still appear the most suitable techniques for the investigation of trabecular bone, but studies comparing high-resolution MRI with QCT and HR-pQCT have documented that MRI performs equally well with trabecular bone measurements [121].

The main clinical use of MRI is for the diagnosis of insufficiency/fragility fractures, characterized by the presence of bone marrow edema, due to trabecular disruption. MRI allows us to confidently rule out malignancy as the cause for fracture [122]. Optimal sequences are T1-weighted and water sensitive ones, such as fat suppressed T2-weighted or short tau inversion recovery (STIR) [10].

Localizer images on MRI are a set of three-plane (axial, coronal, and sagittal), low-resolution, and large field-of-view images that serve to plan the exact position and angulation of slices of the projected MRI sequences. Localizers, despite their limited quality, are able to demonstrate incidental vertebral fractures that can be further confirmed by subsequently acquired T2-weighted sagittal images [90, 92]. MRI features also allow discriminate between benign and malignant vertebral fractures and for the correct identification of recent and old vertebral compression fractures.

14.7 Conclusion

In this chapter, we have summarized the current knowledge on changes in bone metabolism occurring in the elderly and reviewed the possibilities of assessment that each one of the imaging techniques offers for the adequate assessment of bone mineral density in the geriatric population.

The loss of mineral contents in bone and structural changes is a major risk for morbidity, need for institutionalization, and mortality. The most prevalent type of fragility/insufficiency fracture is the vertebral compression fracture, but the effect of osteoporosis on the skeleton is systemic, and there is increased risk of almost all types of fractures.

Findings suggestive of osteoporosis can be frequently found on radiographs, but the typical features are detectable only in the advanced stages of the disease.

Represents the most widely used technique for the assessment of BMD, thanks to its availability, the very low radiation dose, and its low cost. It represents the gold standard for diagnosis and monitoring of osteoporosis and conditions involving low bone mass. DXA and conventional radiography are the techniques of choice for the detection of vertebral fractures.

The use of other techniques, such as QUS, QCT, and pQCT is currently more limited, for different reasons.

MDCT of the thorax and abdomen is one of the most useful tools for opportunistic diagnosis of vertebral fractures in postmenopausal women. Sagittal CT reformations should be a part of standard CT analyses, to improve detection rate.

The main clinical use of MRI is for the diagnosis of insufficiency/fragility fractures and allows to confidently rule out malignancy as the cause for fracture.

References

1. Baumgartner RN, Stauber PM, McHugh D, Koehler KM, Garry PJ. Cross-sectional age differences in body composition in persons 60+ years of age. J Gerontol A Biol Sci Med Sci. 1995;50:M307–16.
2. Hughes VA, Frontera WR, Roubenoff R, Evans WJ, Singh MAF. Longitudinal changes in body composition in older men and women: role of body weight change and physical activity. Am J Clin Nutr. 2002;76:473–81.
3. Ley CJ, Lees B, Stevenson JC. Sex- and menopause-associated changes in body-fat distribution. Am J Clin Nutr. 1992;55:950–4.
4. Hotamisligil GS. Inflammation and metabolic disorders. Nature. 2006;444:860–7.
5. Chumlea WC, Baumgartner RN, Garry PJ, Rhyne RL, Nicholson C, Wayne S. Fat distribution and blood lipids in a sample of healthy elderly people. Int J Obes Relat Metab Disord. 1992;16:125–33.
6. Roche AF. Sarcopenia: a critical review of its measurements and health-related significance in the middle-aged and elderly. Am J Hum Biol. 1994;6:33–42.
7. Schaap LA, Koster A, Visser M. Adiposity, muscle mass, and muscle strength in relation to functional decline in older persons. Epidemiol Rev. 2013;35:51–65.
8. Bouxsein ML, Karasik D. Bone geometry and skeletal fragility. Curr Osteoporos Rep. 2006;4:49–56.
9. Adams JE. Imaging of the musculoskeletal system. Pope T. L.; Bloem H. L.; Beltran J.; Morrison W. B.; Wilson D. J.; Ed. Philadelphia, PA: Saunders Elsevier; 2008. p. 1489–508.
10. Aparisi Gómez MP. Non spinal fragility fractures. Semin Musculoskelet Radiol. 2016;20:330–44.
11. Hamrick MW, McGee-Lawrence ME, Frechette DM. Fatty infiltration of skeletal muscle: mechanisms and comparisons with bone marrow adiposity. Front Endocrinol. 2016;7:69. https://doi.org/10.3389/fendo.2016.00069.
12. Butler L, Santoro N. The reproductive endocrinology of the menopausal transition. Steroids. 2011;76:627–35.
13. Gallagher JC. Vitamin D and aging. Endocrinol Metab Clin N Am. 2013;42:319–32.
14. Pereira-Santos M, Costa PRF, Assis AMO, Santos CAST, Santos DB. Obesity and vitamin D deficiency: a systematic review and meta-analysis: obesity and vitamin D. Obes Rev. 2015;16:341–9.
15. Cheng S, Massaro JM, Fox CS, et al. Adiposity, cardiometabolic risk, and vitamin D status: the Framingham Heart Study. Diabetes. 2010;59:242–8.
16. Wood RJ. Vitamin D and adipogenesis: new molecular insights. Nutr Rev. 2008;66:40–6.
17. Zemel MB, Richards J, Milstead A, Campbell P. Effects of calcium and dairy on body composition and weight loss in African-American adults. Obes Res. 2005;13:1218–25.
18. Garnero P, Munoz F, Sornay-Rendu E, Delmas PD. Associations of vitamin D status with bone mineral density, bone turnover, bone loss and fracture risk in healthy postmenopausal women. The OFELY study. Bone. 2007;40:716–22.
19. Snellman G, Melhus H, Gedeborg R, Byberg L, Berglund L, Wernroth L, Michaëlsson K. Determining vitamin D status: a comparison between commercially available assays. PLoS One. 2010;5:e11555.
20. Lee S-G, Lee Y-H, Kim KJ, Lee W, Kwon OH, Kim J-H. Additive association of vitamin D insufficiency and sarcopenia with low femoral bone mineral density in noninstitutionalized elderly population: the Korea National Health and Nutrition Examination Surveys 2009–2010. Osteoporos Int. 2013;24:2789–99.
21. Tieland M, Brouwer-Brolsma EM, Nienaber-Rousseau C, van Loon LJC, De Groot LCPGM. Low vitamin D status is associated with reduced muscle mass and impaired physical performance in frail elderly people. Eur J Clin Nutr. 2013;67:1050–5.

22. Visser M, Deeg DJH, Lips P. Low vitamin D and high parathyroid hormone levels as determinants of loss of muscle strength and muscle mass (sarcopenia): the longitudinal aging study Amsterdam. J Clin Endocrinol Metab. 2003;88:5766–72.
23. Bélanger C, Luu-The V, Dupont P, Tchernof A. Adipose tissue intracrinology: potential importance of local androgen/estrogen metabolism in the regulation of adiposity. Horm Metab Res. 2002;34:737–45.
24. Kameda T, Mano H, Yuasa T, et al. Estrogen inhibits bone resorption by directly inducing apoptosis of the bone-resorbing osteoclasts. J Exp Med. 1997;186:489–95.
25. Reid IR. Fat and bone. Arch Biochem Biophys. 2010;503:20–7.
26. Ilich JZ, Kelly OJ, Inglis JE, Panton LB, Duque G, Ormsbee MJ. Interrelationship among muscle, fat, and bone: connecting the dots on cellular, hormonal, and whole body levels. Ageing Res Rev. 2014;15:51–60.
27. Zhang P, Peterson M, Su GL, Wang SC. Visceral adiposity is negatively associated with bone density and muscle attenuation. Am J Clin Nutr. 2015;101:337–43.
28. Ilich JZ, Kelly OJ, Kim Y, Spicer MT. Low-grade chronic inflammation perpetuated by modern diet as a promoter of obesity and osteoporosis. Arch Ind Hyg Toxicol. 2014;65:139–48.
29. Liu P-Y, Ilich JZ, Brummel-Smith K, Ghosh S. New insight into fat, muscle and bone relationship in women: determining the threshold at which body fat assumes a negative relationship with bone mineral density. Int J Prev Med. 2014;5:1452–63.
30. Bosch TA, Steinberger J, Sinaiko AR, Moran A, Jacobs DR, Kelly AS, Dengel DR. Identification of sex-specific thresholds for accumulation of visceral adipose tissue in adults: threshold accumulation of VAT in adults. Obesity. 2015;23:375–82.
31. Iwaniec UT, Turner RT. Influence of body weight on bone mass, architecture and turnover. J Endocrinol. 2016;230:R115–30.
32. Scheller EL, Rosen CJ. What's the matter with MAT? Marrow adipose tissue, metabolism, and skeletal health. Ann N Y Acad Sci. 2014;1311:14–30.
33. Bredella MA, Fazeli PK, Daley SM, Miller KK, Rosen CJ, Klibanski A, Torriani M. Marrow fat composition in anorexia nervosa. Bone. 2014;66:199–204.
34. Rosen CJ, Bouxsein ML. Mechanisms of Disease: is osteoporosis the obesity of bone? Nat Rev Rheumatol. 2006;2:35–43.
35. Jafari Nasabian P, Inglis JE, Reilly W, Kelly OJ, Ilich JZ. Aging human body: changes in bone, muscle and body fat with consequent changes in nutrient intake. J Endocrinol. 2017;234:R37–51.
36. Aparisi Gómez MP, Ayuso Benavent C, Simoni P, Aparisi F, Guglielmi G, Bazzocchi A. Fat and bone: the multi perspective analysis of a close relationship. Quant Imag Med Surg. 2020;10:1614–35.
37. Kim TN, Park MS, Ryu JY, et al. Impact of visceral fat on skeletal muscle mass and vice versa in a prospective cohort study: the Korean Sarcopenic Obesity Study (KSOS). PLoS One. 2014;9:e115407.
38. Lang T, Cauley JA, Tylavsky F, Bauer D, Cummings S, Harris TB. Computed tomographic measurements of thigh muscle cross-sectional area and attenuation coefficient predict hip fracture: the health, aging, and body composition study. J Bone Miner Res. 2010;25:513–9.
39. Stefanaki C, Peppa M, Boschiero D, Chrousos GP. Healthy overweight/obese youth: early osteosarcopenic obesity features. Eur J Clin Investig. 2016;46:767–78.
40. Mavros Y, Kay S, Simpson KA, et al. Reductions in C-reactive protein in older adults with type 2 diabetes are related to improvements in body composition following a randomized controlled trial of resistance training. J Cachexia Sarcopenia Muscle. 2014;5:111–20.
41. Visser M, Goodpaster BH, Kritchevsky SB, Newman AB, Nevitt M, Rubin SM, Simonsick EM, Harris TB, for the Health ABC Study. Muscle mass, muscle strength, and muscle fat infiltration as predictors of incident mobility limitations in well-functioning older persons. J Gerontol Ser A Biol Med Sci. 2005;60:324–33.

42. Domiciano DS, Figueiredo CP, Lopes JB, Caparbo VF, Takayama L, Menezes PR, Bonfa E, Pereira RMR. Discriminating sarcopenia in community-dwelling older women with high frequency of overweight/obesity: the São Paulo Ageing & Health Study (SPAH). Osteoporos Int. 2013;24:595–603.
43. Ilich JZ, Inglis JE, Kelly OJ, McGee DL. Osteosarcopenic obesity is associated with reduced handgrip strength, walking abilities, and balance in postmenopausal women. Osteoporos Int. 2015;26:2587–95.
44. Chung JH, Hwang HJ, Shin H-Y, Han CH. Association between sarcopenic obesity and bone mineral density in middle-aged and elderly Korean. Ann Nutr Metab. 2016;68:77–84.
45. Lee AJ, Hodges S, Eastell R. Measurement of osteocalcin. Ann Clin Biochem. 2000;37: 432–46.
46. Luo X-H, Guo L-J, Xie H, Yuan L-Q, Wu X-P, Zhou H-D, Liao E-Y. Adiponectin stimulates RANKL and inhibits OPG expression in human osteoblasts through the MAPK signaling pathway. J Bone Miner Res. 2006;21:1648–56.
47. Lewerin C, Johansson H, Lerner UH, Karlsson MK, Lorentzon M, Barrett-Connor E, Smith U, Ohlsson C, Mellström D. High serum adiponectin is associated with low blood haemoglobin in elderly men: the Swedish MrOS study. J Intern Med. 2015;278:68–76.
48. Oshima K, Nampei A, Matsuda M, Iwaki M, Fukuhara A, Hashimoto J, Yoshikawa H, Shimomura I. Adiponectin increases bone mass by suppressing osteoclast and activating osteoblast. Biochem Biophys Res Commun. 2005;331:520–6.
49. Williams GA, Wang Y, Callon KE, et al. In vitro and in vivo effects of adiponectin on bone. Endocrinology. 2009;150:3603–10.
50. Karsenty G, Ferron M. The contribution of bone to whole-organism physiology. Nature. 2012;481:314–20.
51. Kanis JA. Diagnosis of osteoporosis and assessment of fracture risk. Lancet. 2002;359:1929–36.
52. Link TM. Osteoporosis imaging: state of the art and advanced imaging. Radiology. 2012;263:3–17.
53. Johnell O, Kanis JA. An estimate of the worldwide prevalence and disability associated with osteoporotic fractures. Osteoporos Int. 2006;17:1726–33.
54. Office of the Surgeon General (US). Bone health and osteoporosis: a report of the surgeon general. Rockville, MD: Office of the Surgeon General (US); 2004.
55. Sambrook P, Cooper C. Osteoporosis. Lancet. 2006;367:2010–8.
56. Cauley JA, Hochberg MC, Lui L-Y, Palermo L, Ensrud KE, Hillier TA, Nevitt MC, Cummings SR. Long-term risk of incident vertebral fractures. JAMA. 2007;298:2761.
57. Bazzocchi A, Guglielmi G. Vertebral fracture identification. Semin Musculoskelet Radiol. 2016;20:317–29.
58. Klotzbuecher CM, Ross PD, Landsman PB, Abbott TA, Berger M. Patients with prior fractures have an increased risk of future fractures: a summary of the literature and statistical synthesis. J Bone Miner Res. 2000;15:721–39.
59. Clinton J, Franta A, Polissar NL, Neradilek B, Mounce D, Fink HA, Schousboe JT, Matsen FA. Proximal humeral fracture as a risk factor for subsequent hip fractures. J Bone Joint Surg Am. 2009;91:503–11.
60. Clegg A, Young J, Iliffe S, Rikkert MO, Rockwood K. Frailty in elderly people. Lancet. 2013;381:752–62.
61. Fried LP, Tangen CM, Walston J, et al. Frailty in older adults: evidence for a phenotype. J Gerontol A Biol Sci Med Sci. 2001;56:M146–56.
62. Makizako H, Shimada H, Doi T, Tsutsumimoto K, Suzuki T. Impact of physical frailty on disability in community-dwelling older adults: a prospective cohort study. BMJ Open. 2015;5:e008462.
63. Fugate Woods N, LaCroix AZ, Gray SL, Aragaki A, Cochrane BB, Brunner RL, Masaki K, Murray A, Newman AB. Frailty: emergence and consequences in women aged 65 and older in the women's health initiative observational study: consequences and predictors of frailty in WHI women. J Am Geriatr Soc. 2005;53:1321–30.

64. Yang S, Center JR, Eisman JA, Nguyen TV. Association between fat mass, lean mass, and bone loss: the Dubbo osteoporosis epidemiology study. Osteoporos Int. 2015;26:1381–6.
65. Walston J, McBurnie MA, Newman A, Tracy RP, Kop WJ, Hirsch CH, Gottdiener J, Fried LP, Cardiovascular Health Study. Frailty and activation of the inflammation and coagulation systems with and without clinical comorbidities: results from the Cardiovascular Health Study. Arch Intern Med. 2002;162:2333–41.
66. Xue Q-L. The frailty syndrome: definition and natural history. Clin Geriatr Med. 2011;27:1–15.
67. Zaslavsky O, Rillamas-Sun E, LaCroix AZ, et al. Association between anthropometric measures and long-term survival in frail older women: observations from the women's health initiative study. J Am Geriatr Soc. 2016;64:277–84.
68. Zaslavsky O, Li W, Going S, Datta M, Snetselaar L, Zelber-Sagi S. Association between body composition and hip fractures in older women with physical frailty: adiposity and hip fracture in frailty. Geriatr Gerontol Int. 2017;17:898–904.
69. Yang S, Nguyen ND, Center JR, Eisman JA, Nguyen TV. Association between abdominal obesity and fracture risk: a prospective study. J Clin Endocrinol Metab. 2013;98:2478–83.
70. Chalhoub D, Cawthon PM, Ensrud KE, et al. Risk of non spine fractures in older adults with sarcopenia, low bone mass, or both. J Am Geriatr Soc. 2015;63:1733–40.
71. Harris R, Chang Y, Beavers K, et al. Risk of fracture in women with sarcopenia, low bone mass, or both. J Am Geriatr Soc. 2017;65:2673–8.
72. Bonewald LF, Kiel DP, Clemens TL, Esser K, Orwoll ES, O'Keefe RJ, Fielding RA. Forum on bone and skeletal muscle interactions: summary of the proceedings of an ASBMR Workshop: Forum on Bone and Skeletal Muscle Interactions. J Bone Miner Res. 2013;28:1857–65.
73. Chen Z, Lohman TG, Stini WA, Ritenbaugh C, Aickin M. Fat or lean tissue mass: which one is the major determinant of bone mineral mass in healthy postmenopausal women? J Bone Miner Res. 1997;12:144–51.
74. Crandall CJ, Yildiz VO, Wactawski-Wende J, Johnson KC, Chen Z, Going SB, Wright NC, Cauley JA. Postmenopausal weight change and incidence of fracture: post hoc findings from Women's Health Initiative Observational Study and Clinical Trials. BMJ. 2015;350:h25.
75. Ensrud KE, Ewing SK, Taylor BC, et al. Frailty and risk of falls, fracture, and mortality in older women: the study of osteoporotic fractures. J Gerontol A Biol Sci Med Sci. 2007;62:744–51.
76. Grisso JA, Kelsey JL, Strom BL, Ghiu GY, Maislin G, O'Brien LA, Hoffman S, Kaplan F. Risk factors for falls as a cause of hip fracture in women. N Engl J Med. 1991;324:1326–31.
77. de Rekeneire N, Visser M, Peila R, Nevitt MC, Cauley JA, Tylavsky FA, Simonsick EM, Harris TB. Is a fall just a fall: correlates of falling in healthy older persons. The Health, Aging and Body Composition Study. J Am Geriatr Soc. 2003;51:841–6.
78. Fuller GF. Falls in the elderly. Am Fam Physician. 2000;61:2159–68, 2173–2174.
79. Guglielmi G, Muscarella S, Bazzocchi A. Integrated imaging approach to osteoporosis: state-of-the-art review and update. RadioGraphics. 2011;31:1343–64.
80. Anil G, Guglielmi G, Peh WCG. Radiology of osteoporosis. Radiol Clin N Am. 2010;48:497–518.
81. Singh M, Nagrath AR, Maini PS. Changes in trabecular pattern of the upper end of the femur as an index of osteoporosis. J Bone Joint Surg Am. 1970;52:457–67.
82. Singh M, Riggs BL, Beabout JW, Jowsey J. Femoral trabecular-pattern index for evaluation of spinal osteoporosis. Ann Intern Med. 1972;77:63–7.
83. Jhamaria NL, Lal KB, Udawat M, Banerji P, Kabra SG. The trabecular pattern of the calcaneus as an index of osteoporosis. J Bone Joint Surg (Br). 1983;65:195–8.
84. Adams JE. Radiogrammetry and radiographic absorptiometry. Radiol Clin N Am. 2010;48:531–40.
85. Hyldstrup L, Nielsen SP. Metacarpal index by digital X-ray radiogrammetry: normative reference values and comparison with dual X-ray absorptiometry. J Clin Densitom. 2001;4:299–306.
86. Oei L, Koromani F, Rivadeneira F, Zillikens MC, Oei EHG. Quantitative imaging methods in osteoporosis. Quant Imag Med Surg. 2016;6:680–98.

87. Genant HK, Wu CY, van Kuijk C, Nevitt MC. Vertebral fracture assessment using a semiquantitative technique. J Bone Miner Res. 2009;8:1137–48.
88. Vokes T, Bachman D, Baim S, Binkley N, Broy S, Ferrar L, Lewiecki EM, Richmond B, Schousboe J. Vertebral fracture assessment: the 2005 ISCD official positions. J Clin Densitom. 2006;9:37–46.
89. Bazzocchi A, Spinnato P, Garzillo G, Ciccarese F, Albisinni U, Mignani S, Battista G, Rossi C. Detection of incidental vertebral fractures in breast imaging: the potential role of MR localisers. Eur Radiol. 2012;22:2617–23.
90. Bazzocchi A, Garzillo G, Fuzzi F, Diano D, Albisinni U, Salizzoni E, Battista G, Guglielmi G. Localizer sequences of magnetic resonance imaging accurately identify osteoporotic vertebral fractures. Bone. 2014;61:158–63.
91. Bazzocchi A, Spinnato P, Albisinni U, Battista G, Rossi C, Guglielmi G. A careful evaluation of scout CT lateral radiograph may prevent unreported vertebral fractures. Eur J Radiol. 2012;81:2353–7.
92. Adams JE. Opportunistic identification of vertebral fractures. J Clin Densitom. 2016;19:54–62.
93. Murata K, Endo K, Aihara T, et al. Artificial intelligence for the detection of vertebral fractures on plain spinal radiography. Sci Rep. 2020;10:20031.
94. Johnell O, Kanis JA, Oden A, et al. Predictive value of BMD for hip and other fractures. J Bone Miner Res. 2005;20:1185–94.
95. Guglielmi G, Damilakis J, Solomou G, Bazzocchi A. Quality assurance of imaging techniques used in the clinical management of osteoporosis. Radiol Med. 2012;117:1347–54.
96. Harvey NC, Glüer CC, Binkley N, et al. Trabecular bone score (TBS) as a new complementary approach for osteoporosis evaluation in clinical practice. Bone. 2015;78:216–24.
97. Bazzocchi A, Ponti F, Diano D, Amadori M, Albisinni U, Battista G, Guglielmi G. Trabecular bone score in healthy ageing. Br J Radiol. 2015;88:20140865.
98. Silva BC, Broy SB, Boutroy S, Schousboe JT, Shepherd JA, Leslie WD. Fracture risk prediction by non-BMD DXA measures: the 2015 ISCD official positions part 2: trabecular bone score. J Clin Densitom. 2015;18:309–30.
99. Shevroja E, Lamy O, Kohlmeier L, Koromani F, Rivadeneira F, Hans D. Use of trabecular bone score (TBS) as a complementary approach to dual-energy X-ray absorptiometry (DXA) for fracture risk assessment in clinical practice. J Clin Densitom. 2017;20:334–45.
100. Silva BC, Leslie WD, Resch H, Lamy O, Lesnyak O, Binkley N, McCloskey EV, Kanis JA, Bilezikian JP. Trabecular bone score: a noninvasive analytical method based upon the DXA image. J Bone Miner Res. 2014;29:518–30.
101. Shepherd JA, Schousboe JT, Broy SB, Engelke K, Leslie WD. Executive summary of the 2015 ISCD Position Development Conference on Advanced Measures From DXA and QCT: Fracture Prediction Beyond BMD. J Clin Densitom. 2015;18:274–86.
102. Guglielmi G, Diacinti D, van Kuijk C, Aparisi F, Krestan C, Adams JE, Link TM. Vertebral morphometry: current methods and recent advances. Eur Radiol. 2008;18:1484–96.
103. Glüer C-C. Quantitative ultrasound techniques for the assessment of osteoporosis: expert agreement on current status. J Bone Miner Res. 1997;12:1280–8.
104. Krieg M-A, Barkmann R, Gonnelli S, et al. Quantitative ultrasound in the management of osteoporosis: the 2007 ISCD official positions. J Clin Densitom. 2008;11:163–87.
105. Guglielmi G, Scalzo G, de Terlizzi F, Peh WCG. Quantitative ultrasound in osteoporosis and bone metabolism pathologies. Radiol Clin N Am. 2010;48:577–88.
106. Krug R, Burghardt AJ, Majumdar S, Link TM. High-resolution imaging techniques for the assessment of osteoporosis. Radiol Clin N Am. 2010;48:601–21.
107. Bazzocchi A, Ferrari F, Diano D, Albisinni U, Battista G, Rossi C, Guglielmi G. Incidental findings with dual-energy X-ray absorptiometry: spectrum of possible diagnoses. Calcif Tissue Int. 2012;91:149–56.
108. Li N, Li X, Xu L, Sun W, Cheng X, Tian W. Comparison of QCT and DXA: osteoporosis detection rates in postmenopausal women. Int J Endocrinol. 2013;2013:1–5.

109. Engelke K, Adams JE, Armbrecht G, et al. Clinical use of quantitative computed tomography and peripheral quantitative computed tomography in the management of osteoporosis in adults: the 2007 ISCD official positions. J Clin Densitom. 2008;11:123–62.
110. Engelke K, Lang T, Khosla S, Qin L, Zysset P, Leslie WD, Shepherd JA, Shousboe JT. Clinical use of quantitative computed tomography–based advanced techniques in the management of osteoporosis in adults: the 2015 ISCD official positions—Part III. J Clin Densitom. 2015;18:393–407.
111. Engelke K, Lang T, Khosla S, Qin L, Zysset P, Leslie WD, Shepherd JA, Schousboe JT. Clinical use of quantitative computed tomography (QCT) of the hip in the management of osteoporosis in adults: the 2015 ISCD official positions—Part I. J Clin Densitom. 2015;18:338–58.
112. Bazzocchi A, Fuzzi F, Garzillo G, Diano D, Rimondi E, Merlino B, Moio A, Albisinni U, Battista G, Guglielmi G. Reliability and accuracy of scout CT in the detection of vertebral fractures. Br J Radiol. 2013;86:20130373.
113. Kim YM, Demissie S, Eisenberg R, Samelson EJ, Kiel DP, Bouxsein ML. Intra-and inter-reader reliability of semi-automated quantitative morphometry measurements and vertebral fracture assessment using lateral scout views from computed tomography. Osteoporos Int. 2011;22:2677–88.
114. Gruber M, Bauer JS, Dobritz M, Beer AJ, Wolf P, Woertler K, Rummeny EJ, Baum T. Bone mineral density measurements of the proximal femur from routine contrast-enhanced MDCT data sets correlate with dual-energy X-ray absorptiometry. Eur Radiol. 2013;23:505–12.
115. Ito M, Oishi R, Fukunaga M, Sone T, Sugimoto T, Shiraki M, Nishizawa Y, Nakamura T. The effects of once-weekly teriparatide on hip structure and biomechanical properties assessed by CT. Osteoporos Int. 2014;25:1163–72.
116. Bauer JS, Link TM, Burghardt A, Henning TD, Mueller D, Majumdar S, Prevrhal S. Analysis of trabecular bone structure with multidetector spiral computed tomography in a simulated soft-tissue environment. Calcif Tissue Int. 2007;80:366–73.
117. Nishiyama KK, Shane E. Clinical imaging of bone microarchitecture with HR-pQCT. Curr Osteoporos Rep. 2013;11:147–55.
118. Stein EM, Silva BC, Boutroy S, et al. Primary hyperparathyroidism is associated with abnormal cortical and trabecular microstructure and reduced bone stiffness in postmenopausal women. J Bone Miner Res. 2013;28:1029–40.
119. Patsch JM, Burghardt AJ, Yap SP, Baum T, Schwartz AV, Joseph GB, Link TM. Increased cortical porosity in type 2 diabetic postmenopausal women with fragility fractures. J Bone Miner Res. 2013;28:313–24.
120. Burghardt AJ, Issever AS, Schwartz AV, Davis KA, Masharani U, Majumdar S, Link TM. High-resolution peripheral quantitative computed tomographic imaging of cortical and trabecular bone microarchitecture in patients with type 2 diabetes mellitus. J Clin Endocrinol Metab. 2010;95:5045–55.
121. Krug R, Carballido-Gamio J, Burghardt AJ, Kazakia G, Hyun BH, Jobke B, Banerjee S, Huber M, Link TM, Majumdar S. Assessment of trabecular bone structure comparing magnetic resonance imaging at 3 Tesla with high-resolution peripheral quantitative computed tomography ex vivo and in vivo. Osteoporos Int. 2008;19:653–61.
122. Musa Aguiar P, Zarantonello P, Aparisi Gómez MP. Differentiation between osteoporotic and neoplastic vertebral fractures: state of the art and future perspectives. Curr Med Imag. 2021;18:187. https://doi.org/10.2174/1573405617666210412142758.

Body Composition in Geriatric Patients

15

Maria Pilar Aparisi Gómez, Francisco Aparisi, Giuseppe Guglielmi, and Alberto Bazzocchi

15.1 Introduction

The process of aging is associated with a modification of body composition, with notable consequence on physical abilities and health.

The study of body composition in the geriatric population is gaining momentum, with the aim to mitigate some of the negative effects these changes have and implement existing interventions, such as exercise and diet [1].

As humans age, the lean components of the organism such as total body water, organ mass, mineral bone, and skeletal muscle decrease, while total body fat increases, with an associated redistribution: it becomes more abundant in the abdominal region than in peripheral locations [2].

With age, endocrine and metabolic alterations occur, and besides, an increasingly sedentary lifestyle generates a positive imbalance between intake and use of energy [3, 4]. Aging is characterized by a low-grade chronic inflammatory status known as "inflammaging" which has common features with the metabolism-induced inflammation status known as "metaflammation," mainly driven by nutrient excess [5].

M. P. Aparisi Gómez (✉)
Department of Radiology, Auckland City Hospital, Auckland, New Zealand

Department of Radiology, IMSKE, Valencia, Spain
e-mail: pilara@adhb.govt.nz

F. Aparisi
Department of Radiology, Hospital Nueve de Octubre, Valencia, Spain

G. Guglielmi
Clinical and Experimental Medicine, University of Foggia, Foggia, Foggia, Italy
e-mail: giuseppe.guglielmi@unifg.it

A. Bazzocchi
Diagnostic and Interventional Radiology, IRCCS Istituto Ortopedico Rizzoli, Bologna, Italy
e-mail: abazzo@inwind.it

G. Guglielmi, M. Maas (eds.), *Imaging in Geriatrics*, Practical Issues in Geriatrics, https://doi.org/10.1007/978-3-031-14877-4_15

The increase in body fat and the redistribution of the fat in geriatric population have been demonstrated to be associated with risk factors for non-insulin-dependent diabetes and cardiovascular (CV) disease [6].

The loss of mineral contents in bone and structural changes are a major risk for morbidity, need for institutionalization, and mortality. Sarcopenia, with a decrease in muscle mass and function, has been associated with impaired immunity and functional status [7, 8].

The three tissues (fat, muscle, and bone) have a very close relationship, and therefore analysis and evaluation should be approached in a combined way.

Several methods are available for the assessment of body composition in geriatric population.

Clinical measures such as BMI, waist circumference, waist-to-hip ratio, underwater measurement, and bioelectrical impedance (BIA) are widely used as indicators of body adiposity, but growing evidence demonstrates their inaccuracy and inability to reflect body fat distribution [9].

Imaging tools offer tremendous advantages in research that can be transferred to clinical practice. From dual-energy X-ray absorptiometry (DXA) and ultrasound to computed tomography and magnetic resonance, imaging tools allow a more accurate estimation and characterization of body composition.

In this chapter, we aim to summarize the current knowledge on changes in body composition occurring in the geriatric age and review the possibilities of assessment that each one of the imaging techniques offers for their adequate measurement in the geriatric population.

The contents of this chapter need to be taken into consideration together with the chapter on metabolic bone disease in geriatric patients. The effects of aging on bone are extensively reviewed in a dedicated chapter, but it is important to acknowledge the close relationship and interrelation existing between all components.

15.2 Changes in Body Composition with Aging

Aging induces a decrease in basal metabolic rate (estimated as 5–25%) [10], and this leads to an increase in body weight and body fat, even if there is no change to the dietary intake. In most individuals, body fat increases gradually between the ages of 20–25 and 65 [11].

At the same time, there is a redistribution of the adipose tissue to the abdominal region (android distribution) and visceral organs and fat infiltration into muscle and bone [12]. Bone marrow fatty infiltration occurs with aging [13], but also in the context of diabetes, anorexia nervosa, and starvation [14].

The evaluation of fat as a factor in aging is challenging and made worse by the lack of consensus in the clear cut off for obesity. In the clinical context, obesity classifications are based on BMI values, but the value of this measurement for classification is limited [15]. The quantification of percentage of body fat can be performed with DXA or bioimpedance analysis (BIA) with much more accuracy, but there is still no consensus on the percentage of body fat that constitutes the cut off for obesity

in men or women. The cut off of 32% was suggested recently [16, 17], with the demonstration that 33–38% showed adverse influence on bone mineral density [18].

Muscle and bone tissues decrease with aging. The peak of muscle mass occurs at approximately 30 years of age, with a gradual decrease after that. By the age of 70, a decrease in muscle mass of 20–40% can be expected, leading to sarcopenia [19]. Dynapenia constitutes a different concept [20], consisting of loss of muscle strength and not necessarily muscle mass.

The declines in bone mineral density and muscle mass are more marked in women [21]. Bone mineral density declines with age, starting at about 50 years. At the same time, there is an increase in the bone turnover rate, with increased bone resorption, leading to bone loss [22]. In women, during the 5–7 years after menopause, there is a decrease in bone mass of up to 20%. After this period, in normal conditions, the rate slows down to 0.5–1% per year (National Osteoporosis Foundation). For men, the rate is steady at 0.5–1% and starts later in life (National Osteoporosis Foundation).

The concept of osteosarcopenic obesity syndrome represents a triad of deterioration of bone, muscle, and adipose tissues [16, 23]. The concept was first coined for older women, but a recent study points out that this phenotype may exist in younger overweight populations (18–21 years) [24]. Within this syndrome, two underlining components have been recognized, osteopenic/osteoporotic obesity [12] and sarcopenic obesity [16], which can exist separately.

The three tissues (fat, muscle, and bone) have a very close relationship and therefore evaluation needs to be done in a combined way.

15.3 Analysis of Body Composition Changes

15.3.1 Fat

With aging, there is a global increase in body fat, up to the age of 50–60 [25]. Subsequently, there is a trend of a reduction in fat mass after the age of 80 [26]. The loss of skeletal muscle mass contributes to an increase in body fat percentage [27]. An accelerated loss of lean mass has been associated with greater body fatness in old age [28].

The increase in body fat has an important role in the increase of pro-inflammatory cytokines. Adipose tissue secretes interleukin (IL)-6 and tumor necrosis factor (TNF)-alfa [29, 30]. The relative amount of truncal fat measured with DXA correlates with the levels of these markers in plasma [30].

Intraabdominal fat increases with age quantitatively, but proportionally more than peripheral fat mass [31–33]. The increase of intraabdominal fat starts before the age of 20 in men and women, accelerating with menopause in women. A study performed with DXA showed the ratio of upper to lower body fat increases linearly after 20 years. From 20 to 70, the ratio increases from 1.07 to 1.67 in men and from 0.81 to 1.21 in women [32]. On a study using CT, the increase of intraabdominal fat at L4 increases linearly with advancing age, even without significant changes in fat mass [31].

Besides from the redistribution of body fat, another feature of the changes in body composition with aging is the infiltration of tissues by fat. This has been mostly determined for muscles, thanks to the use of MR. Different studies suggest that the amount of intermuscular fat increases rapidly with age, at a yearly rate of 10% for men and 6% for women. The increase is more noticeable in people with a global increase in body weight, but it is also seen in people who lose weight [34, 35].

15.3.1.1 Causes for the Increase of Intraabdominal Fat with Aging

The redistribution of fat could be caused by different factors, such as age itself, hormonal changes, reduced fatty acid use, reduced physical activity, and resistance to leptin [36]. An increase in intraabdominal fat has been linked with an increase in most markers of cardiovascular risk, such as dyslipidemia, hypertension, and insulin resistance [37].

Withdrawal of estrogens with menopause is an independent factor inducing intraabdominal fat accumulation in women [38], corroborated by the fact that hormonal replacement therapy can prevent negative effects of menopause.

Changes in the production of testosterone can also cause accumulation of intraabdominal fat [36]. Low androgen production in men and high androgen production in women are associated with abdominal obesity. The increased secretion of cortisol could explain the alterations in the production of sexual hormones. Increased cortisol secretion is directly associated with intraabdominal fat accumulation (like in Cushing's syndrome).

The concept of the hypersensitivity of the hypothalamus–pituitary–adrenal (HPA) axis was researched by Bjoerntorp et al. [36]. The HPA is highly activated in cases of abdominal obesity, by different etiology stressors, and the consequences are aggravated by lack of efficient control by the glucocorticoid receptors of the central nervous system. This results in constant pulses of corticotropin-releasing hormone, adrenocorticotropin, cortisol, and adrenal androgens.

The loss of muscle mass and decrease in physical activity are associated with insulin resistance [39] and decreased fatty acid oxidation [40]. In resting conditions, obese people, and type II diabetes, muscle fatty acid uptake is reduced with insulin resistance. Fatty acid uptake was found to be inversely related to visceral fat, suggesting that it is possible that the increase in intraabdominal fat could be a consequence rather than a cause of the alteration of fatty acid utilization [41]. Age may be associated with a decrease in the metabolic activity of muscle, because fatty acids have a smaller contribution to the supply of energy in elderly people than in younger adults [42]. The capacity of respiring tissues to oxidize fat declines with age [43]. The decrease in fat oxidation is related to a reduction in the quantity but also the capacity of skeletal muscle to oxidize fat.

Leptin is secreted by the fatty tissue and is involved in the regulation of energy homeostasis. The circulating leptin level mainly reflects the amount of energy stores in adipose tissue and directs the central nervous system in regulating energy homeostasis, neuroendocrine function, and metabolism [44]. Studies in identical twins that were discordant for obesity demonstrated an increase in circulating leptin in the

obese twin [45], and subsequently, different studies have demonstrated that leptin's effects are largely absent in obese hyperleptinemic state, probably due to resistance or tolerance [46].

15.3.1.2 The Metabolic Consequences of the Intraabdominal Accumulation of Fat

Several descriptive and interventional studies in the past decades demonstrated insulin resistance is related to the increase in intraabdominal fat, as opposed to related to aging per se [47].

Insulin sensitivity was shown to be independently and negatively correlated with intraabdominal fat (measured as waist-to-hip ratio), which was not the case of age or obesity, in an early study by Coon et al. [48]. In studies using MRI in overweight patients, intraabdominal fat was seen to correlate with insulin resistance after controlling for BMI [49, 50]. Studies in identical twins support these results [45].

Intervention studies in rodents such as selective surgical reduction of intraabdominal fat or caloric restriction [51, 52] were seen to reduce hepatic insulin resistance. In human studies, in obese and type II diabetic patients, endurance training inducing loss of intraabdominal was associated with an improvement in peripheral insulin sensitivity [53]. Greater availability and oxidation of fatty acids are suggested as the metabolic link between increased intraabdominal fat and insulin resistance in several studies in type II diabetic patients [36, 54, 55].

Physical inactivity enhances intraabdominal fat accumulation, but also through direct mechanisms, insulin resistance [11, 39].

The effect of menopause on insulin resistance is indirect, through the accumulation of intraabdominal fat, but studies on the direct effects on insulin resistance are not conclusive [47, 56].

15.3.1.3 Fat as an Endocrine Organ

It is well described that fat acts as an endocrine organ. The hormone classically secreted by adipocytes is leptin. This has a structure that resembles the structure of IL-6 and therefore stimulates the pro-inflammatory action of IL-6, but also IL-12 and TNF alfa [57, 58]. The levels of leptin are higher in women and increase proportionally with the volume of fat mass [58]. The levels of leptin decrease progressively with age, more markedly in women than in men, independently from BMI [59].

Leptin has a local effect on bone, enhancing osteoblastogenesis and inhibiting osteoclastogenesis, through the differentiation of marrow stem cell precursors, and in that sense, promotes bone formation [60, 61]. Centrally, the effect of leptin can either be positive or negative, increasing resorption through a hypothalamic–brainstem serotonin mediated mechanism on osteoblasts [62]. Leptin also activates pro-inflammatory pathways in osteoblasts, directly, contributing to bone loss [63].

Decreased serum leptin is found in frail elderly and in cachexia [64]. Obesity leads to leptin resistance and hyperleptinemia, so cases in which there is concomitant osteosarcopenic obesity may go undetected.

Adiponectin is a hormone secreted by adipocytes but also by myocytes and osteoblasts.

Circulating adiponectin is decreased in older individuals.

Some studies demonstrated that adiponectin had a negative impact on bone mass by decreasing osteoblast proliferation [65, 66], but other studies showed that through the same pathway, adiponectin inhibited osteoclastogenesis [67, 68].

Adiponectin also has anti-inflammatory effects, inhibiting the effects of TNF alfa and IL-8 [69]. Hypoadiponectinemia is positively associated with visceral fat and obesity related diseases.

The combined effects appear to favor lean mass and less fat accumulation [70]. Serum concentrations would be lower in osteosarcopenic obesity, due to increased fat mass and decreased lean mass, but since adiponectin increases with age, the decline may be masked.

Adipose tissue has also been seen to have an endocrine effect on muscle metabolism, on an adipo-muscular axis that can modulate changes between physiologic and pathologic situations, including, for example, obesity and inflammation, but also aging.

An increase in loss of lean mass has been associated with an increase in fat accumulation in old age, and a significantly greater quantity of lean mass is lost in weight loss than is gained during weight gain in old men [28, 71].

15.3.1.4 Fat Mass and Its Effects on Mobility and Mortality

In the geriatric population, obesity, as defined by a BMI beyond 30 kg/m^2 was shown to be closely related to a decline in functional performance, with a 60% increased risk of mobility limitations, potentially leading to disability [72].

Recent evidence points toward overweight status (BMI comprised between 25 and 29.9 kg/m^2) also being associated with an increased risk of mobility limitations and disability in the elderly [73–75].

Moreover, increased BMI plays a role in functional performance over time. The Health, Aging, and Body composition study reported that in overweight or obese adults since age 25, the risk of developing mobility limitations as old men or women was 3 times higher compared to adults that maintained normal weight [76]. In people that became overweight or obese during old age, the risk was only 1.7 times higher. Weight instability has been associated with a higher risk of limitation on daily tasks and impaired mobility in the elderly [77].

The correlation between BMI and mortality in the elderly has been described as having "U" or "J" shaped curves. There is an increased risk of death with low BMIs (although this can be biased by cachectic states linked to cancer, for example) and there is also an increased mortality risk in the obese elderly. For overweight adults, reports are conflictive [78], with a recent meta-analysis concluding overweight status is not associated with increased mortality, whereas obesity is. Recent studies support that a high BMI negatively affects healthy life expectancy, and is associated with an increased risk of cancer mortality, in particular colorectal cancer [79, 80].

However, the measurement of body composition through BMI is far from accurate and an increase in weight does not necessarily imply an increase in adiposity,

could reflect an increase in muscle mass, for example. In this regard, other clinical markers, with a better correlation with fat distribution, which in turn has a correlation with specific traits of aging have been used.

As an example, a large waist circumference has been associated with mobility limitation and disabilities in different studies [81, 82], with a greater association in inactive older adults [72]. Interestingly, a longitudinal study found that modification in waist circumference was not associated with a change in self-reported disability and that the main predictor associated with physical decline was the reduction in appendicular fat free mas [83].

In fact, muscle fatty infiltration on CT was associated with a higher risk of incidence of mobility limitations in individuals (men and women) over 70 [84, 85].

An increased waist circumference in old adults has been seen to be a predictor of mortality, even corrected for BMI, and this association was reported to be dependent of cardiorespiratory fitness [86]. In older men, waist circumference has been reported as a stronger predictor for mortality than BMI. In a study assessing associations between BMI, waist circumference, and specific causes for mortality, waist circumference was the only one to show statistically significant positive associations with death from major causes (lung cancer, chronic respiratory disease, among others) [87].

A study using DXA to quantify central adiposity and mortality described a "J" curve between the two [88]. In a study using CT to quantify visceral fat, the conclusions were similar, with an increased risk for men over the age of 50 [89].

Finally, in the subgroup of very old adults, obesity determined by BMI appears unrelated to mortality, so it is possible that the relationship between adiposity and mortality may vary with age [90], but more research is needed in this field.

15.3.2 Skeletal Muscle

Sarcopenia is used to refer to the gradual loss of skeletal muscle mass and strength that takes place with aging. It should be distinguished from cachexia, which corresponds to muscle loss caused by inflammatory diseases and also from the weight loss and wasting that happens in the context of starvation or advanced disease.

There is growing evidence that sarcopenia occurring with aging has important consequences in old age, through its association with weakness, disability, and morbidity [91].

In elderly population, the coexistence of superimposed illnesses will act as an accelerator in the loss of muscle mass, increasing the risk of disability and death.

A unique consensus with the specific cut-off values or the most appropriate technique for the assessment of low skeletal muscle mass in old adults has not been reached yet.

DXA has been used to explore changes in total and regional body composition, including appendicular skeletal muscle mass of legs and arms, which is the sum of lean mass of legs and arms.

The deterioration in skeletal muscle mass in the elderly has been measured in several studies by using CT cross-sectional area, and also whole-body MRI, as techniques that provide an accurate quantification of skeletal muscle mass loss, given they allow for precise segmentation. The yearly decline has been calculated to be between 0.64% and 1.29% per year for old men and between 0.53% and 0.84% per year in old women [28, 83, 91–93].

The loss of muscle mass with age and the increase in body fat put old adults at risk of developing sarcopenic obesity.

Recent studies have used DXA to demonstrate a general decrease of lean mass at the upper and lower limbs with age in both genders. The decrease in lean mass was seen to an increase in fat mass. Lean mass was seen to decrease after 40 years of age in men, particularly after 50, and after 50 years in women. Women seemed to maintain a more favorable lean mass in arms during aging [94].

Anthropometry was also found to not be representative of lean mass of arms in both genders, independently of age, favoring imaging techniques for the correct assessment of body composition of the limbs [95].

15.3.2.1 Causes for the Decrease of Muscle Mass with Aging

Pathophysiologically, sarcopenia has been attributed to a reduction in muscle fiber number and size [96].

Type II fibers (white, fast twitch fibers) are more susceptible than type I fibers (red, slow twitch fibers) to atrophy and loss with aging [96]. Sarcopenia is muscle specific, with some muscles exhibiting substantial loss with age (e.g., vastus lateralis, rectus femoris, soleus, plantaris, gastrocnemius, extensor digitorum longus) and others showing relative preservation (adductor longus, flexor digitorum longus as examples).

The mechanisms of development are thought to be diverse, including selective decline and changes in the motor-unit organization, injuries due to contraction, deficit satellite-cell recruitment, increased free radicals and oxidative stress, and age related accumulation of mitochondrial DNA mutations [96].

As causes of development of sarcopenia, the withdrawal of anabolic stimuli (sex steroids, growth hormones, physical activity, dietary proteins, and insulin action), prevalent in men, and the increase in catabolic activity (inflammation, production of TNF alfa, IL-6, IL-1 beta) more prevalent in women have been considered [97].

Aging is influenced by a decay in the somatotropic axis, a concept that has been coined as “somatopause.” Somatopause is a process that leads to many physiological changes, resulting from DNA and other macromolecule damage [98]. The physiological changes that occur in aging have been seen to be similar to those described in cases of growth hormone deficiency (GHD) [99]. Similar to what happens in this situation, there is an increase in total cholesterol and triglycerides with the subsequent increase in CV risk, a decrease in muscle mass, a decrease in exercise tolerance, and decreased strength.

At the same time, the increase in body fat, as seen, has an important role in the increase of pro-inflammatory cytokines, which may contribute to the onset of

muscle wasting, establishing a link between age related fat mass redistribution and sarcopenia [30].

Sarcopenic change also involves fatty infiltration of the skeletal muscle (myosteatosis), which comes as a result of estrogen deficiency [100]. The pathways involved in the development myosteatosis are two. One of them is the accumulation of intracellular lipids within the myofibers (intramyocellular lipids), and the other one is the disproportioned differentiation of the mesenchymal stem cell population into the "adipogenic lineage," which is responsible for the deposit of fat in between myofibers (inter-myofiber fat). Fatty infiltration in skeletal muscle has a negative effect on muscle health and function and results in decreased sensitivity to insulin [100].

Current evidence suggests that the role of muscle changes per se is minor [101].

Vitamin D

A decreased intake of calcium, added to poor vitamin D levels and reduced renal function during aging may result in secondary hyperparathyroidism, which leads to sarcopenia and reduced strength [102]. Vitamin D controls together with parathyroid hormone (PTH) the intestinal absorption of calcium in a negative feedback loop.

Relatively recent studies have demonstrated that vitamin D deficiency is common in aging [103]. Low levels of vitamin D are therefore associated with impaired muscle strength, leading to disability and falls, through impairment of the negative feedback mechanism and increase in PTH levels.

PTH may have a direct effect on skeletal muscle, reducing energy production and utilization and influencing protein metabolism [104]. PTH also increases free intracellular calcium and decreases plasma phosphate, increasing calcium concentrations and leading to phosphate deficiency in muscle, which alters functionality [102]. It is hypothesized that this could be one of the pathways through which high concentration of PTH has been significantly associated with several parameters implicated in accidental falls and frailty [105].

One of the metabolites of vitamin D is 25-hydroxyvitamin D or calcidiol, a product of the conversion of cholecalciferol by hydroxylases in the liver. Low concentrations of calcidiol have been demonstrated to be associated with overall mortality in older persons. At the same time, the association of high serum concentrations of PTH and higher overall mortality and cardiovascular mortality has only been demonstrated to be significant in older men, but non-significant in women. Calcidiol and PTH can therefore be regarded as important health markers [106].

15.3.2.2 The Metabolic Consequences of the Decrease of Muscle Mass

Sarcopenia is a public health problem, independently associated with health outcomes and disabilities. In cases of advanced sarcopenia, weakness of the muscles is a limiting factor hindering functional capacity and performance. In cases of milder sarcopenia, the relationship between structure and function may be complex. Changes in muscle strength and size in response to inactivity or resistance training

are not always predictable [107, 108]. The loss of skeletal muscle mass and function can be prevented by specific intervention strategies in the fifth decade of life [109].

Sarcopenia is associated with adverse outcomes through a general increase in morbidity and mortality, rates of hospitalization, loss of physical ability, and loss of independence to perform activities of daily life [110, 111].

15.3.2.3 Skeletal Muscle as an Endocrine Organ

Similarly to fat and bone, muscle acts as an endocrine organ.

Troponins, the regulatory proteins associated with the contractility of skeletal muscle are not normally found in blood, except in cases of muscle turnover or muscle damage. Skeletal muscle contraction is regulated by Ca^{2+} through a skeletal muscle specific troponin, and this complex is needed for the cycles of contraction and relaxation. The skeletal muscle is protected by layers of connective tissue, but if the barrier is injured, components of the muscle, particularly these skeletal muscle specific troponins get released into the bloodstream and their presence could be indicative of sarcopenia [112, 113]. Recently, it has been demonstrated that the drop of these troponins in serum is proportional to improvements in handgrip strength and overall physical fitness in older adults [114].

15.3.2.4 Lean Mass and Its Effects on Mobility and Mortality

There is a number of studies which show that sarcopenia is related to a poorer functional status or to a 5-year functional decline in elderly patients [115]; however, other studies show opposite results, but this may be due to the confounding role of excess adiposity [88]. Sarcopenia has been seen to not be associated or only weakly associated with compromised functional capacity [116–118] and future functional decay [74, 84]. It is the high body fat mass that strongly affects functioning in old individuals, suggesting that the impact of an excess body fat is far more important than a low skeletal muscle mass.

Recent cross-sectional studies have not supported either that a mixture of low muscle mass and high body fat mass has worse outcomes regarding functional status than high body fat mass alone. If only sarcopenia is considered, no association with increased risk of poor functional status is found [117, 119, 120].

It has been suggested that prominent muscle mass loss (wasting) in old aging may intensify functional limitations and disability. A study monitoring old individuals for 5.5 years demonstrated that the loss of appendicular mass and leg muscle mass (assessed by DXA) correlated with a decline in disability score [83]. Another study showed changes in the appendicular skeletal muscle mass over 5 years had a faint and positive association with changes in physical function measurements [121].

Yet, it remains unclear if the actual decrease in skeletal muscle mass or the involuntary decrease of body weight could be the crucial factor inducing functional status decline [122].

After voluntary weight loss, the loss of fat mass in the abdomen and thighs compared to changes in skeletal muscle mass was the main determinant of improved functional performance [123].

Regarding mortality, it has been proven that mow muscle mass in the inferior limbs (measured with CT or DXA) was not strongly associated with a 4.9 years mortality risk in individuals aged 70–79 [124]. The In Chianti study concluded that the calf muscle area (measured with peripheral quantitative CT) was not associated with a 6-year mortality risk [125]. The study found no association between sarcopenic obesity and mortality. A large study of Chinese individuals demonstrated that 5 year mortality risk between sarcopenic and non-sarcopenic individuals was similar [121].

However, results may be contradictory, a recent 4.6 year follow-up study in a large population (4331 subjects aged 65–93 years) demonstrated that the loss of appendicular muscle mass (measured by DXA) was associated with an increased mortality risk [126].

15.4 Imaging of Body Composition in the Elderly

Numerous clinical methods are in use for the assessment of body composition. Among the anthropometric methods, BMI measurement has been used as a measurement of body fatness, due to its simplicity; however, it is widely known that it does not reflect the distribution of body fat. In fact, the analysis of BMI together with body composition parameters by DXA reveals that groups with very similar BMI have a different amount of fat, lean, and bone masses [9, 127]. Other clinical methods such as waist circumference measurement, waist-hip ratio, and other techniques such as underwater weighing and bioimpedance analysis are also available.

The attention of clinicians has turned into imaging methods, however. This is due to the great advantages regarding reproducibility and accuracy in research. Imaging methods allow to divide body mass into its components based on their different physical properties.

Imaging methods are the choice for calibration of field methods designed to measure adipose tissue and skeletal muscle in vivo and are the only methods that allow the measurement of internal tissues and organs [128].

Based on the information that is needed, the degree of accuracy, the safety of assessment, time required, and cost, different imaging methods can be used, such as DXA, ultrasound, computed tomography, and magnetic resonance. Each one has its special advantages and limitations (Tables 15.1 and 15.2).

Currently, DXA represents the reference method for the assessment of body composition. It is fast, involves low radiation exposure, and is unexpensive. It is also an imaging tool widely used in research [9]. Recently, it has been used in the NU-AGE study, carried out in five different European countries, among healthy elderly individuals, showing that body composition characteristics are different among the elderly in Europe and that a favorable adipose related inflammatory profile is associated with a favorable profile of fat and lean mass markers in body composition [127].

Table 15.1 Summary of imaging markers for assessment of visceral fat, adipose tissue distribution, and risk of cardiometabolic diseases

Method	Parameters	Uses	Disadvantages
DXA	Visceral adipose tissue (VAT)	Positively correlated with clinical and laboratory parameters associated with cardiovascular and metabolic syndrome risk	Need for advanced segmentation tools (otherwise approximation to android fat)
US	Visceral fat thickness parameters	Satisfactorily correlated with clinical and laboratory parameters	Standard values have not been determined, and therefore the application of the technique is limited
	Subcutaneous fat thickness parameters	Potential use to quantify intracellular fat in liver	
	Intracellular fat thickness parameters		
CT	Linear measurements (similar to US)	Excellent spatial resolution	Radiation Cost Complexity
	Cross-sectional Area (CSA)	Quantification and adipose tissue distribution from different body segments can be achieved with a high level of accuracy	Currently used in research
	Volumetric estimates	Potential opportunistic use	
MRI	Cross-sectional Area (CSA)	High spatial resolution and accuracy	Cost Complexity
	Volumetric estimates	Potential opportunistic use	Currently used in research
	Skeletal muscle fat		
	Bone marrow fat		
	Intracellular fat		

Table 15.2 Summary of imaging markers for assessment of muscle mass and risk of sarcopenia

Method	Parameters	Uses	Disadvantages
DXA	Appendicular lean mass index (ALMI)	Lean mass status could be defined using ALMI with *Z*-scores obtained from an age, ethnicity, and sex-matched population	Definition of low lean mass still has to be established and validated
US	Muscle thickness	Limited use in clinical practice	Parameters vary with aging to a different extent in different studies. Needs further validation
	Cross-sectional Area (CSA)	Potential use	Operator dependent
	Echo intensity		
	Fascicle length		
	Pennation angle		

Table 15.2 (continued)

Method	Parameters	Uses	Disadvantages
CT	Cross-sectional Area (CSA)	Excellent spatial resolution	Radiation Cost Complexity
	Volumetric estimates	High level of accuracy on quantification of skeletal muscle composition	Currently used in research
		Potential opportunistic use	
MRI	Cross-sectional Area (CSA)	Possible to detect changes in muscle structure due to aging and disease progression	Cost Complexity
	Volumetric estimates	Potential opportunistic use.	Currently used in research

15.4.1 Dual-Energy X-ray Absorptiometry (DXA)

DXA is a standard technique for the assessment of human BC, with a good level of correlation between the measurements of skeletal muscle mass at lower limbs derived by DXA and those derived by CT and MRI [129]. DXA has also been validated against post-mortem measurement of muscle, skin, and viscera [130].

DXA is based on the physical principle that X-rays of different energies undergo different attenuation when traversing different tissues. A three compartment model is generated by radiating the body at multiple different points (pixels) using two different energies. The pixels that do not contain bone contain a lean mass and fat mass ratio, and the pixels that contain bone depend on bone mineral content and a soft tissue ratio with subsequent interpolation of fat mass and lean mass ratio, based on pixels in vicinity to the ones with bone. In this way, fat mass (FM), non-bone lean mass (LM), and bone mineral content (BMC) can be obtained. In pixels without bone, soft tissue is further characterized as FM and non-bone LM [131] (Fig. 15.1).

With DXA, total body, and standard regional (trunk, arms, legs, android, and gynoid regions) body composition measures can be obtained.

As we have seen, body composition variation with age involves among others a progressive decrease in LM and increase in FM (sarcopenia and sarcopenic obesity) and also redistribution of FM to the abdomen. These changes can be monitored by DXA [117]. An abdominal or android region distribution of FM has been associated with the development of higher risk profile for cardiovascular and metabolic diseases [132]. The DXA android region was designed to be as representative as possible of abdominal fat, thus to predict metabolic risk of patients.

DXA with dedicated software allows the analysis of visceral and subcutaneous adipose tissue (VAT and SAT, respectively) in the android region (a segment of the abdomen comprised between a lower demarcation line joining the superior limits of the iliac crests and an upper demarcation line drawn at a level representing 20% of the distance in between the iliac crests line and the chin). SAT can be estimated and

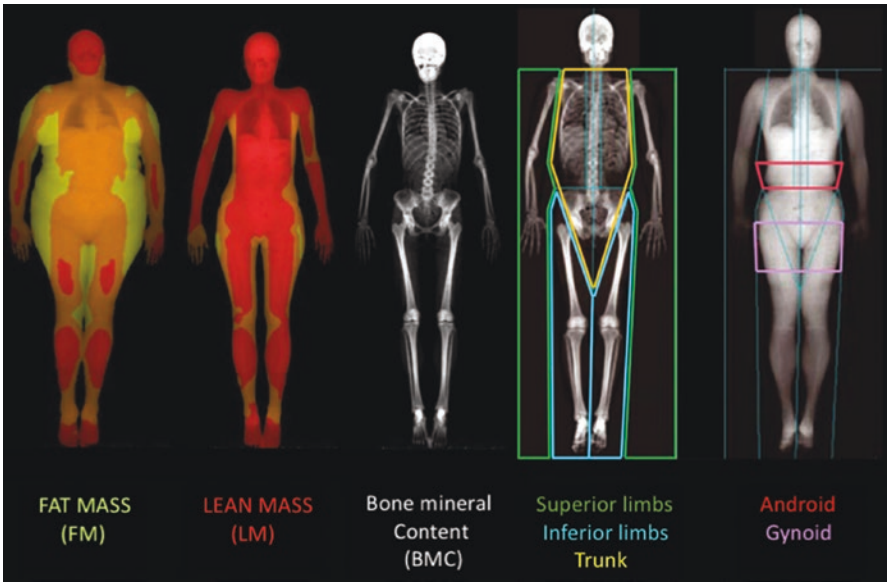

Fig. 15.1 DXA analysis of body composition. Measurements are based on a 3-compartment model that can be simplified into fat mass (FM—yellow), non-bone lean mass (LM—red), and bone mineral content (BMC—white). Body masses and bone mineral density (BMD) can be assessed on a regional or a whole-body basis

then subtracted from android total FM to obtain VAT (in grams and volume). DXA-assessed VAT measurement has been validated against CT in a wide range of age (18–90 years old) and BMI (18–40 kg/m^2) [133] (Fig. 15.2). Most of the risk is related to VAT compartment, while SAT plays a controversial role. The two fat depots are distinct in their endocrine function, with different impacts on glucose metabolism.

DXA specific measurements of LM allow for the calculation of indexes such as lean mass index (LMI: total LM/height^2), appendicular lean mass (ALM: arms LM + legs LM), and appendicular lean mass index (ALMI: ALM/height^2) [134].

ALMI is of clinical significance, because the maintenance of appendicular skeletal muscle mass is critical in the preservation of mobility and functional independence in advanced age, with subsequent impact on morbidity [135]. According to the International Society for Clinical Densitometry (ISCD) guidelines, lean mass status could be defined using ALMI with *Z*-scores obtained from a young adult, race, and sex-matched population; however, the threshold for the definition of low LM is yet to be set and validated [136]. In recent years, age- and sex-specific data on ALM obtained from general population have been collected in different countries and could be useful as a reference standard to monitor the loss of muscle mass [95].

Recent several studies in different populations have focused on collecting body composition data as reference standards, especially in healthy people, to set tools for comparison on groups of patients affected by different conditions. In this context, postmenopausal status is part of normal aging in healthy women [137, 138].

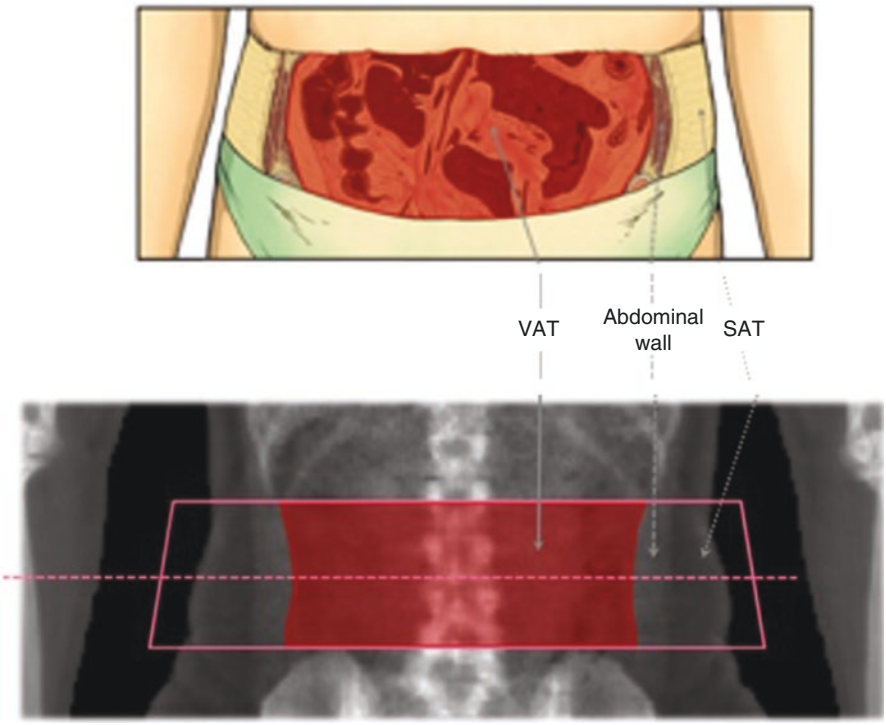

Fig. 15.2 Visceral fat assessment by DXA. DXA with dedicated software allows the analysis of visceral and subcutaneous adipose tissue (VAT and SAT, respectively) in the android region (a segment of the abdomen comprised between a lower demarcation line joining the superior limits of the iliac crests and an upper demarcation line drawn at a level representing 20% of the distance in between the iliac crests line and the chin) (red area in the drawing and DXA image). SAT can be estimated and then subtracted from android total FM to obtain VAT (in grams and volume)

The National Health and Nutrition Examination Survey (NHANES) produced reference body composition values for adults over 60 years old [139].

DXA has the advantages of being non-invasive, quick, and safe. Radiation exposure is very small (less than 1 μSv for whole-body scans), and therefore it has a high degree of safety and makes it ideal for repeated measurements for longitudinal assessment.

It is also substantially cheaper than CT and MRI. DXA also has low precision errors [130, 140]. Another important advantage is that it can be used to assess bone mass.

In the elderly, situations in which there is lack of correct hydration may impair DXA analysis, because the hydration of the lean mass is assumed as constant and uniform [140]. Inaccuracy can also arise from the thickness of the lean tissue [130].

DXA is a projectional technique, and as such measures lean mass as opposed to muscle mass in the body (cannot measure skeletal muscle mass specifically in

non-limb regions of the body, which means it includes other soft tissues in the measurement). Despite this, the measurement of lean mass is frequently used as a proxy to muscle mass.

DXA may underestimate total lean mass in the body depending on hydration status (water retention in heart, liver, kidney failure) and overestimate appendicular lean mass [140].

Individual muscles cannot be evaluated separately, and fatty infiltration cannot be quantified with DXA, which poses a problem for the detection of sarcopenic obesity. DXA does not give information of the quality of muscular tissue.

Additionally, different DXA machines can measure slightly different, with different results. Standardization is necessary and the source of a problem. Phantoms are not anthropometric and cannot be used as reference standards. In vivo cross calibration has been suggested as alternative, but is influenced by many factors, such as ethnicity and health status, besides from age and gender, for example [141]. Ideally also, equations to derive lean mass and standardization of local regions of interest should be standardized across manufacturers, or cross-manufacturer algorithms developed [142].

Another downside of DXA is not being portable, which can pose a problem when assessing elderly population.

15.4.2 Ultrasound

The use of ultrasound has been traditionally based on the possibility it offers to measure thickness of tissue layers. The interfaces between layers are easy to demonstrate. Ultrasound measurement procedures are accurate, reproducible, and fast. Ultrasound is a simple, low cost, real-time innocuous technique to evaluate body composition.

Several parameters and indexes of adipose tissue thicknesses may be measured by ultrasound and have been proved to correlate with clinical and laboratory parameters.

However, standardization is needed: intraabdominal fat thickness, epicardial fat thickness, and peri and para renal fat thickness show good accuracy and reliability, with good correlation with CT and MRI-derived areas and volumes [143]. Abdominal wall fat index, pre-peritoneal fat thickness, and mesenteric fat thickness demonstrate variable accuracy and reliability in different studies, when compared to CT [143] (Fig. 15.3). Other indexes, such as the subcutaneous fat thickness, showed good correlation with MR- and CT-derived areas and minimal and maximal subcutaneous fat thickness good correlation with CT-derived areas [143].

A study demonstrated that reproducibility and repeatability, especially for visceral fat, were more stable in fasting state and expiration [144].

The different parameters demonstrate a variable correlation with clinical and laboratory parameters associated with cardiovascular and metabolic risks, and in different clinical conditions, such as type 2 diabetes mellitus [143].

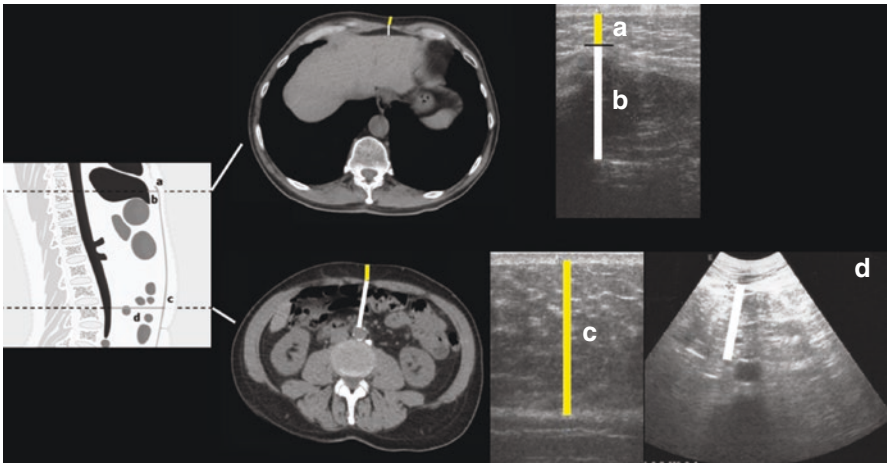

Fig. 15.3 Linear measurements of adipose tissue on ultrasound and CT. (**a**) The minimal abdominal subcutaneous fat thickness (MinASFT) is the distance between the anterior surface of the linea alba and the fat-skin barrier, obtained at a plane through the subxiphoid region. (**b**) Measurement of the pre-peritoneal fat thickness is performed from the anterior surface of the peritoneum covering the liver to the posterior surface of the linea alba, at the plane through the subxiphoid region. (**c**) The maximum abdominal subcutaneous fat thickness (MaxASFT) is the distance between the anterior surface of the linea alba and the fat-skin barrier, measured at the level of the supraumbilical region. (**d**) Most authors measure the intraabdominal fat thickness (IAFT) as the distance from the posterior wall of the abdominal muscle to the anterior wall of the aorta in the supraumbilical region

An in-depth analysis of the correlation of US-derived parameters with clinical and laboratory parameters of cardiovascular and metabolic risk largely exceeds the scope of this chapter. In general, some demonstrate positive correlations with coronary artery stenosis score, serum total cholesterol, triglyceride, and LDL [145], and also hypertension, microalbuminuria, retinopathy, carotid intima-medial thickness (IMT), and fasting Insulin concentration [146]. No correlation has been generally demonstrated with serum HDL cholesterol [145] and insulin sensitivity [147].

US can also give an insight on the intracellular fat contents, through the evaluation of hepatic steatosis, associated with metabolic syndrome and laboratory parameters of cardiovascular disease, and the evaluation of intramuscular fat, but with variable reliability and accuracy.

Ultrasound has been used too to assess muscle tissue [21], but its use remains difficult to standardize and none of the operative definitions of sarcopenia includes ultrasound in its diagnostic algorithm. US-derived measurements of muscle mass have shown a good-to-high level of correlation with those derived from reference methods [148].

Sanada et al. developed regression-based prediction equations to estimate total and regional skeletal muscle mass in healthy Japanese adults using muscle thickness measurements taken at nine sites and a significant and strong site-matched correlation was found with MRI-measured muscle mass [149]. Muscle thickness,

cross-sectional area (CSA), echo intensity, fascicle length, and pennation angle of the lower limbs are the parameters most commonly evaluated by US; in pennate muscles, the pennation angle (angle formed at the attachment site of the fibers into deep and superficial aponeurosis) can be evaluated in static and dynamic conditions and provides information about mechanical and contractile proprieties [150].

All these parameters are affected by aging to a different extent but need to be further validated. The large majority of the available studies have been conducted with small samples and in healthy patients. As a result, no validated site-specific cut-off points for the ultrasound-based assessment of low muscle mass in aging patients exist.

15.4.3 Computed Tomography (CT)

CT and MRI represent the gold standard to investigate body composition at organ-tissue level. Quantification of skeletal muscle composition and adipose tissue distribution from different body segments and individual muscle groups can be achieved with a high level of accuracy using dedicated reconstruction algorithms [151].

Based on the attenuation of an X-ray beam crossing different tissues, a CT scan can differentiate between fat and fat-free mass. Attenuation values in skeletal muscle tissue may vary between 0 and 100. Low attenuation values are proportional to the amount of fat within the muscle (normal density muscles show attenuation values in the range of 31–100 HU, while low-density muscles show attenuation values in the range of 0–30 HU) [152].

For the assessment of fat and skeletal mass, the most frequently used parameters are CT-derived cross-sectional area (CSA), and volumetric estimates, and they show good correlation with cadaver studies [153]. Thickness measurements used on ultrasound, in the case of fat mass, can also be applied, with similar correlation with laboratory and clinical parameters described for ultrasound.

CT has the advantage of being performed routinely for the diagnosis of different conditions. It therefore allows an opportunistic assessment of body composition.

On an axial CT image obtained at L3, information of total, visceral, subcutaneous adipose fat area (and estimation of volume through algorithms) and total psoas area and skeletal muscle index (SMI) (as an estimation) can be obtained [154]. CT has been used to derive a predictive cardiometabolic risk, adjusted to gender and ethnicity [155]. CT has been used to analyze the contribution of pericardial fat, intrathoracic fat, and epicardial fat to cardiometabolic risk [156].

The specific, targeted use of CT to assess body composition is limited in clinical practice by the high radiation dose (risk factor for development of neoplasms), high cost, and operational complexity. On the other side, CT exams performed for other clinical questions are an incredibly big source for body composition assessment. Artificial intelligence (AI) techniques are increasingly being developed, which allow the assessment of body composition from CT images, as collateral information from examinations performed for other clinical reasons.

15.4.4 Magnetic Resonance (MR)

MRI methods have been used in multiple research studies to gain insights into the pathophysiology of metabolic diseases including obesity, metabolic syndrome, or type 2 diabetes mellitus. MRI parameters have been correlated with metabolic control in diabetes and with diet and physical activity intervention in diabetes [157, 158].

Adipose tissue is characterized by a short T1 and long T2 relaxation time. Fat appears as bright on T1-weighted sequences because of a high concentration of immobile protons. Variations of this sequence may be easily applied for the quantification of SAT, VAT, bone marrow fat, and intermuscular adipose tissue (IMAT).

Currently, whole-body scans can be obtained in approximately 5 min, and these allow for the detailed quantification of total and regional fat deposits. Whole-body MR scanning is the most accurate and reproducible protocol to map and measure the amount of body fat, but is obviously expensive, and significantly time consuming, not manually feasible [159]. The calculation of volumes requires semiautomatic segmentation based on signal intensity histograms and thresholds [160]. T2-weighted imaging has been mainly used for fat quantification in the lower extremity muscles and is not suitable for SAT and VAT determination.

As an alternative, the acquisition of the abdominal region, which allows the measurement of fat depots that are usually associated with cardiometabolic risks has been proposed [161]. Single- and multi-slice protocols have also been developed to make analysis faster [161]. Regarding this, the L4–L5 level has been used for single-slice imaging, but poor prediction of visceral and subcutaneous tissue variation in a longitudinal study assessing changes with weight loss was reported [162]. A level close to L2–L3 has been considered as preferred by many groups [163] (Fig. 15.4).

MRI can be used quantitatively. Single-voxel ^{1}H-based MRS has been considered as non-invasive gold standard for ectopic (organ contained) fat quantification using PRESS (point resolved spectroscopy) or STEAM (stimulated echo acquisition mode) sequences. Water and fat signals are identified by their chemical shift

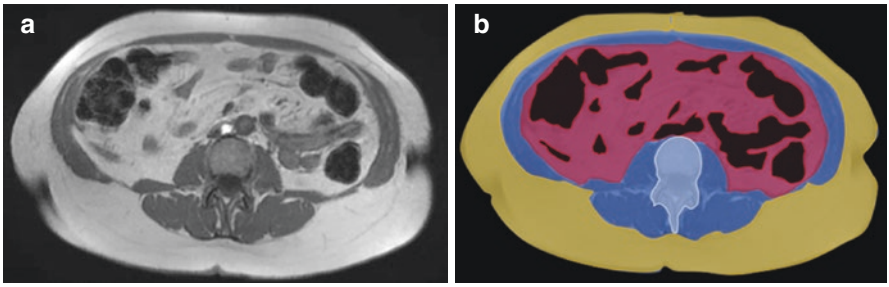

Fig. 15.4 MRI areal measurement of the different fat compartments. (**a**) T1 FSE image through the level of L2-L3. (**b**) segmentation of SAT (yellow), VAT (red), and non-adipose tissue (blue) (the gas within bowel loops is depicted as black and the bone as white)

locations along the frequency spectrum [164]. Chemical shift encoding-based water-fat MRI allows fat quantification with high spatial resolution. This is an advantage when compared to single-voxel MRS as the distribution of fat content can be spatially heterogeneous, particularly in the bone marrow [165]. Both techniques have excellent spatial resolution, allowing for thickness measurements as well as for the analysis of intrinsic tissue composition (intracellular fat content).

MRI represents the gold standard for the investigation of muscle mass and quality in a research setting; however, the high cost, limited access to the equipment and its complexity limit the use of MRI in routine clinical practice.

A key advantage of MRI is the capability to detect changes in the muscle structure occurring with aging and disease progression, which makes it ideal for longitudinal studies. Abnormal edema and the progressive accumulation of adipose tissue and fibrous connective tissue (which are non-contractile tissues) within muscles contribute to loss of muscle strength and quality, a critical aspect of sarcopenia and aging. Two-point Dixon-based technique and chemical shift-based water-fat separation as quantitative MRI techniques have been frequently applied to objectively measure muscle fat content [166]. Finally, the amount of intramyocellular lipid, which is negatively correlated to insulin sensitivity, can be quantified by spectroscopy (H-MRS) [159].

MRI allows for quantification of muscle size (CSA, volume), but also the comprehensive assessment of muscle quality. An excellent level of correlation has been demonstrated between MRI-derived CSA values (cm^2) of adipose tissue-free skeletal muscle (ATFSM), adipose tissue surrounding muscle and adipose tissue embed within muscle (interstitial adipose tissue), and those obtained from cadaveric studies. Good results were also observed between cadaveric and MRI volume estimates for the same three compartments [153].

Yang et al., in a study in old population, demonstrated that a single-slice cross-sectional area at the level of the mid-femur can be used in clinical practice for a fast and non-invasive diagnosis of sarcopenia [167].

Macaluso et al. documented a significantly lower amount of muscle contractile volume and a significantly greater amount of intramuscular non-contractile tissue in older women (mean age: 69.5 ± 2.4 years—postmenopausal bracket) in comparison with young women (mean age: 22.8 ± 5.7 years), in both quadriceps and hamstrings [168]. In women over 50, MRI-measured myosteatosis was reported to be positively associated with increased fracture risk [169], and low extremity muscle fat infiltration was shown to be negatively associated with performance based measures of physical function [170].

In old adults (both gender), the presence of myosteatosis on MRI studies has been detected as a predictor of poor muscle and mobility functions. When comparing intramuscular adipose tissue and in frail and non-frail individuals, higher fat infiltration was detectable in older frail subjects [171].

Compared to CT, MRI has a higher sensitivity in the detection of early fat replacement in muscles [172]. MRI is also independent of the hydration level of fat-free mass, which constitutes a problem with DXA, with great accuracy and

minimal changes detectable in longitudinal studies, but underestimation of fat mass and overestimation of fat-free mass have also been reported [173].

The lack of a standardized assessment protocol in image analysis represents a methodological problem, limiting comparison between the results of different studies [174].

15.5 Conclusion

This chapter has summarized the current knowledge on changes in body composition occurring in the geriatric age. The process of aging is associated with a modification of body composition, with notable consequence on physical abilities and health. Aging is characterized by a low-grade chronic inflammatory status known as "inflammaging."

The increase in body fat and the redistribution of the fat in geriatric population have been demonstrated to be associated with risk factors for non-insulin-dependent diabetes and cardiovascular disease, and besides, the loss of mineral contents in bone and structural changes are a major risk for morbidity, need for institutionalization, and mortality. Sarcopenia, with a decrease in muscle mass and function, has been associated with impaired immunity and functional status. The three tissues (fat, muscle, and bone) have a very close relationship, and therefore analysis and evaluation should be approached in a combined way.

Imaging tools offer tremendous advantages in research that can be transferred to clinical practice. From dual-energy X-ray absorptiometry (DXA) and ultrasound to computed tomography and magnetic resonance, imaging tools allow a more accurate estimation and characterization of body composition.

The accurate analysis of body composition in the geriatric population offers the possibility to mitigate some of the negative effects aging has, with the potential to implement existing interventions, such as exercise and diet, and develop new ways to promote healthy aging in the future.

References

1. Aparisi Gómez MP, Weidekamm C, Aparisi F, Bazzocchi A. Sports and metabolic bone disease. Semin Musculoskelet Radiol. 2020;24:277–89.
2. Baumgartner RN, Stauber PM, McHugh D, Koehler KM, Garry PJ. Cross-sectional age differences in body composition in persons 60+ years of age. J Gerontol A Biol Sci Med Sci. 1995;50:M307–16.
3. Hughes VA, Frontera WR, Roubenoff R, Evans WJ, Singh MAF. Longitudinal changes in body composition in older men and women: role of body weight change and physical activity. Am J Clin Nutr. 2002;76:473–81.
4. Ley CJ, Lees B, Stevenson JC. Sex- and menopause-associated changes in body-fat distribution. Am J Clin Nutr. 1992;55:950–4.
5. Hotamisligil GS. Inflammation and metabolic disorders. Nature. 2006;444:860–7.

6. Chumlea WC, Baumgartner RN, Garry PJ, Rhyne RL, Nicholson C, Wayne S. Fat distribution and blood lipids in a sample of healthy elderly people. Int J Obes Relat Metab Disord. 1992;16:125–33.
7. Roche AF. Sarcopenia: a critical review of its measurements and health-related significance in the middle-aged and elderly. Am J Hum Biol. 1994;6:33–42.
8. Schaap LA, Koster A, Visser M. Adiposity, muscle mass, and muscle strength in relation to functional decline in older persons. Epidemiol Rev. 2013;35:51–65.
9. Santoro A, Bazzocchi A, Guidarelli G, et al. A cross-sectional analysis of body composition among healthy elderly from the European NU-AGE study: sex and country specific features. Front Physiol. 2018;9:1693.
10. St-Onge M-P, Gallagher D. Body composition changes with aging: the cause or the result of alterations in metabolic rate and macronutrient oxidation? Nutrition. 2010;26:152–5.
11. Hunter GR, Gower BA, Kane BL. Age related shift in visceral fat. Int J Body Compos Res. 2010;8:103–8.
12. Ilich JZ, Kelly OJ, Inglis JE, Panton LB, Duque G, Ormsbee MJ. Interrelationship among muscle, fat, and bone: connecting the dots on cellular, hormonal, and whole body levels. Ageing Res Rev. 2014;15:51–60.
13. Aparisi Gómez MP, Ayuso Benavent C, Simoni P, Aparisi F, Guglielmi G, Bazzocchi A. Fat and bone: the multiperspective analysis of a close relationship. Quant Imag Med Surg. 2020;10:1614–35.
14. Bredella MA, Fazeli PK, Daley SM, Miller KK, Rosen CJ, Klibanski A, Torriani M. Marrow fat composition in anorexia nervosa. Bone. 2014;66:199–204.
15. Coutinho T, Goel K, Corrêa de Sá D, et al. Central obesity and survival in subjects with coronary artery disease. J Am Coll Cardiol. 2011;57:1877–86.
16. Ilich JZ, Kelly OJ, Inglis JE. Osteosarcopenic obesity syndrome: what is it and how can it be identified and diagnosed? Curr Gerontol Geriatr Res. 2016;2016:1–7.
17. Wanner M, Martin BW, Autenrieth CS, et al. Associations between domains of physical activity, sitting time, and different measures of overweight and obesity. Prev Med Rep. 2016;3:177–84.
18. Liu P-Y, Ilich JZ, Brummel-Smith K, Ghosh S. New insight into fat, muscle and bone relationship in women: determining the threshold at which body fat assumes negative relationship with bone mineral density. Int J Prev Med. 2014;5:1452–63.
19. Kalyani RR, Corriere M, Ferrucci L. Age-related and disease-related muscle loss: the effect of diabetes, obesity, and other diseases. Lancet Diab & Endocrinol. 2014;2:819–29.
20. Clark BC, Manini TM. Sarcopenia ≠ dynapenia. J Gerontol Ser A Biol Med Sci. 2008;63:829–34.
21. Cruz-Jentoft AJ, Baeyens JP, Bauer JM, et al. Sarcopenia: European consensus on definition and diagnosis: report of the European Working Group on Sarcopenia in Older People. Age Ageing. 2010;39:412–23.
22. Guglielmi G, Muscarella S, Bazzocchi A. Integrated imaging approach to osteoporosis: state-of-the-art review and update. RadioGraphics. 2011;31:1343–64.
23. Jafari Nasabian P, Inglis J, Kelly O, Ilich J. Osteosarcopenic obesity in women: impact, prevalence, and management challenges. Int J Women's Health. 2017;9:33–42.
24. Stefanaki C, Peppa M, Boschiero D, Chrousos GP. Healthy overweight/obese youth: early osteosarcopenic obesity features. Eur J Clin Investig. 2016;46:767–78.
25. Coin A, Sergi G, Inelmen EM, Enzi G. Pathophysiology of body composition changes in elderly people. In: Mantovani G, Anker SD, Inui A, Morley JE, Fanelli FR, Scevola D, Schuster MW, Yeh S-S, editors. Cachexia and wasting: a modern approach. Milan: Springer Milan; 2006. p. 369–75.
26. Ding J, Kritchevsky SB, Newman AB, et al. Effects of birth cohort and age on body composition in a sample of community-based elderly. Am J Clin Nutr. 2007;85:405–10.
27. Zamboni M, Zoico E, Scartezzini T, Mazzali G, Tosoni P, Zivelonghi A, Gallagher D, De Pergola G, Di Francesco V, Bosello O. Body composition changes in stable-weight elderly subjects: the effect of sex. Aging Clin Exp Res. 2003;15:321–7.

28. Koster A, Ding J, Stenholm S, et al. Does the amount of fat mass predict age-related loss of lean mass, muscle strength, and muscle quality in older adults? J Gerontol A Biol Sci Med Sci. 2011;66:888–95.
29. Kern PA, Ranganathan S, Li C, Wood L, Ranganathan G. Adipose tissue tumor necrosis factor and interleukin-6 expression in human obesity and insulin resistance. Am J Physiol Endocrinol Metab. 2001;280:E745–51.
30. Pedersen M, Bruunsgaard H, Weis N, Hendel HW, Andreassen BU, Eldrup E, Dela F, Pedersen BK. Circulating levels of TNF-alpha and IL-6-relation to truncal fat mass and muscle mass in healthy elderly individuals and in patients with type-2 diabetes. Mech Ageing Dev. 2003;124:495–502.
31. Zamboni M, Mazzali G, Fantin F, Rossi A, Di Francesco V. Sarcopenic obesity: a new category of obesity in the elderly. Nutr Metab Cardiovasc Dis. 2008;18:388–95.
32. Horber FF, Gruber B, Thomi F, Jensen EX, Jaeger P. Effect of sex and age on bone mass, body composition and fuel metabolism in humans. Nutrition. 1997;13:524–34.
33. Wang Q, Hassager C, Ravn P, Wang S, Christiansen C. Total and regional body-composition changes in early postmenopausal women: age-related or menopause-related? Am J Clin Nutr. 1994;60:843–8.
34. Rossi AP, Watson NL, Newman AB, Harris TB, Kritchevsky SB, Bauer DC, Satterfield S, Goodpaster BH, Zamboni M. Effects of body composition and adipose tissue distribution on respiratory function in elderly men and women: the health, aging, and body composition study. J Gerontol Ser A Biol Med Sci. 2011;66A:801–8.
35. Delmonico MJ, Harris TB, Visser M, et al. Longitudinal study of muscle strength, quality, and adipose tissue infiltration. Am J Clin Nutr. 2009;90:1579–85.
36. Björntorp P. Body fat distribution, insulin resistance, and metabolic diseases. Nutrition. 1997;13:795–803.
37. Mykkänen L, Laakso M, Pyörälä K. Association of obesity and distribution of obesity with glucose tolerance and cardiovascular risk factors in the elderly. Int J Obes Relat Metab Disord. 1992;16:695–704.
38. Tchernof A, Calles-Escandon J, Sites CK, Poehlman ET. Menopause, central body fatness, and insulin resistance: effects of hormone-replacement therapy. Coron Artery Dis. 1998;9:503–11.
39. Yamanouchi K, Nakajima H, Shinozaki T, Chikada K, Kato K, Oshida Y, Osawa I, Sato J, Sato Y, Higuchi M. Effects of daily physical activity on insulin action in the elderly. J Appl Physiol. 1992;73:2241–5.
40. Mittendorfer B, Klein S. Effect of aging on glucose and lipid metabolism during endurance exercise. Int J Sport Nutr Exerc Metab. 2001;11(Suppl):S86–91.
41. Colberg SR, Simoneau JA, Thaete FL, Kelley DE. Skeletal muscle utilization of free fatty acids in women with visceral obesity. J Clin Invest. 1995;95:1846–53.
42. Horber FF, Kohler SA, Lippuner K, Jaeger P. Effect of regular physical training on age-associated alteration of body composition in men. Eur J Clin Investig. 1996;26:279–85.
43. Toth MJ, Tchernof A. Lipid metabolism in the elderly. Eur J Clin Nutr. 2000;54(Suppl 3):S121–5.
44. Kelesidis T, Kelesidis I, Chou S, Mantzoros CS. Narrative review: the role of leptin in human physiology: emerging clinical applications. Ann Intern Med. 2010;152:93–100.
45. Rönnemaa T, Karonen SL, Rissanen A, Koskenvuo M, Koivisto VA. Relation between plasma leptin levels and measures of body fat in identical twins discordant for obesity. Ann Intern Med. 1997;126:26–31.
46. Mantzoros CS, Magkos F, Brinkoetter M, Sienkiewicz E, Dardeno TA, Kim S-Y, Hamnvik O-PR, Koniaris A. Leptin in human physiology and pathophysiology. Am J Physiol Endocrinol Metab. 2011;301:E567–84.
47. Beaufrère B, Morio B. Fat and protein redistribution with aging: metabolic considerations. Eur J Clin Nutr. 2000;54(Suppl 3):S48–53.

48. Coon PJ, Rogus EM, Drinkwater D, Muller DC, Goldberg AP. Role of body fat distribution in the decline in insulin sensitivity and glucose tolerance with age. J Clin Endocrinol Metab. 1992;75:1125–32.
49. Cefalu WT, Wang ZQ, Werbel S, Bell-Farrow A, Crouse JR, Hinson WH, Terry JG, Anderson R. Contribution of visceral fat mass to the insulin resistance of aging. Metabolism. 1995;44:954–9.
50. Cefalu WT, Werbel S, Bell-Farrow AD, Terry JG, Wang ZQ, Opara EC, Morgan T, Hinson WH, Crouse JR. Insulin resistance and fat patterning with aging: relationship to metabolic risk factors for cardiovascular disease. Metabolism. 1998;47:401–8.
51. Barzilai N, She L, Liu BQ, Vuguin P, Cohen P, Wang J, Rossetti L. Surgical removal of visceral fat reverses hepatic insulin resistance. Diabetes. 1999;48:94–8.
52. Barzilai N, Banerjee S, Hawkins M, Chen W, Rossetti L. Caloric restriction reverses hepatic insulin resistance in aging rats by decreasing visceral fat. J Clin Invest. 1998;101:1353–61.
53. Mourier A, Gautier JF, De Kerviler E, Bigard AX, Villette JM, Garnier JP, Duvallet A, Guezennec CY, Cathelineau G. Mobilization of visceral adipose tissue related to the improvement in insulin sensitivity in response to physical training in NIDDM. Effects of branched-chain amino acid supplements. Diabetes Care. 1997;20:385–91.
54. Girard J. [Role of free fatty acids in the insulin resistance of non-insulin-dependent diabetes]. Diabete Metab. 1995; 21:79–88.
55. Boden G. Role of fatty acids in the pathogenesis of insulin resistance and NIDDM. Diabetes. 1997;46:3–10.
56. Petroni ML, Caletti MT, Dalle Grave R, Bazzocchi A, Aparisi Gómez MP, Marchesini G. Prevention and treatment of sarcopenic obesity in women. Nutrients. 2019;11:E1302.
57. Abenavoli L, Peta V. Role of adipokines and cytokines in non-alcoholic fatty liver disease. Rev Recent Clin Trials. 2015;9:134–40.
58. Pires A, Martins P, Pereira AM, Marinho J, Vaz Silva P, Marques M, Castela E, Sena C, Seiça R. Pro-inflammatory triggers in childhood obesity: correlation between leptin, adiponectin and high-sensitivity C-reactive protein in a group of obese Portuguese children. Rev Port Cardiol. 2014;33:691–7.
59. Isidori AM, Strollo F, Morè M, Caprio M, Aversa A, Moretti C, Frajese G, Riondino G, Fabbri A. Leptin and aging: correlation with endocrine changes in male and female healthy adult populations of different body weights. J Clin Endocrinol Metab. 2000;85:1954–62.
60. Gordeladze JO, Drevon CA, Syversen U, Reseland JE. Leptin stimulates human osteoblastic cell proliferation, de novo collagen synthesis, and mineralization: impact on differentiation markers, apoptosis, and osteoclastic signaling. J Cell Biochem. 2002;85:825–36.
61. Karsenty G, Ferron M. The contribution of bone to whole-organism physiology. Nature. 2012;481:314–20.
62. Motyl KJ, Rosen CJ. The skeleton and the sympathetic nervous system: it's about time! J Clin Endocrinol Metab. 2012;97:3908–11.
63. Upadhyay J, Farr OM, Mantzoros CS. The role of leptin in regulating bone metabolism. Metabolism. 2015;64:105–13.
64. Hubbard RE, O'Mahony MS, Calver BL, Woodhouse KW. Nutrition, inflammation, and leptin levels in aging and frailty: nutrition, inflammation, and leptin levels. J Am Geriatr Soc. 2008;56:279–84.
65. Luo X-H, Guo L-J, Xie H, Yuan L-Q, Wu X-P, Zhou H-D, Liao E-Y. Adiponectin stimulates RANKL and inhibits OPG expression in human osteoblasts through the MAPK signaling pathway. J Bone Miner Res. 2006;21:1648–56.
66. Lewerin C, Johansson H, Lerner UH, Karlsson MK, Lorentzon M, Barrett-Connor E, Smith U, Ohlsson C, Mellström D. High serum adiponectin is associated with low blood haemoglobin in elderly men: the Swedish MrOS study. J Intern Med. 2015;278:68–76.
67. Oshima K, Nampei A, Matsuda M, Iwaki M, Fukuhara A, Hashimoto J, Yoshikawa H, Shimomura I. Adiponectin increases bone mass by suppressing osteoclast and activating osteoblast. Biochem Biophys Res Commun. 2005;331:520–6.

68. Williams GA, Wang Y, Callon KE, et al. In vitro and in vivo effects of adiponectin on bone. Endocrinology. 2009;150:3603–10.
69. Ghoshal K. Adiponectin: probe of the molecular paradigm associating diabetes and obesity. World J Diabetes. 2015;6:151.
70. Fiaschi T, Giannoni E, Taddei ML, Chiarugi P. Globular adiponectin activates motility and regenerative traits of muscle satellite cells. PLoS One. 2012;7:e34782.
71. Newman AB, Lee JS, Visser M, Goodpaster BH, Kritchevsky SB, Tylavsky FA, Nevitt M, Harris TB. Weight change and the conservation of lean mass in old age: the health, aging and body composition study. Am J Clin Nutr. 2005;82:872–8.
72. Koster A, Patel KV, Visser M, et al. Joint effects of adiposity and physical activity on incident mobility limitation in older adults: adiposity, physical activity, and mobility limitation. J Am Geriatr Soc. 2008;56:636–43.
73. Visser M, Langlois J, Guralnik JM, Cauley JA, Kronmal RA, Robbins J, Williamson JD, Harris TB. High body fatness, but not low fat-free mass, predicts disability in older men and women: the cardiovascular health study. Am J Clin Nutr. 1998;68:584–90.
74. Zoico E, Di Francesco V, Mazzali G, Zivelonghi A, Volpato S, Bortolani A, Dioli A, Coin A, Bosello O, Zamboni M. High baseline values of fat mass, independently of appendicular skeletal mass, predict 2- year onset of disability in elderly subjects at the high end of the functional spectrum. Aging Clin Exp Res. 2007;19:154–9.
75. Marsh AP, Rejeski WJ, Espeland MA, et al. Muscle strength and BMI as predictors of major mobility disability in the lifestyle interventions and independence for elders pilot (LIFE-P). J Gerontol Ser A Biol Med Sci. 2011;66A:1376–83.
76. Houston DK, Ding J, Nicklas BJ, Harris TB, Lee JS, Nevitt MC, Rubin SM, Tylavsky FA, Kritchevsky SB, for the Health ABC Study. Overweight and obesity over the adult life course and incident mobility limitation in older adults: the health, aging and body composition study. Am J Epidemiol. 2009;169:927–36.
77. Arnold AM, Newman AB, Cushman M, Ding J, Kritchevsky S. Body weight dynamics and their association with physical function and mortality in older adults: the cardiovascular health study. J Gerontol Ser A Biol Med Sci. 2010;65A:63–70.
78. Flegal KM, Kit BK, Orpana H, Graubard BI. Association of all-cause mortality with overweight and obesity using standard body mass index categories: a systematic review and meta-analysis. JAMA. 2013;309:71.
79. Shaukat A, Dostal A, Menk J, Church TR. BMI is a risk factor for colorectal cancer mortality. Dig Dis Sci. 2017;62:2511–7.
80. Leigh L, Byles JE, Jagger C. BMI and healthy life expectancy in old and very old women. Br J Nutr. 2016;116:692–9.
81. Ramsay SE, Whincup PH, Shaper AG, Wannamethee SG. The relations of body composition and adiposity measures to ill health and physical disability in elderly men. Am J Epidemiol. 2006;164:459–69.
82. Meadows R, Bower JK. Associations of anthropometric measures of obesity with physical limitations in older adults. Disabil Rehabil. 2020;42:1101–6.
83. Fantin F, Francesco VD, Fontana G, Zivelonghi A, Bissoli L, Zoico E, Rossi A, Micciolo R, Bosello O, Zamboni M. Longitudinal body composition changes in old men and women: interrelationships with worsening disability. J Gerontol Ser A Biol Med Sci. 2007;62:1375–81.
84. Visser M, Goodpaster BH, Kritchevsky SB, Newman AB, Nevitt M, Rubin SM, Simonsick EM, Harris TB, for the Health ABC Study. Muscle mass, muscle strength, and muscle fat infiltration as predictors of incident mobility limitations in well-functioning older persons. J Gerontol Ser A Biol Med Sci. 2005;60:324–33.
85. Reinders I, Murphy RA, Koster A, et al. Muscle quality and muscle fat infiltration in relation to incident mobility disability and gait speed decline: the age, gene/environment susceptibility-Reykjavik Study. J Gerontol A Biol Sci Med Sci. 2015;70:1030–6.
86. Sui X, LaMonte MJ, Laditka JN, Hardin JW, Chase N, Hooker SP, Blair SN. Cardiorespiratory fitness and adiposity as mortality predictors in older adults. JAMA. 2007;298:2507–16.

87. Leitzmann MF, Moore SC, Koster A, Harris TB, Park Y, Hollenbeck A, Schatzkin A. Waist circumference as compared with body-mass index in predicting mortality from specific causes. PLoS One. 2011;6:e18582.
88. Kuk JL, Katzmarzyk PT, Nichaman MZ, Church TS, Blair SN, Ross R. Visceral fat is an independent predictor of all-cause mortality in men*. Obesity. 2006;14:336–41.
89. Auyeung TW, Lee JSW, Leung J, Kwok T, Leung PC, Woo J. Survival in older men may benefit from being slightly overweight and centrally obese--a 5-year follow-up study in 4,000 older adults using DXA. J Gerontol Ser A Biol Med Sci. 2010;65A:99–104.
90. Thinggaard M, Jacobsen R, Jeune B, Martinussen T, Christensen K. Is the relationship between BMI and mortality increasingly U-shaped with advancing age? A 10-year follow-up of persons aged 70-95 years. J Gerontol A Biol Sci Med Sci. 2010;65:526–31.
91. Hughes VA, Frontera WR, Wood M, Evans WJ, Dallal GE, Roubenoff R, Fiatarone Singh MA. Longitudinal muscle strength changes in older adults: influence of muscle mass, physical activity, and health. J Gerontol A Biol Sci Med Sci. 2001;56:B209–17.
92. Frontera WR, Reid KF, Phillips EM, Krivickas LS, Hughes VA, Roubenoff R, Fielding RA. Muscle fiber size and function in elderly humans: a longitudinal study. J Appl Physiol. 2008;105:637–42.
93. Song M-Y, Ruts E, Kim J, Janumala I, Heymsfield S, Gallagher D. Sarcopenia and increased adipose tissue infiltration of muscle in elderly African American women. Am J Clin Nutr. 2004;79:874–80.
94. Bazzocchi A, Diano D, Ponti F, Andreone A, Sassi C, Albisinni U, Marchesini G, Battista G. Health and ageing: a cross-sectional study of body composition. Clin Nutr. 2013;32:569–78.
95. Diano D, Ponti F, Guerri S, Mercatelli D, Amadori M, Aparisi Gómez MP, Battista G, Guglielmi G, Bazzocchi A. Upper and lower limbs composition: a comparison between anthropometry and dual-energy X-ray absorptiometry in healthy people. Arch Osteoporos. 2017;12:78.
96. Bua EA, McKiernan SH, Wanagat J, McKenzie D, Aiken JM. Mitochondrial abnormalities are more frequent in muscles undergoing sarcopenia. J Appl Physiol. 2002;92:2617–24.
97. Payette H, Roubenoff R, Jacques PF, Dinarello CA, Wilson PWF, Abad LW, Harris T. Insulin-like growth factor-1 and interleukin 6 predict sarcopenia in very old community-living men and women: the Framingham Heart Study. J Am Geriatr Soc. 2003;51:1237–43.
98. Kolovou G, Katsiki N, Pavlidis A, Bilianou H, Goumas G, Mikhailidis DP. Ageing mechanisms and associated lipid changes. Curr Vasc Pharmacol. 2014;12:682–9.
99. van den Beld AW, Carlson OD, Doyle ME, Rizopoulos D, Ferrucci L, van der Lely AJ, Egan JM. IGFBP-2 and aging: a 20-year longitudinal study on IGFBP-2, IGF-I, BMI, insulin sensitivity and mortality in an aging population. Eur J Endocrinol. 2019;180:109–16.
100. Hamrick MW, McGee-Lawrence ME, Frechette DM. Fatty infiltration of skeletal muscle: mechanisms and comparisons with bone marrow adiposity. Front Endocrinol. 2016;7:69. https://doi.org/10.3389/fendo.2016.00069.
101. Kohrt WM, Holloszy JO. Loss of skeletal muscle mass with aging: effect on glucose tolerance. J Gerontol A Biol Sci Med Sci. 1995;50 Spec No:68–72.
102. Genaro PS, Pinheiro MM, Szejnfeld VL, Martini LA. Secondary hyperparathyroidism and its relationship with sarcopenia in elderly women. Arch Gerontol Geriatr. 2015;60:349–53.
103. on behalf of the IOF Committee of Scientific Advisors (CSA) Nutrition Working Group, Mithal A, Wahl DA, et al. Global vitamin D status and determinants of hypovitaminosis D. Osteoporos Int. 2009;20:1807–20.
104. Baczynski R, Massry SG, Magott M, el-Belbessi S, Kohan R, Brautbar N. Effect of parathyroid hormone on energy metabolism of skeletal muscle. Kidney Int. 1985;28:722–7.
105. Bird M-L, El Haber N, Batchelor F, Hill K, Wark JD. Vitamin D and parathyroid hormone are associated with gait instability and poor balance performance in mid-age to older aged women. Gait Posture. 2018;59:71–5.

106. El Hilali J, de Koning EJ, van Ballegooijen AJ, Lips P, Sohl E, van Marwijk HWJ, Visser M, van Schoor NM. Vitamin D, PTH and the risk of overall and disease-specific mortality: results of the Longitudinal Aging Study Amsterdam. J Steroid Biochem Mol Biol. 2016;164:386–94.
107. Suzuki Y, Murakami T, Haruna Y, Kawakubo K, Goto S, Makita Y, Ikawa S, Gunji A. Effects of 10 and 20 days bed rest on leg muscle mass and strength in young subjects. Acta Physiol Scand Suppl. 1994;616:5–18.
108. Nelson ME, Layne JE, Bernstein MJ, et al. The effects of multidimensional home-based exercise on functional performance in elderly people. J Gerontol A Biol Sci Med Sci. 2004;59:154–60.
109. Roubenoff R. Sarcopenia: a major modifiable cause of frailty in the elderly. J Nutr Health Aging. 2000;4:140–2.
110. Dennison EM, Sayer AA, Cooper C. Epidemiology of sarcopenia and insight into possible therapeutic targets. Nat Rev Rheumatol. 2017;13:340–7.
111. Reginster J-Y, Beaudart C, Buckinx F, Bruyère O. Osteoporosis and sarcopenia: two diseases or one? Curr Opin Clin Nutr Metab Care. 2016;19:31–6.
112. Chase PB, Szczypinski MP, Soto EP. Nuclear tropomyosin and troponin in striated muscle: new roles in a new locale? J Muscle Res Cell Motil. 2013;34:275–84.
113. Kalinkovich A, Livshits G. Sarcopenia – the search for emerging biomarkers. Ageing Res Rev. 2015;22:58–71.
114. Abreu EL, Cheng A-L, Kelly PJ, Chertoff K, Brotto L, Griffith E, Kinder G, Uridge T, Zachow R, Brotto M. Skeletal muscle troponin as a novel biomarker to enhance assessment of the impact of strength training on fall prevention in the older adults. Nurs Res. 2014;63:75–82.
115. Janssen I. Skeletal muscle cutpoints associated with elevated physical disability risk in older men and women. Am J Epidemiol. 2004;159:413–21.
116. Jankowski CM, Gozansky WS, Van Pelt RE, Schenkman ML, Wolfe P, Schwartz RS, Kohrt WM. Relative contributions of adiposity and muscularity to physical function in community-dwelling older adults. Obesity. 2008;16:1039–44.
117. Rolland Y, Lauwers-Cances V, Cristini C, van Kan GA, Janssen I, Morley JE, Vellas B. Difficulties with physical function associated with obesity, sarcopenia, and sarcopenic-obesity in community-dwelling elderly women: the EPIDOS (EPIDemiologie de l'OSteoporose) study. Am J Clin Nutr. 2009;89:1895–900.
118. Hairi NN, Cumming RG, Naganathan V, Handelsman DJ, Le Couteur DG, Creasey H, Waite LM, Seibel MJ, Sambrook PN. Loss of muscle strength, mass (sarcopenia), and quality (specific force) and its relationship with functional limitation and physical disability: the concord health and ageing in men project: age-related muscle changes and physical function. J Am Geriatr Soc. 2010;58:2055–62.
119. Bouchard DR, Dionne IJ, Brochu M. Sarcopenic/obesity and physical capacity in older men and women: data from the nutrition as a determinant of successful aging (NuAge)-the Quebec Longitudinal Study. Obesity. 2009;17:2082–8.
120. Zoico E, Di Francesco V, Guralnik JM, Mazzali G, Bortolani A, Guariento S, Sergi G, Bosello O, Zamboni M. Physical disability and muscular strength in relation to obesity and different body composition indexes in a sample of healthy elderly women. Int J Obes. 2004;28:234–41.
121. Woo J, Leung J, Sham A, Kwok T. Defining sarcopenia in terms of risk of physical limitations: a 5-year follow-up study of 3,153 Chinese men and women: definition of sarcopenia by incident physical limitation. J Am Geriatr Soc. 2009;57:2224–31.
122. Visser M, Pahor M, Tylavsky F, Kritchevsky SB, Cauley JA, Newman AB, Blunt BA, Harris TB. One- and two-year change in body composition as measured by DXA in a population-based cohort of older men and women. J Appl Physiol. 2003;94:2368–74.
123. Santanasto AJ, Glynn NW, Newman MA, Taylor CA, Brooks MM, Goodpaster BH, Newman AB. Impact of weight loss on physical function with changes in strength, muscle mass, and muscle fat infiltration in overweight to moderately obese older adults: a randomized clinical trial. J Obes. 2011;2011:1–10.

124. Newman AB, Kupelian V, Visser M, Simonsick EM, Goodpaster BH, Kritchevsky SB, Tylavsky FA, Rubin SM, Harris TB, on Behalf of the Health, Aging and Body Composition Study Investigators. Strength, but not muscle mass, is associated with mortality in the health, aging and body composition study cohort. J Gerontol Ser A Biol Med Sci. 2006;61:72–7.
125. Cesari M, Pahor M, Lauretani F, Zamboni V, Bandinelli S, Bernabei R, Guralnik JM, Ferrucci L. Skeletal muscle and mortality results from the InCHIANTI study. J Gerontol Ser A Biol Med Sci. 2009;64A:377–84.
126. Lee CG, Boyko EJ, Nielson CM, et al. Mortality risk in older men associated with changes in weight, lean mass, and fat mass: body composition changes and mortality in older men. J Am Geriatr Soc. 2011;59:233–40.
127. Santoro A, Guidarelli G, Ostan R, et al. Gender-specific association of body composition with inflammatory and adipose-related markers in healthy elderly Europeans from the NU-AGE study. Eur Radiol. 2019;29:4968–79.
128. Ross R. Advances in the application of imaging methods in applied and clinical physiology. Acta Diabetol. 2003;40:s45–50.
129. Andreoli A, Scalzo G, Masala S, Tarantino U, Guglielmi G. Body composition assessment by dual-energy X-ray absorptiometry (DXA). Radiol Med. 2009;114:286–300.
130. Buckinx F, Landi F, Cesari M, et al. Pitfalls in the measurement of muscle mass: a need for a reference standard: measurement of muscle mass. J Cachexia Sarcopenia Muscle. 2018;9:269–78.
131. Toombs RJ, Ducher G, Shepherd JA, De Souza MJ. The impact of recent technological advances on the trueness and precision of DXA to assess body composition. Obesity (Silver Spring). 2012;20:30–9.
132. Misra A, Vikram NK. Clinical and pathophysiological consequences of abdominal adiposity and abdominal adipose tissue depots. Nutrition. 2003;19:457–66.
133. Kaul S, Rothney MP, Peters DM, Wacker WK, Davis CE, Shapiro MD, Ergun DL. Dual-energy X-ray absorptiometry for quantification of visceral fat. Obesity. 2012;20:1313–8.
134. Guglielmi G, Ponti F, Agostini M, Amadori M, Battista G, Bazzocchi A. The role of DXA in sarcopenia. Aging Clin Exp Res. 2016;28:1047–60.
135. Janssen I, Heymsfield SB, Ross R. Low relative skeletal muscle mass (sarcopenia) in older persons is associated with functional impairment and physical disability. J Am Geriatr Soc. 2002;50:889–96.
136. Shepherd JA, Baim S, Bilezikian JP, Schousboe JT. Executive summary of the 2013 International Society for Clinical Densitometry Position Development Conference on Body Composition. J Clin Densitom. 2013;16:489–95.
137. Päivi M, Mirja H, Terttu P. Changes in physical activity involvement and attitude to physical activity in a 16-year follow-up study among the elderly. J Aging Res. 2010;2010:1–7.
138. Kyle UG, Genton L, Slosman DO, Pichard C. Fat-free and fat mass percentiles in 5225 healthy subjects aged 15 to 98 years. Nutrition. 2001;17:534–41.
139. Kelly TL, Wilson KE, Heymsfield SB. Dual energy X-ray absorptiometry body composition reference values from NHANES. PLoS One. 2009;4:e7038.
140. Bazzocchi A, Ponti F, Albisinni U, Battista G, Guglielmi G. DXA: technical aspects and application. Eur J Radiol. 2016;85:1481–92.
141. Genant HK, Grampp S, Glüer CC, Faulkner KG, Jergas M, Engelke K, Hagiwara S, van Kuijk C. Universal standardization for dual X-ray absorptiometry: patient and phantom cross-calibration results. J Bone Miner Res. 2009;9:1503–14.
142. Saarelainen J, Hakulinen M, Rikkonen T, Kröger H, Tuppurainen M, Koivumaa-Honkanen H, Honkanen R, Hujo M, Jurvelin JS. Cross-calibration of GE healthcare lunar prodigy and iDXA dual-energy X-ray densitometers for bone mineral measurements. J Osteoporos. 2016;2016:1–11.
143. Bazzocchi A, Filonzi G, Ponti F, Albisinni U, Guglielmi G, Battista G. Ultrasound: which role in body composition? Eur J Radiol. 2016;85:1469–80.

144. Bazzocchi A, Filonzi G, Ponti F, Amadori M, Sassi C, Salizzoni E, Albisinni U, Battista G. The role of ultrasonography in the evaluation of abdominal fat: analysis of technical and methodological issues. Acad Radiol. 2013;20:1278–85.
145. Tadokoro N, Murano S, Nishide T, Suzuki R, Watanabe S, Murayama H, Morisaki N, Saito Y. Preperitoneal fat thickness determined by ultrasonography is correlated with coronary stenosis and lipid disorders in non-obese male subjects. Int J Obes Relat Metab Disord. 2000;24:502–7.
146. Tayama K, Inukai T, Shimomura Y. Preperitoneal fat deposition estimated by ultrasonography in patients with non-insulin-dependent diabetes mellitus. Diabetes Res Clin Pract. 1999;43:49–58.
147. Iacobellis G, Willens HJ. Echocardiographic epicardial fat: a review of research and clinical applications. J Am Soc Echocardiogr. 2009;22:1311–9.
148. Ticinesi A, Meschi T, Narici MV, Lauretani F, Maggio M. Muscle ultrasound and sarcopenia in older individuals: a clinical perspective. J Am Med Dir Assoc. 2017;18:290–300.
149. Sanada K, Kearns CF, Midorikawa T, Abe T. Prediction and validation of total and regional skeletal muscle mass by ultrasound in Japanese adults. Eur J Appl Physiol. 2006;96:24–31.
150. Narici M, Franchi M, Maganaris C. Muscle structural assembly and functional consequences. J Exp Biol. 2016;219:276–84.
151. Guerri S, Mercatelli D, Aparisi Gómez MP, Napoli A, Battista G, Guglielmi G, Bazzocchi A. Quantitative imaging techniques for the assessment of osteoporosis and sarcopenia. Quant Imag Med Surg. 2018;8:60–85.
152. Goodpaster BH, Thaete FL, Kelley DE. Composition of skeletal muscle evaluated with computed tomography. Ann N Y Acad Sci. 2000;904:18–24.
153. Mitsiopoulos N, Baumgartner RN, Heymsfield SB, Lyons W, Gallagher D, Ross R. Cadaver validation of skeletal muscle measurement by magnetic resonance imaging and computerized tomography. J Appl Physiol. 1998;85:115–22.
154. Malietzis G, Aziz O, Bagnall NM, Johns N, Fearon KC, Jenkins JT. The role of body composition evaluation by computerized tomography in determining colorectal cancer treatment outcomes: a systematic review. Eur J Surg Oncol. 2015;41:186–96.
155. Eastwood SV, Tillin T, Wright A, Heasman J, Willis J, Godsland IF, Forouhi N, Whincup P, Hughes AD, Chaturvedi N. Estimation of CT-derived abdominal visceral and subcutaneous adipose tissue depots from anthropometry in Europeans, South Asians and African Caribbeans. PLoS One. 2013;8:e75085.
156. Wang H, Chen YE, Eitzman DT. Imaging body fat: techniques and cardiometabolic implications. Arterioscler Thromb Vasc Biol. 2014;34:2217–23.
157. Machann J, Thamer C, Stefan N, Schwenzer NF, Kantartzis K, Häring H-U, Claussen CD, Fritsche A, Schick F. Follow-up whole-body assessment of adipose tissue compartments during a lifestyle intervention in a large cohort at increased risk for type 2 diabetes. Radiology. 2010;257:353–63.
158. Boettcher M, Machann J, Stefan N, Thamer C, Häring H-U, Claussen CD, Fritsche A, Schick F. Intermuscular adipose tissue (IMAT): association with other adipose tissue compartments and insulin sensitivity. J Magn Reson Imaging. 2009;29:1340–5.
159. Thomas EL, Fitzpatrick JA, Malik SJ, Taylor-Robinson SD, Bell JD. Whole body fat: content and distribution. Prog Nucl Magn Reson Spectrosc. 2013;73:56–80.
160. Kullberg J, Ahlström H, Johansson L, Frimmel H. Automated and reproducible segmentation of visceral and subcutaneous adipose tissue from abdominal MRI. Int J Obes. 2007;31:1806–17.
161. Borga M. MRI adipose tissue and muscle composition analysis-a review of automation techniques. Br J Radiol. 2018;91:20180252.
162. Shen W, Chen J, Gantz M, Velasquez G, Punyanitya M, Heymsfield SB. A single MRI slice does not accurately predict visceral and subcutaneous adipose tissue changes during weight loss. Obesity (Silver Spring). 2012;20:2458–63.
163. Lemos T, Gallagher D. Current body composition measurement techniques. Curr Opin Endocrinol Diabetes Obes. 2017;24:310–4.

164. Tyagi A, Yeganeh O, Levin Y, et al. Intra- and inter-examination repeatability of magnetic resonance spectroscopy, magnitude-based MRI, and complex-based MRI for estimation of hepatic proton density fat fraction in overweight and obese children and adults. Abdom Imaging. 2015;40:3070–7.
165. Eggers H, Börnert P. Chemical shift encoding-based water-fat separation methods: Dixon Methods. J Magn Reson Imaging. 2014;40:251–68.
166. Fischer Michael A, Pfirrmann CWA, Espinosa N, Raptis DA, Buck FM. Dixon-based MRI for assessment of muscle-fat content in phantoms, healthy volunteers and patients with achillodynia: comparison to visual assessment of calf muscle quality. Eur Radiol. 2014;24:1366–75.
167. Yang YX, Chong MS, Lim WS, Tay L, Yew S, Yeo A, Tan CH. Validity of estimating muscle and fat volume from a single MRI section in older adults with sarcopenia and sarcopenic obesity. Clin Radiol. 2017;72:427.e9–427.e14.
168. Macaluso A, Nimmo MA, Foster JE, Cockburn M, McMillan NC, De Vito G. Contractile muscle volume and agonist-antagonist coactivation account for differences in torque between young and older women. Muscle Nerve. 2002;25:858–63.
169. Wong AKO, Beattie KA, Min KKH, Gordon C, Pickard L, Papaioannou A, Adachi JD, Canadian Multicentre Osteoporosis Study (CaMos) Research Group. Peripheral quantitative computed tomography-derived muscle density and peripheral magnetic resonance imaging-derived muscle adiposity: precision and associations with fragility fractures in women. J Musculoskelet Neuronal Interact. 2014;14:401–10.
170. Lorbergs AL, Noseworthy MD, Adachi JD, Stratford PW, MacIntyre NJ. Fat infiltration in the leg is associated with bone geometry and physical function in healthy older women. Calcif Tissue Int. 2015;97:353–63.
171. Addison O, Drummond MJ, LaStayo PC, Dibble LE, Wende AR, McClain DA, Marcus RL. Intramuscular fat and inflammation differ in older adults: the impact of frailty and inactivity. J Nutr Health Aging. 2014;18:532–8.
172. Gloor M, Fasler S, Fischmann A, Haas T, Bieri O, Heinimann K, Wetzel SG, Scheffler K, Fischer D. Quantification of fat infiltration in oculopharyngeal muscular dystrophy: comparison of three MR imaging methods. J Magn Reson Imaging. 2011;33:203–10.
173. Napolitano A, Miller SR, Murgatroyd PR, Coward WA, Wright A, Finer N, De Bruin TW, Bullmore ET, Nunez DJ. Validation of a quantitative magnetic resonance method for measuring human body composition. Obesity (Silver Spring). 2008;16:191–8.
174. Erlandson MC, Lorbergs AL, Mathur S, Cheung AM. Muscle analysis using pQCT, DXA and MRI. Eur J Radiol. 2016;85:1505–11.

Myeloid and Lymphoid Disorders in Geriatric Patients

16

Patrizia Toia, Massimo Galia, Giuseppe Filorizzo, Ludovico La Grutta, Federico Midiri, Pierpaolo Alongi, Emanuele Grassedonio, and Massimo Midiri

16.1 Introduction

Hematological malignancies (HMs) are a type of blood cancer with a large variety of incidence, etiology, prognosis, and survival.

HMs are the fourth most frequent type of cancer in the world with a high impact on elderly patients, resulting in considerable morbidity and mortality. Half of all HMs are diagnosed in patients 65 years of age and older, and this group accounts for 70% of cancer fatalities [1].

An increase in total cancer incidence among older adults is expected [1, 2].

Population aging will have a significant impact on the prevalence of HMs. The prognosis for older patients with HMs varies widely, depending on personal features and treatment options [1].

Aging is a complicated and multifaceted process influenced by both hereditary and environmental factors; older people are more susceptible to infections, and

P. Toia · M. Galia (✉) · G. Filorizzo · F. Midiri · E. Grassedonio · M. Midiri
Department of Biomedicine, Neuroscience and Advanced Diagnostic (BiND), AOUP Paolo Giaccone, University of Palermo, Palermo, Italy
e-mail: massimo.galia@unipa.it; emanuele.grassedonio@unipa.it; massimo.midiri@unipa.it

L. La Grutta
Department of Health Promotion Sciences Maternal and Infantile Care, Internal Medicine and Medical Specialities (ProMISE), AOUP Giaccone, University of Palermo, Palermo, Italy
e-mail: ludovico.lagrutta@unipa.it

P. Alongi
Nuclear Medicine Unit, Fondazione Istituto G. Giglio, Palermo, Italy

G. Guglielmi, M. Maas (eds.), *Imaging in Geriatrics*, Practical Issues in Geriatrics, https://doi.org/10.1007/978-3-031-14877-4_16

functions of several organs are already compromised by chronic diseases. The hematopoietic stem cells (HSCs) are not immune to the aging process, and genetic and epigenetic damage to the HSCs contributes to the onset of malignant hemopathies in older patients [3].

The World Health Organization (WHO) classification divides hematopoietic neoplasms into three types based on their lineage (myeloid, lymphoid, and histiocytic/dendritic) and distinguishes neoplasms composed of precursor cells from those composed of functionally mature ones [4, 5].

In geriatric oncological patients, it is mandatory to evaluate the level of frailty for the best treatment choice.

Frailty is a biological condition caused by aging, comorbidities, and diseases; it is a dynamic state that necessitates a multimodal approach in everyday practice [6] which includes diagnostic imaging evaluation.

Indications and clinical applications of conventional radiography, computed tomography (CT), positron emission tomography/CT (PET/CT), and magnetic resonance imaging (MRI) are all different.

The application of standardized diagnostic criteria is critical for accurate treatment decisions [7].

The aim of the chapter is to describe radiological findings of the main myeloid and lymphoid disorders with special regard to geriatric patients.

16.2 Myeloid Disorders

16.2.1 Myeloproliferative Neoplasms (MPNs)

Polycythemia vera (PV), essential thrombocythemia (ET), primary myelofibrosis (PMF), and chronic myeloid leukemia (CML) are defined as abnormalities in hematopoietic stem cells that lead to clonal proliferation of myeloid lineage cell types [8].

Recognizing the radiologic signs and consequences of myeloid disorders is crucial in the treatment of these hematologic cancers.

As above discussed, some authors suggest that the level of frailty in older patients should be measured to choose the best therapy strategy [9].

Regarding the diagnosis, a significant number of patients with MPNs are detected after undergoing a full blood count and/or peripheral blood film for another cause, as an incidental finding.

Thrombosis, hemorrhage, splenomegaly, and extramedullary hematopoiesis can be associated with MPN. Furthermore, similar conditions, such as splanchnic thrombosis, may occur in the absence of a prior MPN diagnosis or a blood count anomaly, although molecular testing can detect a JAK2 mutation and hence an underlying MPN.

Radiologists should be conversant with these diseases to have more possibilities to diagnose and to suspect occult MPN. The ability to acknowledge the different accompanying radiological abnormalities, as well as the probability of an underlying MPN in the setting of atypical thrombotic episodes, can lead to an early diagnosis [8].

16.2.2 Imaging Findings

The limited literature about imaging features of these disorders may result in underdiagnosis; however there are some imaging findings related to complications of MPN, like thrombotic disease, marrow fibrosis, and extramedullary hematopoiesis (EMH). Although there are no guidelines on the importance of imaging in disease monitoring, radiologists must be aware of the most common imaging findings.

16.2.2.1 Skeletal Findings

Marrow infiltration is one of the most common findings, but cortical bone alterations can also be encountered.

Osteosclerosis is commonly found in PMF on plain radiographs.

The bone marrow appears replaced by an unusually low T1 signal instead of a high T1 signal on MRI. Also bone scintigraphy can help in the diagnosis with an elevated skeletal uptake compared to the kidneys in case of marrow infiltration [10].

16.2.2.2 Solid Lesions

Extramedullary hematopoiesis is one of the most commonly observed solid lesions.

Extra-marrow development of new blood components most typically occurs in the spleen and liver, followed by paravertebral regions [10, 11], but it can affect any tissue or organ, so radiologists may be aware of patient's medical history [12].

EMH of the liver and spleen can determine hepatosplenomegaly leading to symptoms associated with mass effect, such as early satiety, abdominal pain, and dyspnea in severe cases. Although focal hepatic masses have been described, EMH involving the spleen and/or liver most usually results in organomegaly without distinct masses on imaging.

Paraspinal masses especially in the thorax are usually bilateral and well confined.

CT appearance of EMH is determined by hematopoietic activity within the masses, appearing as solid masses at ultrasound.

On contrast-enhanced CT (CECT), active masses tend to show modest homogenous enhancement, whereas older masses are more heterogeneous, with areas of fat attenuation; MRI usually show heterogeneous signal with fat tissue components [12].

16.2.2.3 Thrombosis

Thrombosis is a common complication of MPNs that is often detected on imaging.

ET and PV both increase the risk of thrombotic events, which can manifest in a variety of ways. Arterial thrombi, Budd-Chiari syndrome (BCS), and portal vein thrombosis can all impair splanchnic circulation [13, 14].

Budd-Chiari syndrome describes the clinical signs of hepatic venous outflow obstruction, which can occur anywhere between the hepatic veins and the cavoatrial junction.

BCS is a problem in MPN patients. Intraluminal venous obstruction, such as venous thrombosis, causes primary BCS, whereas extraluminal venous obstruction, such as that caused by extrinsic compression, causes secondary BCS. The sharpness

of the thrombus, as well as the degree of venous blockage, influences imaging findings.

The study of choice for the initial evaluation of BCS is ultrasound with Doppler followed by contrast-enhanced CT.

Because the caudate lobe has its own venous drainage system, compensatory caudate lobe hypertrophy can occur in up to 75% of BCS cases, causing inferior vena cava (IVC) compression in acute situations.

In chronic stages of BCS, portal hypertension and pulmonary embolism can be detected. The liver will seem nodular, with comma-shaped intrahepatic collateral veins visible.

Well-perfused parenchyma tends to compensate for poorly perfused areas, resulting in nodular hyperplasia; because these well-perfused nodular areas, known as large regenerative nodules, show homogenous enhancement on CECT, they are referred to as large regenerative nodules.

Magnetic resonance imaging in acute BCS often demonstrates increased T2-weighted signal intensity in the peripheral part of the liver, comparable to CT findings. The caudate lobe shows normal or increased enhancement after gadolinium administration, but the liver's periphery shows decreased enhancement [8].

The imaging study of choice for detecting portal vein thrombosis (PVT) is ultrasound with Doppler. On ultrasound, a thrombus usually appears as an intraluminal echogenic lesion, albeit a newly formed thrombus may seem hypoechoic or anechoic, with no flow at Doppler imaging or flow around a thrombus that partially obstructs the vein.

Venous thrombus usually appears isodense or hyperdense to surrounding tissue on unenhanced CT, but as an intraluminal filling defect on contrast-enhanced CT; collateral veins and dilatation of the thrombosed venous segment are two indirect CT signs.

When compared to normal hepatic parenchyma, the parenchyma of the hepatic segment supplied by thrombosed vessels appears hypodense on CT.

MRI helps to differentiate acute from chronic thrombosis [8].

16.3 Lymphoid Disorders

B- or T-cell lymphoma, hairy cell leukemia, prolymphocytic leukemia, natural killer cell big granular lymphocytic leukemia, myeloma, and plasmacytoma are few of the lymphocytic illnesses that can be caused by disorders of lymphoid progenitors. Hodgkin lymphoma is also caused by a neoplastic B cell with severely altered immunoglobulin genes that are no longer produced as proteins [7].

Between lymphoid disorders, chronic lymphocytic leukemia (CLL) is a hematological cancer characterized by the proliferation of largely mature but aberrant leukocytes and often affects adults about 65–70 years of age (Fig. 16.1). Splenomegaly, hepatomegaly, and lymphadenopathy are some of the symptoms that might be seen

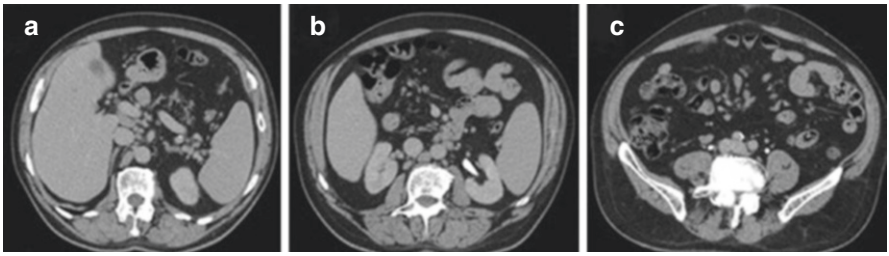

Fig. 16.1 Postcontrast CT axial images in chronic lymphocytic leukemia. (**a**–**c**) show multiple abdominal pathological lymph nodes

on imaging, but they are not specific to the condition, instead lymphomas are characterized by many typical radiological features [15].

16.3.1 Lymphomas

Lymphomas can be unifocal, multifocal, or diffuse, impact solitary lymph nodes or any organ system and show a variety of imaging presentations at nearly every site.

Following the establishment of a histological diagnosis, the imaging-based first staging will impact the treatment options and prognosis.

16.3.1.1 Chest X-Ray (CXR)

CXR plays a limited role in the diagnosis of lymphoma since it is not accurate in the measurement of maximal transverse mass diameter, including nearby normal mediastinal structures, which cannot be distinguished from the tumor mass.

The presence of bulky mediastinal infiltration is a known negative prognosticator in Hodgkin's disease [16–21], initially documented in patients receiving only radiotherapy [16, 20]; treatment advancements with dual modality therapy diminished the importance of the present concept of "bulky disease".

Because of its great concordance with CT, a chest X-ray is not necessary to determine mass [22].

Figure 16.2 shows an example of patients with lymphoma reported by conventional radiography.

16.3.1.2 CT

Computed tomography plays a crucial role in lymphoma imaging.

Normal lymph nodes have an elongated shape and a fatty hilum. Lymph nodes infiltrated by lymphoma cells are frequently visualized incidentally or during a targeted ultrasonography examination.

At ultrasound, pathologic lymph nodes are often rounded, with a hypoechoic, pseudocystic appearance caused by the replacement of the node with lymphomatous tissue.

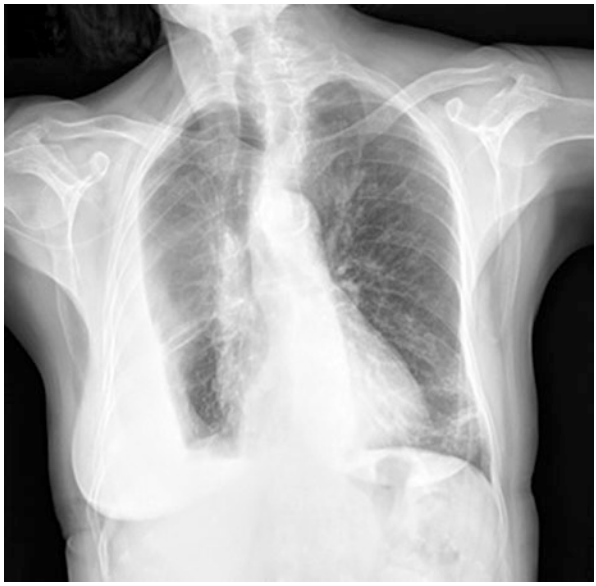

Fig. 16.2 A 76-year-old woman with thoracic lymphoma. Chest X-ray shows pleural opacification of the lower right field and matting of the right lower paraesophageal region with sharp margins

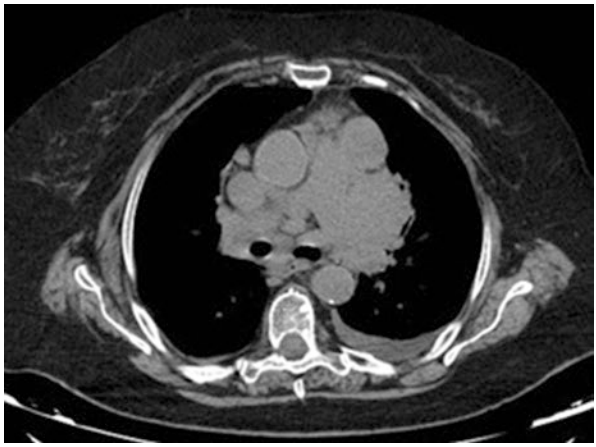

Fig. 16.3 Non-contrast CT scan of a 80-year-old woman with thoracic non-Hodgkin's lymphoma. Presence of multiple enlarged lymph nodes in about all mediastinal sites

At computed tomography, involved lymph nodes are often larger and of homogeneous density.

The location and subtype of lymphoma determine the imaging features.

Nodal lymphoma is a type of lymphoma affecting only lymph nodes. Extranodal lymphoma refers to lymphoma that has spread to other tissues. Primary extranodal lymphoma is a type of lymphoma that affects only one organ, though it can affect many organs.

Lymphoma can affect many sites at the thoracic level (Fig. 16.3).

Pulmonary lymphoma might present as pulmonary masses or extranodal expansion of thoracic nodal masses and is usually diffuse large B-cell lymphoma or

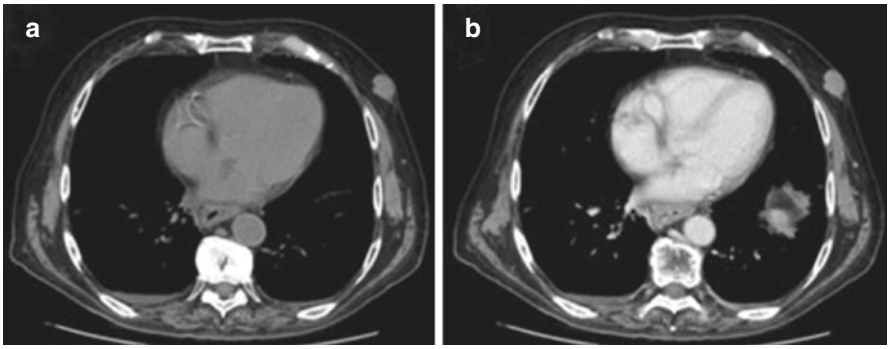

Fig. 16.4 CT of a 84-year-old man with lymphoma of the left breast in external quadrants (non-contrast acquisition in **a** and portal venous phase in **b**)

marginal zone lymphoma developing from bronchial lymphoid tissue, both are uncommon. Multiple ill-defined solid or ground glass nodules or masses, consolidation with air bronchograms, and interlobular septal thickening are all common CT findings in pulmonary lymphoma [23].

Lymphoma can also be found in the breast (Fig. 16.4).

Lymphoma of the abdominal solid organs typically appears on CT scans as solid masses enhancing at contrast-enhanced CT [24].

Diffuse organ involvement is also conceivable, typically in the liver and spleen, resulting in organomegaly and different CT attenuation [25].

Most occurrences of splenic involvement in lymphoma are caused by diffuse large B-cell lymphoma, Hodgkin lymphoma [26], or indolent B-cell lymphomas. Splenomegaly is the most common imaging sign, but a normal spleen does not rule out lymphoma involvement.

In the liver, periportal infiltration has been reported in association with hepatic masses or porto-caval adenopathy. Pancreatic lymphoma is possible even if uncommon, furthermore it may be encased by peripancreatic adenopathy [27].

Renal involvement can manifest as diffuse enlargement or focal renal masses on imaging.

Gastrointestinal tract lymphoma is frequent in non-Hodgkin lymphoma with different CT scan appearance. Stomach is the most usually affected organ, followed by small bowel and colon.

Small bowel lymphoma shows a prevalence in the terminal ileum, due to the enormous proportion of lymphoid tissue at this region. Findings on CT imaging include localized or multifocal intestinal wall or fold thickening, polyps, ulcers, and aneurysmal dilatation [27].

Some examples are shown in Figs. 16.5 and 16.6.

Diffuse large B-cell lymphoma or follicular lymphoma are the most common types of primary lymphoma of the bone. The CT appearance of osseous lymphoma varies; isolated lesions are often lytic, but they can also be sclerotic, as seen in a classic "ivory vertebra," or they might have a mixed lytic/sclerotic appearance [27].

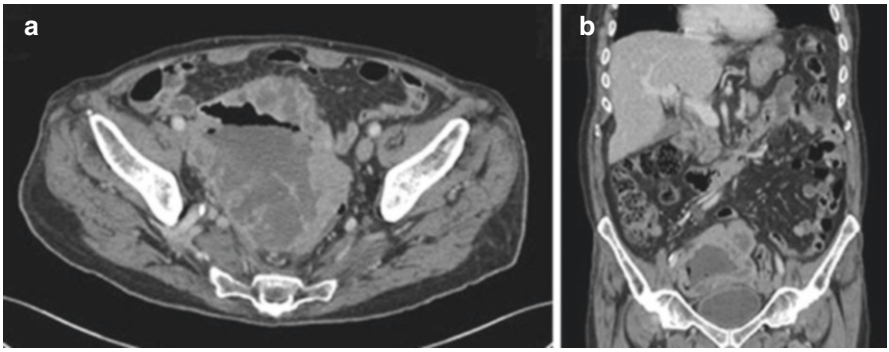

Fig. 16.5 Post-contrast CT of a 76-year-old man with lymphoma involving ileum (axial image in **a** and coronal multiplanar reconstruction in **b**). In the mesenteric fat a mass with inhomogeneous density due to the presence of peripheral tissue quota and central colliquate component is observed, with hydro-air level

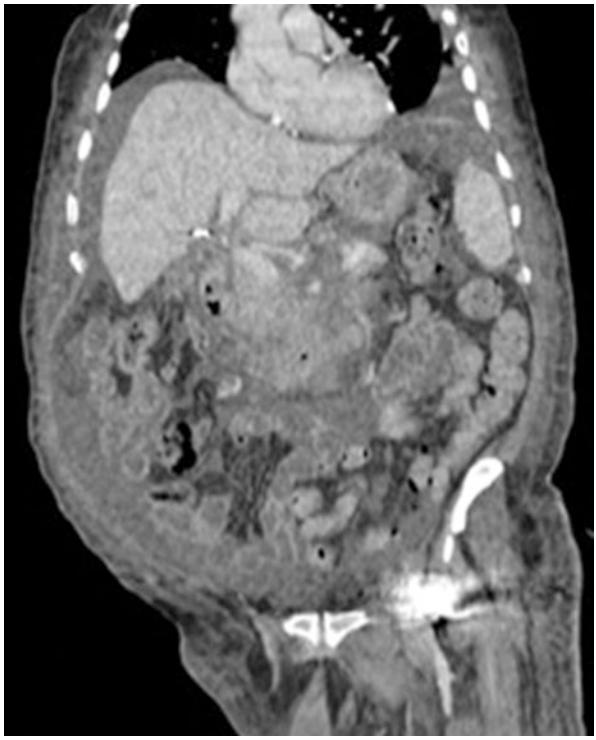

Fig. 16.6 Coronal multiplanar reconstruction of post-contrast CT acquisition in a 76-year-old-man with abdominal lymphoma characterized by multiple confluent lymphadenopathies in retroperitoneal space and in mesenteric fat, abdominal effusion is associated

16.3.2 Lymphoma Staging: Lugano Classification

The Lugano classification is a lymphoma staging system that applies to both non-Hodgkin and Hodgkin lymphoma. Presently, it is the most used staging system and provides criteria for therapy response determined by PET/CT or CT alone.

A universally accepted and reproducible staging system is essential for the standardized management of patients with malignant lymphomas, in fact clinical staging plays a larger role in the selection of patients' treatment than any other clinical factor, and clinical stage is one of the factors that can be used to predict disease prognosis.

A shared classification also allows a clear response evaluation, guiding therapies.

In this staging system, 18F-fluorodeoxyglucose (18F-FDG) PET/CT has been fully integrated into the staging and response assessment of FDG-avid lymphoma. CT should still be used to stage lymphomas with low or variable FDG uptake. Although 18F-FDG PET/CT is strongly recommended for staging FDG-avid lymphomas, a diagnostic contrast-enhanced CT examination should still be included at initial staging for optimal anatomic assessment [28].

CT identifies four categories: (1) complete radiologic response, all lymph nodes less than or equal to 1.5 cm in longest diameter, and disappearance of all lymphoma CT findings; (2) partial remission, 50% or greater reduction in disease burden; (3) stable disease, less than 50% reduction in disease burden; and (4) progressive disease, new or increased adenopathy or new extranodal lymphoma.

Response assessment with 18F-FDG PET/CT is based on metabolic activity, indicated by FDG uptake. The International Work Group criteria for reviewing PET scans were based on visual interpretation and intended for end-of-treatment evaluation, using mediastinal blood pool as the comparator [29].

The Deauville 5-point scale is used by the Lugano classification for documenting response by 18F-FDG PET/CT ranging from no uptake or residual uptake to significantly increased uptake or any new lesion.

Table 16.1 summarizes the Lugano criteria according to CT and 18F-FDG PET/CT [29].

Recent evidences suggest that CT examination may be useful in patients with HL who have a favorable interim or post-treatment PET-CT, with a smaller tumor mass corresponding to a better result [30, 31]. Response evaluation based on CT is

Table 16.1 Lugano criteria

	Response			
Method	Complete response	Partial response	No response	Progressive disease
CT	Nodal sites less than or equal to 1.5 cm	50% or greater reduction in disease burden	Less than 50% reduction in disease burden	New or increased adenopathy
	Complete disappearance of radiological findings			New extranodal lymphoma
18F-FDG PET/CT	Score* of 1, 2, 3 in nodal or extranodal sites	Score* of 4 or 5 with reduced uptake and residual masses of any size	Score* of 4 or 5 with no evident change in FDG uptake	Score* of 4 or 5 in any lesion with an increase in intensity of uptake
				New FDG-avid foci consistent with lymphoma

CT computed tomography, *18F-FDG PET/CT* fluorodeoxyglucose-positron emission tomography/computed tomography
Score* 1–5: according to Deauville 5-point scale

favorite for histologies with low or variable FDG avidity, as well as in regions where PET-CT is not available [31].

Other recommendations are included in the Lugano classification.

Particularly, although 18F-FDG PET/CT is widely accepted as the gold standard for FDG-avid lymphomas, the Lugano classification recognizes the relevance of CT for anatomic assessment, recommending contrast-enhanced CT for initial staging and radiation therapy planning.

At the time of baseline staging, the tumor burden will be estimated. Up to six lymphoma nodes, nodal complexes, or other lymphoma deposits are selected. The lesions picked must be able to be measured accurately in two dimensions.

Although the Lugano classification considers detectable an adenopathy with longest nodal diameter of more than 1.5 cm, radiologists must be aware that a lymph node smaller than 1.0 cm with avid FDG uptake could be connected with lymphoma [29].

Splenomegaly is defined when spleen is >13 cm.

Changes in metabolic activity, expressed by SUV, can be used to quantify response on 18F-FDG PET/CT scans. The highest SUV in any lesion on the baseline and follow-up scan is usually measured.

Furthermore, radiologists must be aware that CT and 18F-FDG PET/CT findings may be discordant, as in case of a significant reduction in tumor burden at CT and increased SUV at 18F-FDG PET/CT [7].

In conclusion, the Lugano classification is used as a unified guideline for all clinicians involved in lymphoma diagnosis and care because it reflects a consensus statement of clinical experts in lymphoma. Therefore, radiologists and nuclear medicine specialists have a better chance of guiding clinical management based on imaging findings thanks to these criteria [7].

Figures 16.7 and 16.8 show an example of an 18F-FDG PET/CT performed in an old patient with a diffuse large B-cell NHL.

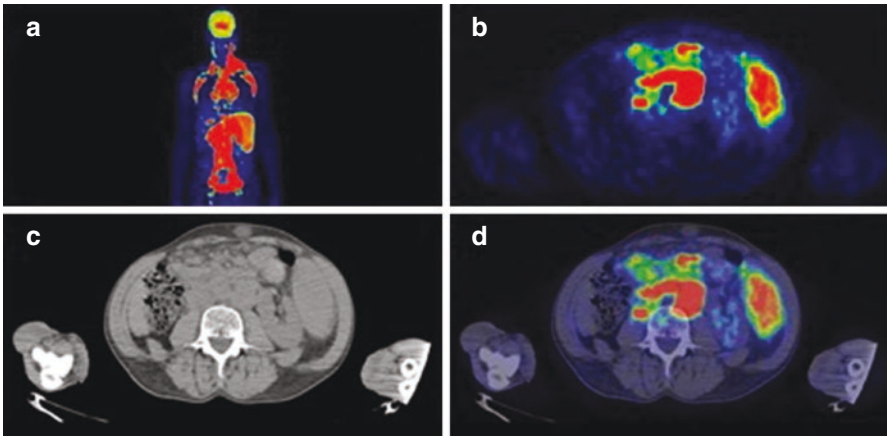

Fig. 16.7 Maximum intensity projection (MIP) representation of 18F-FDG PET (**a**); axial section of PET images corrected for attenuation (**b**); axial section of low-dose CT used for attenuation correction of PET images (**c**); axial section hybrid PET/CT images showing multiple retroperitoneal and mesenteric pathological lymph nodes and diffuse pathological metabolic activity of the lower pole of the spleen (**d**)

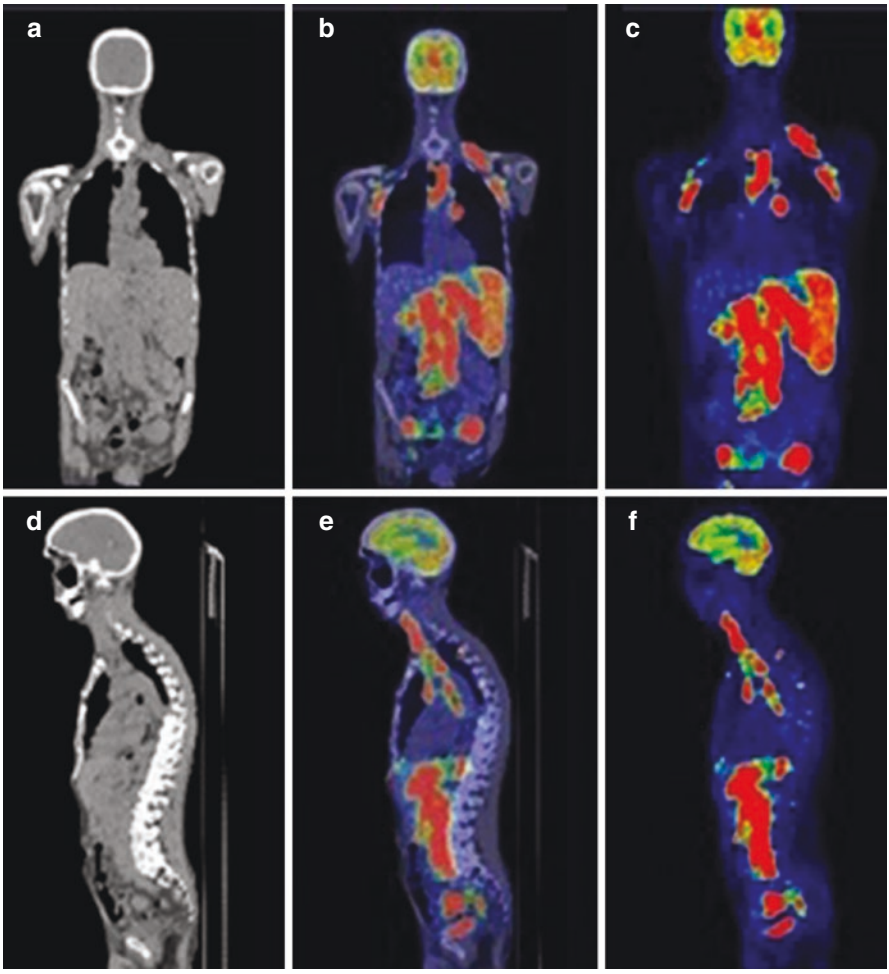

Fig. 16.8 Coronal and sagittal section of low-dose CT used for correction attenuation (**a**, **d**); Coronal and sagittal section hybrid PET/CT images showing multiple supra and subdiaphragmatic pathological lymph nodes, splenic and bone disease with high metabolic activity (**b**, **e**); coronal and sagittal sections of PET images corrected for attenuation (**c**, **f**)

16.3.2.1 Whole-Body Magnetic Resonance Imaging (WB-MRI)

WB-MRI, as a radiation-free alternative to standard imaging procedures, has been prompted by advancements in MRI technology and concerns about an increased cancer risk in lymphoma patients due to radiation exposure associated with imaging examinations.

There is no unanimity on the ideal approach about WB-MRI in lymphoma.

Unenhanced T1- and T2-weighted, short tau inversion recovery, and diffusion-weighted imaging (DWI) sequences have all been proposed and used in prior studies [32, 33].

The functional assessment is based on DWI, which involves the study of random Brownian motion of water molecules in biological tissues, as measured by the apparent diffusion coefficient (ADC) [34].

Lymphoma is characterized by increased cellularity and an elevated nuclear-to-cytoplasm ratio, resulting in restricted water molecule transport compared to normal tissues, high signal intensity on DWI, and low ADC values [35].

In addition to standard dimension criteria, different WB-MRI criteria have been established for the evaluation of lymph node involvement [36] such as DWI signal greater than that of the spinal cord or muscles, high signal intensity at higher *b* values with restriction confirmed by low ADC or in the presence of central necrosis, regardless of dimension; coalesces into a large nodal mass [37].

Despite this, there are no clear established ADC values to distinguish normal lymph nodes from pathological ones; furthermore, no consensus has been reached about mean or minimum ADC values to use in clinical practice.

WB-MRI has also been suggested by some authors as the best imaging tool for monitoring indolent lymphomas (i-NHLs) and aggressive lymphomas in complete remission [38].

Due to artifacts on DWI caused by heart pulse and respiration, WB-MRI has demonstrated some issues in evaluating tiny mediastinal and pulmonary hilar lymph nodes, with ADC values being miscalculated [39]. Furthermore, due to the anisotropic physiologically constrained pattern of diffusion of normal splenic parenchyma on DWI, characterization of focal splenic lesions by WB-MRI can be difficult, so DWI must be combined with standard morphologic WB-MRI images for the evaluation of the spleen [40].

In lymphoma, gadolinium-based contrast agents may increase the accuracy in identifying parenchymal lesions during WB-MRI; it appears to be especially useful in case of high probability of extranodal localization [40, 41].

The time required for a WB-MRI depends on the MRI unit and imaging technique and might take from 30 minutes to more than an hour.

The entire procedure takes less time than 18F-FDG PET/CT [42, 43].

WB-MRI, 18F-FDG PET/CT, and CT all have a high level of patient acceptance when it comes to patient compliance. Claustrophobia, caused by the anxiety of being in the enclosed area of a MRI machine for an extended period of time, is a serious issue for patients undergoing WB-MRI [44].

WB-MRI can be used in HL patients as a complementary imaging modality to replace contrast-enhanced CT in diagnostic work-up and lymphoma surveillance, but it is unlikely to replace 18F-FDG PET/CT for HL staging and response assessment at this time.

T2 signal intensity and contrast enhancement of lymphomatous lesions tend to decrease following treatment, T2 signal reduction may be linked to fibrotic stroma and collagen; however, immature fibrotic tissue, necrosis, or edema might cause an increase in T2 signal, limiting its use in this setting [43].

WB-MRI has also been demonstrated to be useful in detecting certain recently documented sequelae, such as osteonecrosis, in HL patients receiving chemotherapy regimens that include large doses of corticosteroids.

In lymphoma, WB-MRI is an important diagnostic technique, appearing to be less histology-dependent than 18F-FDG PET/CT as a functional imaging test. It also does not necessitate radiation exposure.

According to the European Union directive, a radiation-free imaging method should always be preferred if it gives the same diagnostic results [32].

Figures 16.9 and 16.10 show two examples of lymphomas detected by MRI.

In conclusion, each diagnostic technique has several advantages and disadvantages.

18F-FDG PET/CT has a high reproducibility as CT, but it allows a functional and standardized evaluation with clear SUV cut-off.

CT benefits of short acquisition time and wide availability, but it allows only a morphologic evaluation; both 18F-FDG PET/CT and CT expose patients to ionizing radiations.

WB-MRI has longer acquisition time and lower availability compared to CT but is ionizing radiation free and with enormous potential expanding applications.

16.3.3 Multiple Myeloma

Multiple myeloma (MM) is a malignant hematological condition in which monoclonal plasma cells proliferate uncontrollably in the bone marrow.

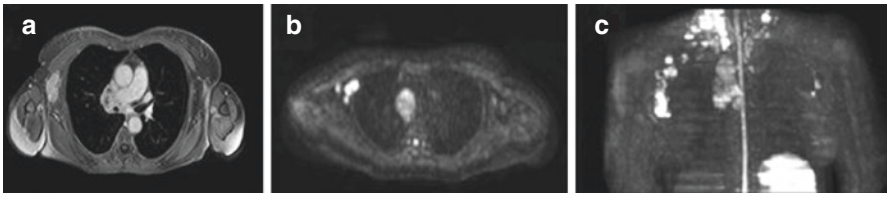

Fig. 16.9 Axial postcontrast 3D-GRE T1-weighted fat suppressed (**a**), axial DWI *b*-value 800 s/mm^2 (**b**) and coronal maximum intensity projection (MIP) diffusion-weighted imaging (DWI) (**c**): multiple lymph nodes increased in size with a tendency to confluence are shown, the largest in the superior mediastinum and right axillary region

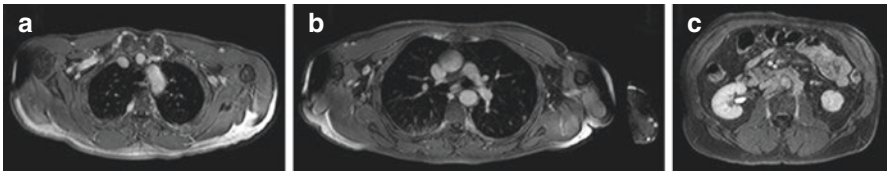

Fig. 16.10 (**a**–**c**) A 66-year-old man with non-Hodgkin's lymphoma. Axial postcontrast 3D-GRE T1-weighted fat-suppressed images: multiple lymph nodes increased in size are shown, in the right axillary site; in the sub-diaphragmatic site there are multiple confluent lymph nodes in the paracaval, interaortocaval, and left para-aortic site

16.3.3.1 Conventional Radiography

Conventional radiography allows the detection of bone anomalies, but current recommendations, such as those issued by the European Myeloma Network or the European Society for Medical Oncology, are increasingly recommending new technologies over traditional radiography [45, 46].

Around 30–50% of trabecular bone must be damaged by osteolysis to be detected in traditional skeletal X-ray. In many facilities, conventional radiography has been replaced with whole-body CT as the primary imaging modality.

16.3.3.2 CT

Unenhanced low-dose CT is commonly used to diagnose bone involvement in MM because of the strong intrinsic contrast of bony structures. The slightly higher radiation dosage is tolerable in view of the much higher sensitivity and improved patient comfort in the typically older patient population. CT has additional benefits, such as enhanced fracture risk assessment and the ability to visualize extraosseous myeloma, in addition to its excellent sensitivity [47].

Some osteolytic lesions in a patient with multiple myeloma are showed in Figs. 16.11 and 16.12.

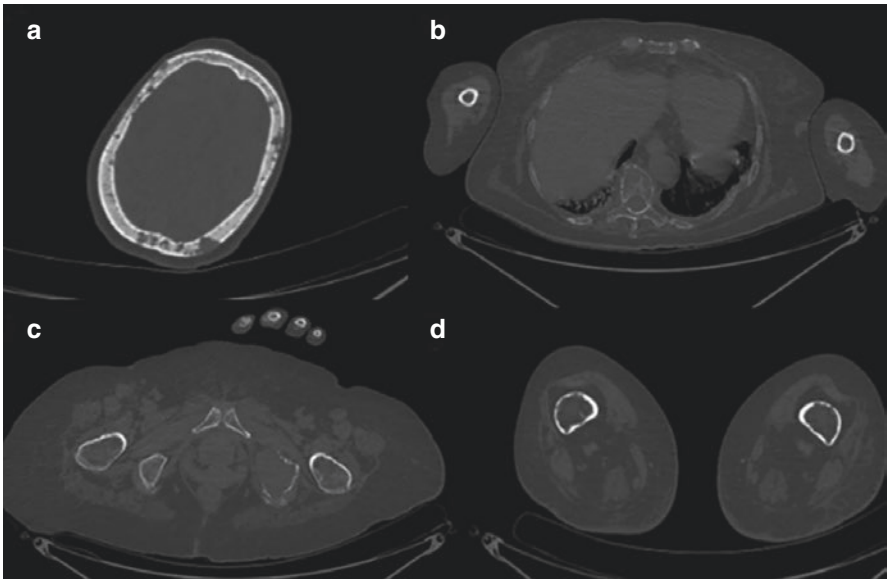

Fig. 16.11 (**a**–**d**) A 73-year-old woman with multiple myeloma. Low-dose CT scan images show multiple and widespread bone lesions of a lytic character, affecting almost all the skeletal segments, between a few millimeters in size and 5 cm, the lesion at the level of the left ischium determines swollen appearance of the bone with thinning and interruption of the cortical profile

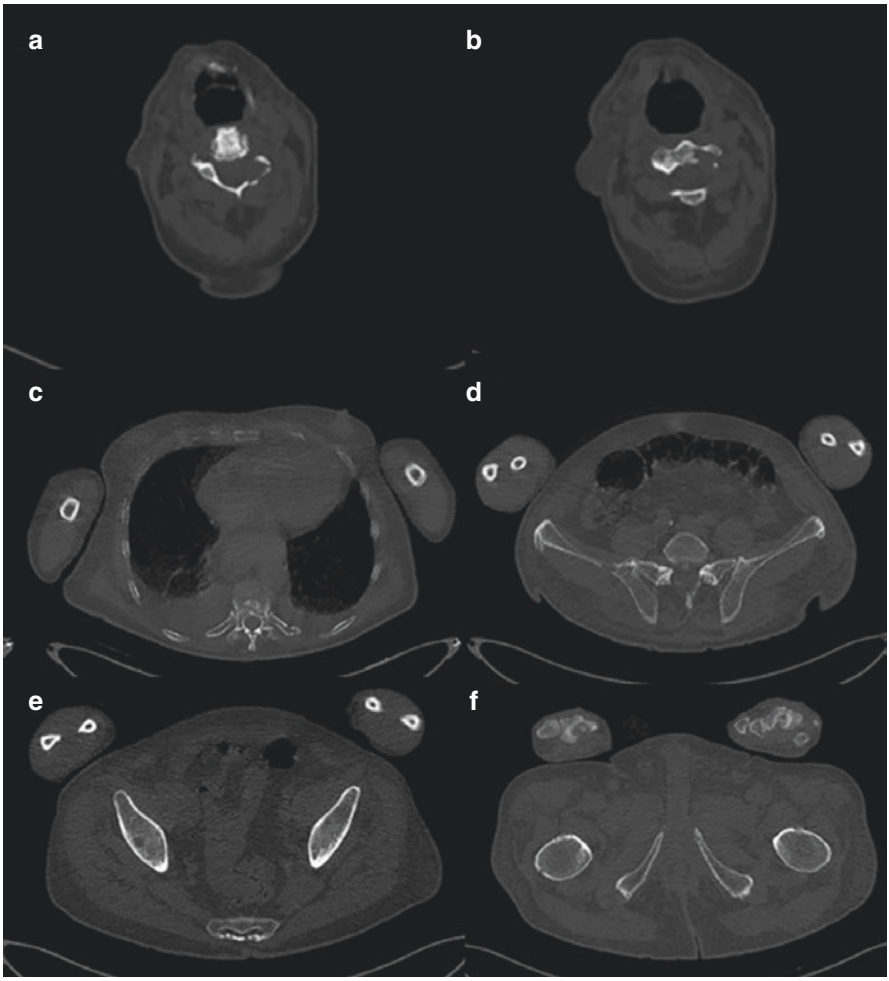

Fig. 16.12 (**a**–**f**) A 77-year-old man with multiple myeloma. CT imaging shows multiple osteolytic lesions and right pleural effusion

16.3.3.3 PET/CT

PET/CT imaging using 18F-fluorodeoxyglucose visualizes glucose hypermetabolism in medullary and extramedullary myeloma; it also allows the morphological detection of osteolysis as an additional functional component. Furthermore, PET/CT allows prognostic statements during the initial diagnosis and treatment [48].

16.3.3.4 MRI

Because nearly half of all patients have focal lesions outside of the axial skeleton, MRI is frequently conducted as a whole-body evaluation including the extremities [49].

Table 16.2 Characteristics of infiltration patterns in patients with myeloma

Patterns	Radiological features
Normal findings	No pathological features
Pattern of focal infiltration	T1w hypointense lesions with a diameter of at least 5 mm
Pattern of homogeneous diffuse infiltration	Bone marrow on unenhanced T1w image commonly more hypointense than adjacent intervertebral disc spaces without degenerative changes
Pattern of mixed infiltration	Focal + diffuse
"Salt and pepper" pattern	Disseminated T1w hypointense lesions

A routine evaluation normally includes coronal and sagittal T1w and T2w sequences, as well as fat-saturated T2w sequences.

On MRI, five different infiltration patterns in myeloma patients can be distinguished (Table 16.2), and the predictive value of MRI infiltration patterns has been demonstrated in several studies.

A normal pattern of the bone marrow, or a "salt and pepper" pattern, was correlated to an early stage of the disease and a better prognosis. Table 16.2 summarizes the radiological features of the various patterns [50].

16.4 Conclusions

The growing expectancy of life is one of the main contributors for the increasing number of older patients with hematologic malignancies.

The role of radiologist is to stage the disease, evaluating the level of frailty, but also to identify possible complications and to assess therapeutic response. Universally accepted and reproducible staging system is essential for the standardized response evaluation.

Magnetic resonance is becoming even more important in clinical practice, especially in lymphoid disorders.

References

1. Krok-Schoen JL, Fisher JL, Stephens JA, et al. Incidence and survival of hematological cancers among adults ages ≥75 years. Cancer Med. 2018;7(7):3425–33.
2. Wang H, Dwyer-Lindgren L, Lofgren KT, Rajaratnam JK, et al. Age-specific and sex-specific mortality in 187 countries, 1970-2010: a systematic analysis for the Global Burden of Disease Study 2010. Lancet. 2012;380(9859):2071–94.
3. Bron D, Ades L, Fulop T, et al. Aging and blood disorders: new perspectives, new challenges. Haematologica. 2015;100(4):415–7.
4. Vardiman JW. The World Health Organization (WHO) classification of tumors of the hematopoietic and lymphoid tissues: an overview with emphasis on the myeloid neoplasms. Chem Biol Interact. 2010;184(1–2):16–20.
5. Swerdlow SH, Campo E, Pileri SA, et al. The 2016 revision of the World Health Organization (WHO) classification of lymphoid neoplasms. Blood. 2016;127:2375.

6. Scheepers ERM, Vondeling AM, Thielen N, et al. Geriatric assessment in older patients with a hematologic malignancy: a systematic review. Haematologica. 2020;105(6):1484–93.
7. Johnson SA, Kumar A, Matasar MJ, et al. Imaging for staging and response assessment in lymphoma. Radiology. 2015;276(2):323–38.
8. Liput J, Smith DA, Beck R, et al. Myeloproliferative neoplasms: a primer for radiologists. J Comput Assist Tomogr. 2019;43:652–63.
9. Extermann M, Aapro M, Bernabei R, et al. Use of comprehensive geriatric assessment in older cancer patients: recommendations from the task force on CGA of the International Society of Geriatric Oncology (SIOG). Crit Rev Oncol Hematol. 2005;55(3):241–25.
10. Murphy IG, Mitchell EL, Raso-Barnett L, et al. Imaging features of myeloproliferative neoplasms. Clin Radiol. 2017;72:801–9.
11. Hanrahan CJ, Shah LM. MRI of spinal bone marrow: part 2, T1-weighted imaging-based differential diagnosis. AJR Am J Roentgenol. 2011;197:1309e21.
12. Orphanidou-Vlachou E, Tziakouri-Shiakalli C, Georgiades CS. Extramedullary hemopoiesis. Semin Ultrasound CT MR. 2014;35:255e62.
13. Potthoff A, Attia D, Pischke S, et al. Long-term outcome of liver transplant patients with Budde Chiari syndrome secondary to myeloproliferative neoplasms. Liver Int. 2015;35:2042e9.
14. Qi X, De Stefano V, Senzolo M, et al. Splanchnic vein thrombosis: etiology, diagnosis, and treatment. Gastroenterol Res Pract. 2015;2015:506136e2.
15. Hallek M. Chronic lymphocytic leukemia: 2017 update on diagnosis, risk stratification, and treatment. Am J Hematol. 2017;92(9):946–65.
16. Matasar MJ, Zelenetz AD. Overview of lymphoma diagnosis and management. Radiol Clin N Am. 2008;46(2):175–98, vii.
17. Costello P, Mauch P. Radiographic features of recurrent intrathoracic Hodgkin's disease following radiation therapy. AJR Am J Roentgenol. 1979;133:201–6.
18. Lee CKK, Bloomfield CD, Goldman AI, et al. Prognostic significance of mediastinal involvement in Hodgkin's disease treated with curative chemotherapy. Cancer. 1980;46:2403–9.
19. Anderson H, Jenkins JPR, Brigg DJ, et al. The prognostic significance of mediastinal bulk in patients with stage IA-IVB Hodgkin's disease: a report from the Manchester Lymphoma Group. Clin Radiol. 1985;36:449–54.
20. Lister TA, Crowther D, Sutcliffe SB, et al. Report of a committee convened to discuss the evaluation and staging of patients with Hodgkin's disease: Cotswolds meeting. J Clin Oncol. 1989;7:1630–6.
21. Thar TL, Millon RR, Hausner RJ, et al. Hodgkin's disease, stages I and II: relationship of recurrence to size of disease, radiation dose, and the number of sites involved. Cancer. 1979;43:1101–5.
22. Castellino RA, Hilton S, O'Brien JP, et al. Non Hodgkin's lymphoma: contribution of chest CT in the initial staging evaluation. Radiology. 1996;199:129–32.
23. Hare SS, Souza CA, Bain G, et al. The radiological spectrum of pulmonary lymphoproliferative disease. Br J Radiol. 2012;85(1015):848–64.
24. Fishman EK, Kuhlman JE, Jones RJ. CT of lymphoma: spectrum of disease. RadioGraphics. 1991;11(4):647–69.
25. Anis M, Irshad A. Imaging of abdominal lymphoma. Radiol Clin N Am. 2008;46(2):265–85, viii–ix.
26. Saboo SS, Krajewski KM, O'Regan KN, et al. Spleen in haematological malignancies: spectrum of imaging findings. Br J Radiol. 2012;85(1009):81–92.
27. Chua SC, Rozalli FI, O'Connor SR. Imaging features of primary extranodal lymphomas. Clin Radiol. 2009;64(6):574–88.
28. Cheson BD, Pfistner B, Juweid ME, et al. Revised response criteria for malignant lymphoma. J Clin Oncol. 2007;25:579–86.
29. Cheson BD, Fisher RI, Barrington SF, et al. Recommendations for initial evaluation, staging, and response assessment of Hodgkin and non-Hodgkin lymphoma: the Lugano classification. J Clin Oncol. 2014;32(27):3059–68.

30. Sattarivand M, Caldwell C, Poon I, et al. Effects of ROI placement on PET based assessment of tumor response to therapy. Int J Mol Imag. 2013;2013:132804.
31. Rossi C, Kanoun S, Berriolo-Riedinger A, et al. Interim 18F-FDG PET SUVmax reduction is superior to visual analysis in predicting outcome early in Hodgkin lymphoma patients. J Nucl Med. 2014;55(4):569–73.
32. Albano D, Bruno A, Patti C, et al. Whole body magnetic resonance imaging (WB-MRI) in lymphoma: state of the art. Hematol Oncol. 2020;38:12–21.
33. Galia M, Albano D, Narese D, et al. Whole-body MRI in patients with lymphoma: collateral findings. Radiol Med. 2016;121(10):793–800.
34. Chianca V, Albano D, Messina C, et al. Diffusion tensor imaging in the musculoskeletal and peripheral nerve systems: from experimental to clinical applications. Eur Radiol Exp. 2017;1(1):12.
35. Kwee TC, Basu S, Torigian DA, Nievelstein RA, Alavi A. Evolving importance of diffusion-weighted magnetic resonance imaging in lymphoma. PET Clin. 2012;7(1):73–82.
36. Stecco A, Buemi F, Iannessi A, et al. Current concepts in tumor imaging with whole-body MRI with diffusion imaging (WB-MRI-DWI) in multiple myeloma and lymphoma. Leuk Lymphoma. 2018;12(11):1–11.
37. Albano D, Patti C, Lagalla R, et al. Whole-body MRI, FDG-PET/CT, and bone marrow biopsy, for the assessment of bone marrow involvement in patients with newly diagnosed lymphoma. J Magn Reson Imaging. 2017;45(4):1082–9.
38. Mayerhoefer ME, Karanikas G, Kletter K, et al. Evaluation of diffusion-weighted MRI for pretherapeutic assessment and staging of lymphoma: results of a prospective study in 140 patients. Clin Cancer Res. 2014;20(11):2984–93.
39. Chavhan GB, Babyn PS. Whole-body MR imaging in children: principles, technique, current applications, and future directions. Radiographics. 2011;31(6):1757–72.
40. Plathow C, Walz M, Lichy MP, et al. Cost considerations for whole body MRI and PET/CT as part of oncologic staging. Radiologe. 2008;48(4):384–96.
41. Albano D, Agnello F, Patti C, et al. Whole-body magnetic resonance imaging and FDG-PET/CT for lymphoma staging: assessment of patient experience. Egypt J Radiol Nucl Med. 2017;48(4):1043–7.
42. Adams HJ, Kwee TC, Vermoolen MA, Ludwig I, Bierings MB, Nievelestein RA. Whole-body MRI vs. CT for staging lymphoma: patient experience. Eur J Radiol. 2014;83(1):163–6.
43. Galia M, Albano D, Tarella C, et al. Whole body magnetic resonance in indolent lymphomas under watchful waiting: the time is now. Eur Radiol. 2018;28(3):1187–93.
44. Rahmouni A, Divine M, Kriaa S, Haioun C, Anglade MC, Kobelter H. Lymphoma: imaging in the evaluation of residual masses. Cancer Imaging. 2002;2(2):93–5.
45. Moreau P, San Miguel J, Sonneveld P, et al. Multiple myeloma: ESMO clinical practice guidelines for diagnosis, treatment and follow-up. Ann Oncol. 2017;28:iv52–61.
46. Terpos E, Kleber M, Engelhardt M, et al. European myeloma network guidelines for the management of multiple myeloma-related complications. Haematologica. 2015;100:1254–66.
47. Gleeson TG, Moriarty J, Shortt CP, et al. Accuracy of whole-body low dose multidetector CT (WBLDCT) versus skeletal survey in the detection of myelomatous lesions, and correlation of disease distribution with whole-body MRI (WB-MRI). Skelet Radiol. 2009;38:225–36.
48. Dimopoulos MA, Hillengass J, Usmani S, et al. Role of magnetic resonance imaging in the management of patients with multiple myeloma: a consensus statement. J Clin Oncol. 2015;33:657–64.
49. Kosmala A, Bley T, Petritsch B, et al. Bildgebende diagnostik des multiplen myeloms. Fortschr Röntgenstr. 2019;191:805–16.
50. Spinnato P, Bazzocchi A, Brioli A, et al. Contrast enhanced MRI and 18F FDG PET-CT in the assessment of multiple myeloma: a comparison of results in different phases of the disease. Eur J Radiol. 2012;81:4013–8.

The Role of Artificial Intelligence (AI) in the Management of Geriatric Patients

17

Salvatore Claudio Fanni, Sherif Mohsen Shalaby, and Emanuele Neri

17.1 Introduction

As of January 2020, the European Union population was estimated at about 447.3 million people; of which there is about 20.6% of population aged 65 years or above. This is according to Eurostat which also declared an expanding population of the older people in Europe; with an increase of 3% as compared to 10 years ago [1].

In fact, it is expected that by the year 2100, there will be about 31.3% of people older than 65 years [2], making old people the typical patients accessing healthcare services within the few upcoming years [3].

The geriatric patients' care is considered very complex due to the coexistence of multiple morbidities, which are often associated with functional impairment and even social withdrawal.

Since age is a well-known nonmodifiable risk factor for numerous morbidities, an increase of their prevalence and incidence is expected, placing healthcare systems under stress. For instance, Alzheimer disease (AD) is the most common neurodegenerative disease of people aged over 65 years, with an estimated prevalence worldwide of 50 million, which should be increased by 2050 to 131.5 million [4]. Additionally, there will be an increase of the incidence of other diseases, such as oncologic, musculoskeletal, or cardiovascular disease with devastating consequences to our society in terms of costs of care, number of family caregivers, hours of care provided, and the impact on caregivers. Also, as age is a common risk factor between these diseases, usually they coexist in the same patient.

The complexity of multimorbidity is closely linked to the combination and synergy of different and numerous clinical, behavioral, environmental and lifestyle variables on onset, progression, and severity of those morbidities [5].

S. C. Fanni · S. M. Shalaby · E. Neri (✉)
Department of Translational Research, Academic Radiology, University of Pisa, Pisa, Italy
e-mail: emanuele.neri@med.unipi.it

G. Guglielmi, M. Maas (eds.), *Imaging in Geriatrics*, Practical Issues in Geriatrics, https://doi.org/10.1007/978-3-031-14877-4_17

The process of clinical decision-making for patients with chronic comorbidities is more challenging due to the multiple coexisting diseases guidelines [6], which additionally are primarily based on clinical trials from which are often excluded people with multiple coexisting morbidities and older age [5].

The rapid demographic growth and complexity of geriatric patients' account for a though challenge, for which the advent of the new technologies may provide important solutions.

Gerontechnology is a term first appeared in the 1990s based on two terms: "gerontology," which is the scientific study of geriatric population and "technology." Gerontechnology is concerned with the research on the application of technology progress to the biological, psychological, social, and medical aspects of the aged people [7]. To name a few of these technologies, telemedicine, wearable devices, robotics, and assistive technologies were already implemented in order to meet the needs of older people and are widely described in the literature [8].

In this chapter, we will discuss the diverse applications and tools of artificial intelligence (AI) in the management of geriatric patients. AI is an area of study of computer science, concerning with the development of computer algorithms able to perform human-like tasks such as learning, self-correction, and even reasoning [9].

Despite it may sound far-fetched, AI is already a part of our daily life, for example, in smartphone speech recognition, spam-filtering, and search engines [10].

A subfield of AI is machine learning (ML), which explores the study of statistical algorithms that can learn from the available data and subsequentially make a prediction [11]. A key feature of ML algorithm is the capability to autonomously adapt to the data and improve its performance in predicting predetermined outcome [12].

Part of the broader ML field is deep learning (DL), defined as the study of artificial neural networks (ANN), implementing a cascade of many layers for feature extraction and transformation to perform tasks such as classification or pattern analysis [13]. ANN own their name to their structure, which resemble the neural cortex: with separate layers (the neurons) connected to each other (synapses). The ANN most frequently described is the convolutional neural network (CNN) which is mostly implemented in image analysis.

While traditional ML algorithms require a hand-crafted feature identification performed by experts, a key component of DL is the capability to autonomously identify correlated features from data during the training phase of the network.

AI could be a brilliant solution to fill the gap of human resources in geriatric clinical care, improving patients' outcomes and quality of life, reducing the cost and the burden of family caregivers [14].

In fact, due to the complexity mentioned above, a multidimensional approach is mandatory in geriatric clinical care, and AI may help to analyze the so far unexploited and heterogeneous amounts of data at our disposal [15]. This mixed data includes clinical data from electronic health records, radiological imaging, radiomics data, genomics data, technical data from wearable devices, and many others.

Radiomics is defined as the processing of medical images into mineable data, by extraction of thousands of hand-crafted or ML-based quantitative features from

images and correlation with outcomes or disease phenotype. Usually, radiomics methods are implemented in oncologic imaging field [16], but it is expected to spread in other fields, such as cardiovascular or neuroradiology.

To date, medicine is rapidly moving toward personalized medicine, which becomes extremely difficult and frequently impracticable in geriatric patients due to the complexity of multimorbidity and their numerical increment. AI models have the potential to change this setting and consequently the future of medicine, contributing to individual-based care.

17.2 Application of Artificial Intelligence in Geriatric Patients

In this chapter we will explore some of the applications of AI in geriatric population following a somatic cranio-caudal approach. We aim to describe how can an accurate and reliable AI solutions provide an effective role for the management of geriatric patients. Additionally, we will inspect those AI algorithms effectiveness as compared to the traditional imaging workflow, which relies on the human healthcare providers.

17.2.1 Neurological Disorders

Neurological disorders, whose burden on healthcare services is expected to increase due to the population growth and aging, are represented mostly by neurodegenerative disorders and stroke; in particular acute ischemic stroke.

The most common neurodegenerative disorders ar Alzheimer's disease (AD) and Parkinson disease (PD). Considering only AD, the affected patients account for 2% of the population over 65 years, increasing to 30% over 85 years [17].

To manage the upcoming increasing number of cases due to the aging of the population and the subsequently unmanageable workload, new instruments need to be evaluated and to be implemented in the clinical practice. With this aim, radiomics features extracted from magnetic resonance imaging (MRI) of the brain combined in ML models have been proposed as valuable instruments to improve early diagnosis, resulting in an early treatment, and prognosis of AD and PD [18].

In AD, the diagnosis of mild cognitive impairment (MCI) and the detection of MCI who will convert to AD are still challenging. The first brain region to be investigated was the hippocampus. Sørensen et al. in 2016 have introduced the use of hippocampal texture, in addition to the traditional hippocampal volume, to provide diagnostic information for association to early cognitive loss beyond that of volumetric changes [19]. From texture analysis to a more comprehensive radiomics approach, the step is short: in 2018 Luk et al. extracted 215 features from hippocampus on MRI T1-W images. A support vector machine (SVM), one of the most described ML algorithm, was implemented to differentiate MCI from healthy controls, achieving an accuracy ranging from 80% to 93.3% [20]. In the same year,

Feng et al. changed the target for radiomics features extraction to the corpus callosum, as it is a major site of disease in the late stage of AD. A logistic regression model was implemented to analyze 385 texture features, with a modest accuracy of 70% in the detection of AD versus controls [21].

As AD is a neurodegenerative disorder with a widespread involvement of the entire brain, the next natural step was the application of radiomics features extraction to a series of brain's region. Nanni et al. achieved an AUC of 94% in differentiating AD versus controls and an interesting 70% in detecting the patients with MCI who faster convert to AD, combining texture and volume features of AD brain [22].

PD is the second most common neurodegenerative disorder and, as AD, an increasing social and economic burden is expected on our society. Shinde et al. in 2019 implemented a CNN to detect PD subject analyzing neuromelanin-sensitive MR images. The CNN showed an interesting performance, locating the most important site involved in the disease, differentiating PD from healthy subject with an accuracy of 80% and even from other parkinsonian syndrome with accuracy of 85.7%. The CNN has outperformed the radiomics classifier with an accuracy of about 60.3% [23].

As for the neurodegenerative disorders, even stroke-related burden on healthcare services is going to increase due to aging of population, with an upcoming and worrying rise in terms of mortality, disability, and economics costs [24].

Neuroimaging, using CT and MRI, plays a pivotal role even in stroke management, as they are crucial to select subject for the most appropriate therapy. Radiomics and machine learning algorithm are expected to manage the incoming increased workload and to improve early diagnosis, prediction of early outcomes, and evaluation of long-term prognosis [25]. As ischemic stroke accounts for approximately 85% of all stroke cases [26], we will focus on applications of AI in management of this entity. Nonenhanced computed tomography (NECT) is the first imaging choice in patients with episode of neurologic deficit. As far as early diagnosis is vital to rapidly treat the patients with the thrombolytic agents, it still remains extremely challenging because the changes in ischemic area often are not easily detectable. Texture analysis has been implemented in order to differentiate healthy tissue from ischemic lesion. With this purpose, Peter et al. built a machine learning model with six texture features extracted from NECT, achieving an AUC of 0.82 [27].

Texture features were also evaluated as a predictor for secondary intracranial hemorrhage in patients with acute ischemic stroke. In a study of Kassner et al. texture parameters extracted from MR T1-weighted images achieved an AUC > 0.75, resulting in a great predictive ability for early outcomes and outperforming visual enhancement score (AUC < 0.6) [28]. Furthermore, radiomics features were analyzed to evaluate the long-term prognosis. Betrouni et al. demonstrated a correlation between the 6-month cognitive impairment and radiomics features extracted at 72 h after stroke from MR images of hippocampus and entorhinal cortex. The support vector machine algorithm achieved an interesting AUC of 0.9 [29].

17.2.2 Lung and Cardiovascular Diseases

In this section, we will be addressing lung and cardiovascular diseases which can benefit from the potential role of AI in the imaging management of these disease.

Chest CT is a medical imaging technique widely performed in elder people, mostly to diagnose, stage, or assess therapy response of lung cancer, to evaluate other pulmonary disease such as chronic obstructive pulmonary disease (COPD) or cardiovascular disease. Building upon this assumption, and in order to take advantage of the large amounts of hidden data not fully exploited in these chest CTs, Carneiro et al. developed a radiomics and a deep-learning approach to predict the 5-year all-cause mortality. The following structures were segmented to extract radiomic features from CT images: lungs, heart, epicardial fat, aorta, spinal column, body fat, and muscles. The deep learning approach, based on two different types of CNNs, achieved a mean classification AUC of 69%, outperforming the radiomics approach, which still presented a good performance (64.6%). Furthermore, the prediction accuracy was similar to currently used clinical risk scores despite the small cohort of patients enrolled and the exclusion from the models of strongly predictive variable as gender or age [30].

Among all the lung disease, COPD has received a great deal of interest, as it is one of the most important cause of death in elder people, and in the next two decades, it is expected to become the leading cause [31]. Furthermore, COPD is a known major risk factor for lung cancer, as they share similar physiopathology and etiology, such as smoking cigarettes [32]. COPD has a heterogeneous CT pattern resulting from the variable combinations of centrilobular emphysema and airway disease [33]. This complexity and the ongoing increase of incidence make it necessary to investigate new tools, in order to improve patient's outcome through an early diagnosis. The first step was represented by quantitative CT (QCT), which is defined as the study of computer-aided methods able to quantify handcrafted features on CT, as the amount of emphysema or airway abnormalities [34]. Though effective, these methods are often time-consuming, consider only a few handcrafted features, and are prone to variability [35]; therefore, more dedicated effort need to be done to explore new hands-on and less time-consuming methods, such as radiomics and machine learning algorithm. Ginsburg et al. in 2012 extracted texture features to train a multiple logistic regression classifier able to differentiate effectively between smokers even without emphysema and never-smokers' lungs [36]. Lafata et al. extracted 39 radiomics features to quantify lung function from CT images. The radiomics signature was then compared to spirometry test as a reference standard, demonstrating an interesting correlation in particular with FEV1 [37].

Another medical imaging technique progressively more used over the years is cardiac computed tomography angiography (CCTA), which is extensively performed to rule out coronary artery disease (CAD) [38]. AI may have a potential role in reducing the time of image analysis, lightening the workload of radiologists, ranging from diagnostic to prognostic tasks [39]. For instance, Muscogiuri et al.

investigated the potential role of a CNN for the classification of CAD-RADS, which is a standardized method to describe coronary artery disease ranging from 0 (absence of stenosis) to 5 (at least one totally occluded coronary artery) [40]. The algorithm effectively distinguishes CAD-RADS ≥1 from 0 with an average time of analysis much shorter compared to radiologists, which is an important result assuming an increase of CCTA in the next few years [41]. Another important quantitative parameter and predictor for adverse cardiovascular events is the coronary artery calcium score (CACS) [42]. Wolterink et al. described the implementation of a CNN to evaluate the CACS on CCTA, achieving an interclass correlation of 0.94 compared to the reference standard [43].

Additionally, CCTA could be source of parameters to build prognostication model. Motwani et al. in 2016 developed an ML model for prognostic stratification in patients followed up for 5 years combining 44 parameters extracted from CCTA and 25 clinical parameters. The severity score computed by the model achieved an AUC of 0.79, outperforming traditional prognostic score such as the Framingham (0.61) and Duke Index (0.62) [44].

17.2.3 Abdomen

Colorectal cancer (CRC) is the third most frequently diagnosed malignancy in both genders [45]. In spite of the availability of screening programs today, about 60–70% of CRC are still diagnosed at advanced stages [46].

Therefore, AI could be implemented to improve the diagnostic performance of routinary screening, such as colonoscopy or computed tomographic colonography (CTC) [47]. One of the challenges of CTC is the detection of flat colorectal adenoma. In 2008 Taylor et al. developed a computer-aided detection system to seek the flat early-stage CRC on supine and prone CTC images. The algorithm achieved a sensitivity of 83.3% and 54.1%, respectively, with 0 and 1 sphericity values [48]. Apart from the detection, AI could improve colorectal lesion classification into neoplastic and non-neoplastic findings. Song et al. in 2014 demonstrated a significant improvement in classification of colorectal lesion by adding to image intensity a texture features analysis, with the AUC rising up from 0.74 to 0.85 [49].

Recently, Grosu et al. implemented an ML method to distinguish more specifically benign and precancerous lesions detected on CTC of asymptomatic patients, with an extremely interesting AUC of 0.91 [50].

Another abdominal oncologic condition whose incidence is expected to increase in the next few years is the hepatocellular carcinoma (HCC). Contrary to CRC, HCC develops from a specific pathologic substrate, the cirrhotic liver, thus leading to screening not of the entire population but only in selected patients. Ultrasound (US) is the main imaging tool to detect new lesion in cirrhotic patients.

To determine the presence of cirrhosis, Liu et al. developed an algorithm based on the analysis of liver capsule. Using the analysis of liver capsule contour, they were able to determine the presence or absence of cirrhosis, with an area under the curve of 0.97 [51]. Once cirrhosis is identified, the challenge is to distinguish benign from malignant lesions. Bharti et al. proposed an ANN model to differentiate four

stages of liver disease using data obtained from US images: normal liver, chronic liver disease, cirrhosis, and HCC. The classification accuracy of the model was 96.6% [52]. Further, images of contrast-enhanced US were used to develop more accurate models. Streba et al. implemented an ANN model to classify HCC, liver metastases, hemangioma, and focal fatty changes with a 94.5% accuracy [53]. When a follow-up ultrasound demonstrates a new lesion suspicious for HCC, other imaging studies like CT or MRI are required to achieve a characterization. AI could play a role in the hepatic nodule with an indeterminate behavior which could help to avoid invasive biopsy. For this purpose, Mokrane et al. retrospectively collect 178 patients with indeterminate nodules subjected to biopsy and developed a DL algorithm to classify nodules as HCC or non-HCC lesion, with an optimistic AUC of 0.70.

17.2.4 Prostate

Prostate carcinoma represents the most common cancer in men worldwide and, despite its low aggressivity, is the third cause of death cancer-related [54]. Overdiagnosis is usually a common issue in the diagnostic process of prostatic adenocarcinoma, which leads to an increased burden on the healthcare system. Accurate prostate segmentation as well as its volume estimation is considered to provide invaluable information for the process of diagnosis and clinical management of benign prostatic hyperplasia (BPH) versus the prostatic carcinoma. Therefore, that can improve BPH treatment, surgical planning, and predictions of PCa prognosis [55]. There are multiple use case domains of using AI or ML in prostate cancer as the detection of prostate cancer with high accuracy both in peripheral and transitional zone, characterization of cancer according to its biological aggressiveness into clinically significant and nonsignificant disease, identification of patients with metastatic prostate cancer as early as possible, establishing the radiologic–histopathologic correlation to provide biology-based validation of AI models, prediction of the risk of disease recurrence and prediction of treatment response in case of radiation therapy or post-prostatectomy as well as the possibility of using AI-powered patient stratification tools for enrollment in Active Surveillance programs.

Accuracy of prostate lesion detection, segmentation, and volume estimation is important at different stages of PCa management. Lesion detection identifies regions for biopsy. Accurate segmentation is crucial for improved fusion biopsy yields as well as improving radiotherapy delivery. Volume estimation can predict prognosis after prostatectomy [56].

The current challenge is the differentiation between aggressive and nonaggressive disease to selectively treat only aggressive type and avoid overdiagnosis and overtreatment. As prostate cancer is a typical elderly disease, its prevalence and incidence are expected to dramatically increase exacerbating the challenge already mentioned. Artificial intelligence could be a solution to achieve the full potential of multiparametric prostate MRI (mpMRI) as a screening, diagnostic, and prognostic tool.

In 2017, Karimi et al. implemented an ML algorithm to differentiate between the benign and malignant lesions. The performance was significantly improved by the combination of the ML algorithm already implemented with a CNN, achieving an AUC of 0.87 [57]. Once a prostate lesion is identified, a correct risk-stratification is vital to guide the decision-making for the possible therapeutic options. With this goal, Zhang et al. in 2019 developed a DL model to predict a Gleason score ≥7 from mpMRI in patients treated with robotic prostatectomy. Adopting lesion ROI definition by adding random cropping into the data augmentation, they were able to further improve the robustness of the model with less potential ROI inconsistency. The algorithm performance was compared to the radiologists one using PI-RADS, with at least a similar result (AUC 0.73 vs. 0.71) [58].

In 2020 Li et al. adopted another approach by extracting radiomics features from biparametric prostate MRI to build a model for predicting the clinically significant prostate cancer. The radiomics features extracted and selected were incorporated into the RAD-SCORE, as the sum of the weighted features. The RAD-SCORE achieved an AUC of 0.98 in the test set, a similar result was obtained when the RAD-SCORE was combined with clinical parameters such as age, prostate volume, or serum PSA [59].

Artificial intelligence algorithm has been applied for automatic and accurate prostate segmentation, which is the first step to compute prostate volume or to extract radiomics features.

In 2017 Rundo et al. used an ML technique to segment prostate on T1-weighted and T2-weighted images from mpMRI. The performance was evaluated with the Sørensen–Dice coefficient, which is a measure of the spatial intersection between the automated segmentation and the ground-truth label. In this paper a great Dice coefficient of 0.91 was achieved [60].

17.2.5 Musculoskeletal

Musculoskeletal radiology is yet another field which could benefit of AI integration in clinical practice since fractures are one of the most common cause of hospitalization, morbidity, and mortality in the elderly. Among many types of fractures, one of the most common is the hip fracture, with a lifetime risk of 27.5 in the women [61]. One issue is the 3–10% rate of occult hip fractures, requiring further investigation as CT or MRI, with a subsequently increased cost and delayed diagnosis [62]. Hence, Mawatari et al. developed a CNN to detect the hip fractures on hip radiographs. Authors compared the CNN performance to seven radiologist readers with different clinical experiences. The CNN achieved an AUC of 88%, while the radiologist's performance ranged from 0.698 to 0.92. Therefore, the most experienced radiologist outperformed the CNN. However, the authors demonstrated an increased performance of all the reader when consulting the CNN outputs, even for the most experienced one, whose AUC increased to 0.934. Therefore, AI/ML can be a useful asset in the radiologist's daily toolbox [63].

A further type of fracture common in the elderly are the vertebral fractures [64]. When a vertebral fracture is diagnosed, it is challenging to differentiate the benign from malignant causes, requiring a different pathway of management.

Li et al. trained a CNN with CT images from 433 patients with benign or malignant fracture. The CNN achieved a good result, with an accuracy of 85% [65].

17.3 Conclusion

It is expected that in the upcoming years the old people will increasingly represent the typical patients accessing healthcare services. Therefore, there is an emerging need for handling that increased workload on the healthcare systems. With the advent of many AI algorithms, the potential of AI applications in geriatric patient management shows a promising spectrum of clinically beneficial uses. The applications can be employed in diverse practical domains as patients' screening, imaging acquisition, pre-reporting, and the further diagnostic process.

References

1. Corselli-Nordblad L, Strandell H, European Commission, Statistical Office of the European Union. Ageing Europe: looking at the lives of older people in the EU. Brussels: European Commission; 2020.
2. EUROSTAT. Population structure and ageing. Luxembourg: EUROSTAT; 2020.
3. Bień B, et al. Disabled older people's use of health and social care services and their unmet care needs in six European countries. Eur J Pub Health. 2013;23(6):1032–8. https://doi.org/10.1093/eurpub/cks190.
4. Martin Prince A, et al. World Alzheimer report 2015. The global impact of dementia an analysis of prevalence, incidence, cost and trends. London: ADI; 2015. www.alz.co.uk/worldreport2015corrections.
5. Cesario A, et al. The role of artificial intelligence in managing multimorbidity and cancer. J Personal Med. 2021;11(4):314. https://doi.org/10.3390/jpm11040314.
6. Tinetti ME, Fried TR, Boyd CM. Designing health care for the most common chronic condition - multimorbidity. JAMA. 2012;307(23):2493–4. https://doi.org/10.1001/jama.2012.5265.
7. Micera S, Bonato P, Tamura T. Gerontechnology. IEEE Eng Med Biol Mag. 2008;27(4):10–4. https://doi.org/10.1109/MEMB.2008.925213.
8. Nevedal AL, Ayalon L, Briller SH, Heyn PC. A qualitative evidence synthesis review of longitudinal qualitative research in gerontology. Gerontologist. 2019;59(6):E791–801. https://doi.org/10.1093/geront/gny134.
9. Kok J, Boers EJW, Kosters WA, van der Putten P, Poel M. Artificial intelligence: definition, trends, techniques and cases. Paris: EOLSS Publishers/UNESCO; 2009.
10. Goldenberg SL, Nir G, Salcudean SE. A new era: artificial intelligence and machine learning in prostate cancer. Nat Rev Urol. 2019;16(7):391–403. https://doi.org/10.1038/s41585-019-0193-3.
11. Kohavi R, Provost F. Glossary of terms. Mach Learn. 1998;2:271–4. https://doi.org/10.1023/A:1017181826899.
12. Brodie A, Dai N, Teoh JYC, Decaestecker K, Dasgupta P, Vasdev N. Artificial intelligence in urological oncology: an update and future applications. Urol Oncol Semin Orig Investig. 2021;39(7):379–99. https://doi.org/10.1016/j.urolonc.2021.03.012.

13. Deng L, Yu D. Deep learning: methods and applications. Found Trends Signal Process. 2013;7(3–4):197–387. https://doi.org/10.1561/2000000039.
14. Javadi-Pashaki N, Ghazanfari MJ, Karkhah S. Machine learning for geriatric clinical care: opportunities and challenges. Ann Geriatric Med Res. 2021;25(2):137–8. https://doi.org/10.4235/agmr.21.0054.
15. Ho A. Are we ready for artificial intelligence health monitoring in elder care? BMC Geriatr. 2020;20(1):358. https://doi.org/10.1186/s12877-020-01764-9.
16. Aerts HJWL, et al. Decoding tumour phenotype by noninvasive imaging using a quantitative radiomics approach. Nat Commun. 2014;5:4006. https://doi.org/10.1038/ncomms5006.
17. Wimo A, Ljunggren G, Winblad B. Costs of dementia and dementia care: a review. Int J Geriatr Psychiatry. 1997;12:841.
18. Salvatore C, Castiglioni I, Cerasa A. Radiomics approach in the neurodegenerative brain. Aging Clin Exp Res. 2021;33(6):1709–11. https://doi.org/10.1007/s40520-019-01299-z.
19. Sørensen L, et al. Early detection of Alzheimer's disease using MRI hippocampal texture. Hum Brain Mapp. 2016;37(3):1148–61. https://doi.org/10.1002/hbm.23091.
20. Luk CC, et al. Alzheimer's disease: 3-dimensional MRI texture for prediction of conversion from mild cognitive impairment. Alzheimer's Dement Diagn Assess Dis Monit. 2018;10:755–63. https://doi.org/10.1016/j.dadm.2018.09.002.
21. Feng Q, et al. Hippocampus radiomic biomarkers for the diagnosis of amnestic mild cognitive impairment: a machine learning method. Front Aging Neurosci. 2019;11:323. https://doi.org/10.3389/fnagi.2019.00323.
22. Nanni L, Brahnam S, Salvatore C, Castiglioni I. Texture descriptors and voxels for the early diagnosis of Alzheimer's disease. Artif Intell Med. 2019;97:19–26. https://doi.org/10.1016/j.artmed.2019.05.003.
23. Shinde S, et al. Predictive markers for Parkinson's disease using deep neural nets on neuromelanin sensitive MRI. NeuroImage Clin. 2019;22:101748. https://doi.org/10.1016/j.nicl.2019.101748.
24. Johnson CO, et al. Global, regional, and national burden of stroke, 1990–2016: a systematic analysis for the Global Burden of Disease Study 2016. Lancet Neurol. 2019;18(5):439–58. https://doi.org/10.1016/S1474-4422(19)30034-1.
25. Chen Q, Xia T, Zhang M, Xia N, Liu J, Yang Y. Radiomics in stroke neuroimaging: techniques, applications, and challenges. Aging Dis. 2021;12(1):143–54. https://doi.org/10.14336/AD.2020.0421.
26. Musuka TD, Wilton SB, Traboulsi M, Hill MD. Diagnosis and management of acute ischemic stroke: speed is critical. CMAJ. 2015;187(12):887–93. https://doi.org/10.1503/cmaj.140355.
27. Peter R, et al. A quantitative symmetry-based analysis of hyperacute ischemic stroke lesions in noncontrast computed tomography. Med Phys. 2017;44(1):192–9. https://doi.org/10.1002/mp.12015.
28. Kassner A, Liu F, Thornhill RE, Tomlinson G, Mikulis DJ. Prediction of hemorrhagic transformation in acute ischemic stroke using texture analysis of postcontrast T1-weighted MR images. J Magn Reson Imaging. 2009;30(5):933–41. https://doi.org/10.1002/jmri.21940.
29. Betrouni N, et al. Texture features of magnetic resonance images: an early marker of post-stroke cognitive impairment. Transl Stroke Res. 2020;11(4):643. https://doi.org/10.1007/s12975-019-00746-3.
30. Carneiro G, Oakden-Rayner L, Bradley AP, Nascimento J, Palmer L. Automated 5-year mortality prediction using deep learning and radiomics features from chest computed tomography. In Proceedings of the International Symposium on Biomedical Imaging. Washington, DC: IEEE; 2017. p. 130–4. https://doi.org/10.1109/ISBI.2017.7950485.
31. Quaderi SA, Hurst JR. The unmet global burden of COPD. Glob Health Epidemiol Genom. 2018;3:e4. https://doi.org/10.1017/gheg.2018.1.
32. Durham AL, Adcock IM. The relationship between COPD and lung cancer. Lung Cancer. 2015;90(2):121–7. https://doi.org/10.1016/j.lungcan.2015.08.017.
33. Washko GR. Diagnostic imaging in COPD. Sem Respir Crit Care Med. 2010;31(3):276–85. https://doi.org/10.1055/s-0030-1254068.

34. Fanni SC, et al. Role of quantitative imaging and deep learning in interstitial lung diseases. J Radiol Rev. 2021;8(2):152. https://doi.org/10.23736/s2723-9284.21.00127-9.
35. Refaee T, et al. The emerging role of radiomics in COPD and lung cancer. Respiration. 2020;99(2):99–107. https://doi.org/10.1159/000505429.
36. Ginsburg SB, Lynch DA, Bowler RP, Schroeder JD. Automated texture-based quantification of centrilobular nodularity and centrilobular emphysema in chest CT images. Acad Radiol. 2012;19(10):1241–51. https://doi.org/10.1016/j.acra.2012.04.020.
37. Lafata KJ, Zhou Z, Liu JG, Hong J, Kelsey CR, Yin FF. An exploratory radiomics approach to quantifying pulmonary function in CT images. Sci Rep. 2019;9(1):11509. https://doi.org/10.1038/s41598-019-48023-5.
38. Neumann FJ, et al. ESC Guidelines for the diagnosis and management of chronic coronary syndromes. Eur Heart J. 2020;41(3):407–77. https://doi.org/10.1093/eurheartj/ehz425.
39. van Assen M, Muscogiuri G, Caruso D, Lee SJ, Laghi A, de Cecco CN. Artificial intelligence in cardiac radiology. Radiol Med. 2020;125(11):1186–99. https://doi.org/10.1007/s11547-020-01277-w.
40. Cury RC, et al. Coronary artery disease - reporting and data system (CAD-RADS): an expert consensus document of SCCT, ACR and NASCI: endorsed by the ACC. JACC Cardiovasc Imaging. 2016;9(9):1099.
41. Muscogiuri G, et al. Performance of a deep learning algorithm for the evaluation of CAD-RADS classification with CCTA. Atherosclerosis. 2020;294:25–32. https://doi.org/10.1016/j.atherosclerosis.2019.12.001.
42. Greenland P, et al. ACCF/AHA 2007 Clinical Expert Consensus Document on Coronary artery calcium scoring by computed tomography in global cardiovascular risk assessment and in evaluation of patients with chest pain. A report of the American College of Cardiology Foundation Clinical Expert Consensus Task Force (ACCF/AHA Writing Committee to Update the 2000 Expert Consensus Document on Electron Beam Computed Tomography). J Am Coll Cardiol. 2007;49(3):378–402. https://doi.org/10.1016/j.jacc.2006.10.001.
43. Wolterink JM, Leiner T, de Vos BD, van Hamersvelt RW, Viergever MA, Išgum I. Automatic coronary artery calcium scoring in cardiac CT angiography using paired convolutional neural networks. Med Image Anal. 2016;34:123–36. https://doi.org/10.1016/j.media.2016.04.004.
44. Motwani M, et al. Machine learning for prediction of all-cause mortality in patients with suspected coronary artery disease: a 5-year multicentre prospective registry analysis. Eur Heart J. 2017;38(7):500–7. https://doi.org/10.1093/eurheartj/ehw188.
45. Bray F, Ferlay J, Soerjomataram I, Siegel RL, Torre LA, Jemal A. Global cancer statistics 2018: GLOBOCAN estimates of incidence and mortality worldwide for 36 cancers in 185 countries. CA Cancer J Clin. 2018;68(6):394–424. https://doi.org/10.3322/caac.21492.
46. Mandel JS, et al. Reducing mortality from colorectal cancer by screening for fecal occult blood. N Engl J Med. 1993;328(19):1365.
47. Mitsala A, Tsalikidis C, Pitiakoudis M, Simopoulos C, Tsaroucha AK. Artificial intelligence in colorectal cancer screening, diagnosis and treatment. A new era. Curr Oncol. 2021;28(3):1581–607. https://doi.org/10.3390/curroncol28030149.
48. Robinson C, et al. CT colonography: computer-assisted detection of colorectal cancer. Br J Radiol. 2011;84(1001):435–40. https://doi.org/10.1259/bjr/17848340.
49. Song B, et al. Volumetric texture features from higher-order images for diagnosis of colon lesions via CT colonography. Int J Comput Assist Radiol Surg. 2014;9(6):1021–31. https://doi.org/10.1007/s11548-014-0991-2.
50. Grosu S, et al. Machine learning-based differentiation of benign and premalignant colorectal polyps detected with CT colonography in an asymptomatic screening population: a proof-of-concept study. Radiology. 2021;299(2):326–35. https://doi.org/10.1148/RADIOL.2021202363.
51. Liu X, Song J, Hong Wang S, Zhao J, Chen Y. Learning to diagnose cirrhosis with liver capsule guided ultrasound image classification. Sensors. 2017;17(1):149. https://doi.org/10.3390/s17010149.

52. Bharti P, Mittal D, Ananthasivan R. Preliminary study of chronic liver classification on ultrasound images using an ensemble model. Ultrason Imaging. 2018;40(6):357–79. https://doi.org/10.1177/0161734618787447.
53. Streba CT, et al. Contrast-enhanced ultrasonography parameters in neural network diagnosis of liver tumors. World J Gastroenterol. 2012;18(32):4427–34. https://doi.org/10.3748/wjg.v18.i32.4427.
54. Siegel RL, Miller KD, Jemal A. Cancer statistics, 2017. CA Cancer J Clin. 2017;67(1):7–30. https://doi.org/10.3322/caac.21387.
55. Bardis MD, et al. Applications of artificial intelligence to prostate multiparametric MRI (mpMRI): current and emerging trends. Cancers. 2020;12(5):1204. https://doi.org/10.3390/cancers12051204.
56. Steenbergen P, et al. Prostate tumor delineation using multiparametric magnetic resonance imaging: inter-observer variability and pathology validation. Radiother Oncol. 2015;115(2):186–90. https://doi.org/10.1016/j.radonc.2015.04.012.
57. Davood K, Ruan D. Synergistic combination of learned and hand-crafted features for prostate lesion classification in multiparametricmagnetic resonance imaging. In: Descoteaux M, et al., editors. Lecture notes in computer science. Cham: Springer; 2017. p. 391–8.
58. Zhong X, et al. Deep transfer learning-based prostate cancer classification using 3 Tesla multi-parametric MRI. Abdom Radiol. 2019;44(6):2030–9. https://doi.org/10.1007/s00261-018-1824-5.
59. Li M, et al. Radiomics prediction model for the improved diagnosis of clinically significant prostate cancer on biparametric MRI. Quantitat Imag Med Surg. 2020;10(2):368–79. https://doi.org/10.21037/qims.2019.12.06.
60. Rundo L, et al. Automated prostate gland segmentation based on an unsupervised fuzzy C-means clustering technique using multispectral T1w and T2w MR imaging. Information. 2017;8(2):49. https://doi.org/10.3390/info8020049.
61. Kannus P, Parkkari J, Siev H, Heinonen A, Vuori I. Epidemiology of hip fractures. Bone. 1996;18:57S.
62. Rizzo PF, Gould ES, Lyden JP, Asnis SE. Diagnosis of occult fractures about the hip. J Bone Joint Surg. 1993;75-A(3):395.
63. Mawatari T, et al. The effect of deep convolutional neural networks on radiologists' performance in the detection of hip fractures on digital pelvic radiographs. Eur J Radiol. 2020;130:109188. https://doi.org/10.1016/j.ejrad.2020.109188.
64. Kendler DL, et al. Vertebral fractures: clinical importance and management. Am J Med. 2016;129(2):221.e1–221.e10. https://doi.org/10.1016/j.amjmed.2015.09.020.
65. Li Y, et al. Differential diagnosis of benign and malignant vertebral fracture on CT using deep learning. Eur Radiol. 2021;31(12):9612–9. https://doi.org/10.1007/s00330-021-08014-5.